Advanced Structured Materials

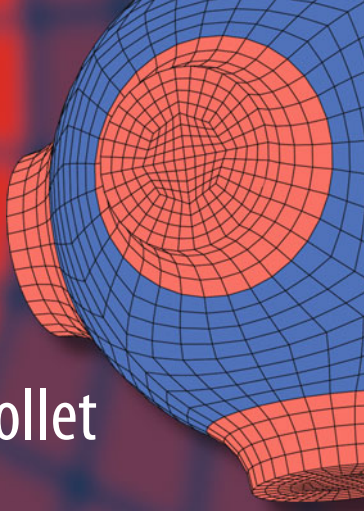

Holm Altenbach · Joël Pouget
Martine Rousseau · Bernard Collet
Thomas Michelitsch *Editors*

Generalized Models and Non-classical Approaches in Complex Materials 2

Springer

Advanced Structured Materials

Volume 90

Common engineering materials reach in many applications their limits and new developments are required to fulfil increasing demands on engineering materials. The performance of materials can be increased by combining different materials to achieve better properties than a single constituent or by shaping the material or constituents in a specific structure. The interaction between material and structure may arise on different length scales, such as micro-, meso- or macroscale, and offers possible applications in quite diverse fields.

This book series addresses the fundamental relationship between materials and their structure on the overall properties (e.g. mechanical, thermal, chemical or magnetic etc.) and applications.

The topics of *Advanced Structured Materials* include but are not limited to

- classical fibre-reinforced composites (e.g. class, carbon or Aramid reinforced plastics)
- metal matrix composites (MMCs)
- micro porous composites
- micro channel materials
- multilayered materials
- cellular materials (e.g. metallic or polymer foams, sponges, hollow sphere structures)
- porous materials
- truss structures
- nanocomposite materials
- biomaterials
- nano porous metals
- concrete
- coated materials
- smart materials

Advanced Structures Material is indexed in Google Scholar and Scopus.

More information about this series at http://www.springer.com/series/8611

Holm Altenbach · Joël Pouget
Martine Rousseau · Bernard Collet
Thomas Michelitsch
Editors

Generalized Models and Non-classical Approaches in Complex Materials 2

Springer

Editors
Holm Altenbach
Institut für Mechanik
Otto-von-Guericke-Universität Magdeburg
Magdeburg
Germany

Joël Pouget
Centre National de la Recherche
Scientifique, UMR 7190,
Institut Jean Le Rond d'Alembert
Sorbonne Université
Paris
France

Martine Rousseau
Centre National de la Recherche
Scientifique, UMR 7190,
Institut Jean Le Rond d'Alembert
Sorbonne Université
Paris
France

Bernard Collet
Centre National de la Recherche
Scientifique, UMR 7190,
Institut Jean Le Rond d'Alembert
Sorbonne Université
Paris
France

Thomas Michelitsch
Centre National de la Recherche
Scientifique, UMR 7190,
Institut Jean Le Rond d'Alembert
Sorbonne Université
Paris
France

ISSN 1869-8433 ISSN 1869-8441 (electronic)
Advanced Structured Materials
ISBN 978-3-319-77503-6 ISBN 978-3-319-77504-3 (eBook)
https://doi.org/10.1007/978-3-319-77504-3

Library of Congress Control Number: 2018934438

Printed on acid-free paper

This Springer imprint is published by the registered company Springer International Publishing AG
part of Springer Nature
The registered company address is: Gewerbestrasse 11, 6330 Cham, Switzerland

Dedicated to the memory of a great creative spirit, G. A. Maugin

Preface

At the beginning of February 2017, the invitation letters for a special remembrance book were sent to approximately 70 friends and colleagues of the great French scientist in the field of Continuum Mechanics (or more general Continuum Physics) Gérard A. Maugin who died on September 22, 2016. As usual in such case that the response is 50% sending a kind reply that they will submit a paper, and finally one gets 15–20 papers. In the case of Gérard, the resonance was overwhelming—the editors got finally approximately 60 papers and the decision was made to publish two volumes. This is the second one including 15 papers from authors living in 13 countries following volume 1 (Altenbach, H., Pouget, J., Rousseau, M., Collet, B., Michelitsch, Th. (Eds.) Generalized Models and Non-classical Approaches in Complex Materials 1, Advanced Structured Materials Vol. 89, Springer International Publishing, 2018).

The scientific interests of Gérard are well reflected by variety of subjects covered by the contributions to this book including the following branches of Continuum Mechanics:

- relativistic continuum mechanics,
- micromagnetism,
- electrodynamics of continua,
- electro-magneto-mechanical interaction,
- mechanics of deformable solids with ferroïc states (ferromagnetics, ferroelectrics, etc.),
- thermomechanics with internal state variables,
- linear and nonlinear surface waves on deformable structures,
- nonlinear waves in continua,
- Lighthill–Whitham wave mechanics, lattice dynamics,
- Eshelbian Mechanics of continua on the material manifold,
- geometry and thermomechanics of material defects,
- material equations, and
- biomechanical applications (tissue and long bones growth).

In addition, he published several papers and books on the history of continuum mechanics. This was reason that the authors of this book have submitted so different papers with the focus on the research interests of Gérard.

We have to thank all contributors for their perfect job. Last but not least, we gratefully acknowledge Dr. Christoph Baumann (Springer Publisher) supporting the book project.

Magdeburg
Paris
February 2018

Holm Altenbach
Joël Pouget
Martine Rousseau
Bernard Collet
Thomas Michelitsch

The original version of the book was inadvertently published without chapter 15. A correction to the book can be found at https://doi.org/10.1007/978-3-319-77504-3_16

Contents

Contributors

Jan D. Achenbach McCormick School of Engineering and Applied Science, Northwestern University, Evanston, IL, USA

Elias C. Aifantis Aristotle University of Thessaloniki, Thessaloniki, Greece; Michigan Technological University, Houghton, MI, USA; Beijing University of Civil Engineering and Architecture, Beijing, China; ITMO University, St. Petersburg, Russia; Togliatti State University, Togliatti, Russia

Weiqiu Chen Department of Engineering Mechanics, Zhejiang University, Hangzhou, China

Youping Chen Department of Mechanical and Aerospace Engineering, University of Florida, Gainesville, FL, USA

Yvon Chevalier Quartz Laboratory, Institute Superior of Mechanic of Paris (ISMEP-SUPMECA), Saint Ouen, France

Naoum Daher Institut FEMTO-ST (UBFC/CNRS/UTBM), Besançon, France

Michel Devel Institut FEMTO-ST (UBFC/CNRS/UTBM), Besançon, France

Adrian Diaz Department of Mechanical and Aerospace Engineering, University of Florida, Gainesville, FL, USA

Sadik Dost Crystal Growth Laboratory, University of Victoria, Victoria, BC, Canada

Khaled ElNady LEMTA, Université de Lorraine, Vandoeuvre-les-Nancy, France

Vladimir I. Erofeev Mechanical Engineering Research Institute of Russian Academy of Sciences, Nizhny Novgorod Lobachevsky State University, Nizhny Novgorod, Russia

Jean-François Ganghoffer LEM3, Université de Lorraine CNRS, Metz Cedex, France

Haralambos G. Georgiadis Mechanics Division, National Technical University of Athens, Zographou, Greece; Office of Theoretical and Applied Mechanics, Academy of Athens, Athens, Greece

Panos A. Gourgiotis School of Engineering and Computing Sciences, Durham University, Durham, UK

Evgeny M. Gromov National Research University Higher School of Economics, Nizhny Novgorod, Russia

Laurent Hirsinger Institut FEMTO-ST (UBFC/CNRS/UTBM), Besançon, France

Nikolas Karathanasopoulos Institute for Computational Science, ETH Zurich, Zurich, Switzerland

Alexander S. Kovalev Verkin Institute for Low Temperature Physics and Engineering, Kharkiv, Ukraine

Hassan Lakiss Faculty of Engineering, Section III, Campus Rafic Hariri, Lebanese University, Beirut, Lebanon

Gautier Lecoutre Institut FEMTO-ST (UBFC/CNRS/UTBM), Besançon, France

James D. Lee Department of Mechanical and Aerospace Engineering, The George Washington University, Washington, DC, USA

Valery Levin Instituto Mexicano del Petróleo, Mexico City, Mexico

Jiaoyan Li School of Engineering, Brown University, Providence, RI, USA

Alexey M. Lomonosov Prokhorov General Physics Institute, Moscow, Russia

Boris A. Malomed Faculty of Engineering, Department of Physical Electronics, Tel Aviv University, Tel Aviv, Israel; ITMO University, St. Petersburg, Russia

Mikhail Markov Instituto Mexicano del Petróleo, Mexico City, Mexico

Andreas P. Mayer Hochschule Offenburg—University of Applied Sciences, Offenburg, Germany

David McDowell School of Materials Science and Engineering, Woodruff School of Mechanical Engineering, Georgia Institute of Technology, Atlanta, GA, USA

David L. McDowell School of Materials Science and Engineering, Woodruff School of Mechanical Engineering, Georgia Institute of Technology, Atlanta, GA, USA

Igor S. Pavlov Mechanical Engineering Research Institute of Russian Academy of Sciences, Nizhny Novgorod Lobachevsky State University, Nizhny Novgorod, Russia

Evgeny Pervago Instituto Mexicano del Petróleo, Mexico City, Mexico

Alexey V. Porubov Institute of Problems in Mechanical Engineering, St. Petersburg State University, Saint-Petersburg, Russia; Institute of Problems in Mechanical Engineering, St. Petersburg State Polytechnical University, Saint-Petersburg, Russia

Pavel D. Pupyrev Prokhorov General Physics Institute, Moscow, Russia; Hochschule Offenburg—University of Applied Sciences, Offenburg, Germany

Yosra Rahali Institut Préparatoire aux Études d'Ingénieur de Bizerte, Bizerte, Tunisia

Hilal Reda LEMTA, Université de Lorraine, Vandoeuvre-les-Nancy, France; Faculty of Engineering, Section III, Campus Rafic Hariri, Lebanese University, Beirut, Lebanon

Ji Rigelesaiyin Department of Aerospace Engineering, Iowa State University, Ames, IA, USA

Kerlin P. Robert Department of Mechanical and Aerospace Engineering, The George Washington University, Washington, DC, USA

Elena S. Sokolova Verkin Institute for Low Temperature Physics and Engineering, Kharkiv, Ukraine

Ioannis Tsagrakis Aristotle University of Thessaloniki, Thessaloniki, Greece

Alexey A. Vasiliev Department of Mathematical Modelling, Tver State University, Tver, Russia

Xiaoyuan Wang Department of Engineering Mechanics, Zhejiang University, Hangzhou, China

Liming Xiong Department of Aerospace Engineering, Iowa State University, Ames, IA, USA

Shuozhi Xu California NanoSystems Institute, University of California, Santa Barbara, Santa Barbara, CA, USA

Chao Yang School of Mechanical Engineering, Beijing Institute of Technology, Beijing, China

Jiashi Yang Department of Mechanical and Materials Engineering, The University of Nebraska-Lincoln, Lincoln, NE, USA

Chunli Zhang Department of Engineering Mechanics, Zhejiang University, Hangzhou, China

Thanasis Zisis Mechanics Division, National Technical University of Athens, Zographou, Greece

Chapter 1
Damping in Materials and Structures: An Overview

Yvon Chevalier

Abstract For ordinary people, mechanical damping is the attenuation of a motion over time under possible eventual external actions. The phenomenon is produced by the loss or dissipation of energy during motion and thus time. The concept of real time is therefore at the center of the phenomenon of damping and given the recent scientific contributions (of gravitational waves in 2016), the notion of space-time calls for reflections and comments. The systemic approach of the phenomenon taking into account the mechanical system, its input and output variables (generalized forces or displacements) allows a very convenient analysis of the phenomenon. We insist on the differences between a phenomenon and a system: the causality, the linearity, the hysteresis are for example properties of phenomena and not properties of system; on the other hand we can consider dissipative or non-dissipative systems. We describe some macroscopic dissipation mechanisms in structures and some microscopic dissipation at the molecular level in materials or mesoscopic dissipation in composites materials. After specifying the notion of internal forces of a system we present some classical dissipative mechanisms currently used: viscous dissipation, friction dissipation, micro-frictions. The purpose of this presentation is not to list new dissipative systems but to point out a number of errors, both scientific and technical, which are frequently committed.

1.1 Introduction

What is the damping of motion in mechanics? For common people that is the motion of a mass Which decreases with time under the eventual action of an excitation called force, the phenomenon is regarded as non-destructive, except in specific cases. This very simple concept currently uses the four general quantities of Newtonian mechanics (Isaac Newton-1638–1723 (see [33])) which are supposed to

Y. Chevalier (✉)
Quartz Laboratory, Institute Superior of Mechanic of Paris (ISMEP-SUPMECA),
3, rue Fernand Hainaut, 93407 Saint Ouen, France
e-mail: yvon.chevalier@supmeca.fr

H. Altenbach et al. (eds.), *Generalized Models and Non-classical Approaches in Complex Materials 2*, Advanced Structured Materials 90,
https://doi.org/10.1007/978-3-319-77504-3_1

be independent: displacement, time, mass and force. This concept that we are going to develop is largely enough to explain and study the common phenomena in the field of engineering.

It should be emphasized, however, that the scientific revolution, which was attacked and vilified by the thurifiers (clerics, flatterers, adulators) of the various religions for three centuries, was again discussed at the beginning of the 20th century by the restricted theory of relativity and general relativity of Albert Einstein and the appearance of quantum mechanics. To try to simplify, in the field of the infinitely large variables, the parameters of the Newtonian mechanics are no longer independent: time and space depend on the reference coordinate system, mass and energy are the same entity and gravitational forces are due to the curvature of space-time. At the same time quantum mechanics is concerned with the infinitely small variables (atomic scale) and the particle-wave duality vision is probabilistic: the famous example is Schrödinger's cat (1925) which can be both dead and alive. It distinguishes 4 types of forces and three fields: electromagnetism linking electrons to the nucleus of the atom (chemistry), strong interaction linking protons and nucleus cohesion (nuclear fusion and fission), nuclear force (radiation) and gravitation. Only the first 3 actions result from a quantum field, since gravitation does not depend on a field. The theory of relativity explains the gravitation by the curvature of space-time. It should be noted that the link between the relativistic mechanics and the quantum mechanics is not yet established despite the efforts of scientists (8 Nobel prizes in physics during the last 20 years) and the technical performances of the experimental devices: CERN particle accelerator in Geneva, the laser interferometers of the centers in Europe-Italy, two in the USA-Washington and Louisiana), and the satellite observations and space probes moving in the universe.

The scientific community is booming over the last two decades and concepts resulting from theories are becoming reality: Higgs boson in 2013, gravitational waves in 2016 for example. Let us return to our preoccupation with damping in a concept of Newtonian mechanics which concerns most of the current engineering problems and where time is still the central variable, while recalling that GPS is an application of relativistic mechanics.

1.2 Mechanisms of Energy Dissipation

The attenuation of the motion of a mass over time can be analyzed from an energy point of view, which gives it a more scientific co-notation than the raw observation presented in the introduction. The mechanical energy dissipated during the movement is transformed, in heat, or else in structural modification of the environment, in electricity, etc. This leads us to consider a systemic approach to the problem which makes it possible to give an intrinsic character to the damping. Let us analyze

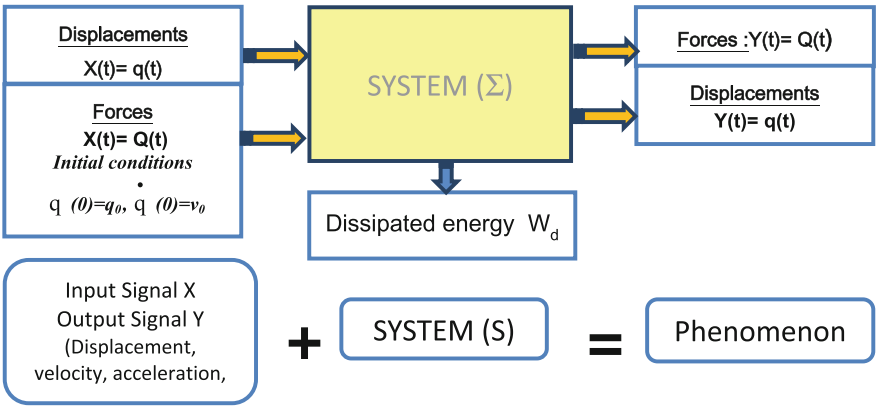

Fig. 1.1 Systemic schematics of damping and energy dissipation

the diagram above (Fig. 1.1) in which the mechanical system is called (Σ), in which the important mechanism is provided with a mass (articulated systems, solid (and/or) fluid structures, …) and is subjected to excitatory actions (input variables X). This results in a response (output variable Y). The nature of the system obviously links the input and output variables which may be scalar, vector or tensor, depending on time t and space coordinates (x, y, z). The nature of these variables provides no information in the interpretation of damping which is a temporal phenomenon which may have spatial effects in wave propagation phenomena for example. We will therefore limit ourselves to scalar variables: q(t) will be a general displacement (length, angle, deformation) and Q(t) will be general force (force, moment, stress) velocity, acceleration can also be considered. The important thing is to note the difference between "phenomenon" and "system": a phenomenon is a system equipped with its input and output variables, we may thus consider damping phenomena and dissipative systems. There is often a confusion between the properties of the phenomenon (causality, stationarity, linearity, hysteresis …) and those of the system. This energy approach is coherent because it is included in the formulation of the principle of virtual powers involving power of internal forces, power of inertia efforts (the system), and power of external forces (the phenomenon). The energy dissipation mechanisms can be schematically classified into 2 categories: macroscopic mechanisms and microscopic mechanisms.

1.2.1 Macroscopic Approach

The macroscopic side appears because the dissipation is produced on the scale of the system itself directly on the variables of input and output (force, displacement, velocity, etc.).

1.2.1.1 Viscous Dissipation

The cause of this energy dissipation is the velocity of motion. The most well-known mechanical device is the hydraulic damper (or oil-filled drilled piston) found in vehicles suspension. In this device the dissipation of energy is due to the viscosity of the oil which goes, with more or less ease, through the holed piston according to his speed. However, we must not forget the role of the spring that compensates for external forces. This simple mechanical vehicle suspension device has led to imagine more integrated systems: the idea is to concentrate the functions of stiffness (spring) and damping (damper) in the same system using the properties of rigidity and damping of materials (composite materials). The advantage is obvious: Small footprint of the device, medium good reliability of the system, good corrosion resistance, reasonable manufacturing cost. Several projects of unidirectional composite blade (glass or carbon/epoxy), which have not been completed industrially, were born in this perspective during the last 2 decades of the 20th century.

1.2.1.2 Friction Dissipation

The cause of this energy dissipation is the presence of frictional forces between two elements of the system. The normal force at the contact surface generates a tangential force which opposes the motion and the phenomenon is therefore damped. The most known device is the vehicle brake consisting of a brake housing containing a pad which rubs on a rotating disc. Compared to viscous-type dissipation, this dissipation by friction can be sudden or softer in the case of micro-friction where the two masses can be clamped in their displacements (see paragraph 1.3.4.4) This is the case for example of assemblies riveted, bolted or even glued. These previous devices are the seat of micro-displacements during external stresses and therefore of micro-frictions which are dissipative.

1.2.1.3 Magneto-Mechanic Dissipation

The cause of this energy dissipation is due to the presence of a magnetic field in which moves a conducting mass which generates eddy currents. These currents generate an own drag force, electromotive force of Laplace which opposes the movement. This concept of dissipation of energy and thus damping, is very recent compared to a pad rubbing on a wheel which is known for millennia. The first patent for electromagnetic retarder was deposited by Steckel in 1903 and realized in practice by Raoul Sarazin in 1936. These systems are known under the trade name of “Telma” and equip heavy trucks and coaches. Unlike the conventional brakes which use the friction of two masses, this braking, or this dissipation of energy,

works without contact and thus without wear of the mechanical parts. The system of damping of motion by dissipation of electric energy is a non-destructive system.

1.2.1.4 Electro-Mechanic Dissipation

The cause of this energy dissipation is due to the presence of an electric field generated by displacements of electric charges caused by external forces: piezo-electricity. If these charges can move in an electrical circuit there is dissipation of energy by Joule effect. This electric current can also excite systems of piezoelectric actuators which correct and attenuate the movement, (see [4, 27]).

1.2.1.5 Plastic Dissipation

The cause of this dissipation of energy is the plasticity of a part of the system. High external loads generate significant internal stresses. If these exceed a threshold the system is irreversibly altered (plasticity of the materials for example) but retains its integrity. The integrity of the system can be destroyed if the efforts are too large and then there is ruin. This device for absorbing energy by plastic deformation of metallic materials (see Fig. 1.2) is used, for example, in the aeronautical sector to absorb the slight shocks and is present at the front of the cockpit of the aircraft. The same principle is used in the automotive sector for absorbing shocks at low speeds: metal profiles in the shape of tubes of rectangular cross-section, attaching the front and rear automobile bumpers to the body of the vehicle, deform by buckling in the event of an impact and thus absorb kinetic energy for low speeds (of the order of 10 km/h).

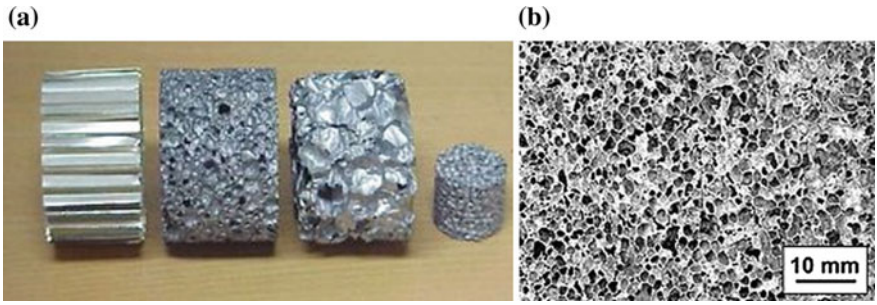

Fig. 1.2 Materials with high absorptive capacity **a** type of aluminum honeycomb **b** type of small-pore aluminum foams

1.2.2 Microscopic Approach

The mechanical dissipative system can also be studied finer by introducing smaller scales in the system to explain the macroscopic phenomenon which is the result of several micro-phenomena working in an intimate way on a smaller scale.

1.2.2.1 Atomic Scale Approach

We can schematically distinguish two close mechanisms that generate damping: one by thermomechanical effects, the other by energy effects:

- Damping in materials by thermomechanical effects
  The most well-known theory is that of the "thermoelastic peaks of Zener" (see [46]) which considers damping in metals can be interpreted by the presence of thermal diffusion phenomena which (the best-known mechanism). An increase in temperature under constant pressure always results in a local increase in volume. Vice versa, the adiabatic application of loads causes a drop-in temperature and, consequently, tends to cause a heat flow from the outside. As the temperature drop gradually relaxes, the specimen undergoes a slow increase in length and generate relaxation. This phenomenon is conditioned by the thermal diffusion coefficient which affects the heat flux. This importance of thermal conductivity was found by Kirchhoff as early as 1860 (see [20]), who noted the importance of thermal conductivity in the damping of acoustic waves. Note that damping in common metals can be neglected (less than 0.1% at ambient temperature) except for some particular ferro-magnetic alloys (Fe–Cr–Al or Mo) (see [36]) where it can reach a few per cent. These metal alloys have approximately the rigidity of steel with cushioning capacities of the polymers, they are used in military applications (submarine discretion for example). An approach also well known in, is those of "*free volumes*". Interpretation assumes that there are "empty volumes" at the atomic or molecular scale inside the material. Under the effect of temperature, forces or other physical phenomena such as moisture, for example, these volumes lose its shape and evolve according to the excitation and then tend to stabilize, with delay and according to a time of their own (material history). Compared to the present time (real time) this phenomenon generates damping and therefore energy dissipation. This interpretation has been developed by chemists concerned with the mechanical behavior of rubber materials. We can mention the work of Knauss and Emri [21, 22] in which the deformation of the free volume is due to temperature (rubber materials and polymers for example), this help to explain William, Landel, Ferry (WLF) curve, (see [13]) and the non-linear viscoelastic behavior of elastomers. In a similar way Schapery proposes that the cause of deformation of the free

volume is the stress that conditions the historical time. This gives rise to non-linear viscoelastic models reflecting the behavior of polymers (see [40, 41]). This approach by the theory of free volume has been taken up more recently by other authors to study non-linear viscoelasticity (see [14, 15]). It should be noted that the scale considered here is "large microscopic" close to those of the mechanics of continuous media.

- Damping in materials by energy effects
  This approach is energetic and based on the notion of internal variables and on the local state, this is also a microscopic point of view but does not explicitly refer to the geometric aspect. The simplest theory, "Theory of transition steps", allows us to study the influence of temperature. It is associated with the name of Eyring who analyses studies chemical reactions and the chemical kinetics (see [12]). The basic idea is that two molecules that react, to lead an activated complex, or possess a transition step, which decomposes to give final reaction products. This reaction, which comes from the theory of transition step, generates an equation which, unlike Arrhenius' law, corresponds to a theoretical model based on statistical thermodynamics (*This equation was established almost simultaneously in 1935 by Henry Eyring, G. Evans, and Michael Polanyi*). The "theory of sites" is a specific approach to damping in polymers which have an amorphous state and a crystalline state according to temperature (see [7]). The theory of sites is based on the "theory of transition steps". It applied to solid crystalline dielectrics and was extended with some success to the mechanical relaxations of polymers. This relaxation is related to the variation of free energy between the crystalline state and the amorphous state generated by the difference between two sites modified by application of a stress. There is a population change between site 1 and site 2 and this change is related to deformation. It is not difficult to imagine how this can happen at the molecular level if, for example, the motion a molecular chain involves internal rotations. Locally, the configurations of strings can be changed from a left configuration to a right configuration. The free energy difference generates a time constant identical to that of the Zener model cited above. This site model is applicable to relaxation processes showing a constant activation energy, that is to say to local motions in the crystalline regions of the semi-crystalline polymers.

1.2.2.2 Molecular Scale Approach

In this approach, the dynamics of the movement of molecules inside the material makes it possible to explain the macroscopic mechanical behavior of the material. In this perspective Rouse's theory is the most well-known (see [38]), it applies to

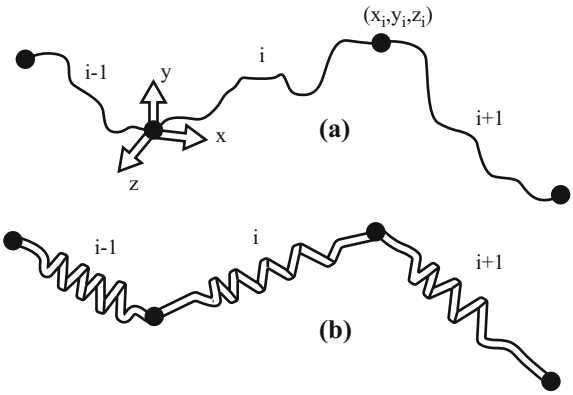

Fig. 1.3 Rouse model—**a** network of chains—**b** representation of the network by a combination of springs and shock absorbers [38, 44]

polymers. It is based on the movement of flexible insulated chains. The aim of this theory is to predict the relaxation spectrum for amorphous polymers as well as the relationship between time scale and temperature. The molecules of polymers are represented as a system of strings (sub-molecules) connected by springs whose behavior is that of a free chain on the basis of the Gaussian theory of elasticity (see Fig. 1.3). If the nodes are moved from their free equilibrium position, the motion is generated by two types of forces:

- the forces due to the friction of the chains,
- forces due to a tendency of the molecular chains to return to their state and the result on a macroscopic scale is that the behavior of the polymer is equivalent to a model of spring and shock absorbers in parallel (Kelvin-Voigt) (see [44]).

1.2.2.3 Mesoscopic Scale Approach

In an approach close to the previous ones, it is possible to envisage composite materials which have damping properties, that is to say media composed of two or more materials that are more or less damping. The scale of analysis is no longer microscopic (atoms or molecules) but intermediate between the latter and the macroscopic approach of the medium: it is called "*mesoscopic scale*". If on the macroscopic scale the composite medium is considered as homogeneous material, its behavior is determined by homogenization processes from a microscopic or mesoscopic scale (see [8, 37]). The most known case is laminated composite (see Fig. 1.4). The behavior of each ply is determined by the microscopic scale as before and the mesoscopic scale corresponds to the behavior of each ply integrated into a homogenization process (see [24]) to arrive at the macroscopic behavior.

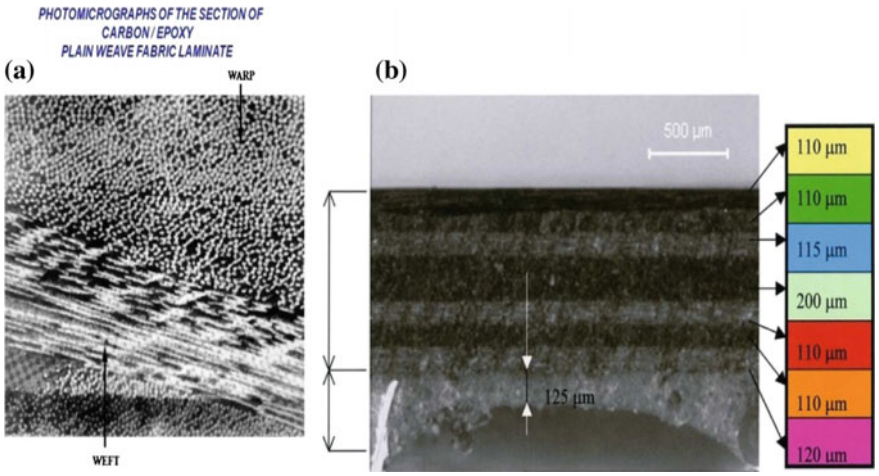

Fig. 1.4 Angle-ply carbon/epoxy composite, 8 plies: 2 × (0° × 60° × 0° × −60°)—thickness 900 µ. **a** Microscopic scale: ply—**b** mesoscopic scale: laminate structure

1.3 Modelling Energy Dissipation

The internal forces and their work in cyclic motions are examined before analyzing some models of dissipation.

1.3.1 Internal Forces

The notion of internal forces specific to a mechanical system (Σ), a thermodynamic concept, manifests only itself in reality when the system is in operation. As we have already pointed out, the energy balance of a mechanical system in operation is governed by the principle of "virtual powers", see [17, 28, 29, 39] in which work of the internal efforts is one of the elements. The real movement is a special case of the virtual movement and is expressed in general by the following equation (or equations) in temporal aspect:

$$m\ddot{q} + \Phi\left(q,\ \dot{q},\ \ldots\ \overset{(n)}{q};\ Q,\ \dot{Q},\ \ldots\ \overset{(n)}{Q},\ t\right) = Q(t) \tag{1.1}$$

in which q(t) is a generalized displacement, Q(t) a generalized effort and Φ the internal forces of the system which are sometimes called "internal frictions". These internal forces depend usually on generalized displacements and their successive

derivatives, on generalized forces and their successive derivatives according to the considered dissipation mechanism. As mentioned previously, q and Q can be scalar, vector or tensor quantities and are all causal signals (q, Q, Φ, etc.) it means they are zero for the negative values of time. This deserves undivided attention for the internal efforts Φ that exist only from the moment 0 beginning of the phenomenon: $\Phi = 0$ when q and $\dot{q}$ are zero. Caution should therefore be exercised in the analysis of aging systems whose properties change over of time.

One technique of analyzing relation (1.1) is to use the classical integral transforms, Laplace or Fourier, which are advantageous because they transform the derivatives into multiplications and the integrations into divisions. Take for example the Fourier transform of the relation of motion (1.1)

$$m\omega^2 \hat{q}(\omega) + \hat{\Phi}\left(q, \dot{q}, \ldots \overset{(n)}{q}; Q, \dot{Q}, \ldots . \overset{(n)}{Q}, t\right) = \hat{Q}(\omega) \tag{1.2}$$

Relation expressed with $\hat{q}(\omega)$ and $\hat{Q}(\omega)$, the Fourier transforms of the generalized displacements and forces q(t) and Q(t), ω is the circular frequency. The relation (1.2) is advantageous only if the Fourier transform of de Φ is expressed as a function of the Fourier transforms of q and Q (linear dependence for example). It is important to note that for any physical signal which is causal, its Fourier transform has **an even real part** and an **odd imaginary part versus circular frequency ω**. This remark must be present in any choice of frequency models. As we shall see later, relations (1.1) (temporal aspect) or (1.2) (frequency aspect), which are the most natural, allow to quantify the elementary mechanisms of energy dissipation in mechanical systems. It should be emphasized, however, that in some dissipation mechanisms the internal forces Φ are only implicitly determined and it is possible to express the generalized displacement q in the following form

$$q(t) = \Theta\left(\Phi, \dot{\Phi}, \ldots \overset{(n)}{\Phi}; Q, \dot{Q}, \ldots \overset{(n)}{Q}, t\right) \tag{1.3}$$

The dependence can be an integro-differential equation, which does not facilitate the analysis of the problem, except in the case of a linear dependence.

1.3.2 Work of Internal Forces: Cycling

The approach of the phenomenon of energy dissipation from the internal forces of the mechanical system is an analytical approach, that means the knowledge and the nature of the internal dissipation of energy is known. If the dissipation models are

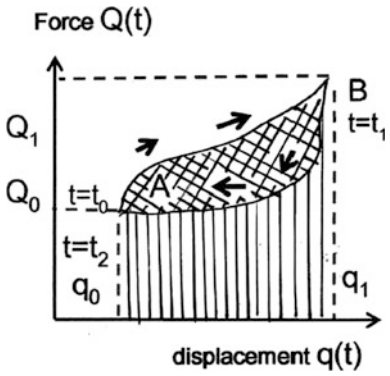

Fig. 1.5 Description of a cycle for a reversible mechanical system: q(t) and Q(t) are respectively the displacements and the generalized forces

numerous and varied (see viscous dissipation Sects. 1.3.3 and 1.3.4 below) they are left to the discretion of the user and the designer. Conversely, a cyclical approach is synthetic in the sense that it does not explicitly take into account the notion of internal efforts of the system but only their work. For example, let us describe a cycle by a system (see Fig. 1.5), the input variable being for example the generalized displacement q(t) and the output variable the generalized force Q(t). The energy balance of this cycle is as follows:

- W_F: energy supplied to the system (surface subtended by the upper curve of Fig. 1.5): Vertical stripes and hatchings
- W_R: energy recovered by the system (surface subtended by the lower curve of Fig. 1.5): Vertical stripes
- $W_D = W_F - W_R$: energy dissipated during the cycle: hatched area of the cycle (Fig. 1.5).

The commonly accepted definition *of Damping* is the "Specific damping Capacity" (SDC) Ψ and is defined as follows

$$\Psi = \frac{W_D}{W_F} = 1 - \frac{W_R}{W_F} \tag{1.4}$$

If the system is non-dissipative $W_D = 0$: the energy returned is equal to the energy supplied and thus the SDC $\Psi = 0$. The system is then thermodynamically called "elastic". This behavior is of course ideal, it is convenient in modeling and simulation, realistic in some cases, but does not correspond to the general physical reality. In a non-destructive mechanical system (excluding explosions, deflagrations, etc.) the energy recovered cannot be greater than the energy supplied and therefore

$$0 < \psi < 1 \tag{1.5}$$

In its general formulation, the SDC Ψ depends on the internal forces of the system (Σ) (relation 1.1) but also on the cycle, that means

$$\Psi[\Phi, q(t), Q(t), t_0, t_1, t_2] \tag{1.6}$$

and consequently, indirectly of q_0 and Q_1 (see Fig. 1.5). In practical aspects a number of remarks deserve to be mentioned which can simplify the analysis.

Comment 3.1 If the system is governed by a potential that means that the energy involved in going from point A to point B of the diagram (q, Q) (see Fig. 1.5) is independent of the path then the energy supplied W_F is identical to the energy recovered W_R. This implies that $\Psi = 0$.

Comment 3.2 If the phenomenon is invariant in time or "stationary" (non-aging), the evolution between times t_0 and t_1 (Fig. 1.5) does not depend on t_0 and t_1 but on the difference $t_1 - t_0$. In this case, we do not restrict the generality by taking $t_0 = 0$.

Comment 3.3 The previous scheme (Fig. 1.5) is described for a cycle but it is possible to envisage several successive cycles. The specific damping thus evolves from one cycle to another. "The Mullins effect" (see [31]) in some viscoelastic media is the best known (see Fig. 1.6).

As in many damping phenomena, when the number of cycles increases, the difference from one cycle to another is very low or nil and the notion of specific damping appears as the consequence of an intrinsic property of the system.

Comment 3.4 In the field of electricity, the notion of quality factor Q (not to be confused with forces) is sometimes used which is the inverse of the specific damping $Q = 2\pi/\Psi$.

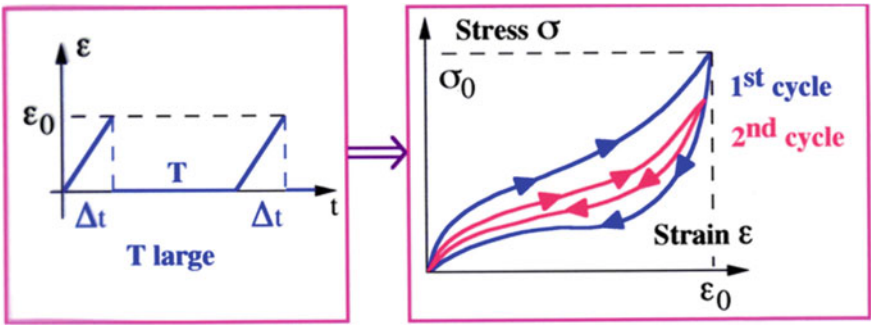

Fig. 1.6 Mullin effect [31] in viscoelastic media. $q = \varepsilon$ (strain), $Q = \sigma$ (stress)

1.3.3 Viscous Dissipation

Mechanisms related to velocity is the most commonly accepted and used because it is the most practical: In the ignorance of the dissipative phenomenon, it is often reduced to viscous damping (under the operating conditions of the system).

1.3.3.1 Linear Behavior of the Phenomenon

The phenomenon is linear (proportionality between the input and output variables (see Fig. 1.1)). The internal efforts of the system (relation 1.1) take the following generic form called "historic integral" (convolution)

$$\Phi(t) = R(0^+)q(t) + \int_0^t \dot{R}(t-\tau)\, q(\tau)d\tau = R(t)q\,(0^+) + \int_0^t R(t-\tau)\,\dot{q}(\tau)d\tau = \frac{D(R * q)}{Dt} \tag{1.7}$$

in which R(t) is the relaxation function of the system and q(t) the generalized displacement which is a causal function (or distribution) not increasing with time. The point symbolizes the temporal derivative and D/Dt the derivative in the sense of the distributions which allows a more synthetic expression of the formulation (see [10] Chapter 2), * represents is the convolution. As we mentioned this relation can be inverted (relation 1.3) and then the generalized displacement q(t) as a function of the internal forces and becomes

$$q(t) = J(0^+)\,\Phi(t) + \int_0^t \dot{J}\,(t-\tau)\Phi(\tau)\,d\tau = J(t)\,\Phi(0^+) + \int_0^t J(t-\tau)\,\dot{\Phi}(\tau)d\tau = \frac{D(J * \Phi)}{Dt} \tag{1.8}$$

In the relation (1.8) J(t) is called creep function. The creep functions and the relaxation are inverse to each other in the sense of convolutions.

Taking the Fourier transform of Eq. (1.7) we obtain the frequency aspect (relation 1.2) of the internal forces.

$$\Phi(\omega) = i\,\omega\,\hat{R}(\omega)\,\hat{q}(\omega) = F(\omega)\hat{q}(\omega) \tag{1.9}$$

$F(\omega) = i\omega\,\hat{R}(\omega) = F'(\omega) + iF''(\omega)$ is called "complex stiffness" in general or "complex modulus" in the context of viscoelasticity, i is the pure imaginary number

($i^2 = -1$). It is convenient to introduce the loss angle δ(ω) defined by its tangent (tg δ), which is the ratio of the imaginary part of the complex stiffness (loss modulus) to its real part (storage modulus), which is commonly called the "damping factor, or loss factor"

$$\eta(\omega) = tg\delta(\omega) = \frac{F''(\omega)}{F'(\omega)} \tag{1.10}$$

These models are frequently used in the field of mechanics of structures and mechanics of material.

Cycling this system makes possible to link the specific damping capacity Ψ (relation 1.4) to the system parameters and provide then energy balance of the evolution of the system. We then consider that a sinusoidal strain $\varepsilon(t) = \varepsilon_0 \sin \omega t$ generates a sinusoidal stress when the transient running has disappeared to give place to a permanent running, the cycle is of the elliptic and symmetrical type as shown in Fig. 1.7.

The choice of the supplied W_F energy leads to several expressions for the SDC Ψ as in the discussion presented by Lee and Hartmann in 1998 (see [25]). The discussion is based on the choice of W_F

$$\begin{aligned}
&\psi = 2\pi \sin\delta \quad \text{Maximum potential energy: } W_F = q_0 Q_0/2 \\
&\psi = \pi \sin\delta \quad \text{Potential energy over one cycle, } W_F = q_0 Q_0 \\
&\psi = \frac{\pi \, tg\,\delta}{1 + \left(\frac{\pi}{2} + \delta\right) tg\,\delta} \quad \text{Energy involved in a cycle}
\end{aligned} \tag{1.11}$$

Depending on the choice the SDC can be greater than one, which is a disadvantage.

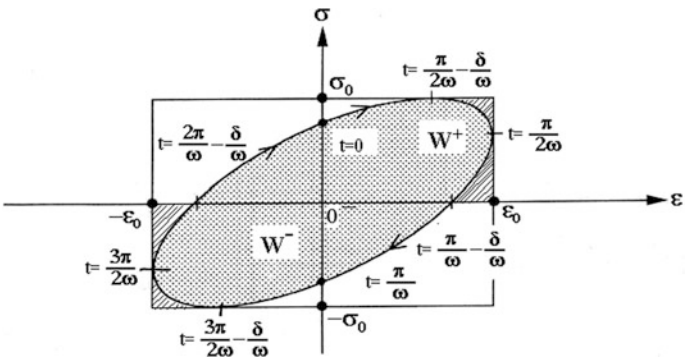

Fig. 1.7 Scheme of the cycling of a damping of the viscous type. cycle of a viscoelastic material: q = ε strain, Φ = σ stress

Discrete Bi-parametric Model (Like Voigt Model)

This model is the most common since internal forces are modelled by a spring and a damper having a linear behavior and placed in parallel. The relaxation function (see relation 1.7) is then of the form:

$$R(t) = C\,\delta(t) + KH(t) \tag{1.12}$$

The parameters C and K are respectively the damping constant and the stiffness, δ(t) is the Dirac distribution and H(t) the Heaviside unit step (H(t) = 0 for t < 0, t) = 1 for t > 0). The internal efforts take the following simple form

$$\Phi(t) = C\,\dot{q}(t) + Kq(t) \tag{1.13}$$

And the the expression of the complex stiffness thus (relationship 1.9) is then

$$F(\omega) = i\,\omega\,C + K \tag{1.14}$$

The relationship (1.14) shows that the damping (relation (1.10) evolves linearly with the circular frequency ω, which can only be realistic within a certain range of circular frequencies. This "two-parameter" model is commonly used in multidimensional formulations (simulations by finite elements for example). The complex stiffness then takes the following matrix form

$$[F(\omega)] = i\,\omega[C] + [K] \tag{1.15}$$

In which [C] and [K] are respectively the symmetric square matrices. If this formulation poses no conceptual problem, it raises some difficulties in solving the equation of motion in the frequency domain.

To solve easily numerically this matrix problem several tricks, having no real physical foundation, are proposed.

Comment 4.1 the first trick t is to introduce the notion of "*structural damping*" which consists in choosing the following complex stiffness

$$[F(\omega)] = i[C] + [K] \tag{1.16}$$

This concept has no physical reality for the simple reason that there is no real time signal whose Fourier transform has a constant and even real part and a constant and odd imaginary part.

This concept of structural damping, which is practical in design, can be explained by considering the notion of a fractional derivative of a function (see [2, 10, 42]). The complex stiffness is then equal to $[F(w)] = (i\omega)^{\alpha}[C] + [K]$ and if α is small and even close to 0, we find that the real and imaginary parts of the previous stiffness are respectively even and odd and almost constant and therefore independent of ω in a given circular frequency bandwidth.

Comment 4.2 the second trick consists in introducing the notion of proportional damping known as the "*Basile hypothesis*". If the system is conservative ([C] = 0), its resolution is done by projection of the displacement {q} on the eigen-modes of this system and in this case the matrix is diagonal. If the system is dissipative ([C] $\neq$ 0), the method consists in express the damping matrix [C] as a linear combination of the mass matrix [M] and stiffness matrix [K], then [C] = ε[K] + γ[M]. Then the matrix equation of motion is projected on the basis of the eigen-modes of the corresponding conservative system. The matrices are then diagonal which facilitates the resolution of the problem. The difficulty lies in the choice of the parameters ε and γ which have no physical reality and are simply a numerical convenience

Continuous Multi-parametric Model (Prony Series)

These models are more complex and include n parameters $(n \geq 2)$ and are used in the behavior of viscoelastic materials (see [10], Chapter 2). The relaxation function R(t) is usually expressed as a linear combination of exponentials or Prony's series

$$R(t) = K_\infty \left(1 + \sum_{p=1}^{p=n} k_p e^{-\frac{t}{\tau_p}} \right) \tag{1.17}$$

The best known of these models is that of generalized Maxwell (see [10]) but the main difficulty lies in the choice of the number of parameters which must be relatively important to correctly represent the behavior of the material (a dozen) but not too important for reasons for determination and measurement. The relation (1.17) easily leads to the complex stiffness (relation 1.9) which is a sum of rational fractions depending on ω. The loss factor varies according to the materials: on the order of a few 10^{-4} for metals, some 10^{-2} for polymers and about 10^{-1} for rubber materials at ambient temperature (20 °C).

1.3.3.2 Non-linear Behavior of the Phenomenon

The notion of nonlinear phenomenon is extremely wide and therefore very varied in representations. The most conventional approach is to admit that in its operation the system has a dissipation of viscous and linear origin and to complete the model with ingredients generating non-linearity in certain cases of motions. We therefore consider the "historic integral" generating internal forces (relations 1.7 or 1.8) by modifying it somewhat.

Schapery Model

This model is adapted to polymers and is based on the notion of free volume (see Sect. 1.2.2.1). It was developed by Shapery in 1966 [41]. The hypothesis is to assume that the real time t is modified by a number of internal variables (temperature, constraint, dilatation, moisture, etc.) and to introduce an artificial time which translates the history of material. In the Schapery model the stress σ of course generates strain but also a modification of time and the model expresses the deformation ε as follows by using the creep functions (relation 1.8)

$$\varepsilon(t) = J(0^+)\ g_1[\sigma(t)]\hat{\sigma}(t) + g_1[\sigma(t)] \int_0^t \dot{J}\ [(\varphi(t) - \varphi(\tau)] \frac{\hat{\sigma}(\tau)}{a[\sigma(\tau)]}\, d\tau \qquad (1.18)$$

In this relation (1.18)

- t is the present (or real) time and τ represents a time specific to the loading history, or historical time (classic case of linear viscoelasticity).
- $g_1[\sigma(t)]$ is a stress factor that expresses the "*nonlinear memory*" of the material. This factor is equal to 1 for the low stress levels (linear viscoelasticity) and increases approximately linearly with the stress: the slope is bounded by 0.04 and 0.05 MPa^{-1} in the case of polymers, (see [45]).
- $\hat{\sigma}(t) = \sigma(t) g_2[\sigma(t)]$ where $g_2[\sigma(t)]$ is known as the "*stiffening stresses factor*" and is equal to 1 for low stresses. It grows proportionally according to the level of stress with a slope by 0.05 and 0.06 MPa^{-1} in the case of polymers, [45].
- $\varphi(t) = \int_0^t \frac{ds}{a_\sigma[\sigma(s)]}$ is the reduced real time and s the time of memory, specific to the history of the phenomenon, a[σ] is the stress-time factor.

The Schapery model allows to describe the dissipative behavior of polymers in the case of low or high deformations or weak or high stresses for polymer materials. It can be noted that the Schapery model is formally similar to the notion of time-temperature superposition (WLF-William-Landel-Ferry, [13]), stress playing the role of temperature in the expression of reduced real time The Schapery model can be generalized by introducing time into the stress-time factor and makes it possible to obtain the behavior of the material for longer times, see [16]. Note that in the case of certain materials, ferro-magnetic alloys for example, the phenomenon of dissipation can depend on the deformation even for small deformations and generate nonlinear phenomena (see [36], Fig. 1.8).

Other kind of alloys, such as "Sonoston" (Manganese, copper, Aluminum, (see [48]), have comparable damping factors like polymers (2 to 5×10^{-2}) with Young's moduli comparable to aluminum, between 73 and 83 GPa. These alloys are used, for example, in the manufacture of submarine propellers for reasons of vibrations damping and acoustic discretion. The disadvantage is the high density,

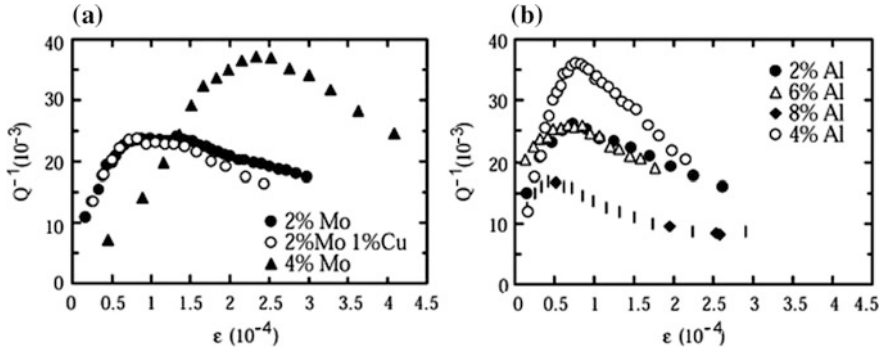

Fig. 1.8 Variations of the damping factor of ferromagnetic alloys versus strain. **a** for various alloys—**b** for various proportions of aluminum (see [36])

7200 kg/m^3, comparable to that of steel, which limits its application in the aeronautical sector.

Valanis-Landel Model

The previous models were generalized by Valanis and Landel (see [43]) and then by O'Down and Knauss (see [34]) for isotropic Hyper-elastic materials, in large deformations. Unlike Schapery, which explicitly introduces stress (or small strains into the "historic integral", these models remain very general by simply using the Green-Lagrange strain tensor in this "historic integral" (relation 1.7). Then

$$S_{ij}(t) = \frac{\partial w}{\partial \mathsf{E}_{ij}} + \int_0^t \frac{\partial}{\partial \tau} \left\{ \mathrm{R_{ijkl}}[\mathsf{E}(\tau), \mathrm{t} - \tau] \right\} \mathsf{E}_{kl}(\tau) d\tau \tag{1.19}$$

- The first part of the relationship (1.19) relates to "hyper-elasticity" where w is the volumetric strain energy, which depends on strain tensor of the Green-Lagrange E = (E_{ij}), and makes it possible to express stress tensor of Piola-Kirchhoff S = (S_{ij}).
- The second part of the relation (1.19) relates to the memory effect provided that the "*condition of validity*" (1.20) is satisfied.

$$\frac{\partial w \mathsf{E}(t)}{\partial \mathsf{E}_{ij}} = \mathrm{R_{ijkl}}[\mathsf{E}(t), 0] \mathsf{E}_{kl}(t) \tag{1.20}$$

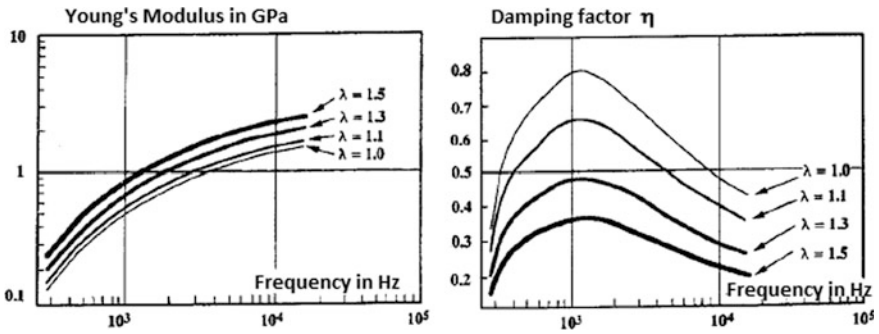

Fig. 1.9 Complex Young's modulus (storage modulus and damping coefficient) of a BX type elastomer with different loading as a function of frequency. Test at room temperature 20 °C [3]

This formulation, which is relatively complex, makes it possible, for example, to study the small oscillations of a rubber material around a large elongation: vibration tests under static preload (see [3]), Fig. 1.9.

In the case of a simple tensile test for example, with a large static elongation λ of the beam (λ = Length L of the beam/Initial length L_0 of the beam), it can be seen that he storage modulus increases with the elongation λ (and the frequency) and that the damping coefficient η decreases with the elongation (for $\lambda > 1$).

Frechet-Volterra Series Model

This model has very mathematical formulation: it stipulates that the internal forces Φ (Relationship 1.1) are expressed by series of multiple convolutions which depend on generalized displacement q(t), the first term of which expresses a linear behavior

$$\Phi(t) = \int_0^t \dot{R}_1(t-\tau_1)\, q(\tau_1) d\tau_1 + \int_0^t \int_0^t \dot{R}_2(t-\tau_1, t-\tau_2) q(\tau_1) q(\tau_2) d\tau_1 d\tau_2 + \ldots$$
$$\ldots + \int_0^t \ldots \int_0^t \dot{R}_n(t-\tau_1, \ldots, t-\tau_n) q(\tau_1) \ldots q(\tau_n) d\tau_1 \ldots d\tau_n + jumps \quad (1.21)$$

The advantage of the relation is that it does not presuppose a priori any model for the phenomenon but the disadvantage is obvious: how to determine the various kernels R1, R2, …, Rn? (see [6]). In practice 2 or 3 term of this series are conserved. This modeling is used in the analysis of structures to bring back various phenomena (plays, micro plasticity, micro-friction, etc.) to a dissipation of viscous type. Let us note the approach of Lai and Finley which is limited to symmetric parabolic kernels of order less or equal to 3, (see [23]), while Locket [26] proposes a method of obtaining kernels, and that Molinari, (see [30]) examines the one-dimensional problem. Huet uses this method to treat the case of aging materials, (see [19]).

Linearization of the Phenomenon

- Two linearization concepts are used: the first concerns weakly nonlinear phenomena and the linearization process consists of expansion in Taylor series, around a reference position: stable equilibrium, for example.
- The second consists in considering a fixed state of the phenomenon and in admitting that the latter is linear around this state. The method of linearization using the **Hilbert Transform** (involution) is a rigorous tool, very efficient and used in software for modal analysis of structures (see [18], [47]). We can consider non-linear-modes which have no fundamental interest but whose role is only qualitative as a point of comparison with other results for example. This linearization makes it possible, for a given state of the system, to use the conventional tools for measuring damping: logarithmic decrement, bandwidth, frequency response functions (FRF).

1.3.4 Friction Dissipation

Friction efforts are often generated by two moving masses, one of which is generally planar. The localized contact generated by a cylindrical, or spherical (most frequent case) surface and the surface contact generated by a flat (less studied) area can be distinguished (see Fig. 1.10).

Models of friction are numerous, see [9], however a large number of laws are based on the model of Coulomb or on the model of Tresca according to the existing phenomenon.

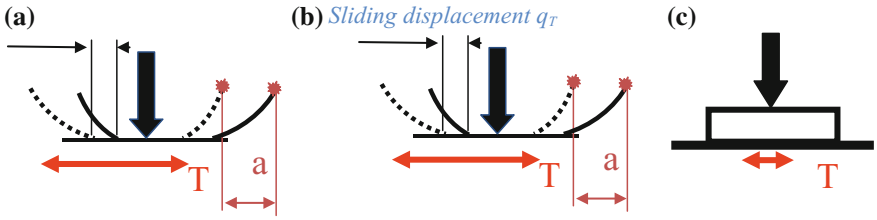

Fig. 1.10 Contact between 2 masses, N: normal force, T: tangential force, q_T: tangential slip, a: amplitude of tangential displacement during cycling. **a** localized contact without sliding. **b** localized contact with sliding **c** plane contact surfaces

1.3.4.1 Coulomb's Friction Modelling

This type of model is the oldest and relatively the simplest (see, for example, [32].) Contact forces have a normal component N and tangential component T (essentially positive) and T is governed by an inequality if masses are immobile and by an equality if one of the masses moves relative to the other (relative motion). Coulomb's law is thus expressed in the following way

$$\begin{cases} T \leq F(N, 0) & \text{si} \quad \dot{q}_T = 0 \\ T = F(N, \dot{q}_T) & \text{si} \quad \dot{q}_T \neq 0 \end{cases} \tag{1.22}$$

q_T being the sliding relative displacement between the two masses (see Fig. 1.10). T represents the forces internal to the system (relation 1.1) which are opposite to the sliding speed. This law is expressed in the following algebraic relationship:

$$\Phi = -T \operatorname{sing}\left(\dot{q}_T\right) \tag{1.23}$$

The function "sing (x)" being equal to 1 if $x > 0$ and -1 if $x < 0$.

The most classic formulation of the Coulomb friction, which states that the function $F(N, \dot{q}_T)$ is proportional to the normal force N, that means

$$F(N, \dot{q}_T) = f\left(\dot{q}_T\right) N \tag{1.24}$$

where $f(\dot{q}_T)$ is dynamic friction coefficient and $f(0)$ is the static coefficient of friction. The coefficient of friction is the ratio of the tangential component of the friction force to the normal component, $f = T/N$. We often represent the friction law in the diagram (f, q_T) for an imposed cyclic tangential displacement q_T, which makes possible to get rid of the normal force N. In the case of the friction of Coulomb this diagram is a rectangle for $q(t) > 0$) and a symmetric rectangle (for $q(t) < 0$). The area of the cycle represents the dissipated energy $W_{D,}$ (relation 1.4), **and therefore the SDC Ψ is greater in the case of a friction dissipation than in the case of a viscous dissipation**. It should be noted that for reasons of simulation convenience, friction damping is often replaced by its viscous equivalent, relations (1.11), thus artificially defining a loss angle of due to the "work of the internal forces".

1.3.4.2 Tresca's Friction Modelling

The friction model of Tresca is very close to that of Coulomb: the upper bound F(N, 0) (relation 1.22) is replaced by a specific quantity g which depends on the 2 solids in contact.

1.3.4.3 Dahl's Friction Modelling

This friction law is introduced by P. Dhal in 1976, [5, 11] for the study of dry friction. In the Coulomb model the adhesion is taken into account by a condition of sliding velocity zero (relation 1.22) while when sliding case, the sliding forces F depends on the speed is imposed, which complicates the resolution. This Dahl's friction model describes the internal forces by the following relation

$$\frac{d\Phi}{dq_T} = K\left(1 - \frac{\Phi}{Tc}\text{sign}\ (\dot{q}_T)\right)^{\alpha} \tag{1.25}$$

in which

- K is the initial tangential rigidity for small displacements around 0,
- Φ is the internal force or the tangential interaction force between the solids,
- T_C is the tangential interaction force when there is slip,
- α is a parameter positive giving the shape of the law of friction.

The law has a non-differential analytical description. For $\alpha = 1$ it can easily be shown that

$$\Phi = T_C\left(\exp\left(\frac{K}{T_C}q_T\right) - 1\right) \tag{1.26}$$

For $\alpha > 1$ and $\alpha < 1$ we can find in [5] the corresponding analytical expressions.

We can also represent the Dahl model in the diagram (f, q_T) for an imposed cyclic displacement (Fig. 1.11).

The literature is generous in friction models, we can mention for example the LuGre's model which is widely used (see [1]).

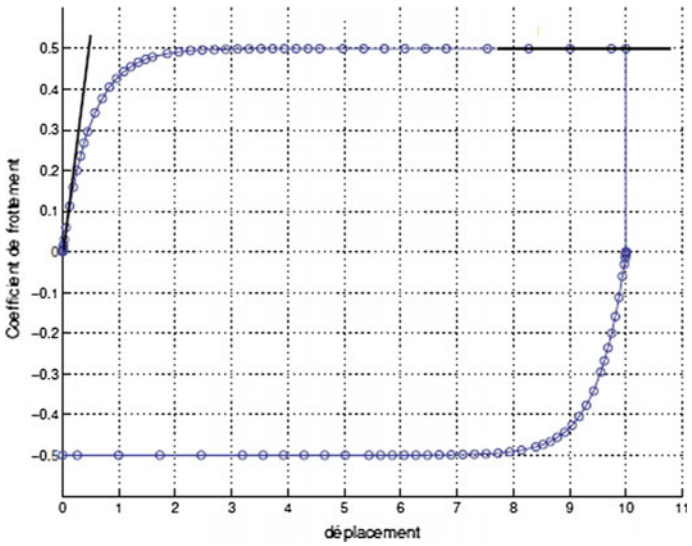

Fig. 1.11 Characteristic of the Dahl model in the plane (f, q_T) for cyclic loading. The diagram is symmetrical with respect to the ordinate axis excluding the rising part close to the origin, according to [9], [11]

1.3.4.4 Micro-friction

The dissipation of energy by micro-friction is more difficult to interpret because this phenomenon is at the level of assemblies where there is no free sliding displacements at the interface of the two masses (see [35]). Unlike the preceding analyzes where the two masses in contact were rigid solids, in this case we assume the masses are deformable under the action of the normal force which generates a variable contact surface and the displacement d considered is taken "far" from the contact surface (see Fig. 1.10a). In the case of cyclic stresses, this displacement d has a maximum amplitude a (see Fig. 1.10a, b) and the area of the cycle (f, d) translates the dissipated energy and thus generate a **SDC Ψ** as before). The friction coefficient depends on the tangential force (relation 1.22) which can be positive or negative.

When there is slip (Fig. 1.10b), the area of the cycle (f, d) is larger. The results in Fig. 1.12 are obtained by plane contact surfaces (contact pin-disc), the track being subjected to an alternating displacement of imposed amplitude and frequency. Special tribometers can also be used.

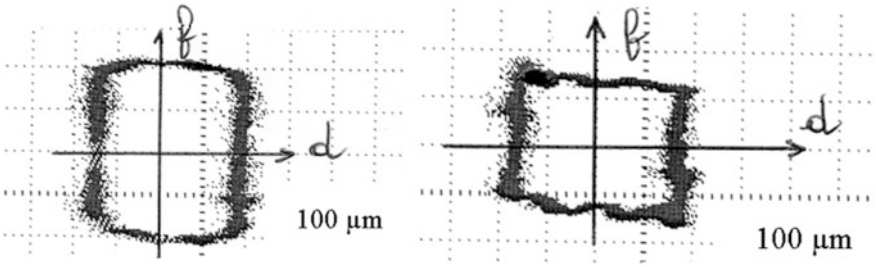

Fig. 1.12 Characteristic of micro-friction s in the plane (f, d), coefficient of friction-displacement. Experimental amplitude 0.1 mm (Institute superior of Mechanics of Paris, Department Tribology)

1.4 Conclusion

The above present developments are conventional and well known since several years but they deserve some reflections on the different concepts used.

- The first concerns the fundamental difference between the notion of damping phenomenon and of the dissipative system. Damping is a phenomenon, a phenomenon that generally decreases over time, the system is a physical reality composed of material elements. The phenomenon is then the union of a system and its input and output variables, it evolves over time. Causality, linearity, stationarity, hysteresis, are not properties of the system, but properties of the phenomenon.
- The second relates to the time which plays a preponderant role in these analyzes and this notion of time deserves some reflections. As we have seen the time and usually an independent parameter related to Newtonian mechanics of the 16th century. But it is possible to generate other times: the reduced historical time which describes the intimate history of a material (see Schapery-1966 models, Valanis model and Landel 1967, etc.), space–time of the relativistic mechanics during beginning of the 20th century, which generates gravitation, permitted to verify the gravitational wave detection in 2016. This current scientific boom will probably generate innovations, long-term in the techniques of mechanical engineering and materials.
- The third concerns the scientific inaccuracies commonly accepted for reasons of simplifying the treatment of problems: We are in an era of abundant digital development and we must constantly create software, and simplify the scientific analysis of phenomena. It should be stressed that these simplifications work correctly within specific ranges of use, and so there is often a scientific reason. The notion of structural damping, for example, can be explained by the fractional derivative, the notion of non-linear modes consists in “linearizing” by abstracting from the real phenomenon. The notion of mode is specific to a linear phenomenon and this notion is advantageous because it makes it possible to

solve the problem by decomposition of the basis of eigenvalues (linear combination).

- The last one concerns the use of current mathematical tools to model the physical phenomena. The notion of distribution, which generalizes the notion of function, makes it possible to introduce in a synthetic way initial conditions in mechanical systems, while convolution schematizes all linear phenomena.

In conclusion, we can observe that nonlinear phenomena are rarely analyzed as such, but by techniques specific to linearity and in sciences the behaviors are like those of mechanics: there is the energy for reflection (potential), there is some energy for applications (kinetics), remains to be seen if the total energy is conserved?

References

1. Aström, K.J., de Wit, C.C.: Revisistings the LuGre friction model. IEEE Control Syst. Mag. **28**(6), 101–114 (2008)
2. Bagley, R.L., Torvik, P.J.: A theoretical basis for the application of fractional calculus to viscoelasticity. J. Rheol. **27**(3), 201–210 (1983)
3. Beda, T., Chevalier, Y.: Sur le comportement statique et dynamique des élastomères en grandes déformations. Mécanique industrielle et Matériaux **50**(5), 228–231 (1997)
4. Berik, P., Benjeddou, A.: Static experimentation of the piezoceramic d15-shear actuation for sanswich structures with opposite or same poled patches-assembled core and composite faces. Int. J. Smart Nano Mat. **2**(4), 230–244 (2011)
5. Bliman, P.A.: Mathematical study of the Dahl's friction model. Eur. J. Mech. A/Solids **11**(6), 835–848 (1992)
6. Bouvier, D., Helic, T., Roze, D.: Représentation en séries de Volterra d'un modèle passif de Haut-parleur électrodynamique avec suspension non-linéaire et perspectives pour identification, Congrès Français d'acoustique, HAL Id: hal-01441060, Le mans; April 2016. https://hal.archives-ouvertes.fr/hal-01441060/document
7. Chatain, M.: Comportement physique et thermodynamique en relation avec la structure, Techniques de l'ingénieur, traité plastiques et composites AM1, A3110, 3111, 3112 (1993)
8. Chevalier, Y.: Micromécanique des composites-Prévision en élasticité, en viscoélasticité et à la rupture, Technique de l'ingénieur, traité A7778 et A7780, 22 pages. Paris (1991)
9. Chevallier, G.: Etude des vibrations de broutement provoquées par le frottement sec-Application aux systèmes d'embrayage, Thèse Université P.M .Curie-ISMEP, 171 pages. Paris (Oct 2005). http://lismma.supmeca.fr/theses/These_Chevallier.pdf
10. Chevalier, Y., Vinh, J.T.: Mechanical characterization of material and waves dispersion, ISTE Ltd, London (U.K) and John Wiley & Sons, Hoboken (NJ-USA), (2010)
11. Dahl, P.: A solid friction damping of mechanical vibrations. AIAA J. **14**, 1675–1682 (1976)
12. Eyring, H.: The activated complex in chemical reactions. J. Chem. Phys. **3**, 107–115 (1935)
13. Ferry, J.D.: Viscoelastic properties of polymers, 3ième edn. Editions John Wiley & Sons, New York (1980)
14. Gacem, H., Chevalier, Y., Dion, J.L., Rezgui, B.: Non-linear dynamic behavior of a preloades thin sanswich plate incorporating Visco-hyperelastic layers. J. Sound Vibrat. **322**(4–5), 941–953 (2009)
15. Gacem, H.: Comportement visco-hyperélastique des élastomères- Viscoélasticité non-linéaire, application aux multicouches, Thèse Université P.M. Curie, Paris (2007)

16. Gacem, H., Chevalier, Y., Dion, J.L., Rezgui, B.: Long term prediction of non-linear viscoelastic creep behavior of elastomers: extended Schapery model. Mech. Ind. **9**(3), 407–416 (2009)
17. Germain, P.: Mécanique des milieux continus. Théorie Générale, Editions Masson, Paris (1973)
18. Haoui, A., Vinh, T., Chevalier, Y.: Application of Hilbert transform in the analysis of non linear structures. In: 2nd International Modal Analysis Conferences. Orland, USA, (Florida) (1984)
19. Huet, C.: Relation between creep and relaxation function in nonlinear viscoelasticity. J. Rheol. **29**(3), 247–257 (1985)
20. Kirchhoff, G.: Über den Einfluß der Wärmeleitung in einem Gas auf die Schallbewegung. Poggendorffs, Ann **134**, 177 (1868)
21. Knauss, W.G., Emri, I.J.: Non-linear viscoelasticity based on free volume consideration. Comput. Struct. **13**, 123–128 (1981)
22. Knauss, W.G., Emri, I.J.: Volume change and the non-linear thermo-viscoelastic constitution of polymers. In: Yee, A. (ed.) Polymer Engineering and Sciences, vol. 27, pp. 86–100 (1987)
23. Lai, J.S., Findley, N.W.: Stress relaxation of non-linear viscoelastic material under uniaxial strain. Trans. Soc. Rheol. **12**, 259–280 (1968)
24. Lene, F.: Technique d'homogénéisation des composites à renforts tissés, Mécanique, matériaux, Electricité, vol. 443 (1990)
25. Lee, G.F., Hartmann, B.: Specific damping capacity for arbitrary loss angle. J. Sound Vibrat. **211**(2), 265–272 (1998)
26. Locket, F.J.: Non-linear viscoelastic solids, Academic Press (1972)
27. Majeed, M., Benjeddou A.: Semi-analytical free-vibrations analysis of piezoelectric adaptive beams using the distributed transfer function approach, structural control ACA structural control and health monitoring, **18**(7), 723–736 (2011)
28. Maugin, G.A.: The method of virtual power in continuum mechanics-Application of coupled fields. Acta Mechanica **35** (1980)
29. Maugin, G.A.: Non Classical Continuum Mechanics dictionary. In: Advanced Structure Materials, Springer, Singapore (2017)
30. Molinari, G. A.: Sur la relaxation entre fluage et relaxation en viscoélasticité non linéaire, C.R. Acad. Sciences, tome 277, série A, pp. 621–623. Paris (1973)
31. Mullins, L.: Softening of rubber by deformation. Rubber Chem. Technol. **42**, 339 (1969)
32. Naejus, C.: Sur la formulation des problèmes de contact avec frottement de Coulomb, Thèse Université de Poitiers, Sept (1995)
33. Naslin, P.: Isaac Newton. La technique moderne **3–4**, 28–35 (1998)
34. O'dowd, N.P., Knauss, W.G., A time dependent large principal deformation of polymers. J. Mech. Phys. Solids **43**(5), 771–792 (1995)
35. Peyret, N., Dion, J.L., Chevallier, G., Argoul, P.: Micro-slip induced damping in planar contact under constant and uniform normal stress. Int. J. Appl. Mech. **02**(02), 281–304 (2010)
36. Pulino-Sagradi, D., Sagradi, M., Martin, J.L.: Noise and vibrations damping of Fe-Cr-X alloys. J. Braz. Soc. Mech. Sci. **23**(2), Rio de Janeiro (2001)
37. Renard, J.: Elaboration, microstructure et comportement des matériaux composites à matrice polymère, Traité MIM série polymère, Editions Hermès. Paris (2005)
38. Rouse, P.E.: A Theory of the linear viscoelastic properties of dilute solutions of coiling polymers. J. Chem. Phys. **21**(7) (1953)
39. Salencon, J.: Mécanique des milieux continus-Concepts généraux, Editions Ellipses de L'école polytechnique. Palaiseau (2007)
40. Schapery, R.A.: Thermodynamical behavior of viscoelastic media with variable properties subjected to cyclic loadin. J. Appl. Mech. **35**, 1451–1465 (1964)
41. Schapery, R.A.: A thermodynamic constitutive theory and its application to various nonlinear materials. Int. J. Sol. Struct. **2**(3), 407–425 (1966)

42. Soula, M., Chevalier, Y.: La dérivée fractionnaire en rhéologie des polymères: Application aux comportements élastiques et viscoélastiques linéaires et non linéaires des élastomères. ESAIM Proc. **5**, 193–204 (1998)
43. Valanis, K.C., Landel, R.F.: Large axial deformation behavior of filled rubber. Tans. Soc. Rheol. **11**(2), 213–256 (1967)
44. Vinh, T., Sorin, P.: Sur la détermination du module complexe d'Young et de l'amortissement des matériaux viscoélastiques par flexion alternée, Sciences et techniques de l'armement, $4^{ième}$ fascicule, pp. 979–1007 (1963)
45. Zaoustos, S.P., Papanicolaou, G.C.: Study of the effect of fibre orientation on the nonlinear viscoelastic behavior of continuous fibre polymer composites. In: Reifsnider, K.L., Verchery, G. (eds.) Recent Developments in Durability Analysis of Composite Systems, pp. 375–379. Cardon, Fukuda, Balkema, Rotterdam (2000)
46. Zener, C.: Elasticité et anélasticité des métaux, Editions Dunod, pp. 55–100. Paris (1955)
47. Vinh, T., Haoui, A., Fei, B.J., Chevalier, Y.: Extension de l'analyse modale aux systèmes non linéaire par la transformée de Hilbert, Matériaux, Mécanique, Electricité, 404, 405, 405, pp. 5–14 (1984)
48. Wang, Y.C., Ludwigson, M., Lakes, R.S.: Deformation of extreme Viscoelastic metals and composites. Mat. Sci. Eng. **A 370**, 41–49 (2004)

Chapter 2
The Principle of Virtual Power (PVP): Application to Complex Media, Extension to Gauge and Scale Invariances, and Fundamental Aspects

Laurent Hirsinger, Naoum Daher, Michel Devel and Gautier Lecoutre

Abstract This work, relative to the principle of virtual power, is composed of three distinct but nevertheless complementary parts. The first part follows the line of thought developed by professor Maugin and his students on complex continuous media subject to the objectivity requirement (translational and rotational invariances). The second part shows that this principle is extensible to other types of invariance such as gauge and scale invariances. Gauge invariance allows to express Maxwell equations, usually derived through a vector approach, by use of a scalar principle having the same formal structure as the principle of virtual power. As to scale invariance, it allows to deal, in a general and unified way whatever the underlying physics, with the passage from a continuous medium to a discontinuous one (singular surfaces, lines or points). The third part concerns the foundations of dynamics where the principle of virtual power appears as a theorem, like other analytical principles, each corresponding to one point of view, deductible from a general intrinsic (viewpoint independent) dynamical framework. The attention will be focused on the origin of the duality notion, at the basis of the principle of virtual power.

L. Hirsinger (✉) · N. Daher · M. Devel · G. Lecoutre
Institut FEMTO-ST (UBFC/CNRS/UTBM), 15b avenue des Montboucons, 25030 Besançon, France
e-mail: laurent.hirsinger@femto-st.fr

N. Daher
e-mail: naoum.daher@femto-st.fr

M. Devel
e-mail: michel.devel@femto-st.fr

G. Lecoutre
e-mail: gautier.lecoutre@femto-st.fr

H. Altenbach et al. (eds.), *Generalized Models and Non-classical Approaches in Complex Materials 2*, Advanced Structured Materials 90,
https://doi.org/10.1007/978-3-319-77504-3_2

2.1 First Part

2.1.1 Complex Media: Modeling of the Different Continua

If one intends to describe semiconduction effects coupled to ferroelectricity and/or ferromagnetism, one must, on the one hand, distinguish between the various species of carriers by decomposing the total charge and current densities in order to account for generation and recombination phenomena as done in [1]. On the other hand, one must introduce polarization and magnetization gradients to account for electromagnetic ordering. Phenomenologically, the conduction (or diffusion) currents per unit charge may be considered as the new generalized velocity fields that, by thermodynamic duality, yield generalized internal forces for which constitutive equations will have to be constructed. That is, we increase the complexity of the general scheme of electromechanical interactions of [2] by considering the self-explanatory scheme of Fig. 2.1 where the continua of charge α, correspond to electrons, holes, ions, impurities, etc. Thus the superscript α labels quantities attached to these species of charge and we have the obvious relations and notations.

The volume density of free charges q_f and the total electric current density $\boldsymbol{J}$ correspond to the contribution of each α charge carriers, such that:

$$q_f = \sum_{\alpha} q_f^{\alpha}, \quad \boldsymbol{J} = \sum_{\alpha} \boldsymbol{J}^{\alpha} \tag{2.1}$$

$$\boldsymbol{v}^{\alpha} = \frac{\boldsymbol{J}^{\alpha}}{q_f^{\alpha}}, \quad \boldsymbol{u}^{\alpha} = \boldsymbol{v}^{\alpha} - \boldsymbol{v} = \frac{\not{\boldsymbol{J}}^{\alpha}}{q_f^{\alpha}} \tag{2.2}$$

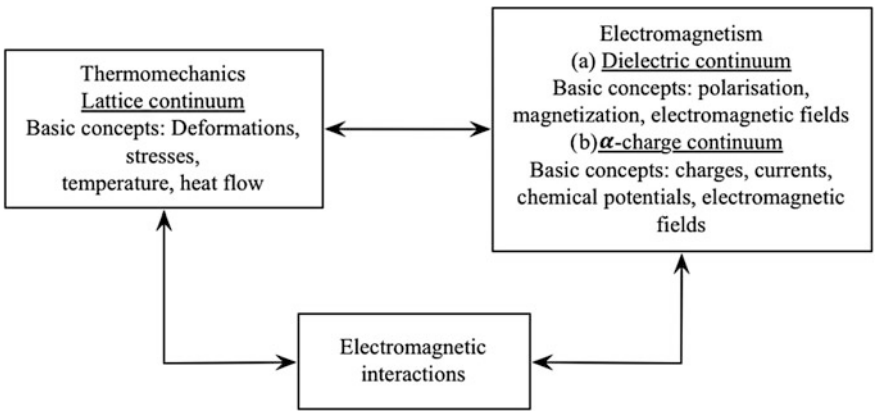

Fig. 2.1 Scheme of interactions in thermo-deformable semiconductors [1]

where q_f^α and $\boldsymbol{J}^\alpha$ denote respectively the volume density and the electric current density of electric charges of type α. The vectors $\boldsymbol{v}$, $\boldsymbol{v}^\alpha$ and $\boldsymbol{u}^\alpha$ denote respectively the velocity fields describing the global deformable material, the αth continuum (or the velocity of α charges carriers with respect to the frame R_G) and the relative velocity (i.e. with respect to the co-moving frame R_C). $\mathcal{J}^\alpha$ denotes the conduction current density of α charge carriers that is diffused within the material with respect to R_C frame. Similarly to the mass conservation but accounting for the possible recombination and generation [1], we can write for the αth continua of charge the following global balance laws $(\alpha = 1, 2, 3 \ldots)$:

$$\frac{d^\alpha}{dt} \int_{\mathcal{D}} q_f^\alpha dv = \int_{\mathcal{D}} r^\alpha dv \tag{2.3}$$

where $d^\alpha/dt = \partial/\partial t + \boldsymbol{v}^\alpha \cdot \nabla$ denotes the "αth continuum" convective-time derivative and r^α the source terms such that $\sum_\alpha r^\alpha = 0$.

Equation (2.3) yields the local conservation-of-charge equations for the αth type of charge carriers as

$$\frac{\partial q_f^\alpha}{\partial t} + \nabla \cdot \boldsymbol{J}^\alpha = r^\alpha \tag{2.4}$$

By summation over α, the latter equation yields the conservation-of-charge equation for the whole continuum.

In the following we use the convective-time derivative of a vector field $\boldsymbol{A}$ such that

$$\overset{*}{A} = \dot{A} - (A \cdot \nabla)\boldsymbol{v} + A(\nabla \cdot \boldsymbol{v}) \tag{2.5}$$

Maxwell's equations can be written in SI units, like other equations in this communication, in order to be close to what is nowadays done by physicists [3]:

$$\nabla \times \mathcal{E} + \overset{*}{\boldsymbol{B}} = 0, \quad \nabla \cdot \boldsymbol{B} = 0 \tag{2.6}$$

$$\nabla \times \left(\frac{\mathcal{B}}{\mu_0} \right) - \varepsilon_0 \overset{*}{\boldsymbol{E}} = \mathcal{J}^{eff}, \quad \nabla \cdot \boldsymbol{E} = \frac{q^{eff}}{\varepsilon_0} \tag{2.7}$$

where $\boldsymbol{E}$ and $\boldsymbol{B}$ denote the vectors of the electric field and the magnetic induction evaluated in the fixed Galilean frame R_G; $\mathcal{E}$ and $\mathcal{B}$ are the same vector fields as $\boldsymbol{E}$ and $\boldsymbol{B}$ but referred to a co-moving frame R_C in movement with the material velocity $\boldsymbol{v}$ with respect to R_G; ε_0 and μ_0 are respectively the vacuum permittivity and permeability such that $\varepsilon_0 \mu_0 c^2 = 1$ (where c denotes the speed of light in vacuum); q^{eff} and $\mathcal{J}^{eff}$ are the effective charges and currents in R_C defined by:

$$q^{eff} = \sum_{\alpha} q_f^{\alpha} - \nabla \cdot \boldsymbol{P} = \sum_{\alpha} q^{\alpha(eff)}, \qquad q^{\alpha(eff)} = q_f^{\alpha}\left(1 - \frac{\nabla \cdot \boldsymbol{P}}{\nabla \cdot \boldsymbol{D}}\right) \tag{2.8}$$

$$\mathcal{J}^{eff} = \mathcal{J} + \overset{*}{\boldsymbol{P}} + \nabla \times \mathcal{M} = \sum_{\alpha} \mathcal{J}^{\alpha(eff)}, \qquad \mathcal{J}^{\alpha(eff)} = \mathcal{J}^{\alpha} + q_f^{\alpha}\left(\overset{*}{\boldsymbol{P}} + \nabla \times \mathcal{M}\right)(\nabla \cdot \boldsymbol{D})^{-1} \tag{2.9}$$

where $\boldsymbol{D}$, $\boldsymbol{P}$ and $\boldsymbol{M}$ denote the vector of the electric displacement, the electric polarization and the magnetization evaluated in R_G; $\mathcal{M}$ and $\mathcal{J} = \sum_{\alpha} \mathcal{J}^{\alpha}$ are the same vector fields as $\boldsymbol{M}$ and $\boldsymbol{J}$ but referred to a co-moving frame R_C. When $\nabla \cdot \boldsymbol{D} = 0$, one uses the first equalities of Eqs. (2.8) and (2.9). In the Galilean approximation, we have the following transformation laws between R_G and R_C:

$$\mathcal{E} = \boldsymbol{E} + \boldsymbol{v} \times \boldsymbol{B}, \qquad \frac{\mathcal{B}}{\mu_0} = \frac{\boldsymbol{B}}{\mu_0} - \boldsymbol{v} \times (\varepsilon_0 \boldsymbol{E}) \tag{2.10}$$

$$\mathcal{M} = \boldsymbol{M} + \boldsymbol{v} \times \boldsymbol{P}, \quad \mathcal{J} = \boldsymbol{J} - q_f \boldsymbol{v}. \tag{2.11}$$

This gives an idea of the effective charge and current densities that must be accounted for the αth species when the material is simultaneously polarized and magnetized.

2.1.2 Thermo-Electro-Magneto-Mechanical Equations

2.1.2.1 General Principles in Global Form

The thermomechanical balance laws of an electromagnetic continuum may be deduced in an elegant manner from three general principles written in global form for the material volume $\mathcal{D}$. These are the principle of virtual power and the first and second principles of thermodynamics [4, 5]. We refer the reader to the review paper [2] and the book [6] for this general approach from which we extract only the required ingredients.

In order to construct the different virtual powers, we construct a space of velocities and velocity gradients $\mathcal{V}$ (see, for instance, [1, 2, 6–8]) from the available "velocities" gathered in $\mathcal{V}^{(0)}$:

$$\mathcal{V}^{(0)} = \left\{v_i, v_i^{\alpha}, \dot{\pi}_i, \dot{\mu}_i\right\} \tag{2.12}$$

where $\pi_i = P_i/\rho$ and $\mu_i = \mathcal{M}_i/\rho$ denote the mass density of polarization and magnetization.

The set of variables is chosen according to the phenomena one is interested in. For simple deformable electro-magneto-mechanical interactions, one needs to account for time rates of polarization $\dot{\pi}_i$ and magnetization $\dot{\mu}_i$, in addition to the

usual mechanical ingredients: velocity v_i and its first gradient $v_{i,j}$ (needed to account for deformation). In the present approach where one deals with complex media including ferroelectricity, ferromagnetism, flexoelectricity, semi-conduction etc., it becomes necessary to add to the time rates of polarization and magnetization first gradients, $(\dot{\pi}_i)_{,j}$ and $(\dot{\mu}_i)_{,j}$, accounting thus for the so-called electromagnetic ordering (ferroelectricity, ferromagnetism …). One also needs to account for a second gradient relative to the velocity $v_{i,jk}$, required to give account of the flexoelectric effect. As to semi-conduction, it is accounted for by introducing new variables reflecting the motion of the different charge carriers (electrons, holes …) i.e. the velocity v_i^α and its first-order gradient $v_{i,j}^\alpha$. In summary, the set of variables $\mathcal{V}^{(0)}$ has been enlarged with these different first and second order gradients to obtain the new set $\mathcal{V}$ such that (see for instance [2, 9]):

$$\mathcal{V} = \left\{ v_i, v_{i,j}, v_{i,jk}, v_i^\alpha, v_{i,j}^\alpha, \dot{\pi}_i, (\dot{\pi}_i)_{,j}, \dot{\mu}_i, (\dot{\mu}_i)_{,j} \right\} \tag{2.13}$$

In order to pave the way for objective quantities, the velocity gradients may be decomposed into their symmetric and anti-symmetric parts. This may be decomposed as:

$$\mathcal{V} = \left\{ v_i, D_{ij}, \Omega_{ij}, v_{i,jk}, u_i^\alpha, D_{ij}^\alpha, \Omega_{ij}^\alpha, \dot{\pi}_i, (\dot{\pi}_i)_{,j}, \dot{\mu}_i, (\dot{\mu}_i)_{,j} \right\} \tag{2.14}$$

where $v_{i,j} = v_{(i,j)} + v_{[i,j]} = D_{ij} + \Omega_{ij}$ and $v_{i,j}^\alpha = v_{(i,j)}^\alpha + v_{[i,j]}^\alpha = D_{ij}^\alpha + \Omega_{ij}^\alpha$.

Since the constitutive equations associated with the different continua must be objective, i.e. frame-independent, we construct a subspace $\mathcal{V}_{obj}$ including only objective fields. In order to do that, the Jaumann derivatives, noted D_J, and the specific time derivative tensors are used with the velocity of the deformable continuum and with the velocities of the αth charge continua [1, 3]. Hence, for the polarization, we introduce:

$$\hat{\pi}_i = (D_J \boldsymbol{\pi})_i = \dot{\pi}_i - \Omega_{ij}\pi_j, \qquad \hat{\pi}_i^\alpha = (D_J^\alpha \boldsymbol{\pi})_i = \dot{\pi}_i - \Omega_{ij}^\alpha \pi_j \tag{2.15}$$

$$\hat{\pi}_{ij} = [D_J(\nabla \boldsymbol{\pi})]_{ij} + D_{kj}\,\pi_{i,k} = (\dot{\pi}_i)_{,j} - \Omega_{ik}\pi_{k,j}, \qquad \hat{\pi}_{ij}^\alpha = (\dot{\pi}_i)_{,j} - \Omega_{ik}^\alpha \pi_{k,j}. \tag{2.16}$$

For the magnetization, the Jaumann derivatives, $\hat{\mu}_i$ and $\hat{\mu}_i^\alpha$, and the specific time derivative tensors, $\hat{\mu}_{ij}$ and $\hat{\mu}_{ij}^\alpha$, are introduced similarly. Thus, the objective space $\mathcal{V}_{obj}$ is composed of the following set of kinematical objective fields

$$\mathcal{V}_{obj} = \left\{ D_{ij}, v_{i,jk}, u_i^\alpha, D_{ij}^\alpha, \hat{\pi}_i, \hat{\pi}_{ij}, \hat{\mu}_i, \hat{\mu}_{ij}, \hat{\pi}_i^\alpha, \hat{\pi}_{ij}^\alpha, \hat{\mu}_i^\alpha, \hat{\mu}_{ij}^\alpha \right\}$$

As to the set of dynamical objective fields $\mathcal{F}_{obj}$, it is introduced by duality to the set $\mathcal{V}_{obj}$. It is composed of generalized internal forces, such that [2]:

$$\mathcal{F}_{obj} = \left\{ \sigma_{ij}, \mu_{ijk}, q_f^{\alpha\, L}\mathcal{E}_i^{\alpha}, \sigma_{ij}^{\alpha}, \rho\, {}^{L}E_i, {}^{L}\mathcal{E}_{ij}, \rho\, {}^{L}B_i, {}^{L}\mathcal{B}_{ij}, \rho\, {}^{L}E_i^{\alpha}, {}^{L}\mathcal{E}_{ij}^{\alpha}, \rho\, {}^{L}B_i^{\alpha}, {}^{L}\mathcal{B}_{ij}^{\alpha} \right\}$$

where σ_{ij}^{α} and σ_{ij} are the symmetric first-order stress tensor's components referred to as the intrinsic-stress tensor respectively for the αth charge continua and for the deformable continuum. μ_{ijk} is the intrinsic second-order stress tensor. A dimensional analysis shows that ${}^{L}B_i$ and ${}^{L}B_i^{\alpha}$ are induction fields, and, ${}^{L}\mathcal{E}_i^{\alpha}$, ${}^{L}E_i$ and ${}^{L}E_i^{\alpha}$ are electric fields. ${}^{L}\mathcal{E}_{ij}$, ${}^{L}\mathcal{B}_{ij}$, ${}^{L}\mathcal{E}_{ij}^{\alpha}$ and ${}^{L}\mathcal{B}_{ij}^{\alpha}$ are generalized forces associated to the gradient of the time derivatives of electric polarization and magnetization.

- **Principle of Virtual Power (PVP)**

In a Galilean frame and for a Newtonian chronology, the total virtual power of inertial forces of the system $\mathscr{P}^{*}_{(a)}$ balances the sum of the virtual powers of internal forces $\mathscr{P}^{*}_{(i)}$, of external volume forces $\mathscr{P}^{*}_{(v)}$ and of external contact forces $\mathscr{P}^{*}_{(c)}$ impressed on the system for any virtual velocity field. With the above notation, this reads:

$$\begin{aligned} &\mathscr{P}^{*}_{(a)}(\mathcal{D}, V^{*} \in \mathcal{V}^{(0)*}) \\ &= \mathscr{P}^{*}_{(i)}(\mathcal{D}, V^{*} \in \mathcal{V}^{*}_{obj}) + \mathscr{P}^{*}_{(v)}(\mathcal{D}, V^{*} \in \mathcal{V}^{*}) + \mathscr{P}^{*}_{(c)}(\partial\mathcal{D}, V^{*} \in \mathcal{V}^{(c)*}) \end{aligned} \tag{2.17}$$

- **First Principle of Thermodynamics**

The time rate of change of the total energy contained in the material domain $\mathcal{D}$, considered as a closed system, is equal to the sum of the power developed by "prescribed" forces $\mathscr{P}_{(e)}$, the energy supply by radiation in the volume of $\mathcal{D}$ and the total flux of energy through the boundary $\partial\mathcal{D}$ [2]. Mathematically, this reads:

$$\frac{d}{dt}\left[K(\mathcal{D}) + E(\mathcal{D}) + U^{em}(\mathcal{D})\right] = \mathscr{P}_{(e)}(\overline{\mathcal{D}}) + \dot{Q}_h(\overline{\mathcal{D}}) \tag{2.18}$$

where $\overline{\mathcal{D}}$ denotes the outside of domain $\mathcal{D}$ in R^3.

- **Second Principle of Thermodynamics**

For any thermodynamical process the time rate of change of the total entropy of the material domain $\mathcal{D}$ is never less than the sum of the total entropy supply in the volume of $\mathcal{D}$ and the total flux of entropy through its boundary $\partial\mathcal{D}$. Mathematically, this reads:

$$\frac{d}{dt}N(\mathcal{D}) \geq \dot{\mathcal{N}}(\overline{\mathcal{D}}) \tag{2.19}$$

For a general magnetizable, electrically polarized, heat conducting deformable semiconductor, the expressions to be carried in Eqs. (2.17)–(2.19) are given as follows:

$$K(\mathcal{D}) = \int_D \left(\frac{1}{2}\rho\, \boldsymbol{v}^2 + \frac{1}{2}\rho\, d\, \dot{\boldsymbol{\pi}}^2\right) dv \tag{2.20}$$

$$E(\mathcal{D}) = \int_{\mathcal{D}} \rho\epsilon dv, \qquad U^{em}(\mathcal{D}) = \int_{\mathcal{D}} \frac{1}{2}\left(\varepsilon_0 \boldsymbol{E}^2 + \frac{\boldsymbol{B}^2}{\mu_0} - 2\mathcal{M}\cdot\mathcal{B}\right) dv \tag{2.21}$$

$$\dot{Q}_h(\overline{\mathcal{D}}) = \int_{\mathcal{D}} \rho h dv - \int_{\partial\mathcal{D}} q\cdot n da \tag{2.22}$$

$$N(\mathcal{D}) = \int_{\mathcal{D}} \rho\eta dv, \qquad \dot{\mathcal{N}}(\overline{\mathcal{D}}) = \int_{\mathcal{D}} \rho\sigma dv - \int_{\partial\mathcal{D}} \boldsymbol{\phi}\cdot n\, da \tag{2.23}$$

where d is the electronic polarization inertia tensor, e is the internal energy per unit mass, η is the entropy per unit mass, h is the radiation heat power source per unit mass, $\boldsymbol{n}$ is the unit exterior normal to the closed surface $\partial\mathcal{D}$ of the material domain $\mathcal{D}$ and $\boldsymbol{q}$ is the total power flux vector, i.e. the sum of the heat power flux vector $\tilde{q}$ and the Poynting's flux vector $\mathcal{S}$ referring to R_C [2]:

$$\boldsymbol{q} = \tilde{\boldsymbol{q}} + \mathcal{S}, \qquad \mathcal{S} = \mathcal{E}\times\mathcal{H}. \tag{2.24}$$

The fields σ and $\boldsymbol{\phi}$ are usually related to h, q and the thermodynamical temperature θ (where $\theta > 0$, $\inf(\theta) = 0$). These relations will be specified later on.

The other expressions to be carried in Eqs. (2.17)–(2.19) are constructed as follows:

Total virtual power of inertial forces $\mathscr{P}^*_{(a)}$

$$\mathscr{P}^*_{(a)}(\mathcal{D}, V^* \in \mathcal{V}^{(0)*}) = \int_{\mathcal{D}} \rho\left[\dot{v}_i v_i^* + d\ddot{\pi}_i \dot{\pi}_i^* + \beta' \gamma^{-1} \dot{\mu}_i \omega_i^*\right] dv \tag{2.25}$$

where γ is the gyromagnetic ratio of electrons. β' is equal to 1 when the spin precession plays an important role (i.e. when the material is ferromagnetic at low temperature) which can be expressed as a constraint on the magnetization velocity $\dot{\boldsymbol{\mu}} = \boldsymbol{\omega}\times\boldsymbol{\mu}$, where $\boldsymbol{\omega}$ is the precession velocity. Otherwise, β' can be set equal to 0 as shown in [1, 2, 6, 8].

Total virtual power of internal forces $\mathscr{P}^*_{(i)}$

The internal forces that reflect the interactions associated with the crystal lattice and polarizable, magnetizable and semi-conducting continua, have to be objective [1, 2, 6, 8]:

$$\mathscr{P}^*_{(i)}(\mathscr{D}, V^* \in \mathscr{V}^*_{obj}) = -\int_{\mathscr{D}} p^*_{(i)} dv \tag{2.26}$$

with

$$\begin{aligned} p^*_{(i)} = {} & \sigma_{ij} D^*_{ij} + \mu_{ijk} v^*_{i,jk} - \rho\, {}^L E_i \hat{\pi}^*_i - \rho\, {}^L B_i \hat{\mu}^*_i + {}^L \mathscr{E}_{ij} \hat{\pi}^*_{ij} + \beta\, {}^L \mathscr{B}_{ij} \hat{\mu}^*_{ij} - \sum_\alpha q_f^\alpha\, {}^L \mathscr{E}_i^\alpha u_i^{\alpha *} \\ & + \sum_\alpha \left(\sigma_{ij}^\alpha D_{ij}^{\alpha *} - \rho\, {}^L E_i^\alpha \hat{\pi}_i^{\alpha *} - \rho\, {}^L B_i^\alpha \hat{\mu}_i^{\alpha *} + {}^L \mathscr{E}_{ij}^\alpha \hat{\pi}_{ij}^{\alpha *} + \beta\, {}^L \mathscr{B}_{ij}^\alpha \hat{\mu}_{ij}^{\alpha *} \right) \end{aligned} \tag{2.27}$$

where, β is equal to 1 when the exchange forces play an important role, via variables ${}^L\mathscr{B}_{ij}$ and ${}^L\mathscr{B}^\alpha_{ij}$ (i.e. when the material is ferromagnetic). Otherwise, β can be set equal to 0.

Total virtual power of external volume forces $\mathscr{P}^*_{(v)}$

$$\mathscr{P}^*_{(v)}(\mathscr{D}, V^* \in \mathscr{V}^*) = \int_{\mathscr{D}} \left(\left(f_i + f_i^{em}\right) v_i^* + \rho \mathscr{E}_i \dot{\pi}_i^* + \rho B_i \dot{\mu}_i^* + \sum_\alpha f_i^\alpha u_i^{\alpha *} \right) dv \tag{2.28}$$

where f and f^α represent volume densities of forces and f^{em} is the volume density of ponderomotive forces. Here, we have assumed for the sake of simplicity that the cofactors of $v_{i,jk}$, $(\dot{\mu}_i)_{,j}$ and $(\dot{\pi}_i)_{,j}$ take the value zero (in fact no physical interpretation of these fields has been found up to now [2]).

Total virtual power of external contact forces $\mathscr{P}^*_{(c)}$

For the external contact power, we obtain the following expression (see [3, 5, 9–13]):

$$\begin{aligned} \mathscr{P}^*_{(c)}(\partial\mathscr{D}, V^* \in \mathscr{V}^{(0)*}) = {} & \int_{\partial\mathscr{D} - \Gamma_\nearrow} \left(\left(T_i + T_i^{em}\right) v_i^* + R_i \frac{\partial v_i^*}{\partial n} + \frac{\rho\, Q_i}{\varepsilon_0} \dot{\pi}_i^* \right) da \\ & + \int_{\partial\mathscr{D} - \Gamma_\nearrow} \left(\beta\, \mu_0\, \rho\, \mathscr{F}_i\, \dot{\mu}_i^* + \sum_\alpha T_i^\alpha u_i^{\alpha *} \right) da + \int_{\Gamma_\nearrow} L_i v_i^*\, ds \end{aligned} \tag{2.29}$$

where $\boldsymbol{T}$ and $\boldsymbol{T}^\alpha$ represent surface densities of forces, $\boldsymbol{T}^{em}$ is the electromagnetic surface density of forces, R_i, L_i, Q_i and $\mathscr{F}_i$ denote respectively the normal double traction (per unit length), the reduced linear density of strength along the discontinuous line Γ (i.e. an edge where the unit exterior normal $\boldsymbol{n}$ on the closed surface $\partial\mathscr{D}$ is discontinuous) and the surface distribution of electric and magnetic dipoles.

Total power of "prescribed" forces $\mathscr{P}_{(e)}$

The total power of the "prescribed" forces is obtained by the construction of the principle of virtual power for an actual velocity field [2, 9, 11]. Using the global energetic identity for the electromagnetic fields U^{em} given by Maugin in [6], we obtain the total power of the "prescribed" forces $\mathscr{P}_{(e)}(\overline{\mathscr{D}})$ as

$$\begin{aligned}\mathscr{P}_{(e)}(\overline{\mathscr{D}}) = &\int_{\mathscr{D}} f_i v_i dv + \int_{\partial\mathscr{D}-\Gamma_\nearrow} \left(T_i v_i + R_i \frac{\partial v_i}{\partial n} + \frac{\rho Q_i}{\varepsilon_0}\dot{\pi}_i \right) da \\ &+ \int_{\partial\mathscr{D}-\Gamma_\nearrow} \left(\beta\mu_0 \rho \mathscr{F}_i \dot{\mu}_i + \sum_\alpha T_i^\alpha u_i^\alpha \right) da + \int_{\Gamma_\nearrow} L_i v_i ds\end{aligned} \tag{2.30}$$

In the above-set of Eqs. (2.25)–(2.30), $\boldsymbol{f}$ and $\boldsymbol{T}$ are respectively the volume and surface densities of forces of purely mechanical origin. f^α and T^α are respectively the volume and surface densities of forces associated with the αth charge continuum. The symmetric tensor with the component σ_{ij} is called the intrinsic stress tensor (not to be mistaken for the Cauchy stress tensor to which it is only a symmetric contribution). Constitutive equations will have to be constructed for this tensor. The quantities σ_{ij}^α, ${}^L E_i$, ${}^L B_i$ ${}^L E_i^\alpha$, ${}^L B_i^\alpha$ and ${}^L \mathscr{E}_i^\alpha$ all introduced by duality (we need constitutive equations for these) reflect the interactions between, respectively, the neighboring elements of the αth charge continuum; the polarization field and the crystal lattice; the magnetization field and the crystal lattice; the polarization field and the αth charge continuum; the magnetization field and the αth charge continuum; the crystal lattice and the αth charge continuum (this clearly is a "diffusion" process). Finally, the presence of μ_{ijk}, ${}^L \mathscr{E}_{ij}$, ${}^L \mathscr{B}_{ij}$, ${}^L \mathscr{E}_{ij}^\alpha$ and ${}^L \mathscr{B}_{ij}^\alpha$ are explained by the inclusion of the gradients ($\nabla\nabla\boldsymbol{v}$, $\nabla\boldsymbol{\mu}$ and $\nabla\boldsymbol{\pi}$) and the principle of objectivity. These quantities (we also need constitutive equations for these) reflect, respectively, the second order interaction between the neighboring elements of the deformable continuum, and, the interactions between the polarization gradient field and the crystal lattice; the magnetization gradient field and the crystal lattice; the polarization gradient field and the αth charge continuum; the magnetization gradient field and the αth charge continuum. Finally, $\boldsymbol{f}^{em}$ is the volume density of the ponderomotive force and T^{em} is the corresponding electromagnetic surface density of force.

According to a semi microscopic approach [14] accounting for the effects of only charges and dipoles, the ponderomotive volume density of force is [1, 6, 8, 14–19]:

$$\boldsymbol{f}^{em} = q^{eff}\mathscr{E} + \left(\mathscr{J}^{eff} - \nabla\times\mathscr{M}\right)\times\boldsymbol{B} + \nabla\cdot(\mathscr{E}\otimes\boldsymbol{P}) + (\nabla\boldsymbol{B})\cdot\mathscr{M} \tag{2.31}$$

where one has set: $[\nabla\cdot(\mathscr{E}\otimes\boldsymbol{P})]_i = \left(\mathscr{E}_i\, P_j\right)_{,j}$ and $[(\nabla\boldsymbol{B})\cdot\mathscr{M}]_i = B_{j,i}\,\mathscr{M}_j$

This latter expression is equivalent to the following:

$$\boldsymbol{f}^{em} = \nabla \cdot \boldsymbol{t}^{em} - \frac{\partial G}{\partial t} = {}_{L}\boldsymbol{f} + \nabla \cdot \bar{\boldsymbol{t}}^{em} \tag{2.32}$$

where we have singularized the "Lorentz force" ${}_{L}f$

$${}_{L}\boldsymbol{f} = q^{eff}\mathscr{E} + \mathscr{J}^{eff} \times \boldsymbol{B} = \nabla \cdot t^{F} - \frac{\partial G}{\partial t} \tag{2.33}$$

$$t_{ij}^{em} = t_{ij}^{F} + \bar{t}_{ij}^{em}, \qquad G = \varepsilon_0 \boldsymbol{E} \times \boldsymbol{B} \tag{2.34}$$

$$t_{ij}^{F} = \varepsilon_0 E_i E_j + \frac{B_i B_j}{\mu_0} - \frac{1}{2}\left(\varepsilon_0 \boldsymbol{E}^2 + \frac{\boldsymbol{B}^2}{\mu_0}\right)\delta_{ij}, \qquad \bar{t}_{ij}^{em} = \mathscr{E}_i P_j - \mathscr{M}_i B_j + \mathscr{M} \cdot \boldsymbol{B}\ \delta_{ij}. \tag{2.35}$$

The electromagnetic surface density of forces T^{em} is defined on $\partial\mathscr{D}$ as [1, 6, 8]:

$$T_i^{em} = -(t_{ij}^{em} + G_i v_j) n_j \tag{2.36}$$

Finally, the ponderomotive couple $\boldsymbol{C}^{em}$ (of electromagnetic origin) is accounted for through the pseudo-vector of the electromagnetic stress tensor $\boldsymbol{C}^{em}$ such that

$$C_{ij}^{em} = -t_{[ij]}^{em} = -\bar{t}_{[ij]}^{em}, \qquad c_k^{em} = \varepsilon_{klm} C_{lm}^{em} = (\boldsymbol{P} \times \mathscr{E} + \mathscr{M} \times \boldsymbol{B})_k \tag{2.37}$$

where ε_{ijk} denotes the classical Levi-Civita symbol.

2.1.2.2 Local Electro-Magneto-Mechanical Balance Equations

For any virtual fields $\boldsymbol{v}^*$, $\boldsymbol{v}^{\alpha *}$, $\dot{\boldsymbol{\pi}}^*$, $\dot{\boldsymbol{\mu}}^*$ and $\partial \boldsymbol{v}^*/\partial n$ and for any element of volume and surface, we obtain the following local field equations from (2.17) that govern the motion and the interactions in a moving magnetized, polarized and semiconducting, material medium (see [1, 2, 4, 9]):

$$\boxed{\forall \frac{\partial v^*}{\partial n}} \quad \mu_{ijk} n_j n_k = R_i \qquad on\ \partial\mathscr{D} - \Gamma_{\nearrow} \tag{2.38}$$

$$\boxed{\forall \boldsymbol{v}^*} \quad t_{ij,j} + f_i + f_i^{em} - \sum_{\alpha} q_f^{\alpha}\left(\mathscr{E}_i^{\alpha} + {}^{L}\mathscr{E}_i^{\alpha}\right) = \rho\ \dot{v}_i \qquad in\ \mathscr{D} \tag{2.39}$$

$$t_{ij} n_j = T_i + T_i^{em} + \left(\nabla_j - n_j\left(\nabla_p n_p\right)\right)\mu_{ijk} n_k - \sum_{\alpha} T_i^{\alpha} \qquad on\ \partial\mathscr{D} - \Gamma_{\nearrow} \tag{2.40}$$

$$L_i = \varepsilon_{jpq}[\![\mu_{ijk} n_k \tau_p n_q]\!] \qquad on\ \Gamma_{\nearrow} \tag{2.41}$$

where the nonsymmetric Cauchy stress tensor's component t_{ij} is defined by:

$$t_{ij} = \sigma_{ij} - \mu_{ijk,k} + \rho \left({}^{L}E_{[i}\pi_{j]} + {}^{L}B_{[i}\mu_{j]} \right) - \left({}^{L}\mathcal{E}_{[i|k|}\pi_{j],k} + \beta\, {}^{L}\mathcal{B}_{[i|k|}\mu_{j],k} \right) \tag{2.42}$$

and where the symbol $[\![\ldots]\!]$ denotes here the jump across the edge Γ, $\boldsymbol{\tau}$ denotes the unit vector tangent to Γ and oriented in the direct sense about the normal $\boldsymbol{n}$, and, $\hat{\nabla}$ denotes the surface gradient operator.

$$\boxed{\forall \boldsymbol{v}^{\alpha^*}} \quad t^{\alpha}_{ij,j} + q^{\alpha}_{f} \left(\mathcal{E}^{\alpha}_{i} + {}^{L}\mathcal{E}^{\alpha}_{i} \right) = 0 \qquad in\ \mathcal{D} \tag{2.43}$$

$$t^{\alpha}_{ij} n_j = T^{\alpha}_{i} \qquad on\ \partial\mathcal{D} - \Gamma_{\nearrow} \tag{2.44}$$

where the nonsymmetric stress tensor's component t^{α}_{ij} is defined by:

$$t^{\alpha}_{ij} = \sigma^{\alpha}_{ij} + \rho \left({}^{L}E^{\alpha}_{[i}\pi_{j]} + {}^{L}B^{\alpha}_{[i}\mu_{j]} \right) - \left({}^{L}\mathcal{E}^{\alpha}_{[i|k|}\pi_{j],k} + \beta\, {}^{L}\mathcal{B}^{\alpha}_{[i|k|}\mu_{j],k} \right) \tag{2.45}$$

$$\boxed{\forall \dot{\boldsymbol{\pi}}^{*}} \quad {}^{L}\mathcal{E}^{T}_{ij,j} + \rho \mathcal{E}^{eff}_{i} = \rho\, d\ddot{\pi}_i \qquad in\ \mathcal{D} \tag{2.46}$$

$${}^{L}\mathcal{E}^{T}_{ij} n_j = \frac{\rho Q_i}{\varepsilon_0} \qquad on\ \partial\mathcal{D} - \Gamma_{\nearrow} \tag{2.47}$$

with the effective electric field $\mathcal{E}^{eff}$, and, the local interaction electric fields of the first order ${}^{L}\boldsymbol{E}^{T}$ and of the second order with components ${}^{L}\mathcal{E}^{T}_{ij}$ defined by:

$$\mathcal{E}^{eff}_{i} = \mathcal{E}_i + {}^{L}E^{T}_{i} \tag{2.48}$$

$${}^{L}E^{T}_{i} = {}^{L}E_i + \sum_{\alpha} {}^{L}E^{\alpha}_{i} \quad \text{and} \quad {}^{L}\mathcal{E}^{T}_{ij} = {}^{L}\mathcal{E}_{ij} + \sum_{\alpha} {}^{L}\mathcal{E}^{\alpha}_{ij} \tag{2.49}$$

$$\boxed{\forall \dot{\boldsymbol{\mu}}^{*}} \quad \beta^{L}\mathcal{B}^{T}_{ij,j} + \rho B^{eff}_{i} = -\beta^{'} \rho \frac{\omega_i}{\gamma} \text{ with } \boldsymbol{\omega} \text{ such that } \dot{\boldsymbol{\mu}} = \boldsymbol{\omega} \times \boldsymbol{\mu}\ in\ \mathcal{D} \tag{2.50}$$

$$\beta \varepsilon_{ipq} \left({}^{L}\mathcal{B}^{T}_{pj} n_j - \rho \mu_0 \mathcal{F}_p \right) \mu_q = 0 \qquad on\ \partial\mathcal{D} - \Gamma_{\nearrow} \tag{2.51}$$

with $\beta^{'} = \beta = 1$, when the material is ferromagnetic at low temperature [13, 15]; $\beta = 1, \beta^{'} = 0$, when the material is ferromagnetic near the Curie temperature; $\beta^{'} = \beta = 0$, otherwise, and, with the effective magnetic induction $\boldsymbol{B}^{eff}$, and, the local interaction magnetic inductions of the first order ${}^{L}\boldsymbol{B}^{T}$ and of the second order with components ${}^{L}\mathcal{B}^{T}_{ij}$ defined by:

$$B_i^{eff} = B_i + {}^L B_i^T \tag{2.52}$$

$${}^L B_i^T = {}^L B_i + \sum_\alpha {}^L B_i^\alpha \quad \text{and} \quad {}^L \mathcal{B}_{ij}^T = {}^L \mathcal{B}_{ij} + \sum_\alpha {}^L \mathcal{B}_{ij}^\alpha \tag{2.53}$$

2.1.2.3 Local Thermodynamical Equations

Combining the first principle of thermodynamic (2.18) with the principle of virtual power (taken for actual velocities), we obtain the following global statement corresponding to the global form of the energy theorem as:

$$\dot{E}(\mathcal{D}) + \mathscr{P}_{(i)}(\mathcal{D}, \mathcal{V}_{obj}) = \dot{Q}_h(\overline{\mathcal{D}}) + \dot{Q}_{em}(\overline{\mathcal{D}}) \tag{2.54}$$

where we have set

$$\dot{Q}_{em}(\overline{\mathcal{D}}) = \int_{\mathcal{D}} \dot{q}_{em} dv + \int_{\partial\mathcal{D}} \mathscr{S} \cdot \boldsymbol{n} da \tag{2.55}$$

with

$$\dot{q}_{em} = \sum_\alpha \left(\mathscr{J}^{\boldsymbol{\alpha}} \cdot \mathscr{E} - \boldsymbol{f}^{\boldsymbol{\alpha}} \cdot \boldsymbol{u}^{\boldsymbol{\alpha}} \right) \tag{2.56}$$

Accounting for the generalized transport theorems and balances of mass, from these latter eqns, we deduce the local forms of the first principle of thermodynamics (2.18) (or the local form of the energy theorem) as

$$\rho \dot{\varepsilon} = p_{(i)} + \dot{q}_{em} - \nabla \cdot \tilde{\boldsymbol{q}} + \rho h \tag{2.57}$$

The second principle of thermodynamics remains to be exploited. To that purpose we assume that $\sigma = h/\theta$ and $\phi_i = \tilde{q}_i/\theta$. Only the volume entropy flux differs from the usual ratio of the heat vector to the temperature, which means that non-simple thermodynamic processes are involved (cf. [20], p. 129). The local form of the second principle of thermodynamics (2.19) then reads

$$\rho\theta \frac{d\eta}{dt} \geq \rho h - \nabla \cdot \tilde{\boldsymbol{q}} + \boldsymbol{\phi} \cdot \nabla\theta \tag{2.58}$$

2.1.3 Clausius-Duhem Inequality

The Helmholtz free energy density $\psi = \varepsilon - \eta\,\theta$ is introduced. And we are led to the Clausius-Duhem inequality in the local form:

$$-\rho\left(\frac{d\psi}{dt}+\eta\frac{d\theta}{dt}\right)+p_{(i)}+\ \dot{q}_{em}-\boldsymbol{\phi}\cdot\nabla\theta\geq 0 \tag{2.59}$$

Introducing the relations between Jaumann derivatives and convective-time ones and a scalar chemical potential, we can evaluate [3]:

$$\begin{aligned} p_{(i)}+\dot{q}^{em}=&\tilde{t}_{ij}^{T}D_{ij}+\mu_{ijk}v_{i,jk}-{}^{L}E_{i}^{T}\overset{*}{P}_{i}-{}^{L}B_{i}^{T}\overset{*}{\mathscr{M}}_{i}+{}^{L}\mathscr{E}_{ij}^{T}\widehat{\pi}_{ij}+\beta\,{}^{L}\mathscr{B}_{ij}^{T}\widehat{\mu}_{ij}\\ &+\sum_{\alpha}\left[\mathscr{E}^{\alpha(eff)}\cdot\mathscr{J}^{\alpha}-\mu^{\alpha}\nabla\cdot\mathscr{J}^{\alpha}\right] \end{aligned} \tag{2.60}$$

where we have also introduced the effective electromotive field of the α charge carriers by $\mathscr{E}^{\alpha(eff)}=\mathscr{E}-\nabla\mu^{\alpha}$, where $\tilde{t}^{T}$ is a symmetric tensor such that:

$$\tilde{t}_{ij}^{T}=\sigma_{ij}+\sum_{\alpha}\sigma_{ij}^{\alpha}-{}^{L}E_{(i}P_{j)}-{}^{L}B_{(i}\mathscr{M}_{j)}+{}^{L}\mathscr{E}_{(i|,k|}\pi_{j),k}+\beta\,{}^{L}\mathscr{B}_{(i|,k|}\mu_{j),k} \tag{2.61}$$

and where ${}^{L}E_{i}^{T}$, ${}^{L}B_{i}^{T}$, ${}^{L}\mathscr{E}_{ik}^{T}$ and ${}^{L}\mathscr{B}_{ik}^{T}$ are respectively defined previously.

Recalling that $\boldsymbol{\phi}=\tilde{\mathbf{q}}/\theta$ and accounting for the latter eqns, we can rewrite the Clausius-Duhem inequality (2.59) in the useful form [3]:

$$\begin{aligned} &-\rho\left(\frac{d\psi}{dt}+\eta\frac{d\theta}{dt}\right)+\tilde{t}_{ij}^{T}D_{ij}+\mu_{ijk}v_{i,jk}-{}^{L}E_{i}^{T}\overset{*}{P}_{i}-{}^{L}B_{i}^{T}\overset{*}{\mathscr{M}}_{i}+{}^{L}\mathscr{E}_{ik}^{T}\widehat{\pi}_{ij}+\beta\,{}^{L}\mathscr{B}_{ik}^{T}\widehat{\mu}_{ij}\\ &+\sum_{\alpha}\mathscr{E}_{i}^{\alpha(eff)}\mathscr{J}_{i}^{\alpha}+\sum_{\alpha}\mu^{\alpha}\left(\rho\frac{dc_{\lambda}^{\alpha}}{dt}-r^{\alpha}\right)+\theta\,\tilde{\boldsymbol{q}}\cdot\nabla\left(\frac{1}{\theta}\right)\geq 0 \end{aligned} \tag{2.62}$$

As is well known, the Clausius-Duhem inequality plays a major role in the building of constitutive relations.

2.2 Second Part

2.2.1 Extension of the PVP to Gauge and Scale Invariances

The scalar method known as the principle of virtual power—applied to mechanics with microstructures by Germain [4, 5], then to electro-magneto-mechanics by Maugin and his students [7, 8, 10, 11]—has brought remarkable advances. This method based on the duality notion subject to translational and rotational invariances is extended here to gauge and scale invariances, leading thus to a more unifying principle, apt to account for a wider range of applications as shown in [21–24].

After having extended the principle of virtual power to complex structures including conduction and diffusion effects of various charge carriers (semi-conduction), it seemed advisable to acquire a more unifying, systematic and universal framework, adapting this formal and reliable method to other types of symmetries and invariances thanks to its use of the fruitful concepts of modern geometry.

This was done by borrowing concepts from theoretical physics, particularly gauge theories (serious candidates for the unification of the four forces of interaction of fundamental physics). Thus, scale and gauge invariances were introduced into the physics of continuous media. These two types of invariances add to the well-known translational and rotational invariances (objectivity requirement) already dealt with in electro-magneto-mechanics. Gauge invariance allows to account for Maxwell's electromagnetism analogously to rotational invariance for deformable bodies. As to scale invariance, it allows to deal with the various forms of discontinuities and interfacial properties that occur at singular surfaces, lines and/or points.

These aspects have been presented succinctly in congresses [22–24] and in a synthetic paper [21] more than twenty years ago, both in Newtonian and Einsteinian chronologies, but this theoretical theme, considered too remote from the immediate concerns of the laboratory, had not been pursued further at that time.

In the last decade, some works together with Hirsinger and Devel showed the need for such a general and systematic methodology (see for instance [3]) that will be succinctly recalled here and developed in future works.

2.2.2 *Extended form of d'Alembert's Principle*

Statical continuum mechanics and magnetism are the simplest examples where the basic ideas are brought out clearly. In addition, since a boundary may be regarded as a particular case of a moving singular surface, one may omit its expression in the present derivation. Only the essential elements are kept here. The attention is focused on the three different invariance principles that govern discontinuities as well as Maxwell electromagnetism and deformable mechanics.

2.2.3 *Unified Global Statement*

The basic postulate may be expressed in the form of an orthogonality relation as follows:

$$\delta W^{*} = \langle \boldsymbol{D}, \delta \overset{*}{G} \rangle = 0 \tag{2.63}$$

where δG is an infinitesimal variation of the geometrical parameter $\boldsymbol{G}$ and $\boldsymbol{D}$ is the dynamical contribution introduced by duality. A star * on a field denotes its virtual character. In the present framework, it is convenient to distinguish between three types of energies as follows:

$$\delta W^* = \delta W^*_{GIV} + \delta W^*_{GRI} + \delta W^*_{SCI} = 0 \tag{2.64}$$

In a first-order gradient framework associated with volume and surface physical contributions, one may write:

$$\delta W^*_{GIV} = \int\limits_{\mathcal{D}-\Sigma} \left(K_i \delta R^*_i + K_{ij} \nabla_j \, \delta R^*_i\right) dv + \int\limits_{\Sigma} \left(\hat{K}_i \hat{\delta} \hat{R}^*_i + \hat{K}_{ij} \nabla_j \, \hat{\delta} \hat{R}^*_i\right) da \tag{2.65}$$

$$\delta W^*_{GRI} = \int\limits_{\mathcal{D}-\Sigma} \left(A_i \delta R^*_i + A_{ij} \nabla_j \, \delta R^*_i\right) dv + \int\limits_{\Sigma} \left(\hat{A}_i \hat{\delta} \hat{R}^*_i + \hat{A}_{ij} \hat{\nabla}_j \, \hat{\delta} \hat{R}^*_i\right) da \tag{2.66}$$

$$\delta W^*_{SCI} = \int\limits_{\Sigma} \left(Z^+_i \delta^+ R^{*+}_i - Z^-_i \delta^- R^{*-}_i + \hat{Z}_i \hat{\delta} \hat{R}^*_i\right) da \tag{2.67}$$

where dv is the volume element of the bulk medium $\mathcal{D} - \Sigma$, da is the surface element of the interface Σ and $\hat{\nabla}$ denotes the surface gradient, + and − denote quantities on either side of the singular surface and ^ the quantity at the singular surface.

The expressions of δW^*_{GIV} and δW^*_{GRI} (*GIV* for given fields, *GRI* for gauge and rotational invariance) are introduced in a systematic manner. $\left(K_i, K_{ij}\right)$ and their surface counterparts $\left(\hat{K}_i, \hat{K}_{ij}\right)$ correspond to given fields. A quantity for which no physical support is available can be dropped from Eq. (2.65). As to the expression of δW^*_{GRI}, it should be specified through a physical invariance principle. More precisely, gauge invariance (Electromagnetism) and rotational invariance (Mechanics) will impose restrictions on the form of δW^*_{GRI}. As shown below, the dual field A_{ij} will be skew-symmetrical (in Electromagnetism) and symmetrical (in Mechanics). And the dual fields A_i and $\hat{A}_i$ will vanish in both cases since they violate the invariance requirements. Physically, these invariance principles will give the correct form of the field-field interaction energy (magnetic energy) and of the matter-matter interaction energy (deformation energy). Thus, a net distinction is made between given fields and those deduced from a physical invariance principle.

Across the interface, one loses differentiability, thus, a general form of the interaction energy between the bulk and the interface is given by Eq. (2.67). Its construction is performed by taking all the energies that one may construct at the interface and its surrounding. This leads to the introduction of three vector fields, to be coupled together as well as with the fields present in Eqs. (2.65) and (2.66). A full determination is obtained in two steps. First, the scale invariance principle

relates $\hat{Z}$ to $Z^{\pm}$, then the use of the virtual character through the application of the principle for any $\delta R^{\pm}$ will lead to the determination of $Z^{\pm}$. The scale invariance principle asserts that Eq. (2.67) must remain invariant under the addition of any continuous infinitesimal vector field. This requirement governs the passage from a continuous to a discontinuous medium. Before dealing with the three invariance principles, let us recall that the present formulation may be regarded as a generalization of the well-known Lagrangian approach, (recovered for integrable systems, $A_i \equiv \partial L/\partial R_i$). In the present formulation, no hypothesis of integrability is imposed. This offers richer possibilities, particularly in the framework of dissipative phenomena and irreversible processes.

2.2.4 *Derivation of Scale, Gauge and Rotational Invariances*

The attention is focused here on the formal unifying structure. The physical details are provided in Refs. [21–24]. One way to deal with invariance principles consists in requiring that the energy remains invariant under the addition of a certain infinitesimal field. Mathematically, one writes

$$\overset{\alpha}{\boldsymbol{\delta}} \overset{\alpha}{R'} = \overset{\alpha}{\boldsymbol{\delta}} \overset{\alpha}{R} + \boldsymbol{\delta} r \quad \alpha = \{+, -, \wedge\} \tag{2.68}$$

A—Scale invariance corresponds to $r = a$, where a is any continuous vector field (i.e. $[\![a]\!] = 0$)

This requirement transforms Eq. (2.67) into

$$\delta W^{*}_{SCI} = \int [\![Z_i \left(\delta R^{*}_i - \delta \hat{R}^{*}_i \right)]\!] \, da \tag{2.69}$$

where $[\![A]\!] \equiv A^{+} - A^{-}$ denotes the jump from the + to the – side of the interface.

B—Gauge invariance consists in taking $r = \nabla\psi$, where ψ is any scalar field. As to $\boldsymbol{\delta R}$, it coincides here with an infinitesimal variation of a vector potential $\boldsymbol{\delta A}$. The consequence of this invariance on Eq. (2.66) leads to

$$A_i = 0, \qquad \hat{A}_i = 0, \qquad H_{ij} \equiv A_{ij} \tag{2.70}$$

such that

$$H_{ij} + H_{ji} = 0$$

and

$$\overset{S}{H}_{ij} \equiv \hat{A}_{ij} \tag{2.71}$$

such that

$$\overset{S}{H}_{ij} + \overset{S}{H}_{ji} = \overset{S}{H}_{ik}\, n_k\, n_j + \overset{S}{H}_{jk}\, n_k\, n_i$$

where H_{ij} and $\overset{S}{H}_{ij}$ are respectively volume and surface magnetic fields which are pseudo-vectors expressed here in tensorial form.

C—Rotational invariance (or objectivity requirement) is expressed through a rigid body motion transformation $r = X + \boldsymbol{\omega} \times x$ ($\boldsymbol{X}$: translations, $\boldsymbol{\omega}$: Rotations). This leads to

$$A_i = 0, \qquad \hat{A}_i = 0, \qquad \sigma_{ij} \equiv -A_{ij} \tag{2.72}$$

such that

$$\sigma_{ij} - \sigma_{ji} = 0$$

and

$$\overset{S}{\sigma}_{ij} \equiv -\hat{A}_{ij} \tag{2.73}$$

such that

$$\overset{S}{\sigma}_{ij} - \overset{S}{\sigma}_{ji} = \overset{S}{\sigma}_{ik}\, n_k\, n_j - \overset{S}{\sigma}_{jk}\, n_k\, n_i$$

In this case $\boldsymbol{\delta R}$ coincides with an infinitesimal displacement and σ_{ij} is none other than the mechanical stress tensor.

2.2.5 *Local Equations*

On assuming that Eq. (2.64) holds good for all virtual fields and any element of volume and surface, one obtains the following local equations after using the volume and surface divergence theorems:

$$K_i = \nabla_i\, A_{ij}, \quad \hat{K}_i = \tilde{\nabla}_i\, \hat{A}_{ij} + [\![A_{ij}]\!] n_j \tag{2.74}$$

$$\tilde{\nabla} = \hat{\nabla} + 2\overset{m}{\Omega}\,\boldsymbol{n}, \qquad 2\overset{m}{\Omega} = -\hat{\nabla}\cdot\boldsymbol{n} \tag{2.75}$$

($\overset{m}{\Omega}$: mean curvature, $\hat{\nabla}$: surface gradient).

Notice that a tensorial framework offers interesting similarities between mechanical and electromagnetic energies. Here $K_{ij}\,\delta A_{\{i,j\}}$ is none other than deformation energy (mechanics) or magnetic energy (magneto-statics).

2.2.6 Relativistic Framework

Another important feature in such a derivation is its natural generalization to a relativistic framework. Indeed, the basic postulates (2.63)–(2.64) and the invariance requirements (2.68)–(2.73) still hold. The only difference is that one needs to express the fields in a Lorentzian 4-dimensional space. Thus, Eq. (2.74) is to be replaced by

$$K^{\alpha} = \partial_{\beta}\,A^{\alpha\beta}, \quad \hat{K}^{\alpha} = \hat{\partial}_{\beta}\,\hat{A}^{\alpha\beta} + [\![A^{\alpha\beta}]\!]N_{\beta} \tag{2.76}$$

$$\alpha,\ \beta = \{1,\ \ldots 4\}$$

where ∂_{β}, $\hat{\partial}_{\beta}$ and N_{β} are the 4 dimensional analogues of ∇_j, $\hat{\nabla}_j$ and n_j. For lack of space, we only recall the relation between $\boldsymbol{N}$ and $\boldsymbol{n}$

$$N_i = n_i/\sqrt{1-\hat{v}_n^2}, \qquad N_4 = -\hat{v}_n/\sqrt{1-\hat{v}_n^2} \tag{2.77}$$

when $\hat{v}_n^2 \ll 1$, $\hat{\partial}_i \to \nabla_i$ and $\hat{\partial}_4 \to \hat{\partial}/\partial t = \partial/\partial t + \hat{v}_n\left(n\cdot\nabla - 2\overset{m}{\Omega}\right)$.

It is important to note here, that dealing with interfaces in a relativistic framework does not only yield more general solutions but also leads to simple covariant expressions. The simplicity criterion is essential here to verify the coherence of the theory. Indeed, the lack of symmetry between space and time in a Galileen framework leads to complicated expressions. When applied to electromagnetism, Eq. (2.76) may be explicitly written as:

$$J^{\alpha} = \partial_{\beta}\,H^{\alpha\beta}, \qquad \hat{J}^{\alpha} = P^{\gamma}_{\beta}\,\partial_{\gamma}\,\hat{H}^{\alpha\beta} + \hat{H}^{\beta\gamma}\Gamma^{\alpha}_{\gamma\beta} + [\![H^{\alpha\beta}]\!]N_{\beta} \tag{2.78}$$

$$P^{\gamma}_{\beta} = \delta^{\gamma}_{\beta} - N_{\beta}N^{\gamma}, \quad \Gamma^{\alpha}_{\gamma\beta} = N_{\gamma}\left\{P^{\theta}_{\beta}\,\partial_{\theta}\,N^{\alpha} - \hat{\partial}\cdot N\,\delta^{\alpha}_{\beta}\right\}, \quad \overset{s}{J}{}^{\alpha} = P^{\alpha}_{\beta}\,\hat{J}^{\beta} \tag{2.79}$$

Let us recall that the passage from 4 to (3 + 1) dimensions transforms $J^{\alpha} = \partial_{\beta}\,H^{\alpha\beta}$ such that $H^{\alpha\beta} + H^{\beta\alpha} = 0$ into $q_f = \nabla\cdot\boldsymbol{D}$ and $\boldsymbol{J} = -\partial\boldsymbol{D}/\partial t + \nabla\times H$.

The interfacial expression is written in such a manner that one may distinguish between three contributions: (i) the spatio-temporal variation of $\hat{H}^{\alpha\beta}$ (counterpart of the volume expression), (ii) its coupling with the surface curvature $\Gamma^{\alpha}_{\gamma\beta}$ and (iii) the jump relation.

This energy formulation may also account for singular lines by analogy to singular surfaces as explicitly shown in [21–23].

In conclusion, let us recall that the second part of this work extends the ideas expressed in the works of professors Germain and Maugin who developed d'Alembert's principle in different contexts by exploiting the invariance under a rigid body motion.

2.3 Third Part

2.3.1 Foundation of the Principle of Virtual Power (PVP)

The principle of virtual power is a scalar (geometrical) approach, based on the duality notion that corresponds to one point of view among others. We shall go back to the source of this notion thanks to an intrinsic (viewpoint independent) dynamical framework conceptualized by Leibniz and formalized recently in Refs. [25–28]. This framework clearly distinguishes between worlds and points of view. A dynamical world is formally expressed through a relation that links directly the two conserved entities (energy and impulse): $E = F(p)$ or more generally $R(E,\ p) = C$ (constant). As to a point of view attached to a specific world, it consists in expressing impulse and energy in terms of a motion parameter x: $p = g(x),\ E = f(x)$. Obviously, if this point of view is relative to the above world $E = F(p)$, then the three functions F, g and f cannot be independent anymore. They must satisfy: $E = F(p) = F(g(x)) = f(x)$.

Unlike usual physics, limited to one world (Newtonian, Einsteinian, Finslerian …) dealt with through one point of view (variational, geometrical, group theoretical …), Leibniz's conception accounts for all physically admissible worlds (i.e. compatible with the relativity and conservation requirements) independently of any a priori imposed point of view whatsoever. Such a conception is characterized by its intrinsic (viewpoint independent) nature where the different dynamical worlds are deduced before the determination, by self-organization, of the appropriate points of view attached to each world.

The principle of virtual power, like other analytical principles such as the principle of least action, appears henceforth as a theorem. These turn out to be deductible from a weaker principle, using qualitative mathematics, from which different quantitative dynamical structures—each constituting one point of view—are derived. Among these dynamical structures, one recognizes the ones that correspond to the well-identified physical principles developed in the history of

dynamics. Here, the attention will be focused on the source of the duality notion which is at the basis of the principle of virtual power.

2.3.2 Main Points of the Leibnizian Dynamical Framework

The Leibnizian formulation takes its origin from a dynamical procedure, due to Huygens, based on the relativity and conservation principles, in (1 + 1) dimensions, recalled in Eqs. (9.11)–(9.14) of Ref. [29], by the physicist and historian of science Barbour.

Elevated to the rank of a principle and expressed in the Leibnizian language of infinitesimal calculus, Huygens dynamics is formally expressed by: $M = d^2E/dw^2$, with $M = m$, $p = dE/dw$ and the limit conditions $w = 0$, $p = 0$, $E = E_0$, where the motion parameter w satisfies an additive composition law $\left(w' = w + W\right)$. Its integration leads to: $p = m\ w$ and $E = 1/2\ m\ w^2 + E_0$. This method (recently justified by a theorem borrowed from group theory) was revived by many authors [30–34] and applied to Einstein's dynamics where the constant $(M = m)$ is replaced by the linear relation $(M = E/c^2)$.

In order to account for all physically admissible worlds and associated points of view, we have extended Huygens procedure according to Leibniz's conceptualization, characterized by the simultaneous presence of an infinity of points of view on each dynamical world [25–28]. Such a conceptualization is called architectonical by opposition to the usual analytical conceptualization, limited to one point of view a priori imposed from the start.

As a consequence, instead of the above differential equation $M = d^2E/dw^2$, relative to Huygens conception, that accounts for one world $(M = m)$, corresponding to: $E = p^2/2\ m + E_0$, dealt with through one point of view $(p = dE/dw)$, expressed by the motion parameter w attached to the operator d/dw, one is led, as shown explicitly in [25, 26], to an infinity of differential equations $M = d_\mu^2 E/dv_\mu^2$, corresponding to Leibniz's conception, that account for all dynamically admissible worlds $\left(M = \lambda E + \gamma d_\mu E/dv_\mu + \eta\right)$, each one dealt with through an infinity of points of view $\left(p = d_\mu E/dv_\mu\right)$, expressed by the motion parameters v_μ attached to the infinitely multiple μ-operator: $d_\mu/dv_\mu = I_\mu d/dv_\mu$ where the functions I_μ that depend on v_μ are yet indeterminate. The functions I_μ reflect the non-additive composition laws $\left(v_\mu' \neq v_\mu + V_\mu\right)$ that accompany the additive one $\left(v_a' = v_a + V_a\right)$ for which I_a reduces to unity $(I_a = 1)$.

In brief, the passage from the Huygensian analytical conception to the Leibnizian architectonical one, amounts to replace: $M = m = d^2E/dw^2$ with $p = dE/dw$ by the following under-determinate structure: $M = \lambda E + \gamma d_\mu E/dv_\mu + \eta = d_\mu^2 E/dv_\mu^2$ with $p = d_\mu E/dv_\mu$ expressed explicitly by:

$$M = \lambda E + \gamma\ I_\mu dE/dv_\mu + \eta = \left[I_\mu d/dv_\mu\right]\left[I_\mu d/dv_\mu\right]E \\ = I_\mu^2 d^2E/dv_\mu^2 + \left[I_\mu dI_\mu/dv_\mu\right]\ dE/dv_\mu \tag{2.80}$$

At first sight, it seems contradictory to associate the term "world" with the above expression of M because of its viewpoint dependence. But this apparent contradiction vanishes by showing, as done in [25], that Eq. (2.80) transform into an intrinsic (viewpoint independent) framework, expressed uniquely in terms of the conserved entities E and p as follows: $M = \lambda E + \gamma p + \eta = [pd/dE][pd/dE]E = [p^2d^2/dE^2 + (pd/dE)d/dE]E = pdp/dE$. When integrated, this differential equation becomes formally expressed through a relation that links together the two conserved entities (energy and impulse): $R(E,\ p) = C$. One recovers thus what is called above a dynamical world. This procedure, called in [25–28] a "filtering procedure", characterizes the Leibnizian intrinsic approach where the determination of the worlds precedes and contributes to the specification of the points of view.

2.3.3 *Determination of the Yet Under-Determinate Framework*

The attention will be focused here on the Newtonian (parabolic) and Einsteinian (hyperbolic) worlds that correspond respectively to: $(\lambda,\ \gamma,\ \eta) = (0,\ 0,\ m)$ and $(\lambda, \gamma, \eta) = (E/c^2, 0, 0)$, getting thus: $M = m$ and $M = E/c^2$. These two dynamical worlds can be expressed in a unified differential form by: $M = m(E/m\,c^2)^k = p\,dp/dE$ with $k = 0$ for Newton and $k = 1$ for Einstein.

Its integration will provide valuable information that will actively contribute to the determination of the infinity of the yet indeterminate points of view as shown in [25]. Thus, one is led to the multiple scale law:

$$I_\mu = (M/m)^{2-\mu} = \left[\left(E/m\ c^2\right)^k\right]^{2-\mu} \tag{2.81}$$

Having specified the functions I_μ, the under-determinate structure (2.80) becomes well determinate: it includes an infinity of quantitative equations, each value of μ corresponding to a particular point of view. Among the infinity of points of view, the formal structure singles out four basic (singular, remarkable and operational) points of view, the others corresponding to more or less complicated combinations of the four basic ones. The three well-identified points of view relative to the three different principles (Lagrangian formulation, d'Alembert's principle and Huygens procedure) expressed in mathematical terms by the calculus of variations, modern geometry and group theory, turn out to be deductible from the points of view of orders $\mu = \{4,\ 1\ and\ 2\}$ respectively as shown in [25–28]. Since we are mainly concerned here with d'Alembert's (or virtual power) principle, the

attention will be focused on the procedure that allows deriving it from the present general Leibnizian approach.

2.3.4 Deduction of the PVP Based on Duality

As shown in [25–28] for the point of view of order one $(\mu = 1)$, we get: $I_1 = M/m = (E/m\,c^2)^k$ and $p = I_1\,dE/dv_1 = m\,v_1$ from which one deduces: $p\,dv_1 = v_1\,dp$ (since $dp = m\,dv_1$), at the basis of the duality notion. Its combination with $p = I_1 dE/dv_1$ leads to: $I_1\,dE - p\,dv_1 = I_1\,dE - v_1\,dp = 0$ so that one is finally left with: $M\,c = m\,c\,I_1$, $p = m\,v_1$ and $I_1\,dE - v_1\,dp = 0$.

With the well-known compact notation: $(M\,c, p) = \boldsymbol{P} = \{P^i\}$, $(E/c, p) = \boldsymbol{p} = \{p^i\}$ and $(c\,I_1, v_1) = \boldsymbol{u} = \{u^i\}$ with $i = 0, 1$, one gets: $\boldsymbol{P} = m\,\boldsymbol{u}$ and $\boldsymbol{u} \cdot d\boldsymbol{p} = 0$ where the scalar product: $\boldsymbol{u} \cdot d\boldsymbol{p} = 0$ is associated with Minkowski's signature $\eta = (1, -1)$.

In order to replace the infinitesimal form: $\boldsymbol{u} \cdot d\boldsymbol{p} = 0$ by a finite one: $\boldsymbol{u} \cdot \boldsymbol{f} = 0$, leading thus to the concept of force, we set: $\boldsymbol{f} = d\boldsymbol{p}/d\tau$, then analogously: $\boldsymbol{F} = d\boldsymbol{P}/d\tau$ and $\boldsymbol{a} = d\boldsymbol{u}/d\tau$. This allows writing: $\boldsymbol{F} = m\,\boldsymbol{a}$ and $\boldsymbol{u} \cdot \boldsymbol{f} = 0$. These two vector and scalar expressions can be unified into a unique scalar formalism: $(\boldsymbol{F} - m\,\boldsymbol{a}) \cdot \boldsymbol{u}^* = 0$ and $\boldsymbol{u} \cdot \boldsymbol{f} = 0$, provided one accounts for a virtual motion $\boldsymbol{u}^*$. This formulation that goes back to d'Alembert corresponds to the principle of virtual power.

2.3.5 Derivation of Einstein's Dynamics

For $k = 1$ (Einstein's world), $\boldsymbol{f}$ reduces to $\boldsymbol{F}$ because $\boldsymbol{p} = \boldsymbol{P}$ since $E/c = M\,c$, getting thus: $(F - m\,a) \cdot \boldsymbol{u}^* = 0$ and $\boldsymbol{u} \cdot F = 0$.

Let us firstly show that this general dynamical approach, will naturally lead to space-time thanks to the duality property. Indeed, by combining: $\boldsymbol{u} \cdot d\boldsymbol{p} = \boldsymbol{u} \cdot \boldsymbol{f}\,d\tau$ with: $\boldsymbol{u} \cdot \boldsymbol{f} = \boldsymbol{f} \cdot \boldsymbol{u}$, one gets the following expressions: $\boldsymbol{u} \cdot d\boldsymbol{p} = \boldsymbol{u} \cdot \boldsymbol{f}\,d\tau = \boldsymbol{f} \cdot \boldsymbol{u}\,d\tau = \boldsymbol{f} \cdot d\boldsymbol{x}$, where we have set: $d\boldsymbol{x} = \boldsymbol{u}\,d\tau$. In the same way as $\boldsymbol{u}$ is the dual of $d\boldsymbol{p}$, $\boldsymbol{f}$ appears as the dual of $d\boldsymbol{x}$. As shown below, when $\boldsymbol{f} = \boldsymbol{F}$, $d\boldsymbol{x}$ corresponds to space-time variation.

On assuming that the relation $(\boldsymbol{F} - m\,\boldsymbol{a}) \cdot \boldsymbol{u}^* = 0$ subject to: $\boldsymbol{u} \cdot \boldsymbol{F} = 0$ holds true for any virtual motion $\boldsymbol{u}^*$, one derives: $\boldsymbol{F} = m\,\boldsymbol{a}$ and $\boldsymbol{u} \cdot \boldsymbol{a} = 0$. Their integration leads to: $\boldsymbol{p} = m\,\boldsymbol{u}$ and $\boldsymbol{u} \cdot \boldsymbol{u} = C$ where C is a constant of integration. On setting $C = c^2$, with c having the dimension of a velocity and accounting for $d\boldsymbol{x} = \boldsymbol{u}\,d\tau$, one is left with: $\boldsymbol{p} = m\,d\boldsymbol{x}/d\tau$ and $d\boldsymbol{x} \cdot d\boldsymbol{x} = c^2 d\tau^2$ where one recognizes Einstein's dynamics with its metrical structure.

Final remark: In order to establish a direct link with the present approach, let us note that the metrical structure may be explicitly written as: $\Gamma^2 - u^2/c^2 = 1$, with $\Gamma = dt/d\tau$ and $u = dx/d\tau$. The couple (Γ, u) that reflects the relativistic factor and

the celerity respectively corresponds to: $(I_1,\ v_1)$ subject to: $I_1^2 - v_1^2/c^2 = 1$. It is easily deduced from the general relation between I_μ and v_μ:

$$I_\mu^{2/(2-\mu)} - \frac{1}{c^2}\left(\int I_\mu^{(\mu-1)/(2-\mu)} dv_\mu\right)^2 = 1 \tag{2.82}$$

derived from the Leibnizian architectonical approach. Indeed, for $\mu = 1$, this expression greatly simplifies getting: $I_1^2 - v_1^2/c^2 = 1$ which is formally similar to: $I^2 - u^2/c^2 = 1$ but with a different interpretation.

According to the architectonical approach where dynamics precedes kinematics and determines it, the principle of virtual power, based on the duality notion between kinematical and dynamical entities $(\boldsymbol{u}\ and\ f)$ is not postulated anymore: it corresponds to the point of view of order one $(\mu = 1)$ deduced from a higher intrinsic principle apt to include various singular, remarkable and operational points of view including those developed in the history of science as shown in [26, 27].

Acknowledgements This study relative to the principle of virtual power, based on the notions of duality and invariance, owes much to the scientific formation that one of us received directly, in Paris, from Professor Maugin and his first students and collaborators, mainly B. Collet and J. Pouget. As for its extension to gauge and scale invariances and the search for a more solid conceptual basis likely to go back to the origin of the notion of duality, they would not have been possible without the contributions, remarks and criticism of the members (epistemologists, physicists and mathematicians) of the "Epiphymaths" group (an interdisciplinary seminar held weekly at Besançon), especially, J. Merker who presented, in the nineties of the last century, recent studies concerning an autonomous dynamical framework, dealt with through group theory, and C. A. Risset who, later on, accompanied this research over the years, bringing different suggestions and improvements.

References

1. Daher, N., Maugin, G.A.: Deformable semiconductors with interfaces: basic continuum equations. Int. J. Eng. Sci. **25**, 1093–1129 (1987). https://doi.org/10.1016/0020-7225(87)90076-0
2. Maugin, G.: The method of virtual power in continuum mechanics: application to coupled fields. Acta Mech. **35**, 1–70 (1980)
3. Lecoutre, G., Daher, N., Devel, M., Hirsinger, L.: Principle of virtual power applied to deformable semiconductors with strain, polarization, and magnetization gradients. Acta Mech. **228**, 1681–1710 (2017). https://doi.org/10.1007/s00707-016-1787-y
4. Germain, P.: La méthode des puissances virtuelles en mécanique des milieux continus. Première partie: Théorie du second gradient. J. Mécanique **12**, 236–274 (1973)
5. Germain, P.: The Method of virtual power in continuum mechanics. Part 2: microstructure. SIAM J. Appl. Math. **25**, 556–575 (1973)
6. Maugin, G.A.: Continuum mechanics of electromagnetic solids. North-Holland (1988)
7. Maugin, G.A., Pouget, J.: Electroacoustic equations for one-domain ferroelectric bodies. J. Acoust. Soc. Am. **68**, 575–587 (1980). https://doi.org/10.1121/1.384770

8. Daher, N., Maugin, G.A.: Virtual power and thermodynamics for electromagnetic continua with interfaces. J. Math. Phys. **27**, 3022–3035 (1986). https://doi.org/10.1063/1.527231
9. Collet, B.: Higher order surface couplings in elastic ferromagnets. Int. J. Eng. Sci. **16**, 349–364 (1978). https://doi.org/10.1016/0020-7225(78)90025-3
10. Collet, B., Maugin, G.A.: Sur l'électrodynamique des milieux continus avec interactions. C r À Académie Sci t. **279**, 379–382 (1974)
11. Collet, B., Maugin, G.A.: Thermodynamique des milieux continus électromagnétiques avec interactions. C r À Académie Sci t. **279**, 439–442 (1974)
12. Collet, B.: Sur une théorie des premier et second gradients des milieux continus électromagnétiques. Ph.d. Thesis, Pierre et Maire Curie (1976)
13. Maugin, G.A.: A continuum theory of deformable ferrimagnetic bodies. I. Field equations. J. Math. Phys. **17**, 1727–1738 (1976). https://doi.org/10.1063/1.523101
14. Eringen, A.C., Maugin, G.A.: Electrodynamics of Continua I: Foundations and Solid Media (1990)
15. Maugin, G.A.: The principle of virtual power: from eliminating metaphysical forces to providing an efficient modelling tool. Contin. Mech. Thermodyn. **25**, 127–146 (2011). https://doi.org/10.1007/s00161-011-0196-7
16. Fousek, J., Cross, L.E., Litvin, D.B.: Possible piezoelectric composites based on the flexoelectric effect. Mater. Lett. **39**, 287–291 (1999). https://doi.org/10.1016/S0167-577X(99)00020-8
17. Cross, L.E.: Flexoelectric effects: charge separation in insulating solids subjected to elastic strain gradients. J. Mater. Sci. **41**, 53–63 (2006). https://doi.org/10.1007/s10853-005-5916-6
18. Majdoub, M.S., Sharma, P., Cagin, T.: Enhanced size-dependent piezoelectricity and elasticity in nanostructures due to the flexoelectric effect. Phys. Rev. B **77**, 125424 (2008)
19. Maugin, G.A., Eringen, A.C.: On the equations of the electrodynamics of deformable bodies of finite extent. J. Mécanique **16**, 101–147 (1977)
20. Eringen, A.C.: Mechanics of Continua, 2nd edn. Krieger Pub Co, Huntington, N.Y. (1980)
21. Daher, N.: On a general non integrable, multiple scale continuum energy formulation. Application to acoustic, optics and coupled effects. Curr. Top. Acoust. Res. (1994)
22. Daher, N.: Leibniz-D'Alembert energy formulation, application to piezoelctric media with interfaces. In: Proceedings Vol II Poster Contributions (1994)
23. Daher, N.: Energy formulation for electronic, optical and acoustical applications including interfacial properties and irreversible processes. Synth. Met. **67**, 287–291 (1994). https://doi.org/10.1016/0379-6779(94)90058-2
24. Daher, N.: Electromagnetomechanical media including irreversible processes and interfacial properties. Synth. Met. **76**, 327–330 (1996). https://doi.org/10.1016/0379-6779(95)03482-Y
25. Daher, N.: Approche multi-échelle de la mécanique. 20ème Congrès Fr. Mécanique 28 Août2 Sept 2011-25044 Besançon Fr. FR (2011)
26. Daher, N.: Objectivité, Rationalité et Relativité Scientifiques Le cas de la Dynamique. In: Ann. Fr. Microtech. Chronométrie. Société française des microtechniques et de chronométrie, pp. 78–95 (2009)
27. Daher, N.: D'une Esthétique Analytique vers une Ethique Architectonique au service des Fondements de la Physique, X International Leibniz Congress, Hannover (Germany), July 18–23, 2016
28. Daher, N.: Leibniz's intrinsic dynamics: from principles to theorems. In: XVII International Congress on Mathematical Physics (ICPM12). Aalborg, Denmark, Aug 6–11, 2012
29. Barbour, J.B.: The Discovery of Dynamics: A Study from a Machian Point of View of the Discovery and the Structure of Dynamical Theories, Oxford University Press (2001)
30. Landau, B.V., Sampanthar, S.: A new derivation of the Lorentz transformation. Am. J. Phys. **40**, 599–602 (1972). https://doi.org/10.1119/1.1988057

31. Lévy-Leblond, J.-M., Provost, J.-P.: Additivity, rapidity, relativity. Am. J. Phys. **47**, 1045–1049 (1979)
32. Lévy-Leblond, J.-M.: Speed (s). Am. J. Phys. **48**, 345–347 (1980)
33. Comte, C.: Leibniz aurait-il pu découvrir la relativité. Eur. J. Phys. **7**, 225–235 (1986)
34. Comte, C.: Langevin et la dynamique relativiste. ln Epistémologiques, V 01.2, 1-2. EDP Sci Paris, pp. 225–235 (2002)

Chapter 3
The Limitations and Successes of Concurrent Dynamic Multiscale Modeling Methods at the Mesoscale

Adrian Diaz, David McDowell and Youping Chen

Abstract Dynamic concurrent multiscale modeling methods are reviewed and then analyzed based on their governing equations in terms of consistency in material descriptions between different scales, wave propagation across the numerical interfaces between the different descriptions, and advances in describing defects in the coarse-grained domain. The analysis finds that most methods suffer from the consequences of inconsistent materials descriptions between representations at different scales; a few methods such as Concurrent Atomistic Continuum (CAC), Coupled Atomistic Discrete Dislocation (CADD), and the coupled Extended Finite Element Method (XFEM) are capable of simulating moving defects in the coarse-scale domain to improve practicality and prediction. Application of multi-scale simulation to coupled thermal and mechanical problems is showing promise. Mesoscale evolution of defects, largely beyond the reach of conventional atomistic methods, is still beyond the reach of many concurrent multiscale methods.

A. Diaz (✉) · Y. Chen
Department of Mechanical and Aerospace Engineering, University of Florida, Gainesville, FL 32611-6250, USA
e-mail: adriandiaz@ufl.edu

Y. Chen
e-mail: ypchen2@ufl.edu

D. McDowell
Woodruff School of Mechanical Engineering, Georgia Institute of Technology, Atlanta, GA 30332-0405, USA
e-mail: david.mcdowell@me.gatech.edu

D. McDowell
School of Materials Science and Engineering, Georgia Institute of Technology, Atlanta, GA 30332-0245, USA

H. Altenbach et al. (eds.), *Generalized Models and Non-classical Approaches in Complex Materials 2*, Advanced Structured Materials 90,
https://doi.org/10.1007/978-3-319-77504-3_3

3.1 Introduction

The development of many multiscale methodologies today has been in the interest of seeking enhanced efficiency to address higher length and time scales [1]. Ideally, a multiscale method would provide a vehicle by which the scientific community can overcome the current limiting length and time scales in the established methods of atomistic simulation. The current drive to develop multiscale methods is the simulation of mesoscale defect evolution since atomistic simulations cannot model these processes.

The mesoscale is an inherently dynamic regime, "where energy and information captured at the nanoscale is processed and transformed to create novel outcomes" [2]. The mesoscale also connects the enormously different descriptions between the behavior of atoms at the nanoscale and the functionality and behavior of materials at the higher scales of applications. A multiscale simulation method is useful only if it surpasses the practical challenges of nanoscale methods to tackle challenging mesoscale problems with similar predictive capabilities.

Metamaterials are an emerging class of mesoscale materials [3]; an example is a photonic material of dimension of 1–100 μm with internal surfaces and phase interfaces shown in Fig. 3.1 [4]. Metamaterials are synthetic periodic structures that provide specific functionality through ordering of interfaces; these interfaces alter the dynamics of waves and, consequently, the dynamic properties of the materials [5–13]. For the understanding of a metamaterial, a simulation method should have one or all of the following capabilities:

(1) The ability to reproduce wave propagation. This is essential since physical properties of metamaterials and the underlying mechanisms have been described in terms of waves. In addition, dynamic phenomena in crystalline materials are typically waves, e.g., stress waves, heat waves, sound, and light; each of these possesses characteristic wavelengths.

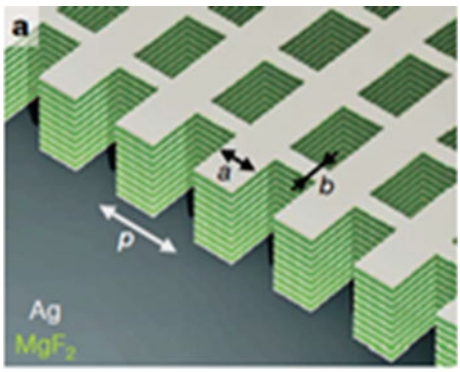

Fig. 3.1 A metamaterial made of Ag and MgF_2 layers (a = 565 nm, b = 265 nm, and p = 860 nm) [4]

(2) The ability to simulate nucleation and propagation of defects. In contrast to nanoscale materials, defects are ubiquitous in mesoscale materials. They determine mechanical properties and alter the functionalities of the materials.
(3) Coupling thermal transport and mechanical behavior. Like defects, thermal behavior is also ubiquitous at the mesoscale. Consequently, thermal and mechanical coupling becomes crucially important to the understanding and prediction of mesoscale material behavior.

This paper aims to assess concurrent multiscale modeling methods, including their theoretical foundations and their capabilities in the simulation of mesoscale material behavior. The objective of a typical concurrent multiscale method designed for mesoscale simulations is to couple the response of a domain modeled at full atom.

Istic resolution to another represented by coarse-graining approximations. The multiscale methodologies encompassed in this review focus on dynamic multiscale methods pursued in the last five years. The specific properties of the Coupled Atomistic Discrete Dislocation (CADD), the coupled Extended Finite Element Method (XFEM), Concurrent Atomistic Continuum (CAC), maximum entropy Quasi-Continuum (HotQC), and Atomistic to Continuum (AtC) methods will be reviewed. The limitations unique to the governing equations, interface treatments, and supplemental equations for each method will be analyzed. Limitations that are shared by most of the methods that affect their utility will also be discussed.

The paper is divided into four sections. After the introduction, each of the dynamic multiscale methods will be described in Sect. 3.2.2. Common challenges to capability will be analyzed in Sect. 3.2.3. Conclusions will be presented in Sect. 3.2.4.

3.2 Review of Dynamic Multiscale Methods

3.2.1 Coupled Atomistic and Discrete Dislocation Dynamics

Coupled Atomistic and Discrete Dislocation Dynamics (CADD) is interested in interfacing phenomenon that require atomistic resolution such as dislocation nucleation, mobility, crack formation, and growth with a continuum model that can represent dislocations through the Discrete Dislocation method [14–16]. The CADD formulation involves the linear superposition of three different problem types, shown in Fig. 3.2, to apply appropriate boundary conditions [17].

The energy and forces of the atomistic region are treated as in a MD model. The atoms are coupled to the continuum at the interface by a set of “pad” atoms that affect the environment for the atoms at the interface. These pad atoms and interface atoms adhere to the continuum displacement field on the continuum side of the interface, i.e., strong compatibility [18]. The nodes of the finite elements present at

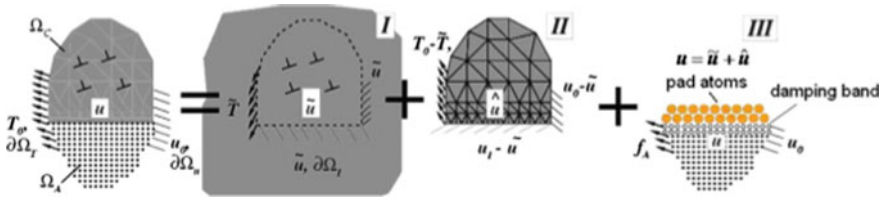

Fig. 3.2 Schematic representation of the CADD problem superposition. The first is the infinite discrete dislocation solution, the second is the corrections required to create the finite element model from the DD solution. Then the atomic conditions are applied [14]

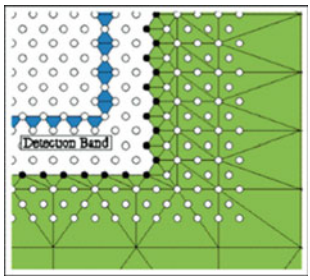

Fig. 3.3 Schematic representation of CADD interface with detection elements shown [14]

the interface must then correspond to interface atoms in the atomistic representation (Fig. 3.3). This completes the description of the coupling on the atomistic region.

The superposition of the problem types for the continuum region necessitates the definition of displacement fields $\tilde{u}$ for the pure DD solution and $\hat{u} = u - \tilde{u}$ for a corrective solution resulting from the Finite Element solution subject to boundary and loading conditions due to the external environment and the coupling interface. The stress fields likewise are superimposed as $\boldsymbol{\sigma} = \hat{\boldsymbol{\sigma}} + \tilde{\boldsymbol{\sigma}}$. The solution for the corrective accelerations $\hat{u}$ follows from the discretization present in problem II. CADD employs linear elastic constitutive laws for the stress within the continuum; the elasticity tensor corresponds to the atomistic crystal structure and potential in a manner that will be described towards the end. The corrective accelerations can thus be solved with the typical mass and stiffness matrices, i.e.,

$$M\ddot{\hat{u}} = K\hat{u} + F_{ext}. \tag{3.1}$$

The last term F_{ext} represents the external equivalent nodal forces. Problem I (The DD model) can then be updated using constitutive laws by computing the Peach-Koehler forces for each dislocation using the resulting stress field $\boldsymbol{\sigma} = \hat{\boldsymbol{\sigma}} + \tilde{\boldsymbol{\sigma}}$. The constitutive relationship ensures the dislocation moves in its specified slip direction. The new dislocation positions are then used to compute the new DD strain field to start the next time-step.

An additional feature of the algorithm is the detection of dislocations in the atomistic region to artificially pass them into the continuum. The lack of this mechanism would result in spurious movement of the dislocation at the interface of the atomistic to continuum region. A detection band of elements is defined near the interface in the atomistic region to this end as in Fig. 3.2; the deformation of these elements is then analyzed and compared to all the known allowable dislocation slip strains in the crystal structure [14, 16].

Spurious reflections of waves emanating from the atomistic domain into the continuum at the interface are removed or minimized by dampening atomic motion. Recently, a parallel CADD algorithm was implemented enabling 3D simulation in LAMMPS [19]. The wave reflection in this implementation is mitigated by dampening only atoms near the interface. Additionally, this method foregoes the passing of dislocations across the interface. The calculation of the continuum elastic modulus tensor C_{ijkl} is performed by performing an MD simulation of an atomistic unit cell.

3.2.2 Coupled Extended Finite Element Method

A method pioneered by Belytschko involves the use of the Extended Finite Element Method (XFEM), a discontinuous framework for finite element analysis, to introduce dislocation slip directions and crack surfaces as part of the continuum description [20]. The method also aims to be adaptive to encapsulate the moving defects with the minimum required atomic resolution; it coarse grains when atomic displacements appear regular enough and refines where defects might move or propagate. The continuum is governed by the use of the "Cauchy Born Rule" in the latest implementations [20, 21]. The purely atomistic region with no enforced coupling is treated just as in MD. The continuum displacement is additively decomposed into the continuous and discontinuous part, i.e.,

$$u(x) = u^C(x) + u^D(x) \tag{3.2}$$

$$u^D(x) = u^{Dd}(x) + u^{Dc}(x) \tag{3.3}$$

where the additional lowercase d signifies dislocation and the lowercase c signifies crack. These two are then defined with Heaviside step functions $H(x)$ as:

$$u^{Dd}(x) = b \sum_{J \in N^\psi} N_J[H(\psi(x)) - H(\psi(x_J))] \tag{3.4}$$

$$u^{Dc}(x) = \sum_{J \in N^\psi} N_J[H(\psi(x)) - H(\psi(x_J))]a_K \tag{3.5}$$

The Heaviside functions present in each of the discontinuous enrichment terms ensures that the only non-zero contribution is made over those elements that are

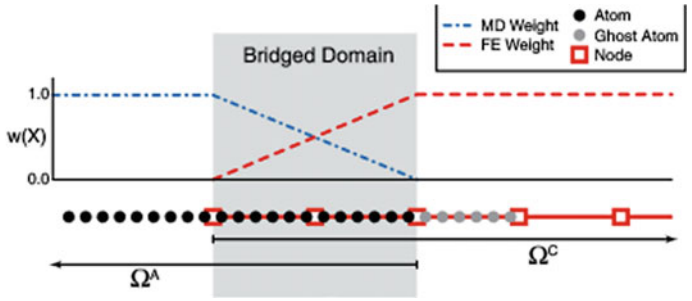

Fig. 3.4 One dimensional example of a bridging domain with linear weighting function [20]

intersected by the crack or the slip direction. The function $\psi(x)$ is defined for a specific slip plane or crack surface; defect location is denoted by $\psi(x) = 0$.

The coupled XFEM method imposes a pair of weighting functions, as shown in Fig. 3.4, to the energy contributions of the atomistic and continuum regions. In this manner, the energy is not double counted at the interface between the atomistic and continuum regions.

The governing equation for the entire system is the Euler Lagrange equations; the Lagrangian is treated discretely in the atomistic and bridging domains while being described with a density in the continuum domain. The Euler-Lagrange equations can be solved with the superposition of all three Lagrangians:

$$L_A = \sum_i \left[w(X_i) m_i v_i^2 - \bar{w}(X_i) U_i) \right] \tag{3.6}$$

$$L_B = \sum_{i \in S^B} \lambda_i [u(X_i) - u_i] \tag{3.7}$$

$$L_C = \int_{V_0^C} \left[(1 - w(X)) \left(\frac{\rho_0(X)}{2} \dot{u}^2(X) - W^C(C(X)) \right) \right] dV_0^C \tag{3.8}$$

The barred weight function in the atomistic Lagrangian represents the effective weight computed for a non-local interaction; typically this involves an average of the sum of weights for the interacting atoms. The two properties inherently enforcing the coupling are the weight function and the Lagrange multipliers applying constraint forces in the bridging domain. The procedure is spatially scalable due to its adaptive remeshing tactics; it coarsens where atomistic displacements are smooth enough and transitions to an atomistic description where finite elements may cause inaccuracy as shown schematically in Fig. 3.5.

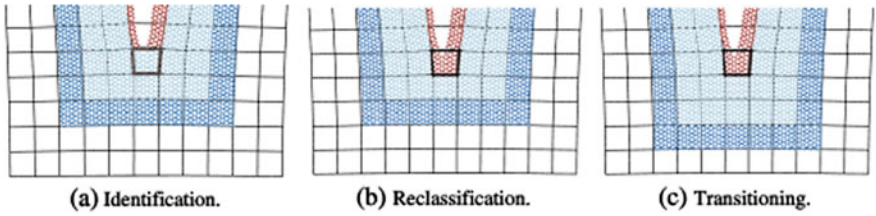

Fig. 3.5 Example of mesh refinement into atomistic degrees of freedom [20]

3.2.3 Concurrent Atomistic Continuum Method

The concurrent atomistic-continuum (CAC) method is a coarse-grained atomistic method employing a two-level structural description of crystalline materials [22]. It builds on the solid-state physics description of crystals and the nonequilibrium statistical mechanics of transport processes. Solid state physics describes the structure of all crystals in terms of a periodic lattice with a basis of atoms attached to each lattice point [23] (cf. Fig. 3.6). As the size of the lattice increases, the structure and its response become increasingly amenable to a continuous field representation [2]. In contrast to many existing multiscale methods that coarse-grain the atomic-level structure or displacements, CAC reduces the degrees of freedom by assuming continuous deformation of the lattice while retaining the internal degrees of freedom within any given unit cell in the case of polyatomic crystals.

The CAC balance laws are formulated using the formalism of Kirkwood for the "statistical mechanical theory of transport processes" [25, 26]. CAC extends Kirkwood's theory of transport processes for "single phase single component systems" to the description of materials having internal degrees of freedom first envisioned by Kirkwood [26]. Consequently, a crystalline material is viewed as a continuous collection of lattice cells with a group of discrete atoms embedded within each lattice cell. This two-level description is also employed in Micromorphic theory and other generalized continuum mechanics (GCM) [27–36], but CAC contrasts with these GCM in that the subscale description consists of discrete atoms. Following the Irving-Kirkwood formalism [25], this concurrent two-level description leads to a concurrent atomistic-continuum representation of the conservation laws of mass, momentum, and energy [37–39], i.e.,

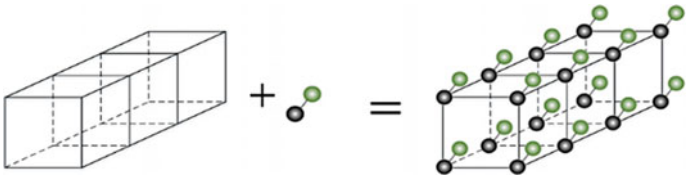

Fig. 3.6 Solid state physics description: "crystal structure = lattice + basis" [24]

$$\begin{aligned} \frac{d\rho^\alpha}{dt} + \rho^\alpha(\nabla_x \cdot v + \nabla_{y^\alpha} \cdot \Delta v^\alpha) &= 0 \\ \rho^\alpha \frac{d}{dt}(v + \Delta v^\alpha) &= \nabla_x \cdot t^\alpha + \nabla_{y^\alpha} \cdot \boldsymbol{\tau}^\alpha + f^\alpha_{\text{ext}} \\ \rho^\alpha \frac{de^\alpha}{dt} &= \nabla_x \cdot q^\alpha + \nabla_{y^\alpha} \cdot j^\alpha + t^\alpha : \nabla_x(v + \Delta v^\alpha) + \boldsymbol{\tau}^\alpha : \nabla_{y^\alpha}(v + \Delta v^\alpha) \end{aligned} \tag{3.9}$$

where x is the physical space coordinate of the continuously distributed lattice; $y^\alpha(\alpha = 1, 2, \ldots, N_a$, where N_a is the total number of atoms in a unit cell) is the internal variable describing the position of atom α relative to the mass center of the lattice located at x; ρ^α, $\rho^\alpha(v + \boldsymbol{\Delta} v^\alpha)$, and $\rho^\alpha e^\alpha$ are the local densities of mass, linear momentum and total energy, respectively; $v + \boldsymbol{\Delta} v^\alpha$ is the atomic-level velocity and v is the velocity field; f^α_{ext} is the external force field; t^α and q^α are the momentum flux and heat flux due to the homogeneous deformation of lattice cells; $\boldsymbol{\tau}^\alpha$ and j^α are the momentum flux and heat flux resulted from the reorganizations of atoms within the lattice cells.

The new conservation equations, supplemented by the underlying interatomic potential, solve for both the continuous lattice deformation and the rearrangement of atoms within the lattice cells, thus leading to a concurrent atomistic-continuum methodology. The same single set of governing equations govern both the atomistic and continuum regions; in the two limiting cases, i.e., the atomic and the macroscopic scales, the atomistic and continuum descriptions of transport processes are recovered. Noteworthy features of CAC include:

(1) There is no need for an artificial interface between atomistic-continuum descriptions that limits most multiscale methods to static phenomena.
(2) CAC can simulate complex crystalline materials and reproduce both acoustic and optical branches of phonons due to its incorporation of internal degrees of freedom; in the coarse-grained regions modeled by finite elements CAC can reproduce accurate phonon dynamics for phonons with wavelengths sufficiently longer than the element size.
(3) The CAC formulation can be solved efficiently using continuum simulation approaches with the only constitutive relation being the interatomic potential. In addition, due to its use of a nonlocal force field, continuity between elements is not required; consequently, nucleation and propagation of dislocations or cracks can be simulated via sliding and separation between elements as direct consequences of the governing equations.

The CAC formulation has been numerically implemented using a modified finite element (FE) method. It differs from traditional FE implementations of classical continuum mechanics since each finite element in CAC contains a collection of primitive unit cells and each FE node corresponds to a primitive unit cell that further contains a group of atoms. Applications of CAC for simulations of mechanical behavior have been demonstrated through reproducing dynamic phenomena, such as crack propagation and branching [40–42], phase transitions [43], nucleation of dislocations and formation of dislocation loops and networks [44–49], defect-interface interactions [50–56], phonon-dislocation interactions [57, 58] and

phonon-grain boundary interactions [59], and crack-dislocation-grain boundary interaction in polyatomic ionic crystals [60, 61].

3.2.4 The Hot Quasi-Continuum Method

The "Hot" quasicontinuum method utilizes the principle of maximum entropy [62]. Unlike the canonical ensemble associated with a global constraint, the method begins by enforcing a distribution per atom energy for the entropy function to be maximized:

$$S(\bar{\mathbf{q}}, \bar{\mathbf{p}}, \boldsymbol{\beta}, \boldsymbol{\omega}) = -k_B\langle \log(\rho)\rangle + \boldsymbol{\beta} \cdot \langle \mathbf{h}(\mathbf{q}, \mathbf{p})\rangle \tag{3.10}$$

where angle brackets denote ensemble averages with respect to the probability distribution. This results in a similar exponential distribution to the canonical ensemble that is a function of per particle energies and temperatures:

$$\rho = \frac{1}{Z}\exp\left(\sum_a \frac{h_a}{T_a}\right) \tag{3.11}$$

where Z is the normalization constant and T_a represents the particle temperature. The Lagrange multipliers β_i are redefined as particle temperatures via $T_i = 1/k_B\beta_i$, where k_B is Boltzmann's constant. The non-local per particle Hamiltonian h_a would introduce great difficulty and impracticality in the calculation of Eq. (3.10), and thus the energies must be approximated with local forms. The quantity h_a in the distribution function is then approximated by

$$h_a = \frac{1}{2m_a}|\mathbf{p} - \bar{\mathbf{p}}|^2 + \frac{m_a\omega_a^2}{2}|\mathbf{q} - \bar{\mathbf{q}}|^2, \tag{3.12}$$

which involves the introduction of mean positions $\bar{\mathbf{q}} = \langle \mathbf{q}\rangle$ and momenta $\bar{\mathbf{p}} = \langle \mathbf{p}\rangle$ along with frequencies ω_a for each particle a in the system. This is called the "meanfield" approximation of the entropy [63]. The local approximation of the Hamiltonian introduces a larger free energy by the Gibbs-Bogoliubov inequality [64]. The equations of motion used by the authors, [65, 66], in terms of an average Hamiltonian $\bar{H} = \frac{1}{k_B}\sum_i \partial S/\partial\beta_i = \langle H(\mathbf{q}, \mathbf{p})\rangle$ are then

$$\frac{d\bar{\mathbf{p}}_i}{dt} = -\frac{\partial \bar{H}}{\partial \bar{\mathbf{q}}_i} \tag{3.13}$$

$$\frac{d\bar{\mathbf{q}}_i}{dt} = \frac{\partial \bar{H}}{\partial \bar{\mathbf{p}}_i} \tag{3.14}$$

These two equations are coupled with a stationary requirement on the entropy with respect to the previously defined particle frequencies:

$$\frac{\partial S}{\partial \omega_i} = 0 \tag{3.15}$$

The temperatures are updated with an additional constitutive law; in recent works on nanovoid growth [65, 66] Fourier's law of heat conduction is utilized. The method is then used to reduce the degrees of freedom with a typical finite element interpolation of the variables in terms of specified nodes, called "repatoms". After this approximation, some local quantities such as kinetic energy can be computed, but the potential energy is nonlocal and requires further approximation. QC uses the Cauchy-Born rule (CBR) with a specified cluster summation rule such as is depicted in Fig. 3.7 to approximate the energy at proscribed quadrature points [18].

A typical summation rule approximates the total energy for the reference atom an as average of the energy in selected cluster around the atom:

$$\bar{E}_i(X^i) = \frac{1}{m}\sum_a^m E(u(X^a - X^i)) \tag{3.16}$$

The total energy of the model is then computed using a set of weights assigned to each representative atom's average energy:

$$E_{tot} = \sum_i^{n_r} w_i \bar{E}_i \tag{3.17}$$

The weights (w) are selected according to the number of atoms that the average energy represents. The method then requires the ensemble average of energy:

$$\langle E \rangle = \int \rho(\bar{\mathbf{q}}, \bar{\mathbf{p}}, \boldsymbol{\beta}, \boldsymbol{\omega}, \mathbf{q}, \mathbf{p}) E(\mathbf{q}, \mathbf{p}) \mathbf{dqdp} \tag{3.18}$$

The integral average increases in dimensionality with the number of relevant degrees of freedom needed to describe the neighboring deformation and this imposes the famous "curse of dimensionality" on the associated quadrature rule.

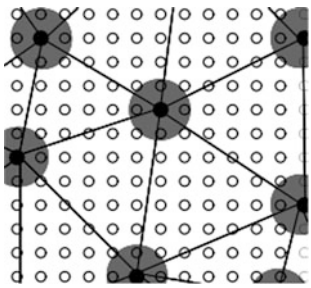

Fig. 3.7 Clusters of "repatoms", which are the nodes of the CST elements [18]

Sparse gridded methods exist to alleviate the burden of increasing dimension but they only become practical by the time the dimension is quite large [67].

A persistent issue in the CQC method is the presence of ghost-forces. Many of the recent publications are aimed at minimizing the influence of the ghost forces through various methods, such as optimal summation weights, displacement basis enrichment such as higher order shape functions and Krylov subspace bases, and bridging methods [68–70].

3.2.5 The Atomistic to Continuum Method

AtC is intended to provide a means by which energy can flow from the continuum to the atomistic domain [71, 72]. The governing equation of the continuum representation is the heat equation with the assumption of Fourier's law.

The procedure can be divided into three steps: computing an effective set of nodal temperatures for the FE mesh overlaid on the MD region; damping the atomistic forces in the MD region to conserve the total energy of the model in the coupled system; and finally find the solution of the heat equation using the previous computations for the current state along with their effect on the energy flow rates.

The first step requires computation of nodal temperatures for the background mesh overlaid on the MD region (Fig. 3.8) by minimizing the squared difference between the finite element temperature interpolation and the atomistic temperature field, i.e.,

$$R = \int_{\Omega_A} \left(T(X) - T^h(X)\right)^2 dV \tag{3.19}$$

where $T^h(X)$ is the finite element interpolation using a set of nodal temperatures $\theta_I(t)$. The temperature field $T(X)$ is defined using a dirac delta distribution for each atom. The coupling of the thermal boundary conditions on the atomistic domain is enforced by altering the interatomic force as.

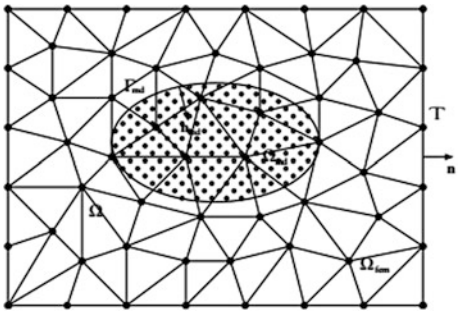

Fig. 3.8 Depiction of the domains to be coupled in the thermal AtC problem [72]

$$f_i = f_i^{MD} + f_i^{\lambda}. \tag{3.20}$$

The alteration f_i^{λ} is expressed as a damping force

$$f_i^{\lambda} = \frac{m_i}{2} v_i \lambda_i, \tag{3.21}$$

in which the multiplier λ_i is expressed as a finite element interpolation using the same mesh over the MD region, i.e.,

$$\lambda_i = \sum_{I=1}^{M} N_I(X_i)\lambda_I. \tag{3.22}$$

The λ_I are then solved for in two steps. First, the method imposes the global conservation of energy with this new dissipative force term. The result of that is still non-unique since there are many possible per atom damping force combinations. The chosen solution is a linear regression evaluated at all the atomic sites which results in the second linear system the procedure needs to solve:

$$M\boldsymbol{\lambda}_I = -P_I \tag{3.23}$$

where P_I is the inner product of the Ith shape function and the effective surface flux out of the MD region.

The final step to complete procedure is the solution of the heat equation with the two previous steps of computation and Galerkin's method:

$$\int_{\Omega} N_I \dot{T}^h dV = \sum_{a=1}^{N} V_a N_I(X_a)\dot{T}_a + \int_{\Omega_C} \frac{\kappa}{\rho c_p} N_I \nabla^2 T^h dV, \tag{3.24}$$

which is then coupled to the atomistic region through

$$\int_{\Gamma_{md}} N_I Q \cdot dA = \int_{\Gamma_{md}} N_I \kappa \nabla T \cdot dA \tag{3.25}$$

where Γ_{md} is the surface separating the continuum and atomistic regions. This heat flux is then expressed in terms of the drag forces on the atom. This completes the effect of the coupling and the equations are integrated numerically in time.

3.3 Analysis

A concurrent multiscale simulation method capable of describing the example mesoscale problem shown in Fig. 3.1 should, with few if any additional constitutive laws that riskily assume the mesoscale behavior, be capable of several or all of the following: wave propagation, defect nucleation and multiplication, and thermo-mechanical coupling. Two important necessities for a wider applicability of such a method are the accurate description of polyatomic materials when coarse-graining and the ability to model moving defects without impractically increasing the degrees of freedom through adaptive remeshing. In this section, we explain their applicability based on the governing equations. Table 3.1 summarizes the laws and equations that govern the motion of the system for each method and the additional equations needed to define the interface or describe unknowns with supplemental constitutive equations in addition to the interatomic potential.

3.3.1 Modeling Materials Beyond Monoatomic Crystals

The spurious reflection problem has two common sources in dynamic multiscale modeling methods: (1) material mismatch between two different spatial domains of the model trying to describe the same material with different definitions, and (2) the interfaces between regions of different numerical resolution, i.e., a non-uniform mesh [74]. The abundance of reflection then forces implementers to create a specially treated numerical interface that somehow absorbs the spurious waves. The cause for case (1) is commonly neglected even in recent works that focus on the numerical cause (2) for XFEM coupling [20, 75] with graphene. Most of the multiscale methods, excluding CAC, do not provide a two-level description for each material point in the continuum domain. This limits the methods to monoatomic crystals and introduces error for polyatomic materials.

No methods are capable of conveying all fine-scale dynamics of waves, such as an input wave packet excitation, from one atomistic region to another separated by a continuum representation. This is due to that the second source of spurious reflection is purely a consequence of the finite element discretization where only wavelengths that are sufficiently longer than the length of the finite elements can propagate. Typical wavelengths range from 6 to 10 times the element size [76]. This last problem is a difficult limitation to overcome for a non-uniform mesh and caution must be taken to determine the impact of this spurious wave reflection contribution on simulation accuracy, assuming the reflections do not cause instability and prevent a practical simulation in the first place.

In CADD, the use of an elasticity tensor C_{ijkl} will introduce a mismatch between the frequency response of the atomistic and continuum domains and thus be a source of spurious wave reflection. Significant spurious forces are also noted by [19] when dislocations are close to the interface.

Table 3.1 Governing equations of each method along with supplemental equations

Name	Governing law and representations	Supplemental equations
CADD	Momentum conservation Atomic: $m\frac{d^2u}{dt^2} = -\frac{\partial U}{\partial r}$ Continuum: $\rho\frac{d^2\hat{u}}{dt^2} + \nabla_x \cdot \hat{\boldsymbol{\sigma}} = b + \iint -21mu\bigcirc\, \boldsymbol{\tau} \cdot dS$ where $\tilde{\boldsymbol{\sigma}}^{(k)}$ refers to the kth dislocation's stress contribution. This is computed with an analytical model [73]. $u = \hat{u} + \tilde{u}$ $\tilde{\boldsymbol{\sigma}} = \sum_k \tilde{\boldsymbol{\sigma}}^{(k)}$	• Dislocation detection and dampening at the interface • Peach-Koehler Force: $f^{(k)} = n^{(k)T}(\hat{\boldsymbol{\sigma}} + \sum_{l \neq k} \tilde{\boldsymbol{\sigma}}^{(l)})b^{(k)}$ where (k) refers to the kth dislocation and $f^{(k)}$ is the force along the slip plane
Coupled XFEM	Lagrangian Mechanics $L_A = \sum_i \left[w(\mathbf{X}_i)m_i\mathbf{v}_i^2 - \bar{w}(\mathbf{X}_i)U_i)\right]$ $L_B = \sum_{i \in S^B} \boldsymbol{\lambda}_i[u(\mathbf{X}_i) - u_i]$, $L_C = \int_{V_0^C} \ell dV_0^C$ $\ell = \left[(1 - w(\mathbf{X}))\left(\frac{\rho_0(\mathbf{X})}{2}\dot{\mathbf{u}}^2(\mathbf{X}) - W^C(\mathbf{C}(\mathbf{X}))\right)\right]$ $L = L_A + L_B + L_C$ $\frac{\partial}{\partial t}\frac{\partial L}{\partial \dot{\mathbf{U}}_i} - \frac{\partial L}{\partial \mathbf{U}_i} = 0$, $\frac{\partial}{\partial t}\frac{\partial L}{\partial \dot{\mathbf{v}}_i} - \frac{\partial L}{\partial \mathbf{u}_i} = 0$	• Constraint forces: $A_{ji}\boldsymbol{\lambda}_i = \frac{-2}{\Delta t} g_j$ $A_{ji} = \sum_{I \in B} \frac{\Phi_I(X_j)\Phi_I(X_i)}{\bar{m}_I} + \frac{\delta_{ji}}{\bar{m}_\alpha}$ $g_j = v_i^h - \Phi_I(X_i)U_I^h$ where h refers to half timestep
CAC	Conservation laws $\frac{d\rho^\alpha}{dt} + \rho^\alpha(\nabla_x \cdot v + \nabla_{y^\alpha} \cdot \Delta v^\alpha) = 0$ $\rho^\alpha \frac{d}{dt}(v + \Delta v^\alpha) = \nabla_x \cdot t^\alpha + \nabla_{y^\alpha} \cdot \boldsymbol{\tau}^\alpha + f_{\text{ext}}^\alpha$ $\rho^\alpha \frac{de^\alpha}{dt} = \nabla_x \cdot q^\alpha + \nabla_{y^\alpha} \cdot j^\alpha + t^\alpha : \nabla_x(v + \Delta v^\alpha) + \boldsymbol{\tau}^\alpha : \nabla_{y^\alpha}(v + \Delta v^\alpha)$	None
HotQC	Maximum Entropy $S(\bar{\mathbf{q}}, \bar{\mathbf{p}}, \boldsymbol{\beta}, \boldsymbol{\omega}) = -k_B\langle \log(\rho)\rangle + \boldsymbol{\beta} \cdot \langle \mathbf{h}(\mathbf{q}, \mathbf{p})\rangle$ $\bar{H}(\bar{q}, \bar{p}) = \langle H(q, p)\rangle = \sum_i \dot{e}_i$	• Depends on whether ghost force mitigation is employed • The definition of the probability density function: $\rho = \frac{1}{Z}\exp\left(\sum_i \frac{h_i}{T_i}\right)$

(continued)

Table 3.1 (continued)

Name	Governing law and representations	Supplemental equations
	$\frac{d\bar{\mathbf{p}}_i}{dt} = -\frac{\partial \bar{H}}{\partial \bar{\mathbf{q}}_i}$, $\frac{d\bar{\mathbf{q}}_i}{dt} = \frac{\partial \bar{H}}{\partial \bar{\mathbf{p}}_i}$ $\frac{\partial S}{\partial \omega_i} = 0$ $\dot{e}_j = \dot{w} + \sum_{j \neq i} R_{ij}$	• Local Hamiltonian approximation: $h_a = \frac{1}{2m_a}\lvert\mathbf{p} - \bar{\mathbf{p}}\rvert^2 + \frac{m_a\omega_a^2}{2}\lvert\mathbf{q} - \bar{\mathbf{q}}\rvert^2$• Heat Equation to update local temperatures: $P_{ij} = \frac{1}{T_i} - \frac{1}{T_j}$, $R_{ij} = \frac{\partial \psi}{\partial P_{ij}}$ • ψ is a function of the P_{ij}
AtC	Conservation of Energy Atomic: $f_i = f_i^{MD} + f_i^{\lambda}, f_i^{\lambda} = \frac{m_i}{2} v_i \lambda_i$ Continuum: $\rho c_p \frac{\partial T}{\partial t} - \nabla \cdot (k \nabla T) = \dot{q}_V$	• Temperature Projection procedure • Calculation of damping constant

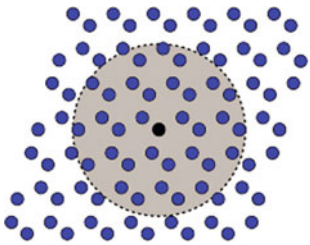

Fig. 3.9 Example of a virtual atom cluster to compute the stress at a quadrature point [20]

The use of the Cauchy Born rule (CBR) in methods such as coupled XFEM and HotQC is intended to reduce the mismatch between the atomic and continuum regions; it eliminates short-wavelength acoustic phonons and all optical phonons. The stress for CBR is typically computed by mapping the strain to a reference lattice surrounding a reference atom at a quadrature point, as shown in Fig. 3.9. The strain tensor defines a state of continuous deformation applied to all atoms in the unit cell and the rest of the neighborhood in a CBR procedure; this generally leads to unstable configurations if no further treatment is provided for polyatomic materials [20]. A further approximation is to minimize the energy of the neighborhood after the continuous deformation. Since energy minimization does not move internal atoms in accordance with Newton's second law, even for linear dynamics, this is then a source of spurious wave reflections at the interface since this approximation cannot reproduce the frequency response of material in the lattice even at long wavelengths.

The CAC formulation is based on the solid-state physics description of all crystals, i.e., crystal = lattice + basis. As a result, it naturally applies to any crystalline materials beyond monoatomic crystals. This ability has been demonstrated through simulation of phase transition in Si [43], dislocations in MgO [77], the nucleation and propagation of cracks and dislocations as well as dislocation-GB interaction in $SrTiO_3$ [60, 61, 78].

3.3.2 Modeling of Defects and Waves

The dynamic simulation of metamaterials shown in Fig. 3.1 requires effective coupling between the wave dynamics and defects to reproduce the transport processes; these are generally non-equilibrium in space and time and may involve phonon-interface and phonon-dislocation scattering in addition to defect-defect and defect-interface interactions. Applicability of the multiscale methods for the simulation of these dynamic phenomena is discussed in Table 3.2.

The CAC method provides consistency between the atomistic and continuum propagation of waves due to its two-level description of materials. It is possible to obtain accurate dynamic wave propagation, as shown in Fig. 3.10, for long wavelength phonons. The spurious wave reflection will nonetheless be present for

Table 3.2 Evaluation of applicability for each method in the simulation of waves and defects

Name	Wave propagation	Nucleation and propagation of defects	Thermal-mechanical coupling
CADD	Waves will reflect spuriously due to the description of the continuum with linear elasticity. The method requires interface damping which influences waves and energy conservation	Dislocations must be detected before the interface and artificially reintroduced into the DD domain. Significant spurious forces are also noted by [19] when dislocations are close to the interface	The DD constitutive laws are not suitable to describe the interaction with phonons even if they overcame the dampening and interface reflection
Coupled XFEM	Bridging region influences the propagation of waves. The material description in the continuum with the CB rule + energy minimization represents a different material since atoms internal to the unit cell don't obey newton's second law; this results in unphysical scattering	The method enables defects to move practically with mesh refinement when dislocation cores arrive at interfaces between different descriptions. Coarsening takes place where defects are no longer present Defects cannot nucleate naturally in the coarse-grained description	The discontinuous description of defects is simplified with a Heaviside function. Coupled with the material description, this alters phonon propagation
CAC	Long wavelength waves can propagate while shorter wavelengths only suffer numerical scattering in non-uniform meshes	Propagates naturally if near element edges but fails to do so if incident on element surfaces; would require mesh refinement by at least splitting elements [79]. Defects can emerge naturally in the coarse-scale regions	CAC is robust for coarse-grained simulation of phonon thermal transport, phonon-defect interaction, but inaccurate for short wavelength phonons due to the scattering caused by non-uniform mesh
HotQC	The governing law is not Newton's laws of motion and thus wave representation is dramatically altered. Waves would scatter at the numerical interfaces	Mesh must be refined to atomistic resolution for defects. This leads to the well documented increasing DOF problem, Fig. 3.11 [80]	Waves cannot be modeled accurately as previously stated. Defects can only be modeled in the atomistic domain
AtC	The constitutive description of the continuum would scatter waves introduced in the atomistic description [72, 81]	Defects in the atomistic domain would encounter a boundary unless mesh is refined	Only possible within the atomistic domain

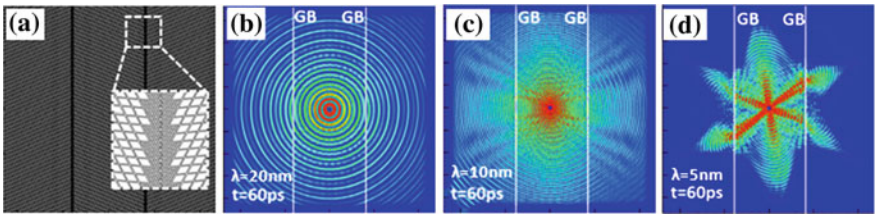

Fig. 3.10 Phonon propagation across grain boundaries in a CAC model [59]

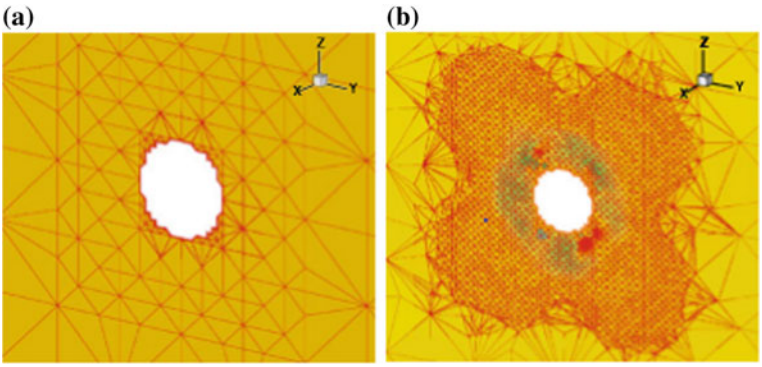

Fig. 3.11 Quasicontinuum mesh initially (**a**) and after adaptive refinement (**b**) [80]

systems involving short wavelength phonons under the critical mesh threshold as commonly seen in dynamic FEA simulations [82]; this can be negligible but there is no guarantee for a general system and process.

A common challenge in the modeling of defects using atomistic resolution is the threat of rapidly increasing numbers of degrees of freedom as defects propagate. An example of HotQC simulation, shown in Fig. 3.11, exemplifies this problem; this incentivizes use of coarse-grained models to describe defects in the continuum, using the interatomic potential, to resolve the discontinuities and their propagation.

3.4 Conclusions

In this work, we have attempted to evaluate the applicability of concurrent multiscale modeling methods for dynamic simulation of mesoscale materials. We have reviewed in detail the governing equations of each method. The governing equations, i.e., the mathematical representation of the governing laws, determine the fundamental nature of each method. They distinguish static from dynamic models, simple lattice from general materials, zero temperature from finite temperature

problems, constant temperature from thermo-mechanical coupling, and hence define the domains of applications.

Within the domain of applications, the applicability of each method is further determined by another key element for concurrent multiscale methods, namely the internal consistency of its laws. A Philosophy professor, Dr. Winsberg, commented on existing "parallel (concurrent) multiscale models" as "models of an inconsistent set of laws" and a "common philosophical intuition about scientific theories" is that "the internal consistency of its laws is a necessary condition that all successful theories have to satisfy" [83]. Using different governing laws for different scales results in internal inconsistency. The internal inconsistency gives rise to artificial interfaces. These a physical interfaces are the source of ghost forces for many static multiscale methods; they are also the origin of spurious wave reflections for most dynamic methods. The presence of such interfaces can degrade the ability of a concurrent multiscale method to simulate dynamic problems involving waves or vibrations. From this viewpoint, many dynamic methods are inapplicable to realistic dynamic problems. This is indicated in Table 3.1 and explained in Table 3.2.

The formulations of many dynamic multiscale methods have been unable to preserve the essential features of the dynamics of atoms: internal motion of atoms relative to the lattice, the interatomic potential as the only materials description, and discontinuities as a result of naturally occurring defects. This has placed many dynamic methods in a position where they are unable to accurately simulate polyatomic materials with existing interatomic potentials even with uniform meshes and no critical defects. The inclusion of these requirements in CAC has generated a potentially general and consistent framework for modeling the coupling between thermal and mechanical features accurately with uniform meshes. Multiscale modeling methods must provide consistency between the descriptions of the atomistic and the continuum domains. Strengths of some methods might be synergized; such as the two-level description of CAC being employed in other methods and XFEM support possibly augmenting CAC. Additionally, all multiscale methods today still require physical problems to have a negligible reliance on short wavelength propagation only currently available in MD.

Nonetheless, with enough synthesis and improvements the abstraction of concurrent multiscale modeling methods may very well be a powerful tool for the solution of mesoscale technological problems such as the design of multifunctional or mechanical metamaterials. A modern inspiration for this role of powerful predictive simulation comes from the continuum scale with ubiquitous finite element methods solving structural dynamics, heat transport problems, electrical conduction, and other problems. With continued effort, concurrent multiscale simulation methodologies might conceive a similar advance with their predictive power.

Acknowledgements This paper is written in honor of Dr. Gerald Maugin. This material is based upon research supported by the U.S. Department of Energy, Office of Basic Energy Sciences, Division of Materials Sciences and Engineering under Award #DE-SC0006539.

References

1. Gracie, R., Belytschko, T.: Concurrently coupled atomistic and XFEM models for dislocations and cracks. Int. J. Numer. Methods Eng. **78**(3), 354–378 (2009)
2. Hemminger, J., Crabtree, G., Sarrao J.: From quanta to the continuum: opportunities for mesoscale science. A Report from the Basic Energy Sciences Advisory Committee, Technical Report, pp. 1601–1606 (2012)
3. Ziolkowski, R.W.: Metamaterials: the early years in the USA. EPJ Appl. Metamaterials **1** (2014)
4. Valentine, J., et al.: Three-dimensional optical metamaterial with a negative refractive index. Nature **455**(7211), 376 (2008)
5. Tsu, R.: Man-made superlattice and quantum wells: past and future. Waves Random Complex Media **24**(3), 232–239 (2014)
6. Valentine, J., et al.: Three-dimensional optical metamaterial with a negative refractive index. Nature **455**(7211), 376–379 (2008)
7. Wegener, M.: Metamaterials beyond optics. Science **342**(6161), 939–940 (2013)
8. Gorishnyy, T., et al.: Hypersonic phononic crystals. Phys. Rev. Lett. **94**(11), 115501 (2005)
9. Hopkins, P.E., et al.: Reduction in the thermal conductivity of single crystalline silicon by phononic crystal patterning. Nano Lett. **11**(1), 107–112 (2010)
10. Maldovan, M.: Sound and heat revolutions in phononics. Nature **503**(7475), 209–217 (2013)
11. Zen, N., et al.: Engineering thermal conductance using a two-dimensional phononic crystal. Nat. Commun. **5** (2014)
12. Liu, Y., Zhang, X.: Metamaterials: a new frontier of science and technology. Chem. Soc. Rev. **40**(5), 2494–2507 (2011)
13. Tsu, R., Fiddy, M.A.: Waves in man-made materials: superlattice to metamaterials. Waves Random Complex Media **24**(3), 250–263 (2014)
14. Shiari, B., Miller, R.E., Klug, D.D.: Multiscale modeling of solids at the nanoscale: dynamic approach. Can. J. Phys. **86**(2), 391–400 (2008)
15. Shilkrot, L., Miller, R., Curtin, W.: Coupled atomistic and discrete dislocation plasticity. Phys. Rev. Lett. **89**(2), 025501 (2002)
16. Shilkrot, L., Miller, R.E., Curtin, W.A.: Multiscale plasticity modeling: coupled atomistics and discrete dislocation mechanics. J. Mech. Phys. Solids **52**(4), 755–787 (2004)
17. Shiari, B., Miller, R.E.: Multiscale modeling of crack initiation and propagation at the nanoscale. J. Mech. Phys. Solids **88**, 35–49 (2016)
18. Miller, R.E., Tadmor, E.B.: A unified framework and performance benchmark of fourteen multiscale atomistic/continuum coupling methods. Model. Simul. Mater. Sci. Eng. **17**(5), 053001 (2009)
19. Pavia, F., Curtin, W.A.: Parallel algorithm for multiscale atomistic/continuum simulations using LAMMPS. Model. Simul. Mater. Sci. Eng. **23**(5), 055002 (2015)
20. Moseley, P., Oswald, J., Belytschko, T.: Adaptive atomistic-to-continuum modeling of propagating defects. Int. J. Numer. Method Eng. **92**(10), 835–856 (2012)
21. Talebi, H., Silani, M., Rabczuk, T.: Concurrent multiscale modeling of three dimensional crack and dislocation propagation. Adv. Eng. Softw. **80**, 82–92 (2015)
22. Chen, Y., et al.: Assessment of atomistic coarse-graining methods. Int. J. Eng. Sci. **49**(12), 1337–1349 (2011)
23. Dove, M.T.: Introduction to Lattice Dynamics. null. vol. null. (1993). null
24. Kittel, C.: Introduction to Solid State Physics. null. vol. null. (1967). null
25. Irving, J., Kirkwood, J.G.: The statistical mechanical theory of transport processes. IV. The equations of hydrodynamics. J. Chem. Phys. **18**(6), 817–829 (1950)
26. Kirkwood, J.G.: The statistical mechanical theory of transport processes I. General theory. J. Chem. Phys. **14**(3), 180–201 (1946)
27. Eringen, A.C.: Microcontinuum Field Theories: Foundations and Solids, vol. 487. Springer, New York (1999)

28. Chen, Y., Lee, J.D., Eskandarian, A.: Examining the physical foundation of continuum theories from the viewpoint of phonon dispersion relation. Int. J. Eng. Sci. **41**(1), 61–83 (2003)
29. Eringen, A.C.: Mechanics of Micromorphic Continua. Springer (1968)
30. Chen, Y., Lee, J.D.: Connecting molecular dynamics to micromorphic theory. (I). Instantaneous and averaged mechanical variables. Phys. A **322**, 359–376 (2003)
31. Chen, Y., Lee, J.D.: Connecting molecular dynamics to micromorphic theory. (II). Balance laws. Phys. A **322**, 377–392 (2003)
32. Chen, Y., Lee, J., Eskandarian, A.: Atomistic counterpart of micromorphic theory. Acta Mech. **161**(1–2), 81–102 (2003)
33. Chen, Y., Lee, J.D.: Determining material constants in micromorphic theory through phonon dispersion relations. Int. J. Eng. Sci. **41**(8), 871–886 (2003)
34. Maugin, G.A.: Some remarks on generalized continuum mechanics. Math. Mech. Solids **20** (3), 280–291 (2015)
35. Maugin, G.A.: Generalized continuum mechanics: various paths. In: Continuum Mechanics Through the Twentieth Century, pp. 223–241. Springer (2013)
36. Maugin, G.A.: Generalized continuum mechanics: what do we mean by that? In: Mechanics of Generalized Continua, pp. 3–13 (2010)
37. Chen, Y.: Reformulation of microscopic balance equations for multiscale materials modeling. J. Chem. Phys. **130**(13), 134706 (2009)
38. Chen, Y.: Local stress and heat flux in atomistic systems involving three-body forces. J. Chem. Phys. **124**(5), 054113 (2006)
39. Chen, Y., Lee, J.: Atomistic formulation of a multiscale field theory for nano/micro solids. Philos. Mag. **85**(33–35), 4095–4126 (2005)
40. Deng, Q., Xiong, L., Chen, Y.: Coarse-graining atomistic dynamics of brittle fracture by finite element method. Int. J. Plast. **26**(9), 1402–1414 (2010)
41. Deng, Q., Chen, Y.: A coarse-grained atomistic method for 3D dynamic fracture simulation. J. Multiscale Comput. Eng. **11**(3), 227–237 (2013)
42. Deng, Q.: Coarse-Graining Atomistic Dynamics of Fracture by Finite Element Method Formulation, Parallelization and Applications. Fla: University of Florida, Gainesville (2011)
43. Xiong, L., Chen, Y.: Coarse-grained simulations of single-crystal silicon. Model. Simul. Mater. Sci. Eng. **17**, 035002 (2009)
44. Xiong, L., et al.: Coarse-grained elastodynamics of fast moving dislocations. Acta Mater. **104**, 143–155 (2016)
45. Xu, S., et al.: An analysis of key characteristics of the Frank-Read source process in FCC metals. J. Mech. Phys. Solids **96**, 460–476 (2016)
46. Xiong, L., et al.: A concurrent scheme for passing dislocations from atomistic to continuum domains. Acta Mater. **60**(3), 899–913 (2012)
47. Xiong, L., et al.: Coarse-grained atomistic simulations of dislocations in Al, Ni and Cu crystals. Int. J. Plast. **38**, 86–101 (2012)
48. Xiong, L., McDowell, D.L., Chen, Y.: Nucleation and growth of dislocation loops in Cu, Al and Si by a concurrent atomistic-continuum method. Scr. Mater. **67**(7), 633–636 (2012)
49. Xiong, L., et al.: Coarse-grained atomistic simulation of dislocations. J. Mech. Phys. Solids **59** (2), 160–177 (2011)
50. Yang, S., Chen, Y.: Concurrent atomistic-continuum simulation of polycrystalline strontium titanate (2014) (in preparation)
51. Xu, S., et al.: Comparing EAM Potentials to Model Slip Transfer of Sequential Mixed Character Dislocations Across Two Symmetric Tilt Grain Boundaries in Ni. JOM, 1–8 (2017)
52. Xu, S., et al.: Validation of the concurrent atomistic-continuum method on screw dislocation/stacking fault interactions. Crystals **7**(5), 120 (2017)
53. Xu, S., et al.: Sequential slip transfer of mixed-character dislocations across Σ3 coherent twin boundary in FCC metals: a concurrent atomistic-continuum study. npj Comput. Materials **2**, 15016 (2016)

54. Xu, S., et al.: Edge dislocations bowing out from a row of collinear obstacles in Al. Scr. Mater. **123**, 135–139 (2016)
55. Xiong, L., et al.: Concurrent atomistic–continuum simulations of dislocation–void interactions in fcc crystals. Int. J. Plast. **65**, 33–42 (2015)
56. Xu, S., et al.: A quasistatic implementation of the concurrent atomistic-continuum method for FCC crystals. Int. J. Plast. **72**, 91–126 (2015)
57. Xiong, L., McDowell, D.L., Chen, Y.: Sub-THz Phonon drag on dislocations by coarse-grained atomistic simulations. Int. J. Plast. **55**, 268–278 (2014)
58. Chen, X., et al.: Effects of phonons on mobility of dislocations and dislocation arrays. Scr. Mater. **137**, 22–26 (2017)
59. Chen, X., et al.: Ballistic-diffusive phonon heat transport across grain boundaries. Acta Mater. **136**(Supplement C), 355–365 (2017)
60. Yang, S., Chen Y.: Concurrent Atomistic-Continuum Simulation of Defects in Polyatomic Ionic Materials, in Multiscale Materials Modeling for Nanomechanics, pp. 261–296. Springer International Publishing (2016)
61. Yang, S., Chen, Y.: Concurrent atomistic and continuum simulation of bi-crystal strontium titanate with tilt grain boundary. Proc. R. Soc. A Math. Phys. Eng. Sci. **471**(2175) (2015)
62. Jaynes, E.T.: Information theory and statistical mechanics. Phys. Rev. **106**(4), 620–630 (1957)
63. Venturini, G., et al.: Atomistic long-term simulation of heat and mass transport. J. Mech. Phys. Solids **73**, 242–268 (2014)
64. Isihara, A.: The Gibbs-Bogoliubov inequality dagger. J. Phys. A: Gen. Phys. **1**(5), 539 (1968)
65. Ponga, M., Ortiz, M., Ariza, M.P.: Finite-temperature non-equilibrium quasi-continuum analysis of nanovoid growth in copper at low and high strain rates. Mech. Mater. **90**, 253–267 (2015)
66. Mauricio, P., et al.: Dynamic behavior of nano-voids in magnesium under hydrostatic tensile stress. Model. Simul. Mater. Sci. Eng. **24**(6), 065003 (2016)
67. Gerstner, T., Griebel, M.: Numerical integration using sparse grids. Numer. Algorithms **18**(3), 209 (1998)
68. Ming, P., Yang, J.Z.: Analysis of a one-dimensional nonlocal quasi-continuum method. Multiscale Model. Simul. **7**(4), 1838–1875 (2009)
69. Amelang, J.S., Venturini, G.N., Kochmann, D.M.: Summation rules for a fully nonlocal energy-based quasicontinuum method. J. Mech. Phys. Solids **82**, 378–413 (2015)
70. Ortner, C., Zhang, L.: Atomistic/continuum blending with ghost force correction. SIAM J. Sci. Comput. **38**(1), A346–A375 (2016)
71. Jeremy, A.T., Reese, E.J., Gregory, J.W.: Application of a field-based method to spatially varying thermal transport problems in molecular dynamics. Model. Simul. Mater. Sci. Eng. **18** (8), 085007 (2010)
72. Wagner, G.J., et al.: An atomistic-to-continuum coupling method for heat transfer in solids. Comput. Methods Appl. Mech. Eng. **197**(41), 3351–3365 (2008)
73. Giessen, E.V.d., Needleman, A.: Discrete dislocation plasticity: a simple planar model. Model. Simul. Materials Sci. Eng. **3**(5), 689 (1995)
74. Jiang, L., Rogers, R.J.: Spurious wave reflections at an interface of different physical properties in finite-element wave solutions. Commun. Appl. Numer. Methods **7**(8), 595–602 (1991)
75. Xu, M., Belytschko, T.: Conservation properties of the bridging domain method for coupled molecular/continuum dynamics. Int. J. Numer. Methods Eng. **76**(3), 278–294 (2008)
76. Bažant, Z.P., Celep, Z.: Spurious reflection of elastic waves in nonuniform meshes of constant and linear strain unite elements. Comput. Struct. **15**(4), 451–459 (1982)
77. Xiong, L., Chen, Y.: Multiscale modeling and simulation of single-crystal MgO through an atomistic field theory. Int. J. Solids Struct. **46**(6), 1448–1455 (2009)
78. Yang, S., Zhang, N., Chen, Y.: Concurrent atomistic–continuum simulation of polycrystalline strontium titanate. Philos. Mag. **95**(24), 2697–2716 (2015)

79. Xu, S., et al.: Mesh refinement schemes for the concurrent atomistic-continuum method. Int. J. Solids Struct. **90**, 144–152 (2016)
80. Ariza, M.P., et al.: HotQC simulation of nanovoid growth under tension in copper. Int. J. Fract. **174**(1), 75–85 (2012)
81. Chernatynskiy, A., Phillpot, S.R.: Phonon-mediated thermal transport: confronting theory and microscopic simulation with experiment. Curr. Opin. Solid State Mater. Sci. **17**(1), 1–9 (2013)
82. Bažant, Z.P.: Spurious reflection of elastic waves in nonuniform finite element grids. Comput. Methods Appl. Mech. Eng. **16**(1), 91–100 (1978)
83. Winsberg, E.: Models and theories at the nano-scale. Spontaneous Gener. J. Hist. Philos. Sci. **2**(1), 139 (2009)

Chapter 4
Modeling Semiconductor Crystal Growth Under Electromagnetic Fields

Sadik Dost

Abstract Growth of semiconductor single crystals under electric and magnetic fields is of interest to increase and better control of crystal growth rate, to suppress and control the adverse effect of natural convection and to obtain better mixing in the growth melt (liquid solution) for better crystal uniformity, which all are favorable conditions for a prolonged growth of high quality crystals. To this end, in parallel to well-designed experiments, modeling is essential to shed light on various aspects of these growth processes and also to better understand the transport phenomena involved. In this article the models developed over the years, mostly based on Professor Gerard Maugin's well-known contributions to "electromagnetic interactions", are briefly presented for "solution growth" conducted under electric and magnetic fields. Basic and constitutive equations of a binary electromagnetic continuum mixture are specialized for two important solution growth techniques—Liquid Phase Electroepitaxy (LPEE) and Travelling Heater Method (THM). As an application, an LPEE growth of GaAs bulk crystals under a strong static magnetic field is considered. Experimental results, that have shown that the growth rate under an applied static magnetic field is also proportional to the applied magnetic field and increases with the field intensity level, are predicted from these models. The contribution of a third-order material constant in LPEE is also predicted from these models. The prediction of increasing growth rate in THM growth under rotating magnetic fields from modeling was verified by experiments.

4.1 Introduction

Modeling some electromagnetic continua has been a great interest for many disciplines of engineering sciences. The literature on this topic is rich. The related fundamental and constitutive equations of a *single* continuum, and also a comprehensive list of related literature can be found in the treatment of Eringen and

S. Dost (✉)
Crystal Growth Laboratory, University of Victoria, Victoria, BC V8W 3P6, Canada
e-mail: sdost@uvic.ca

H. Altenbach et al. (eds.), *Generalized Models and Non-classical Approaches in Complex Materials 2*, Advanced Structured Materials 90,
https://doi.org/10.1007/978-3-319-77504-3_4

Maugin [1]. Linear and nonlinear constitutive equations of various single continuum electromagnetic media were presented in [1]. Fundamental equations of a continuum (non electromagnetic) of mixtures, and the related literature can also be found in Bowen [2]. Based on [1] and [2] the *linear* equations of binary and ternary conducting metallic liquid mixtures under electric and magnetic fields were given in [3] and [4]. However, as presented in [1] and [5], when an electromagnetic medium is under a strong external magnetic field, contributions of nonlinear and higher order interactions may become significant. Therefore, for accurate predictions such nonlinear effects must be included in the model. To this end, the *nonlinear* equations of a binary metallic liquid mixture under electric and magnetic fields were developed in [6, 7] where in the development of the model equations the focus was on the solution crystal growth techniques of Liquid Phase Electroepitaxy (LPEE) and Travelling Heater Method (THM).

Solution growth techniques such as LPEE and THM are of significant technological interest in growth of bulk single crystals of alloy semiconductors. However, in these techniques the natural convection occurring in the solution zone adversely affects the quality of grown crystals and leads to growth instabilities. The use of an applied magnetic field is an option in suppressing natural convection. A strong static magnetic field aligned perfectly with the axis of the growth cell gives rise to a magnetic body force that balances the vertical gravitational body force and, as a result, suppresses convection in the liquid solution. A weak rotating magnetic field is also used for better mixing in the melt. Literature on the use of magnetic field in crystal growth is rich. There are numerous studies examining the effect of applied magnetic field. We cite here only a brief list for the sake of brevity (see for instance [3–46].

The high growth rates observed in LPEE growth of bulk crystals under magnetic field [39, 40] could not be predicted from a model based only on linear constitutive coefficients (see [36, 45, 46]). As mentioned earlier, this requires the development of nonlinear equations for accurate predictions [6, 7]. To provide the needed background for modeling, we first briefly introduce the LPEE and THM crystal growth techniques.

4.1.1 Liquid Phase Electroepitaxy

In Liquid Phase Electroepitaxy (LPEE), growth is achieved by passing an electric current through the growth cell while the overall furnace temperature is kept constant during the entire growth period (see Fig. 4.1). The applied electric current is the sole driving force for growth, and gives rise to two growth mechanisms that are known as “electromigration” and “Peltier cooling/heating”. The electromigration of species in the liquid solution is believed to take place due to electron-momentum exchange and electrostatic field forces, and sustains a controlled-growth [47, 48]. The Peltier heating/cooling, on the other hand, is a thermoelectric effect occurring when electric current passes through an interface of

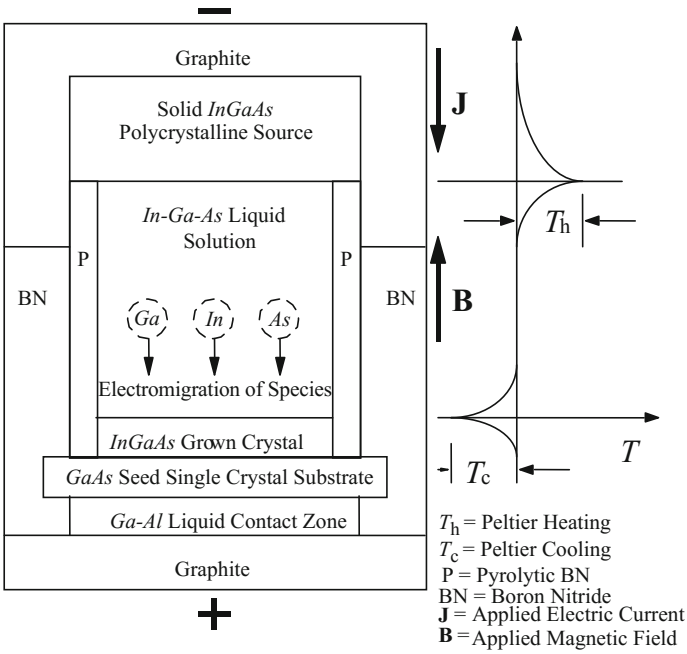

Fig. 4.1 Schematic view of a typical LPEE growth cell

two materials with different Peltier coefficients. The Peltier cooling at the growth interface (the interface between the seed and the liquid solution, see Fig. 4.1) supersaturates the solution in the immediate vicinity of the substrate and leads to epitaxial growth. The Peltier heating at the dissolution interface (the interface between the source and the liquid solution, see Fig. 4.1), on the other hand, causes the dissolution of the source material into the solution and provides constantly the needed feed material for growth. The growth rate is proportional to the applied electric current density [39, 40, 47–57]. The Joule heating due to the passage of electric current may also become very significant, particularly in growth of bulk crystals that require longer growth periods [58].

LPEE has a number of advantages over other bulk crystal growth techniques such as relatively lower temperature gradients, the ability of well-controlled growth, and the growth of ternary single crystals with uniform compositions. Such features make LPEE technologically very promising for commercial growth of high quality, bulk crystals such as GaInAs, GaInSb, CdZnTe, and SiGe (see [39, 40, 47–57]). However, the combined effect of the Joule heating in the solid crystals and the Peltier heating/cooling at the growth and dissolution interfaces gives rise to natural convection in the solution, which leads to interface instability and limits the achievable crystal thickness [4]. In order to reduce the adverse effect of convection, the LPEE growth of single crystals has been studied under a strong static magnetic field both theoretically and experimentally. The objective of the related modeling

studies (i.e., [3–7, 22–24, 31, 35, 36, 38–40] was to examine the effect of an applied static magnetic field in minimizing the adverse effect of natural convection. These studies have shown that lower convection in the solution may allow the use of higher electric current densities that will be translated into higher growth rates. A detailed account of application of magnetic field and related literature can be found in [5–7, 36].

A large number of bulk GaAs and InGaAs single crystals with 25 mm diameter and up to 9 mm thicknesses have been grown [39, 40] with and without the application of a strong magnetic field. It was shown experimentally that the application of a static magnetic field, up to a critical field strength [35, 38, 40], indeed suppresses convection, and leads to thick and very flat crystals of uniform compositions.

In addition, LPEE experiments in [39] under static magnetic field also led to very significant results. The mass transport was extraordinarily enhanced in the presence of applied magnetic field. Experiments showed that the growth rate is proportional to the field, and increases with the field intensity level. For instance, the growth rate at $J = 3$ A/cm^2 electric current density was more than ten times higher for the 0.45 T magnetic field level than that under no magnetic field. In addition, the LPEE growth was independent of the direction of the magnetic field. A number of experiments were conducted at three levels of magnetic field intensities taking the magnetic field vector **B** both upward and downward. All the experiments were successful and the grown crystals were single crystals. The growth rates in these experiments were the same whether **B** was up or down. This showed that the mass transport due to electromigration was only dependent on the magnetic field intensity but not on the field direction. Measured growth rates are presented in Table 4.1. Details of LPEE experimental procedures can be found in [39, 46].

4.1.2 Traveling Heater Method

The Traveling Heater Method (THM) is also a solution growth technique in which a metallic liquid solution is placed between a polycrystalline source and a single crystal seed in a quartz ampoule (see Fig. 4.2: a laboratory THM system used at the Crystal Growth Lab of University of Victoria is shown [44]). A predetermined temperature profile is then imposed on the growth ampoule. Then, the imposed temperature profile, by moving either the heater or the growth ampoule, is slowly moved upward at a predetermined rate (with a continuous motion as much as

Table 4.1 Summary of experimental results [39, 46] at $J = 3$ A/cm^2

Magnetic field intensity (T)	0.0	0.1	0.2	0.45
Experimental growth rate (mm/day)	0.50	1.62	2.35	6.10

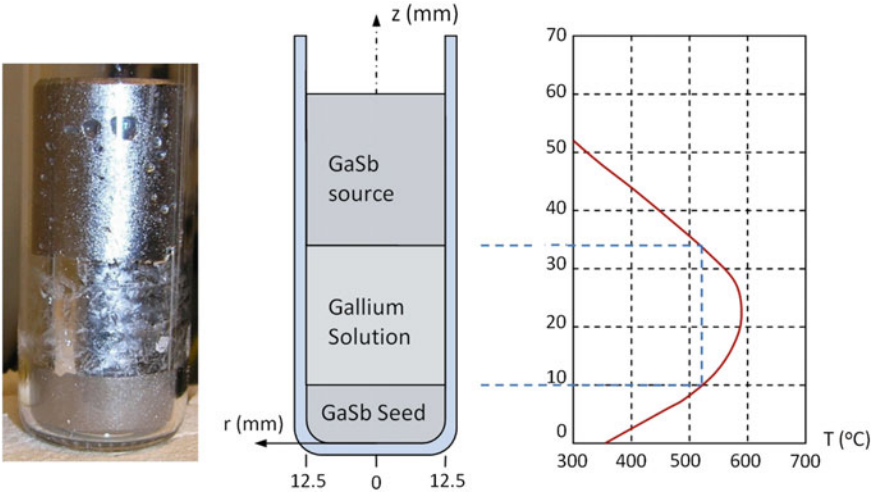

Fig. 4.2 The THM GaSb system used at University of Victoria: (i) a sample of grown crystal (left), (ii) the schematics of the growth crucible (middle), and (iii) the actual applied temperature profile (right) [44]

possible). When the temperature profile (the right figure in Fig. 4.2) moves upwards, the dissolution interface (the interface between the source and the liquid solution; see the middle figure in Fig. 4.2) hits the hotter section of the temperature profile and dissolves the source material. This dissolution provides constantly the needed material to the liquid solution. With the movement of the temperature profile, at the same time, the growth interface (the interface between the substrate and the liquid solution) hits the cooler section of the temperature profile, and the supersaturated solution in the vicinity of the growth interface solidifies on the seed crystal. With this process, a constant, controlled, but slow growth is achieved.

The quality of grown crystals in THM is very sensitive to the relative movement of the temperature profile that determines the growth rate. It is important to mention that the growth rate (which is the rate (speed) of the heater or the ampoule movement) is determined by the crystal grower based on his/her experience. If the rate is lower than the actual mass transport in the liquid zone, the material yield will be less and the grown crystals will be more expensive. On the other hand, if the growth rate is selected higher, the grown crystals will be of poor quality due to possible inclusions of elements of the solution mixture. For instance, in growth of GaSb we may have elemental Ga or Sb trapped in the grown GaSb crystals. Therefore, the availability of accurate models for THM is very important for the growth of high quality crystals with a sufficient yield.

In a typical THM system, temperature gradients in the liquid solution zone are very large compared with that of an LPEE system. It may reach a maximum of about 30 °C/cm. Naturally such a large temperature gradient gives rise to very strong convection in the solution zone. In order to reduce the adverse effect of

convection, a large number of studies are conducted considering the application of an external magnetic field [15, 21, 25, 26, 28, 35, 37, 42]. These studies have shown that a strong magnetic field is beneficial in suppressing convection. A weak but rotating magnetic field has also been used to provide better mixing in the solution zone for growth of better quality crystals [15, 16, 21, 25, 26, 33, 42]. In addition, THM experiments conducted in our laboratory under a weak rotating magnetic field are showing the possibility of increasing the THM growth about two or three times compared with that of no magnetic field [44]. Such results are very important for THM, and definitely show the importance of mathematical modeling for a better understanding of the effects of magnetic field on mass transport in crystal growth. In order to make more accurate predictions, the availability of a model that also includes some nonlinear effects would be beneficial for researchers in this field.

4.2 Basic Equations of an Electromagnetic Liquid Continuum

In this section we present the basic equations of an electromagnetic liquid continuum of a binary mixture. Solutions used in both LPEE and THM are metallic liquids and are generally good conductors. We will therefore assume that the liquid phase is a conductive, viscous fluid with no polarization and magnetization. Following closely the procedures given by Eringen and Maugin [1] and [3, 4], the basic and general constitutive equations of a binary mixture under the assumption of the classical magnetohydrodynamic (MHD) approximation were obtained [6, 7].

4.2.1 Basic Equations

Under the assumption of magnetohydrodynamic approximation the Maxwell equations take the following forms in the RMKS unit system [1]:

$$\nabla \times \mathbf{E} + \frac{\partial \mathbf{B}}{\partial t} = \mathbf{0}, \quad \nabla \cdot \mathbf{B} = \mathbf{0}, \quad \nabla \times \mathbf{H} - \mathbf{J} = \mathbf{0}, \quad \nabla \cdot \mathbf{J} = \mathbf{0} \tag{4.2.1}$$

where $\mathbf{B} = \mu_0 \mathbf{H}$ and $\mathrm{E} = \mathbf{E} + \mathbf{v} \times \mathbf{B}$. Here $\mathbf{E}$, $\mathbf{B}$, $\mathbf{H}$, and $\mathbf{J}$ denote the electric field, magnetic induction, magnetic field, and electric current density, respectively, and μ_0 is the permeability of vacuum. The contribution of the free charge density is neglected. This is a good approximation for metallic liquids [4], and for the same reason, the partial derivative of the electric displacement was also neglected in Eq. $(4.2.1)_3$. The associated jump conditions on a surface of discontinuity $\sigma(t)$, moving with a velocity $\mathbf{V}$ can be found in [1].

The metallic binary liquid solution (for instance, a Ga-As solution for the growth of GaAs, or Cd-Te for CdTe, or Ga-Sb for GaSb, etc.) is assumed to be a non-polarizable, non-magnetizable, Newtonian viscous liquid mixture. Under the above assumptions and also based on the magnetohydrodynamic approximation, the thermomechanical balance laws of such a medium, namely the overall conservation of mass, the balance of linear momentum, the conservation of mass for the solute (for instance *As* in a *Ga*-rich solvent), the balance of energy, and the second laws of thermodynamics yields the following local balance equations (see [1, 4, 6, 7] for derivation).

Continuity

$$\frac{\partial \rho}{\partial t} + \nabla \cdot (\rho \mathbf{v}) = 0 \tag{4.2.2}$$

Momentum

$$-\nabla \pi + \nabla . {}_D\mathbf{t} + \rho \left(\mathbf{f} - \frac{\partial \mathbf{v}}{\partial t} - \mathbf{v} . \nabla \mathbf{v} \right) + \mathbf{f}^{em} = \mathbf{0} \tag{4.2.3}$$

Mass transport

$$\rho \left(\frac{\partial C}{\partial t} + \mathbf{v} . \nabla C \right) = \nabla . \mathbf{i} \tag{4.2.4}$$

Energy

$$\rho \vartheta \left(\frac{\partial \eta}{\partial t} + \mathbf{v} . \nabla \eta \right) = tr({}_D\mathbf{t} . \mathbf{d}) + \nabla . \mathbf{q} - \mu \nabla . \mathbf{i} + \rho h + \mathbf{J} . \mathrm{E} \tag{4.2.5}$$

Entropy inequality

$$tr({}_D\mathbf{t} . \mathbf{d}) + \frac{1}{\vartheta} (\mathbf{q} - \mu \mathbf{i}) . \nabla \vartheta + \mathbf{i} . \nabla \mu + \mathbf{J} . \mathrm{E} \geq 0 \tag{4.2.6}$$

In Eqs. (4.2.2)–(4.2.6) ρ denotes the mass density of the binary mixture defined in terms of mass densities of the solute ρ_1 and the solvent ρ_2 by $\rho = \rho_1 + \rho_2$, C is the mass concentration of the solute defined by $C = \rho_1 / \rho$, π is the thermodynamic pressure, ${}_D\mathbf{t}$ is the dissipative part of the stress tensor, $\mathbf{f}$ is the body force due to gravitation, $\mathbf{i}$ and $\mathbf{q}$ are the concentration and heat fluxes, respectively, h is the internal heat source, ϑ and η denote respectively the absolute temperature and the entropy density function. $\mathbf{f}^{em} = \mathbf{J} \times \mathbf{B}$ represents the magnetic body force [42] where the convection current is assumed to be negligible compared with the conduction current. The effective chemical potential is defined by $\mu = \mu_1 - \mu_2$ where μ_1 and μ_2 are the chemical potentials of the solute and solvent, respectively. The deformation

rate tensor, $\mathbf{d}$ is given by $2\mathbf{d} = \nabla \otimes \mathbf{v} + (\nabla \otimes \mathbf{v})^T$ where T denotes transpose, and ∇ is the gradient operator. The associated interface conditions related to overall mass balance, momentum balance, mass transport, and energy balance can be found in [4, 6, 7].

4.2.2 Constitutive Equations

A complete set of nonlinear constitutive equations of an electromagnetic fluid is given by Eringen and Maugin in [1] for a single conductive continuum, taking into account both polarization and magnetization. The *linear* constitutive equations of a binary metallic liquid mixture were obtained in [3, 4] where the mixture was assumed nonpolarizable and nonmagnetizable. Following the same procedure of [1] and [3, 4] the *nonlinear* constitutive equations for a nonpolarizable and nonmagnetizable binary metallic liquid mixture were given in [6, 7]. After lengthy manipulations, the constitutive equations for the mass flux $\mathbf{i}$, the heat flux $\mathbf{q}$, and the electric current $\mathbf{J}$ were obtained as

$$\begin{aligned}\rho^{-1}\mathbf{i} = {} & D_1\nabla C + D_2\nabla T + D_3\mathrm{E} + D_4\mathbf{d}\nabla C + D_5\mathbf{d}\nabla T + D_6\mathbf{d}\mathrm{E} + D_7\nabla C\times\mathbf{B} \\ & + D_8\nabla T\times\mathbf{B} + D_9\mathrm{E}\times\mathbf{B} + D_{10}\mathbf{d}^2\nabla C + D_{11}\mathbf{d}^2\nabla T + D_{12}\mathbf{d}^2\mathrm{E} + D_{13}(\mathbf{B}\cdot\nabla C)\mathbf{B} \\ & + D_{14}(\mathbf{B}\cdot\nabla T)\mathbf{B} + D_{15}(\mathbf{B}\cdot\mathrm{E})\mathbf{B} + D_{16}\{\mathbf{d}(\nabla C\times\mathbf{B}) - \mathbf{d}(\mathbf{B}\times\nabla C)\} \\ & + D_{17}\{\mathbf{d}(\nabla T\times\mathbf{B}) - \mathbf{d}(\mathbf{B}\times\nabla T)\} + D_{18}\{\mathbf{d}(\mathrm{E}\times\mathbf{B}) - \mathbf{d}(\mathbf{B}\times\mathrm{E})\}\end{aligned} \tag{4.2.7}$$

$$\begin{aligned}\mathbf{q} = {} & k_1\nabla T + k_2\nabla C + k_3 E + k_4\mathbf{d}\nabla T + k_5\mathbf{d}\nabla C + k_6\mathbf{d}\mathbf{E} + k_7\nabla T\times\mathbf{B} + k_8\nabla C\times\mathbf{B} \\ & + k_9\mathrm{E}\times\mathbf{B} + k_{10}\mathbf{d}^2\nabla T + k_{11}\mathbf{d}^2\nabla C + k_{12}\mathbf{d}^2\mathrm{E} + k_{13}(\mathbf{B}\cdot\nabla T)\mathbf{B} + k_{14}(\mathbf{B}\cdot\nabla C)\mathbf{B} \\ & + k_{15}(\mathbf{B}\cdot\mathrm{E})\mathbf{B} + k_{16}\{\mathbf{d}(\nabla T\times\mathbf{B}) - \mathbf{d}(\mathbf{B}\times\nabla T)\} + k_{17}\{\mathbf{d}(\nabla C\times\mathbf{B}) \\ & - \mathbf{d}(\mathbf{B}\times\nabla C)\} + k_{18}\{\mathbf{d}(\mathrm{E}\times\mathbf{B}) - \mathbf{d}(\mathbf{B}\times\mathrm{E})\}\end{aligned} \tag{4.2.8}$$

$$\begin{aligned}\mathbf{J} = {} & \sigma_1 E + \sigma_2\nabla T + \sigma_3\nabla C + \sigma_4\mathbf{d}\mathrm{E} + \sigma_5\mathbf{d}\nabla C + \sigma_6\mathbf{d}\nabla T + \sigma_7\mathrm{E}\times\mathbf{B} + \sigma_8\nabla C\times\mathbf{B} \\ & + \sigma_9\nabla T\times\mathbf{B} + \sigma_{10}\mathbf{d}^2 E + \sigma_{11}\mathbf{d}^2\nabla T + \sigma_{12}\mathbf{d}^2\nabla T + \sigma_{13}(\mathbf{B}\cdot\mathrm{E})\mathbf{B} + \sigma_{14}(\mathbf{B}\cdot\nabla C)\mathbf{B} \\ & + \sigma_{15}(\mathbf{B}\cdot\nabla T)\mathbf{B} + \sigma_{16}\{\mathbf{d}(\mathrm{E}\times\mathbf{B}) - \mathbf{d}(\mathbf{B}\times\mathrm{E})\} + \sigma_{17}\{\mathbf{d}(\nabla C\times\mathbf{B}) - \mathbf{d}(\mathbf{B}\times\nabla C)\} \\ & + \sigma_{18}\{\mathbf{d}(\nabla T\times\mathbf{B}) - \mathbf{d}(\mathbf{B}\times\nabla T)\}\end{aligned} \tag{4.2.9}$$

where the stress tensor ${}_D\mathbf{t}$ (dissipative) was not presented here for the sake of space (see [6, 7]) and $W_{kl} = \varepsilon_{klm}B_m$ and ε_{klm} is the permutation symbol, and subscript S indicates symmetrization. In these equations, the notation of [1] was adopted, i.e., a

tensor product sign was used between two vectors, but no sing was used between a second order tensor and a vector to denote the operation of contraction. Coefficients $D_1, \ldots, D_{18}$; $k_1, \ldots, k_{18}$; $\sigma_1, \ldots, \sigma_{18}$ and $\alpha_1, \ldots, \alpha_{25}$ are functions of temperature T, concentration C, and also the joint invariants of **d**, E, **B**, ∇T, and ∇C. These invariants can be read from Table E1 in [1]. They are not presented here for the sake of brevity. However, some that are essential for the models of LPEE and THM will be presented later. These equations will be simplified based on physical grounds. The physical significance of some of the coefficients, related to the LPEE and THM growth processes, will be discussed. Previous numerical simulations have shown that the concentration field (mass transport) is more sensitive to nonlinear interactions than the thermal and flow fields [58, 59]. We therefore focus on the mass flux given in Eq. (4.2.7).

In this constitutive equation, the first three terms, $D_1\nabla C$, $D_2\nabla T$, and $D_3 E$ are linear in ∇C, ∇T, and E, but the coefficients D_1, D_2, and D_3 are still arbitrary functions of T, C, and the joint invariants of **d**, E, **B**, ∇T, and ∇C. We first expand these coefficients into a Taylor series about a reference temperature T_0, and concentration C_0. This process is straightforward but very lengthy. We only present the procedure for the mass flux, and then write the resulting equations for the others. Let us begin with $D_1 = D_1(T, C, I_1, I_2, I_3, \ldots, I_K)$, $D_2 = D_2(T, C, I_1, I_2, I_3, \ldots, I_K)$, $D_3 = D_3(T, C, I_1, I_2, I_3, \ldots, I_K)$ where some of the invariants are $I_1 = tr(\mathbf{d}) = I$, $I_2 = tr(\mathbf{d}^2) = I^2 - 2(II)$, $I_3 = tr(\mathbf{d}^3) = I^3 - 2(I)(II) + III$, $I_4 = \mathrm{E}\cdot\mathrm{E}$, $I_5 = \mathbf{B}\cdot\mathbf{B}$, $I_6 = (\mathrm{E}\cdot\mathbf{B})^2$, etc. [1]. The remaining invariants can be read from Table E1 of [1], of course, by adding the concentration gradient to the list of independent variables. We expand D_1, D_2, and D_2 into a Taylor series:

$$D_1 = \{D_C + D_{CE}E + D_{CB}B\} + \ldots\} + \{D_{CC} + D_{CCE}E + D_{CCB}B + \ldots\}C + \{D_{CT} + D_{CTE}E + D_{CTB}B + \ldots\}T \ldots\ldots \tag{4.2.10}$$

$$D_2 = \{D_T + D_{TE}E + D_{TB}B\} + \ldots\} + \{D_{TC} + D_{TCE}E + D_{TCB}B + \ldots\}C + \{D_{TT} + D_{TTE}E + D_{TTB}B + \ldots\}T \ldots. \tag{4.2.11}$$

$$D_3 = \{D_E + D_{EE}E + D_{EB}B\} + \ldots\} + \{D_{EC} + D_{ECE}E + D_{ECB}B + \ldots\}C + \{D_{ET} + D_{ETE}E + D_{ETB}B + \ldots\}T \ldots. \tag{4.2.12}$$

where $E = \sqrt{I_4}$, $B = \sqrt{I_5}$, and the material constants appearing in the above equations are functions of the reference temperature and the reference concentration only. Now using Eqs. (4.2.10)–(4.2.12) in Eq. (4.2.7), and also dropping some higher order terms we obtain the mass flux as

$$\begin{aligned}\rho^{-1}\mathbf{i} = &\{(D_C + D_{CE}E + D_{CB}B) + (D_{CC} + D_{CCE}E + D_{CCB}B)C \\ &+ (D_{CT} + D_{CTE}E + D_{CTB}B)T + \ldots.\}\nabla C + \{(D_T + D_{TE}E + D_{TB}B) \\ &+ (D_{TC} + D_{TCE}E + D_{TCB}B)C + (D_{TT} + D_{TTE}E + D_{TTB}B)T + D_{TCC}C^2 + \ldots\}\nabla T \\ &+ \{(D_E + D_{EE}E + D_{EB}B) + (D_{EC} + D_{ECE}E + D_{ECB}B)C \\ &+ (D_{ET} + D_{ETE}E + D_{ETB}B)T + \ldots.\}\mathrm{E} + \ldots..\end{aligned} \tag{4.2.13}$$

where we have not written the remaining higher order cross terms for the sake of space. In the above equations, the following convention was used for the subscripts in material constants. In the expanded parts, we used only letters, and the first letter indicates the direct contribution of the field to the related flux, while the second and third letters describe higher order contributions of the other fields. For instance, D_C is the coefficient of the direct contribution of ∇C to the mass flux, and D_{EC} represents the interactive contribution of $\boldsymbol{E}$ with C to the mass flux. In addition, the number of letters describes the rank of the order of contribution. For instance, D_C is a first order contribution while D_{EC} and D_{ECB} are the second and third order contributions. The coefficients in the cross terms, the first index (letter) refer to the depended variable (fluxes), for the second indices we kept the numbering indexing to make the identification tractable.

Equation (4.2.13) can be further simplified based on physical grounds and experimental observations. At this point, considering the applications only in LPEE and THM growth of crystals, we will leave only the terms up to second order with the exception of two third order coefficients in the coefficient of $\boldsymbol{E}$, and one in the coefficient of ∇T. The significance of higher order coefficients will be discussed later. It is important to mention that the decision of leaving coefficients in a model in or out depends on how the model is being developed. This can either be the result of experimental observations that may force us to reexamine the significance of such coefficients in a model to make more accurate predictions, or can be brought about in the development of a general theory which can be tried to be proven by experiments. The former is the reason in this work. Based on the purpose in mind, Eq. (4.2.13) is simplified further to

$$\begin{aligned}\rho^{-1}\mathbf{i} = &\{D_C + D_{CC}C + D_{CT}T + D_{CE}E + D_{CB}B\}\nabla C + \{D_T + D_{TC}C + D_{TT}T \\ &+ D_{TCC}C^2\}\nabla T + \{D_E + (D_{EC} + D_{ECB}B)C + (D_{ET} + D_{ETB}B)T\}\mathrm{E} \\ &+ D_{C4}\mathbf{d}\nabla C + D_{C5}\mathbf{d}\nabla T + D_{C6}\mathbf{d}\mathrm{E} + D_{C7}\nabla C \times \mathbf{B} + D_{C8}\nabla T \times \mathbf{B} + D_{C9}\mathrm{E} \times \mathbf{B}\end{aligned} \tag{4.2.14}$$

We will leave the mass flux in its form at the moment. We will later make further simplifications specific to each crystal growth technique. Also when we use Eq. (4.2.14) in the mass balance equation, further simplifications can be made by dropping higher order terms depending on their significance to the process under consideration, and also due to the restrictions imposed by the entropy inequality on material coefficients.

Following the same procedure and arguments, the heat flux, electric current and stress tensor can be simplified further. In these equations, for the sake of brevity, we will leave only the terms that are significant for discussion, i.e.,

$$\begin{aligned}\mathbf{q} = k_T\nabla T + k_C\nabla C + k_E\mathrm{E} \; + k_{T4}\mathbf{d}\nabla T + k_{T5}\mathbf{d}\nabla C + k_{T6}\mathbf{d}\mathrm{E} \; + \mathrm{k}_{T7}\nabla T\times\mathbf{B} \\ + k_{T8}\nabla C\times\mathbf{B} + k_{T9}\mathrm{E}\times\mathbf{B}\end{aligned} \tag{4.2.15}$$

$$\mathbf{J} = \sigma_E\mathrm{E} \; + \sigma_T\nabla T \quad \text{and} \quad {}_D\mathbf{t} = 2\mu_v\mathbf{d} \tag{4.2.16}$$

Equations (4.2.15)–(4.2.16) must satisfy the entropy inequality in Eq. (4.2.6). The material constants are functions of the reference temperature and concentration only. The physical significance of the constitutive constants appearing in these constitutive equations has been discussed in details in regard to crystal growth of semiconductors in [6, 7].

4.3 Liquid Phase Electroepitaxial Growth of Binary Systems Under Magnetic Field

We only present here the equations of the liquid phase. The equations of the solid phases for a binary system are the same as those given in [4]. We will now develop the model equations for the growth of *GaAs* crystals by LPEE under an applied magnetic field, specific to the LPEE growth system used in our Crystal Growth Laboratory. Here we make the following assumptions and simplifications in obtaining the field equations, and the boundary and interface conditions.

(i) The so-called Boussinesq approximation holds, that is, the density of the liquid phase is constant everywhere in the field equations except in the body force term due to gravitation. In order to allow density variations, we write

$$\rho\mathbf{f} = \mathbf{g}\{-\rho_L\beta_T(T-T_0) + \rho_L\beta_C(C-C_0)\} \tag{4.3.1}$$

where ρ_L is the constant density of the liquid solution, and β_T and β_C are the thermal and solutal expansion coefficients, respectively, and T_0 and C_0 are the reference temperature and concentration. In this special case the continuity equation will reduce to the incompressibility condition, i.e., $\nabla\cdot\mathbf{v} = 0$.

(ii) In the LPEE systems used in our Laboratory, the electric field and the magnetic field are aligned vertically with the symmetry axis of the growth crucible. The magnetic field measurements made in the absence of growth crucible also shown that the magnetic field is almost uniform in the space where the growth cell is located (see [17]). The fields are also constant; do not vary in time. These reduce the Maxwell equations to a single equation, i.e., $\nabla\cdot\mathbf{J} = 0$. The electric field in the solution will be obtained from the solution of $\nabla\cdot\mathbf{J} = 0$, as was the case in [35, 36]. However, since the LPEE growth

crucible was designed so as to have an almost uniform electric current distribution in the liquid zone, and also since the computed electric field was almost uniform in [35, 36], in this work we will consider the electric current distribution is uniform for computational convenience. Otherwise, $\nabla \cdot \mathbf{J} = 0$ must be added to the field equations. In addition, the induced magnetic field due to the applied electric current is small, so is neglected.

(iii) Since the electromigration of species is the dominant mechanism of mass transport in LPEE, we further assume that the contributions of (a) nonlinear terms, such as $D_{C7}\nabla C \times \mathbf{B}$, $D_{C8}\nabla T \times \mathbf{B}$, $D_{C9}\mathrm{E} \times \mathbf{B}$, $k_{T7}\nabla T \times \mathbf{B}$, $k_{T8}\nabla C \times \mathbf{B}$, $k_{T9}\mathrm{E} \times \mathbf{B}$, $\sigma_{J7}\mathrm{E} \times \mathbf{B}$, $\sigma_{J8}\nabla C \times \mathbf{B}$, $\sigma_{J8}\nabla T \times \mathbf{B}$, $\mu_{vT}T$, and $\mu_{vC}C$, and (b) the Soret (D_T) and Dufour (k_C) effects are negligible.

(iv) In Fig. 4.1 the applied static magnetic field is shown upward, but as mentioned earlier, the two sets of LPEE growth experiments performed specifically for the work in [43] showed that the growth is in the direction of applied electric current, and the growth rate is almost the same regardless whether the applied magnetic field is upward or downward. This eliminates the possibility of the explicit dependence of the mass flux on the magnetic field vector. Indeed, the constitutive equations developed so far are in compliance with this observation; there was no magnetic induction vector dependence in the constitutive equations.

(v) The contribution of the Joule heating can be neglected since the liquid is a good conductor. However, it must be taken into account in the solid phases (source, seed, and grown crystal). In addition, the contribution of $(\mathbf{v} \times \mathbf{B}) \times \mathbf{B}$ to the electric current can also be neglected based on our previous numerical simulations in [36, 42, 45, 46] that the contribution of $(\mathbf{v} \times \mathbf{B}) \times \mathbf{B}$ with respect to $\mathbf{E}$ is very small. Then the constitutive equations for the case considered become

$$\frac{1}{\rho_L}\mathbf{i} = D_C\nabla C + (D_{EC} + D_{ECB}B)C\mathrm{E}, \quad \mathbf{q} = k_T\nabla T, \quad \mathbf{J} = \sigma_E\mathrm{E}, \quad {}_D\mathbf{t} = 2\mu_v\mathbf{d} \tag{4.3.2}$$

Based on the foregoing assumptions, the use of Eq. (4.3.2) in Eqs. (4.2.2)–(4.2.5) yields respectively the following field equations

$$\begin{aligned}
&\nabla \cdot \mathbf{v} = 0,\\
&-\nabla p + 2\mu_v\nabla \cdot \mathbf{d} + \mathbf{g}\{-\rho_L\beta_T(T - T_0) + \rho_L\beta_C(C - C_0)\} + \sigma_E\mathrm{E} \times \mathbf{B}\\
&\quad = \rho_L\left(\frac{\partial \mathbf{v}}{\partial t} + \mathbf{v} \cdot \nabla\mathbf{v}\right),\\
&(D_{EC} + D_{ECB}B)\mathrm{E} \cdot \nabla C + D_C\nabla^2 C = \frac{\partial C}{\partial t} + \mathbf{v} + \nabla C,\\
&k_T\nabla^2 T = \rho_L\gamma_L\left(\frac{\partial T}{\partial t} + \mathbf{v} \cdot \nabla T\right)
\end{aligned} \tag{4.3.3}$$

where γ_L is the specific heat of the liquid solution. The above equations will be supplemented by appropriate boundary and interface conditions for a selected specific domain (the growth cell). These conditions can be found in our earlier simulation studies for specific growth crucibles [36, 42, 45, 46].

4.3.1 Electromagnetic Mobility

The first term in the mass transport equation, Eq. $(4.3.3)_3$, i.e., $\mu_t = D_{EC} + D_{ECB}B \equiv \mu_E + \mu_{EB}B$ represents the contribution of applied electric current density to mass transport under the effect of a static external magnetic field. This effect is known as *electromigration*. Its coefficient, which will be called from now on "*the total mobility*", is written in the following form for convenience $\mu_t = D_{EC} + D_{ECB}B \equiv \mu_E + \mu_{EB}B$ where the material constant μ_E (a second order material coefficient) is the *classical electric mobility* of the solute (*As*) in the liquid solution (Ga-As solution) due to the applied electric current in the absence of an applied magnetic field. The constant μ_{EB} is a third order material coefficient that represents the contribution of the applied magnetic field intensity to the electromigration of species. It is zero (or insignificant) in the absence of applied electric current. This term is new, and defined for the *first time* by the Author. It is called *"Electromagnetic effect" or Electromagnetic mobility"*. Below we will give an estimate for its numerical value using the experimental results of [39] and [46].

Experiments show that the growth rate is proportional to the applied electric current density, and we have evaluated the value of μ_E in the Ga-As (and also in *In-Ga-As*) solution in the absence of applied magnetic field. The numerical simulations based on this value verify the experimental growth rates at all three electric current levels (J = 3, 5, and 7 A/cm^2) (see [31]). Of course, the diffusion (the second term, $D_C\nabla^2 C$) and also the natural convection (the last term on the right-hand side, $\mathbf{v}\cdot\nabla C$) contribute to the growth rate [4, 17, 22, 23, 35, 38, 40]. However, in LPEE the contribution of the first term (electromigration) is dominant [23], and the growth rate can be assumed proportional to this term. Experiments also show that the growth rate increases significantly in the presence of a static magnetic field, and is also proportional to the field intensity level as long as the field level is below a critical value above which the growth is not stable [39, 45].

The numerical values of μ_E and μ_{EB} are calculated using the results of a large number of experiments of [39, 46] in which the magnetic field vector **B** was used both upward and downward. The growth rates in these experiments were almost the same whether **B** was up or down. In other words the mass transport due to electromigration was only dependent on the magnetic field intensity but not on its direction. This is also in compliance with the defined constitutive equations. Using the measured growth rates given in Table 4.1, the *total magnetic mobility* was computed as $\mu_t = \mu_E + \mu_{EB}B \cong 0.7\times10^{-5} + 1.4\times10^{-5}B$ where the above mobility values are computed as $\mu_E = 0.7\times10^{-5}\text{m}^2/\text{Vs}$ and $\mu_{EB} = 1.4\times10^{-4}\text{m}^2/\text{Vs}$ (tesla)

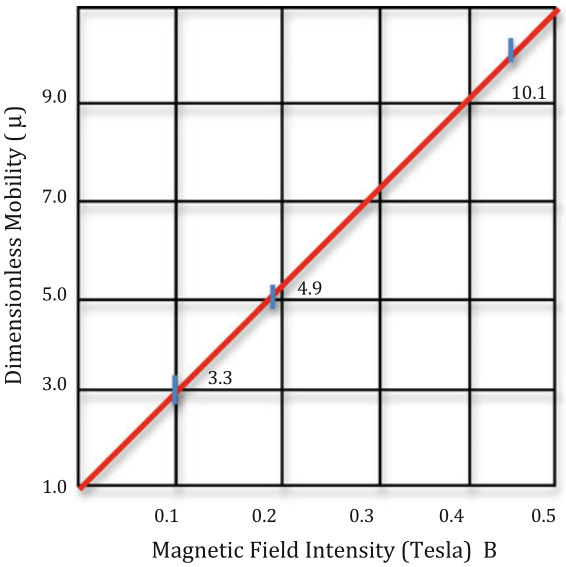

Fig. 4.3 Dependence of the total mobility on magnetic field intensity

(electromagnetic effect). Equation (4.3.4) can be expressed in terms of a dimensionless mobility as

$$\mu = \frac{\mu_t}{\mu_E} = 1 + \frac{\mu_{EB}}{\mu_E} B \cong 1 + 20B \tag{4.3.4}$$

which is plotted in Fig. 4.3. As seen the total mobility is almost linearly dependent on the magnetic field intensity, within the limits of experimental measurements.

Growth rate under the effect of applied magnetic field will then be calculated by using the total mobility (instead of using only electric mobility) given by

$$V_g = \frac{\rho_L}{\rho_S}\left(D_C \frac{\partial C}{\partial n} + \mu_t E_z C\right)\frac{1}{C_S - C} \tag{4.3.5}$$

which predicts the experimental growth rate accurately.

4.4 Growth of Binary Systems by the Traveling Heater Method Under Magnetic Fields

As described in the introduction section, the Traveling Heater Method (THM) is a solution growth technique and the driving force is the applied temperature profile. There is no applied electric current imposed on the system. However, an external static magnetic field has been used in THM to suppress the convective flow in the solution zone. The interaction of the applied magnetic field with other field

gradients may induce an electric current. In this case the simplified constitutive equation for the mass flux can be written from Eq. (4.2.14) as

$$\rho^{-1}\mathbf{i} = D_C\nabla C + D_T\nabla T + D_{C4}\mathbf{d}\nabla C + D_{C5}\mathbf{d}\nabla T + D_{C7}\nabla C\times\mathbf{B} + D_{C8}\nabla T\times\mathbf{B} + k_{T9}\mathrm{E}\times\mathbf{B} \tag{4.4.1}$$

where $\mathrm{E} = \mathbf{E}_{ind} + \mathbf{v}\times\mathbf{B}$ and where $\mathbf{E}_{ind}$ represent the induced electric field due to the applied magnetic field. When the applied magnetic field is constant in time and also uniform in space, the contribution of the induced electric field can be neglected; leaving only the term $\mathbf{v}\times\mathbf{B}$ in the electric field term above.

Below we now present the constitutive equations and also the associated field equations for the THM growth of a binary system such as CdTe or GaSb under certain simplifying assumptions in view of metallic solutions involved in the growth of such semiconductor single crystal materials. These assumptions, however, must be re-examined, whenever in doubt, based on experimental observations.

4.4.1 Growth by the Traveling Heater Method Under Static Magnetic Field

In this section we develop the model equations step by step, making certain simplifying assumptions and also discussing the implications of the simplifications made or not made. Lets us begin with the mass transport equation, in Eq. (4.2.4), and evaluate $\nabla.(\rho^{-1}\mathbf{i})$ using Eq. (4.4.1) with the assumption of negligible $\mathbf{E}_{ind}$. Then we have

$$\nabla.(\rho^{-1}\mathbf{i}) = D_C\nabla^2 C + D_T\nabla^2 T + D_{C4}\cdot(\mathbf{d}\nabla C) + D_{C5}\nabla\cdot(\mathbf{d}\nabla T) + D_{C7}\nabla\cdot(\nabla C\times\mathbf{B}) + D_{C8}\nabla\cdot(\nabla T\times\mathbf{B}) + D_{C9}\nabla\cdot((\mathbf{v}\times\mathbf{B})\times\mathbf{B}) \tag{4.4.2}$$

The first term in Eq. (4.4.2), $D_C\nabla^2 C$, represents the molecular diffusion with a constant effective diffusion coefficient, D_C. This is the only term considered in most modeling studies for THM. The second term, $D_T\nabla^2 T$, is the Soret effect which is the contribution of temperature gradient to mass transport. Depending on the material (the value of the Soret coefficient, D_T) considered, it may or may not be significant. It must be taken into account if there is a physical evidence of its significance. For instance, this effect was considered in [60, 61] by not taking D_T into account but the nonlinear terms $D_{TC}C$ and $D_{TCC}C^2$, and was shown that their contribution was significant. The third and the fourth terms, $D_{C4}\nabla\cdot(\mathbf{d}\nabla C)$ and $D_{C5}\nabla\cdot(\mathbf{d}\nabla T)$, are the second order terms, and represent respectively the interaction of fluid flow with concentration and temperature gradients. In most models their contribution is neglected.

In the presence of an applied magnetic field, the last term, $D_{C7}\nabla\cdot(\nabla C\times\mathbf{B})$, represents the contribution of the applied magnetic field to the mass transport.

$$D_{C7}(\varepsilon_{klm}C_{,l}B_m)_{,k}=D_{C7}(\varepsilon_{klm}C_{,lm}B_m+\varepsilon_{klm}C_{,l}B_{m,k})=D_{C7}\varepsilon_{klm}C_{,l}B_{m,k} \tag{4.4.3}$$

We now examine this term closely. Here we used the index notation for convenience. As can be seen this term will not vanish if the magnetic field is not constant in space (not uniform). In such a case, it must be included in a model, and its significance can only be determined by experiments. It is possible that it may contribute to the growth rate in THM, for instance the growth rate may be increased by a proper application of the external magnetic field.

In the THM system in our Laboratory at the University of Victoria, a strong static magnetic field up to 1.25 T can be applied in the vertical direction that is aligned with the growth direction. The superconducting magnet (with 13 "opening) is designed so as to provide an almost uniform field in the central region where the liquid solution zone will be located in the growth ampoule. Indeed in the absence of growth crucible the field is uniform in this space. However, the field distribution may be altered when the growth ampoule is lowered into the magnet opening. If the field is assumed to be uniform in the liquid solution, then the contribution of the last term can be neglected. Otherwise this term must be taken into account in modeling.

Then Eq. (4.4.2) can be simplified to

$$\nabla\cdot\left(\frac{1}{\rho_L}\right)\mathbf{i}=D_C\nabla^2C+D_T\nabla^2T+D_{C9}\nabla\cdot((\mathbf{v}\times\mathbf{B})\times\mathbf{B}) \tag{4.4.4}$$

Following a similar reasoning, the constitutive equations for the heat flux and electric current can be simplified to

$$\mathbf{q}=k_T\nabla T+k_C\nabla C,\quad \mathbf{J}=\sigma_E\mathrm{E}\ +\sigma_T\nabla T+\sigma_C\nabla C+\sigma_{J7}(\mathbf{v}\times\mathbf{B})\times\mathbf{B} \tag{4.4.5}$$

The field equations in this case take the following forms

$$\begin{aligned}
&\nabla\cdot\mathbf{v}=0,\\
&-\nabla p+2\mu_v\nabla.\mathbf{d}+\mathbf{g}\{-\rho_L\beta_L(T-T_0)+\rho_L\beta_C(C-C_0)\}+\sigma_E(\mathbf{v}\times\mathbf{B})\times\mathbf{B}\\
&\quad=\rho_L\left(\frac{\partial\mathbf{v}}{\partial t}+\mathbf{v}.\nabla\mathbf{v}\right),\\
&D_C\nabla^2C+D_T\nabla^2T+D_{C9}\nabla\cdot((\mathbf{v}\times\mathbf{B})\times\mathbf{B})=\frac{\partial C}{\partial t}+\mathbf{v}.\nabla C,\\
&k_T\nabla^2T+k_C\nabla^2C-\mu\{D_C\nabla^2C+D_T\nabla^2T+D_{C9}\nabla\cdot((\mathbf{v}\times\mathbf{B})\times\mathbf{B})\}+\sigma_EE^2\\
&\quad+\{\sigma_T\nabla T+\sigma_C\nabla C+\sigma_{J7}((\mathbf{v}\times\mathbf{B})\times\mathbf{B})\}\cdot((\mathbf{v}\times\mathbf{B})\times\mathbf{B})=\rho_L\gamma_L\left(\frac{\partial T}{\partial t}+\mathbf{v}.\nabla T\right)
\end{aligned} \tag{4.4.6}$$

In addition, the remaining Maxwell equation, i.e.,

$$\sigma_E \nabla \cdot \mathrm{E} + \sigma_T \nabla^2 T + \sigma_C \nabla^2 C + \sigma_{J7} \nabla \cdot \{(\mathbf{v} \times \mathbf{B}) \times \mathbf{B}\} = 0 \tag{4.4.7}$$

must be added to these equations.

The energy equation can be further simplified if the Joule heating in the liquid zone is neglected, and also higher order interaction terms are dropped, i.e.,

$$k_T \nabla^2 T + k_C \nabla^2 C - \mu\{D_C \nabla^2 C + D_T \nabla^2 T\} = \rho_L \gamma_L \left(\frac{\partial T}{\partial t} + \mathbf{v}.\nabla T\right) \tag{4.4.8}$$

These equations can be further simplified if the Soret and Dufour effects are neglected. In that case the mass transport and energy equations become

$$D_C \nabla^2 C + D_{C9} \nabla \cdot ((\mathbf{v} \times \mathbf{B}) \times \mathbf{B}) = \frac{\partial C}{\partial t} + \mathbf{v}.\nabla C \tag{4.4.9}$$

$$k_T \nabla^2 T = \rho_L \gamma_L \left(\frac{\partial T}{\partial t} + \mathbf{v}.\nabla T\right) \tag{4.4.10}$$

In a microgravity environment such as the International Space Station, second and third order terms may become significant. As mentioned earlier, the results of microgravity solidification experiment (Mephisto in [60]) could only be predicted by a model in [61] that included the second and third order Soret effects in the mass transport equation, in the form of $D_{CT} C(1 - C) \nabla^2 T$.

4.4.2 *Growth by the Traveling Heater Method Under Rotating Magnetic Field*

As mentioned earlier a weak rotating applied magnetic field is of great interest in THM to obtain good mixing in the solution zone in order to grow crystals with uniform composition. On this topic the literature is relatively rich (see for instance [15, 16, 21, 25, 26, 32, 42]). The application of a weak rotating field can also be considered together with a strong static external magnetic field. While the strong field can provide the required control of natural convection in the liquid zone, the weak rotating field gives rise to better mixing in the solution. In this direction such a facility has been developed in our Laboratory and used to conduct experiments in growth of bulk crystals of CdTe, CdZnTe, GaSb, etc. We have also performed numerical simulations for THM growth in order to determine the feasibility of using static and rotating magnetic fields [42].

In the presence of a small rotating magnetic field, the magnetic body force will have two parts, one from the applied strong field, and the other from the rotating field; $\mathbf{f}^{em} = \mathbf{f}^{em}_{sta} + \mathbf{f}^{em}_{rot}$ where $\mathbf{f}^{em}_{sta}$ is the same given earlier and $\mathbf{f}^{em}_{rot}$ is given by

$\mathbf{f}_{rot}^{em} = \mathbf{J} \times \mathbf{B}^{rot} = \sigma_E(\mathbf{E}_{ind} + \mathbf{v} \times \mathbf{B}^{rot}) \times \mathbf{B}^{rot}$ where we have neglected the effects of temperature and concentration gradients in $\mathbf{J}$. Since the field is not stationary the Maxwell equations must be added to the system equations as

$$\nabla \times \mathbf{E}_{ind} + \frac{\partial \mathbf{B}^{rot}}{\partial t} = 0, \quad \nabla \cdot \mathbf{E}_{ind} = 0, \quad \nabla \cdot \mathbf{B}^{rot} = 0, \quad \nabla \times \mathbf{B}^{rot} - \frac{1}{\mu_0}\mathbf{J} = 0,$$
$$\nabla \cdot \mathbf{J} = 0$$

Now assuming that electric and magnetic fields can be obtained from a scalar potential ϕ, and a vector potential $\mathbf{A}$ as follows

$$\mathbf{B}^{rot} = \nabla \times \mathbf{A} \quad \text{and} \quad \mathbf{E}_{ind} = -\left(\nabla\phi + \frac{\partial \mathbf{A}}{\partial t}\right)$$

A specific application of the above components can be found in [42].

Naturally, the question of whether the growth rate in THM will be affected by the presence of an applied magnetic field (fixed or rotating) comes in mind. In this direction, we have performed THM experiments under rotating magnetic fields (RMF) for the growth of GaSb single crystals [44]. Typical industrial THM growth rate (translation rate) is about 2–3 mm/day. Faster than this rate leads to more Te inclusions in the growth crystals.

In our THM growth experiments we tested a higher growth rate: 5 mm/day and performed a number of experiments to determine the optimum RMF level. At this translation rate the THM experiments produced polycrystalline structures under the RMF of 0.8 mT field intensity and 75 Hz frequency. The crystals grown in the experiments under a 1.94 mT rotating magnetic field at 50 Hz were however predominantly single crystals with a few large grains near the crucible wall. Results of the experiments performed in [44] suggest that the growth rate of the THM growth process may be increased significantly (*more than double*) with the proper (optimum) selection of rotating magnetic field levels. It must be mention that the optimum level of RMF will be different for different materials due to different electric conductivities. For instance, in the growth of CdTe crystals the optimum level of RMF could be higher due to the lower electric conductivity of this material.

4.5 Conclusions

The models developed over the years, based on Professor Gerard Maugin's contributions to "electromagnetic interactions", are briefly presented for "solution growth" techniques under electric and magnetic fields. Basic and constitutive equations are specialized for the solution growth techniques of LPEE and THM. As an application, the LPEE growth of GaAs bulk crystals under a strong static magnetic field is considered. Experimental results, that have shown that the growth rate under an applied static magnetic field is also proportional to the applied

magnetic field and increases with the field intensity level, are predicted from these models. The contribution of a third-order material constant in LPEE is also predicted from these models. The prediction of increasing growth rate in THM growth under rotating magnetic fields was also verified by experiments.

Acknowledgements The financial support provided by the Natural Sciences and Engineering Research Council of Canada (NSERC) and the Canada Research Chairs (CRC) Program is gratefully acknowledged.

References

1. Eringen, A.C., Maugin, G.A.: Electrodynamics of Continua, vol. I and II. Springer, New York (1989)
2. Bowen, R.M.: Theory of mixtures. In: Eringen, A.C. (ed.) Continuum Physics, vol. 3, pp. 1–127. Academic Press, New York
3. Dost, S., Erbay, H.A.: A continuum model for liquid-phase electroepitaxy. Int. J. Eng. Sci. **33**, 1385–1402 (1995)
4. Dost, S., Qin, Z.: A model for liquid phase electroepitaxy under an external magnetic field I. Theory. J. Cryst. Growth **153**, 123–130 (1995)
5. Series, R.W., Hurle, D.T.J.: The use of magnetic fields in semiconductor crystal-growth. J. Cryst. Growth **113**, 305–328 (1991)
6. Dost, S., Sheibani, H.: A mathematical model for solution growth of bulk crystals under electric and magnetic fields. Philos. Mag. **85**(33–35), 4331–4351 (2005)
7. Dost, S., Lent, B.: Single crystal growth of semiconductors from metallic solutions. Elsevier, Amsterdam, The Netherlands (2007). ISBN: 0 444 52232
8. Kim, D.H., Adornato, P.M., Brown, R.A.: Effect of vertical magnetic field on convection and segregation in vertical Bridgman crystal growth. J. Cryst. Growth **89**, 339–356 (1988)
9. Hirata, H., Hoshikawa, K.: 3-dimensional numerical analyses of the effects of a cusp magnetic field on the flows, oxygen transport and heat transfer in a Czochralski silicon melt. J. Cryst. Growth **125**, 181–207 (1992)
10. Baumgartl, J., Muller, G.: Calculation of the effects of magnetic field damping on fluid flow: comparison of magnetohydrodynamic models of different complexity. In: Proceedings of the VIIIth Enropean Symposium on Materials and Fluid Sciences in Microgravity, Noordwijk, The Netherlands, pp. 161–164 (1992)
11. Baumgartl, J., Hubert, A., Muller, G.: The use of magnetohydrodynamic effects to investigate fluid flow in electrically conducting melts. Phys. Fluids A **5**, 3280–3289 (1993)
12. Salk, M., Lexow, B., Benz, K.W., et al.: CdTe crystal growth in the soviet facility ZONA 4. Microgravity Sci. Technol. **6**, 88 (1993)
13. Hurle, D.T.J. (ed.): Handbook of Crystal Growth 2: Bulk crystal growth, Part B: Growth Mechanisms and Dynamics, North-Holland (1994)
14. Oshima, M., Taniguchi, N., Kobayashi, T.: Numerical investigation of 3-dimensional melt convection with the magnetic Czochralski method. J. Crystal Growth **137**, 48–53 (1994)
15. Salk, M., Fiederle, M., Benz, K.W., Senchenkov, A.S., Egorov, A.V., Matioukhin, D.G.: CdTe and CdTe0.9Se0.1 crystal grown by the traveling heater method using a rotating magnetic field. J. Cryst. Growth **138**, 161–167 (1994)
16. Price, M.W., Andrews, R.N., Su, C.H., Lehoczky, S.L., Szofran, F.R.: The effect of a transverse magnetic field on the microstructure of directionally solidified CdTe. J. Cryst. Growth **137**, 201–207 (1994)
17. Qin, Z., Dost, S., Djilali, N., Tabarrok, B.: A model for liquid phase electroepitaxy under an external magnetic field II. Application. J. Cryst. Growth **153**, 131–139 (1995)

18. Ben Hadid, H., Henry, D.: Numerical study of convection in the horizontal Bridgman configuration under the action of a constant magnetic field. Part 1. Two dimensional flow. J. Fluid Mech. **333**, 23–56 (1996)
19. Ben Hadid, H., Henry, D.: Numerical study of convection in the horizontal Bridgman configuration under the action of a constant magnetic field. Part 2. Three-dimensional flow. J. Fluid Mech. **333**, 57–83 (1996)
20. Kakimoto, K., Yi, K.W., Eguchi, M.: Oxygen transfer during single silicon growth in Czochralski system with vertical magnetic fields. J. Cryst. Growth **163**, 238–242 (1996)
21. Fiederle, M., Eiche, C., Joerger, W., Salk, M., Senchenkov, A.S., Egorov, A.V., Ebling, D.G., Benz, K.W.: Radiation detector properties of $CdTe_{0.9}Se_{0.1}Cl$ crystals grown under microgravity in a rotating magnetic field. J. Cryst. Growth **166**, 256–260 (1996)
22. Dost, S.: Recent developments in modeling of liquid phase electroepitaxy: a continuum approach. Appl. Mech. Rev. **49**(12), 477–495 (1996)
23. Qin, Z., Dost, S.: A model for liquid phase electroepitaxial growth of ternary alloy semiconductors. Int. J. Electromagnet. Mech. **7**(2), 129–142 (1996)
24. Dost, S., Qin, Z.: A numerical simulation model for liquid phase electroepitaxial growth of GaInAs. J. Cryst. Growth **187**, 51–64 (1998)
25. Senchenkov, A.S., Barmin, I.V., Tomson, A.S., Krapukhin, V.V.: Seedless THM growth of $Cd_{(x)}Hg_{(1-x)}Te$ (approximately x = 0.2) single crystals within rotating magnetic field. J. Cryst. Growth **197**, 552–556 (1999)
26. Ghaddar, C.K., Lee, C.K., Motakef, S., Gillies, D.C.: Numerical simulation of THM growth of CdTe in presence of rotating magnetic fields (RMF). J. Cryst. Growth **205**, 97–111 (1999)
27. Davoust, L., Cowley, M.D., Moreau, R., Bolcato, R.: Buoyancy-driven convection with an uniform magnetic field. Part 2. Experimental investigation. J. Fluid Mech. **400**, 59–90 (1999)
28. Meric, R.A., Dost, S., Lent, B., Redden, R.F.: A finite element model for the growth of ternary alloy GaInSb by the travelling heater method. Int. J. Electromagnet. Mech. **10**, 505–526 (1999)
29. Dost, S.: Numerical simulation of liquid phase electroepitaxial growth of GaInAs under magnetic field. ARI-the Bull. ITU **51**, 235–246 (1999)
30. Jing, C.J., Imaishi, N., Yasuhiro, S., Sato, T., Miyazawa, Y.: Three-dimensional numerical simulation of rotating spoke pattern in an oxide melt under a magnetic field. Inter. J. Heat Mass Transf. **43**, 4347–4359 (2000)
31. Dost, S., Sheibani, H.: In Mechanics of Electromagnetic Materials and Structures in Studies in Appl. Electr. Mech., (Eds. J.S. Yang, G.A. Maugin), 19, pp. 17–29. IOS Press, Amsterdam (2000)
32. Vizman, D., Friedrich, J., Muller, G.: Comparison of the predictions from 3D numerical simulation with temperature distributions measured in Si Czochralski melts under the influence of different magnetic fields. J. Cryst. Growth **230**, 73–80 (2001)
33. Ben Hadid, H., Vaux, Samuel, Kaddeche, Slim: Three dimensional flow transitions under a rotating magnetic field. J. Cryst. Growth **230**, 57–62 (2001)
34. Akamatsu, M., Higano, M., Ozoe, H.: Elliptic temperature contours under a transverse magnetic field computed for a Czochralski melt. Int. J. Heat Mass Transf. **44**, 3253–3264 (2001)
35. Dost, S., Liu, Y.C., Lent, B.: A numerical simulation study for the effect of applied magnetic field in liquid phase electroepitaxy. J. Cryst. Growth **240**, 39–51 (2002)
36. Liu, Y.C., Okano, Y., Dost, S.: The effect of applied magnetic field on flow structures in liquid phase electroepitaxy—a three-dimensional simulation model. J. Cryst. Growth **244**, 12–26 (2002)
37. Okano, Y., Nishino, S.-S., Ohkubo, S.-S., Dost, S.: Numerical study of transport phenomena in the THM growth of compound semiconductor crystal. J. Cryst. Growth **238–239**, 1779–1784 (2002)
38. Liu, Y.C., Sheibani, H., Sakai, S., Okano, Y., Dost, S.: In: Kleijn, C.R., Kawano, S. (eds.) Computational Technologies for Fluid/Thermal/Structural/Chemical Systems with Industrial Applications. ASME Proceedings, New York, PVP-vol. 448-1, pp. 65–72 (2002). ISBN: 0-7918-4659-8

39. Sheibani, H., Dost, S., Sakai, S., Lent, B.: Growth of bulk single crystals under applied magnetic field by liquid phase electroepitaxy. J. Cryst. Growth **258**(3–4), 283–295 (2003)
40. Sheibani, H., Liu, Y.C., Sakai, S., Lent, B., Dost, S.: The effect of applied magnetic field on the growth mechanisms of liquid phase electroepitaxy. Int. J. Eng. Sci. **41**, 401–415 (2003)
41. Okano, Y., Kondo, H., Dost, S.: Control of transport structures in a rotating liquid cylinder by means of an applied magnetic field. Int. J. Electromagnet. Mech. **18**(4), 217–226 (2003)
42. Dost, S., Liu, Y.C., Lent, B.: A numerical simulation study for the effect of applied magnetic field in growth of CdTe single crystals by the traveling heater method. Int. J. Electromagnet. Mech. **17**, 271–288 (2003)
43. Liu, Y.C., Dost, S., Lent, B., Redden, R.F.: A three-dimensional numerical simulation model for the growth of CdTe single crystals by the traveling heater method under magnetic field. J. Cryst. Growth **254**, 285–297 (2003)
44. Roszmann, J., Dost, S., Lent, F.: Crystal growth by the travelling heater method using tapered crucibles and applied rotating magnetic field. Cryst. Res. Technol. **45**(8), 785–790 (2010)
45. Liu, Y.C., Dost, S., Sheibani, H.: A three dimensional numerical simulation for the transport structures in liquid phase electroepitaxy under applied magnetic field. Int. J. Transp. Phenom. **6**, 51–62 (2004)
46. Dost, S., Lent, B., Sheibani, H., Liu, Y.C.: Recent developments in liquid phase electroepitaxial growth of bulk crystals under magnetic field. Comptes rendus de mecanique **332**(5–6), 413–428 (2004)
47. Jastrzebski, L., Gatos, H.C., Witt, A.F.: Electromigration in current-controlled LPEE. J. Electrochem. Soc. **123**, 1121 (1976)
48. Jastrzebski, L., Imamura, Y., Gatos, H.C.: Thickness uniformity of GaAs layers grown by electroepitaxy. J. Electrochem. Soc. **125**, 1140–1146 (1978)
49. Okamoto, A., Lakowski, L., Gatos, H.C.: Enhancement of interface stability in liquid-phase electroepitaxy. J. Appl. Phys. **53**, 1706–1713 (1982)
50. Nakajima, K.: Liquid-phase epitaxial-growth of very thick $In_{1-x}Ga_xAs$ layers with uniform composition by source-current-controlled method. J. Appl. Phys. **61**(9), 4626–4634 (1987)
51. Bryskiewicz, T., Boucher Jr., C.F., Lagowski, J., Gatos, H.C.: Bulk GaAS crystal growth by liquid phase electroepitaxy. J. Cryst. Growth **82**, 279–288 (1987)
52. Nakajima, K.: Layer thickness calculation of In1-vGavAs grown by the source-current-controlled method—diffusion and electromigration limited growth. J. Cryst. Growth **98**, 329–340 (1989)
53. Bryskiewicz, T., Edelman, P., Wasilewski, Z., Coulas, D., Noad, J.: Properties of very uniform InxGa1-xAs single-crystals grown by liquid-phase electroepitaxy. J. Appl. Phys. **68**, 3018–3020 (1990)
54. Nakajima, K., Kusunoki, T., Takenaka, C.: Growth of ternary $In_xGa_{1-x}As$ bulk crystals with a uniform composition through supply of GaAs. J. Cryst. Growth **113**, 485–490 (1991)
55. Bryskiewicz, T., Laferriere, A.: Growth of alloy substrates by liquid phase electroepitaxy—Theoretical considerations. J. Cryst. Growth **129**, 429–442 (1993)
56. Zytkiewicz, Z.R.: Influence of convection on the composition profiles of thick GaAlAs layers grown by liquid-phase electroepitaxy. J. Cryst. Growth **131**, 426–430 (1993)
57. Zytkiewicz, Z.R.: Joule effect as a barrier for unrestricted growth of bulk crystals by liquid phase electroepitaxy. J. Cryst. Growth **172**, 259–268 (1996)
58. Minakuchi, H., Okano, Y., Dost, S.: A three-dimensional numerical simulation study of the Marangoni convection occurring in the crystal growth of Si_xGe_{1-x} by the Float-zone technique in zero gravity. J. Cryst. Growth **266**, 140–144 (2004)
59. Minakuchi, H., Okano, Y., Dost, S.: A three dimensional numerical study of marangoni convection in a floating full zone. In: Dost, S. (ed.) Crystal Growth of Semiconductor from the Liquid Phase. IJMPT **22**(1/2/3), 151–171 (2005)

60. Timchenko, V., Chen, P.Y.P., de Vahl Davis, G., Leonardi, E., Abbaschian, R.: A computational study of transient plane front solidification of alloys in a Bridgman apparatus under microgravity conditions. Int. J. Heat Mass Transf. **43**, 963–980 (2000)
61. Timchenko, V., Chen, P.Y.P., de Vahl Davis, G., Leonardi, E., Abbaschian, R.: A computational study of binary alloy solidification in the Mephisto experiment. Int. J. Heat Mass Transf. **23**, 258–268 (2002)

Chapter 5
Dispersion Properties of a Closed-Packed Lattice Consisting of Round Particles

Vladimir I. Erofeev, Igor S. Pavlov, Alexey V. Porubov and Alexey A. Vasiliev

Abstract A two-dimensional discrete model for a hexagonal (closed-packed) lattice with elastically interacting round particles possessing two translational and one rotational degrees of freedom is considered. The linear differential-difference equations are obtained by the method of structural modeling to describe propagation of longitudinal, transverse and rotational waves in the medium. The dispersion properties of the model are analyzed. Existence of a backward wave is revealed. The numerical estimations of threshold frequencies of acoustic and rotational waves are given for some values of microstructure parameters.

Keywords Structural modeling · Hexagonal lattice · Round particles Microstructure parameters · Dispersion properties

V. I. Erofeev (✉) · I. S. Pavlov
Mechanical Engineering Research Institute of Russian Academy of Sciences,
85 Belinskogo str., 603024 Nizhny Novgorod, Russia
e-mail: erof.vi@yandex.ru

V. I. Erofeev · I. S. Pavlov
Nizhny Novgorod Lobachevsky State University, 23 Gagarin av., 603950
Nizhny Novgorod, Russia

A. V. Porubov
Institute of Problems in Mechanical Engineering, 61 Bolshoy, V.O.,
199178 Saint-Petersburg, Russia
e-mail: alexey.porubov@gmail.com

A. V. Porubov
St. Petersburg State University, 7–9 Universitetskaya nab., V.O., 199034 Saint-Petersburg, Russia

A. V. Porubov
St. Petersburg State Polytechnical University, 29 Polytechnicheskaya st.,
195251 Saint-Petersburg, Russia

A. A. Vasiliev
Department of Mathematical Modelling, Tver State University, 35 Sadoviy per.,
170002 Tver, Russia
e-mail: alvasiliev@yandex.ru

H. Altenbach et al. (eds.), *Generalized Models and Non-classical Approaches in Complex Materials 2*, Advanced Structured Materials 90,
https://doi.org/10.1007/978-3-319-77504-3_5

5.1 Introduction

Prediction of physical and mechanical properties of media with microstructure and adequate description of dynamic (wave) processes [1] require mathematical models taking into account the presence of several scales (structural levels) in a medium, their self-consistent interaction and the possibility of energy transfer from one level to another [2]. It should be emphasized that the actual values of the "microstructure" of the medium in a specific problem can lie both in the range of nanometers or angstroms, and in the field of microns and even on larger scales. From the viewpoint of the methodology of theoretical research, the absolute values of the "microstructure" are not so important, as the smallness of some scales with respect to others.

Investigation of wave processes in crystal lattices can be carried out by the method of structural modeling [3–7]. Modeling by this method starts with a selection of a certain minimum volume (a structural cell that is analog of the periodicity cell in the crystalline material) in the bulk of a material represented by a regular or a quasiregular lattice consisting of particles of finite sizes. Such a cell is capable of reflecting the main features of the macroscopic behavior of this material [8]. First, a discrete model is elaborated within the scope of this method. Only at the next stage, one can pass to the continuum approximation. Structural models in explicit form contain the geometric parameters of the structure—the size and shape of the particles, on which, ultimately, the effective moduli of elasticity depend [5]. By changing these parameters, we can control the physical and mechanical properties of a medium. Such investigations are very important, for instance, for the *photonic* and *phononic* crystals [9–11].

The term "photonic crystals" appeared in the early 1990s for media having a periodic system of dielectric inhomogeneities giving rise to emergence of zones opaque both for light and electromagnetic waves [12]. From a general viewpoint, a photonic crystal is a superlattice or a medium, in which an additional field has been artificially created, and its period is of some orders greater than the basic lattice period. The behavior of photons is radically different from their behavior in the ordinary crystal lattice if the optical superlattice period is comparable with the length of the electromagnetic wave. They do not transmit the light with a wavelength comparable with the lattice period of the photonic crystal and determine the effect of the light localization. Photonic lattices are in the gap between the atomic crystal lattices and the macroscopic artificial periodic structures.

Subsequently, natural or artificial periodic structures became known as "phononic" crystals (acoustic superlattices) by analogy if they consist of nonpointwise particles, in which the length of the acoustic waves is comparable with the lattice period [9, 13–15]. The velocity of propagation of elastic waves in solids is about 10^5 times less than the light wave velocity. Therefore, all effects inherent to photonic crystals should take place in acoustics, but for significantly lower frequencies. High interest in materials of this type is caused by the unique properties of the materials that enables one to apply them in many fields, primarily, in nanoelectronics. The ordering of the geometric structure is typical for the periodic (crystalline)

media. It is a decisive factor leading to anisotropy of the properties of crystals and to the predominance of the collective motions of the wave type in the crystal lattice [16]. The dispersion properties of the phononic crystal representing a rectangular lattice consisting of ellipse-shaped particles were analyzed in [17].

It is interesting to note that examples of materials, in which the presence of various structural levels is very clearly manifested, can be also found in geophysics. For instance, the internal structure of rocks, in particular, hydrocarbon reservoirs, is different on various scales and determines their specific physical properties. First of all, it concerns such physical properties as thermal and electrical conductivity, hydraulic and dielectric permittivity. Methods of the theory of effective media are employed in geophysics for elaboration of different-scale mathematical models of such media. The construction of models is performed according to the principle "from small inhomogeneities to large ones". For each scale, a model medium is constructed with the given parameters. Its equations establish relationships between the parameters of the model and the measured physical properties of the rock. The role of the model parameters can be played by the characteristics of the shape and orientation, degree of ordering of the inhomogeneities, and the degree of their connectivity [18, 19]. In this case, inhomogeneities mean the grains of minerals, particles of organic matter, cracks and pores filled with various fluids. In addition, such models can be used, in particular, for solving problems of geomechanical modeling [20]. Obviously, such approach to construction of models for physical properties of media resembles with the structural modelling method in mechanics of microstructured solids.

In exploration geophysics, interest has recently increased to unconventional reservoirs of hydrocarbons and to reservoirs with complicated production conditions [20]. Such objects include gas-hydrate formations and rocks of "shale oil/gas". In particular, gas hydrates, as distinct from traditional hydrocarbons, have a crystalline structure. "Shale oil/gas" rocks are characterized by a rather large (more than 30%) content of clay minerals, the crystal lattice of which contains intracrystalline water. Due to that, the elastic properties of clay minerals are drastically changed. Therefore, studies of processes occurring at the level of the crystal lattices of such media, which influence and give rise to the interrelationships of the physical properties mentioned above, are of great importance. When different-scale mathematical models of physical properties of such rocks are constructed, these studies should precede the study of properties on nano-and micro-scales.

Using the structural modeling method, a discrete model of a two-dimensional close-packed lattice consisting of rigid non-deformable round particles is elaborated in this paper. Between the particles there is the so-called porous space—a medium, through which force and moment interactions between the particles are transmitted. If the appropriate model is used to solve a geophysical problem, it is possible to suppose that this porous space is filled with a fluid, for example, an intracrystalline water. Next, the dispersion properties [21] of such a lattice are analyzed. An influence of the microstructure of the crystal on its dispersion properties is also shown, and theoretical estimates of the threshold frequencies of the acoustic and optical phonons are obtained for some values of the microstructure parameters.

5.2 Discrete Model for a Hexagonal Lattice Consisting of Round Particles

We consider a two-dimensional hexagonal closed-packed lattice (or *triangle*, as it is mentioned in [22]) consisting of homogeneous round particles (grains or granules) with masses M and diameter d. In the initial state, they are located in the lattice sites and the distance between the mass centers of the neighboring granules are equal to a, see Fig. 5.1. Each particle has three degrees of freedom: translational degrees of freedom $u_{i,j}$ and $w_{i,j}$ for the displacement of the mass center of the particle with the number $N = N(i,j)$ along the axes $x$and y, and the rotational degree of freedom $\varphi_{i,j}$ for the rotation with respect to the mass center (Fig. 5.2). The kinetic energy of the particle $N(i, j)$ is

$$T_{i,j} = \frac{M}{2}\left(\dot{u}_{i,j}^2 + \dot{w}_{i,j}^2\right) + \frac{J}{2}\dot{\varphi}_{i,j}^2, \tag{5.1}$$

where $J = Md^2/8$ is the moment of inertia of the particle about the axis passing through its mass centre. The upper dot denotes derivatives with respect to time.

It is assumed that each particle interacts only with six nearest neighbors in the lattice. Simulation of the interactions between the particles is performed by means of the so-called "spring" model. Such a model is used in many works, see, e.g., [3, 23–29]. In this paper, the central and non-central interactions of the neighboring granules are simulated by elastic springs of three types [30]: central (the corresponding spring is designated by number 1 and has rigidity K_0), non-central (2 and 3 with rigidity K_1), and "diagonal" (4 and 5 with rigidity K_2). The interactions of tension-compression type are modeled by the central and non-central springs. The torques

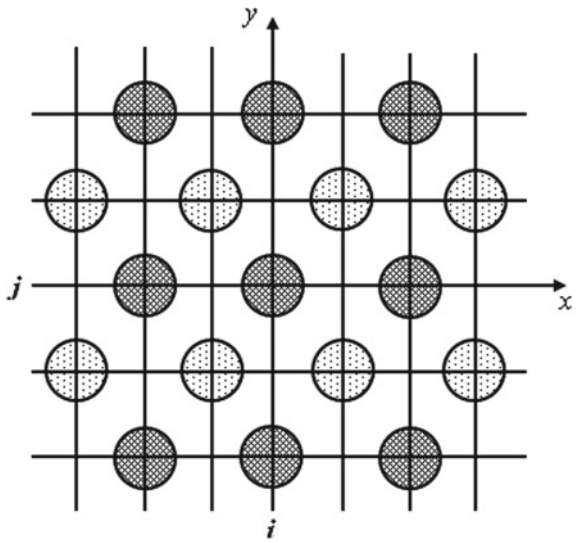

Fig. 5.1 Hexagonal lattice with round particles

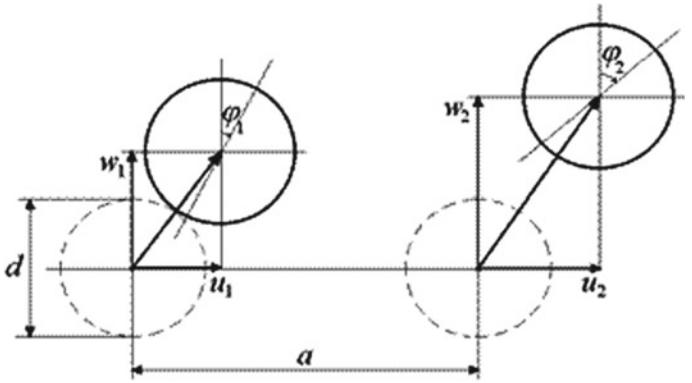

Fig. 5.2 Kinematical scheme

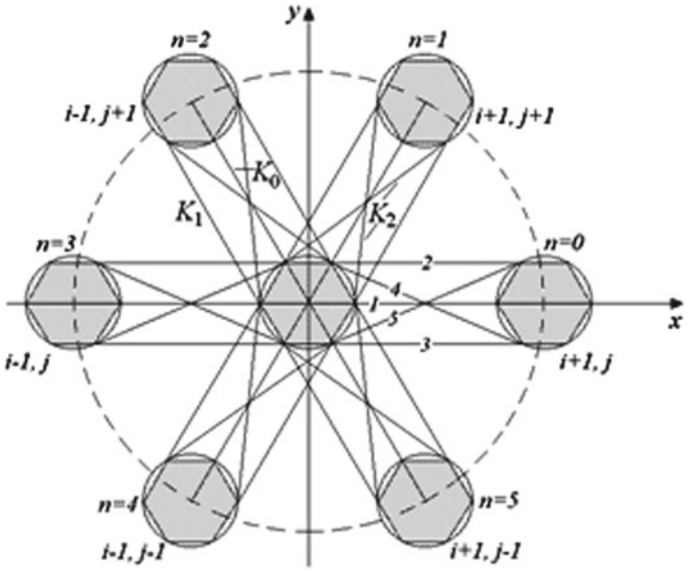

Fig. 5.3 Scheme of the force interactions and introduced notations

of the particles are provided by the springs of the K_1 type. Springs with the rigidity K_2 characterize the force interactions of the particles at the shear deformations. The points of junctions of the springs K_1 and K_2 coincide with the apexes of the regular hexagon inscribed in the round particle (Fig. 5.3).

It should be noted that six pairs of diagonal springs connecting the central particle with the six nearest neighbors in the lattice have the same rigidity K_2. But if the rigidities of the diagonal springs in pairs are different, then there is a lattice with a chiral microstructure. Dynamical properties of such lattices were discussed, particularly, in Refs. [31, 32].

The displacements of the granules are supposed to be small in comparison with the sizes of the elementary cell of the lattice. The energy of each particle provided by deviation of the particle from the equilibrium state is determined by the strain energy of the springs connecting this particle with the six nearest neighbors in the lattice. These six particles can be numbered by two ways: either by the number of the row, where the particle is located (Fig. 5.3), or by the coordinates of the mass centers of these particles on the circle of unit radius. In order to construct a discrete model, it is more convenient to use the first method. In this case, 1 is added to the first index of the particles, if they are located to the right of the particle $N(i, j)$ (in Fig. 5.3, these particles have the numbers $n = 0, 1, 5$), and -1 is added, if the particles are to the left of it (these are particles $n = 2, 3, 4$). Similarly, 1 is added to the second index of the particles located above the particle $N(i, j)$ and -1 is added, if the particles are below it (respectively, for particles with numbers $n = 0$ and $n = 5$, the second index remains equal to j). Thus, the potential energy due to the interaction of the particle $N(i, j)$ with six nearest neighbors in the lattice $(i + m_1, j + m_2)$, where $m_1 = \pm 1$ is the shift of the number along the horizontal axis and $m_2 = 0, \pm 1$ is the shift of the number along the vertical axis, is described by the formula

$$U_{i,j} = \frac{1}{2} \sum_{(m_1, m_2)} \left(\frac{K_0}{2} D^2_{1(m_1, m_2)} + + \frac{K_1}{2} (D^2_{2(m_1, m_2)} + D^2_{3(m_1, m_2)}) + \right. \\ \left. + \frac{K_2}{2} (D^2_{4(m_1, m_2)} + D^2_{5(m_1, m_2)}) \right). \tag{5.2}$$

Here $D_{l(m_1, m_2)}$ are the elongations of the springs connecting the central particle N with its six neighbors, $l = 1, 2, 3, 4, 5$ is the spring number in Fig. 5.3. Equation (5.2) contains an additional factor 1/2, since the potential energy of each spring is equally divided between two particles connected by this spring. Expressions for the elongations of the springs $D_{l(m_1, m_2)}$ calculated in the approximation of smallness of the quantities $\Delta u_{m_1, m_2} = = (u_{i+m_1, j+m_2} - u_{i,j})/a \sim \Delta w_{m_1, m_2} = (w_{i+m_1, j+m_2} - w_{i,j})/a \sim \sim \varphi_{i,j} \sim \varepsilon$ (here $\varepsilon << 1$ is a measure of the cell deformation, $m_1 = \pm 1$, $m_2 = 0, \pm 1$) and $\Phi_{m_1, m_2} = \left(\varphi_{i,j} + \varphi_{i+m_1, j+m_2}\right)/2 = = \varphi_{i,j} - 0,5a\Delta\varphi_{m_1, m_2} << \pi/2$ have the form:

$$D_{1(m_1, m_2)} = \frac{a}{2} \left(m_1 \Delta u_{m_1, m_2} + m_2 \sqrt{3} \Delta w_{m_1, m_2} \right),$$

$$D_{1(m_1, 0)} = m_1 a \Delta u_{m_1, 0},$$

$$D_{2,3m_1, m_2)} = \frac{a}{4} \left(2m_1 \Delta u_{m_1, m_2} + 2m_2 \sqrt{3} \Delta w_{m_1, m_2} \mp m_2 d \sqrt{3} \Delta \varphi_{m_1, m_2} \right),$$

$$D_{2,3(p, 0)} = m_1 a \left(\Delta u_{m_1, 0} \pm \frac{d\sqrt{3}}{4} \Delta \varphi_{m_1, 0} \right), \tag{5.3}$$

$$D_{4(m_1, m_1)} = \frac{m_1 a}{2r_0} \left((a - 2d) \Delta u_{m_1, m_1} + a\sqrt{3} \Delta w_{m_1, m_1} + d\sqrt{3} \Phi_{m_1, m_1} \right),$$

$$D_{5(m_1,\,m_1)} = \frac{m_1 a}{2r_0}\left((a+d)\Delta u_{m_1,\,m_1} + (a-d)\sqrt{3}\Delta w_{m_1,\,m_1} - d\sqrt{3}\Phi_{m_1,\,m_1}\right),$$

$$D_{4,5(m_1,0)} = \frac{a}{2r_0}\left(m_1(2a-d)\Delta u_{m_1,\,0} \pm d\sqrt{3}\Delta w_{m_1,0} \pm m_1 d\sqrt{3}\Phi_{m_1,0}\right),$$

$$D_{4,5(\mp1,\pm1)} = \frac{a}{2r_0}\left(\mp(a+d)\Delta u_{\mp1,\,\pm1} \pm (a-d)\sqrt{3}\Delta w_{\mp1,\pm1} + d\sqrt{3}\Phi_{\mp1,\pm1}\right),$$

$$D_{4,5(\pm1,\mp1)} = \frac{a}{2r_0}\left(\pm(a-2d)\Delta u_{\pm1,\,\mp1} \mp (a-d)\sqrt{3}\Delta w_{\pm1,\mp1} - d\sqrt{3}\Phi_{\pm1,\mp1}\right),$$

where $r_0 = \sqrt{a^2 - ad + d^2}$ is the length of the undisturbed spring K_2. In expressions for $D_{2,3}$ and $D_{4,5}$, the upper symbols in $\pm$ and $\mp$ are taken for the springs of types 2 and 4, whereas the lower ones are necessary for the springs 3 and 5.

It should be noted that Eq. (5.3) have been obtained with the accuracy up to the linear terms having the order ε^1. Substitution of these expressions in Eq. (5.2) leads to the following expression for the potential energy per cell with the number $N = N(i, j)$ with accuracy up to quadratic terms:

$$\begin{aligned}
U_{i,j} &= \gamma_1(\Delta u_{1,0}^2 + \Delta u_{-1,0}^2) + \gamma_2(\Delta u_{1,1}^2 + \Delta u_{-1,-1}^2 + \Delta u_{1,-1}^2 + \Delta u_{-1,1}^2) + \\
&+ \gamma_3(\Delta w_{1,0}^2 + \Delta w_{-1,0}^2 + \Phi_{1,0}^2 + \Phi_{-1,0}^2 + \Phi_{1,1}^2 + \Phi_{-1,-1}^2 + \Phi_{1,-1}^2 + \Phi_{-1,1}^2 + \\
&+ \Delta w_{1,1}\Phi_{1,1} - \Delta w_{-1,-1}\Phi_{-1,-1} + \Delta w_{1,-1}\Phi_{1,-1} - \Delta w_{-1,1}\Phi_{-1,1}) + \\
&+ \sqrt{3}\gamma_3(-\Delta u_{1,1}\Phi_{1,1} + \Delta u_{-1,-1}\Phi_{-1,-1} + \Delta u_{1,-1}\Phi_{1,-1} - \Delta u_{-1,1}\Phi_{-1,1}) + \\
&+ 2\gamma_3(\Delta w_{1,0}\Phi_{1,0} - \Delta w_{-1,0}\Phi_{-1,0}) + \\
&+ \gamma_4(\Delta w_{1,1}^2 + \Delta w_{-1,-1}^2 + \Delta w_{1,-1}^2 + \Delta w_{-1,1}^2) + \\
&+ \gamma_5(\Delta\varphi_{1,0}^2 + \Delta\varphi_{-1,0}^2 + \Delta\varphi_{1,1}^2 + \Delta\varphi_{-1,-1}^2 + \Delta\varphi_{1,-1}^2 + \Delta\varphi_{-1,1}^2) + \\
&+ \gamma_6(\Delta u_{1,1}\Delta w_{1,1} + \Delta u_{-1,-1}\Delta w_{-1,-1} - \Delta u_{1,-1}\Delta w_{1,-1} - \Delta u_{-1,1}\Delta w_{-1,1}).
\end{aligned} \tag{5.4}$$

Here the coefficients $\gamma_1, \ldots, \gamma_6$ are

$$\gamma_1 = \frac{a^2}{2}(K_0 + 2K_1 + \frac{(2a-d)^2}{2r_0^2}K_2),$$

$$\gamma_2 = \frac{a^2}{8}(K_0 + 2K_1 + \frac{2a^2 - 2ad + 5d^2}{r_0^2}K_2), \gamma_3 = \frac{3a^2d^2}{4r_0^2}K_2,$$

$$\gamma_4 = \frac{3}{8}a^2(K_0 + 2K_1 + \frac{2a^2 - 2ad + d^2}{r_0^2}K_2), \tag{5.5}$$

$$\gamma_5 = \frac{3a^2d^2}{16}K_1, \gamma_6 = \frac{\sqrt{3}}{4}a^2(2K_1 - \frac{2a^2 - 2ad - d^2}{r_0^2}K_2).$$

The linear equations of motion for our lattice are obtained using the variational principle, where parts of the Lagrangian are defined by Eqs. (5.1) and (5.4),

$$\begin{gathered} M\ddot{u}_{i,j} - \frac{2\gamma_1}{a^2}(u_{i+1,j} - 2u_{i,j} + u_{i-1,j}) - \\ - \frac{2\gamma_2}{a^2}(u_{i+1,j+1} + u_{i-1,j-1} + u_{i+1,j-1} + u_{i-1,j+1} - 4u_{i,j}) - \\ - \frac{\gamma_6}{a^2}(w_{i+1,j+1} + w_{i-1,j-1} - w_{i+1,j-1} - w_{i-1,j+1}) - \\ - \frac{\sqrt{3}\gamma_3}{2a}(-\varphi_{i+1,j+1} + \varphi_{i-1,j-1} + \varphi_{i+1,j-1} - \varphi_{i-1,j+1}) = 0, \end{gathered} \tag{5.6}$$

$$\begin{gathered} M\ddot{w}_{i,j} - \frac{2}{a^2}\gamma_1(w_{i+1,j} - 2w_{i,j} + w_{i-1,j}) - \\ - \frac{2}{a^2}\gamma_2(u_{i+1,j+1} + u_{i-1,j-1} + u_{i+1,j-1} + u_{i-1,j+1} - 4u_{ij}) - \\ - \frac{1}{a^2}\gamma_6(w_{i+1,j+1} + w_{i-1,j-1} - w_{i+1,j-1} - w_{i-1,j+1}) - \\ - \frac{1}{a}\gamma_3(\varphi_{i+1,j} - \varphi_{i-1,j}) - \\ - \frac{1}{2a}\gamma_3(\varphi_{i+1,j+1} - \varphi_{i-1,j-1} + \varphi_{i+1,j-1} - \varphi_{i-1,j+1}) = 0, \end{gathered} \tag{5.7}$$

$$\begin{gathered} M\ddot{\varphi}_{i,j} - (\tfrac{16}{a^2}\gamma_5 - 4\gamma_3)(\varphi_{i+1,j} + \varphi_{i-1,j} + \varphi_{i+1,j+1} + \varphi_{i-1,j-1} + \\ + \varphi_{i+1,j-1} + \varphi_{i-1,j+1} - 6\varphi_{i,j}) + \tfrac{8}{a}\gamma_3(w_{i+1,j} - w_{i-1,j}) + \\ + 48\gamma_3\varphi_{i,j} - \tfrac{4\sqrt{3}}{a}\gamma_3(u_{i+1,j+1} - u_{i-1,j-1} - u_{i+1,j-1} + u_{i-1,j+1}) - \\ - \tfrac{4}{a}\gamma_3(-w_{i+1,j+1} + w_{i-1,j-1} - w_{i+1,j-1} + w_{i-1,j+1}) = 0. \end{gathered} \tag{5.8}$$

Here $R = \sqrt{J/M} = d/8$ is the radius of inertia of the microparticles of the medium with respect to the mass center.

Equations (5.6)–(5.8) obtained in this section can be used for numerical simulation of the response of the system to the external dynamic effects in a wide range of

frequencies up to the threshold values [30]. It should be noted that non-neighboring interactions are frequently introduced, if the particles are the material points [24]. It leads to the differences in the Lagrangian, which gives the higher-order derivatives in the continuum limit. In this paper the particles of the lattice are finite size bodies. They possess both translational and rotational degrees of freedom. In the low-frequency long-wavelength approximation, when the rotational mode does not propagate, the three-mode system is reduced to the two-mode system containing the fourth-order derivatives in equations for the longitudinal and transverse modes [30]. These equations are called *equations of the second-order gradient elasticity*. Thus, we achieve appearance of the higher-order derivatives in the governing equations by another way. Further, the dispersion properties of Eqs. (5.6)–(5.8) will be analyzed.

5.3 Derivation of the Dispersion Equation

The lattice with round particles considered in Sect. 5.2 represents a system with N degrees of freedom, which is described by coupled equations (5.6)–(5.8), see [16]. Introduction of normal mode variables, makes equations of motion independent [33], and the arbitrary motion of the system can be represented as a superposition of normal vibrations. This approach is very convenient both for the theoretical analysis of the problem and for the physical interpretation of the obtained results. Similar concepts can be also introduced for distributed systems, where interacting waves of various types can propagate. A generalization of the concept of the normal vibrations of concentrated systems to "not closed" wave systems (boundless media, waveguides, tubes, rods, strings, and etc.) gives rise to the *normal wave*, i.e. traveling harmonic waves in the linear systems with constant parameters, in which an absorption and scattering of energy are negligible [34, 35].

In order to study the collective motions arising in an arranged crystalline structure, we will pass to the normal oscillations. Let us consider solutions of the equations of motion representing plane monochromatic waves, for which the displacements are

$$\begin{aligned} u\left(\vec{N},t\right) &= u_0 \exp\left[i\left(\omega\left(\vec{q}\right)\ t - \vec{q}\vec{N}\right)\right] \\ w\left(\vec{N},t\right) &= w_0 \exp\left[i\left(\omega\left(\vec{q}\right)\ t - \vec{q}\vec{N}\right)\right] \\ \varphi\left(\vec{N},t\right) &= \varphi_0 \exp\left[i\left(\omega\left(\vec{q}\right)\ t - \vec{q}\vec{N}\right)\right] \end{aligned} \tag{5.9}$$

Here $\omega = \omega\left(\vec{q}\right)$ is a wave frequency regarded as a continuous function of the wave vector $\vec{q} = \left(q_1, q_2\right)$ that defines both the direction of the wave propagation in the Cartesian coordinate system (x, y) and the wave length $\lambda = 2\pi/q$ $\left(q = \left|\vec{q}\right|\right)$. The vector $\vec{N} = (i, j)$ fixes the lattice sites. Arbitrary collective motions can be represented as a superposition of monochromatic waves. Substitution of Eq. (5.9) into

Eq. (5.6)–(5.8) results in a set of equations in the matrix form for determination of the amplitudes of displacements,

$$\begin{pmatrix} M\omega^2 - d_{11} & d_{12} & d_{13} \\ d_{21} & M\omega^2 - d_{22} & d_{23} \\ d_{31} & d_{32} & M\omega^2 - d_{33} \end{pmatrix} \cdot \begin{pmatrix} u_0 \\ w_0 \\ \varphi_0 \end{pmatrix} = \begin{pmatrix} 0 \\ 0 \\ 0 \end{pmatrix}, \tag{5.10}$$

where the matrix elements are

$$\begin{gathered} d_{11} = \frac{8\gamma_1}{a^2}\sin^2\left(\frac{q_1 a}{2}\right) + \frac{8\gamma_2}{a^2}\left(1 - \cos\left(\frac{q_1 a}{2}\right)\cos\left(\frac{q_2 a\sqrt{3}}{2}\right)\right), \\ d_{22} = \frac{16\gamma_3}{a^2}\sin^2\left(\frac{q_1 a}{2}\right) + \frac{8\gamma_4}{a^2}\left(1 - \cos\left(\frac{q_1 a}{2}\right)\cos\left(\frac{q_2 a\sqrt{3}}{2}\right)\right), \\ d_{33} = \frac{8}{a^2}\left[\frac{8\gamma_5 + 4a^2\gamma_3}{d^2} + \left(\gamma_6\sqrt{3} - \gamma_3\left(1 + \frac{2a}{d}\right)\right) \times \right. \\ \left. \times \left(\sin^2\left(\frac{q_1 a}{2}\right) - \cos\left(\frac{q_1 a}{2}\right)\cos\left(\frac{q_2 a\sqrt{3}}{2}\right)\right)\right], \\ d_{12} = d_{21} = \frac{8\sqrt{3}}{3a^2}(\gamma_3 - \gamma_4)\sin\left(\frac{q_1 a}{2}\right)\sin\left(\frac{q_2 a\sqrt{3}}{2}\right), \\ d_{13} = -\frac{d^2}{8}d_{31} = i\frac{2\sqrt{3}\gamma_3}{a}\cos\left(\frac{q_1 a}{2}\right)\sin\left(\frac{q_2 a\sqrt{3}}{2}\right), \\ d_{23} = -\frac{d^2}{8}d_{32} = -i\frac{2\gamma_3}{a}\sin\left(\frac{q_1 a}{2}\right)\left(\cos\left(\frac{q_2 a\sqrt{3}}{2}\right) + 2\cos\left(\frac{q_1 a}{2}\right)\right). \end{gathered} \tag{5.11}$$

The solvability condition for Eq. (5.10) with coefficients defined by Eq. (5.11) leads to a bi-cubic dispersion equation for ω,

$$M^3\omega^6 + F_1\omega^4 + F_2\omega^2 + F_3 = 0, \tag{5.12}$$

where $F_{1,2,3}$ are the wave vector functions:

$$\begin{gathered} F_1 = d_{11} + d_{22} + d_{33}, \\ F_2 = d_{11}d_{22} + d_{11}d_{33} + d_{22}d_{33} - d_{12}d_{21} - d_{13}d_{31} - d_{23}d_{32}, \\ F_3 = -d_{11}d_{22}d_{33} + d_{11}d_{23}d_{32} + d_{22}d_{13}d_{31} + d_{33}d_{12}d_{21} + d_{12}d_{23}d_{31} + d_{13}d_{32}d_{21}. \end{gathered} \tag{5.13}$$

Dividing Eq. (5.12) by K_0^3 and substituting the relationship, $\varpi = \omega\sqrt{M/K_0}$, one can obtain the dispersion equation in the dimensionless form:

$$\varpi^6 - f_1\varpi^4 + f_2\varpi^2 + f_3 = 0, \tag{5.14}$$

where $f_1 = F_1/K_0$, $f_2 = F_2/K_0^2$, and $f_3 = F_3/K_0^3$. Thus, the left-hand side of Eq. (5.14) contains three variables: frequency ω and the components of the wave vector, q_1 and q_2. Moreover, the coefficients of Eq. (5.14) depend on the relative particle size d/a and on two parameters of the force and couple interactions: K_1/K_0 and K_2/K_0.

Two lattices correspond to each of the crystal structure: a direct lattice and a reciprocal one. A direct lattice is a lattice in ordinary space and a reciprocal one is a lattice in abstract reciprocal space, where distances have a dimension of the reciprocal length, in fact, it is the Fourier transform of the direct lattice [36]. The diffraction pattern represents a reciprocal crystal lattice map, just as the microscopic image is a map of the real crystal structure.

The primitive unit cells which constitute the periodic reciprocal lattice in the Bloch wave vector space are referred to as *Brillouin zones* [36]. The first Brillouin zone can be regarded as a primitive cell of the reciprocal lattice that possesses point symmetry of this lattice. Indeed, if we construct the first Brillouin zone around each node of the reciprocal lattice (the origin should be located in the node), then such zone would entirely fill the entire space without overlapping with each other. From this fact it follows, in particular, that the volume of the first Brillouin zone is equal to the volume of the primitive cell of the reciprocal lattice.

The structure of the Brillouin zones is defined only by crystal structure and depends neither on the type of particles forming the crystal, nor on their interaction. The physical meaning of the Brillouin zone boundaries consists in that they show the following values of the wave vectors or the electron quasi-pulses, in which the electron wave cannot propagate in a solid [36].

Next, we will analyze the dispersion properties of the medium in the first Brillouin zone and on its boundary depending on the values of the microstructure parameters.

5.4 Dispersion Properties of Normal Waves

Like in the solid-state physics, each normal lattice vibration can be associated with a certain type of quasiparticle—phonon [37]. The considered system has a longitudinal acoustic (LA) phonon, a transverse acoustic (TA) one, and an optical rotational (OR) phonon [38]. We pass to the polar coordinate system $q_1 = q\cos\theta$, $q_2 = q\sin\theta$, in Eq. (5.12), where q is the wave vector module and the angle θ indicates the direction of the plane wave propagation with respect to x-axis in the direct lattice. In particular, in the case of propagation of the plane waves, when $q_2 \equiv 0$ and, hence, $d_{12} \equiv d_{13} \equiv d_{21} \equiv d_{31} \equiv 0$, Eq. (5.14) is substantially simplified since the longitudinal phonons become independent in it:

$$(\varpi^2 - \frac{d_{11}}{K_0})\left((\varpi^2 - \frac{d_{22}}{K_0})(\varpi^2 - \frac{d_{33}}{K_0}) - \frac{d_{23}}{K_0}\frac{d_{32}}{K_0}\right) = 0, \tag{5.14a}$$

where $\varpi = \omega/\omega_0$, $\omega_0 = \sqrt{M/K_0}$ and the coefficients of Eq. (5.14a) have the form:

$$d_{11} = \frac{8}{a^2}\left[\gamma_1 \sin^2(\frac{qa}{2}) + \gamma_2(1 - \cos(\frac{qa}{2}))\right],$$

$$d_{22} = \frac{8}{a^2}\left[2\gamma_3 \sin^2(\frac{qa}{2}) + \gamma_4(1 - \cos(\frac{qa}{2}))\right], \tag{5.15}$$

$$d_{33} = \frac{8}{a^2}\left[\frac{8\gamma_5 + 4a^2\gamma_3}{d^2} + \left(\gamma_6\sqrt{3} - \gamma_3(1 + \frac{2a}{d})\right)\left(\sin^2(\frac{qa}{2}) - \cos(\frac{qa}{2})\right)\right],$$

$$d_{23} = -\frac{d^2}{8}d_{32} = -i\frac{2\gamma_3}{a}\left(\sin(\frac{qa}{2}) + \sin(qa)\right).$$

From Eqs. (5.14a) and (5.15) it follows that each wave mode has both minimum and maximum, which values depend on microstructure parameters. Thus, for example, along the $\Gamma - K$-axis the frequency of the longitudinal phonons has a local maximum $\omega_{LA}^{\max} = \sqrt{2\left(4(\gamma_1 + \gamma_2) + \gamma_2^2/\gamma_1\right)/Ma^2}$ at the point $q = 2\left(\pi - \arccos\left(\gamma_2/2\gamma_1\right)\right)/a$. Consequently, by varying the microstructure parameters, it is possible to specify certain dispersion properties of the crystal [17, 39].

Analysis of solutions of the dispersion Eq. (5.14) is performed for the following values of the microstructure parameters: $d/a = 0.1$, $K_1/K_0 = 0.5$, $K_2/K_0 = 0.3$. The dispersion curves calculated along directions $\theta = 0°$ (Γ–K), $\theta = 30°$ (Γ–M) and along the boundary of the Brillouin zone ($K - M$) are shown in Fig. 5.4.

From Fig. 5.4 it is visible that in the $\Gamma - M$-direction the frequency increases monotonically, when the wave number grows, up to the boundary of the Brillouin zone, and in the $\Gamma - K$-direction the frequency of the longitudinal phonons has a local maximum $\varpi \approx 2.96$ located at the point $q = 2\left(\pi - arctg\left(3\sqrt{7}\right)\right)/a$. In the interval $2\left(\pi - arctg\left(3\sqrt{7}\right)\right)/a < q < 4\pi/3a$ the group velocity of rotational phonons is negative: $v_{gr} = d\omega/dq < 0$. This area is called a *backward-wave region* [36]. Usually, a field of the negative group velocity exists for optical phonons in lattices with a complex structure, when more than one particle is present in the Bravais lattice [36]. Here, a similar situation takes place for acoustic phonons in a simple lattice. The presence of a backward wave in a medium is associated with the phenomenon of negative refraction provided that the surface of equal frequencies is convex. The longitudinal mode has the maximum frequency $\varpi \approx 3.65$ that is achieved on the boundary of the first Brillouin zone at point ($q = 2\pi/\sqrt{3}a$). At this point, the group velocity is equal to zero and therefore a signal with such a frequency cannot propagate in a crystal lattice. This restriction can be dropped only for nonlinear perturbations [35], when anharmonic terms are taken into account in equations of

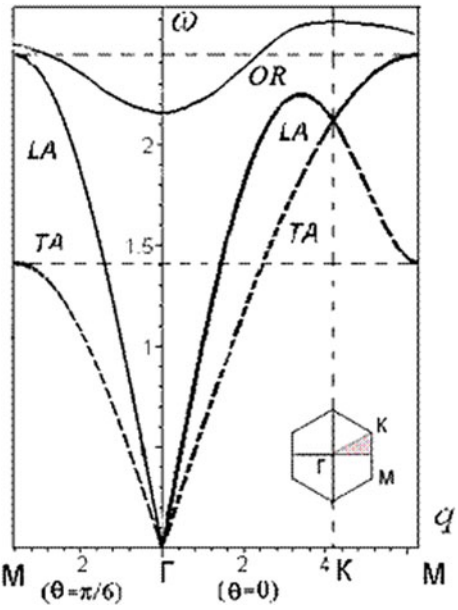

Fig. 5.4 Dispersion curves of the hexagonal lattice

motion. The frequency of the transverse phonons has the maximal value $\varpi \approx 3.38$ at the point K. The rotational (optical) mode has two threshold frequencies: the minimum $\varpi(0) \approx 3.44$ and maximum $\varpi \approx 4.15$ ones. In the frequency range $0 \leq \varpi \leq 3.38$ the system has LA-and TA-modes. In the interval $3.28 < \varpi < 3.44$ there is only a longitudinal mode and for frequencies $3.44 \leq \varpi \leq 3.65$ there are longitudinal and rotational modes. And, finally, in the high-frequency range $3.65 < \varpi \leq 4.15$, only the rotational mode is present in the system (Fig. 5.4).

It should be noted that in the continuum approximation the rotational mode has only one threshold frequency—minimal, whereas the longitudinal and transverse modes have no threshold frequencies [39]. If a medium consists of material points ($d = 0$), then there are no rotational phonons in the medium.

Figure 5.5 shows maps of equal frequencies for longitudinal, transverse, and rotational phonons (for LA-mode $\varpi = 0.7, 1.0, 1.5, 2.1, 2.7, 3.0, 3.2, 3.3$, for TA-mode $\varpi = 0.7, 1.0, 1.5, 2.1, 2.7, 3.0$ and for OR mode $\varpi = 3.2, 3.3, 3.5, 3.6, 3.7, 3.8$). The horizontal axis represents the projection q_x of the wave vector, and along the vertical axis—q_y. The boundaries of the first Brillouin zone are indicated by a dashed line.

Figure 5.5 shows that lines of equal frequencies are circles for small values of the wave number. Hence, the crystal structure behaves like an isotropic medium in the long-wavelength range. However, when the wavelength decreases (the magnitude of the wave vector increases), the properties of acoustic anisotropy begin to appear. In this case, the transverse waves become anisotropic ones faster than the longitudinal waves do. For $\varpi = 3.22$ the map of equal frequencies reproduces completely the structure of the hexagonal lattice at issue.

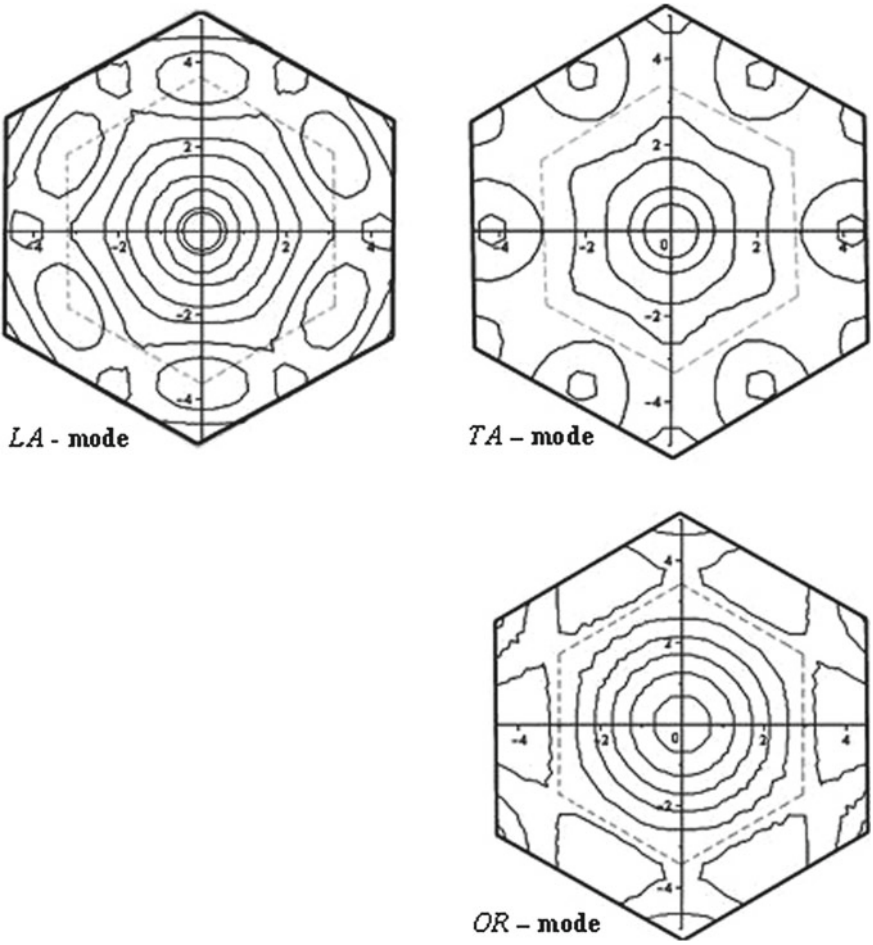

Fig. 5.5 Maps of equal frequencies for the hexagonal lattice

5.5 Conclusions

A two-dimensional discrete model of a close-packed (hexagonal) lattice consisting of rigid non-deformable round particles of finite sizes is elaborated in this paper using the structural modeling method. This model can be used, for example, for description of wave processes in phononic crystals and in geophysics—for studying physical properties of rocks.

Dispersion properties of such a medium have been analyzed for some values of the microstructure parameters. The analysis showed the existence of a backward wave, i.e. the wave whose phase and group velocities are oppositely directed. Moreover, if in the long-wavelength (continuum) approximation (when the characteris-

tic length of an acoustic wave is much larger than the lattice period) the hexagonal lattice with round particles is isotropic in terms of acoustic properties, then in the short-wavelength (discrete) approximation it is anisotropic, and the transverse waves become anisotropic ones faster than the longitudinal waves do. The rotational mode has two threshold frequencies: maximum and minimum. In the ranges of low ($0 \le \varpi < 2.33$) and high ($2.98 < \varpi \le 3.28$) frequencies, there are two wave modes in the system, whereas for $2.33 < \varpi \le 2.98$ all three wave modes (longitudinal, transverse and rotational) are present in the system. The greatest value of the frequency of longitudinal phonons is reached at the boundary of the Brillouin zone at the point M ($q = 2\pi/\sqrt{3}a$).

The similar results were obtained in [17], where the dispersion properties of the discrete model of the rectangular lattice consisting of ellipse-shaped particles were analyzed. But, in contrast to the hexagonal lattice considered here, the rectangular and square lattices are anisotropic in terms of acoustic properties even in the long-wavelength approximation. Moreover, the continuum approximations of the hexagonal and square lattice were considered in [30], where the analytical relationships between the macroelasticity constants of the medium and microstructure parameters were found. These relationships appeared to be different for the hexagonal and square lattices.

Dispersion properties of elastic waves in 3D phononic crystals, where rotational degrees of freedom had been taken into account, were considered in [40].

Transformation from a discrete model to a continuum one is suitable when the long-wavelength processes are studied [30]. In this case, a comparison of the elaborated model with the well-known continuum theories becomes possible. For adequate description of the dispersion properties in the short-wavelength range (for instance, frequency band gaps), it is necessary either to remain within a discrete model, or to pass to a generalized continuum model, for example, in the framework of the multi-field approach [25, 26] or on the base of Pade approximations [41].

Nonlinear plane waves in media with a hexagonal lattice consisting of material points were studied in the scope of multi-field models in Refs. [6, 7]. The lattice models with finite-size particles generalize such models and enable one to take into account rotational wave effects. Earlier, multi-field models were elaborated only for square lattices [25, 26]. Nowadays, construction of multi-field models for hexagonal lattices with finite-size particles is, in our opinion, of prime interest.

The results obtained in this work can be suggested for modeling of artificial periodic structures consisting of particles of non-zero sizes comparable with the wavelengths of the considered phenomena, and possessing predetermined dispersion properties.

Acknowledgements The research was carried out within the framework of the Russian State assignment to IAP RAS (topic No 0035-2014-0402, State Registration No 01201458047, V.I.E. and I.S.P.), as well as under the financial support of the Russian Foundation for Basic Research (projects No 18-08-00715-a, 16-08-00776-(V.I.E. and I.S.P.), 16-08-00971-a (I.S.P. and A.A.V.), and 16-01-00068-a (A.V.P.)) and the Ministry of Education and Science of the Russian Federation within the framework of the basic part of State Work for scientific activity (project 9.7446.2017/8.9, A.A.V.).

References

1. Erofeyev, V.I.: Wave Processes in Solids with Microstructure. World Scientific Publishing, New Jersey-London-Singapore-Hong Kong-Bangalore-Taipei (2003)
2. Ghoniem, N.M., et al.: Multiscale modelling of nanomechanics and micromechanics: an overview. Phil. Mag. **83**, 3475–3528 (2003)
3. Berglund, K.: Structural Models of Micropolar Media. In: Brulin, O., Hsieh, R.K.T. (eds.) Mechanics of Micropolar Media, pp. 35–86. World Scientific, Singapore (1982)
4. Li, Chunyu, Chou, Tsu-Wei: A structural mechanics approach for the analysis of carbon nanotubes. Int. J. Solids Struct. **40**, 2487–2499 (2003)
5. Pavlov, I.S., Potapov, A.I.: Structural models in mechanics of nanocrystalline media. Dokl. Phys. **53**, 408–412 (2008)
6. Porubov, A.V., Berinskii, I.E.: Non-linear plane waves in materials having hexagonal internal structure. Int. J. Non-Linear Mech. **67**, 27–33 (2014)
7. Porubov, A.V., Berinskii, I.E.: Two-dimensional nonlinear shear waves in materials having hexagonal lattice structure. Math. Mech. Solids **21**, 94–103 (2016)
8. Broberg, K.B.: The cell model of materials. Comput. Mech. **19**, 447–452 (1997)
9. Bogomolov, V.N., Parfen'eva, L.S., Smirnov, I.A., Misiorek, H., Jzowski, A.: Phonon propagation through photonic crystals—media with spatially modulated acoustic properties. Phys. Solis State **44**, 181–185 (2002)
10. Steurer, W., Sutter-Widmer, D.: Photonic and phononic quasicrystals. J. Phys. D **40**, R229–R247 (2007)
11. Vetrov, S.Ya., Timofeev, I.V., Rudakova, N.V.: Band structure of a two-dimensional resonant photonic crystal. Phys. Solid State **52**, 527–532 (2010)
12. Yablonovitch, E., Gmitter, T.J., Leung, K.M.: Photonic band structure (2003) The face-centered cubic case employing nonspherical atoms. Phys. Rev. Lett. **67**, 2295 (1991)
13. Fujii, M., Kanzaea, Y., Hayashi, S., Yamamoto, K.: Raman scattering from acoustic phonons confined in Si nanocrystals. Phys. Rev. B **54**, R8373 (1996)
14. Sigalas, M.M., Economou, E.N.: Elastic and acoustic-wave band-structure. J. Sound Vib. **158**, 377–382 (1992)
15. Pichard, H., Duclos, A., Groby, J.-P., Tournat, V., Gusev, V.E.: Two-dimensional discrete granular phononic crystal for shear wave control. Phys. Rev. B **86**, 134307 (2012)
16. Kushwaha, M.S., Halevi, P., Martinez, G., Dobrzynski, L., Djafari-Rouhani, B.: Theory of band structure of periodic elastic composites. Phys. Rev. B **49**, 2313 (1994)
17. Pavlov, I.S., Vasiliev, A.A., Porubov, A.V.: Dispersion properties of the phononic crystal consisting of ellipse-shaped particles. J. Sound Vib. **384**, 163–176 (2016)
18. Bayuk, I., Ammerman, M., Chesnokov, E.: Upscaling of elastic properties of anisotropic sedimentary rocks. Geophys. J. Int. **172**, 842–860 (2008)
19. Yalaev, T., Bayuk, I., Tarelko, N., Abashkin, A.: Connection of elastic and thermal properties of Bentheimer sandstone using effective medium theory (rock physics). ARMA-2016-128. 50th U.S. Rock Mechanics/Geomechanics Symposium, 26–29 June, Houston, Texas, pp. 1–7 (2016)
20. Dubinya, N., Tikhotsky, S., Bayuk, I., Beloborodov, D., Krasnova, M., Makarova, A., Rusina, O., Fokin, I. Prediction of physical-mechanical properties and in-situ stress state of hydrocarbon reservoirs from experimental data and theoretical modeling. In: SPE Russian Petroleum Technology Conference (SPE-187823-MS), pp. 1–15 (2017)
21. Porubov, A.V., Aero, E.L., Maugin, G.A.: Two approaches to study essentially nonlinear and dispersive properties of the internal structure of materials. Phys. Rev. E **79**, 046608 (2009)
22. Krivtsov, A.M.: Deformation and Destruction of Microstructured Solids. Fizmatlit Publishers, Moscow (in Russian) (2007)
23. Askar, A.: Lattice Dynamical Foundations of Continuum Theories. World-Scientific, Singapore (1985)
24. Metrikine, A.V., Askes, H.: An isotropic dynamically consistent gradient elasticity model derived from a 2D lattice. Philos. Mag. **86**(21–22), 3259–3286 (2006)

25. Vasiliev, A.A., Dmitriev, S.V., Miroshnichenko, A.E.: Multi-field approach in mechanics of structural solids. Int. J. Solids Struct. **47**, 510–525 (2010)
26. Vasiliev, A.A., Miroshnichenko, A.E., Dmitriev, S.V.: Multi-field modeling of a Cosserat lattice: models, wave filtering, and boundary effects. Eur. J. Mech. A/Solids **46**, 96–105 (2014)
27. Erofeev, V.I., Kazhaev, V.V., Pavlov, I.S.: Nonlinear localized strain waves in a 2D medium with microstructure In: Altenbach H. et al. (eds.), Generalized Continua as Models for Materials, 91 Advanced Structured Materials 22, pp. 91-110. Springer, Berlin, Heidelberg (2013). https://doi.org/10.1007/978-3-642-36394-8_6,
28. Erofeev, V.I., Pavlov, I.S., Leontiev, N.V.: A mathematical model for investigation of nonlinear wave processes in a 2D granular medium consisting of spherical particles. Compos. Mech. Comput. Appl. Int. J. **4**, 239–255 (2013)
29. Pavlov, I.S., Potapov, A.I., Maugin, G.A.: A 2D granular medium with rotating particles. Int. J. Solids Struct. **43**, 6194–6207 (2006)
30. Potapov, A.I., Pavlov, I.S., Lisina, S.A.: Acoustic identification of nanocrystalline media. J. Sound Vib. **322**, 564–580 (2009)
31. Spadoni, A., Ruzzene, M., Gonella, S., Scarpa, F.: Phononic properties of hexagonal chiral lattices. Wave Motion **46**, 435–450 (2009)
32. Spadoni, A., Ruzzene, M., Scarpa, F.: Dynamic response of chiral truss-core assemblies. J. Intell. Mater. Syst. Struct. **17**, 941–952 (2006)
33. Pierce, J.R.: Almost All about Waves. Dover Publications (2006)
34. Ostrovsky, L.A., Papko, V.V., Pelinovsky, E.N.: Solitary electromagnetic waves in nonlinear lines. Radiophys. Quantum Electron. **15**, 438–446 (1972)
35. Ostrovsky, L.A., Potapov, A.I.: Modulated Waves: theory and applications. The Johns Hopkins University Press, Baltimore, MD (1999)
36. Kittel, C.: Introduction to Solid State Physics, 8th edn. Wiley (2005)
37. Reisland, J.A.: Phys. Phon. Wiley, London-New York-Sydney-Toronto (1973)
38. Stroscio, M., Dutta, M.: Phon. Nanostruct. Cambridge University Press, Cambridge (2001)
39. Potapov, A.I., Pavlov, I.S., Lisina, S.A.: Identification of nanocrystalline media by acoustic spectroscopy methods. Acoust. Phys. **56**, 588–596 (2010)
40. Merkel, A., Tournat, V., Gusev, V.: Dispersion of elastic waves in three-dimensional noncohesive granular phononic crystals: properties of rotational modes. Phys. Rev. E **82**(031305), 8 (2010)
41. Andrianov, I.V., Kholod, E.G., Weichert, D.: Application of quasi-continuum models for perturbation analysis of discrete kinks. Nonlinear Dyn. **68**, 1–5 (2012)

Chapter 6
Emulating the Raman Physics in the Spatial Domain with the Help of the Zakharov's Systems

Evgeny M. Gromov and Boris A. Malomed

Abstract Dynamics of solitons is considered in the framework of the extended nonlinear Schrödinger equation (NLSE), which is derived from a system of the Zakharov's type for the interaction between high- and low-frequency (HF and LF) waves, in which the LF field is subject to diffusive damping. The model may apply to the propagation of HF waves in plasmas. The resulting NLSE includes a *pseudo-stimulated-Raman-scattering* (pseudo-SRS) term, i.e., a spatial-domain counterpart of the SRS term which is well known as an ingredient of the temporal-domain NLSE in optics. Also included is inhomogeneity of the spatial second-order diffraction (SOD). It is shown that the wavenumber downshift of solitons, caused by the pseudo-SRS, may be compensated by an upshift provided by the SOD whose coefficient is a linear function of the coordinate. An analytical solution for solitons is obtained in an approximate form. Analytical and numerical results agree well, including the predicted balance between the pseudo-SRS and the linearly inhomogeneous SOD.

6.1 Introduction

The great interest to the dynamics of solitons is motivated by their ability to travel long distances keeping the shape and transferring the energy and information with no or little loss. Soliton solutions are relevant to nonlinear models in various areas

E. M. Gromov (✉)
National Research University Higher School of Economics, Nizhny Novgorod 603155, Russia
e-mail: egromov@hse.ru

B. A. Malomed
Faculty of Engineering, Department of Physical Electronics, Tel Aviv University, 69978 Tel Aviv, Israel
e-mail: malomed@post.tau.ac.il

B. A. Malomed
ITMO University, St. Petersburg 197101, Russia

H. Altenbach et al. (eds.), *Generalized Models and Non-classical Approaches in Complex Materials 2*, Advanced Structured Materials 90,
https://doi.org/10.1007/978-3-319-77504-3_6

of physics which deal with the propagation of intensive wave fields in dispersive media: optical pulses and beams in fibers and spatial waveguides, electromagnetic waves in plasma, surface waves (SW) on deep water, etc. [1–7]. Recently, solitons have also drawn a great deal of interest in plasmonics [8–10].

The propagation of broad high-frequency (HF) wave packets is modeled by the second-order nonlinear dispersive wave theory. In isotropic media, the basic equation of the theory is the nonlinear Schrödinger equation (NLSE) [11, 12], which combines the second-order dispersion (SOD) and the self-phase modulation. Its soliton solutions provide for the equilibrium of the dispersive dilatation and nonlinear compression of the wave packets. In particular, permanent-shape solutions for damped solitons were found in the framework of the NLSE including linear losses of HF waves and spatially-decreasing SOD [4, 13].

In anisotropic media, the copropagation of wave modes with different polarizations gives rise to coupled NLSEs [14–17], which include cross-phase-modulation (XPM) terms. Interactions of vector solitons in the framework of coupled NLSEs were studied in detail too, see, e.g., [18–20].

The dynamics of narrow HF wave packets is described by the third-order nonlinear dispersive wave theory [1], which takes into account the nonlinear dispersion (self-steeping) [21], stimulated Raman scattering (SRS) [22–24] and third-order dispersion (TOD). In isotropic media the basic equation of the theory is the third-order NLSE [24–28]. Soliton solutions in the framework of the third-order NLSE with TOD and nonlinear dispersion were found in Refs. [29–36]. In Refs. [37, 38], stationary kink waves were found as solutions of the extended NLSE with SRS and nonlinear dispersion terms. This solution exists as the equilibrium between the nonlinear dispersion and SRS. For localized nonlinear wave packets (solitons), the SRS gives rise to the downshift of the soliton spectrum [22–24] and eventually to destabilization of the solitons. The use of the balance between the SRS and the slope of the gain for the stabilization of solitons in long telecom links was proposed in [25]. The compensation of the SRS by emission of linear radiation fields from the soliton's core was considered in [26]. In addition, the compensation of the SRS in inhomogeneous media was considered in several situations, viz., with periodic SOD [27, 28], shifted zero-dispersion point of SOD [29], and in dispersion-decreasing fibers [30].

In anisotropic media the dynamics of narrow vector wave packets is described by coupled third-order NLSEs, which take into account third-order cross-nonlinear terms [31–34]. In the framework of this system, which does not include SRS terms, vector-soliton solutions were found in [32]. Interactions of vector solitons in the framework of coupled third-order NLSEs were considered in [35].

Intensive short pulses of HF electromagnetic or Langmuir wave in plasmas, as well as HF SW in deep stratified water, suffer effective induced damping due to scattering on LF waves, which, in turn, are subject to the action of viscosity. These LF modes are ion-sound waves in the plasma, and internal waves (IW) in the stratified fluid. The first model for the damping induced by the interaction with the LF waves was proposed in [35] (see Sect. 6.2). This model gives rise to an extended NLSE with the spatial-domain counterpart of the SRS term, that was call a

pseudo-SRS one (*pseudo-Raman*). The equation was derived from the system of the Zakharov's type equations [37, 38] for the coupled Langmuir and ion-acoustic waves in plasmas. The pseudo-SRS leads to the self-wavenumber downshift, similar to what is well known in the temporal domain [1, 21–24] and, eventually, to destabilization of the solitons. The model elaborated in [36] also included smooth spatial variation of the SOD, accounted for by a spatially decreasing SOD coefficient, which leads to an increase of the soliton's wavenumber, making it possible to compensate the effect of the pseudo-SRS on the soliton by the spatially inhomogeneous SOD, neglecting the direct effect of the LF-wave loss.

The objective of this article is to produce a review of models derived, starting from systems of the Zakharov's type, in the form of NLSEs which include the pseudo-Raman term and other terms which produce soliton pulses as a result of competition with the pseudo-Raman effect. After reviewing the basic model equation in Sect. 6.2, in Sect. 6.3 we consider the dynamics of intensive HF wave packets in dispersive nonlinear media, taking into account the scattering on the damped LF waves (pseudo-Raman), exponentially decreasing SOD, and linear losses of HF waves [39].

In Sect. 6.4 the soliton dynamics is considered in the framework of an higher-order NLSE with a pseudo-Raman effect, decreasing SOD, taking into account nonlinear dispersion and TOD too [40]. The equilibrium between the pseudo-SRS and decreasing SOD is considered. The equilibrium state is a stable focus for negative nonlinear dispersion and positive TOD, and an unstable focus for positive nonlinear dispersion and negative TOD.

In Sect. 6.5 we address the dynamics of vector solitons in the framework of coupled extended NLSEs, taking into account pseudo-Raman, cross-pseudo-SRS, XPM and inhomogeneous SOD [41]. Using analytical and numerical methods, the compensation of the soliton's Raman self-wavenumber downshift by the upshift caused by the decreasing SOD is shown. An analytical vector-soliton solution is found in the framework of coupled extended NLSEs, representing the equilibrium of pseudo-SRS and inhomogeneous SOD. The soliton exists with an additional wavenumber lower than a certain critical value, which is proportional to the amplitude of the wave packet. By means of direct simulations, we also address evolution initiated by an input with spatially even and odd components, which reveals different outcomes, depending on the value of the relative amplitude of the two components.

In Sect. 6.6 dynamics of solitons is considered in the framework of an extended nonlinear NLSE, which is derived from a Zakharov-type model for wind-driven HF SW in the ocean, coupled to damped LF IW [42]. The drive gives rise to a convective (but not absolute) instability in the system. The resulting NLSE includes a pseudo-SRS term, which is a spatial-domain counterpart of the SRS term. Analysis of the field-momentum balance and direct simulations demonstrate that wavenumber downshift by the pseudo-SRS may be compensated by the upshift induced by the wind traction, thus maintaining robust bright solitons in both stationary and oscillatory forms; in particular, they are not destroyed by the underlying convective instability.

6.2 Soliton Dynamics in an Extended Nonlinear Schrödinger Equation with a Pseudo-Raman Effect and Inhomogeneous Dispersion

We consider the evolution of slowly varying envelope $U(\xi, t)$ of the intense HF wave field in the nonlinear medium with inhomogeneous SOD, taking into account the interaction with LF variations of the medium's parameter $n(\xi, t)$ (such as the refractive index in optics), which suffers the action of effective diffusion. The unidirectional propagation of the fields along coordinate ξ is described by the system of the Zakharov's type [37, 38]:

$$2i\frac{\partial U}{\partial t} + \frac{\partial}{\partial \xi}\left(q(\xi)\frac{\partial U}{\partial \xi}\right) - nU = 0, \tag{6.1}$$

$$\frac{\partial n}{\partial t} + \frac{\partial n}{\partial \xi} - \mu\frac{\partial^2 n}{\partial \xi^2} = -\frac{\partial |U|^2}{\partial \xi}, \tag{6.2}$$

where μ is the diffusion coefficient. In particular, this system may describe intense electromagnetic or Langmuir waves in plasmas, taking into account the scattering on ion-acoustic waves, which are subject to the viscous damping. In the third-order approximation of the theory (for short HF wave packets, with $k\Delta \ll \mu$, where k and Δ are the spatial extension and characteristic wave number of the wave packet), Eq. (6.2) may approximated by the nonlinear response of the medium, $n = -|U|^2 - \mu\partial\left(|U|^2\right)/\partial\xi$, which leads to the following extended NLSE for the HF amplitude:

$$2i\frac{\partial U}{\partial t} + \frac{\partial}{\partial \xi}\left[q(\xi)\frac{\partial U}{\partial \xi}\right] + 2\alpha U|U|^2 + \mu U\frac{\partial\left(|U|^2\right)}{\partial \xi} = 0, \tag{6.3}$$

where $\alpha = 1/2$. Below, we fix $\alpha = 1$ by means of obvious scaling. The last term in Eq. (6.3) represents the above-mentioned pseudo-Raman effect in the spatial domain.

Equation (6.3) with zero boundary conditions at infinity, $U|_{\xi\to\pm\infty} \to 0$, gives rise to the following integral relations for field moments, which will be used below:

$$\frac{dN}{dt} \equiv \frac{d}{dt}\int_{-\infty}^{+\infty} |U|^2 d\xi = 0, \tag{6.4}$$

$$2\frac{d}{dt}\int_{-\infty}^{+\infty} K|U|^2 d\xi = -\mu \int_{-\infty}^{\infty} \left[\frac{\partial\left(|U|^2\right)}{\partial\xi}\right]^2 d\xi - \int_{-\infty}^{\infty} \frac{dq}{d\xi}\left|\frac{\partial U}{\partial\xi}\right|^2 d\xi, \tag{6.5}$$

$$\frac{d}{dt}\int_{-\infty}^{+\infty} \xi|U|^2 d\xi = \int_{-\infty}^{+\infty} qK|U|^2 d\xi, \tag{6.6}$$

where the complex field is represented as $U \equiv |U|\exp(i\phi)$, and $K \equiv \partial\phi/\partial\xi$ is the local wavenumber.

For the analytical consideration of the wave-packet dynamics, we assume that scale of the inhomogeneity of the SOD term is much larger than the spatial width of the wave-packet envelope, $D_q \gg D_{|U|}$. Then, a solution of system (6.5)–(6.6) may be obtained in the adiabatic approximation, based on the use of the sech-like ansatz:

$$U(\xi,t) = A(t)\mathrm{sech}\left[\frac{\xi-\bar{\xi}(t)}{\Delta(t)}\right]\exp\left[ik(t)\xi - i\int \Omega(t)dt\right], \tag{6.7}$$

where $\Delta(t) = \sqrt{q(\bar{\xi})}/A(t), \Omega(t) = A^2(t)/2, A^2(t)\Delta(t) = \mathrm{const}, \bar{\xi}(t) = N^{-1}\int_{-\infty}^{+\infty}\xi|U|^2 d\xi$. Substituting (6.7) in (6.5)–(6.6) we derive a system of evolution equations the system for free parameters k and $\bar{\xi}$:

$$2\frac{dk}{dt} = -\frac{8}{15}\frac{\mu A_0^4 q_0^2}{q^3(\bar{\xi})} - \frac{q'(\bar{\xi})A_0^2 q_0}{3q^2(\bar{\xi})} - q'(\bar{\xi})k^2,\ \frac{d\bar{\xi}}{dt} = kq(\bar{\xi}), \tag{6.8}$$

where initial values are $q_0 \equiv q\left(\bar{\xi}(t=0)\right), A_0 \equiv A(t=0)$, which obey the above-mention relation, $A^2(t)q\left(\bar{\xi}(t)\right) = A^2(t=0)q\left(\bar{\xi}(t=0)\right) \equiv A_0^2 q_0$, and $q'(\bar{\xi}) \equiv dq/d\xi|_{\xi=\bar{\xi}}$ is the derivative (*slope*) of the SOD coefficient at the soliton's center. Equation (6.8) give rise to an obvious equilibrium state (alias a fixed point, FP):

$$8\mu q_0 A_0^2 = -5q'(\bar{\xi}_*)q(\bar{\xi}_*), k_* = 0, \tag{6.9}$$

where $\bar{\xi}_*$ is the equilibrium position of the soliton. For $\mu = \mu_* \equiv -(5/8)q'(\bar{\xi}_0)/A_0^2$ the equilibrium position of the soliton coincides with its initial position, $\bar{\xi}_* = \bar{\xi}_0 \equiv \bar{\xi}(t=0)$. For $\mu \neq \mu_*$ soliton's parameters are time-varying. To analyze the evolution around the FP, we assume linearly decreasing SOD, $q' = \mathrm{const} < 0$, and rescale the variables by defining $\tau \equiv -tq'A_0/\sqrt{3q_0}$,

$$y(\tau) \equiv k(\tau)\sqrt{3q_0}/A_0, n(\tau) = q\left(\bar{\xi}(\tau)\right)/q_0. \tag{6.10}$$

Then system (6.8) is reduced to

$$2\frac{dy}{d\tau} = -\frac{\lambda}{n^3} + \frac{1}{n^2} + y^2, \quad \frac{dn}{d\tau} = -ny, \tag{6.11}$$

where $\lambda \equiv -8\mu A_0^2/\left(5q'\right) \equiv \mu/\mu_*$. The first integral of Eq. (6.11) is

$$2y^2n^3 - \left(2y_0^2 + \lambda - 2\right)n^2 - 2n + \lambda = 0, \tag{6.12}$$

where $y_0 = y(\tau = 0)$. Dynamical invariant (6.12) is drawn in the plane of (y, n) in Fig. 6.1a, for $y_0 = 0$ and different values of λ. Trajectories in the plot are closed for $0 < \lambda < 2$, and open otherwise.

Further, at $y_0^2 > 0$ straightforward analysis of Eq. (6.11) demonstrates that the closed trajectories, which are shown in Fig. 6.1a for $y_0^2 = 0$, stretch in both positive and negative vertical directions (along the axis of n). In the same case, the critical value of the pseudo-SRS coefficient, which leads to the destruction of the soliton, decreases to $\lambda_{\rm cr} = 2\left(1 - y_0^2\right)$, the destruction being signaled by the disappearance of closed trajectories. Thus, the solitons do not exist at $y_0^2 > 1$; in other words, they exist with the wavenumber smaller than a critical value, $k^2 < A_0^2\alpha/(3q_0)$. Contours of dynamical invariant (6.12) are plotted in the plane of (y, n) in Fig. 6.1b, for $0 < y_0^2 < 1$ and several values of λ.

We look for stationary solutions to Eq. (6.3), where the SOD with linear spatial profile is adopted, in the form of a stationary wave profile, $U(\xi, t) = \psi(\xi)\exp(i\Omega t)$:

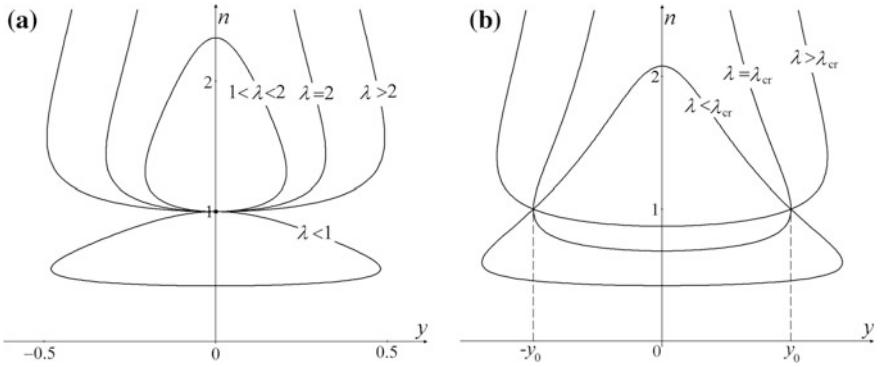

Fig. 6.1 Contour plots of dynamical invariant (6.12) in the plane of (y, n) of the soliton's rescaled dispersion and wavenumber (see Eq. (6.10)) for $y_0 = 0$ (**a**) and $0 < y_0^2 < 1$ (**b**), and different values of constant λ

$$\left(q_0 + q'\xi\right)\frac{d^2\psi}{d\xi^2} + q'\frac{d\psi}{d\xi} + 2\psi^3 - 2\Omega\psi + \mu\psi\frac{d(\psi^2)}{d\xi} = 0. \tag{6.13}$$

Next, with regard to the underlying assumption that the soliton's width is much smaller than the scale of the spatial inhomogeneity for the SOD, a solution to Eq. (6.13) is found in the form of $\psi = \psi_0 + \psi_1$, where ψ_1 is a small correction produced by terms $\sim q'$ and $\sim \mu$ in Eq. (6.13). In this approximation, we obtain

$$q_0\frac{d^2\psi_0}{d\xi^2} + 2\psi_0^3 - 2\Omega\psi_0 = 0, \tag{6.14}$$

$$q_0\frac{d^2\psi_1}{d\xi^2} + \left(6\psi_0^2 - 2\Omega\right)\psi_1 = -q'\frac{d^2\psi_0}{d\xi^2}\xi - \frac{2}{3}\mu\frac{d\left(\psi_0^3\right)}{d\xi} - q'\frac{d\psi_0}{d\xi}. \tag{6.15}$$

Equation (6.14) gives rise to the classical soliton solution, $\psi_0 = A_0\mathrm{sech}(\xi/\Delta)$, where $\Delta \equiv \sqrt{q_0}/A_0$ and $\Omega \equiv A_0^2/2$. Then substitutions $\eta = \xi/\Delta$ and $\Psi = \psi_1 q_0/\left(A_0 q_\eta'\right)$ cast Eq. (6.15) in the form of

$$\frac{d^2\Psi}{d\eta^2} + \left(\frac{6}{\cosh^2\eta} - 1\right)\Psi = \frac{\eta}{\cosh\eta} - \frac{2\eta}{\cosh^3\eta} - \frac{5}{4}\frac{\mu}{\mu_*}\frac{\sinh\eta}{\cosh^4\eta} + \frac{\sinh\eta}{\cosh^2\eta}, \tag{6.16}$$

where the equilibrium value of the pseudo-SRS coefficient is $\mu_* \equiv -5q'/(8A_0)$. For $\mu = \mu_*$ Eq. (6.16) has an *exact* localized solution for the correction to the standard sech soliton,

$$\Psi(\eta) = (1/4)\tanh\eta(\mathrm{sech}\eta)\left[\eta^2 - \ln(\cosh\eta)\right], \tag{6.17}$$

cf. a similar solution reported by [43]. It satisfies boundary conditions $\Psi(\eta \to \pm\infty) \to 0$. This spatially antisymmetric solution exists due to the balance between the pseudo-SRS term and linearly decreasing SOD.

6.3 Damped Solitons in an Extended Nonlinear Schrödinger Equation with a Pseudo-Raman Effect and Exponentially Decreasing Dispersion

We consider the evolution of a slowly varying envelope, $U(\xi, t)$, of the intensive HF wave field in the nonlinear medium with inhomogeneous SOD, taking into account the interaction with the damped LF wave, which is represented by the local perturbation of the effective refractive index, $n(\xi, t)$. The respective system of the

Zakharov's type for the unidirectional propagation of the HF and LF waves is [37, 38]

$$2i\left(\frac{\partial U}{\partial t}+V\frac{\partial U}{\partial x}\right)+\frac{\partial}{\partial x}\left[q(x)\frac{\partial U}{\partial x}\right]-nU+i\nu U=0, \tag{6.18}$$

$$\frac{\partial n}{\partial t}+V_S\frac{\partial n}{\partial x}-\delta\frac{\partial^2 n}{\partial x^2}=-\frac{\partial\left(|U|^2\right)}{\partial x}, \tag{6.19}$$

where ν is the linear-losses coefficient of the HF waves, δ is the viscosity of the LF waves, V is the HF group velocity, and V_S is the velocity of LF waves. As mentioned above, this system may describe intensive Langmuir waves in isotropic plasmas coupled to ion-sound waves, which are subject to the viscous damping.

In the third-order approximation of the theory (see Sect. 6.2) system (6.18)–(6.19) leads to the following evolution equation for the HF envelope amplitude:

$$2i\frac{\partial U}{\partial t}+\frac{\partial}{\partial\xi}\left[q(\xi+Vt)\frac{\partial U}{\partial\xi}\right]+2\alpha U|U|^2+\mu U\frac{\partial\left(|U|^2\right)}{\partial\xi}+i\nu U=0, \tag{6.20}$$

where $\xi=x-Vt$, term $\mu U\partial\left(|U|^2\right)/\partial\xi$, with $\mu\equiv\delta(V_S-V)^{-2}$, is, as above, the spatial counterpart of the SRS effect in the temporal domain, and $\alpha\equiv(1/2)(V_S-V)^{-1}$. Below, we fix $\alpha=1$ by means of obvious scaling. After the substitution of $U\equiv W\exp(-\nu t/2)$, Eq. (6.3) takes the form of

$$2i\frac{\partial W}{\partial t}+\frac{\partial}{\partial\xi}\left[q(\xi+Vt)\frac{\partial W}{\partial\xi}\right]+2W|W|^2\exp(-\nu t)+\mu W\frac{\partial\left(|W|^2\right)}{\partial\xi}\exp(-\nu t)=0. \tag{6.21}$$

Equation (6.21) with zero boundary conditions at infinity, $W|_{\xi\to\pm\infty}\to 0$, gives rise to the following integral relations for the field moments:

$$\frac{dN}{dt}\equiv\frac{d}{dt}\int_{-\infty}^{+\infty}|W|^2d\xi=0, \tag{6.22}$$

$$2\frac{d}{dt}\int_{-\infty}^{+\infty}K|W|^2d\xi=-\mu\exp(-\nu t)\int_{-\infty}^{\infty}\left[\frac{\partial\left(|W|^2\right)}{\partial\xi}\right]^2d\xi-\int_{-\infty}^{\infty}\frac{\partial q}{\partial\xi}\left|\frac{\partial W}{\partial\xi}\right|^2d\xi, \tag{6.23}$$

$$\frac{d}{dt}\int_{-\infty}^{\infty}\xi|W|^2d\xi=\int_{-\infty}^{+\infty}qK|W|^2d\xi. \tag{6.24}$$

For the analytical consideration of the wave-packet dynamics, we again assume that the scale of the inhomogeneity of the SOD term is much larger than the spatial width of the wave-packet envelope, $D_q \gg D_{|W|}$.

We take the HF wave packet as

$$W(\xi,t)=A(t)\mathrm{sech}\left[\frac{\xi-\overline{\xi}(t)}{\Delta(t)}\right]\exp\left[ik(t)\xi-i\int\Omega(t)dt\right], \tag{6.25}$$

cf. Eq. (6.7), where $\Delta(t)=\sqrt{q\left(\overline{\xi}+Vt\right)}/\left(A(t)\sqrt{\exp(-\nu t)}\right), \Omega(t)=A^2(t)\exp(-\nu t)/2, A^2(t)\Delta(t)=\text{const}$, $\overline{\xi}(t)=N^{-1}\int_{-\infty}^{+\infty}\xi|U|^2d\xi$. Substituting (6.25) in (6.23)–(6.24), we derive the dynamical system:

$$2\frac{dk}{dt}=-\frac{8}{15}\frac{\mu A_0^4\exp(-4\nu t)q_0^2}{q^3\left(\overline{\xi}+Vt\right)}-\frac{q'\left(\overline{\xi}+Vt\right)A_0^2\exp(-2\nu t)q_0}{3q^2\left(\overline{\xi}+Vt\right)}-q'\left(\overline{\xi}+Vt\right)k^2,$$

$$\frac{d\overline{\xi}}{dt}=kq\left(\overline{\xi}+Vt\right), \tag{6.26}$$

where $A_0=A(0)$. We now select the spatial variation of SOD in the form corresponding to an exponentially decreasing profile of the SOD,

$$q=q_0\exp(-\nu x/V). \tag{6.27}$$

In particular, the realization of fibers with exponentially decreasing profiles of the SOD was demonstrated experimentally in [44]. Such profiles are created by variation of the fiber's diameter. Then system (6.14)–(6.18), with the time, wavenumber and the soliton's coordinate redefined as $\theta\equiv\nu t$, $y\equiv k\sqrt{3q_0}/A_0, \eta\equiv\nu\overline{\xi}/V$, is reduced to

$$2\sigma\exp\theta\frac{dy}{d\theta}=-\lambda\exp(3\eta)+y^2\exp(-\eta)+\exp(\eta), \tag{6.28}$$

$$\sigma\exp\theta\frac{d\eta}{d\theta}=y\exp(-\eta), \tag{6.29}$$

where new constants are defined as $\sigma\equiv V\sqrt{3}/\left(A_0\sqrt{q_0}\right), y_0=y(0), \lambda\equiv(8/5)\mu A_0^2V/\nu$. An equilibrium state of Eqs. (6.25)–(6.26) is achieved under conditions

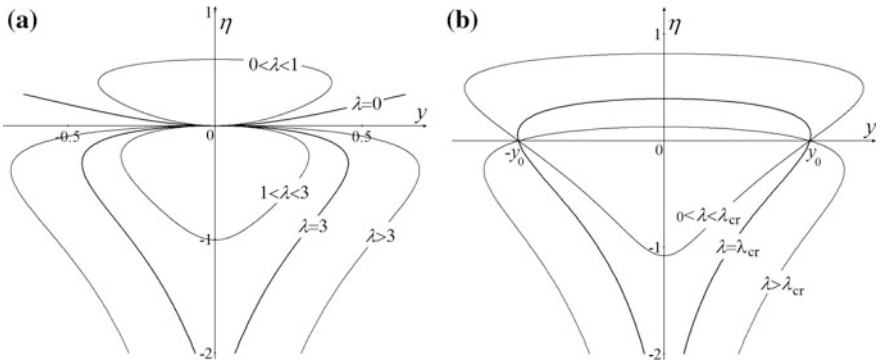

Fig. 6.2 First integral (6.31) in the plane (y, η) of the soliton's rescaled wavenumber and coordinate for $y_0 = 0$ (**a**) and $0 < y_0^2 < 1$ (**b**), and different values of constant λ

$$k_* = 0, \eta_* = -(1/2)\ln\lambda. \tag{6.30}$$

In the equilibrium regime, the wave packet W propagates with the integral moment, N, keeping their initial value, N, and zero wavenumber. Therefore, the field moments for original wave packet, $U = W\exp(-\theta/2)$ decay exponentially, $N_U(\theta) = N\exp(-\theta)$, that $\theta \equiv \nu t$. The first integral of these equations is

$$3y^2\exp(-\eta) + \lambda[\exp(3\eta) - 1] + 3[1 - \exp(\eta)] = 3y_0^2. \tag{6.31}$$

In Fig. 6.2a, first integral (6.31) is drawn in the plane of (y, η) for $y_0 = 0$ and different values of λ. Trajectories in the plot are closed for $0 < \lambda < 3$, and open otherwise. In Fig. 6.2b, first integral (6.31) is drawn in the plane of (y, η) for $0 < y_0^2 < 1$ and different values of λ. Trajectories in the plot are closed for $0 < \lambda < \lambda_{\rm cr} \equiv 3\left(1 - y_0^2\right)$, and open otherwise, cf. Fig. 6.1. The temporal evolution $y(\theta)$ following from Eqs. (6.28)–(6.29) is shown in Fig. 6.3 for initial condition $y_0 = 0$ with different σ and λ.

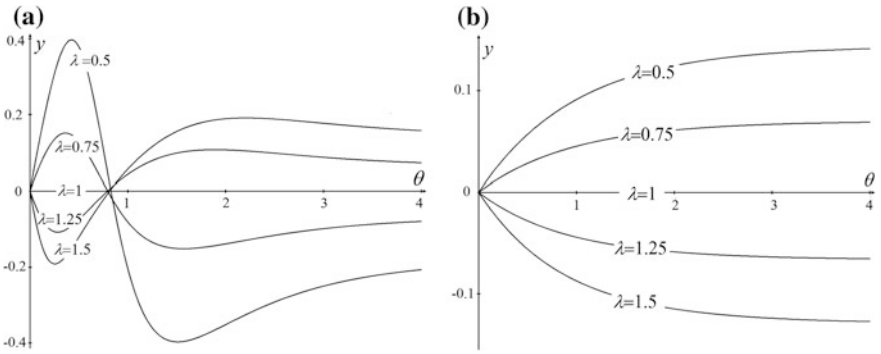

Fig. 6.3 Time evolution $y(\theta)$ obtained from Eqs. (6.28)–(6.29) for initial condition $y_0 = 0$ with different values of σ [**a**: $\sigma = 1/10$, **b**: $\sigma = 1$], and different λ

6.4 Soliton in a Higher-Order Nonlinear Schrödinger Equation with Pseudo-Raman Effect and Inhomogeneous Second-Order Diffraction

Here we consider the dynamics of the HF wave, field $U(\xi,t)\exp(-i\omega t+i\kappa\xi)$, in the framework of inhomogeneous higher-order NLSE with pseudo-Raman, nonlinear-dispersion, TOD and inhomogeneous-SOD terms:

$$2i\frac{\partial U}{\partial t}+\frac{\partial}{\partial\xi}\left[q(\xi)\frac{\partial U}{\partial\xi}\right]+2U|U|^2+2i\chi\frac{\partial\left(U|U|^2\right)}{\partial\xi}+i\gamma\frac{\partial^3U}{\partial\xi^3}+\mu U\frac{\partial\left(|U|^2\right)}{\partial\xi}=0, \tag{6.32}$$

where the following notation is used: μ is, as above, the pseudo-SRS strength, χ is the nonlinear dispersion, and γ is the TOD. Equation (6.1) with zero boundary conditions on infinity, $U|_{\xi\to\pm\infty}\to 0$, gives rise to the following evolution equations for integral moments:

$$\frac{dN}{dt}\equiv\frac{d}{dt}\int_{-\infty}^{+\infty}|U|^2d\xi=0, \tag{6.33}$$

$$2\frac{d}{dt}\int_{-\infty}^{+\infty}K|U|^2d\xi=-\mu\int_{-\infty}^{\infty}\left[\frac{\partial\left(|U|^2\right)}{\partial\xi}\right]^2d\xi-\int_{-\infty}^{\infty}\frac{dq}{d\xi}\left|\frac{\partial U}{\partial\xi}\right|^2d\xi, \tag{6.34}$$

$$N\frac{d\bar{\xi}}{dt}\equiv\frac{d}{dt}\int_{-\infty}^{\infty}\xi|U|^2d\xi=\int_{-\infty}^{+\infty}qK|U|^2d\xi+\frac{3}{2}\chi\int_{-\infty}^{+\infty}|U|^4d\xi-\frac{3}{2}\gamma\int_{-\infty}^{\infty}\left|\frac{\partial U}{\partial\xi}\right|^2d\xi. \tag{6.35}$$

For analytical consideration of the system (6.33)–(6.35), we assume that values of nonlinear dispersion, TOD, and wavenumber are small, $\chi,\gamma,K\sim\varepsilon\ll 1$. In this case, from the imaginary part of (6.32), where terms of order ε^2 are neglected, we derive equation

$$\frac{\partial\left(|U|^2\right)}{\partial t}+\frac{\partial}{\partial\xi}\left(qK|U|^2+\frac{3}{2}\chi|U|^4\right)+\gamma|U|\frac{\partial^3(|U|)}{\partial\xi^3}=0. \tag{6.36}$$

Assuming that wave packets move keeping their shapes, $\partial\left(|U|^2\right)/\partial t\approx -V\partial\left(|U|^2\right)/\partial\xi$, where V is the velocity of the packet, we obtained from Eq. (6.36)

$$\frac{\partial}{\partial\xi}\left(-V|U|^2+qK|U|^2+\frac{3}{2}\chi|U|^4\right)+\gamma|U|\frac{\partial^3(|U|)}{\partial\xi^3}=0. \tag{6.37}$$

Integrating (6.37) for localized wave packets, $|U|_{\xi\to-\infty}\to 0$, and assuming (as above) that the scale of the inhomogeneity of SOD is much larger than the inhomogeneity scale of the wave-packet envelope, $D\gg D_{|U|}$, gives rise to a relation for the wavenumber:

$$K=k(t)-\frac{3\chi}{2q(\bar{\xi})}|U|^2+\frac{3\gamma}{2q(\bar{\xi})|U|^2}\left[\frac{\partial(|U|)}{\partial\xi}\right]^2-\frac{\gamma}{2q(\bar{\xi})|U|^2}\frac{\partial^2\left(|U|^2\right)}{\partial\xi^2}, \tag{6.38}$$

where $k(t)=V/q\left(\bar{\xi}(t)\right)$. Solution of the system of Eqs. (6.34) and (6.35) can be found in the adiabatic approximation, presenting the solution in sech-like form with wavenumber distribution (6.38):

$$U(\xi,t)=A(t)\operatorname{sech}\left[\frac{\xi-\bar{\xi}}{\Delta(t)}\right]\exp\left[i\int K(\xi,t)d\xi-\frac{i}{2}\int A^2(t)dt\right], \tag{6.39}$$

$$K(\xi,t)=k(t)-\frac{3}{2}\frac{\chi A^2(t)}{q(\bar{\xi})}\operatorname{sech}^2\left[\frac{\xi-\bar{\xi}}{\Delta(t)}\right]-\frac{3}{2}\frac{\gamma}{q(\bar{\xi})\Delta^2(t)}\tanh^2\left[\frac{\xi-\bar{\xi}}{\Delta(t)}\right]+\frac{\gamma}{q(\bar{\xi})\Delta^2(t)}, \tag{6.40}$$

where $\Delta(t)\equiv\sqrt{q(\bar{\xi})}/A(t)$ and $A^2(t)\Delta(t)=\text{const}$. Solution (6.39)–(6.40) has two free parameters: an additional wavenumber $k(t)$ and a center-of-mass coordinate $\bar{\xi}(t)$. Substituting Eqs. (6.39)–(6.40) in (6.34)–(6.35) and keeping terms of order ε, we derive a system of equations for k and $\bar{\xi}$:

$$2\frac{dk}{dt}=-\frac{8q_0^2A_0^4\mu}{15q^3(\bar{\xi})}-\frac{q_0A_0^2q'(\bar{\xi})}{3q^2(\bar{\xi})}+\frac{2q_0\gamma A_0^2q'(\bar{\xi})k}{q^3(\bar{\xi})}-\frac{2\chi A_0^2q'(\bar{\xi})k}{q^2(\bar{\xi})}-q'(\bar{\xi})k^2,$$

$$\frac{d\bar{\xi}}{dt}=qk, \tag{6.41}$$

where $q_0=q(0), A_0=A(0)$, and $q'(\bar{\xi})=(dq/d\xi)_{\bar{\xi}}$. System (6.41) gives rise to an obvious equilibrium state (alias a fixed point, FP): $8q_0A_0^2\mu=-5q'(\bar{\xi}_*)q(\bar{\xi}_*), k_*=0$. In particular, for $\mu=\mu_*\equiv-5q'(0)/(8A_0^2)$ the FP corresponds to initial soliton parameters: $\bar{\xi}=0,\ k=0$. For $\mu\neq\mu_*$ soliton's parameters are time-varying. To analyze the evolution around the FP, we assume linearly decreasing SOD, $q'=\text{const}<0$, and rescale the variables by defining $\tau\equiv-tq'A_0/\sqrt{3q_0}, y\equiv k\sqrt{3q_0}/A_0$ and $n=q(\bar{\xi})/q_0$. Then system (6.41) is reduced to

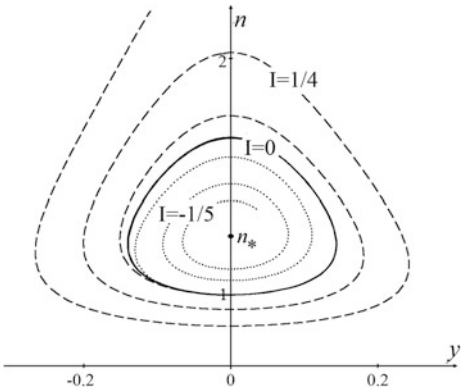

Fig. 6.4 Trajectories (6.42) in the plane (y, n) for $\lambda = 5/4$, initial conditions $y_0 = 0, n_0 \equiv 1$, and different values of $\mathrm{I} = \upsilon - (5/4)\varsigma \equiv \upsilon - \lambda\varsigma$

$$2\frac{dy}{d\tau} = -\frac{\lambda}{n^3} + \frac{1}{n^2} + y^2 - \upsilon\frac{y}{n^3} + \varsigma\frac{y}{n^2}, \quad \frac{dn}{d\tau} = -ny, \tag{6.42}$$

where $\lambda \equiv -8\mu A_0^2/(5q') \equiv \mu/\mu_*, \upsilon \equiv 2\sqrt{3}\gamma A_0/\sqrt{q_0^3}, \varsigma \equiv 2\sqrt{3}\chi A_0/\sqrt{q_0^3}$. The FP of Eq. (6.42) in the rescale variables is $y_* = 0, n_* = \lambda$. For $\mathrm{I} \equiv \upsilon - \lambda\varsigma > 0$ the FP is a stable focus, for $\mathrm{I} = 0$ it is a center, and for $\mathrm{I} < 0$ the FP is an unstable focus. Trajectories in the (y, n) plane, obtained from Eq. (6.42) with initial conditions $y_0 = 0, n_0 \equiv 1$ for $\lambda = 5/4$, and different values of $\mathrm{I} = \upsilon - (5/4)\varsigma \equiv \upsilon - \lambda\varsigma$, are shown in Fig. 6.4.

For $\mu = \mu_* \equiv 5q'/(8A_0^2)$, corresponding to $\lambda = 1$, the FP's coordinates coincide with the initial soliton parameters, $n_0 \equiv 1, y_0 = 0$. In this case, the soliton's parameters remain constant in time.

6.5 Vector Solitons in Coupled Nonlinear Equations with the Pseudo-Raman Effect and Inhomogeneous Dispersion

We consider dynamics of the two-component (vector) HF wave field $\vec{E}(\xi, t) = U_1(\xi, t)\exp(i\omega t - i\kappa\xi)\vec{e}_1 + U_2(\xi, t)\exp(i\omega t - i\kappa\xi)\vec{e}_2$, where $\vec{e}_{1,2}$ are unit vectors of two orthogonal polarizations, and $U_{1,2}$ are the corresponding amplitudes. The consideration is carried out in the framework of two coupled NLSEs including pseudo-SRS, cross-pseudo-SRS, XPM and inhomogeneous SOD:

$$2i\left(\frac{\partial U_{1,2}}{\partial t}\mp\delta\frac{\partial U_{1,2}}{\partial\xi}\right)+\frac{\partial}{\partial\xi}\left[q(\xi)\frac{\partial U_{1,2}}{\partial\xi}\right]$$
$$+2U_{1,2}\left(|U_{1,2}|^2+|U_{2,1}|^2\right)+\mu U_{1,2}\frac{\partial\left(|U_{1,2}|^2+|U_{2,1}|^2\right)}{\partial\xi}=0, \tag{6.43}$$

where δ is the group-velocity mismatch between the components, and μ is, once again, the pseudo-SRS strength. The substitution of $U_{1,2}=u_{1,2}\exp\left[\pm i\delta\int d\xi/q(\xi)\right]$ transforms Eq. (6.43) into

$$2i\frac{\partial u_{1,2}}{\partial t}+\frac{\partial}{\partial\xi}\left[q(\xi)\frac{\partial u_{1,2}}{\partial\xi}\right]+\frac{\delta^2}{q(\xi)}u_{1,2}+2u_{1,2}\left(|u_{1,2}|^2+|u_{2,1}|^2\right)+\mu u_{1,2}\frac{\partial\left(|u_{1,2}|^2+|u_{2,1}|^2\right)}{\partial\xi}=0, \tag{6.44}$$

with an effective potential $\delta^2/q(\xi)$ (this definition implies that $q(\xi)$ does not vanish; it may be interesting too to consider a setting with a zero-dispersion point, at which $q(\xi)=0$, but in that case it necessary to take into regard the third-order-dispersion term, which is not included here).

6.5.1 Analytical Results

Equation (6.44) with zero boundary conditions at infinity, $u_{1,2}|_{\xi\to\pm\infty}\to 0$, gives rise to the following exact integral relations for a localized wave packet:

$$\frac{dN_{1,2}}{dt}\equiv\frac{d}{dt}\int_{-\infty}^{+\infty}|u_{1,2}|^2d\xi=0, \tag{6.45}$$

$$2\frac{d}{dt}\int_{-\infty}^{+\infty}k_{1,2}|u_{1,2}|^2d\xi=-\mu\int_{-\infty}^{\infty}\frac{\partial\left(|u_{1,2}|^2\right)}{\partial\xi}\frac{\partial\left(|u_{1,2}|^2+|u_{2,1}|^2\right)}{\partial\xi}d\xi-\int_{-\infty}^{\infty}\frac{dq}{d\xi}\left(\left|\frac{\partial u_{1,2}}{\partial\xi}\right|^2+\frac{\delta^2}{q^2}|u_{1,2}|^2\right)d\xi$$
$$+2\int_{-\infty}^{+\infty}|u_{1,2}|^2\frac{\partial\left(|u_{2,1}|^2\right)}{\partial\xi}d\xi, \tag{6.46}$$

$$N_{1,2}\frac{d\bar{\xi}_{1,2}}{dt}\equiv\frac{d}{dt}\int_{-\infty}^{\infty}\xi|u_{1,2}|^2d\xi=\int_{-\infty}^{+\infty}qk_{1,2}|u_{1.2}|^2d\xi, \tag{6.47}$$

where $u_{1,2}=|u_{1,2}|\exp\left(i\varphi_{1,2}\right)$, and $k_{1,2}=\partial\varphi_{1,2}/\partial\xi$ are wavenumbers of wave packets $u_{1,2}$.

To analyze of the wave-packet dynamics, we assume, as above, that the scale of the spatial inhomogeneity of SOD is much larger than the packet's width, $D_q \gg \Delta$. A solution to system (6.3)–(6.5) is then looked for in the form of a sech ansatz, with two components proportional to each other:

$$u_1(\xi,t)=A(t)\mathrm{sech}\left[\frac{\xi-\overline{\xi}(t)}{\Delta(t)}\right]\exp\left[ik(t)\xi-i\int\Omega(t)dt\right],\quad u_2(\xi,t)=\sigma u_1(\xi,t), \tag{6.48}$$

where σ is a free real parameter, $\overline{\xi}(t)=\overline{\xi}_{1,2}(t)$ is the coordinate of the soliton's center $2\Omega(t)=(1+\sigma^2)A^2(t)+\delta^2/q\left(\overline{\xi}(t)\right)$, $\Delta(t)=(1/A(t))\sqrt{q\left(\overline{\xi}(t)\right)/(1+\sigma^2)}$ $k(t)\equiv k_{1,2}(t)$, and it is set $A^2(t)\Delta(t)=\mathrm{const}$, which is the usual relation between the amplitude and width of sech-shaped solitons. Substituting ansatz (6.48) in Eqs. (6.46) and (6.47), and taking into account the above condition $\Delta \ll D_q$, leads to the following evolution equations:

$$2\frac{dk}{dt}=-\mu\frac{8}{15}\frac{(1+\sigma^2)^2q_0^2A_0^4}{q^3\left(\overline{\xi}\right)}-\frac{(1+\sigma^2)q_0A_0^2q'\left(\overline{\xi}\right)}{3q^2\left(\overline{\xi}\right)}-\frac{\delta^2q'\left(\overline{\xi}\right)}{q^2\left(\overline{\xi}\right)}-q'\left(\overline{\xi}\right)k^2,$$

$$\frac{d\overline{\xi}}{dt}=kq\left(\overline{\xi}\right), \tag{6.49}$$

where initial values are $q_0\equiv q\left(\overline{\xi}(t=0)\right)$, $A_0\equiv A(t=0)$, which obey the above-mention relation, $A^2(t)q\left(\overline{\xi}(t)\right)=A^2(t=0)q\left(\overline{\xi}(t=0)\right)\equiv A_0^2q_0$, and $q'\left(\overline{\xi}\right)\equiv dq/d\xi|_{\xi=\overline{\xi}}$ is the derivative (*slope*) of the SOD coefficient at the soliton's center. Equation (6.49) give rise to an obvious equilibrium state (alias a fixed point, FP):

$$8\mu\left(1+\lambda^2\right)^2q_0^2A_0^4=-5q'\left(\overline{\xi}_*\right)q\left(\overline{\xi}_*\right)\left[\left(1+\lambda^2\right)q_0A_0^2+3\delta^2\right],\ k_*=0, \tag{6.50}$$

where $\overline{\xi}_*$ is the equilibrium position of the soliton. In the particular case of $\lambda=\delta=0$, relation (6.50) reduces to its counterpart for the single NLSE derived in [38]. For $\mu=\mu_*\equiv-(5/8)q'\left(\overline{\xi}_0\right)\left[(1+\sigma^2)q_0A_0^2+3\delta^2\right]/\left[(1+\sigma^2)^2q_0A_0^4\right]$ the equilibrium position of the soliton coincides with its initial position, $\overline{\xi}_*=\overline{\xi}_0\equiv\overline{\xi}(t=0)$.

To analyze the evolution near the FP, we assume a constant value of the SOD slope around the FP, $q'=\mathrm{const}$, and rescale the variables by defining $\tau\equiv-tq'\sqrt{q_0A_0^2(1+\sigma^2)+3\delta^2}/\left(\sqrt{3}q_0\right)$, $y(\tau)\equiv k(\tau)-tq'\sqrt{3}q_0/\sqrt{q_0A_0^2(1+\sigma^2)+3\delta^2}n(\tau)\equiv q\left(\overline{\xi}(\tau)\right)/q_0$, thus deriving a simple mechanical system from Eq. (6.49), coinciding with Eq. (6.11).

Here we address steady-state solutions of Eq. (6.44) for a linear profile of the inhomogeneous SOD, viz., $q(\xi)=q_0+q'\xi$, in the form of $U_2(\xi,t)=\sigma U_1(\xi,t)\equiv\sigma\psi(\xi)\exp(i\Omega t)$:

$$-2\Omega\psi+\frac{\delta^2}{q_0+q'\xi}\psi+\left(q_0+q'\xi\right)\frac{d^2\psi}{d\xi^2}+q'\frac{d\psi}{d\xi}+2\left(1+\sigma^2\right)\psi^3+\mu\left(1+\sigma^2\right)\psi\frac{d\left(\psi^2\right)}{d\xi}=0. \tag{6.51}$$

Similar to what was adopted above, we again assume that the wave-packet's width is much smaller than the scale of the SOD's spatial inhomogeneity, $\Delta\ll 1/|q'|$. Introducing the corresponding small parameter, $\varepsilon\sim\Delta\cdot q'\sim\mu\ll q_0$, a solution to Eq. (6.51) can be looked for as $\psi=\Phi+\phi$, where ϕ is a correction $\sim\varepsilon$. Separating terms of orders ε^0 and ε^1, we obtain

$$q_0\frac{d^2\Phi}{d\xi^2}+2\Phi^3\left(1+\sigma^2\right)-\left(2\Omega-\frac{\delta^2}{q_0}\right)\Phi=0, \tag{6.52}$$

$$q_0\frac{d^2\phi}{d\xi^2}+\left[6\left(1+\sigma^2\right)\Phi^2-2\Omega+\frac{\delta^2}{q_0}\right]\phi=q'\frac{\delta^2}{q_0^2}\Phi\xi-q'\frac{d^2\Phi}{d\xi^2}\xi-q'\frac{d\Phi}{d\xi}-\frac{2}{3}\mu\left(1+\sigma^2\right)\frac{d\left(\Phi^3\right)}{d\xi}. \tag{6.53}$$

Equation (6.52) has the standard sech-soliton solution, $\Phi=A\,\mathrm{sech}(\xi/\Delta)$, where $\Delta=\sqrt{q_0/(1+\sigma^2)}/A$, and $2\Omega=(1+\sigma^2)A^2+\delta^2/q_0$. Then, in terms of rescaled variables, $\eta\equiv\xi/\Delta$ and $\phi\equiv q'\Psi/\sqrt{q_0\left(1+\lambda^2\right)}$, Eq. (6.53) takes the form of

$$\frac{d^2\Psi}{d\eta^2}+\left(\frac{6}{\cosh^2\eta}-1\right)\Psi=\left[\frac{\delta^2}{q_0(1+\sigma^2)A_0^2}-1\right]\frac{\eta}{\cosh\eta}+\frac{2\eta}{\cosh^3\eta}+\frac{\sinh\eta}{\cosh^2\eta}+\frac{2\mu(1+\sigma^2)A_0^2}{q'}\frac{\sinh\eta}{\cosh^4\eta}. \tag{6.54}$$

An essential result is that, at

$$\mu=\mu_*\equiv-(5/8)q'(1+3\mathrm{H})/\left[\left(1+\sigma^2\right)A_0^2\right], \tag{6.55}$$

where $\mathrm{H}\equiv\delta^2/\left[q_0(1+\sigma^2)A_0^2\right]$, Eq. (6.54) has an *exact* localized solution for the correction to the standard sech soliton,

$$\Psi(\eta)=(1/4)(\mathrm{sech}\eta)\left[2\mathrm{H}\eta+(1-\mathrm{H})\eta^2\tanh\eta-(1+3\mathrm{H})(\tanh\eta)\ln(\cosh\eta)\right]. \tag{6.56}$$

In the particular case of $H=0$, which corresponds to $\delta=0$, i.e., in the absence of the group-velocity mismatch between the polarization components, solution (6.56) carries over into one obtained above in Sect. 6.2, see Eq. (6.17).

6.5.2 Numerical Results

To check the above analytical results, we here aim to report findings produced bysimulations of the evolution of initial wave packet $u_{1,2}(\xi,0)=\left(1/\sqrt{2}\right)\mathrm{sech}\xi$ in the framework of Eq. (6.44) with a typical linear profile of the inhomogeneous SOD, $q=1-\xi/20, \delta=1, \sigma=1$ and different values of strength μ of the pseudo-SMS effect. The respective point (6.50) of the equilibrium between the pseudo-SRS and inhomogeneous SOD is $\mu_*=1/8$. In the simulations performed with $\mu=1/8$, at times $t>10$ the pulse evolves into a stationary localized profile with zero wavenumber. Figure 6.5 shows the deviation of the absolute value of the numerically found stationary profile from the sech-soliton input, i.e., $\phi_{\mathrm{num}}(\xi)=|u_{1,2}(\xi)|-\left(1/\sqrt{2}\right)\mathrm{sech}\xi$ (the solid curve in the figure). The deviation is very close to the respective analytically predicted correction, given by Eq. (6.56):

$$\phi=-\left(\sqrt{2}/80\right)(\mathrm{sech}\xi)[\xi-2\tanh\xi\,\ln(\cosh\xi)], \tag{6.57}$$

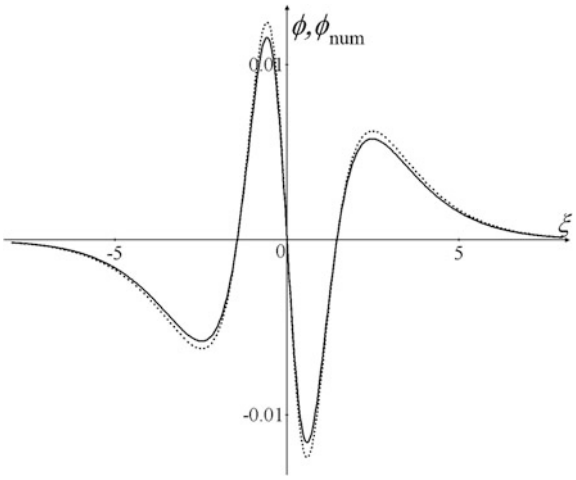

Fig. 6.5 Numerical results: deviation of the absolute value of the numerically found stationary pulse from the standard soliton shape, $\phi_{\mathrm{num}}(\xi)=|u_{1,2}(\xi)|-\left(1/\sqrt{2}\right)\mathrm{sech}\xi$ (the solid curve). The analytical correction ϕ to the absolute value of the standard soliton solution, given by Eq. (6.57), is shown by the dashed curve

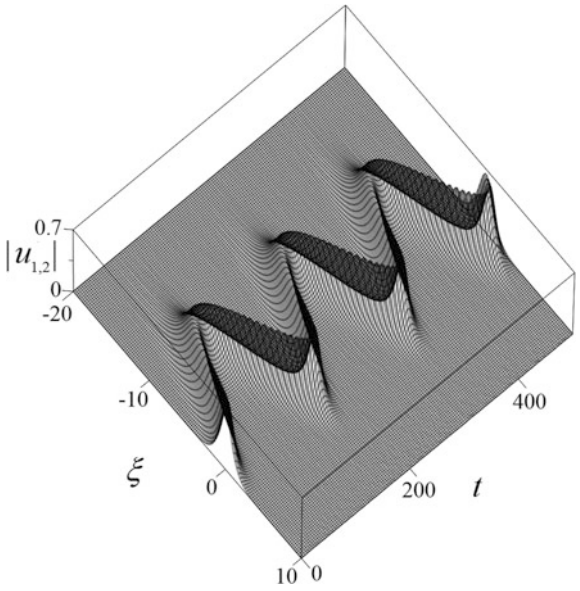

Fig. 6.6 Results of the simulations of the evolution of the sech-shaped pulse for $\mu = (4/3)\mu_* \equiv 1/6$

as shown by the dashed curve in Fig. 6.5. Change of the pseudo-SMS strength μ leads to variation of soliton's wavenumber and amplitude. In particular, Fig. 6.6 shows the simulated spatiotemporal evolution of $|u_{1,2}(\xi, t)|$ for $\mu = (4/3)\mu_* \equiv 1/6$. In this case, the soliton performs oscillations without any visible radiation loss, i.e., the soliton is dynamically stable in the case, in the oscillatory state.

The above considerations were focused on two-component solitons with similar shapes of the components. It is an issue of straightforward interest too to consider the evolution of inputs with opposite parities of the components. For this purpose, we carried out the simulations initiated by the input with an even profile in one component, and an odd one in the other:

$$u_1(\xi, 0) = \text{sech}\xi, u_2(\xi, 0) = A[\text{sech}(\xi + 1) - \text{sech}(\xi - 1)], \tag{6.58}$$

in the framework of Eq. (6.44) with $q = 1 - x/20, \delta = 0$, and different values of A and μ. Figures 6.7, 6.8, and 6.9 display the resulting spatiotemporal evolution of $|u_1(\xi, t)|$ (a) and $|u_2(\xi, t)|$ (b). For the relative amplitude of the odd component $A = 0.8$ (with $\mu = 1/10$), initial pulse (6.58) transforms into an *essentially novel* dynamical mode, in the form of a breather which keeps the opposite parities in its components (Fig. 6.7). Further, for $A = 1$ (with $\mu = 1/25$) initial pulse (6.58) splits into two separating vector solitons of the usual type, with identical parities in the two components (Fig. 6.8), which is possible as the odd component in Eq. (6.58), $u_2(\xi, 0)$, is built as a set of two pulses with opposite signs. Lastly, for $A = 0.5$ (with

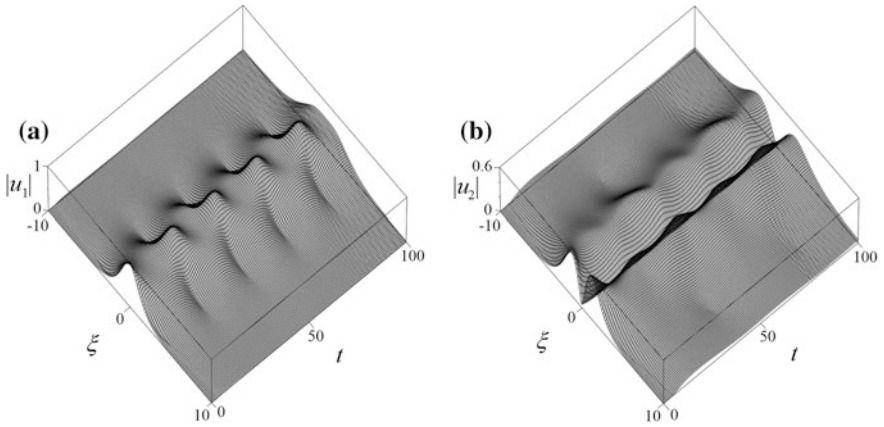

Fig. 6.7 The result of simulations of the evolution of the initial pulse (6.58) with opposite parities of the components, for $A = 0.8$ and $\mu = 1/10$: formation of a breather with coupled even and odd components

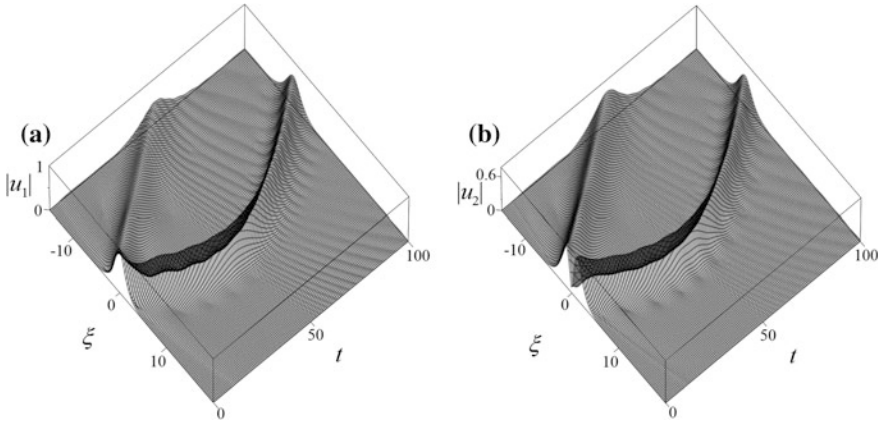

Fig. 6.8 The result of simulations of the evolution of the initial pulse (6.58) for $A = 1$ and $\mu = 1/25$: splitting into two vector solitons of the usual type

$\mu = 1/30$) the weaker component u_2 tends to spread out into a small-amplitude pedestal, into which a dark soliton is embedded (Fig. 6.9b), while the even component u_1 shows no essential evolution (Fig. 6.9a). In the latter case, the u_2 component keeps the spatially odd structure, as dark solitons are odd kink-like solutions.

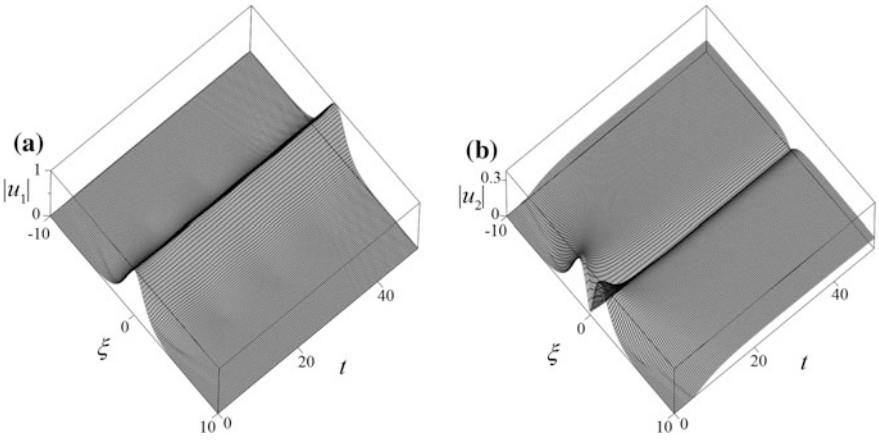

Fig. 6.9 The result of simulations of the evolution of the initial pulse (6.58) for $A = 0.5$ and $\mu = 1/30$: the transformation of the weak odd component into a small-amplitude dark soliton

6.6 Solitons in a Forced Nonlinear Schrödinger Equation with the Pseudo-Raman Effect

In this section, we consider the unidirectional copropagating of a slowly varying envelope, $U(x,t)$, of the complex HF wave field, $U(x,t)\exp(ik_0x - i\omega_0 t)$, and its real LF counterpart, $n(x,t)$ (as said above, it may be realized as a local perturbation of the refractive index, in terms of the optical or quasi-optical propagation). If the HF and LF fields represent the SW (surface waves) and IW (internal waves), respectively, in the ocean, the corresponding Zakharov-type system is composed of the Schrödinger equation for the SW and Boussinesq (Bq) equation for the IW, coupled by the quadratic terms [45–48]. Although the underlying geometry of the fluid motion is two-dimensional, the derivation of the coupled system simplifies the model to the one-dimensional form, as the crucially important geometric elements which guide the propagating waves, viz., the free surface and interface between the layers with different densities of water, are one-dimensional. Under the commonly adopted assumption of the unidirectional wave propagation, the Bq equation may be reduced to one of the Korteweg–de Vries type. Taking into regard LF viscosity δ and the linear gain with real coefficient β applied to the SW, which, as said above, represents the wind forcing in the ocean [49], the system of equations takes the form of:

$$2i\left(\frac{\partial U}{\partial t} + V\frac{\partial U}{\partial x}\right) - \frac{\partial^2 U}{\partial x^2} - \beta\frac{\partial U}{\partial x} - nU = 0, \tag{6.59}$$

$$\frac{\partial n}{\partial t} + V_L \frac{\partial n}{\partial x} - \delta \frac{\partial^2 n}{\partial x^2} = -\frac{\partial \left(|U|^2 \right)}{\partial x}, \tag{6.60}$$

where V and V_L are the HF and LF group velocities.

The interplay of the wind, SW and IW is strong enough if the group velocities of the SW and IW at some (widely different, see below) wavelengths, Λ_{SW} and Λ_{IW}, are in resonance, and, additionally, the wind's friction velocity, W, is in resonance with the SW group velocity [45, 49]. Taking a characteristic value, $W \sim 10$ cm/s [50], the classical dispersion relation for the SW on deep water, $\omega_{\mathrm{SW}} = \sqrt{gk}$, and the characteristic value for the Brunt-Väisälä (buoyancy) frequency, $\omega_{\mathrm{BV}} \sim 0.01$ Hz, which gives rise to the IW at the interface between the top mixed layer and the underlying undisturbed one in the ocean (at the depth of a few hundred meters) [51], one can conclude that the corresponding characteristic HF is $\omega_{\mathrm{SW}} \sim 50$ Hz, which exceeds the above-mentioned LF, ω_{BV} by three or four orders of magnitude, thus completely justifying the HF-LF frequency distinction. The difference in the respective wavelength is dramatic too, the estimate yielding $\Lambda_{\mathrm{SW}} \sim 2$ cm and $\Lambda_{\mathrm{IW}} \sim 10$ m.

In the third-order approximation of the theory (see Sect. 6.2) system (6.59)–(6.60) leads to the following evolution equation for the HF envelope amplitude:

$$2i \frac{\partial U}{\partial t} = \frac{\partial^2 U}{\partial \xi^2} + \beta \frac{\partial U}{\partial \xi} + 2\alpha U |U|^2 - \mu U \frac{\partial \left(|U|^2 \right)}{\partial \xi}, \tag{6.61}$$

where $\xi \equiv x - Vt, \alpha \equiv (1/2)(V - V_L)^{-1}, \mu \equiv \delta (V_L - V)^{-2}$. Below, we fix $\alpha = 1$ by means of obvious scaling, as it was done above in a different context.

The gain term in Eq. (6.61) may be formally absorbed by a transition into a reference frame moving with imaginary velocity, i.e., replacement of real coordinate ξ by $\Xi \equiv \xi - i(\beta/2)t$, which makes it possible to obtain exact soliton solutions to Eq. (6.62) that explicitly feature growth effects induced by the gain [49]. However, we prefer to consider Eq. (6.61) in terms of the real coordinate and time. Then, it is natural to analyze the dispersion relation for small-amplitude excitations, governed by the linearized versions of Eq. (6.61), by substituting $U \sim \exp(i\kappa\xi - i\omega t)$, which produces a complex frequency as a function of real wavenumber κ:

$$\omega = -\kappa^2/2 + (i/2)\beta\kappa.$$

The same branch of the HF dispersion relation is valid for system (6.59)–(6.60), as the nonlinear HF-LF coupling does not affect the dispersion relation. The real part of the frequency gives rise to the group velocity, $V_{\mathrm{gr}} \equiv d\omega/d\kappa = -\kappa$, hence the excitation traveling at this velocity grows with the distance, $-\xi$, as

$$U \sim \exp(\mathrm{Im}\omega \cdot t) \equiv \exp\left(\mathrm{Im}\omega \cdot \xi / V_{\mathrm{gr}}\right) = \exp(-\beta\xi/2) \tag{6.62}$$

(note that it does not depend on the wavenumber, κ), which represents a typical manifestation of the *convective instability* [52]. This type of the instability implies that (in contrast with the *absolute instability*, which drives the growth of quiescent perturbations), the perturbations grow as they travel away, hence they usually do not destroy the underlying patterns. Namely, if a soliton of size L, maintained by the balance between the linear gain and pseudo-SRS term, does not move on the average (see below), it follows from Eq. (6.62) that the soliton is not hurt by the convective instability, provided that it is narrow enough, $\mathrm{L} \ll \beta^{-1}$.

Equation (6.61) with zero boundary conditions at infinity, $U|_{\xi \to \pm\infty} \to 0$, gives rise to the following integral relations for field moments:

$$\frac{dN}{dt} \equiv \frac{d}{dt} \int_{-\infty}^{+\infty} |U|^2 d\xi = \beta \int_{-\infty}^{+\infty} k|U|^2 d\xi \equiv -\beta P, \tag{6.63}$$

$$\frac{dP}{dt} = -\beta \int_{-\infty}^{+\infty} \left|\frac{\partial U}{\partial \xi}\right|^2 d\xi + \frac{\mu}{2} \int_{-\infty}^{+\infty} \left[\frac{\partial\left(|U|^2\right)}{\partial \xi}\right]^2 d\xi, \tag{6.64}$$

$$\frac{d}{dt} \int_{-\infty}^{+\infty} \xi |U|^2 d\xi = P + \beta \int_{-\infty}^{+\infty} k\xi |U|^2 d\xi, \tag{6.65}$$

The moments introduced in Eqs. (6.63), (6.64), and (6.65) determine the norm, N, momentum, P, and center-of-mass coordinate, $\overline{\xi}$, of the wave packet.

The system of exact evolution equations for the moments may be used, as done above in different contexts, for the derivation of approximate evolution equations for parameters of a soliton, see Refs. [53–56] and references therein. To this end, we adopt the usual ansatz for the moving soliton, with amplitude $A(t)$, wavenumber $k(t)$, and coordinate $\overline{\xi}$ defined above:

$$U(\xi, t) = A(t)\mathrm{sech}\left[A(t)\left(\xi - \overline{\xi}\right)\right] \exp\left[ik(t)\xi - (i/2)\int A^2(t)dt\right]. \tag{6.66}$$

The substitution of the ansatz into Eqs. (6.63)–(6.65) leads to the following evolution equations:

$$\frac{dk}{dt} = \frac{\beta}{3}A^2 - \frac{4}{15}\mu A^4, \frac{dA}{dt} = \beta A k, \frac{d\overline{\xi}}{dt} = -k, \tag{6.67}$$

which give rise to an obvious equilibrium state (alias fixed point, FP):

$$\mu_* \equiv 5\beta/\left(4A_0^2\right), k_* = 0, \tag{6.68}$$

where A_0 is an arbitrary amplitude if the stationary soliton. To analyze the evolution around the FP, we rescale the variables by defining $\tau \equiv t\beta A_0/\sqrt{6}, a \equiv A/A_0, y \equiv k\sqrt{6}/A_0$, thus deriving a simple mechanical system from Eq. (6.67):

$$\frac{dy}{d\tau} = 2a^2\left(1 - \lambda a^2\right), \frac{da}{d\tau} = ay, \tag{6.69}$$

where $\lambda \equiv \mu/\mu_*$. Obviously, Eq. (6.69) conserves the corresponding Hamiltonian,

$$y^2 + \lambda\left(a^4 - 1\right) - 2\left(a^2 - 1\right) = y_0^2, \tag{6.70}$$

where y_0 is the value of y at $a = 1$. Dynamical invariant (6.70) is drawn in the plane of (y, a) in Fig. 6.10a, for $y_0 = 0$ and different values of λ. Evidently, at $\lambda < 1$ (i.e., if the pseudo-SRS effect is relatively weak), the soliton's amplitude periodically oscillates between maximum and minimum values $a_{\max} \equiv A_{\max}/A_0 = \sqrt{(2-\lambda)/\lambda}$ and $a_{\min} = 1$. These values swap if the pseudo-SRS effect is stronger, viz., $1 < \lambda < 2$ (the amplitude remains constant at $\lambda = 1$). As it follows from Eq. (6.70), oscillations of the soliton's amplitude translate into oscillations of its velocity, which are symmetric with respect to the positive and negative values.

Lastly, if the pseudo-SRS term is too large, with $\lambda \geq 2$, it destroys the soliton, as the evolution leads to the decay of the amplitude to $a = 0$, while the rescaled wavenumber takes the limit value $y_\infty \equiv \sqrt{\lambda - 2}$.

Further, at $y_0^2 > 0$ straightforward analysis of Eq. (6.70) demonstrates that the loop trajectories, which are seen in Fig. 6.10a for $y_0^2 = 0$, stretch in both positive and negative vertical directions (along the axis of a). In the same case, the critical value

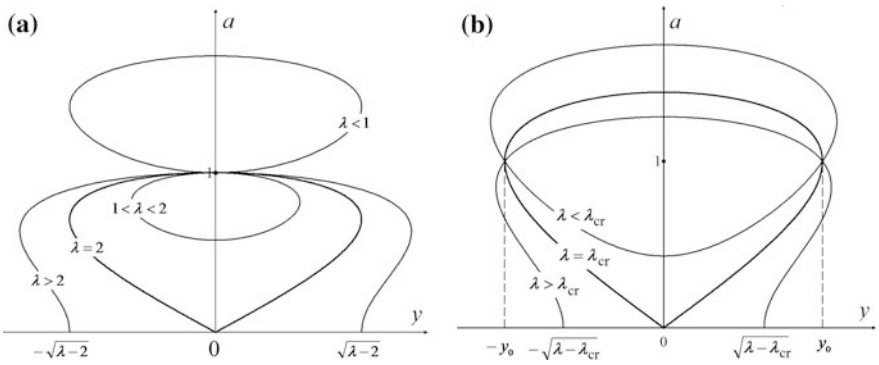

Fig. 6.10 Plots of dynamical invariant (6.70) in plane (y, a) of the soliton's rescaled wavenumber and amplitude for $y_0 = 0$ (**a**) and $0 < y_0^2 < 2$ (**b**), and different values of constant λ

of the pseudo-SRS coefficient, which leads to the destruction of the soliton, decreases to $\lambda_{cr} = 2 - y_0^2$; thus, the solitons do not exist at all at $y_0^2 > 2$. Dynamical invariant (6.70) is schematically drawn in the plane of (y, a) in Fig. 6.10b, for $0 < y_0^2 < 2$ and different values of λ.

6.7 Conclusion

In this article we have produced a review of results obtained in modelsbased on the extended NLSEs (nonlinear Schrödinger equations) which contain the spatial-domain counterpart of the SRS (stimulated Raman scattering) term, viz., the pseudo-SRS one). The NLSEs are derived from the systems of the Zakharov's type for electromagnetic or Langmuir waves in plasmas and similar media, in which the LF field is subject to the diffusive damping. We have studied the soliton dynamics is the framework of the extended NLSEs, which may also include the smooth spatial variation of the SOD (second-order dispersion) coefficient. The analytical predictions were produced by integral relations for the field moments, and numerical results were generated by systematic simulations of the pulse evolution in the framework of the extended NLSEs. Stable stationary solitons are maintained, in particular, by the balance between the self-wavenumber downshift, driven by the pseudo-SRS, and the upshift induced by the linearly decreasing SOD. The analytical solutions are found to be in close agreement with their numerical counterparts.

Acknowledgements The work of B.A.M. is supported, in part, by grant No. 2015616 from the joint program in physics between National Science Foundation (US) and Binational (US-Israel) Science Foundation, and by grant No. 1287/17 from the Israel Science Foundation.

References

1. Infeld, E., Rowlands, G.: Nonlinear Waves, Solitons, and Chaos. Cambridge University Press, Cambridge (2000)
2. Agrawal, G.P.: Nonlinear Fiber Optic. Academic Press, San Diego (2001)
3. Yang, J.: Solitons in Field Theory and Nonlinear Analysis. Springer, New York (2001)
4. Kivshar, Y.S., Agrawal, G.P.: Optical Solitons: From Fibers to Photonic Crystals. Academic, San Diego (2003)
5. Dickey, L.A.: Soliton Equation and Hamiltonian Systems. World Scientific, New York (2005)
6. Malomed, B.A.: Soliton Management in Periodic Systems. Springer, New York (2006)
7. Dauxois, T., Peyrard, M.: Physics of Solitons. Cambridge University Press, Cambridge (2006)
8. Sich, M., Krizhanovskii, D.N., Skolnick, M.S., Gorbach, A.V., Hartley, R., Skryabin, D.V., Cerda-Méndez, E.A., Biermann, K., Hey, R., Santos, P.V.: Observation of bright solitons in a semiconductor microcavity. Santos Nature Phot. **6**, 50–55 (2012)
9. Kauranen, M., Zayats, A.V.: Nonlinear plasmonics. Nature Phot. **6**, 737–748 (2012)

10. Cerda-Ménde, E.A., Sarkar, D., Krizhanovskii, D.N., Gavrilov, S.S., Biermann, K., Skolnick, M.S., Santos, P.V.: Polaritonic two-dimensional nonlinear crystals. Phys. Rev. Lett. **111**, 146401 (2013)
11. Zakharov, V.E., Shabat, A.B.: Exact theory of two-dimensional self-focusing and one-dimensional self-modulation of waves in nonlinear media. Sov. Phys. JETP **34**, 62–69 (1972)
12. Hasegawa, A., Tappert, F.: Transmission of stationary nonlinear optical physics in dispersive dielectric fibers I: anomalous dispersion Appl. Phys. Lett. **23**, 142–144 (1973)
13. Tajima, K.: Compensation of soliton broadening in nonlinear optical fibers with loss. Opt. Lett. **12**, 54–56 (1987)
14. Manakov, S.V.: On the theory of two-dimensional stationary self-focusing of electromagnetic waves. Sov. Phys. JETP **38**, 248–253 (1974)
15. Fordy, A.P., Kullish, P.P.: Commun. Math. Phys. **89**, 427–443 (1983)
16. Menyuk, C.R., Josa, B.: Nonlinear Schrödinger equations and simple Lie algebras **5**, 392–402 (1988)
17. Lazarides, N., Tsironis, G.P.: Coupled nonlinear Schrödinger equations for electromagnetic wave propagation in nonlinear left-handed materials. Phys. Rev. E **71**, 036614 (2005)
18. Yang, J.: Interactions of vector solitons. Phys. Rev. E **64**, 026607 (2001)
19. Ablowitz, M.J., Prinari, B., Trubatch, A.D.: Soliton interactions in the vector NLS equation. Invers. Probl. **20**, 1217–1237 (2004)
20. Vahala, G., Yepes, L.V.: Inelastic vector soliton collisions: a quantum lattice gas representation. J. Phil. Trans. Roy. Soc. L A **362**, 1677–1690 (2004)
21. Oliviera, J.R., Moura, M.A.: Analytical solution for the modified nonlinear Schrödinger equation describing optical shock formation. Phys. Rev. E **57**, 4751–4755 (1998)
22. Mitschke, F.M., Mollenauer, L.F.: Discovery of the soliton self-frequency shift. Opt. Lett. **11**, 659–661 (1986)
23. Gordon, J.P.: Theory of the soliton self-frequency shift. Opt. Lett. **11**, 662–664 (1986)
24. Kodama, Y.: Optical solitons in a monomode fiber. J. Stat. Phys. **39**, 597–614 (1985)
25. Malomed, B.A., Tasgal, R.S.: Matching intrapulse self-frequency shift to sliding-frequency filters for transmission of narrow solitons. J. Opt. Soc. Am. B **15**, 162–170 (1998)
26. Biancalama, F., Skrybin, D.V., Yulin, A.V.: Theory of the soliton self-frequency shift compensation by the resonant radiation in photonic crystal fibers. Phys. Rev. E **70**, 011615 (2004)
27. Essiambre, R.-J., Agraval, G.P.: Timing jitter of ultra short solitons in high-speed communication systems. I. General formulation and application to dispersion-decreasing fibers. J. Opt. Soc. Am. B **14**, 314–322 (1997)
28. Essiambre, R.-J., Agrawal, G.P.: Timing jitter of ultra short solitons in high-speed communication systems. II. Control of jitter by periodic optical phase conjugation. J. Opt. Soc. Am. B **14**, 323–330 (1997)
29. Andrianov, A., Muraviev, S., Kim, A., Sysoliatin, A.: DDF-based all-fiber optical source of femtosecond pulses smoothly tuned in the telecommunication range. Laser Phys. **17**, 1296–1302 (2007)
30. Chernikov, S., Dianov, E., Richardson, D., Payne, D.: Soliton pulse compression in dispersion-decreasing fiber. Opt. Lett. **18**, 476–478 (1993)
31. Kim, J.: A coupled higher-order nonlinear Schrodinger equation including higher-order bright and dark solitons. ETRI J. **23**, 9–15 (2001)
32. Lu, F., Lin, W.H., Knox, W.H., Agrawal, G.P.: Vector soliton fission. Phys. Rev. Lett. **93**, 183901 (2004)
33. Gromov, E.M., Piskunova, L.V., Tyutin, V.V., Vorontzov, D.E.: Short vector solitons. Phys. Lett. A **287**, 233–239 (2001)
34. Wen, S.C., et al.: Theoretical models for ultrashort electromagnetic pulse propagation in nonlinear metamaterials. Phys. Rev. A **75**, 033815 (2007)
35. Aseeva, N.V., Gromov, E.M., Tyutin, V.V.: Phase interaction of short vector solitons. Phys. Lett. A **376**, 718–722 (2012)

36. Gromov, E.M., Malomed, B.A.: Soliton dynamics in an extended nonlinear Schrödinger equation with a spatial counterpart of the stimulated Raman scattering. J. Plasma Phys. **79**, 1057–1062 (2013)
37. Zakharov, V.E.: Hamiltonian formalism for hydrodynamic plasma model. Sov. Phys. JETP **33**, 927–932 (1971)
38. Zakharov, V.E.: The Hamiltonian formalism for waves in nonlinear media having dispersion. Radiophys. Quant. Electr. **17**, 326–343 (1974)
39. Gromov, E.M., Malomed, B.A.: Damped solitons in an extended nonlinear Schrödinger equation with a spatial stimulated Raman scattering and decreasing dispersion. Opt. Comm. **320**, 88–93 (2014)
40. Aseeva, N.V., Gromov, E.M., Onosova, I.V., Tyutin, V.V.: Soliton in a higher-order nonlinear Schrödinger equation with spatial stimulated scattering and spatially inhomogeneous second-order dispersion. JETP Lett. **103**, 736–741 (2016)
41. Gromov, E.M., Malomed, B.A., Tyutin, V.V.: Vector solitons in coupled nonlinear Schrödinger equations with spatial stimulated scattering and inhomogeneous dispersion. Commun. Nonlinear Sci. Numer. Simulat. **54**, 13–20 (2018)
42. Gromov, E.M., Malomed, B.A.: Solitons in a forced nonlinear Schrödinger equation with the pseudo-Raman effect. Phys. Rev. E **92**, 062926 (2015)
43. Blit, R., Malomed, B.A.: Propagation and collisions of semidiscrete solitons in arrayed and stacked waveguides. Phys. Rev. A **86**, 043841 (2012)
44. Bogatyrev, V.A., et al.: Single-mode fiber with chromatic dispersion varying along the length. J. Lightwave Tech. **9**, 561–566 (1991)
45. Janssen, P.: The Interaction of Ocean Waves and Wind. Cambridge University Press, Cambridge (2009)
46. Colin, T., Lannes, D.: Long-wave short-wave resonance for nonlinear geometric optics. Duke Math. J. **107**, 351–419 (2001)
47. Duchêne, V.: Asymptotic shallow water models for internal waves in a two-uid system with a free surface. SIAM J. Math. Anal. **42**, 2229–2260 (2010)
48. Craig, W., Guyenne, P., Sulem, C.: Coupling between internal and surface waves. Nat. Hazards **57**, 617–642 (2011)
49. Brunetti, M., Marchiando, N., Berti, N., Kasparian, J.: Nonlinear fast growth of surface gravity waves under the action of wind. Phys. Lett. A **378**, 1025–1030 (2014)
50. Kharif, C., Kraenkel, R.A., Manna, M.A., Thomas, R.: The modulational instability in deep water under the action of wind and dissipation. J. Fluid Mech. **664**, 138–149 (2010)
51. Wahl, R.J., Teague, W.J.: Estimation of Brunt-Väisälä frequency from temperature profiles. J. Phys. Oceanogr. **13**, 2236–2245 (1983)
52. Lifshitz, E.M., Pitaevskii, L.P.: Physical Kinetics. Nauka Publishers, Moscow (1979)
53. Turitsyn, S.K., Schaefer, T., Mezentsev, V.K.: Dispersion-managed solitons. Phys. Rev. E **58**, R5264 (1998)
54. Belanger, P.A., Pare, C.: Dispersion management in optical fiber links: self-consistent solution for the RMS pulse parameters. J. Lightwave Tech. **17**, 445–458 (1999)
55. Pérez-García, V.M., Torres, P.J., Montesinos, G.D.: The method of moments for nonlinear Schrodinger equations: theory and applications. SIAM J. Appl. Math. **67**, 990–1115 (2007)
56. Chen, Z., Taylor, A.J., Efimov, A.: Soliton dynamics in non-uniform fiber tapers: analytical description through an improved moment method. J. Opt. Soc. Am. B **27**, 1022–1030 (2010)

Chapter 7
Generalized Differential Effective Medium Method for Simulating Effective Physical Properties of 2D Percolating Composites

Mikhail Markov, Valery Levin and Evgeny Pervago

Abstract In this paper, we propose an approach for calculating the effective physical properties of composite materials taking into account the percolation phenomena. This approach is based on the Generalized Differential Effective Medium (GDEM) method and, in contrast to the commonly used self-consistent methods, allows us to incorporate the percolation threshold into the homogenization scheme for simulation of the effective elastic moduli and electrical conductivity of a 2D medium. In this case, the composite is treated as a conductive elastic host where elliptical inclusions of two types are embedded: (1) non-conductive soft inclusions and (2) conductive elastic inclusions that have the same properties as the host. The comparison of theoretical simulations with the experimental data for metal plates containing holes has shown that the proposed GDEM approach describes well the elastic moduli and electrical conductivity of materials of such type in the wide range of hole concentration including the area near the percolation threshold.

7.1 Introduction

The problem of determination of effective properties of inhomogeneous materials is important for various areas of physics of condensed matter such as physics of composite materials, optics, rock physics, biophysics etc. Theoretical methods for the solution of this problem were developed since the 19th century in the pioneer articles by Rayleigh and Maxwell. Different homogenization methods were

M. Markov (✉) · V. Levin · E. Pervago
Instituto Mexicano del Petróleo, Mexico City, Mexico
e-mail: mmarkov@imp.mx

V. Levin
e-mail: vlevine@imp.mx

E. Pervago
e-mail: epervago@imp.mx

H. Altenbach et al. (eds.), *Generalized Models and Non-classical Approaches in Complex Materials 2*, Advanced Structured Materials 90,
https://doi.org/10.1007/978-3-319-77504-3_7

discussed in the review articles by Bergman and Stroud [1], Berryman [2], Markov [3], Goncharenko [4], Brosseau [5], and in the book by Kanaun and Levin [6]. There are several approximation schemes which are applied widely for the simulation of effective physical properties of micro-inhomogeneous media. Two methods, the self-consistent approximation (EMA) and the differential effective medium (DEM), both proposed by Bruggeman are known to be realizable (Milton [7], Avellaneda [8]). The effective physical constants of an inhomogeneous material obtained with the help of both methods obey the rigorous bound of Hashin and Strickman [9]. Both methods were proposed by Bruggeman [10] for the calculation of conductivity.

The EMA method was developed for N-component media where all components are treated equally with no material distinguished as a host [11]. In contrast to the EMA method, the differential effective medium approximation is based on the concept that a composite material can be built up by infinitesimal additions of inclusions into a host material and the material is asymmetrical on the components. Then, as the included material accumulates to a finite amount, the new composite becomes the host material, and so on until the described concentration of included material is achieved [12–14]. In the framework of this method for composite media with multiple constituents, the effective physical properties depend not only on the final volume fractions and shapes of the constituents but also on the order in which the incremental additions are made (see Norris [9], Berryman and Berge [11], Nemat-Nasser and Hori [15], Chinh [16]).

It was shown that depending on the material microstructure and the contrast between constituents' properties, the effective physical properties are described better using the DEM or the EMA method (Berryman [2]). It is known from Tobochnik et al. [17] that both methods cannot describe the effective properties of micro-inhomogeneous media near the percolation threshold. For example, in the 2D case the DEM approximation overestimates the effective conductivity (Zimmerman [18]) in the range of the conducting inclusion concentration close and less than the percolation threshold. The EMA underestimates the effective conductivity predicting zero-electrical conductivity for the circular conducting inclusion concentration equal to 0.5 [4, 17].

An interesting extension of the DEM approximation was presented in the papers by Norris [9] and Norris et al. [19]. The authors of the General DEM model (GDEM) considered two types of inclusions embedded in a host material. Norris [9] showed that this model contains both DEM and EMA approximations as a particular case. The physical properties of the composite calculated using the GDEM depend on the manner by which the solution is constructed [9, 15, 19]. In this case, the possible solution must be restricted by introducing reasonable assumptions. In the GDEM model, the construction process of a composite material is uniquely specified by parametrizing the volume fractions of the included phases. This scheme leads to an ordinary differential equation for the electric conductivity and to a system of differential equations in the case of elasticity that can be solved numerically, and it contains both the EMA and DEM approximations as special

cases. Later, the GDEM was discussed by Hashin [20], Nemat-Nasser and Hori [15] and Berryman and Berge [11].

In the current paper, we apply the GDEM approximation for the simulation of effective elastic moduli and electrical conductivities of 2D composites in the wide concentration area including the percolation threshold. The modeling results are presented for experimentally well-examined media that consist of elastic and conducting hosts containing holes.

The layout of this paper is as follows. In Sect. 7.2 we present the short description of the GDEM, in Sect. 7.3 we give the modeling results for elastic moduli and in Sect. 7.4 we demonstrate the calculation results for electric conductivity. The comparison with the experimental data is presented in this section too. In Sect. 7.5 we discuss the results obtained and present our concluding remarks.

7.2 Generalized Differential Effective Medium Method for Elastic Moduli and Conductivity Prediction

To calculate the effective properties of composite media, Norris [9] used the following procedure: he considered a volume V_0 of a linear homogeneous material 0 that is characterized by the tensor $\mathbf{A_0}$ of physical properties (conductivity or elastic moduli). Grains of materials 1 and 2 are embedded in the material 0 in such a way that the total volume is a constant $\varphi_0 + \varphi_1 + \varphi_2 = 1$, where φ_i is the volume fraction of the i-th component.

The construction process continues by removing the current material and replacing it with grains of materials 1 and 2. At each stage the material is assumed to be homogeneous. The construction process is uniquely defined by a path in the φ_1, φ_2 plane. If we assume that φ_1, φ_2 are functions of parameter t, the process of homogenization results in a system of differential equations for the tensor of effective physical properties.

According to the Norris scheme for 2D systems, two types (phase 1 and phase 2) of inclusions embedded in a host material are considered. Assuming that the changes of surface phase concentration are functions of the parameter $t(\varphi_1 = \varphi_1(t)$ and $\varphi_2 = \varphi_2(t))$, we obtained the system of equations that describes the elastic moduli and the equation for the conductivity of an inhomogeneous two-component medium.

In the case of isotropic medium containing elliptical inclusions, the equations for elastic moduli have the form:

$$\frac{dK(t)}{dt} = (K_1 - K)P_1\left(\frac{d\varphi_1}{dt} + \frac{d\varphi}{dt}\frac{\varphi_1}{1-\varphi}\right) + (K_2 - K)P_2\left(\frac{d\varphi_2}{dt} + \frac{d\varphi}{dt}\frac{\varphi_2}{1-\varphi}\right), \quad (7.1)$$

$$\frac{d\mu(t)}{dt} = (\mu_1 - \mu)Q_1\left(\frac{d\varphi_1}{dt} + \frac{d\varphi}{dt}\frac{\varphi_1}{1-\varphi}\right) + (\mu_2 - \mu)Q_2\left(\frac{d\varphi_2}{dt} + \frac{d\varphi}{dt}\frac{\varphi_2}{1-\varphi}\right), \quad (7.2)$$

where K and μ are bulk and shear moduli of effective medium respectively, K_i and μ_i are the bulk and shear moduli of i-th component, $\varphi = \varphi_1 + \varphi_2$, where φ_1, φ_2 are the surface phase concentrations, and

$$P^{(i)} = \frac{1}{3}T^{(i)}_{jjll}, Q^{(i)} = \frac{1}{5}\left(T^{(i)}_{jjll} - P_i\right), \quad (7.3)$$

where repeated subscripts are summed.

The tensor $T^{(i)}$ is obtained from the solution of one-particle problem for the strain of an ellipse placed in the infinite effective medium and affected by a given uniform strain field far from the inclusion. In the case of elliptical inclusions, Thorpe and Sen [21] found that for the inclusions of the i-th type

$$\begin{aligned} P &= \left[1 + Z - \frac{ZY}{X+Y}\left(\frac{a-b}{a+b}\right)^2\right]^{-1}, \\ 2Q &= P\frac{(1+Z)}{X+Y} + (2 + A - X)^{-1}, \end{aligned} \quad (7.4)$$

where

$$\begin{aligned} X &= 1 + \left[\frac{Aab}{(a+b)^2}\right](1+s), \\ Y &= \frac{A}{2}(1-s), Z = \frac{C}{2}(1+s) \end{aligned} \quad (7.5)$$

and

$$A = \left(\frac{\mu_i}{\mu}\right) - 1, C = \left(\frac{K_i}{K}\right) - 1, s = \left(\frac{K-\mu}{K+\mu}\right), i = 1, 2 \quad (7.6)$$

where a and b are the ellipse semi-axes, indices j in Eqs. 7.4 and 7.5 are omitted for simplicity. In Eq. 7.6 the subscript i refers to the inclusions and unsubscribed quantities that correspond to the effective medium.

As in the 3D case, the sum of the surface phase concentrations obeys the equation $\varphi_0 + \varphi_1 + \varphi_2 = 1$, where φ_0 is the host material concentration. The initial conditions for the Eqs. (7.1) and (7.2) are $K(0) = K_0, \mu(0) = \mu_0$, where K_0 and μ_0 are the elastic moduli of the host material. The equation of the GDEM approximation for conductivity of an isotropic material is:

$$\frac{d\sigma}{dt} = -\left(G_1\frac{d\varphi_1}{dt} + G_2\frac{d\varphi_2}{dt}\right) - [G_1\varphi_1(t) + G_2\varphi_2(t)]\frac{d\varphi}{dt}\frac{1}{(1-\varphi)}, \tag{7.7}$$

where

$$G_j = \sigma\sum_{k=1}^{2}\frac{(\sigma-\sigma_j)}{\left(1-L_k^{(j)}\right)\sigma + L_k^{(j)}\sigma_j}, j = 1,\ 2; \tag{7.8}$$

the coefficients $L_k^{(j)}$ are the depolarization coefficients of the ellipses associated with material j and σ is a function of variable t $(\sigma = \sigma(t))$. In the case of elliptical inclusions, the depolarization coefficients are given by Osborn [22] and Landau and Lifshitz [23]

$$L_1 = \frac{a}{a+b}, L_2 = \frac{b}{a+b}. \tag{7.9}$$

The initial condition for the Eq. (7.4) is $\sigma(0) = \sigma_0$ where σ_0 is electrical conductivity of the host material.

To describe the properties of a bi-component composite, Norris [9] has made an assumption that the physical properties of inclusions of the second type (phase 2) coincide with the properties of the host. In this case, when $\varphi = \varphi_1 + \varphi_2$ tends to unity, the Eqs. (7.1), (7.2) and (7.7) lead to the EMA approximation:

$$\begin{gathered}(K_1 - K)P_1\varphi_1 + (K_2 - K)P_2\varphi_2 = 0,\\ (\mu_1 - \mu)Q_1\varphi_1 + (\mu_2 - \mu)Q_2\varphi_2 = 0\\ G_1\varphi_1 + G_2\varphi_2 = 0.\end{gathered} \tag{7.10}$$

In the case when $\varphi_2 = \frac{d\varphi_2}{dt} = 0$, Eqs. (7.1), (7.2) and (7.7) lead to the usual DEM equations:

$$\begin{aligned}\frac{dK}{d\varphi_1} &= \frac{1}{1-\varphi_1}(K_1 - K)P_1\\ \frac{d\mu}{d\varphi_1} &= \frac{1}{1-\varphi_1}(\mu_1 - \mu)Q_1,\\ \frac{d\sigma}{d\varphi_1} &= -G_1\frac{1}{(1-\varphi_1)}.\end{aligned} \tag{7.11}$$

Both methods give us similar results in the case of low inclusion concentration range. Unfortunately, these methods lead to different results that lie far from the experimental data near the percolation threshold. Below we demonstrate that the GDEM model describes the experimental data up to percolation threshold.

Generally, Eqs. (7.1), (7.2) and (7.7) can be solved numerically, in some cases it is possible to obtain the analytical solution, but the analysis of this analytical solution is out of our consideration. To calculate the electrical conductivity and elastic moduli we have to determine the functions $\varphi_1 = \varphi_1(t), \varphi_2 = \varphi_2(t)$. In the calculation process, we consider that:

1. The inclusions of the first phase are holes and inclusions of the second phase have the same physical properties as the host.
2. The host material concentration tends to zero near the percolation threshold, $\varphi_0(t) \to 0$ as φ_1 approaches φ_C, where φ_C corresponds to the critical concentration of the non-conducting phase.
3. The sum of concentrations obeys the condition $\varphi_0 + \varphi_1 + \varphi_2 = 1$.

In this paper, we make an assumption that the concentrations of both phases are a power functions of the parameter t:

$$\varphi_1(t) = a_1 t^{\gamma} \quad \text{and} \quad \varphi_2(t) = a_2 t^{\beta} \tag{7.12}$$

Here we consider a more general case that in the paper [24] where we used the model with $\gamma = 1$. In order to solve the GDEM equations, we apply the classical fourth-order Runge-Kutta method [25].

7.3 Elastic Properties Calculations

As the first example of calculations, we present the results for the elastic medium containing circular holes. It is known from Xia and Thorpe [26], Garboczi et al. [27] that the percolation threshold for this medium corresponds to elastic phase concentration equal to 0.33. The dependencies of effective elastic moduli on the elastic phase concentration $(\varphi_0 + \varphi_2)$ obtained by DEM and GDEM approximations are presented in Fig. 7.1. The shear and the compression moduli of the host are 1 and 1.667, respectively. The calculations were fulfilled for linear dependence of component concentration on the parameter $t(\gamma = \beta = 1)$. The effective moduli obtained by GDEM method coincide with the classical DEM results (Fig. 7.1) in high concentration range of the elastic component (the sum of the host and the component 2 concentrations). However, the GDEM application describes the percolation threshold at the elastic phase concentration equal to 0.33 while the elastic moduli calculated by DEM maintain non-zero values for the elastic phase concentration less than 0.33.

The effective moduli obtained by GDEM method coincide with the classical DEM results (Fig. 7.1) in high concentration range of the elastic component (the sum of the host and the component 2 concentrations). However, the GDEM application describes the percolation threshold at the elastic phase concentration equal to 0.33 while the elastic moduli calculated by DEM maintain non-zero values for the elastic phase concentration less than 0.33.

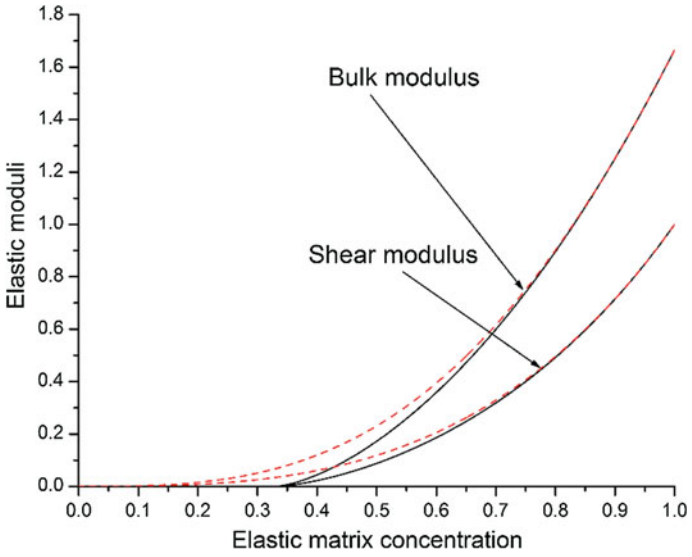

Fig. 7.1 Normalized effective elastic moduli of isotropic medium containing circular holes as an elastic matrix concentration function. Solid lines correspond to the GDEM and dashed lines are the DEM approximation

The decreasing of the aspect ratio of elastic inclusions leads to the increasing of the effective elastic moduli (Fig. 7.2). The aspect ratio of the second phase inclusions affects the elastic moduli only near the percolation threshold (Fig. 7.2b).

Figure 7.3 presents the calculation results for different integration paths. Inclusions of both types are circular. The results obtained demonstrate the influence of different path on the elastic module near the percolation threshold. In the low hole concentration (φ_1) range, this influence is negligible.

To verify the feasibility of application of the GDEM approach for the effective elastic moduli prediction we compare the predicted Young module with the experimental data presented in [28]. The measurements were fulfilled for square metal sheets containing randomly drilled holes. Holes could overlap or miss each other by any amount. To minimize finite-size effects the authors used relatively large samples.

The ratio of the sample size to the hole diameter was 49. In Fig. 7.4, we compare the experimental data with the modeling results from EMA, DEM, and GDEM approximations. The effective Young module simulated by EMA was taken from Thorpe and Sen [21]. The GDEM's results are obtained for linear dependencies of surface concentrations φ_1, φ_2 on the parameter t. The results (Fig. 7.4) for GDEM are shown for circular inclusions of both phases. The GDEM method describes the experimental data better than the classical self-consistent methods, which can be used for the low hole concentration only; the DEM approximation overestimates the

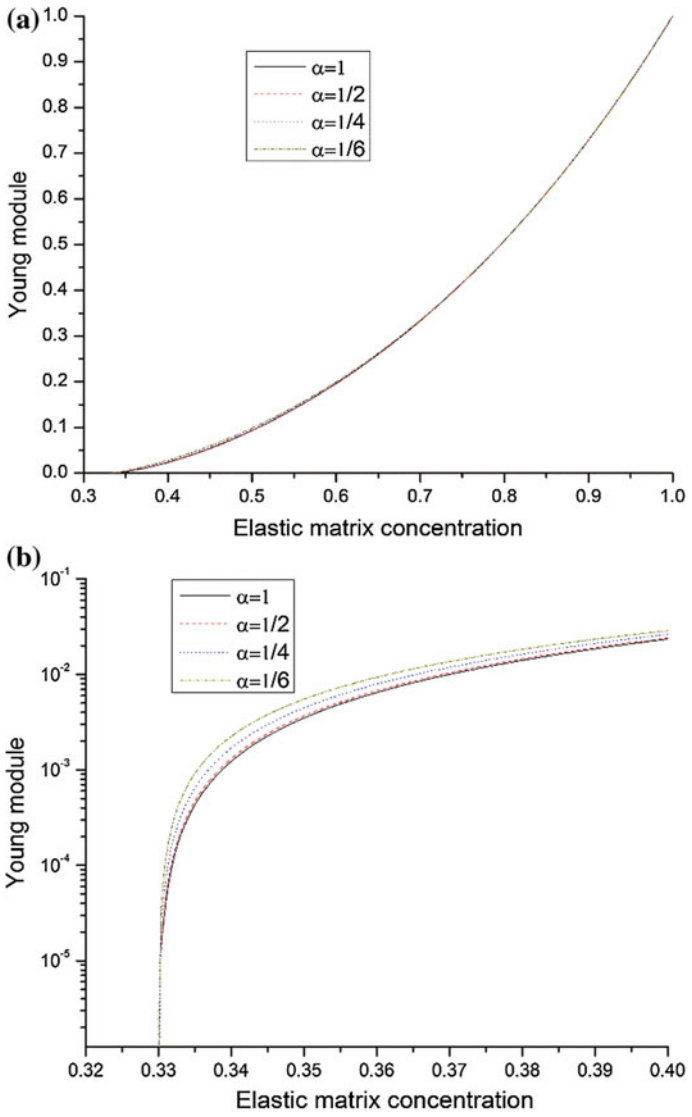

Fig. 7.2 Normalized Young module of a 2D composite as a function of the elastic phase concentration. Different curves correspond to different aspect ratios of the elastic inclusions α_2 (inclusions of the second type)

Young module near the percolation threshold, while the EMA method underestimates this module.

Near the percolation threshold, the value of physical parameter varies as $(p - p_C)^{\delta}$, [29] where p is an area concentration of matrix phase $(\varphi_0 + \varphi_2)$ and p_C is the surface concentration corresponding to the percolation threshold.

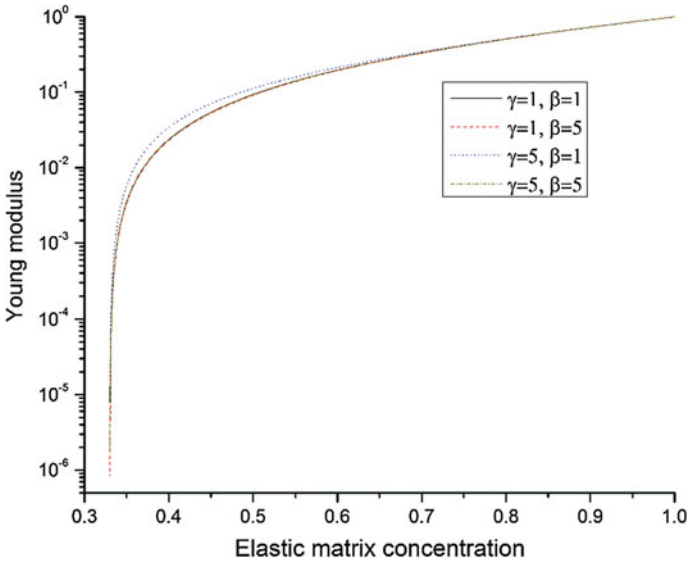

Fig. 7.3 Normalized Young module for different powers γ and β in Eq. 7.12

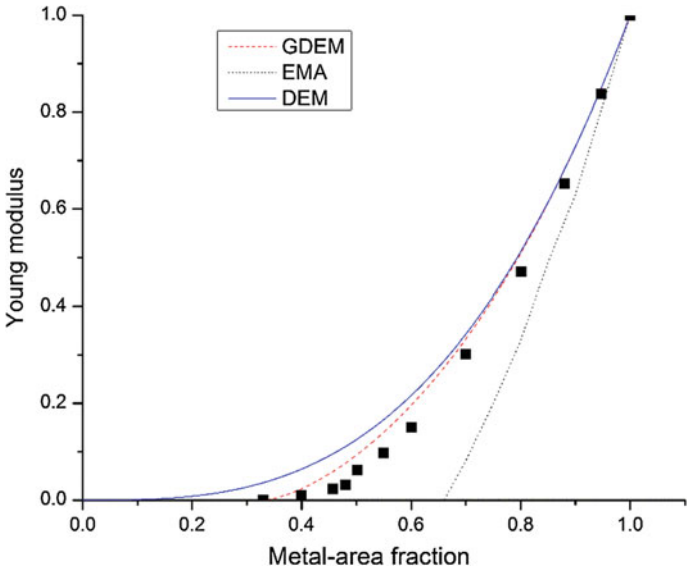

Fig. 7.4 The comparison of the effective conductivity simulated by using the EMA (dot line), the DEM (solid line), and the GDEM (dash line), approximations with experimental data. The squares represent the experimental data obtained by Lobb and Forrester [28]

Our calculations for elastic moduli have shown that the GDEM gives the value of critical exponent δ in the range of 1.6–2 depending on the model parameters (integration path and aspect ratio of elastic inclusions). In the cases of lattice simulation [17] and experimental data [28], δ is smaller.

7.4 Effective Conductivity Calculations

As in the case of elastic moduli, the influence of integration path (different powers γ and β in Eq. 7.12) on the conductivity is small for the hole concentrations lying far from the percolation threshold (Fig. 7.5).

In contrast to the elastic moduli, the aspect ratio of the second phase inclusions (conducting inclusions) significantly influences the electrical conductivity. The decreasing of the aspect ratio of conducting inclusion leads to the decreasing of the effective conductivity (Fig. 7.6). Near the percolation threshold the electrical conductivity varies as $\sigma \propto (p - p_C)^{\delta}$, where p is the surface concentration of the conducting phase $(\varphi_0 + \varphi_2)$ and p_C is the surface concentration of the conducting phase corresponding to the percolation threshold. In the case of a 2D system containing circular holes, computer simulations and experimental measurements give the value of the critical exponent δ in the range 1.2–1.4. The GDEM model gives the value of critical exponent that is in this range (Fig. 7.6b).

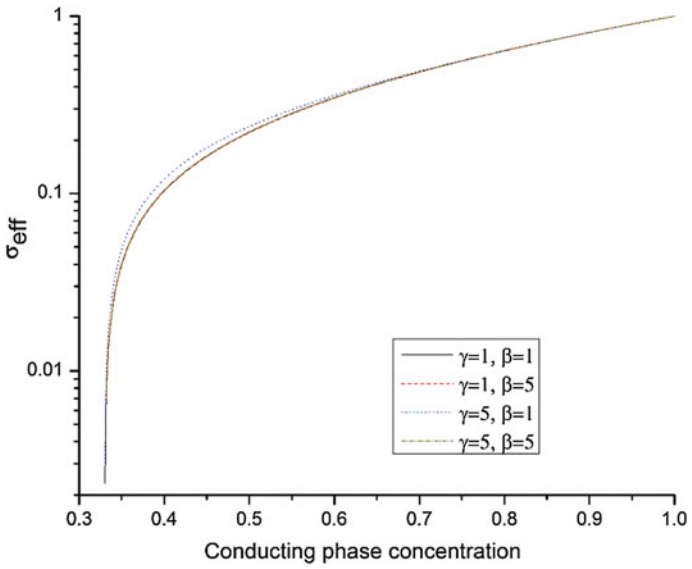

Fig. 7.5 Normalized effective conductivity as a conducting phase concentration. The calculations are presented for different powers γ and β in Eq. 7.12

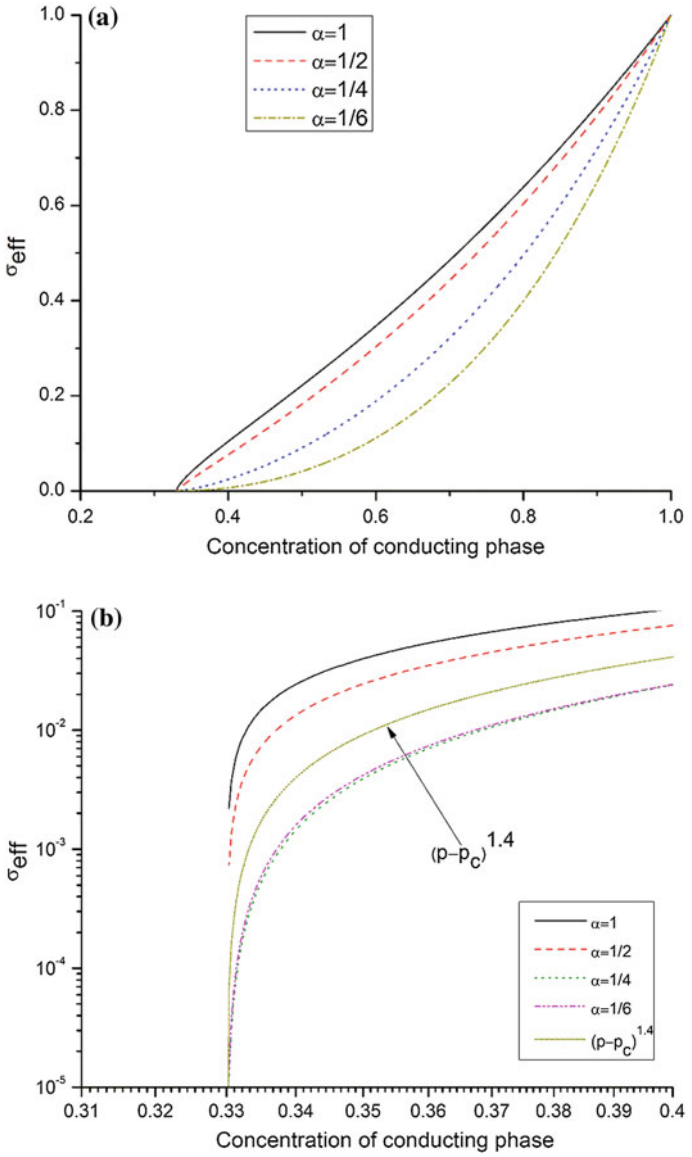

Fig. 7.6 Normalized effective conductivity calculated by the GDEM for $\gamma = \beta = 1$ and the power law dependence $(p - p_c)^{\delta}$, where p is the conductive phase concentration $(\varphi_0 + \varphi_2)$ and p_c is the percolation threshold of the conductive phase concentration. Different curves correspond to different aspect ratios of conducting phase (α_2)

We compare the electrical conductivities obtained by using the different self-consistent methods with the experimental data presented in Lobb and Forrester [28] for an aluminum plate containing circular holes and with the results of random-walk calculation of Tobochnik et al. [17] (Fig. 7.7). The DEM approximation overestimates the conductivity, while the EMA method underestimates it. The results for the GDEM method are presented for the linear dependence of phase concentrations on the parameter $t(\gamma = \beta = 1)$. The comparison of the experimentally measured data and the simulation of Tobochnik et al. [17] with the GDEM predictions demonstrates their good correspondence.

The experimental data for a composite medium containing elliptical inclusions was obtained by Tobochnik et al. [30]. The samples are aluminized Mylar sheets consisting of 0.5 in. thick Mylar plastic covered with a 500 Å film of aluminum. The sample is a square sheet with the length of 23.1 cm and the slit length is 1/50 of that. The measurements were fulfilled for non-conductive inclusions (phase 1) with the aspect ratio $\alpha_1 = 1/43$. In Fig. 7.8, we show these experimental data and the GDEM results for the linear dependence of phase concentrations on the parameter t.

The comparison of our calculations with the experimental data set has shown that the GDEM predictions are in satisfactory agreement with measured data.

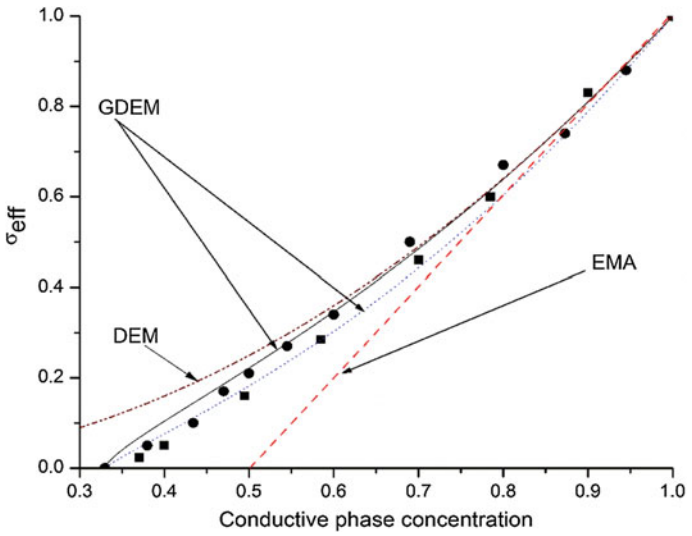

Fig. 7.7 The comparison of the normalized effective conductivity simulated by using the EMA (dash line), the DEM (dash dot-dot line), and the GDEM approximations for $\gamma = \beta = 1$ with experimental data. The solid and dot lines correspond to the GDEM method with $\alpha_2 = 1$, and 0.5, respectively. The squares represent the experimental data obtained by Lobb and Forrester [28]. The circles represent the lattice simulation data obtained by Tobochnik et al. [17]

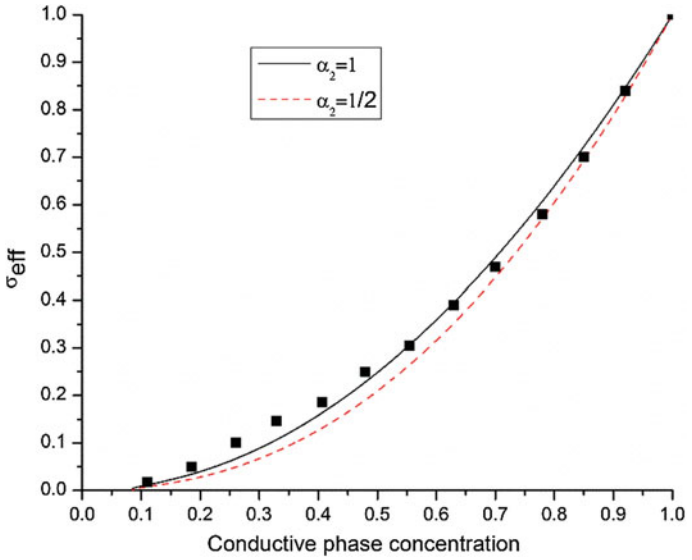

Fig. 7.8 Effective conductivity predicted by the GDEM method for the 2D conducting medium containing a random distribution of elliptical holes ($\alpha = 1/43$). The solid and dashed lines correspond to the models with different shapes of the conducting phase $\alpha_2 = 1$ and $\alpha_2 = 1/2$, respectively. The calculations are fulfilled for $\gamma = \beta = 1$. The squares are the experimental data by Tobochnik et al. [30]

7.5 Concluding Remarks

It is well known that the classical effective medium theories such as the EMA or DEM approximations predict effective physical properties of 2D composite materials in the case of sufficiently low inclusion concentrations [26]. The DEM approximation overestimates effective physical properties of inhomogeneous media near the percolation threshold. In contrast, the EMA method by Bruggeman [10] gives us zero value of elastic moduli and conductivity of composites far from the real value of critical porosity corresponding to the percolation threshold. In this paper, we adopted for 2D media the GDEM approximation developed by Norris and co-authors firstly for 3D composite materials for determination of elastic moduli and conductivity of 2D inhomogeneous material prediction. As in the case of DEM approximation, this scheme leads to a system of ordinary differential equations of the first order that can be solved numerically. In contrast to the classical DEM approximation, the physical properties of a composite calculated by the GDEM approach depend on the manner by which the solution is constructed [9, 19]. In our case, the construction process of a composite material is uniquely specified by parametrizing the surface concentration of the included phases. The GDEM method does not predict the percolation threshold but the application of

this method allows us include the information about the value of critical porosity to improve the calculation scheme.

Our calculations show that the GDEM approximation describes the experimental data in the high inclusion concentration better than the classical self-consistent schemes. In the low concentration range all methods give similar results.

To our mind, the GDEM approximation is a powerful tool for prediction of physical properties of inhomogeneous media containing high contrast inclusions. It is possible to find many applications of this method in rock physics and physics of composite materials. One of the possible applications of the GDEM approximation is the description of rocks near the critical porosity, i.e., the porosity that separates their mechanical and acoustic behavior into two distinct domains. For porosities lower than critical, the mineral grains are load-bearing, whereas for porosities greater than critical, the rock simply "falls apart" and becomes a suspension, in which the fluid phase is load bearing. The other feasible application of GDEM approximation is the calculation of electric conductivity of low-porosity rocks near the percolation threshold.

Acknowledgements We are grateful to Professors Christopher Lobb, Sergey Kanaun and Dr. Irina Markova for useful discussions.

References

1. Bergman, D.J., Stroud, D.: Physical properties of macroscopically inhomogeneous media. Solid State Phys. **46**, 148 (1992). https://doi.org/10.1016/S0081-1947(08)60398-7
2. Berryman, J.G.: Mixture theories for rock properties. In: Ahrens, T.J. (ed.) A Handbook of Physical Constants, p. 205. American Geophysical Union, Washington, D.C. (1995)
3. Markov, K.Z.: Elementary micromechanics of heterogeneous solids. In: Markov, K.Z., Preziosi, L. (eds.) Heterogeneous Media: Micromechanics Modeling Methods and Simulation, p. 1. Birkhauser, Boston (2000)
4. Goncharenko, A.V.: Generalizations of the Bruggeman equations and a concept of shape-distributed composites. Phys. Rev. E **68**, 041108 (2003)
5. Brosseau, C.: Modelling and simulation of dielectric heterostructures: a physical survey from an historical perspective. J. Phys. D: Appl. Phys. **39**, 1277 (2006)
6. Kanaun, S., Levin, V.: Self-consistent methods for composites. In: Static Problems, vol. 1, p. 376. Springer (2008)
7. Milton, G.: The coherent potential approximation is a realizable effective medium scheme. Comm. Math. Phys. **99**, 463 (1985)
8. Avellaneda, M.: Iterated homogenization, differential effective medium theory and applications. Commun. Pure Appl. Math. **40**, 527 (1987). https://doi.org/10.1002/cpa.3160400502
9. Norris, A.N.: A differential scheme for the effective moduli of composites. Mech. Mater. **4**, 1 (1985)
10. Bruggeman, D.A.: Berechnung verschiedener physikalischer Konstanten von heterogenen Substanzen. Ann. Phys. Lpz. **24**, 636 (1935)
11. Berryman, J.G., Berge, P.A.: Critique of two explicit schemes for estimating elastic properties of multiphase composites. Mech. Mater. **22**, 149 (1996)

12. Landauer, R.: Electrical conductivity in inhomogeneous media. In: Garland, J.C., Tanner, D. B. (eds.) Electrical, Transport and Optical Properties of Inhomogeneous Media. AIP, New York (1978)
13. Sen, P., Scala, C., Cohen, M.H.: A self similar model for sedimentary rocks with application to the dielectric constant of fused glass beads. Geophysics **46**, 781 (1981)
14. Sheng, P.: Effective-medium theory of sedimentary rocks. Phys. Rev. B **41**, 4507 (1990)
15. Nemat-Nasser, S., Hori, M.: Micromechanics: Overall Properties of Heterogeneous Materials, North-Holland, Amsterdam (1993)
16. Chinh, P.D.: Modeling the conductivity of highly consolidated, bi-connected porous rocks. J. Appl. Phys. **84**, 3355 (1998)
17. Tobochnik, J., Laing, D., Wilson, G.: Random-walk calculation of conductivity in continuum percolation. Phys. Rev. A **41**, 3052 (1990)
18. Zimmerman, R.W.: Effective conductivity of a two-dimensional medium containing elliptical inclusions. Proc. R. Soc. Lond. A **452**, 1713 (1996)
19. Norris, A.N., Callegary, A.J., Sheng, P.: A generalized differential effective medium theory. J. Mech. Phys. Solids **33**, 525 (1985)
20. Hashin, Z.: The differential scheme and its application to cracked materials. J. Mech. Phys. Solids **36**, 719 (1988)
21. Thorpe, M.F., Sen, P.: Elastic moduli of two-dimensional composite continua with elliptical inclusions. J. Acoust. Soc. America **77**, 1674 (1985)
22. Osborn, J.A.: Demagnetizing factors of the general ellipsoid. Phys. Rev. **67**, 351 (1945)
23. Landau, L.D., Lifshitz, E.: Electrodynamics of Continuous Media. Pergamon press, N.Y (1984)
24. Markov, M., Levin, V., Mousatov, A., Kazatchenko, E.: Generalized DEM model for the effective conductivity of a two-dimensional percolating medium. Int. J. Eng. Sci. **58**, 78 (2012)
25. Butcher, J.C.: Numerical methods for ordinary differential equations, Wiley (2003)
26. Xia, W., Thorpe, M.F.: Percolation properties of random ellipses. Phys. Rev. A **38**, 2650 (1988). https://doi.org/10.1103/PhysRevA.38.2650
27. Garboczi, E., Thorpe, M.F., DeVries, M., Day, A.R.: Universal conductivity curve for a plane containing random holes. Phys. Rev. A **43**, 6473 (1991)
28. Lobb, C.J., Forrester, M.G.: Measurement of nonuniversal critical behavior in a two-dimensional continuum percolating system. Phys. Rev. B **35**, 1899 (1987). https://doi.org/10.1103/PhysRevB.35.1899
29. Stauffer, D., Aharony, A.: Introduction to Percolation Theory. Taylor K Francis, Bristol (1991)
30. Tobochnik, J., Dubson, M.A., Wilson, M.L., Thorpe, M.F.: Conductance of a plane containing random cuts. Phys. Rev. A **40**, 5370 (1989). https://doi.org/10.1103/PhysRevA.40.5370

Chapter 8
Nonlinear Acoustic Wedge Waves

Pavel D. Pupyrev, Alexey M. Lomonosov, Elena S. Sokolova, Alexander S. Kovalev and Andreas P. Mayer

Abstract Among the various types of guided acoustic waves, acoustic wedge waves are non-diffractive and non-dispersive. Both properties make them susceptible to nonlinear effects. Investigations have recently been focused on effects of second-order nonlinearity in connection with anisotropy. The current status of these investigations is reviewed in the context of earlier work on nonlinear properties of two-dimensional guided acoustic waves, in particular surface waves. The role of weak dispersion, leading to solitary waves, is also discussed. For anti-symmetric flexural wedge waves propagating in isotropic media or in anisotropic media with reflection symmetry with respect to the wedge's mid-plane, an evolution equation is derived that accounts for an effective third-order nonlinearity of acoustic wedge waves. For the kernel functions occurring in the nonlinear terms of this equation, expressions in terms of overlap integrals with Laguerre functions are provided, which allow for their quantitative numerical evaluation. First numerical results for the efficiency of third-harmonic generation of flexural wedge waves are presented.

P. D. Pupyrev · A. M. Lomonosov
Prokhorov General Physics Institute, Moscow, Russia
e-mail: pavel.pupyrev@hs-offenburg.de

A. M. Lomonosov
e-mail: lom@kapella.gpi.ru

P. D. Pupyrev · A. P. Mayer (✉)
Hochschule Offenburg - University of Applied Sciences, Offenburg, Germany
e-mail: andreas.mayer@hs-offenburg.de

E. S. Sokolova · A. S. Kovalev
Verkin Institute for Low Temperature Physics and Engineering, Kharkiv, Ukraine
e-mail: esokolova@ilt.kharkov.ua

A. S. Kovalev
e-mail: kovalev@ilt.kharkov.ua

H. Altenbach et al. (eds.), *Generalized Models and Non-classical Approaches in Complex Materials 2*, Advanced Structured Materials 90,
https://doi.org/10.1007/978-3-319-77504-3_8

8.1 Introduction

Since the nineteen-seventies and especially in the nineteen-eighties and nineteen-nineties, nonlinear phenomena in connection with guided acoustic waves constituted a very active field of research, bringing together researchers in different fields like mechanical and electrical engineering, applied mathematics, geophysics and solid state physics. Gérard Maugin took a very important part in these activities as one of his numerous research topics. Not only did he advance the theory of nonlinear guided waves, considering a model that contains the essentials for nonlinear surface waves of shear-horizontal polarization [1–4]. He also efficiently helped this topic to develop as a conference organizer, editor and textbook author [5]. At an early stage, he recognized the necessity of having reliable data for the nonlinear material properties. His compilation of linear and nonlinear material constants in his well-known book "Nonlinear electromechanical effects and applications" [6] was a valuable source that enabled researchers to obtain quantitative results for estimating the size of the effects they predicted.

The nonlinear wave phenomena considered by Gérard Maugin in the above-mentioned publications refer to the regime of large dispersion, where envelope solitons of the nonlinear Schrödinger-type occur. They are modulations of a guided acoustic carrier wave, and apart from the second harmonic of this carrier wave, higher harmonics are largely irrelevant [7, 8]. This regime of large dispersion was also considered in the context of acoustic wedge waves in an early theoretical work [9]. At the same time, nonlinear phenomena have been investigated in connection with guided acoustic waves that are not dispersive. The prototype of this type of guided acoustic waves are Rayleigh waves or, more generally, surface acoustic waves (SAWs) in elastic media that may be anisotropic and, in addition, piezoelectric. We briefly review these theoretical investigations on nonlinear SAWs here since they bear many similarities with the case of acoustic wedge waves. In the absence of linear dispersion, second-order nonlinearity leads to rapid growth of higher harmonics of a fundamental monochromatic input wave. The nonlinearity is small, since maximum strains below the breaking limit of most common materials are below 10^{-2}, and the third-order elastic constants are normally not larger than the second-order elastic constants by more than one order of magnitude. This allows asymptotic methods to be used. Their application to SAWs has been pioneered by Reutov [10], Kalyanasundaram [11], Lardner [12], Parker [13], Zabolotskaya [14] and others. (For reviews with more references to the original literature see [15–17]. Reference [16] also contains a comparison between different approaches). A nonlinear evolution equation was derived by these authors for the waveforms of SAWs at the surface. With the help of this evolution equation, steepening or spiking of initially sinusoidal waveforms [13, 14, 18, 19] or pulses [20] with propagation distance up to shock formation was found. The shock formation distance as well as the waveforms for the components of the displacement field vertical or parallel to the surface are governed by a kernel in the evolution equation which depends on the second-order and third-order elastic constants of the elastic medium.

The nonlinearity-induced evolution of the displacement components of an initially sinusoidal Rayleigh wave was experimentally observed as early as 1984 [21]. Nonlinear evolution of surface acoustic pulses including shock formation was demonstrated experimentally by laser ultrasound techniques [20, 22] in excellent agreement with theory.

When small linear dispersion is introduced, for example by coating the elastic medium with a thin film of a different material, the evolution equation for nonlinear SAWs becomes similar to the Benjamin-Ono- or Korteweg-de Vries (KdV) equation with a non-local nonlinearity [16]. The interplay between dispersion and nonlinearity gives rise to solitary waves, which have been predicted and verified experimentally in laser-ultrasound experiments [16]. In case of anisotropic substrates, the shape of these solitary pulses (i.e. the displacement or displacement gradient components at the surface as function of arrival time at a certain observation point on the surface) strongly depends on the kernel in the nonlinear evolution equation. For a simplified version of this evolution equation including weak linear dispersion of the KdV type, analytic solutions for solitary pulses and stationary periodic wave profiles (analogs to the cnoidal wave solutions of the KdV equation) have been found [16].

Other types of guided acoustic waves which are non-dispersive and which exhibit straight-crested wave-fronts, characterized by a two-dimensional wave-vector (2D guided waves), are Stoneley waves, propagating at the planar interface of two homogeneous solid media, Scholte waves, propagating at the planar interface between a solid and a fluid, and Bleustein-Gulyaev waves. The latter are surface acoustic waves with shear-horizontal polarization, which owe their surface localization to the coupling to the electric field in piezoelectric elastic media. The equation governing nonlinear waveform evolution of Stoneley and Scholte waves was found to be very similar to that of Rayleigh waves [23]. In the case of Bleustein-Gulyaev waves, even harmonics of a sinusoidal straight-crested input wave are polarized in the sagittal plane and have no shear-horizontal displacement component in common propagation geometries. As a consequence of this different symmetry type of even and odd harmonics, the evolution equation for nonlinear Bleustein-Gulyaev waves contains an effective third-order instead of a second-order nonlinearity [24].

The absence of linear dispersion in surface and interface waves is due to the absence of any length scale in these systems. A further type of non-dispersive guided acoustic waves are wedge waves, i.e. acoustic waves propagating along the apex of a wedge made of an homogeneous elastic material. The apex line is the intersection line of two planar surfaces of the elastic medium. Obviously, this system is lacking a length scale, too. Unlike surface and interface waves, wedge waves are one-dimensionally (1D) guided waves in the sense that their associated displacement field is localized at the wedge tip and decays to zero away from the apex line. Monochromatic acoustic wedge waves (AWWs) may be characterized by a one-dimensional wave-vector parallel to the wedge tip. Because of their 1D character, they propagate without diffraction. Acoustic wedge waves were discovered in numerical calculations in the early seventies [25, 26]. In isotropic media

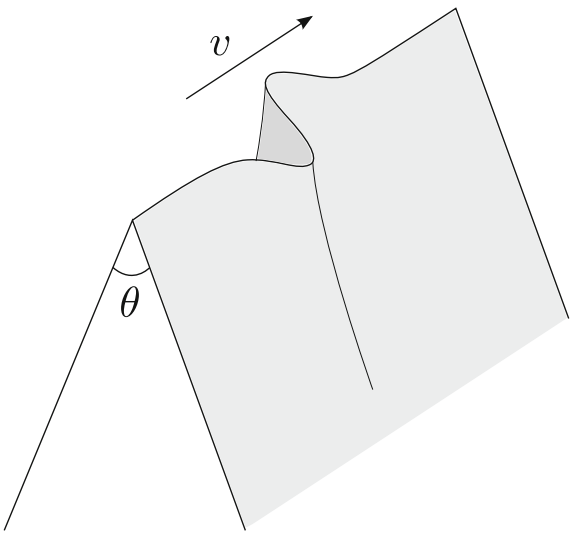

Fig. 8.1 Anti-symmetric flexural (ASF) acoustic wedge wave. θ : opening angle of the wedge

as well as anisotropic media with the mid-plane of the wedge being a reflection plane, wedge waves may be distinguished by their symmetry properties. They are either symmetric (even) or anti-symmetric flexural (ASF, odd) modes [27]. The latter symmetry type of acoustic wedge waves is illustrated in Fig. 8.1. The numerical findings of [27] and later systematic studies on wedge wave existence in isotropic media [28] revealed that for Poisson ratios in the range of practical materials and wedge angles equal to or smaller than 90°, only ASF modes exist. In anisotropic media, the situation is much more complex [29]. For slender wedges (opening angles typically smaller than 60° in isotropic media), more than one wedge wave branch exists, and the velocity of wedge waves belonging to a certain branch decreases with decreasing opening angle of the wedge.

For precise calculations of the speeds and displacement patterns of linear AWWs, numerical methods have to be used. In the pioneering works [25, 26], two approaches were used, namely the finite element method [25] and an expansion of the displacement field in a double series of Laguerre functions. This expansion is carried out after having applied a conformal mapping of the wedge with arbitrary opening angle into a rectangular wedge [27, 30]. This latter method has been extended for the computation of the kernel in the equation governing wave-form evolution of AWWs due to second-order nonlinearity [31]. In order to obtain analytic results in the limiting case of slender wedges, approximations like thin-plate theory with varying plate thickness [32] and an expansion in powers of the wedge angle [33] have been introduced. A wealth of results was obtained on the basis of ray theory, i.e. geometric acoustics [34, 35].

The geometric acoustics approximation and the direct expansion of the wedge wave displacement field in powers of the wedge angle have been used in investigations of nonlinear properties of AWWs, the prior to harmonic generation and

nonlinear mixing [36, 37], the latter to self-interaction and third-harmonic generation due to third-order nonlinearity [38].

Already shortly after the discovery of AWWs, first experiments on nonlinear properties were carried out [39, 40]. Adler et al. [40] investigated experimentally harmonic generation and nonlinear mixing of two input waves at a rectangular edge of $LiNbO_3$. Effects due to second-order nonlinearity were found to be relatively small in comparison to those on surface waves, unlike third-order nonlinear effects, which had appreciable magnitude. The authors attributed this finding to the symmetry of the wedge modes in this system. Later, Krylov and Parker derived nonlinear evolution equations for wedge waves of even and odd symmetry. In the case of even wedge modes, the evolution equation contains an effective second-order nonlinearity similar to the corresponding equation for Rayleigh waves. However, for ASF modes, i.e. wedge waves of odd symmetry, it is an effective third-order nonlinearity that occurs in the evolution equation, and no second-order term is present. Unfortunately, this work remained unpublished.

In the following section, we shall first present a derivation of a nonlinear evolution equation for nonlinear AWWs which are either of even symmetry or which propagate in a wedge that has no reflection symmetry with respect to its mid-plane. This derivation differs to some extent from the one given in [31] and is closer to numerical calculations of the kernel functions arising in this equation. In Sect. 8.3, consequences of the evolution equation and their experimental verification with laser ultrasound will be discussed. Especially the tendency towards shock formation at anisotropic wedges will be briefly compared with the corresponding phenomenon for surface and bulk acoustic waves.

When weak dispersion of AWWs, which arises if the tip of the wedge is truncated, for example, is taken into account in the evolution equation, solitary wave solutions of this equation can be found numerically. For a simplified version of this evolution equation including weak linear dispersion with a specific dependence of the frequency on wavelength, we derive an analytic expression for a solitary wave solution, which is compared with a corresponding solution of the nonlinear evolution equation for SAWs with a specific dispersion law [16].

In the last section, the derivation of a nonlinear evolution equation for AWWs is extended to account for third-order nonlinearity. This is especially relevant for ASF modes in isotropic wedges, where the effective second-order nonlinearity vanishes. From a mathematical point of view, the situation is comparable to the nonlinear evolution equation for Bleustein-Gulyaev waves mentioned above [24]. Very recently, nonlinear effects on guided acoustic waves have gained renewed interest, partly because of their relevance for non-destructive evaluation (NDE) to detect pre-fatigue at an early stage [41]. Defects give rise to modifications of the elastic properties of a material, which may affect especially its higher-order elastic constants [42]. The defects arising as a result of cyclic load, for example, may cause the elastic medium to become weakly anisotropic with no reflection symmetry with respect to the mid-plane of the wedge. For this situation, an evolution equation is

derived that governs waveform evolution of "largely anti-symmetric flexural" wedge waves and which contains simultaneously an effective second-order and third-order nonlinearity.

8.2 Evolution Equation with Second-Order Nonlinearity Only

The following derivations refer to a wedge geometry with a Cartesian coordinate system defined in Fig. 8.2. We start with the Lagrangian L for a nonlinear elastic medium,

$$L = \int_V \left(\frac{1}{2} \rho \, \dot{u}_\alpha \dot{u}_\alpha - \Phi \right) d^3x \,, \tag{8.2.1}$$

where ρ is the mass density of the elastic medium and $u_\alpha(x_1, x_2, x_3, t)$, $\alpha = 1, 2, 3$, are the Cartesian components of the displacement field, depending on the material coordinates x_β, $\beta = 1, 2, 3$, and time t. Cartesian indices are denoted by lower-case Greek letters, and summation over repeated Cartesian indices is implied. A dot on a symbol denotes derivative with respect to time of the corresponding quantity. The integration in (8.2.1) has to be performed over the volume V of the undeformed elastic medium. The density of potential energy Φ is expanded in powers of displacement gradients ($u_{\alpha,\beta}$ is the partial derivative of the displacement component u_α with respect to x_β),

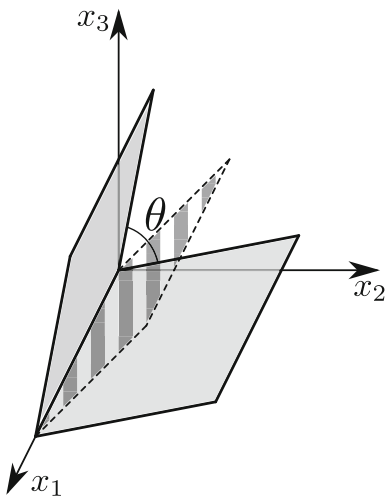

Fig. 8.2 Wedge geometry and coordinate system. Mid-plane of wedge indicated with dashed boundary

$$\Phi = \frac{1}{2} C_{\alpha\beta\mu\nu}\, u_{\alpha,\beta}\, u_{\mu,\nu} + \frac{1}{6} S_{\alpha\beta\mu\nu\gamma\delta}\, u_{\alpha,\beta}\, u_{\mu,\nu}\, u_{\gamma,\delta} + \frac{1}{24} S_{\alpha\beta\mu\nu\gamma\delta\kappa\lambda}\, u_{\alpha,\beta}\, u_{\mu,\nu}\, u_{\gamma,\delta}\, u_{\kappa,\lambda} + O\Big((\nabla u)^5\Big)\,. \tag{8.2.2}$$

In an elastic medium without pre-stress, the components of the fourth-rank tensor C are the second-order elastic constants, the components of the sixth-rank tensor S are linear combinations of second-order and third-order elastic constants and those of the eighth-rank tensor S are linear combinations of second-order, third-order and fourth-order elastic constants [43].

The displacement field is now expanded in a complete set of functions in the following way:

$$u_\alpha(x_1, x_2, x_3, t) = \int_{-\infty}^{\infty} \sum_I f_I(x_2, x_3; q)\, e^{iqx_1}\, a_I^{(\alpha)}(q,t)\, \frac{dq}{2\pi}. \tag{8.2.3}$$

The functions f_I may, but need not, depend on the 1D wave-vector q. The reality of the displacement field is guaranteed by the requirements

$$f_I(x_2, x_3; -q) = f_I^*(x_2, x_3; q), \quad a_I^{(\alpha)}(-q,t) = a_I^{(\alpha)*}(q,t)\,. \tag{8.2.4}$$

In (8.2.4) and the following, a star at a symbol denotes the complex conjugate.

The quantities $a_I^{(\alpha)}(q, t)$ may be the node displacements in a 2D finite element scheme with f_I being shape functions, for example. A perfect homogeneous wedge does not contain any length scale. This suggests the form

$$f_I(x_2, x_3; q) = \hat{f}_I(|q|x_2,\ |q|x_3) \tag{8.2.5}$$

for the functions f_I. (We note that for finite element calculations of nonlinear quantities, the ansatz (8.2.5) may not be favorable as it makes the mesh q-dependent.) In our numerical calculations, we follow [26, 27, 30, 31] and choose f_I as a product of two Laguerre functions φ_n with I being a combined index of the two non-negative integer indices of the two Laguerre functions,

$$\hat{f}_{(m,n)}(y, z) = \varphi_m(s_1\eta(y, z))\ \varphi_n(s_2\zeta(y, z)), \tag{8.2.6}$$

where $\eta(y, z)$, $\zeta(y, z)$ is a linear transformation that maps the wedge with opening angle θ into a rectangular one [27], and s_1, s_2 are dimensionless factors that may be chosen to optimize convergence in the numerical calculations [44].

After inserting (8.2.3) with (8.2.5) in (8.2.1) with (8.2.2), Hamilton's principle yields the following equation of motion for the expansion coefficients $a_I^{(\alpha)}(q, t)$:

$$
\begin{aligned}
&-\sum_J N_{IJ}(q)\ \ddot{a}_J^{(\alpha)}(q) = \sum_J M_{IJ}^{(\alpha\beta)}(q)\ a_J^{(\beta)}(q) \\
&+\frac{1}{2}\sum_{J,K}\int_{-\infty}^{\infty} V_{IJK}^{(\alpha\beta\gamma)}(-q,k,q-k)\ a_J^{(\beta)}(k)\, a_K^{(\gamma)}(q-k)\frac{dk}{2\pi} \\
&+\frac{1}{6}\sum_{J,K,L}\int_{-\infty}^{\infty}\int_{-\infty}^{\infty} W_{IJKL}^{(\alpha\beta\gamma\delta)}(-q,k,k',q-k-k') \\
&\qquad \times a_J^{(\beta)}(k)\ a_K^{(\gamma)}(k')\ a_L^{(\delta)}(q-k-k')\frac{dk}{2\pi}\frac{dk'}{2\pi} \quad + O(a^4).
\end{aligned}
\tag{8.2.7}
$$

The "mass matrix" N,

$$
N_{IJ}(q) = \iint_A \hat{f}_I^*(|q|x_2, |q|x_3)\,\rho\hat{f}_J(|q|x_2, |q|x_3)\,dx_2\,dx_3, \tag{8.2.8}
$$

where A is the cross section of the infinite wedge, becomes a positive real multiple of the unit matrix if the functions f_I are orthogonal and normalized appropriately. With the choice (8.2.5), (8.2.6) we obtain

$$
N_{IJ}(q) = \delta_{IJ} N_0(q) \tag{8.2.9}
$$

with $N_0(q) = \rho/(q^2\ s_1\ s_2\ d)$, where d is the determinant of the linear map $\eta(y, z)$, $\zeta(y, z)$. Explicit expressions for the quantities M, V, W on the right-hand side of (8.2.7) in terms of the material constants in (8.2.2) and the functions f_I are given in Appendix A.

We now write the time-dependent coefficients $a_I^{(\alpha)}(q, t)$ in the form of an expansion in powers of a typical strain ε and introduce a stretched time coordinate $\tau = \varepsilon\ t$,

$$
a_I^{(\alpha)}(q,t) = \varepsilon\,\tilde{a}_I^{(\alpha)}(q,t,\tau) + \varepsilon^2\, b_I^{(\alpha)}(q,t,\tau) + \varepsilon^3 c_I^{(\alpha)}(q,t,\tau) + O(\varepsilon^4), \tag{8.2.10}
$$

which is inserted in the equation of motion (8.2.7) with (8.2.9). At first order of ε the equation of motion admits a solution of the form

$$
\tilde{a}_I^{(\alpha)}(q,t,\tau) = w_I^{(\alpha)}(q)\, A(q,\tau)\, e^{-iqv_W t}, \tag{8.2.11}
$$

where w is an eigenvector of the matrix M corresponding to a wedge wave. It depends only on the sign, not on the modulus of q, and we have to require $w(q) = w^*(-q)$. The eigenvalue that corresponds to this eigenvector is $N_0\ (q\ v_W)^2$, and v_W is the phase velocity of the wedge wave.

At second order of ε we obtain from the equation of motion (8.2.7)

$$
\begin{aligned}
&-N_0(q)\ \ddot{b}_I^{(\alpha)}(q) - \sum_J M_{IJ}^{(\alpha\beta)}(q)\ b_J^{(\beta)}(q) \\
&= \left\{ -2iN_0(q)qv_W w_I^{(\alpha)}(q)\ \frac{\partial}{\partial\tau}A(q) + \frac{1}{2}\int_{-\infty}^{\infty} \sum_{J,K} V_{IJK}^{(\alpha\beta\gamma)}(-q,k,q-k) \right. \\
&\qquad \left. \times\, w_J^{(\beta)}(k)\, w_K^{(\gamma)}(q-k) A(k)\, A(q-k) \frac{dk}{2\pi} \right\}\ e^{-iqv_W t}.
\end{aligned}
\tag{8.2.12}
$$

Equation (8.2.12) constitutes a system of linear inhomogeneous differential equations for the unknown functions $b(q, t)$. To ensure for this system of equations the existence of a solution that is bounded as function of t, a compatibility condition has to be satisfied, which can be brought into the form

$$
\begin{aligned}
2iN_0(q)qv_W \sum_{I,\alpha} |w_I^{(\alpha)}|^2\ \frac{\partial}{\partial\tau}A(q) = \frac{1}{2}\int_{-\infty}^{\infty} \sum_{I,J,K} V_{IJK}^{(\alpha\beta\gamma)}(-q,k,q-k) \\
\times\, w_I^{(\alpha)}(-q) w_J^{(\beta)}(k)\, w_K^{(\gamma)}(q-k) A(k)\, A(q-k) \frac{dk}{2\pi}\,.
\end{aligned}
\tag{8.2.13}
$$

This is the nonlinear evolution equation for the amplitudes $A(q)$ of AWWs with wavevectors q. The scaling properties of the function V, which follow from Eqs. (A.3) and (A.9) in Appendix A, allow (8.2.13) to be cast into the form

$$
\begin{aligned}
i\,\frac{\partial}{\partial\tau}B(q) = qv_W \left\{ \int_0^q G(k/q)\ B(k)B(q-k)\frac{dk}{2\pi} \right. \\
\left. +2\int_q^{\infty} (q/k)^2\ G^*(q/k)\ B(k)B^*(k-q)\frac{dk}{2\pi} \right\}
\end{aligned}
\tag{8.2.14}
$$

in terms of displacement gradient amplitudes $B(q) = \mathrm{i}qA(q)$. This equation involves only positive 1D wavevectors q, k. The (in general complex) dimensionless function $G(X)$ has the property $G(X) = G(1 - X)$ and hence needs to be computed for arguments X in the interval [0, 1/2] only. Explicitly,

$$
G(X) = \frac{-i}{\hat{N}\,X(1-X)} \sum_{I,J,K} V_{IJK}^{(\alpha\beta\gamma)}(-1,X,1-X)\ w_I^{(\alpha)*}(1)\ w_J^{(\beta)}(1)\ \ w_K^{(\gamma)}(1), \tag{8.2.15}
$$

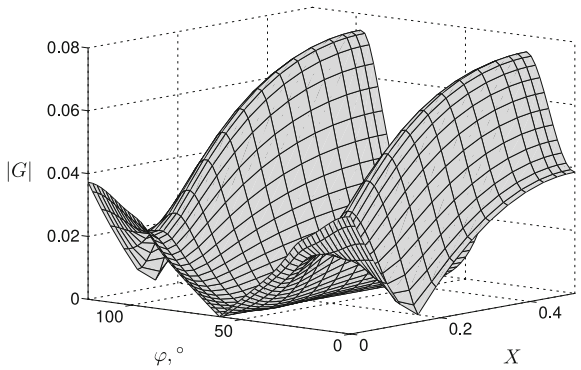

Fig. 8.3 Modulus of kernel $G(X)$ in the evolution Eq. (8.2.14) for silicon as wedge material. The rotation angle φ is defined in Fig. 8.4. Wedge angle $\theta = 70.5°$

where

$$\hat{N} = 4N_0(1)v_W^2 \sum_{I,\alpha} \left|w_I^{(\alpha)}\right|^2. \tag{8.2.16}$$

In Fig. 8.3, the modulus of the complex function G is shown for wedge geometries in the anisotropic material silicon. One of the two surfaces of the wedge is a (111) surface. The angle between the apex line of the wedge and the [1 −1 0] direction is denoted by φ (Fig. 8.4). Figure 8.3 shows $|G|$ as function of X and φ for wedges with opening angle $\theta = \arccos(1/3) = 70.53°$. A strong dependence of $|G|$ on the angle φ is clearly seen. The second-order and third-order elastic constants of silicon used in the calculation of $|G|$ were taken from [45] and for the density, the value 2328 kg/m^3 was chosen. The eigenvectors $w(q)$ were normalized such that the energy density associated with a linear wedge wave, integrated over the wedge's cross section and divided by $|A(q)|^2$, has a fixed value.

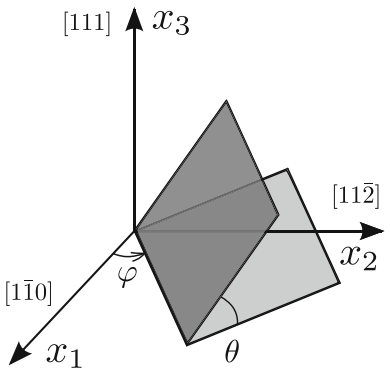

Fig. 8.4 Rotation of wedge geometry with respect to a crystallographic coordinate system

8.3 Nonlinear Evolution of Acoustic Wedge Pulses

The right-hand side of the evolution Eq. (8.2.14) for AWWs is a sum of two integrals. The first represents frequency up-conversion, as it drives high-frequency waves by combining two waves with lower frequencies. The second integral gives rise to frequency down-conversion, i.e. driving a wave with frequency lower than the frequency of one of the two waves that it combines in the nonlinear driving term. When comparing (8.2.14) with the nonlinear evolution equation for SAWs propagating on the planar surface of a homogeneous elastic medium that may be anisotropic, the essential difference is found to be the power of (q/k) in front of the complex-conjugate of the kernel function in the second integral. In the case of wedge waves, this power is equal to two, while in the evolution equation for SAWs it is equal to one. A consequence of this finding is that in the case of wedge waves, frequency down-conversion is less efficient than for SAWs, which means that phenomena like steepening of a wave front and shock formation happen more rapidly with wedge waves than with surface waves.

Recently, detailed experimental investigations of nonlinear pulse shape evolution have been carried out at rectangular silicon wedges with the help of laser excitation and detection of the acoustic pulses [46]. Pulse shapes were recorded at two observation points at the wedge tip having different distances from the excitation point. In this way, pulse shortening, steepening and the tendency to shock formation was clearly observed. Similarly to the situation with SAW pulses, the qualitative behavior of the pulse shape is largely determined by the phase angle of $G(1/2)$, i.e. the value of the complex kernel function at its argument $X = 1/2$. On the other hand, shock formation at a solid surface, generated by a pulsed line source on the surface, strongly differs from its counterpart at solid wedges as in the latter case, the strain pulse contracts to a quasi one-dimensional object at the tip of the wedge.

Numerical simulations of wedge wave pulses with the evolution Eq. (8.2.14), including a small linear damping term, over distances up to and even beyond the shock-formation distance, revealed that the high-frequency part of the power spectrum of the pulse develops a power-law behavior, $|B(q)| \sim q^{\kappa}$. The value for the exponent κ found in the numerical simulations was very close to the value $-1/3$, which is the exponent occurring in the formal solution $B(q) = B_{\mathrm{W}}\, q^{-1/3}$ of the evolution Eq. (8.2.14), where $q > 0$ and B_{W} is a complex constant. These findings are analogous to results obtained earlier by Hunter [47] for nonlinear SAWs. He pointed out that a slightly simplified version of the nonlinear evolution equation for SAWs has formally a power-law solution with exponent $-2/3$, and he found a power-law spectrum with this exponent in numerical simulations over long propagation distances. These results for nonlinear wedge and surface waves may also be compared to the shock wave solution of the Burger's equation. Its power spectrum develops the well-known q^{-1} power law [48].

For various reasons, wedge waves can become weakly dispersive [49], which can be accounted for in the derivation of the evolution equation. It leads to a linear term of the form $q^2\ \Delta_W(q)\ B(q)$ on the right-hand side of (8.2.14). The explicit

dependence of Δ_W on q is most easily determined for small variations of the mass density or elastic moduli of the material over the cross section of the wedge. For this purpose, we decompose the mass density ρ and tensor of linear elastic constants C into their averages over the cross section, denoted by an overbar, and a position-dependent deviation that we scale as being proportional to the expansion parameter ε,

$$\rho(x_2, x_3) = \overline{\rho} + \varepsilon\, \delta\rho(x_2,\ x_3), \quad C(x_2, x_3) = \ \overline{C} + \varepsilon\, \delta C(x_2, x_3)\,, \tag{8.3.1}$$

and obtain

$$\begin{aligned}\Delta_W(q) = \frac{2v_W}{q\hat{N}} \sum_{I,J} \Big\{ & w_I^{(\alpha)*}(q)\ \ w_J^{(\beta)}(q) \\ & \times \iint_A \Big[g_I^{(\mu)*}(x_2, x_3;\, q)\ \delta C_{\alpha\mu\beta\nu}(x_2, x_3)\ g_J^{(\nu)}(x_2, x_3;\, q) \\ & - \delta_{\alpha\beta} \hat{f}_I^*(|q|x_2, |q|x_3)\ (qv_W)^2\, \delta\rho(x_2, x_3) \hat{f}_J(|q|x_2, |q|x_3) \Big] dx_2\, dx_3 \Big\}.\end{aligned} \tag{8.3.2}$$

Other sources for linear dispersion are truncation of the tip of the edge and coating of one or both of the wedge's surfaces with a film of different material. In the long-wavelength limit, the quantity $\Delta_W(q)$ is independent of q in the case of coating and proportional to q in the case of truncation [49].

Solitary pulse solutions of the evolution equation including the linear dispersion term have been determined numerically [50, 51] as limiting cases of periodic pulse train solutions with a numerical approach applied earlier to the analogous case of SAWs. (Details are given in [51]). In the special case of the linear dispersion law $\Delta_W(q) = -Z\, q^2$ with constant coefficient Z and the kernel function $G(X)$ approximated by a complex constant $G_0 = -i\ |G_0|\ e^{i\phi}$, an analytic solitary wave solution can be found. In terms of the displacement amplitudes $A(q)$, the evolution equation with the above choice for the kernel and the linear dispersion law becomes for $q > 0$

$$\begin{aligned} i\,\frac{\partial}{\partial\tau} A(q) = v_W |G_0| \Bigg\{ & e^{i\phi} \int_0^q k(q-k) A(k) A(q-k)\, \frac{dk}{2\pi} \\ & + 2e^{-i\phi} q^2 \int_q^\infty k^{-1}(k-q)\, A(k) A(k-q)\, \frac{dk}{2\pi} \Bigg\} + Z q^4\, A(q). \end{aligned} \tag{8.3.3}$$

Inserting the ansatz

$$A(q,\tau) = A_0 e^{i\phi} q \, \exp[-q(\beta + i\kappa v_W \tau)] \tag{8.3.4}$$

for $q > 0$ in (8.3.3), two relations are obtained for the three parameters A_0, β and κ. The parameter A_0 is fixed by the constants in the evolution Eq. (8.3.3),

$$A_0 = 60\pi Z/|G_0|, \tag{8.3.5}$$

while the two remaining parameters are related via

$$\kappa = 15\, Z/\beta^3. \tag{8.3.6}$$

The displacement amplitudes are usually defined as the Fourier transform of a Cartesian component u_α (or a linear combination of components) of the displacement field at the wedge tip,

$$\begin{aligned} u_\alpha(x_1, 0, 0, t) &= \varepsilon 2\mathrm{Re} \int_0^\infty \exp(iq\xi)\, A(q,\tau) \frac{dq}{2\pi} \; + \; O(\varepsilon^2) \\ &= \varepsilon U(\xi,\tau) \; + \; O(\varepsilon^2), \end{aligned} \tag{8.3.7}$$

where $\xi = x_1 - v_W\, t$. For the solitary wave solution with displacement amplitudes (8.3.4) we find the algebraic form

$$U(\xi,\tau) \; = \frac{2A_0}{\left[\beta^2 + (\xi - \kappa\, v_W \tau)^2\right]^2} \left\{ \cos\phi \; \left[\beta^2 - (\xi - \kappa v_W \tau)^2\right] - 2\sin\phi \; \beta(\xi - \kappa v_W \tau) \right\}, \tag{8.3.8}$$

which differs from the Lorentzian form of the solitary wave solutions of a simplified evolution equation for SAWs with a KdV-type dispersion law (Eq. 3.14 in [16]). This one-parameter family of solitary wave solutions is analogous to the corresponding family of one-soliton solutions of the Benjamin-Ono or KdV type, where width, peak height and speed are governed by one parameter.

For a linear dispersion law corresponding to truncation of the wedge tip in the long-wavelength limit and a kernel function corresponding to a wedge cut out of a silicon crystal, solitary pulse solutions have been determined numerically and first numerical simulations of their collision behavior have been performed. A result is shown in Fig. 8.5. If the ratio of the peak amplitudes of the two incoming pulses is 1/5, it was found that both pulses largely survive the collision, and the collision scenario is reminiscent of that for KdV solitons (Fig. 8.5a). However, in the case of the peak ratio being 1/10, the smaller of the two pulses appears to break up after the collision.

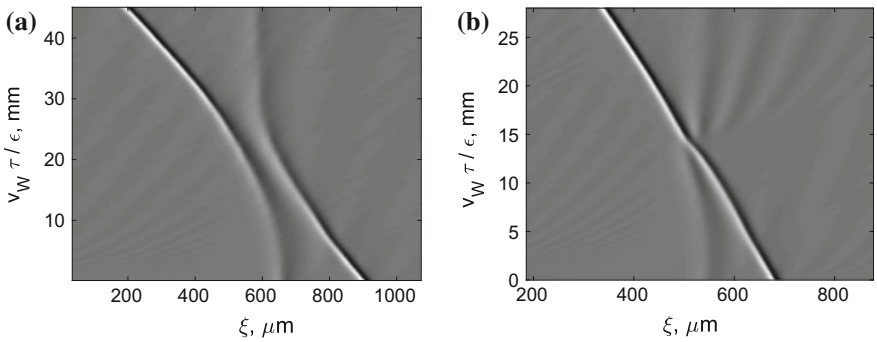

Fig. 8.5 Collision of two solitary pulse solutions of the evolution Eq. (8.2.14) with a linear dispersion term. For details see text. Ratio of peak amplitudes 1/5 (**a**) and 1/10 (**b**)

8.4 Evolution Equation with Second- and Third-Order Nonlinearity

The kernel function G in the evolution Eq. (8.2.14) vanishes in the case of ASF modes (odd wedge modes) if the mid-plane of the wedge is a reflection plane, which is always the case in isotropic elastic media. We shall now address this situation. Simultaneously, we treat the case of the reflection symmetry with respect to the mid-plane being slightly broken. This is accounted for by decomposing the tensor of second-order elastic constants C and the sixth-rank and eighth-rank tensors S, occurring in (8.2.2), in a part that satisfies the reflection symmetry and a small deviation that we scale to be of order ε,

$$C = C^{(0)} + \varepsilon\, C^{(1)},\ \ S = S^{(0)} + \varepsilon\, S^{(1)}. \tag{8.4.1}$$

As a consequence, the Hermitian matrix M and the quantities V and W may be decomposed in the same way,

$$M = M^{(0)} + \varepsilon\, M^{(1)},\ \ V = V^{(0)} + \varepsilon\, V^{(1)},\ \ W = W^{(0)} + \varepsilon\, W^{(1)}, \tag{8.4.2}$$

where, with the definitions in Appendix A,

$$M_{IJ}^{(n,\alpha\beta)}(q) = \iint\limits_A g_I^{(\mu)*}(x_2, x_3; q) C_{\alpha\mu\beta\nu}^{(n)} g_J^{(\nu)}(x_2, x_3; q)\, dx_2\, dx_3\,, \tag{8.4.3}$$

for $n = 0{,}1$, and analogous expressions for $V^{(n)}$ and $W^{(n)}$. In the following derivation, we shall again use the expansion (8.2.10) and introduce a second stretched time coordinate $T = \varepsilon^2\, t$.

Proceeding as in Sect. 8.2, we obtain at first order of ε Eq. (8.2.11), where w is now an eigenvector of the matrix $M^{(0)}$, corresponding to a wedge wave of odd

symmetry with velocity v_W in the absence of the small symmetry-breaking part $\varepsilon\ C^{(1)}$ of the tensor of second-order elastic constants.

At second order of ε we obtain (8.2.12) with V replaced by $V^{(0)}$ and with the additional term

$$\sum_J M_{IJ}^{(1,\alpha\beta)}(q)\ w_J^{(\beta)}(q)A(q)e^{-iqv_W t} \tag{8.4.4}$$

on the right-hand side. Since the symmetry with respect to the mid-plane of the wedge implies

$$\sum_{I,J,K} V_{IJK}^{(0,\alpha\beta\gamma)}(-q,k,q-k)\, w_I^{(\alpha)*}(q) w_J^{(\beta)}(k)\, w_K^{(\gamma)}(q-k) = 0, \tag{8.4.5}$$

the compatibility condition, which has to be satisfied to guarantee a bounded solution for b, reduces to

$$\begin{aligned} &2iN_0(q)qv_W \sum_{I,\alpha} |w_I^{(\alpha)}(q)|^2\ \frac{\partial}{\partial\tau}A(q) \\ &\quad = \sum_{I,J} w_I^{(\alpha)*}(q) M_{IJ}^{(1,\alpha\beta)}(q) w_J^{(\beta)}(q)\, A(q). \end{aligned} \tag{8.4.6}$$

This implies that $A(q)$ depends on τ via

$$A(q,\tau,T) \sim\ \exp(-iq\,\Delta v_{W,1}\tau). \tag{8.4.7}$$

In the following, we shall include the correction $\varepsilon\ \Delta v_{W,1}$ of the wedge wave velocity due to the symmetry breaking part $\varepsilon\ C^{(1)}$ of the second-order elastic constants in v_W. This implies that the amplitudes $A(q)$ no longer depend on τ .

The coefficients b are decomposed into two parts,

$$b_I^{(\alpha)}(q,t) = e^{-iqv_W t}\left\{\Delta w_I^{(\alpha)}(q)\, A(q) + \int_{-\infty}^{\infty} h_I^{(\alpha)}(q,k)\, A(k)\, A(q-k)\, \frac{dk}{2\pi}\right\}. \tag{8.4.8}$$

The first term in the curly brackets on the right-hand side of (8.4.8) yields a correction to the displacement field of the linear wedge wave with wavevector q due to the symmetry-breaking part $\varepsilon\ C^{(1)}$ of the second-order elastic constants. The quantities $h_I^{(\alpha)}(q,\ k)$ in the second term in the curly brackets are the unique solutions of the inhomogeneous linear equations

$$\begin{aligned} &\sum_J \left[N_0(q)\ (qv_W)^2 \delta_{IJ}\,\delta_{\alpha\beta} - M_{IJ}^{(0,\alpha\beta)}(q)\right] h_J^{(\beta)}(q,k) \\ &\quad = \frac{1}{2}\sum_{J,K} V_{IJK}^{(\alpha\beta\gamma)}(-q,k,q-k)\, w_J^{(\beta)}(k)\, w_K^{(\gamma)}(q-k) \end{aligned} \tag{8.4.9}$$

for fixed q and k. We note that the right-hand side of (8.4.9) corresponds to even symmetry with respect to the mid-plane of the wedge. Therefore, (8.4.9) has a unique solution, and the matrix H with elements

$$H_{IJ}^{(\alpha\beta)}(q) = N_0(q)\ (qv_W)^2 \delta_{IJ}\, \delta_{\alpha\beta} - M_{IJ}^{(0,\alpha\beta)}(q), \tag{8.4.10}$$

i.e. the contents of the square brackets on the left-hand side of (8.4.9), can be inverted in the subspace of even symmetry. Note that $H(q)$ is independent of the modulus of q and $H(-q) = H^*(q)$. The inverse of the matrix $H(q)$ in this subspace will be denoted by $\Gamma(q)$.

At third order of ε, the equation of motion (8.2.7) yields

$$\begin{aligned}
&-N_0(q)\ \ddot{c}_I^{(\alpha)}(q) - \sum_J M_{IJ}^{(\alpha\beta)}(q)\ c_J^{(\beta)}(q) \\
&= \Bigg\{ -2iN_0(q) q v_W w_I^{(\alpha)}(q)\ \frac{\partial}{\partial T} A(q) + Q_I^{(\alpha)}(q)\, A(q) \\
&+ \frac{1}{2} \int_{-\infty}^{\infty} \Bigg[\sum_{J,K} V_{IJK}^{(1,\alpha\beta\gamma)}(-q,k,q-k) w_J^{(\beta)}(k)\, w_K^{(\gamma)}(q-k) \\
&+ \sum_{J,K} V_{IJK}^{(0,\alpha\beta\gamma)}(-q,k,q-k)\ \left(\Delta w_J^{(\beta)}(k)\ w_K^{(\gamma)}(q-k) + w_J^{(\beta)}(k)\ \Delta w_K^{(\gamma)}(q-k) \right) \\
&- \sum_J \left(2N_0(q) q^2 v_W\, \Delta v_{W,1}\, \delta_{\alpha\beta}\, \delta_{IJ} - M_{IJ}^{(1,\alpha\beta)}(q) \right) h_J^{(\beta)}(q,k) \Bigg] A(k)\, A(q-k)\, \frac{dk}{2\pi} \\
&+ \int_{-\infty}^{\infty} \int_{-\infty}^{\infty} \Bigg[\frac{1}{2} \sum_{J,K} V_{IJK}^{(0,\alpha\beta\gamma)}(-q,k,q-k) \Big(h_J^{(\beta)}(k,k')\, w_K^{(\gamma)}(q-k)\, A(q-k)\, A(k-k') \\
&+ w_J^{(\beta)}(k)\, h_K^{(\gamma)}(q-k,k') A(k) A(q-k-k') \Big) A(k') \\
&+ \frac{1}{6} W_{IJKL}^{(0,\alpha\beta\mu\nu)}(-q,k,k',q-k-k')\, w_J^{(\beta)}(k)\, w_K^{(\mu)}(k')\, w_L^{(\nu)}(q-k-k') \\
&\times A(k) A(k') A(q-k-k') \Big] \frac{dk}{2\pi} \frac{dk'}{2\pi} \Bigg\}\ e^{-iqv_W t}.
\end{aligned} \tag{8.4.11}$$

The terms on the right-hand side of (8.4.11) are ordered according to their degree of nonlinearity with respect to the displacement amplitudes A. The linear term involving the quantity Q is related to higher-order corrections to the velocity and displacement field of the linear wedge waves due to the symmetry-breaking part $\varepsilon\, C^{(1)}$ of the second-order elastic constants. The inhomogeneous system of differential equations (8.4.11) has solutions for the quantities c that are bounded functions of t, if a compatibility condition is satisfied that is obtained by multiplying the right-hand side of (8.4.11) by $w_I^{(\alpha)}(-q)$, summing over I and α and equating the

result with zero. In the equation obtained in this way, the linear term involving Q gives rise to a correction of order ε^2 to the wedge wave velocity. The linear term is eliminated by including this second-order correction in v_W. After transition from displacement amplitudes $A(q, T)$ to displacement-gradient amplitudes $B(q, T) = iqA(q, T)$, the compatibility condition for (8.4.11) takes on the form

$$i\frac{\partial}{\partial T}B(q) = v_W q \int_{-\infty}^{\infty} K_2(-q,k,q-k)\,B(k)\,B(q-k)\,\frac{dk}{2\pi} + v_W q \int_{-\infty}^{\infty}\int_{-\infty}^{\infty} K_3(-q,k,k',q-k-k')B(k)B(k')\,B(q-k-k')\frac{dk}{2\pi}\frac{dk'}{2\pi}, \tag{8.4.12}$$

which is the nonlinear evolution equation for the displacement-gradient amplitudes. It contains both an effective second-order and third-order nonlinearity. Explicit expressions for the two kernel functions K_2 and K_3 in terms of the quantities defined above are given in Appendix B. These expressions allow for a quantitative determination of the two kernel functions, once the second-order, third-order and fourth-order elastic constants of the wedge material are known. In analogy to the case of nonlinear shear-horizontal surface waves in piezoelectric media (Bleustein-Gulyaev waves) [24], the function K_3 results as a sum of a direct part (B.2), involving the eighth-rank tensor S in the expansion of the potential energy in (8.2.2) (third-order nonlinearity) and an indirect contribution (B.3) due to cascaded second-order nonlinearity.

In the case of perfect reflection symmetry with respect to the mid-plane of the wedge, i.e. $K_2 = 0$, the growth rate of the third harmonic of a wedge wave with wave-vector q is governed by

$$T = K_3(-3q,q,q,q). \tag{8.4.13}$$

The quantity

$$S = K_3(-q,-q,q,q) + K_3(-q,q,-q,q) + K_3(-q,q,q,-q) \tag{8.4.14}$$

determines the size of a self-induced frequency shift of this wave. (Note that T and S are independent of the modulus of q.) For the isotropic material fused quartz, the quantity T has been evaluated numerically, using an expansion of the displacement field in a double series of Laguerre functions, (8.2.3)–(8.2.6). The second-, third-, and fourth-order elastic constants of fused quartz were taken from [52–54], respectively. For the mass density, the value 2203 kg/m^3 was chosen. Figure 8.6 contains first results for the dependence of T on the wedge angle θ for the slowest wedge mode. The direct and indirect contributions to T are displayed, too. The data shown in Fig. 8.6 reveal a strong compensation of both contributions for wedge

angles below 60°, which substantially reduces the efficiency of third-harmonic generation. The normalization of the eigenvectors $w(q)$ was chosen such that at the tip of the wedge, the component $u_n = -\sin((0.5\pi - \theta)/2)\, u_2 + \cos((0.5\pi - \theta)/2)\, u_3$ of the displacement field normal to the lower wedge surface in Fig. 8.2 is given by

$$u_n(x_1, t) = \int_{-\infty}^{\infty} A(q)\, \exp[iq(x_1 - v_W t)]\, \frac{dq}{2\pi}. \tag{8.4.15}$$

A quantitative determination of K_3 requires much higher numerical efforts than calculations of K_2, and it has been found difficult to obtain convergent results for the direct contribution to T for wedge angles larger than 70° with the approach chosen.

For the slowest wedge wave branch in slender isotropic wedges, the leading-order terms in an expansion of T and S in powers of the wedge angle θ were evaluated [38, 55], using the results for the displacement field of linear wedge waves [33]. It was found that the ratio T/S vanishes linearly with θ . This means that for the lowest wedge wave branch in wedges with sufficiently small wedge angle, the effect of a self-induced frequency shift should be dominant over higher harmonic generation. It was also found that to leading order in θ, the kernel K_3 (both the direct and the indirect contribution) is independent of third-order and fourth-order elastic constants and depends on the second-order Lamé constants and the mass density of the wedge material only.

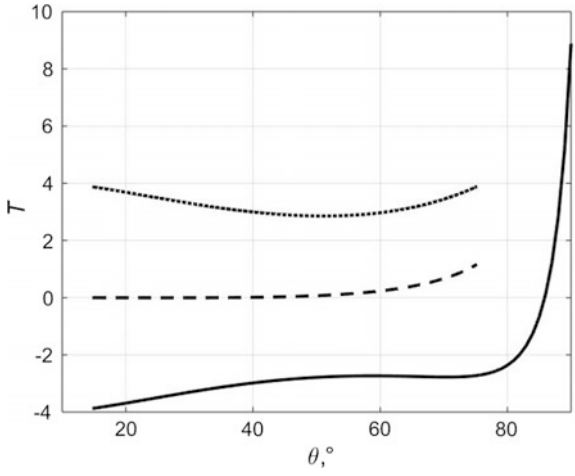

Fig. 8.6 Efficiency T of third-harmonic generation, defined in (8.4.13), as function of wedge angle θ (dashed). Direct contribution (dotted) and indirect contribution (solid) to T

8.5 Conclusions

Acoustic wedge waves exhibit a variety of nonlinear propagation effects which are investigated since their discovery in the early seventies. For the nonlinear properties of these 1D guided waves in the non-dispersive or weakly dispersive regime, the reflection symmetry with respect to the mid-plane of the wedge plays a key role.

If this symmetry is broken by anisotropy of the wedge material, nonlinear propagation properties of wedge waves are governed by an evolution equation containing a non-local second-order nonlinearity, which is similar to the corresponding nonlinear evolution equation for Rayleigh-type surface acoustic waves or for Stoneley waves. However, there is a subtle but important difference, which is related to the 1D character of wedge waves in contrast to acoustic waves guided by a 2D surface or interface. In the non-dispersive regime, this difference leads to faster build-up of higher harmonics and a different exponent in the power-law behavior of the Fourier spectrum of wedge waves near the shock-formation distance. The typical features of nonlinear pulse evolution of acoustic wedge waves, following from the evolution equation in the absence of dispersion, have recently been demonstrated in laser-ultrasound experiments for rectangular silicon wedges [46].

In the presence of weak dispersion, the evolution equations for surface waves and for wedge waves both admit solitary wave solutions. The characteristic difference in the evolution equations mentioned above influences to some extent the shape of solitary pulses, but it does not affect the scaling relation between peak height, width and speed of a solitary pulse, which exists if the linear dispersion can be approximated by a power law.

If the mid-plane of the wedge is a mirror plane, which pertains especially to isotropic wedges, the effective nonlinearity in the evolution equation for wedge waves is of third order. Computations of the kernel function in the third-order nonlinear term require considerable numerical efforts, but are feasible with an approach based on an expansion of the displacement field in a double series of Laguerre functions. If the mirror symmetry with respect to the mid-plane is only weakly broken, for example by defects with a texture in an isotropic matrix material, both second-order and third-order nonlinearity are present, which should lead to interesting phenomena.

The nonlinear effects on acoustic wedge waves discussed here pertain to elastic media with density of potential energy that can be expanded in powers of displacement gradients. Defects like dislocations or cracks may give rise to nonlinearities which are associated with potential energy terms that do not allow for such an expansion [56]. First experiments with wedge waves in materials, which are expected to contain such nonlinearities, have been reported in [57] and open up a new direction in the field of nonlinear wedge waves.

Acknowledgements The authors would like to thank Peter Hess for helpful discussions. Financial support by Deutsche Forschungsgemeinschaft (Grant No. MA 1074/11) is gratefully acknowledged.

Appendix A

We define the operator

$$D_\alpha(q) = \begin{cases} iq & \text{for } \alpha = 1 \\ \partial/\partial x_\alpha & \text{for } \alpha = 2, 3, \end{cases} \tag{A.1}$$

and the quantities

$$g_I^{(\alpha)}(x_2, x_3; q) = D_\alpha(q)\hat{f}_I(|q|x_2, |q|x_3)\,, \tag{A.2}$$

which possesses the scaling property for $q > 0$

$$g_I^{(\alpha)}(x_2, x_3; q) = X g_I^{(\alpha)}(Xx_2, Xx_3; q/X) \tag{A.3}$$

and, if the function f_I is real,

$$g_I^{(\alpha)}(x_2, x_3; -q) = g_I^{(\alpha)*}(x_2, x_3; q). \tag{A.4}$$

The elements of the matrix M in (8.2.7) may then be expressed in the form

$$M_{IJ}^{(\alpha\beta)}(q) = \iint_A g_I^{(\mu)*}(x_2, x_3; q) C_{\alpha\mu\,\beta\nu} g_J^{(\nu)}(x_2, x_3; q)\, dx_2\, dx_3\,. \tag{A.5}$$

The right-hand side of (A.2) implies that M does not depend on $|q|$, that

$$M_{IJ}^{(\alpha\beta)}(q) = M_{JI}^{(\beta\alpha)*}(q) \tag{A.6}$$

and, if the functions f_I are all real, which is the case with the choice (8.2.6), that

$$M_{IJ}^{(\alpha\beta)}(-q) = M_{IJ}^{(\alpha\beta)*}(q). \tag{A.7}$$

For the quantities V and W we obtain expressions analogous to (A.5),

$$\begin{aligned} V_{IJK}^{(\alpha\beta\gamma)}(-q, k, q-k) = \iint_A & S_{\alpha\mu\,\beta\nu\,\gamma\lambda}\; g_I^{(\mu)}(x_2, x_3; -q) \\ & \times g_J^{(\nu)}(x_2, x_3; k)\, g_K^{(\lambda)}(x_2, x_3; q-k) dx_2\, dx_3, \end{aligned} \tag{A.8}$$

$$\begin{aligned} W_{IJKL}^{(\alpha\beta\gamma\delta)}(-q, k, k', q-k-k') = \iint_A & S_{\alpha\mu\,\beta\nu\,\gamma\lambda\,\delta\kappa}\; g_I^{(\mu)}(x_2, x_3; -q) \\ & \times g_J^{(\nu)}(x_2, x_3; k)\, g_K^{(\lambda)}(x_2, x_3; k') g_L^{(\kappa)}(x_2, x_3; q-k-k') dx_2\, dx_3 \end{aligned} \tag{A.9}$$

with scaling properties that follow from (A.3).

Appendix B

The kernel function in the effective second-order nonlinearity of the evolution Eq. (8.4.12) may be expressed in the form

$$K_2(-q,k,q-k) = \frac{-iq}{\hat{N}\,k(q-k)} \times \sum_{I,J,K} \Big\{ V_{IJK}^{(1,\alpha\beta\gamma)}(-q,k,q-k)\, w_I^{(\alpha)}(-q)\, w_J^{(\beta)}(k)\, w_K^{(\gamma)}(q-k) + V_{IJK}^{(0,\alpha\beta\gamma)}(-q,k,q-k) \Big[w_I^{(\alpha)}(-q)\, w_J^{(\beta)}(k)\ \Delta w_K^{(\gamma)}(q-k) + w_I^{(\alpha)}(-q)\ \Delta w_J^{(\beta)}(k)\, w_K^{(\gamma)}(q-k) + \Delta w_I^{(\alpha)}(-q)\ w_J^{(\beta)}(k)\, w_K^{(\gamma)}(q-k) \Big] \Big\}. \tag{B.1}$$

It depends only on the signs and on ratios of the 1D wavevectors q, k, $q - k$, and it vanishes if the reflection symmetry with respect to the mid-plane of the wedge is not broken.

The kernel function in the effective third-order nonlinearity in (8.4.12) consists of a direct contribution, which is linear in the components of the eighth-rank tensor S, and an indirect contribution, which is quadratic in the sixth-rank tensor S, $K_3 = K_{3,\mathrm{d}} + K_{3,\mathrm{i}}$, where

$$K_{3,d}(-q,k,k',q-k-k') = \frac{-q}{3\hat{N}\,k\,k'\,(q-k-k')} \times \sum_{I,J,K,L} \Big[W_{IJKL}^{(0,\alpha\beta\gamma\delta)}(-q,k,k',q-k-k')\ w_I^{(\alpha)}(-q)\ w_J^{(\beta)}(k)\ w_K^{(\gamma)}(k')\ w_L^{(\delta)}(q-k-k') \Big], \tag{B.2}$$

and

$$K_{3,i}(-q,k,k',q-k-k') = \frac{-q}{\hat{N}\,k\,k'\,(q-k-k')} \times \sum_{I,J,K,L} \Big[w_I^{(\alpha)}(-q)\ w_J^{(\beta)}(k)\ V_{IJK}^{(0,\alpha\beta\gamma)}(-q,k,q-k)\ \Gamma_{KL}^{(\gamma\lambda)}(q-k) \times V_{LMN}^{(0,\lambda\mu\nu)}(-q+k,k',q-k-k') w_M^{(\mu)}(k')\ w_N^{(\nu)}(q-k-k') \Big]. \tag{B.3}$$

References

1. Hadouaj, H., Maugin, G.A.: Une onde solitaire se propageant sur un substrat élastique recouvert d'un film mince. C. R. Acad. Sci. Paris **309**, 1877–1881 (1989)
2. Maugin, G.A., Hadouaj, H.: Solitary surface transverse waves on an elastic substrate coated with a thin film. Phys. Rev. B **44**, 1266–1280 (1991)
3. Maugin, G.A., Hadouaj, H., Malomed, B.A.: Nonlinear coupling between SH surface solitons and Rayleigh modes on elastic structures. Phys. Rev. B **45**, 9688–9694 (1992)
4. Hadouaj, H., Maugin, G.A.: Surface solitons on elastic surfaces: numerics. Wave Motion **16**, 115–123 (1992)
5. Maugin, G.A.: Nonlinear waves in elastic crystals. Oxford University Press, Oxford (1999)
6. Maugin, G.A.: Nonlinear electromechanical effects and applications. World Scientific, Singapore (1985)
7. Parker, D.F.: Nonlinear surface acoustic waves on elastic and piezoelectric materials. In: Borissov, M., Spassov, L., Georgiev, Z., Avramov, I. (eds.) 2nd International Symposium on Surface Waves in Solids and Layered Structures and 4th International Scientific Technical Conference Acoustoelectronics '89, Varna, September 1989, pp. 389–405. World Scientific, Singapore (1990)
8. Mayer, A.P., Maradudin, A.A.: Effects of nonlinearity and dispersion on the propagation of surface acoustic waves. In: Maugin, G.A. (ed.) Continuum Models and Discrete Systems, vol. 2, pp. 306–315. Longman, London (1991)
9. Andersen, D.R., Datta, S., Gunshor, R.L.: A coupled mode approach to modulational instability and envelope solitons. J. Appl. Phys. **54**, 5608–5612 (1983)
10. Reutov, V.P.: Use of the averaged variational principle for describing multiwave interactions of elastic surface waves. Izv. Vyssh. Uchebn. Zaved., Radiofiz. **16**, 1690–1702 (1973) [Radiophys. Quantum Electron. **16**, 1307–1316 (1973)]
11. Kalyanasundaram, N., Ravindran, R., Prasad, P.: Coupled amplitude theory of nonlinear surface acoustic waves. J. Acoust. Soc. Am. **72**, 488–493 (1982)
12. Lardner, R.W.: Nonlinear surface waves on an elastic solid. Int. J. Eng. Sci. **21**, 1331–1342 (1983)
13. Parker, D.F.: Waveform evolution for nonlinear surface acoustic waves. Int. J. Eng. Sci. **26**, 59–75 (1988)
14. Zabolotskaya, E.A.: Nonlinear propagation of plane and circular Rayleigh waves in isotropic solids. J. Acoust. Soc. Am. **91**, 2569–2575 (1992)
15. Mayer, A.P.: Surface acoustic waves in nonlinear elastic media. Phys. Rep. **256**, 237–366 (1995)
16. Eckl, C., Kovalev, A.S., Mayer, A.P., Lomonosov, A.M., Hess, P.: Solitary surface acoustic waves. Phys. Rev. E **70**, 046604-1–15 (2004)
17. Hess, P., Lomonosov, A.M., Mayer, A.P.: Laser-based linear and nonlinear guided elastic waves at surfaces (2D) and wedges (1D). Ultrasonics **54**, 39–55 (2014)
18. Parker, D.F.: Stratification effects on nonlinear elastic surface waves. Phys. Earth Planet. Inter. **50**, 16–25 (1988)
19. Hamilton, M.F., Il'insky, Yu.A., Zabolotskaya, E.A.: Evolution equations for nonlinear Rayleigh waves. J. Acoust. Soc. Am. **97**, 891–897 (1995)
20. Lomonosov, A.M., Mikhalevich, V.G., Hess, P., Knight, E.Yu., Hamilton, M.F., Zabolotskaya, E.A.: Laser-generated nonlinear Rayleigh waves with shocks. J. Acoust. Soc. Am. **105**, 2093–2096 (1999)
21. Brysev, A.P., Krasilnikov, V.A., Podgornov, A.A., Solodov, I.Yu.: Direct observation of the form of an elastic wave with finite amplitude on a solid surface. Fiz. Tverd. Tela **26**, 2104–2106 (1984) [Moscow University Physics Bulletin **26**, 2104–2106 (1984)]
22. Lomonosov, A.M., Hess, P.: Nonlinear surface acoustic waves: Realization of solitary pulses and fracture. Ultrasonics **48**, 482–487 (2008)

23. Meegan, G.D., Hamilton, M.F., Il'inskii, Yu.A., Zabolotskaya, E.A.: Nonlinear Stoneley and Scholte waves. J. Acoust. Soc. Am. **106**, 1712–1723 (1999)
24. Mayer, A.: Evolution equation for nonlinear Bleustein-Gulyaev waves. Int. J. Engng. Sci. **29**, 999–1004 (1991)
25. Lagasse, P.: Analysis of a dispersion-free guide for elastic waves. Electron. Lett. **8**, 372–373 (1972)
26. Maradudin, A.A., Wallis, R.F., Mills, D.L., Ballard, R.L.: Vibrational edge modes in finite crystals. Phys. Rev. B **6**, 1106–1111 (1972)
27. Moss, S.L., Maradudin, A.A., Cunningham, S.L.: Vibrational edge modes for wedges with arbitrary interior angles. Phys. Rev. B **8**, 2999–3008 (1973)
28. Zavorokhin, G.L., Nazarov, A.I.: On elastic waves in a wedge. J. Math. Sci. **175**, 646–650 (2011)
29. Pupyrev, P.D., Lomonosov, A.M., Nikodijevic, A., Mayer, A.P.: On the existence of guided acoustic waves at rectangular anisotropic edges. Ultrasonics **71**, 278–287 (2016)
30. Datta, S., Hunsinger, B.J.: Analysis of line acoustical waves in general piezoelectric crystals. Phys. Rev. B **16**, 4224–4229 (1977)
31. Sokolova, E.S., Kovalev, A.S., Mayer, A.P.: Second-order nonlinearity of wedge acoustic waves in anisotropic media. Wave Motion **50**, 246–252 (2013)
32. McKenna, J., Boyd, G.D., Thurston, R.N.: Plate theory solution for guided flexural acoustic waves along the tip of a wedge. IEEE Trans. Sonics Ultrason. **21**, 178–186 (1974)
33. Parker, D.F.: Elastic wedge waves. J. Mech. Phys. Solids **40**, 1583–1593 (1992)
34. Krylov, V.V.: Wedge acoustic waves: new theoretical and experimental results. In: Borissov, M., Spassov, L., Georgiev, Z., Avramov, I. (eds.) 2nd International Symposium on Surface Waves in Solids and Layered Structures and 4th International Scientific Technical Conference Acoustoelectronics '89, Varna, September 1989, pp. 389–405. World Scientific, Singapore (1990)
35. Mozhaev, V.G.: Ray theory of wedge acoustic waves. Moscow Univ. Phys. Bull. **30**, 38–42 (1989)
36. Krylov, V.V., Parker, D.F.: Harmonic generation and parametric mixing in wedge acoustic waves. Wave Motion **15**, 185–200 (1992)
37. Krylov, V.V., Mayer, A.P., Parker, D.F.: Nonlinear evolution of initially sine-like wedge acoustic waves. In: Proceedings of the 1993 IEEE International Ultrasonics Symposium, pp. 765–768
38. Mayer, A.P., Garova, E.A., Mozhaev, V.G.: Nonlinear surface and wedge acoustic waves in the presence of weak dispersion. Proc. Estonian Acad. Sci. Phys. Math. **46**, 85–93 (1997)
39. Mason, I.M., Motz, M.D., Chambers, J.: Parametric interaction of acoustic surface wedge waves. Electron. Lett. **8**, 429–430 (1972)
40. Adler, R., Hoskins, M., Datta, S., Hunsinger, B.J.: Unusual parametric effects on line acoustic waves. IEEE Trans. Sonics Ultrason. **SU-26**, 345–347 (1979)
41. Matlak, K.H., Kim, J.Y., Jacobs, L.J., Qu, J.: Review of second harmonic generation measurement techniques for material state determination in metals. J. Nondestruct. Eval. **34**, 273–296 (2015)
42. Nazarov, V.E., Sutin, A.M.: Nonlinear elastic constants of solids with cracks. J. Acoust. Soc. Am. **102**, 3349–3354 (1997)
43. Leibfried, G., Ludwig, W.: Gleichgewichtsbedingungen in der Gittertheorie. Z. Phys. **160**, 80–92 (1960)
44. Sharon, T.M., Maradudin, A.A., Cunningham, S.L.: Vibrational edge modes for small-angle wedges. Phys. Rev. B **8**, 6024–6026 (1973)
45. Hall, J.J.: Electronic Effects in the Elastic Constants of n-Type Silicon. Phys. Rev. **161**, 756–761 (1967)
46. Lomonosov, A.M., Pupyrev, P.D., Hess, P., Mayer, A.P.: Nonlinear one-dimensional guided wedge waves. Phys. Rev. B **92**, 014112-1–5 (2015)

47. Hunter, J.K.: Nonlinear hyperbolic surface waves. In: Bressan, A., Chen, G.-Q.G., Lewicka, M., Wang, D. (eds.) Nonlinear Conservation Laws and Applications, pp. 303–314. Springer, Boston (2011)
48. Chorin, A.J., Hald, O.H.: Viscosity-dependent inertial spectra of the Burgers and Korteweg–deVries–Burgers equations. Proc. Natl. Acad. Sci. U.S.A. **102**, 3921–3923 (2005)
49. Sokolova, E.S., Kovalev, A.S., Timler, R., Mayer, A.P.: On the dispersion of wedge acoustic waves. Wave Motion **50**, 233–245 (2013)
50. Mayer, A.P., Lomonosov, A.M., Hess, P.: Nonlinear acoustic waves localized at crystal edges. In: Proceedings of the 2009 IEEE International Ultrasonics Symposium, pp. 1088–1091
51. Pupyrev, P.D.: Linear and nonlinear wedge waves in solids. Dissertation, Prokhorov General Physics Institute of the Russian Academy of Sciences (2017)
52. De Jong, B.H.W.S., Beerkens, R.G.C., van Nijnatten, P.A. (eds.): Ullmann's Encyclopedia of Industrial Chemistry. Wiley-VCH, Weinheim (2000)
53. Bogardus, E.H.: Third-order elastic constants of Ge, MgO, and fused SiO_2. J. Appl. Phys. **36**, 2504–2513 (1965)
54. Kondo, K., Iio, S., Sawaoka, A.: Nonlinear pressure dependence of the elastic moduli of fused quartz up to 3 GPa. J. Appl. Phys. **52**, 2826–2831 (1981)
55. Mayer, A.P., Mozhaev, V.G., Krylov, V.V., Parker, D.F.: Nonlinear acoustic waves in a slender wedge. In: Spatschek, K.H., Mertens, F.G. (eds.) Nonlinear Coherent Structures in Physics and Biology, pp. 279–282. Plenum, New York (1994)
56. Ostrovsky, L.A., Johnson, P.A.: Dynamic nonlinear elasticity in geomaterials. Rivista del Nuovo Cimento **24**, 1–46 (2001)
57. Korobov, A., Izossimova, M., Kokshaiskii, A., Agafonov, A.: Elastic waves in a wedge of aluminum alloy with permanent residual deformations. AIP Conf. Proc. **1685**, 080005-1–4 (2015)

Chapter 9
Analysis of Nonlinear Wave Propagation in Hyperelastic Network Materials

Hilal Reda, Khaled ElNady, Jean-François Ganghoffer, Nikolas Karathanasopoulos, Yosra Rahali and Hassan Lakiss

Abstract We analyze the acoustic properties of microstructured repetitive network material undergoing configuration changes leading to geometrical nonlinearities. The effective constitutive law of the homogenized network is evaluated successively as an effective first nonlinear 1D continuum, based on a strain driven incremental scheme written over the reference unit cell, taking into account the changes of the lattice geometry. The dynamical equations of motion are next written, leading to specific dispersion relations. The inviscid Burgers equation is obtained as a specific wave propagation equation for the first order effective continuum when the expression of the energy includes third order contributions, whereas a perturbation method is used to solve the dynamical properties for the effective medium including fourth order terms. This methodology is applied to analyze wave propagation within different microstructures, including the regular and reentrant hexagons, and plain weave textile pattern.

H. Reda (✉) · K. ElNady
LEMTA, Université de Lorraine, 2 Avenue de la Forêt de Haye,
TSA 60604, 54504 Vandoeuvre-les-Nancy, France
e-mail: hilal_reda@hotmail.com

K. ElNady
e-mail: khaled-elnady@outlook.fr

H. Reda · H. Lakiss
Faculty of Engineering, Section III, Campus Rafic Hariri, Lebanese University,
Beirut, Lebanon
e-mail: hassanlakiss@yahoo.com

N. Karathanasopoulos
Institute for Computational Science, ETH Zurich, Clausiusstrasse 33, 8092 Zurich,
Switzerland
e-mail: karathanasopoulosn@gmail.com

Y. Rahali
Institut Préparatoire aux Études d'Ingénieur de Bizerte, 7000 Bizerte, Tunisia
e-mail: rahali.yosra@gmail.com

J.-F. Ganghoffer
LEM3, Université de Lorraine CNRS, 7, rue Félix Savart., 57073 Metz Cedex, France

H. Altenbach et al. (eds.), *Generalized Models and Non-classical Approaches in Complex Materials 2*, Advanced Structured Materials 90,
https://doi.org/10.1007/978-3-319-77504-3_9

9.1 Introduction

The analysis of wave propagation in hyperelastic media depends initially on the type of constitutive law. When considering microstructured solids prone to large deformations, the effective constitutive law written in the large strains regime reflects the impact of the microstructure, and can be obtained thanks to suitable homogenization schemes instead of being postulated directly in a phenomenological manner.

In recent years, different materials have been analyzed in the context of anisotropic finite-strain elasticity; these include composites, foam-like structures, 2D and 3D textile preforms and synthetic solids [1, 2]. Cellular solids, by contrast to compact materials, are two or three dimensional bodies divided into cells, the walls of which are made of a solid material capable of undertaking large elastic deformations in the elastic regime, before plastic failure or fracture occurs. There are numerous examples of such network structures, including repetitive large scale deployable structures like antenna, 3D textiles, cellular materials and especially auxetic structures (those with negative Poisson's ratio) having excellent damping and impact absorption capabilities [3].

We shall in the current paper use the discrete asymptotic homogenization method [3–5] which is perfectly suited to the discrete architecture of different types of networks which can be modeled with beam like structural elements, in order to compute their effective nonlinear static and dynamic response. Due to the very small bending rigidity of the beams building such networks, the nonlinear response is essentially due to the change of network configuration, meaning that the beam orientation and length change with ongoing deformation. We shall thus mostly account for geometrical nonlinearities at the microlevel of the network. The geometrical nonlinear behavior of cellular structures and network materials has been extensively studied in [6, 7], considering especially foams, and using simplified pin jointed models for which the bending contribution of the skeleton struts has been neglected. Wang and Cuitino [8] proposed another approach accounting for axial, bending and twisting deformations at local level. One study based on a homogenization technique was given in [9]. Linear effective models developed to analyze structures on the basis of a beam model were presented in homogenization of the underlying microstructure [10, 11], in which stretching and simultaneous bending occur. This initial linear was extended more recently in [12] to build the stress-strain relation and strain energy function for an effective hyperelastic cellular material with arbitrary symmetry. An alternative approach was proposed in [13] using a computational homogenization to derive a nonlinear constitutive model for lattice materials [14, 15].

A lot of attention has been paid in the literature to the propagation of elastic waves in the linear context [16–19], with comparatively less work devoted to wave propagation in nonlinear media.

The propagation of elastic waves in nonlinear materials and structures is accompanied by a number of new phenomena such as amplitude-dependent dispersion relations, or the occurrence of subsonic and supersonic modes that can

never be observed in homogeneous linear media [20–23]. As another aspect, the propagation of waves in a nonlinear medium enriched by second gradient terms is studied in [24]; the authors show that two modes can propagate: an evanescent subsonic mode that disappears after a certain wavenumber and a supersonic mode characterized by an increase of the frequency with the wavenumber.

These features entail that the solutions of the wave propagation equations are more complex compared to the linear case, and they depend on the form of the dynamical equilibrium equations derived from the constitutive law. For example, the solitary surface waves discovered by John Scott Russell [25] in 1834 have been developed as solution of the Boussinesq equation [26], the Benjamin-Bona-Mahony (BBM) equation [27], the Korteweg & de Vries (KdV) equation [28], the Camassa-Holm (CH) equation [29]. The shock displacement wave can be used for nonlinear dynamical problems in the form of Burger's equation; as an alternative, the perturbation method can be used for certain kinds of constitutive laws [30].

Dispersion has been accounted for by higher-order derivatives of the displacement field due to the underlying discrete structure of the elastic medium in Maradudin [31] and more, recently in Hao et al. [32].

We rely in the present work on the discrete homogenization method developed in [14, 15] for predicting the effective nonlinear elastic responses of repetitive lattices, taking into consideration changes of the microstructure geometry under applied loads. The predictive nature of the employed homogenization technique allows in the present contribution the identification of a strain energy density of hyperelastic models at the mesoscopic level, that characterize the effective continuum. The identified hyperelastic constitutive models are then involved in the analysis of nonlinear wave propagation in repetitive network materials (represented by the constructed effective substitution medium). We advocate thereby novel aspects in this paper. The obtained forms of the nonlinear constitutive law identified for three different network materials leads to different types of waves, the dispersive behavior of which is analyzed.

The outline of this contribution is as follows: Sect. 9.2 is devoted to a synthetic description of the discrete homogenization method in a large strains context, which constitutes the basis of this work. The incremental update of the kinematic and static variables at the mesoscopic level of the effective Cauchy continuum accounting for the evolution of the network geometry will be described in algorithmic format. In Sect. 9.3, virtual simulations based on the developed discrete homogenization technique will be used for the calibration of a strain energy density of a hyperelastic model for three different lattices, leading to two different forms of the strain energy density function. Wave propagation analysis is done in Sect. 9.4, based on the identified strain energy hyperelastic functions. We conclude by a summary of the work and perspectives of developments in Sect. 9.5.

Regarding notations, vectors and tensors are denoted by boldface symbols; the transpose of t second order tensor is denoted with a superscript T, for instance $\mathbf{F}^{\mathrm{T}}$.

9.2 Incremental Scheme for the Computation of the Effective Hyperelastic Effective Models

The adopted computational method of the effective nonlinear response of lattice materials relies on a two steps methodology: the ground state effective moduli are first evaluated in the initial small strains regime, followed by the evaluation of the nonlinear subsequent response, based on the update of the lattice configuration (geometry) when subjected to an increased kinematic loading imposed over the identified unit cell. We rely for the purpose of computing the effective nonlinear response on the discrete homogenization method (abbreviated DH method in the sequel) to replace the initially discrete structure by a nonlinear elastic effective continuum.

The homogenization of the periodic network towards a Cauchy continuum at the mesoscopic level relies on the condensation of the existing nodal rotations (which exist at the crossing nodes between the structural elements of the network), which are expressed versus the deformation applied over the unit cell, using the equilibrium equations. We refer the reader for more details related to the asymptotic homogenisation technique to [14, 15]. The homogenization methods accounts for the large changes of network configurations occurring due to the large imposed kinematic loadings. The lattice geometry is updated at each new increment of the external load applied to the unit cell boundary, based on which new effective properties are evaluated. The main steps of the DH method leading to the nonlinear response of the homogenized continuum are written in algorithmic format in Box 1. Note that although the main source of nonlinearities at microscopic level is the modification of the network geometry, the obtained constitutive law at the mesoscopic level is a nonlinear relation between stress and strain.

A dedicated code has been constructed to solve the nodal kinematical unknowns (displacements) of each beam within the repetitive unit cell, which defines the so-called localization problem that has to be solved at each new increment. The code is written in symbolic language and it uses an input file including the initial reference unit cell topology and the mechanical properties of the structural elements (treated as Timoshenko beams); it delivers as an output the homogenized mechanical response in both the linear and nonlinear regimes (for different kinematic loadings imposed over the repetitive unit cell), from which the tangent effective moduli can be extracted.

Box 1 Algorithm for the nonlinear discrete homogenization of repetitive lattices

For each increment n, impose the Lagrangian strain tensor $\Delta \mathbf{E}_{Gn}^{(k)}$ applied over the unit cell boundary;

For each iteration k:

1. Initialization: compute the effective mechanical properties in the linear regime based on discrete homogenization in the linear framework [1, 5].

2. Compute the incremental Second Piola-Kirchhoff stress tensor [14, 15], based on the tangent stiffness matrix $K_{T,n}$

$$\Delta \mathbf{S}_n^{(k)} = K_{T,n} : \Delta \mathbf{E}_{Gn}^{(k)}$$

3. If convergence is reached, go to next step, otherwise loop again.
4. Update Cauchy stress at increment $(n+1)$ by a push-forward of the Lagrangian stress from configurations Ω_n to Ω_{n+1}

$$\boldsymbol{\sigma}_{n+1}^{(k)} = J_n^{-1} \mathbf{F}_n \cdot \left\{ \mathbf{S}_n^{(k)} + \Delta \mathbf{S}_n^{(k)} \right\} \cdot \mathbf{F}_n^T = \underbrace{\left(J_n^{-1} \mathbf{F}_n \cdot \mathbf{S}_n^{(k)} \cdot \mathbf{F}_n^T \right)}_{\boldsymbol{\sigma}_n^{(k)}} + \underbrace{\left(J_n^{-1} \mathbf{F}_n \cdot \left(\Delta \mathbf{S}_n^{(k)} \right) \cdot \mathbf{F}_n^T \right)}_{\Delta \boldsymbol{\sigma}_n^{(k)}}$$

5. Update the network configuration from Ω_n to Ω_{n+1}.
6. Repeat steps 1–5 up to the maximum applied strain over the unit cell.

Since the DH method is predictive, it can be conceived as a virtual testing method (instead of doing real measurements, which can be costly) to provide a database of uniaxial loading response to identify a strain energy density for an assumed hyperelastic effective homogeneous material.

9.3 Identification of a Hyperelastic Strain Energy Density for the Hexagonal Lattice, the Re-entrant Lattice and Plain Weave Textile

We shall calibrate a strain energy function of two preselected hyperelastic models for the three investigated lattices (Fig. 9.1), considering the 1D context of microstructured beams operating under pure tensile loadings, as pictured in Fig. 9.1.

In such situations, the sole kinematic degree of freedom is the scalar displacement along the beam, variable $u(x)$, with a spatial gradient denoted by the scalar quantity $u_{,x}$ (the comma denotes the partial derivative).

We use in the sequel the following microstrucrural geometrical and mechanical parameters for the three considered microstructures. The hexagonal reentrant lattice is one the most known and studied auxetic lattice in the literature, since the work of Gibson and Ashby in the late eighties. The re-entrant lattice geometry we adopt is based on three beams (Fig. 9.2): beams b2 and b3 have a negative angle with respect to the horizontal line ($\theta = -15°$, Fig. 9.1b). The geometrical parameters and material properties for plain weave and twill are given in Tables 9.1 and 9.2.

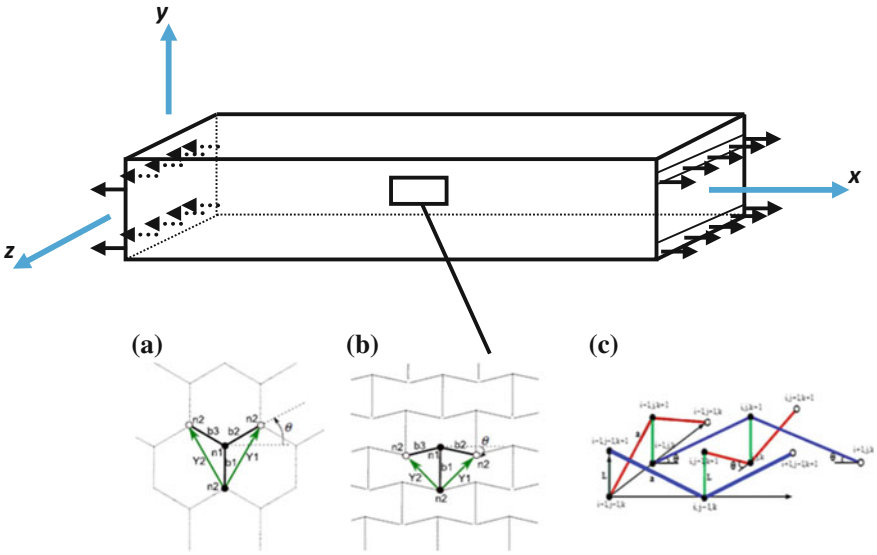

Fig. 9.1 Configuration of 1D micro-structured beams including either of the three investigated lattices: **a** classical hexagonal lattice, **b** re-entrant hexagonal lattice and **c** textile plane weave

Mechanical properties of weft and warp made of PET are given in Table 9.2; we intentionally choose very different moduli to represent an unbalanced fabric, leading to an expected anisotropic behavior.

The tensile, flexural, and torsion rigidities of the beam segments resulting from the weft and warp moduli are given in Table 9.3.

The following two forms of the hyperelastic function $W = W(F)$ are selected, depending upon the transformation gradient $F = 1 + u_{,x}$ in the present 1D situation, representative of classical elastic Cauchy materials, which are coined Form 1 and Form 2 here and in the sequel:

- Form 1: The strain energy density takes the folllowing quartic expression in the deformation form [24]

$$W = Au_{,x} + B\frac{(u_{,x})^2}{2} + C\frac{(u_{,x})^4}{4}$$

- Form 2: The strain energy density takes the cubic expression of the deformation form (we use the same notation for the material coefficients as for previous form of the strain energy density)

$$W = Au_{,x} + B\frac{(u_{,x})^2}{2} + C\frac{(u_{,x})^3}{3}$$

The coefficients (A, B, C) therein are microstructure dependent material coefficients that shall be identified in the sequel. Note that the coefficients A,B and C may

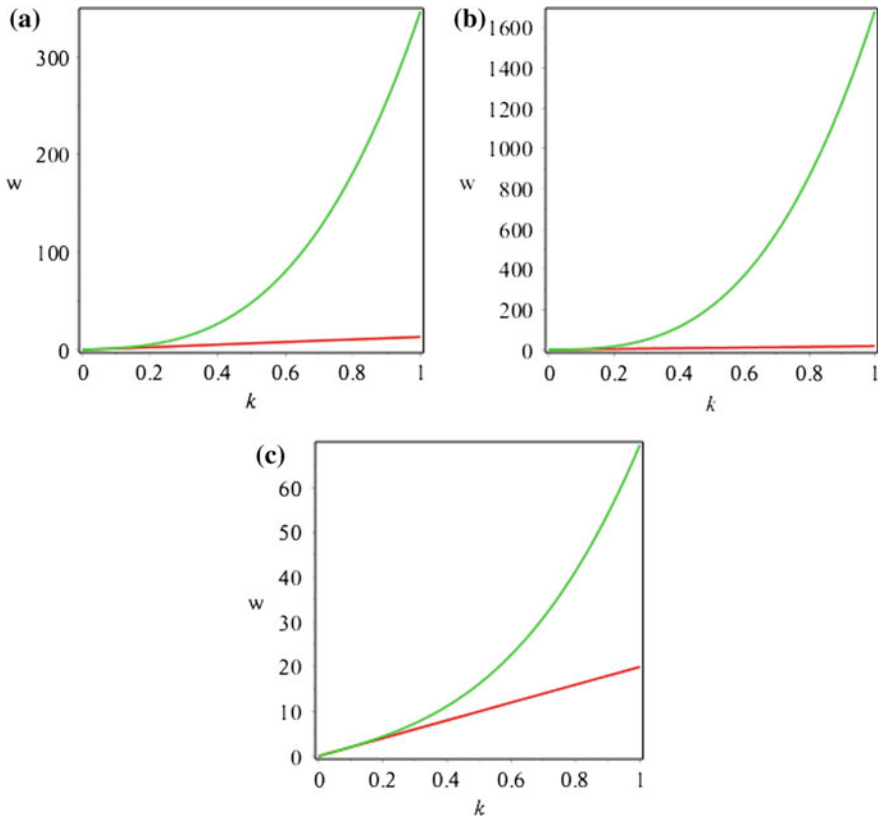

Fig. 9.2 Linear (red) and nonlinear (green) dispersion curves for **a** the hexagonal network, **b** the re-entrant network and **c** the textile plane weave

Table 9.1 Plain weave fabric configuration parameter

Plain weave	Set of input geometric data				
	Weft	Lf1 = 0.618 mm	–	θf = 40°	df = 0.27 mm
	Warp	Lp1 = 0.56 mm	–	θp = 40°	dp = 0.25 mm

Table 9.2 Elastic properties of weft and warp yarns

Set of input material data			
Weft	E_{sf} = 1889 MPa	G_{sf} = 756 MPa	$\nu_f = 0.25$
Warp	E_{sp} = 13,853 MPa	G_{sp} = 5541 MPa	$\nu_p = 0.25$

differ in respective expressions Form 1 and Form 2, but we nevertheless use the same notations for the material coefficients.

The successive higher order powers of the displacement gradients can be conceived as an enrichment of the constitutive law to account for higher order

Table 9.3 Mechanical properties of weft and warp

Beam rigidity	Beams at	
	Weft	Warp
Tensile rigidity	$k_{lf_{1,2}} = \frac{E_{sf}A_f}{L_{f_{1,2}}}$	$k_{lp_{1,2}} = \frac{E_{sp}A_p}{L_{p_{1,2}}}$
Flexural rigidity	$k_{tf1} = \frac{12E_{sf}I_f}{\left(L_{f1}\right)^3}$	$k_{tp1} = \frac{12E_{sp}I_p}{\left(L_{p1}\right)^3}$
Torsional fi	$k_{rf1} = \frac{G_{sf}J_f}{L_{f1}}$	$k_{rp1} = \frac{G_{sp}J_p}{L_{p1}}$

nonlinearities that are activated depending on the intensity of the applied loading. Restricting the energy density to a quadratic expansion clearly would correspond to a linear elastic material. Since the reference configuration can be selected such that the stress is nil, it implies that the coefficient A can be discarded.

Note that there is no unique choice of the mesoscopic (homogenized) constitutive law; observe further that the adopted choice of the strain energy density there above means that we restrict the mesoscopic stress to be at most a cubic function of its conjugated strain.

The constitutive law can be derived from the form taken by the strain energy density of the hyperelastic model; the first Piola-Kirchhoff stress is computed as the partial derivative of the strain energy density, thus it holds for the two forms of energy

$$T = \frac{\partial W}{\partial F} \Rightarrow \begin{cases} T = A + Bu_{,x} + C(u_{,x})^3 & \text{for Form 1} \\ T = A + Bu_{,x} + C(u_{,x}) & \text{for Form 2} \end{cases} \tag{9.1}$$

In the present 1D context, it holds the identity between the first Piola-Kirchhoff stress and Cauchy stress measure

$$T(x) = \sigma(x) \tag{9.2}$$

We shall in the sequel and as a matter of simplification of notations omit the x dependency. Note that the strain energy density can easily be expressed versus the stretch, due to the relation $\lambda = F$ in the present 1D context.

The material parameters are identified based on a combination of virtual tensile test performed over the unit cell of the three considered lattices; their identification proceeds from the minimization of the following function with respect to the set of material parameters A, B, C

$$\underset{\mathrm{A,B,C}}{\mathrm{Min}}\ \mathrm{T(A,\ B,\ C)}: = \left\{ \left\| \mathrm{T^{DH}} - \mathrm{T^{model}} \right\|^2 \right\}^{1/2} \tag{9.3}$$

The function T(A, B, C) there above is built as the quadratic measure of the error between the DH stress component $\mathrm{T^{DH}}$ and its analytical counterpart $\mathrm{T^{model}}$, obtained from one of the hyperelastic potential given there above.

The material constants of the model are identified from a least square method (9 sampling points are used), relying on uniaxial tension as the kinematic loading

Table 9.4 Coefficients in [MPa] of the two forms of the hyperelastic strain energy potential

	Form 1			Form 2		
	A	B	C	A	B	C
Hexagonal	−0.1	40.1	1469.3	0.0604	22.218	316.5386
Re-entrant	−0.4939	244.775	10220.08	0.0999	156.3594	1896.04
Plain weave	−0.0929	124.129	330.3384	0.0103	116.0903	101.9276

imposed over the lattice unit cell. The function Lsqcurve fit in the Optimization Toolbox of MATLAB has been used [14, 15] to identify the coefficients (A, B, C and D) of the strain energy density for these three lattices (Fig. 9.1) based on the incremental scheme developed in Sect. 9.2; they are listed in Table 9.4.

We shall in the next section rely on the two different selected forms of the strain energy density to analyze nonlinear wave propagation.

9.4 Analysis of Nonlinear Wave Propagation in the Homogenized Hyperelastic Continua

Different types of nonlinear wave propagation equations are considered in this work: harmonic plane waves based on the perturbation method [30], solitary waves for the Boussinesq type equation, and shock waves for Burger's equation [33].

We shall consider the following non-dimensional system parameters:

$k\,L$ the dimensionless wave number,

$\frac{\omega_0^L}{\sqrt{\frac{E}{\rho}}}$ the dimensionless frequency,

$\frac{c^p}{\sqrt{\frac{E}{\rho^*}}}$, $\frac{c^g}{\sqrt{\frac{E}{\rho^*}}}$ the dimensionless phase and group velocities respectively, built from the effective density ρ^*,

E, ρ, L the Young modulus, density and length of the beam structures respectively.

9.4.1 Wave Propagation Analysis for the Form 1 of the Hyperelastic Effective Medium Energy

Considering first Form 1 of the nonlinear strain energy, we can write the dynamical equilibrium equation as:

$$\left(\frac{\partial \sigma_{ij}}{\partial x_j}\right) = \rho^* \ddot{u}_j \tag{9.4}$$

Inserting the constitutive law into the dynamical equilibrium, Eq. 9.8, leads to

$$\left(\frac{\partial\left(A+Bu_{,x}+Cu_{,x}^{3}\right)}{\partial x}\right)=\rho^{*}\ddot{u}\Rightarrow\underbrace{\left(B\frac{\partial^{2}u}{\partial x^{2}}\right)}_{\text{Linear part}}+\underbrace{\left(3C\frac{\partial^{2}u}{\partial x^{2}}\left(\frac{\partial u}{\partial x}\right)^{2}\right)}_{\text{Non Linear part}}=\rho^{*}\ddot{u}\qquad(9.5)$$

The first step in the analysis of the nonlinear dispersion relation in the effective continuum medium is the introduction of the dimensionless time $\tau=\omega t$ (with ω the frequency) and the parameter ν to enforce the non-linearity in the dynamical equation, $\overline{C}=\upsilon C$, thus leading to the asymptotic expansion of frequency and axial displacement (here truncated to the first order), successively

$$\begin{aligned}\omega&=\omega_0+\upsilon\,\omega_1,\\ u&=u_0+\upsilon\,u_1,\end{aligned}\qquad(9.6)$$

Substituting those asymptotic developments (Eq. 9.6) into the nonlinear wave equation Eq. 9.8 and ordering versus the successive powers of the small parameter υ produces a set of equation as follows:

$$\begin{aligned}&O(\upsilon^{0}):\ B\tfrac{\partial^{2}u_0}{\partial x^{2}}-\rho^{*}\omega_0^{2}\tfrac{\partial^{2}u_0}{\partial\tau^{2}}=0\\ &O(\upsilon^{1}):\ B\tfrac{\partial^{2}u_1}{\partial x^{2}}-\rho^{*}\omega_0^{2}\tfrac{\partial^{2}u_1}{\partial\tau^{2}}=-2\rho_0^{*}\omega_0\omega_1\tfrac{\partial^{2}u_0}{\partial\tau^{2}}-3\overline{C}\tfrac{\partial^{2}u_0}{\partial x^{2}}\left(\tfrac{\partial u_0}{\partial x}\right)^{2}\end{aligned}\qquad(9.7)$$

The first order equation at order $O(\upsilon^0)$ describes linear wave propagation in the effective (linear) medium.

We take planar harmonic waves as a solution of the $O(\upsilon^0)$ equation:

$$u_0=A\ \exp i(\tau-kx)=A\ \cos(\tau-kx)\qquad(9.8)$$

in which k is the wavenumber and A the wave amplitude. Subsequent substitution of the expression of the wave solution into the $O(\upsilon^1)$ term results in the partial differential equation

$$O(\upsilon^{1}):\ B\frac{\partial^{2}u_1}{\partial x^{2}}-\rho^{*}\omega_0^{2}\frac{\partial^{2}u_1}{\partial\tau^{2}}=-2\rho^{*}\omega_0\omega_1 A\ \cos(kx-\tau)+\frac{3}{4}\overline{C}A^{3}k^{4}\ \cos(kx-\tau)\qquad(9.9)$$

Removing the secular terms (those in factor of $\cos(kx-\tau)$) leads to the algebraic equation

$$-2\rho^{*}\omega_0\omega_1 A+\frac{3}{4}CA^{3}k^{4}=0\Rightarrow\omega_1=\frac{3\,\overline{C}A^{2}k^{4}}{8\rho^{*}\omega_0}\qquad(9.10)$$

where ω_1 is the corrected frequency based on the nonlinear terms. The frequency is then updated versus the wave amplitude as follows:

$$\omega = \omega_0 + \frac{3\,CA^2k^4}{8\rho^*\,\omega_0} \tag{9.11}$$

The dispersion relation for the three investigated lattices involves an amplitude-dependent frequency in the context of a nonlinear effective medium, based on Eq. 9.11.

Figure 9.2 illustrates the dispersion relation based on Eq. 9.11 for the classical and reentrant hexagonal networks and the textile plane weave structure. Dispersion shifts occur for the longitudinal wave through the introduction of the nonlinear parts represented by the corrected frequency ω_1 this behavior is observed for the three investigated lattices.

9.4.2 Wave Propagation Analysis for Form 2 of the Hyperelastic Energy

Recall that the strain energy density is selected as a cubic function of the linearized strain

$$W = Au_{,x} + B\frac{(u_{,x})^2}{2} + C\frac{(u_{,x})^3}{3} \tag{9.12}$$

which entails the following expression of Cauchy stress

$$\sigma = A + Bu_{,x} + Cu_{,x}^2 \tag{9.13}$$

The dynamical equilibrium equation based on this constitutive law writes:

$$\left(\frac{\partial\left(A + Bu_{,x} + Cu_{,x}^2\right)}{\partial x}\right) = \rho^*\ddot{u} \Rightarrow \underbrace{\left(B\frac{\partial^2 u}{\partial x^2}\right)}_{\text{Linear part}} + \underbrace{\left(3C\frac{\partial^2 u}{\partial x^2}\left(\frac{\partial u}{\partial x}\right)\right)}_{\text{Non Linear part}} = \rho^*\ddot{u} \tag{9.14}$$

Note that for this type of equation, harmonic plane waves cannot be considered as solutions, due to the non-vanishing secular term.

Using the change of variable $y = x - \frac{\omega}{k}t$ and $f = \frac{\partial u}{\partial y}$ and after a simple transformation, Eq. (9.14) writes as follows:

$$\underbrace{\left(B\frac{\partial^2 u}{\partial y^2}\right)}_{\text{Linear part}} + \underbrace{\left(3C\frac{\partial^2 u}{\partial y^2}\left(\frac{\partial u}{\partial y}\right)\right)}_{\text{Non Linear part}} = \rho^*\left(\frac{\omega}{k}\right)^2\frac{\partial^2 u}{\partial y^2} \Rightarrow \left(\left(B - \rho^*\left(\frac{\omega}{k}\right)^2\right)\frac{\partial f}{\partial y}\right) + \left(3Cf\left(\frac{\partial f}{\partial y}\right)\right) = 0 \tag{9.15}$$

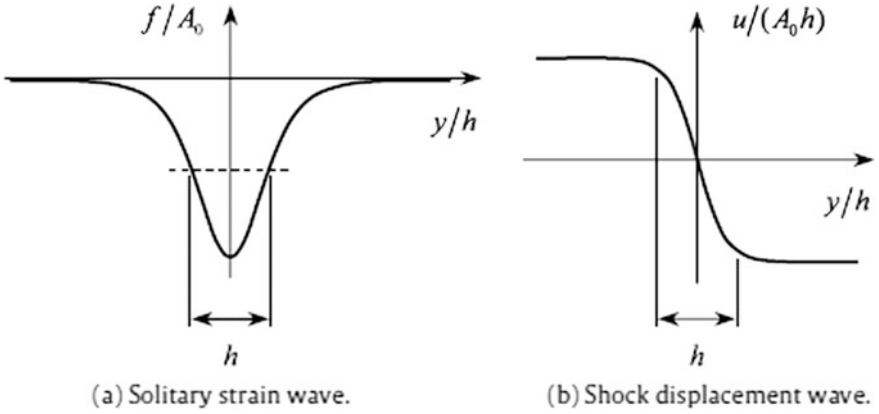

Fig. 9.3 **a** Shape of the solitary strain wave and **b** shock wave

Equation (9.15) is of inviscid Burger's type, a fundamental partial differential equation occurring in various areas of applied mathematics, such as fluid mechanics, nonlinear acoustics, gas dynamics, traffic flow. The inviscid Burgers' equation is a conservation equation, more generally a first order quasi-linear hyperbolic equation. Shock waves are solution of the above equation; mathematically, a shock wave type solution can be obtained by the integration of the solitary wave (Fig. 9.3).

The solution of the dynamical equilibrium equation can then be expressed in terms of the displacement as

$$u(y) = \int f(y)\, dy = \int \left(-\frac{A}{2} + \frac{A\, s^2}{2(1 - E(s)/K(s))} sn^2(h, s) \right) dy, \tag{9.16}$$

in which function f(y) describes solitary waves propagation and u(y) shock waves, where s is the universal constant describing the degree of nonlinearity $(0 \le s \le 1)$, sn(.) the elliptic Jacobin sine, and K(s), E(s) are the complete elliptic integrals of the first and second kind respectively, $h = \frac{k_0}{2} y$ and k_0 is the propagation constant related to the wavenumber k as follows:

$$k = \frac{\pi}{2\, K(s)} k_0 \tag{9.17}$$

The strain amplitude can be calculated from the following equation

$$3(1 - E(s)/K(s)) = \frac{-3CA}{k_0^2} \tag{9.18}$$

In the limiting case $s \to 0$ (which corresponds to the linear situation), the solution of Eq. (9.16) is reduced to the harmonic plane wave,

$$f(y) = -\frac{A}{2}\cos(ky) \to u = -\frac{A}{2k}\sin(ky), \quad \text{with } k = k_0$$

In the opposite case, when $s \to 1$, the solution (9.16) describes a localized solitary strain wave with

$$f(y) = -\frac{A}{2}\operatorname{sech}^2(k_0 y) \to u(y) = -\frac{A}{k_0}\tanh(k_0 y).$$

Compression solitary waves can exist for negative coefficients $A < 0$, whereas dilatation solitary waves (tension waves) will be obtained when $A > 0$. From the results, we expect based on the definition of shock waves the occurrence of a set of supersonic modes, describing the propagation of waves with a velocity higher than the linear velocity (the velocity of non-dispersive waves); this phenomenon can indeed be observed in Fig. 9.4 for the three investigated lattices. When moving

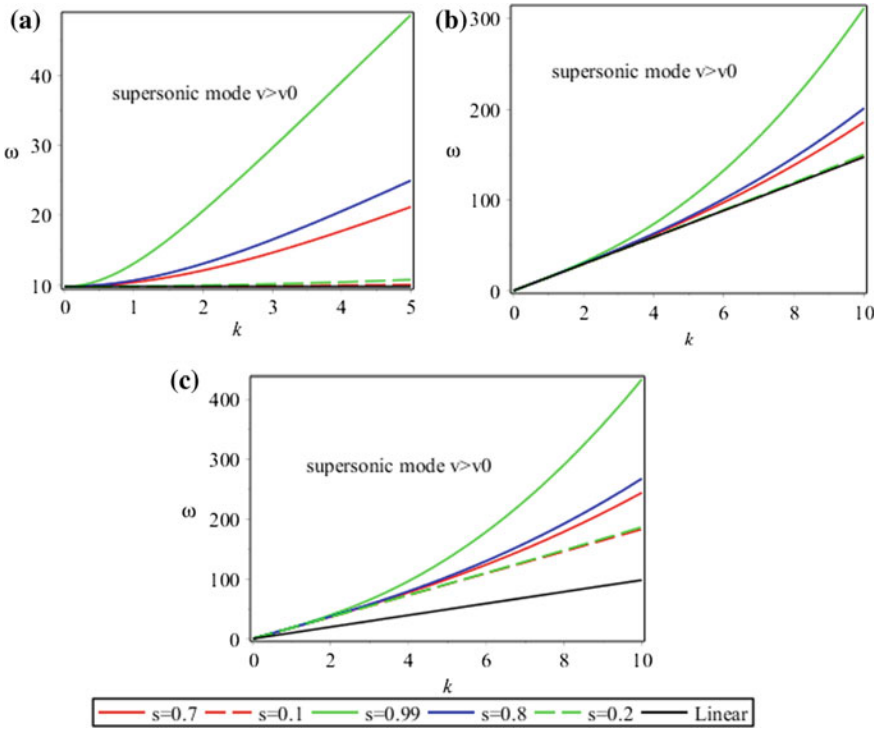

Fig. 9.4 Dispersion relation with different values of parameter s based on Burger's equation for **a** the hexagonal lattice, **b** the re-entrant lattice and, **c** textile plane weave

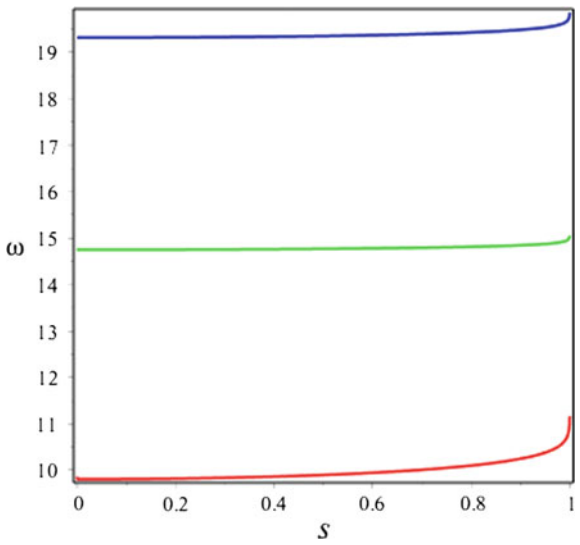

Fig. 9.5 Frequency band structure versus the degree of nonlinearity (parameter s) for the hexagonal lattice (in red), the re-entrant lattice (in green) and textile plane weave (in blue)

from a weak nonlinearity (for low values of s) to a high nonlinearity (at high values of s), an important shift in the frequency band structure occurs. The influence of the nonlinearity is more pronounced for the hexagonal lattice and the textile structure in comparison to the re-entrant lattice, due to the presence of a large partial band gap between the linear mode and the nonlinear modes in these two configurations.

Figure 9.5 shows the frequency for the supersonic longitudinal mode for the three lattices versus the degree of nonlinearity s. It appears from Fig. 9.5 that for all values of parameter s between 0 and 1, the supersonic mode always occurs; these results are in very good arguments with those obtained in Fig. 9.4.

9.5 Conclusion

We analyze in this contribution nonlinear wave propagation occurring within microstructured beams including a repetitive network material undergoing configuration changes under pure tensile loadings, leading to geometrical nonlinearities. Three types of repetitive microstructures have been considered in order to exemplify the analysis of (nonlinear) wave propagation: the hexagonal network, its re-entrant version, and plain wave textile.

The effective nonlinear constitutive law has been identified from a micromechanical scheme in terms of the strain energy density expressed as a nonlinear function of the small strain tensor; first order grade 1D homogenized continuum have been thereby identified in the nonlinear range, based on a strain driven

incremental scheme written over a reference unit cell taking into account the variation of the lattice geometry. The coefficients of the selected constitutive models have been identified for three specific network materials based on the proposed homogenization scheme.

The dynamical equations of motion have been next written for two different Forms of the constitutive law - successively discarding and including second order terms - originating from the selected strain energy density, leading to specific dispersion relations. The inviscid Burgers equation is obtained as a specific wave propagation equation for the first order effective continuum, whereas a perturbation method was used for the second form of energy density.

The generalization of such nonlinear wave propagation analyses to 2D situations will be performed in future work, based on suitable hyperelastic constitutive laws obtained from the homogenization of the existing microstructure.

References

1. Goda, I., Assidi, M., Ganghoffer, J.F.: Equivalent mechanical properties of textile monolayers from discrete asymptotic homogenization. J. Mech. Phys. Solids **61**, 2537–2565 (2013)
2. Goda, I., Ganghoffer, J.F.: Construction of first and second order grade anisotropic continuum media for 3D porous and textile composite structures. Compos. Struct. **141**(141), 292–327 (2016)
3. Dos Reis, F., Ganghoffer, J.F.: Equivalent mechanical properties of auxetic lattices from discrete homogenization. Comput. Mater. Sci. **51**, 314–321 (2012)
4. Raoult, A., Caillerie, D., Mourad, A.: Elastic lattices: equilibrium, invariant laws and homogenization. Ann. Univ. Ferrara **54**, 297–318 (2008)
5. Dos Reis, F., Ganghoffer, J.F.: Construction of micropolar continua from the asymptotic homogenization of beam lattices. Comput. Struct. **112–113**, 354–363 (2012)
6. Warren, W.E., Kraynik, A.M., Stone, C.M.: A constitutive model for two-dimensional nonlinear elastic foams. J. Mech. Phys. Solids **37**, 717–733 (1989)
7. Warren, W.E., Kraynik, A.M.: The nonlinear elastic behaviour of open-cell foams. Trans. ASME **58**, 375–381 (1991)
8. Wang, Y., Cuitino, A.M.: Three-dimensional nonlinear open cell foams with large deformations. J. Mech. Phys. Solids **48**, 961–988 (2000)
9. Hohe, J., Becker, W.: Effective mechanical behavior of hyperelastic honeycombs and two dimensional model foams at finite strain. Int. J. Mech. Sci. **45**, 891–913 (2003)
10. Janus-Michalska, M., Pęcherski, R.P.: Macroscopic properties of open-cell foams based on micromechanical modeling. Tech. Mech. Band, **23**(Heft, 2–4), 221–231 (2003)
11. Janus-Michalska, J.: Effective models describing elastic behavior of cellular materials. Arch. Metall. Mater. **50**, 595–608 (2005)
12. Janus-Michalska, J.: Hyperelastic behavior of cellular structures based on micromechanical modeling at small strain. Arch. Mech. **63**(1), 3–23 (2011)
13. Vigliotti, A., Deshpande, V.S., Pasini, D.: Nonlinear constitutive models for lattice materials. J. Mech. Phys. Solids **64**, 44–60 (2014)
14. El Nady, K., Ganghoffer, J.F.: Computation of the effective mechanical response of biological networks accounting for large configuration changes. J. Mech. Behave. Biomed. Mat. **58**, 28–44 (2015)

15. El Nady, K., Goda, I., Ganghoffer, J.F.: Computation of the effective nonlinear mechanical response of lattice materials considering geometrical nonlinearities. Comput. Mech. **58**, 1–23 (2016)
16. Langley, R.S.: The response of two dimensional periodic structures to point harmonic forcing. J. Sound Vib. **197**, 447–469 (1996)
17. Phani, A.S., Woodhouse, J., Fleck, N.A.: Wave propagation in two-dimensional periodic lattices. J. Acoust. Soc. Am. **119**, 1995–2005 (2006)
18. Gonella, S., Ruzzene, M.: Analysis of in-plane wave propagation in hexagonal and re-entrant lattices. J. Sound Vib. **312**, 125–139 (2008)
19. Reda, H., Rahali, Y., Ganghoffer, J.F., Lakiss, H.: Wave propagation in 3D viscoelastic auxetic and textile materials by homogenized continuum micropolar models. Compos. Struct. **141**, 328–345 (2016)
20. Bhatnagar, P.L.: Nonlinear Waves in One-dimensional Dispersive Systems. Clarendon Press, Oxford (1979)
21. Ogden, R.W., Roxburgh, D.G.: The effect of pre-stress on the vibration and stability of elastic plates. Int. J. Eng. Sci. **31**, 1611–1639 (1993)
22. Norris, A.N.: Finite amplitude waves in solids. In: Hamilton, M.F., Blackstock, D.T. (eds.) Nonlinear Acoustics, pp. 263–277. Academic Press, San Diego (1998)
23. Porubov, A.: Amplification of Nonlinear Strain Waves in Solids, vol. 9. World Scientific (2003)
24. Reda, H., Rahali, Y., Ganghoffer, J.F., Lakiss, H.: Wave propagation analysis in 2D nonlinear hexagonal periodic networks based on second order gradient nonlinear constitutive models. Int. J. Nonlinear Mech. **87**, 85–96 (2016)
25. Russell, J.S.: Report on waves. In: Fourteenth Meeting of the British Association for the Advancement of Science (1844)
26. Boussinesq, J.: Théorie des ondes et des remous qui se propagent le long d'un canal rectangulaire horizontal, en communiquant au liquide contenu dans ce canal des vitesses sensiblement pareilles de la surface au fond. J. Math. Pures Appl. Deuxième Série **17**, 55–108 (1872)
27. Korteweg, D.J., Vries, G.D.: On the change of form of long waves ad-vancing in a rectangular canal, and on a new type of long stationary waves. Phil. Mag. **39**, 422–443 (1985)
28. Benjamin, B., Bona, J.L., Mahony, J.J.: Model equations for long waves in nonlinear dispersive systems. Philos. Trans. Roy. Soc. London **272**, 47–78 (1972)
29. Camassa, R., Holm, D.D.: An integrable shallow water equation with peaked solitons. Phys. Rev. Lett. **71**, 1661–1664 (1993)
30. Manktelow, L.K., Narisetti, R.K., Leamy, J.M., Ruzzene, M.: Finite-element based perturbation analysis of wave propagation in nonlinear periodic structures. Mech. Syst. Signal Process. **39**, 32–46 (2013)
31. Maradudin, A.A.: Nonequilibrium Phonon Dynamics. Bron, W.E. (ed.), p. 395. Plenum, New York (1985)
32. Hao, Y., Singhsomroje, W., Maris, H.J.: Phys. B **316–317**, 147–149 (2002)
33. Reda, H., Rahali, Y., Ganghoffer, J.F., Lakiss, H.: Nonlinear dynamical analysis of 3D textiles based on second gradient homogenized media. Compos. Struct. **154**, 538–555 (2016)

Chapter 10
Multiscale Modeling of 2D Material MoS_2 from Molecular Dynamics to Continuum Mechanics

Kerlin P. Robert, Jiaoyan Li and James D. Lee

Abstract Research on two dimensional (2D) materials, such as Graphene and Molybdenum disulfide (MoS_2), now involves thousands of researchers worldwide, implementing cutting edge technology to study them. Due to the extraordinary properties of 2D materials, research extends from fundamental science to novel applications of 2D materials. This work introduces atomistic simulation methodologies, based on interatomic potential, as a tool to unveil the mechanical and thermal properties at nanoscale of MoS_2, a material that has attracted most research interests among all 2D materials. Young's modulus, Poison's ratio, heat conductivity and heat capacity at atomic scale are studied. These findings lend compelling insights into the atomistic mechanism of MoS_2. Then, based on these useful information, we perform concurrent multiscale modeling of MoS_2 from molecular dynamics simulation in atomic region to finite element analysis in continuum region.

10.1 Introduction

Free-standing 2D crystals were believed to be unstable at nonzero temperatures [10]. This point of view has been disproved since Geim and his colleague discovered a simple but novel method to isolate single atomic layers of graphene from graphite [7]. Since then, 2D materials are being heavily studied due to many valuable properties they exhibit. MoS_2, a 2D dichalcogenide, that has attracted a

K. P. Robert · J. D. Lee (✉)
Department of Mechanical and Aerospace Engineering,
The George Washington University, Washington, DC 20052, USA
e-mail: jdlee@gwu.edu

K. P. Robert
e-mail: kerlinrobert@gwu.edu

J. Li
School of Engineering, Brown University, Providence, RI 02860, USA
e-mail: jiaoyan_li@brown.edu

H. Altenbach et al. (eds.), *Generalized Models and Non-classical Approaches in Complex Materials 2*, Advanced Structured Materials 90,
https://doi.org/10.1007/978-3-319-77504-3_10

great deal of attention recently because of its unique properties in electronic and optoelectronic applications, is the core material studied in our paper. Due to its layered structure, low coefficient of friction and reactivity, it is widely used as a solid lubricant and hydrodesulfurization catalyst. MoS_2 has been attracting plentiful research interests in order to overcome the shortage of graphene and broadening the range of applications of 2D materials.

From an engineering point of view, understanding the material properties of 2D materials under various conditions is crucial for tailoring the electrical and mechanical properties of 2D-material-based devices at nanoscale. Even at nanoscale, molecular systems typically consist of a vast number of atoms. Molecular dynamics (MD) simulations enable us to understand the assemblies of molecules in a structure, and the microscopic interactions between them. In the microscopic region where critical physical phenomena occur we perform MD and solve for the atomistic trajectory of the atoms using the velocity verlet method. This theoretical model of classical MD provides a solid foundation for our bottom-up sequential multiscale modeling, through which we obtained material properties including the elastic constants, thermal conductivity, specific heat, and thermal expansion coefficients for thermoelasticity of MoS_2. We then perform concurrent multiscale modeling from MD to thermoelasticity for MoS_2. Lee et al. [11] performed similar multiscale modeling for graphene.

10.2 Crystal Structure and Interatomic Potential of MoS_2

MoS_2 identifies as a hexagonal crystal system where the layer of Mo is sandwiched between two layers of S. The crystal structure of MoS_2 can be described as follows: each primitive cell has three atoms with position vectors: one Mo atom at $(0, 0, 0)$, and two S atoms at $(0, \frac{c^1}{\sqrt{3}}, \pm c^2)$. The three base vectors are: $(c^1, 0, 0)$, $(-\frac{1}{2}c^1, \frac{\sqrt{3}}{2}c^1, 0)$ and $(0, 0, 2c^2 + c^3)$, where $c^1 = 0.316$ nm, $c^2 = \left[0.242^2 - (c^1)^2/3\right]^{1/2}$ nm, and $c^3 = 0.350$ nm (Fig. 10.1).

Within a 2D layer of MoS_2 the major interaction is due to the covalent bonds between atoms. In our case the weak van-der Waals forces acting between two layers of MoS_2, which is only found in a bulk system, can be ignored. That being said, we incorporate the two-body and three-body Stillinger-Weber (SW) potential based on covalent bonding, developed by Jiang et al. [9], in our MD simulation of Mo-S system. This potential is able to yield good agreements with experimental observations and Density Functional Theory (DFT) calculations on structure and energetics of Mo molecules, 2D Mo structures, 3D Mo Crystals, S molecules, and Mo-S binary crystal structures. The SW potential treats the bond bending by a

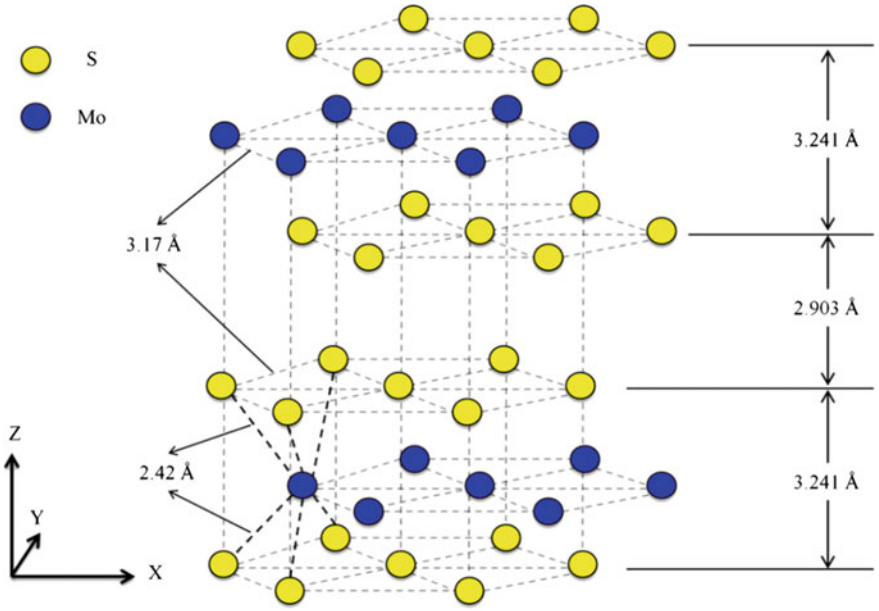

Fig. 10.1 Crystal structure of MoS_2. Schematic shows Mo-Mo, S-S, Mo-S bond distances and S-S planar distances [17]

two-body interaction, while the angle bending is described by a three-body interaction. The total potential energy within a system of N atoms is

$$V = \sum_{i<j} V_2(i,j) + \sum_{i<j<k} V_3(i,j,k), \tag{10.1}$$

where

$$V_2 = \varepsilon A\left(B\sigma^p r_{ij}^{-p} - \sigma^q r_{ij}^{-q}\right) \exp\left[\sigma\left(r_{ij} - a\sigma\right)^{-1}\right], \tag{10.2}$$

$$V_3 = \varepsilon\lambda \exp\left[\gamma\sigma\left(r_{ij} - a\sigma\right)^{-1} + \gamma\sigma\left(r_{ik} - a\sigma\right)^{-1}\right]\left(\cos\,\theta_{jik} - \cos\,\theta_0\right)^2. \tag{10.3}$$

Then the interatomic forces acting on *atom i*, *atom j*, and *atom k* can be simply obtained as

$$\mathbf{f}_i = -\frac{\partial V}{\partial \mathbf{r}_i}, \quad \mathbf{f}_j = -\frac{\partial V}{\partial \mathbf{r}_j}, \quad \mathbf{f}_k = -\frac{\partial V}{\partial \mathbf{r}_k}. \tag{10.4}$$

10.3 Molecular Dynamics

MD was first introduced by Alder and Wainwright [1, 2] to study the interactions of hard spheres. Rahman [16] carried out the first simulation using a realistic potential for liquid argon. The first MD simulation of a realistic system was done by Stillinger and Rahman [18] for liquid water. MD simulations enable us to study 2D materials in the nanometer scale with over a million molecules. In classical MD the trajectories of atoms are then determined by the Newton's law

$$m^i \dot{\mathbf{v}}^i = \mathbf{f}^i + \boldsymbol{\varphi}^i, \quad i = [1, 2, 3, \ldots, N], \tag{10.5}$$

where N is the total number of atoms in the system, i.e. including Mo and S atoms; m^i, $\dot{\mathbf{v}}^i$, and $\mathbf{f}^i$ are the mass, acceleration, and interatomic force of *atom i*, respectively; $\boldsymbol{\varphi}^i$ represents forces other than interatomic force acting on *atom i*, i.e. $\boldsymbol{\varphi}^i$ could be any combination of applied force, body force including Lorentz force, fictitious force due to the translation and rotation of the coordinate system, and thermal force due to the presence of thermostat.

A detailed formulation of Maxwell's equations and Lorentz force at atomistic level was given by de Groot and Suttorp [5]. For non-relativistic electromagnetics, $\boldsymbol{\varphi}^i$ was obtained

$$\boldsymbol{\varphi}^i = q^i \{\mathbf{E}^e + c^{-1} \mathbf{v}^i \times \mathbf{B}^e\} + \sum_{j=1, j\neq i}^{N} q^i q^j \frac{\mathbf{r}^{ij}}{(r^{ij})^3}, \tag{10.6}$$

where q^i is the electric charge of *atom i*; $\mathbf{E}^e$ and $\mathbf{B}^e$ are the external electric and magnetic fields, respectively; c is the speed of light; $\mathbf{r}^{ij} \equiv \mathbf{r}^i - \mathbf{r}^j$; $r^{ij} \equiv \|\mathbf{r}^{ij}\|$. It is seen that the last term on the right-hand side of Eq. (10.6) is the Coulomb forces between *atom i* and *atom j*. It is worthwhile to note that, due to the non-relativistic approximation, i.e., $\|\mathbf{v}^i\| << c$, the Lorentz force exists only between charged atoms and the external $\mathbf{E}^e$ and $\mathbf{B}^e$ fields; between charged atoms themselves only Coulomb forces exist.

It is noticed that, in MD simulation, temperature is a dependent variable. Usually, but not correctly, it was expressed as

$$T = \frac{\sum_{i=1}^{N} m^i (\mathbf{v}^i \cdot \mathbf{v}^i)}{N_{dof} k_B}, \tag{10.7}$$

where N_{dof} is the number of degrees of freedom of the system; k_B is the Boltzmann constant.

Temperature Control: Nosé-Hoover Thermostat

The revolutionary Nosé-Hoover dynamics, originally introduced by Nosé [14, 15] and developed further by Hoover [8], modified Newtonian dynamics so as to

reproduce canonical and isobaric-isothermal ensemble equilibrium systems. However, there is an increasing interest in conducting MD simulations which do not fall within the classification of these classical ensembles. Li and Lee [12] pointed out the need to reformulate the Nosé-Hoover thermostat to locally regulate the temperatures at many distinct regions without introducing the unphysical linear and angular momenta. In this way, the trajectories of atoms and molecules can be generated more rigorously and accurately by Non-equilibrium Molecular Dynamic (NEMD) simulations.

After the reformulation, we define the ***Nose-Hoover thermal velocity*** as

$$\tilde{\mathbf{v}}^i \equiv \mathbf{v}^i - \bar{\mathbf{v}} - \boldsymbol{\eta}^i, \tag{10.8}$$

where $\bar{\mathbf{v}}$ is the average velocity of a group of atoms in question; $\boldsymbol{\eta}^i = \boldsymbol{\omega} \times \tilde{\mathbf{r}}^i$; $\boldsymbol{\omega}$ is the angular velocity; $\tilde{\mathbf{r}}^i$ is the relative position vector of *atom i* in the group considered. Now, the temperature of *group g* is calculated as

$$T_g = \frac{1}{N_g^{dof} k_B} \sum_{i=1}^{n_g} m^i \tilde{\mathbf{v}}^i \cdot \tilde{\mathbf{v}}^i, \tag{10.9}$$

where $N_g^{dof} = 3n_g - 6$ is the number of degrees of freedom of *group g*. One may readily prove that rigid body translation and rotation have no contribution to the temperature [11]. The subtraction of 6 from $3n_g$ is due to the elimination of linear and angular momenta from the velocity field in the calculation of the Nose-Hoover thermal velocity.

The governing equations for a material system with ***upgraded Nosé-Hoover Thermostats*** should now be expressed as

$$m^i \dot{\mathbf{v}}^i = \mathbf{f}^i + \boldsymbol{\varphi}^i - \chi_g m^i \tilde{\mathbf{v}}^i, \quad i \in group\ g, \tag{10.10}$$

where $-\chi_g m^i \tilde{\mathbf{v}}^i$ is named as ***Nosé-Hoover temperature force***. The role of χ_g is similar to damping coefficient, except that χ_g is not a constant—instead it is governed by

$$\dot{\chi}_g = \frac{1}{\tau_g^2 T_g^o}(T_g - T_g^o), \tag{10.11}$$

where τ_g is a specified time constant associated with *group g*; T_g^o is the target temperature of the Nose-Hoover thermostat. It is noticed that if *group g* doesn't have a thermostat, then it is a special case with $\chi_g = \dot{\chi}_g = 0$. From now on, if there is no ambiguity, we use the general case for description and derivation.

The ***Hamiltonian*** of the entire system can be generalized as,

$$H = \sum_{g=1}^{N_g} \sum_{i \in g} \left\{ \frac{1}{2} m^i \mathbf{v}^i \cdot \mathbf{v}^i - \int_0^t \boldsymbol{\varphi}^i(s) \cdot \mathbf{v}^i(s) ds \right\} + \sum_{g=1}^{N_g} \left\{ \frac{1}{2} Q_g \chi_g^2 + \frac{Q_g}{\tau_g^2} \int_0^t \chi_g(s) ds \right\} + V(\mathbf{r}^1, \mathbf{r}^2, \mathbf{r}^3, \ldots, \mathbf{r}^N), \tag{10.12}$$

where V is the total interatomic potential energy of the entire system, and

$$Q_g \equiv N_g^{dof} k_B T_g^o \tau_g^2. \tag{10.13}$$

It is seen that the Hamiltonian, H, consists of four parts: (1) the kinetic energy which is the sum of kinetic energies of all atoms, i.e., $\frac{1}{2} m^i \mathbf{v}^i \cdot \mathbf{v}^i (i = 1, 2, 3, \ldots, N)$, (2) the potential energy $U(\mathbf{r}^1, \mathbf{r}^2, \mathbf{r}^3, \ldots, \mathbf{r}^N)$, which in principle cannot be divided into a summation of subsets, (3) the work done by force $\boldsymbol{\varphi}^i \quad [i = 1, 2, 3, \ldots, N]$, and (4) the sum of thermal energy $E_g \quad [g = 1, 2, 3, \ldots, N_g]$ of all groups, where

$$E_g \equiv \left\{ \frac{1}{2} Q_g \chi_g^2 + \frac{Q_g}{\tau_g^2} \int_0^t \chi_g(s) ds \right\}. \tag{10.14}$$

One may also prove that the Hamiltonian is a constant. We also notice that

$$\dot{E}_g = N_g^{dof} k_B \chi_g T_g. \tag{10.15}$$

Actually $\dot{E}_g$ is the flow of energy per unit time out of *group g* due to the action of Nosé-Hoover thermostat.

10.4 Thermoelasticity and Sequential Multiscale Modeling

10.4.1 Governing Equations of Thermoelasticity

In small-strain thermoelasticity (a branch of continuum mechanics), the relevant balance laws and constitutive equations may be expressed as [3, 4, 6]:

$$\rho^o \dot{\mathbf{v}} = \nabla \cdot \boldsymbol{\sigma} + \rho^o \boldsymbol{\varphi}, \tag{10.16}$$

$$\rho^o \dot{e} - \boldsymbol{\sigma} : \nabla \mathbf{v} + \nabla \cdot \mathbf{q} - \rho^o h = 0, \tag{10.17}$$

$$\sigma_{ij} = -\beta_{ij}(T - T^{ref}) + A_{ijkl}e_{kl}, \tag{10.18}$$

$$\rho^o \dot{e} = \rho^o \gamma \dot{T} + A_{ijkl}e_{ij}\dot{e}_{kl}, \tag{10.19}$$

$$q_i = -\kappa_{ij}T_{,j}, \tag{10.20}$$

where ρ^o is the mass density in the reference state; $\mathbf{u}$ is the displacement vector and $\mathbf{v} = \dot{\mathbf{u}}$ is the velocity vector; $\boldsymbol{\sigma}$ is the Cauchy stress tensor; e is the internal energy density; $\mathbf{q}$ is the heat flux; T is the absolute temperature; T^{ref} is the reference temperature; $\mathbf{e}$ is the strain tensor, i.e. $(e_{ij} \approx (u_{i,j} + u_{j,i})/2)$; $\boldsymbol{\beta}$ is named as the thermal expansion coefficients; $\mathbf{A}$ are the elastic constants; $\boldsymbol{\kappa}$ is the thermal conductivity; γ is the specific heat; $\boldsymbol{\varphi}$ is the body force per unit mass. Notice that, in thermoelasticity, the Cauchy stress is derivable from a scalar-valued Helmholtz free energy density function; stress tensor and strain tensor are both symmetric. Therefore, one has

$$\beta_{ij} = \beta_{ji}, \quad A_{ijkl} = A_{jikl} = A_{ijlk} = A_{klij}. \tag{10.21}$$

It is emphasized that in continuum mechanics (CM), temperature is an independent variable. Therefore an energy equation, Eq. (10.17) is needed. On the contrary, ***Nosé-Hoover Thermostat*** is not needed—all one needs to do is to set temperature-specified boundary conditions. Of course, one may set heat-flux-specified boundary conditions too. Also, the temperature field and displacement field in CM are functions of spatial and temporal variables—that is why we see terms such as $\nabla \cdot \boldsymbol{\sigma}, \nabla \mathbf{u}, \nabla \mathbf{v}, \nabla \cdot \mathbf{q}$, and ∇T in Eqs. (10.16)–(10.20). From now on, we refer the temperature in continuum mechanics as continuum temperature, to distinguish it from atomistic temperature in molecular dynamics.

In finite element analysis, relate the displacement and temperature fields with their nodal values as

$$\begin{array}{ll} u_i = N_{i\alpha}U_\alpha, & e_{ij} = B_{ij\alpha}U_\alpha \\ T = N_\xi T_\xi, & T_{,k} = C_{k\xi}T_\xi \end{array}, \tag{10.22}$$

Then it is straightforward to obtain the dynamic finite element equations as

$$\mathbf{M}\ddot{\mathbf{U}} + \mathbf{K}\mathbf{U} = \mathbf{P}\mathbf{T} + \mathbf{F}^{\mathbf{1}} + \mathbf{F}^{\mathbf{2}}, \tag{10.23}$$

$$\mathbf{G}\dot{\mathbf{T}} + \mathbf{H}\mathbf{T} + T^{ref}\mathbf{P}^{\mathbf{T}}\dot{\mathbf{U}} = -\mathbf{Q}^1 + \mathbf{Q}^2. \tag{10.24}$$

The detailed expressions of $\mathbf{M}$, $\mathbf{K}$, $\mathbf{P}$, $\mathbf{G}$, $\mathbf{H}$, $\mathbf{F}^1$, $\mathbf{F}^2$, $\mathbf{Q}^1$, and $\mathbf{Q}^2$ are given by Lee et al. [11].

Now it is noticed that, if one has the values of $\mathbf{A}, \boldsymbol{\beta}, \boldsymbol{\kappa}$, and γ, then one may proceed to solve Eqs. (10.23), (10.24) for $\mathbf{U}(\mathbf{X}, t)$ and $T(\mathbf{X}, t)$. If further we can

obtain those material properties from ***molecular dynamics*** (MD) simulation, then this approach is named as a ***sequential multiscale modeling***.

10.4.2 Elastic Constants

In experimental works, the mechanical properties of 2D material nanosheets are usually measured by performing AFM nano-indentation. In theoretical works, there are several atomistic modeling and simulation tools, such as DFT, molecular mechanics (MM), and MD. MD simulations can realize a variety of loading cases, including nano-indentation, tension, compression, and bending, to calculate the Young's modules and Poisson's ratio. In Voigt's convention, one may rewrite Eq. 10.18 as

$$\begin{vmatrix}\sigma_{11}\\ \sigma_{22}\\ \sigma_{33}\\ \sigma_{23}\\ \sigma_{31}\\ \sigma_{12}\end{vmatrix} = -\begin{vmatrix}\beta_{11}\\ \beta_{22}\\ \beta_{33}\\ \beta_{23}\\ \beta_{31}\\ \beta_{12}\end{vmatrix}(T-T^{ref}) + \begin{vmatrix} A_{1111} & A_{1122} & A_{1133} & A_{1123} & A_{1131} & A_{1112}\\ A_{1122} & A_{2222} & A_{2233} & A_{2223} & A_{2231} & A_{2212}\\ A_{1133} & A_{2233} & A_{3333} & A_{3323} & A_{3331} & A_{3312}\\ A_{1123} & A_{2223} & A_{3323} & A_{2323} & A_{2331} & A_{2312}\\ A_{1131} & A_{2231} & A_{3331} & A_{2331} & A_{3131} & A_{3112}\\ A_{1112} & A_{2212} & A_{3312} & A_{2312} & A_{3112} & A_{1212}\end{vmatrix}\begin{vmatrix}e_{11}\\ e_{22}\\ e_{33}\\ \gamma_{23}\\ \gamma_{31}\\ \gamma_{12}\end{vmatrix}, \tag{10.25}$$

where $\gamma_{23}=2e_{23}$, $\gamma_{31}=2e_{31}$, $\gamma_{12}=2e_{12}$.

In simple strain problem, the deformation can be expressed as

$$\begin{vmatrix}x\\ y\\ z\end{vmatrix} = \begin{vmatrix}1+e_1 & \gamma_{12} & \gamma_{13}\\ \gamma_{21} & 1+e_2 & \gamma_{23}\\ \gamma_{31} & \gamma_{32} & 1+e_3\end{vmatrix}\begin{vmatrix}X\\ Y\\ Z\end{vmatrix} \quad \text{or} \quad x_k = F_{kK}X_K, \tag{10.26}$$

which implies the Green's deformation tensor, and Lagrangian strain tensor can be calculated as

$$C_{KL}=F_{kK}F_{kL}, \quad E_{KL}=(C_{KL}-\delta_{KL})/2. \tag{10.27}$$

From the Lagrangian strains one may obtain their approximate small-strain counter-parts. We employ SW potential to describe the interatomic interactions among atoms. The interatomic forces acting on atoms can be obtained as mentioned in Sect. 10.2. In MD simulation, let the whole specimen have N atoms. There are six independent simple strains that can be created, from which the position vectors, $\mathbf{r}^i\ i\in[1,2,3,\ldots.,N]$, of all atoms can be determined. Because these six cases are static cases, the virial stress tensor are reduced to

$$\mathbf{S} = -\frac{1}{\Omega}\sum_{i=1}^{N}\mathbf{r}^i \otimes \mathbf{f}^i, \tag{10.28}$$

where Ω is the volume of the whole specimen. For each case, we obtain six components of the virial stress, from which the elastic constants can now be deduced as

$$A_{klmn} = S_{kl}/e_{mn}. \tag{10.29}$$

In general, the stress-strain relation is nonlinear and we focus our attention to small strain theory, therefore, to evaluate the elastic constants, those specified strains, e_{11}, e_{22}, e_{33}, γ_{12}, γ_{23}, and γ_{31}, should be in the linear elastic range.

10.4.3 Thermal Conductivity

Now suppose we have several atomic groups lined up in series and let the 1st group be subjected to Nose-Hoover thermostat at atomistic temperature T_H and let the last group be subjected to Nose-Hoover thermostat at atomistic temperature T_L. Those groups in between do not have Nosé-Hoover thermostat. After the system reaches steady state, one may obtain the thermal energies E_H and E_L as

$$E_H \equiv \left\{\frac{1}{2}Q_H\chi_H^2 + \frac{Q_H}{\tau_H^2}\int_0^t \chi_H(s)ds\right\}, \tag{10.30}$$

$$E_L \equiv \left\{\frac{1}{2}Q_L\chi_L^2 + \frac{Q_L}{\tau_L^2}\int_0^t \chi_L(s)ds\right\}. \tag{10.31}$$

Because, in MD simulation, atomistic temperature is a statistical quantity and involves significant amount of noises, one may plot the thermal energies E_H and E_L as functions of time, which can be approximated by two straight lines. Numerically one should obtain (cf. Eq. (10.15))

$$\frac{\Delta E_H}{\Delta t} \approx \dot{E}_H = N_H^{dof} k_B \chi_H T_H, \quad \frac{\Delta E_L}{\Delta t} \approx \dot{E}_L = N_L^{dof} k_B \chi_L T_L, \tag{10.32}$$

where $\dot{E}_H$ and $\dot{E}_L$ should be approximately equal in magnitude but opposite in sign. The heat flux $\mathbf{q}$ in magnitude is equal to $\dot{E}_H$ and $\dot{E}_L$ divided by cross sectional area; the temperature gradient is equal to $\Delta T/\Delta L$, where $\Delta T = T_H - T_L$ and ΔL is the

distance between the centers of mass of the two atomic groups controlled by Nose-Hoover thermostats.

Rewriting Eq. 10.20 in Voigts convention as

$$\begin{vmatrix} q_1 \\ q_2 \\ q_3 \end{vmatrix} = - \begin{vmatrix} \kappa_{11} & \kappa_{12} & \kappa_{13} \\ \kappa_{21} & \kappa_{22} & \kappa_{23} \\ \kappa_{31} & \kappa_{32} & \kappa_{33} \end{vmatrix} \begin{vmatrix} T_{,1} \\ T_{,2} \\ T_{,3} \end{vmatrix}, \tag{10.33}$$

one can calculate the thermal conductivity κ from heat flux density $\mathbf{q}$ and temperature gradient along the transportation direction.

10.4.4 Specific Heat and Thermal Expansion Coefficient

We now recall two constitutive equations in small strain thermoelasticity

$$\rho^o \dot{e} = \rho^o \gamma \dot{T} + A_{ijkl} e_{ij} \dot{e}_{kl}, \tag{10.18*}$$

$$\sigma_{ij} = -\beta_{ij} T + A_{ijkl} e_{kl}, \tag{10.19*}$$

where γ and $\boldsymbol{\beta}$ are the specific heat and thermal expansion coefficients, respectively. In MD simulation, one may consider a group of atoms in relaxed and idealized state, i.e., absolute zero temperature, vanishing interatomic forces, and vanishing virial stresses. Then imagine that this group of atoms is put into a rigid box and prohibited to move out of the box. In this situation, the strain and the strain rate are zero, Eqs. (10.18*), (10.19*) are re-written as

$$S_{ij} = -\beta_{ij} T, \quad \dot{e} = \gamma \dot{T}. \tag{10.34}$$

Here we assume that the Cauchy stress tensor in continuum mechanics is equivalent to the virial stress tensor in MD simulation [19]. This may be considered as an approximation. But, without it, it is very difficult, even impossible to bridge the gap between atoms and genuine continuum.

Now let the atomistic temperature of atoms in the box be raised to a specified temperature T by Nose-Hoover thermostat and, after steady state is reached, one may calculate virial stresses S_{ij} and internal energy density e (sum of potential energy and thermal energy divided by total mass of atoms). It results

$$\beta_{ij} = -S_{ij}/T, \quad \gamma = \frac{e}{T}. \tag{10.35}$$

10.5 Concurrent Multiscale Modeling from Atoms to Genuine Continuum

To implement the concurrent multiscale modeling, we divide the solution domain into two regions, namely the non-critical region (or far field) and the critical region (or the atomic region) where the stress concentrations, crack initiation and propagation, dislocations, and other critical physical phenomena may occur. We have successfully modeled the critical region (the atomic region) using MD Simulations and the non-critical region (continuum region) using Finite Element Methods.

The atomic region is further divided into N_g groups, each consisting of n_g atoms, which results in a total of N atoms. Let the first M_g groups have Nosé-Hoover thermostats, $N_g > M_g$. For example, Fig. 10.2b shows $N_g = 22$ and $M_g = 17$. These M_g groups are linked to the first M_g nodes in the GC region (cf. Fig. 10.2a). It is noticed that there are $N_g - M_g = 5$ groups not controlled by thermostats because they are not linked to any node in the genuine continuum (GC) region. By considering the N_g groups as nodes and incorporating into the finite element mesh of GC (cf. Fig. 10.2a), we can obtain an apparent FE mesh as shown in Fig. 10.2c. This results in the formation of an ***interface*** between the atomic region and continuum region. In the ***interface*** each node is corresponding to a group of atoms, not just a single atom (cf. Fig. 10.2a, b).

At this moment we make the following 2 major assumptions

Assumption 1 Each node in the interface is anchored at the mass center of its corresponding group.

Assumption 2 The sum of heat fluxes into the node and its corresponding group is zero.

Now, we recall the equations governing the atomic region as

$$m^i \dot{\tilde{\mathbf{v}}}^i = \mathbf{f}^i + \boldsymbol{\varphi}^i + \mathbf{f}^i_{\text{int}} - \chi_g m^i \tilde{\mathbf{v}}^i, \tag{10.10*}$$

$$\dot{\chi}_g = \frac{1}{\tau_g^2 T_g^c}(T_g^a - T_g^c), \tag{10.11*}$$

$$T_g^a = \frac{1}{N_g^{dof} k_B} \sum_{i=1}^{n_g} m^i \tilde{\mathbf{v}}^i \cdot \tilde{\mathbf{v}}^i, \tag{10.9*}$$

$$\dot{E}_g = N_g^{dof} k_B \chi_g T_g^a. \tag{10.15*}$$

However, we replace T_g to T_g^a to emphasize that now it is the atomistic temperature of group g calculated through the Nose Hoover thermal velocity $\tilde{\mathbf{v}}^i$ in the atomic region. Similarly target temperature T_g^o is replaced by T_g^c to indicate the target temperature of the *group g* is no longer a constant, but the nodal temperature of the corresponding node g in the GC region, $g \in [1, 2, 3, \ldots, M_g]$. The term $\mathbf{f}^i_{\text{int}}$

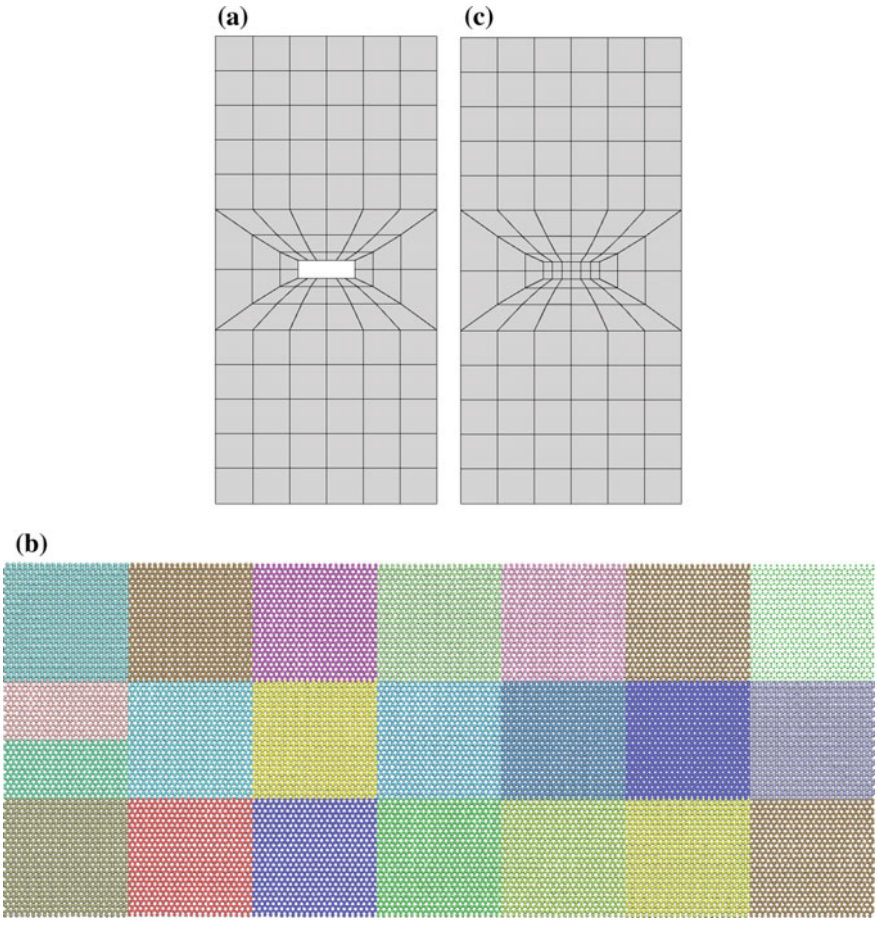

Fig. 10.2 **a** Finite element mesh in the genuine continuum region, **b** groups of atoms in the atomic region, **c** apparent FE mesh

introduced into Eq. (10.10*) represents the interaction between the atoms in group g and their corresponding node g in the GC region.

We recall and rewrite the finite element equations for the GC region as

$$\mathbf{M}\ddot{\mathbf{U}} + \mathbf{K}\mathbf{U} = \mathbf{P}\mathbf{T} + \mathbf{F}^1 + \mathbf{F}^2 + \mathbf{F}_{\text{int}}, \tag{10.23*}$$

$$\mathbf{G}\dot{\mathbf{T}} + \mathbf{H}\mathbf{T} + T^{ref}\mathbf{P}^T\dot{\mathbf{U}} = -\mathbf{Q}^1 + \mathbf{Q}^2 + \mathbf{Q}_{\text{int}}. \tag{10.24*}$$

It is seen that, for those nodes anchored in groups of atoms in the atomic region, we add $\mathbf{F}_{\text{int}}$ and $\mathbf{Q}_{\text{int}}$ to the governing equations; for other nodes, $\mathbf{F}_{\text{int}} = \mathbf{Q}_{\text{int}} = 0$.

The time step used in the atomic region and the continuum region is denoted by Δt^a and Δt^c, respectively. Ratio of time steps N^{time}, which should be an integer, is defined as

$$N^{time} \equiv \Delta t^c / \Delta t^a \quad \text{or} \quad \Delta t^c = N^{time} \Delta t^a. \tag{10.36}$$

We employ the velocity verlet method to solve Eqs. (10.10*), (10.11*) and central difference method to solve Eqs. (10.23*), (10.24*).

10.5.1 Interfacial Conditions

At each node/group in the interface, one should have the following two conditions:

$$\sum_{i \in g} \mathbf{f}^i_{\text{int}} + \mathbf{F}^g_{\text{int}} = 0, \tag{10.37}$$

$$Q^g_{\text{int}} = \dot{E}_g = N^{dof}_g k_B \chi_g T^a_g. \tag{10.38}$$

The first condition, Eq. (10.37), simply means the sum of interactive forces of the node/group pair should be vanishing. Recall that $\dot{E}_g$ is the flow of energy per unit time out of *group g* due to the action of Nosé-Hoover thermostat. Therefore, the second condition simply says $\dot{E}_g$ should be the inward flow of energy per unit time to the corresponding *node g*.

We now re-write Eq. (10.10*) and Eq. (10.23*) respectively as

$$m^i \dot{\mathbf{u}}^i = m^i \dot{\mathbf{v}}^i = \mathbf{f}^i + \boldsymbol{\varphi}^i + \mathbf{f}^i_{\text{int}} - \chi_g m^i \tilde{\mathbf{v}}^i \equiv \bar{\mathbf{f}}^i + \mathbf{f}^i_{\text{int}}, \tag{10.39}$$

$$\mathbf{M}\ddot{\mathbf{U}} = -\mathbf{K}\mathbf{U} + \mathbf{P}\mathbf{T} + \mathbf{F}^1 + \mathbf{F}^2 + \mathbf{F}_{\text{int}} \equiv \bar{\mathbf{F}} + \mathbf{F}_{\text{int}}, \tag{10.40}$$

where $\mathbf{u}^i$ denotes the position vector of *atom i*. In this work, lumped-mass system is adopted, i.e. the mass matrix $\mathbf{M}$ is diagonalized and hence nodal mass is well defined. Similarly, the $\mathbf{G}$ matrix in Eq. (10.24*) is also diagonalized. Equation (10.37) leads to

$$M^g \ddot{\mathbf{U}}^g + \sum_{i \in g} m^i \dot{\mathbf{u}}^i = \bar{\mathbf{F}}^g + \sum_{i \in g} \bar{\mathbf{f}}^i. \tag{10.41}$$

Assumption 10.1, that we made, says *node g* is anchored at the mass center of *group g*. It implies

$$\ddot{\mathbf{U}}^g = \frac{\sum_{i\in g} m^i \ddot{\mathbf{u}}^i}{\sum_{i\in g} m^i} \equiv \frac{\sum_{i\in g} m^i \ddot{\mathbf{u}}^i}{m^g} \equiv \ddot{\mathbf{u}}^g_{avg}. \tag{10.42}$$

To ensure Eq. (10.42), one needs

$$\ddot{\mathbf{u}}^i = \frac{\bar{\mathbf{f}}^i}{m^i} + \ddot{\mathbf{U}}^g - \frac{\sum_{i\in g} \bar{\mathbf{f}}^i}{m^g}. \tag{10.43}$$

Substituting Eq. (10.42) into Eq. (10.41) results

$$\ddot{\mathbf{U}}^g = \frac{1}{M^g + m^g}\left\{\bar{\mathbf{F}}^g + \sum_{i\in g} \bar{\mathbf{f}}^i\right\}. \tag{10.44}$$

In addition to the interfacial conditions, we need to impose boundary condition, either displacement-specified or force specified, at each component of each node, similarly, impose boundary condition, either temperature-specified or heat flow-specified, at each node, at outer boundary of GC region, but not at inner boundary, which is the interface.

10.5.2 Multiple Time Scale Algorithm

There are two regions, atomic and continuum, and therefore there are two time scales, n and m. Then time t equals

$$t(n,m) = n\Delta t^c + m\Delta t^a. \tag{10.45}$$

It is seen that $t(n+1,0) = t(n, N^{time})$. First, suppose at $t(n,0)$ we know $\mathbf{u}^{n,0}$, $\mathbf{a}^{n,0} \equiv \ddot{\mathbf{u}}^{n,0}$, $\chi^{n,0}$,$\mathbf{v}^{n,-\frac{1}{2}} = \dot{\mathbf{u}}^{n,-\frac{1}{2}}$, $\mathbf{U}^{n,0}$, $\mathbf{V}^{n,0} \equiv \dot{\mathbf{U}}^{n,0}$, $\mathbf{A}^{n,0} \equiv \ddot{\mathbf{U}}^{n,0}$, $\mathbf{T}^{n,0}$, and $\dot{\mathbf{T}}^{n,0}$. The numerical procedures to solve Eqs. (10.10*), 10.11*), 10.23*), (10.24*) are described in detail by Lee et al. [11]. Then all the unknown variables are updated as

$$\mathbf{U}^{n,0},\ \mathbf{V}^{n,0},\ \mathbf{T}^{n,0},\ \mathbf{A}^{n,0},\ \mathbf{T}^{n,0} \rightarrow \mathbf{U}^{n+1,0},\ \mathbf{V}^{n+1,0},\ \mathbf{T}^{n+1,0},\ \mathbf{A}^{n+1,0},\ \mathbf{T}^{n+1,0}, \tag{10.46}$$

$$\mathbf{u}^{n,m},\ \mathbf{v}^{n,m-\frac{1}{2}},\ \mathbf{a}^{n,m},\ \boldsymbol{\chi}^{n,m} \rightarrow \mathbf{u}^{n,m+1}, \mathbf{v}^{n,m+\frac{1}{2}},\ \mathbf{a}^{n,m+1},\ \boldsymbol{\chi}^{n,m+1}. \tag{10.47}$$

10.5.3 Sample Problems and Numerical Results

To show the flexibility and extent of the concurrent multiscale theory, in this work we have studied MoS_2, a 2D material consisting two kinds of atoms, characterized by strong in-plane covalent bonding and weak out of plane van der Waals bonding which give them a layered structure.

10.5.3.1 Material Constants Obtained from MD Simulations

The interatomic potential for MoS_2 used in this work is Stillinger Weber potential. In the continuum region, we model the material as a 2D thermoelastic solid with its material properties obtained from MD simulation (cf. Sect. 10.4). The material properties may be summarized as follows:

$$\begin{vmatrix} \sigma_{11} \\ \sigma_{22} \\ \sigma_{12} \end{vmatrix} = - \begin{vmatrix} 0.3675 \text{ x } 10^{-5} \\ 0.3408 \text{ x } 10^{-5} \\ 0.3981 \text{ x } 10^{-5} \end{vmatrix} (T - T^{ref}) + \begin{vmatrix} 0.00489 & 0.00181 & 0 \\ 0.00181 & 0.00488 & 0 \\ 0 & 0 & 0.001505 \end{vmatrix} \begin{vmatrix} e_{11} \\ e_{22} \\ \gamma_{12} \end{vmatrix}, \tag{10.48}$$

$$\begin{vmatrix} q_1 \\ q_2 \end{vmatrix} = - \begin{vmatrix} 0.8924 \text{ x } 10^{-9} & 0 \\ 0 & 0.7637 \text{ x } 10^{-9} \end{vmatrix} \begin{vmatrix} T_{,1} \\ T_{,2} \end{vmatrix}, \tag{10.49}$$

$$\gamma = 0.5444 \text{ x } 10^{-2}. \tag{10.50}$$

In this work, we use atomic units, i.e., the dimensions and units of stress, temperature, heat expansion coefficient, heat flux, thermal conductivity, and specific heat are

$$\begin{aligned} &[\sigma] = \frac{\text{Hartree}}{\text{Bohr}^3}, \quad [T] = \text{Kelvin}, \quad [\beta] = \frac{\text{Hartree}}{\text{Bohr}^3 \,\text{Kelvin}} \\ &[q] = \frac{\text{Hartree}}{\tau \,\text{Bohr}^2}, \quad \text{k}[\kappa] = \frac{\text{Hartree}}{\tau \,\text{Bohr Kelvin}}, \quad [\gamma] = \frac{\text{Hartree}}{\text{m}_e \,\text{Kelvin}} \end{aligned}, \tag{10.51}$$

where

$$\begin{aligned} &\text{Hartree} = 4.3597482 \times 10^{-18} \,\text{J} \\ &\text{Bohr} = 5.29177249 \times 10^{-11} \,\text{m} \\ &\tau = 2.418884326555 \times 10^{-17} \,\text{s} \\ &\text{m}_e = 9.10938291 \times 10^{-31} \,\text{kg} \end{aligned}. \tag{10.52}$$

10.5.3.2 Case Study

The entire specimen is divided into two regions: (1) the finite element mesh of the continuum region has 138 nodes and 108 2D 4-noded plane elements, shown in Fig. 10.2a; (2) the atomic region is further divided into 22 groups, as shown in Fig. 10.2b. There are 756 atoms in *group* 1 and in *group* 17, 1512 atoms in each of the other 20 groups, i.e. 504 Mo atoms each associated with 2 S atoms. There are 31,752 atoms in the atomic region. One may take a close look and find that *group i* and its corresponding *node i*$(i = 1, 2, 3, \ldots, 17)$ form 17 node/group pairs. For the purpose of presentation, one may consider, and view later, the finite element mesh of the entire specimen has 143 nodes (143 = 138 + 5 groups) and 120 elements (120 = 108 + 2(5 + 1)), as shown in Fig. 10.2c. In this view, one may say this specimen had a crack and the crack tip is located at the centroid of *group* 18. In this work the time steps are set at $\Delta t^a = 20\,\tau = 0.4838$ femto second and $\Delta t^c = 20\,\Delta t^a$. It is emphasized that, from the concurrent multiscale modeling, one can obtain the positions of the centroids, the atomistic temperatures, and the virial stress tensors of the 22 groups. Therefore, later in the Tecplot, one may see the graphic representations of a mixture of Cauchy stress tensors and continuum temperatures at 121 nodes (121 = 138 – 17) together with virial stress tensors and atomistic temperatures at 22 groups. The boundary conditions are specified as

Along top edge

$$T = T^{ref}$$
$$u_y = \begin{cases} 85\dfrac{t}{t^r}(\text{Bohr}), & t \le t^r \\ 85(\text{Bohr}), & t \ge t^r \end{cases}. \tag{10.53}$$

Along the bottom edge

$$T = T^{ref}$$
$$u_y = \begin{cases} -85\dfrac{t}{t^r}(\text{Bohr}), & t \le t^r \\ -85(\text{Bohr}), & t \ge t^r \end{cases}. \tag{10.54}$$

where $t^r = 2500\,\Delta t^c = 50000\,\Delta t^a$; $T^{ref} = 300\,\text{K}$. It means there is no temperature gradient; the elongation, after time $t \ge t^r$, is a constant. The positions of 31,752 atoms at different time steps are shown in the *VMD* plots in Fig. 10.3. One may observe the crack opening and crack propagations along multiple fronts. It means, in critical region, MD simulation can be and should be utilized to investigate problems in fracture mechanics and fatigue crack propagation. The temperatures (continuum and atomistic), virial stresses are shown in the Tecplots (cf. Fig. 10.4).

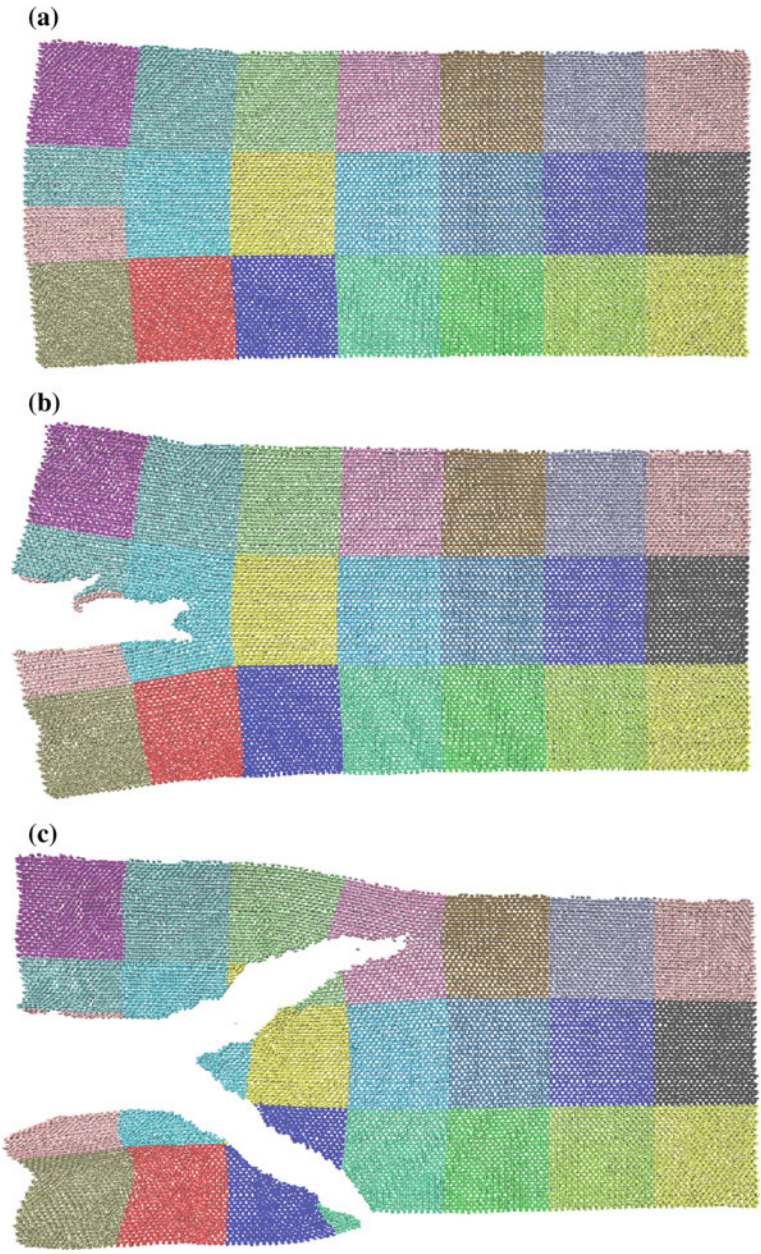

Fig. 10.3 VMD plots at various time steps: **a** $t = 5000\,\Delta t^c$; **b** $t = 6000\,\Delta t^c$, right before crack branching; **c** $t = 7000\,\Delta t^c$, crack propagating and branching

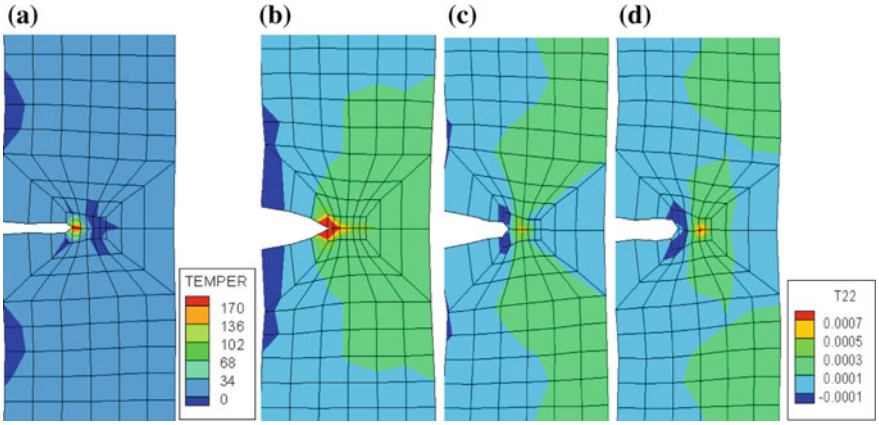

Fig. 10.4 **a** Continuum and atomistic temperature variations at $t = 7000\,\Delta t^c$; Cauchy stress σ_{22} and virial stress S_{22} (Hartree/Bohr^3) at **b** $t = 5000\,\Delta t^c$, **c** $t = 6000\,\Delta t^c$, **d** $t = 7000\,\Delta t^c$

10.6 Conclusion and Future Work

In this work, the atomic region of the specimen we studied is in the range of nanometers to tens of nanometers. Although MD simulation has established itself as a widely employed simulation technique for the study of material behaviors at nanoscale, the extension of MD into computational science over a realistic range of length and time is limited, even with a state-of-the-art supercomputer. On the other hand, continuum physics is simply invalid for material systems at nanoscale because, to say the least, stress-strain relation cannot replace interatomic potential; treatment of temperature is totally different from that in MD. Therefore, this development of a unified theory and associated computational methods for strongly coupled simulations in order to investigate materials from atomic scale to macroscale, becomes necessary in a practical viewpoint.

In addition to drawing attention based on some of its admirable properties, MoS_2 also became popular because it has superior properties than graphene. Although graphene possesses good electrical conductivity thanks to its electron mobility, it fails at switch control due to its gapless band structure. MoS_2 helps implement switch control with its direct band gap of 1.8 eV; this influences the sensitivity of the material allowing it to be used as an effective transistor. However it cannot match graphene in electron mobility. Therefore, fabrication of hybrid structures based on 2D materials by taking advantages of the individual component is one of latest research trends [13].

References

1. Alder, B.J., Wainwright, T.E.: Phase transition for a hard sphere system. J. Chem. Phys. **27**(5), 1208 (1957)
2. Alder, B.J., Wainwright, T.E.: Studies in molecular dnamics. I. General method. J. Chem. Phys. **31**(2), 459–466 (1959)
3. Boresi, A.P., Chong, K.P., Lee, J.D.: Elasticity in Engineering Mechanics. Wiley (2011)
4. Chen, Y., Lee, J.D., Eskandarin, A.: Meshless Methods in Solid Mechanics. Springer (2006)
5. de Groot, S.R., Suttorp, L.G.: Foundations of Electrodynamics. North-Holland Pub, Co (1972)
6. Eringen, A.C.: Microcontinuum Field Theories I: Foundation and Solids. Springer (1999)
7. Geim, A.K., Novoselov, K.S.: The rise of graphene. Nat. Mater. **6**, 183–191 (2007)
8. Hoover, W.G.: Canonical dynamics: equilibrium phase-space distributions. Phys. Rev. A **31** (3), 1695 (1985)
9. Jiang, J.P.: Molecular dynamics simulations of single-layer molybdenum disulfide (MoS2): Stillinger-Weber parametrization, mechanical properties, and thermal conductivity. J. Appl. Phys. **114**(6), 064307 (2013)
10. Laudau, L.D.: Theory of phase changes. I. Physikalische Z. Sowjetunion **11**, 26–47 (1937)
11. Lee, J.D., Li, J., Zhang, Z., Wang, L.: Sequential and concurrent multiscale modeling of multiphysics: from atoms to continuum. In: Meguid, S.A., Weng, G. J. (eds.) Micromechanics and Nanomechanics of Composite Solids. Springer (2017)
12. Li, J., Lee, J.D.: Reformulation of the Nose-Hoover thermostat for heat conduction simulation at nanoscale. Acta Mech. **225**, 1223–1233 (2014)
13. Li, X., Zhu, H.: Two-dimensional MoS_2: properties, preparation, and applications. J. Mater. **1**, 33–44 (2015)
14. Nosé, S.: A unified formulation of the constant temperature molecular dynamics methods. J. Chem. Phys. **81**, 511–519 (1984)
15. Nosé, S.: A molecular dynamics method for simulations in the canonical ensemble. Mol. Phys. **53**, 255–268 (1984)
16. Rahman, A.: Correlations in the motion of atoms in liquid argon. Phys. Rev. **136**(2A), A405–A411 (1964)
17. Stewart, J., Spearot, D.: Atomistic simulations of nanoindentation on the basal plane of crystalline molybdenum disulfide (MoS_2). Model. Simul. Mater. Sci. Eng. **21**(4), 045003 (2013)
18. Stillinger, F.H., Rahman, A.: Improved simulation of liquid water by molecular dynamics. J. Chem. Phys. **60**(4), 1545–1557 (1974)
19. Subramaniyan, A.K., Sun, C.T.: Continuum interpretation of virial stress in molecular simulations. Int. J. Solids Struct. **45**(14–15), 4340–4346 (2008)

Chapter 11
Gradient Elasticity Effects on the Two-Phase Lithiation of LIB Anodes

Ioannis Tsagrakis and Elias C. Aifantis

Abstract A coupled gradient chemoelasticity theory is employed to model the two-phase mechanism that occurs during lithiation of silicon nanoparticles used to fabricate next generation Li-ion battery (LIB) anodes. It is shown that the strain gradient length scale is able to predict the propagation of an interface front of nonzero thickness advancing from the lithiated to unlithiated region without necessarily including higher-order concentration gradients of the Li ions. Larger strain gradient coefficients (elastic internal lengths) induce more diffused interfaces and faster lithiation, which affect both internal strain and stress distributions in a similar way. Estimates for the migration velocity of the phase boundary are obtained and a range of values of the strain gradient length scale is shown to simulate the observed experimental results.

11.1 Introduction

It is with great pleasure and honor to dedicate this article to the memory of a dear mentor, colleague and honorary doctorate of Aristotle University of Thessaloniki—the hometown of his long-time companion Eleni. Professor Maugin advanced pioneered works in coupled continuum mechanics to model synergistic effects

I. Tsagrakis · E. C. Aifantis (✉)
Aristotle University of Thessaloniki, Thessaloniki 54124, Greece
e-mail: mom@mom.gen.auth.gr

I. Tsagrakis
e-mail: itsagrakis@tem.uoc.gr

E. C. Aifantis
Michigan Technological University, Houghton, MI 49931, USA

E. C. Aifantis
Beijing University of Civil Engineering and Architecture, Beijing 100044, China

E. C. Aifantis
ITMO University, St. Petersburg 197101, Russia

E. C. Aifantis
Togliatti State University, Togliatti 445020, Russia

H. Altenbach et al. (eds.), *Generalized Models and Non-classical Approaches in Complex Materials 2*, Advanced Structured Materials 90,
https://doi.org/10.1007/978-3-319-77504-3_11

between mechanical, thermal, chemical and electromagnetic effects. The present contribution is strongly motivated by his work; i.e. on the development and use of generalized coupled continuum theories to interpret mechanically-induced nonlinear phenomena observed in natural and modern engineering systems. The particular chemomechanical problem considered herein concerns the internal stress development and propagation of a lithiated front wave observed during Li-intercalation of nanostructured silicon-based composite anodes.

A first attempt for using elasticity theory to model the huge volumetric expansions occurring in rechargeable Li-ion battery (LIB) anodes containing active Si or Sn nanoparticles embedded within a glass or ceramic matrix, was provided in [1]. Soon after that, linear elastic fracture mechanics (LEFM) considerations were employed in [2] to model crack patterns in nanostructured composite anodes and assess the optimum configuration of nanodomains (nanospheres, nanofibers, nanodiscs) that prevent cracking. Later, a rather complex gradient damage theory was used [3] to derive estimates for the local geometry, volume fraction and spacing of the "active" nanodomains which minimize anode damage during Li insertion/de-insertion under electrochemical cycling.

A first mechanics-oriented review on lithium-ion batteries with emphasis on the synergy between elasticity and electrochemistry was provided in [4]. In addition to anode chemomechanical degradation, detrimental phase separation in cathodes was also discussed by coupling elasticity to Cahn's theory [5, 6] of spinodal decomposition. Concurrently, the topic became quite popular in the mechanics community [7–12] and a number of rigorous but often complex formulations on elasticity or plasticity coupled with diffusion were proposed and applied to interpret cracking in anodes and phase separation in cathodes. With the exception of [13], none of these formulations takes into account the higher-order gradients due to the strain field, even though higher-order gradients for the concentration field are often considered. Moreover, with the exception of [14, 15], the nonlinear nature of the lithiation phenomenon and the influence of different internal lengths (elastic and chemical) on the accompanied phase transition-like process is not addressed. A related "phase field" theory based on the introduction of higher-order gradients of the order parameter do not explicitly separate between the effects of higher-order strain gradients and higher-order concentration gradients.

Our modest aim here is to provide and utilize a relatively simple thermodynamic framework considering higher-order gradients in both the strain and the concentration field for modeling the lithiation of Si anodes during electrochemical cycling. Experimental results on crystalline [16] as well as amorphous silicon [17] have shown that this process occurs through a two-phase mechanism, where an amorphous Li_xSi $(x \cong 3.75)$ phase grows and separated from the unlithiated phase by a sharp interface of about 1 nm thick. Accordingly, the kinetics of lithiation is characterized by the migration of this interface which can interpreted either by employing diffusion arguments of Cahn–Hilliard type [18] or by considering the interfacial chemical reaction of lithium and silicon [19].

In the present contribution, we build on a revision of our previously published model [14] on coupled higher-order strain gradient—concentration gradient phase

transformations of spinodal type and utilize it to simulate the development and front propagation of the lithiated phase that a spherical Si particle undergoes during electrochemical charging. The implications of the strain gradient and concentration gradient coefficients (internal lengths) on the Li concentration distributions, as well as, on the induced stress and strain profiles are also investigated.

11.2 Theoretical Framework of Gradient Chemoelasticity

In a recent article of the authors [14], it has been shown that the thermodynamic coupling of strain gradient elasticity with Cahn-Hilliard diffusion can be originated by assuming that the Helmholtz free energy density is non-convex and depends in addition to the concentration (c) and the strain $(\boldsymbol{\varepsilon})$, on the concentration gradient ∇c of the chemical species (Li-ions) and the gradient of the hydrostatic strain field $(\nabla \mathrm{tr}\,\boldsymbol{\varepsilon})$. We relax somewhat this assumption here to include the gradient of the full strain field $\nabla\boldsymbol{\varepsilon}$. In other words, our starting constitutive assumption for the free energy density is of the form $\psi = \hat{\psi}(c, \nabla c, \boldsymbol{\varepsilon}, \nabla\boldsymbol{\varepsilon})$, where c denotes the local nominal concentration (in moles per unit volume) of the diffusing species (e.g. Li in $\mathrm{Li_xSi}$), $\boldsymbol{\varepsilon}$ is the displacement compatible infinitesimal strain tensor, i.e. $\boldsymbol{\varepsilon} = \left[\nabla\boldsymbol{u} + (\nabla\boldsymbol{u})^T\right]/2$, while $\nabla\boldsymbol{\varepsilon} = \frac{\partial\boldsymbol{\varepsilon}}{\partial x_i} \otimes \hat{\boldsymbol{e}}_i$ is its gradient (a 3rd order tensor). The thermodynamically consistent constitutive equations for the chemical potential μ and the Cauchy stress σ_{ij} derived for this general model read (see also in [15])

$$\mu = \frac{\partial\hat{\psi}}{\partial c} - \frac{\partial}{\partial x_i}\left(\frac{\partial\hat{\psi}}{\partial c_{,i}}\right), \quad \sigma_{ij} = \frac{\partial\hat{\psi}}{\partial\varepsilon_{ij}} - \frac{\partial}{\partial x_k}\left(\frac{\partial\hat{\psi}}{\partial\varepsilon_{ij,k}}\right), \tag{11.1}$$

while the components of the associated traction-like vectors have the form

$$\xi_i = \frac{\partial\hat{\psi}}{\partial c_{,i}}, \quad t_i = \sigma_{ij}n_j + \tau_i D_m n_m - D_j\left(n_k\frac{\partial\hat{\psi}}{\partial\varepsilon_{ij,k}}\right), \quad \tau_i = \frac{\partial\hat{\psi}}{\partial\varepsilon_{ij,k}}n_j n_k, \tag{11.2}$$

where $D_j \equiv \partial_j - n_j n_k \partial_k$ is the tangential component of the gradient operator $\nabla = \{\partial_j\}$ on the boundary ∂P of the material domain P.

In the present work, the following specific constitutive equation for $\hat{\psi}$ is considered

$$\hat{\psi}(c, \nabla c, \boldsymbol{\varepsilon}, \nabla\boldsymbol{\varepsilon}) = f(c) + \frac{\kappa}{2}\nabla c\cdot\nabla c + \frac{1}{2}\boldsymbol{\varepsilon}^e\cdot\mathcal{C}\,\boldsymbol{\varepsilon}^e + \frac{\ell_\varepsilon^2}{2}\nabla\boldsymbol{\varepsilon}^e\cdot\mathcal{C}\nabla\boldsymbol{\varepsilon}^e, \tag{11.3}$$

where $\boldsymbol{\varepsilon}^e = \boldsymbol{\varepsilon} - \rho M$ is the infinitesimal elastic strain tensor with $\rho := c/c_{\max}$ $(0 \le \rho \le 1)$ denoting the normalized concentration, while $c_{\max}$ is the concentration when all the accommodating sites in the host material are filled (i.e. at the fully lithiated state). The term ρM represents the lattice misfit (stress-free) strain of the

two materials which varies linearly with the composition (Vegard's law). For simplicity, we assume that the intercalation process induces only isotropic compressions and expansions of the surrounding material and consequently $M = M_o \mathbf{1}$, where M_o is a constant scalar strain measure. Moreover, $\mathcal{C}\boldsymbol{\varepsilon}^e = 2G\boldsymbol{\varepsilon}^e + \lambda(\mathrm{tr}\,\boldsymbol{\varepsilon}^e)\mathbf{1}$ for an isotropic host material, where G, λ are the Lamé parameters which are assumed to be constants, though in a more general consideration they will depend on concentration. It is noted that Eq. (11.3) is different from that proposed in [15], where the gradient $\nabla\boldsymbol{\varepsilon}$ of the total strain was used instead of $\nabla\boldsymbol{\varepsilon}^e$.

The first two terms in Eq. (11.3) are identical with the original Cahn-Hilliard expression for the free energy density of a non-homogeneous binary solution [5], where $f(c)$ is the chemical free energy density of a stress-free system of uniform concentration c. This function is able to describe the co-existence of two phases provided that it is non-convex with two minima and a maximum in between (i.e. a double-well function). For this reason, the well-known regular solution model of the form

$$f(c) = \mu^0 c + RTc_{\max}[\rho\ \ln\ \rho + (1-\rho)\ln(1-\rho) + \alpha\rho(1-\rho)] \tag{11.4}$$

is adopted, where R is the universal gas constant, T is the absolute temperature, and μ^0 is a reference value of the chemical potential of the diffusing species. Equation (11.4) is able to describe phase transition or phase separation phenomena as long as $\alpha > 2$. In this connection, it is noted that amorphous phases (e.g. Li_xSi) are simply considered to evolve according to an ideal hypothesis for regular solutions, and hence Eq. (11.4) should be viewed only as a mathematical function with double energy wells [18], without loss of generality.

For the specific form of the Helmholtz free energy density defined by Eqs. (11.3) and (11.4), Eq. (11.1) gives the following gradient dependent constitutive expressions for the chemical potential and the stress tensor

$$\left.\begin{aligned}\mu = \mu^0 + RT\left[\ln\left(\tfrac{\rho}{1-\rho}\right) + \alpha(1-2\rho)\right] - \kappa c_{\max}\nabla^2\rho \\ -(2G+3\lambda)M_o\left[\left(\mathrm{tr}\,\boldsymbol{\varepsilon} - \ell_\varepsilon^2\nabla^2\mathrm{tr}\,\boldsymbol{\varepsilon}\right) - 3M_o(\rho - \ell_\varepsilon^2\nabla^2\rho)\right]/c_{\max}\end{aligned}\right\}, \tag{11.5}$$

$$\boldsymbol{\sigma} = 2G\boldsymbol{\varepsilon} + \lambda(\mathrm{tr}\,\boldsymbol{\varepsilon})\mathbf{1} - \ell_\varepsilon^2\nabla^2[2G\boldsymbol{\varepsilon} + \lambda(\mathrm{tr}\,\boldsymbol{\varepsilon})\mathbf{1}] - (2G+3\lambda)M_o(\rho - \ell_\varepsilon^2\nabla^2\rho)\,\mathbf{1}, \tag{11.6}$$

where $\mathbf{1}$ is the 2nd order identity tensor. By calculating the hydrostatic stress $\sigma_h = \mathrm{tr}\boldsymbol{\sigma}/3$ from Eq. (11.6), it is rather straightforward to show that Eq. (11.5) can be recast into the following standard stress-dependent form of the chemical potential

$$\mu = \mu^0 + RT\left[\ln\left(\frac{\rho}{1-\rho}\right) + \alpha(1-2\rho)\right] - \kappa c_{\max}\nabla^2\rho - \Omega_{\mathrm{Li}}\sigma_h, \tag{11.7}$$

where $\Omega_{\mathrm{Li}} = 3M_o/c_{\max}$ is the partial molar volume of the diffusing species. Moreover, Eq. (11.6) can be also recast into the form $\boldsymbol{\sigma} = \boldsymbol{\sigma}^c - \ell_\varepsilon^2\nabla^2\boldsymbol{\sigma}^c$, where

$\boldsymbol{\sigma}^c := 2G\boldsymbol{\varepsilon} + \lambda(\mathrm{tr}\,\boldsymbol{\varepsilon})\mathbf{1} - (2G + 3\lambda)M_o\rho\mathbf{1}$ denotes the classical (non-gradient) part of the stress. Then, the traction-like parameters in Eq. (11.2) obtain the form

$$\boldsymbol{\xi} = \kappa c_{\max}\nabla\rho - \ell_\varepsilon^2\Omega_{\mathrm{Li}}\nabla\boldsymbol{\sigma}_h^c, \quad t = \boldsymbol{\sigma}\boldsymbol{n} + (D_m n_m)\boldsymbol{\tau} - \ell_\varepsilon^2\nabla_s\cdot(\nabla_{\boldsymbol{n}}\boldsymbol{\sigma}^c), \quad \boldsymbol{\tau} = \ell_\varepsilon^2(\nabla_{\boldsymbol{n}}\boldsymbol{\sigma}^c)\boldsymbol{n}, \tag{11.8}$$

where $\nabla_{\boldsymbol{n}}\boldsymbol{\sigma}^c = n_k\sigma^c_{ij,k}\,\hat{\boldsymbol{e}}_i\otimes\hat{\boldsymbol{e}}_j$ is the normal gradient of $\boldsymbol{\sigma}^c$ on the boundary ∂P, while $\nabla_s\cdot\boldsymbol{T} = D_j T_{ij}\,\hat{\boldsymbol{e}}_i$ is the tangential divergence of the 2nd order tensor $\boldsymbol{T}$.

The set of the constitutive equations is completed by the flux versus chemical potential expression

$$\boldsymbol{j} = -c\boldsymbol{B}\nabla\mu; \quad \boldsymbol{B} = \frac{D_o}{RT}(1-\rho)\mathbf{1}, \tag{11.9}$$

where $\boldsymbol{B}$ denotes the mobility tensor which has been assumed diagonal and isotropic, and D_o is the inter-diffusion coefficient. Substituting Eq. (11.8) into the local mass conservation law $\frac{\partial c}{\partial t} + \nabla\cdot\boldsymbol{j} = 0$ and dividing the resulting equation by $c_{\max}$ yields

$$\frac{\partial\rho}{\partial t} = \frac{D_o}{RT}\left[(1-2\rho)\nabla\rho\cdot\nabla\mu + \rho(1-\rho)\nabla^2\mu\right]. \tag{11.10}$$

Finally, the set of the governing equations is completed by the standard equilibrium condition $\nabla\cdot\boldsymbol{\sigma} = \mathbf{0}$, which with the aid of the previously stated linear approximation for the strain-displacement relation $\boldsymbol{\varepsilon} = \left[\nabla\boldsymbol{u} + (\nabla\boldsymbol{u})^T\right]/2$ gives

$$G(\nabla^2\boldsymbol{u} - \ell_\varepsilon^2\nabla^4\boldsymbol{u}) + (\lambda+G)\nabla\left[\nabla\cdot\boldsymbol{u} - \ell_\varepsilon^2\nabla^2(\nabla\cdot\boldsymbol{u})\right] - (2G+3\lambda)M_o\nabla\left(\rho - \ell_\varepsilon^2\nabla^2\rho\right) = \mathbf{0}. \tag{11.11}$$

In this connection, it is noted that the quasi-static form $\nabla\cdot\boldsymbol{\sigma} = \mathbf{0}$ of the momentum balance equation used in the present analysis implies that body forces and inertial effects are considered negligible. The feasibility of this approximation is based on the fact that time scales associated with species diffusion are usually considerably longer than those associated with wave propagation (see, e.g. in [11], and references quoted therein), as well as, external gravitational forces exerted in the micro-specimens are much smaller than the mechanical forces between adjacent micro-volumes.

11.3 Modeling Lithiation of a Spherical Silicon Particle

11.3.1 Governing Equations

Under spherically symmetric conditions, i.e., $\rho = \rho(r,t)$ and $\boldsymbol{u} = u(r,t)\hat{\boldsymbol{e}}_r$, Eq. (11.11) obtains the form

$$\frac{\partial}{\partial r}\left\{\frac{1}{r^2}\frac{\partial}{\partial r}\left[r^2\left(u-\ell_\varepsilon^2\frac{\partial}{\partial r}\left[\frac{1}{r^2}\frac{\partial(r^2u)}{\partial r}\right]\right)\right]\right\}=\frac{2G+3\lambda}{2G+\lambda}M_o\frac{\partial(\rho-\ell_\varepsilon^2\nabla^2\rho)}{\partial r}. \quad (11.12)$$

Taking into account that the non-vanishing components of strain are $\varepsilon_{rr}=\partial u/\partial r$ and $\varepsilon_{\theta\theta}=\varepsilon_{\varphi\varphi}=u/r$, and thus, $\mathrm{tr}\,\boldsymbol{\varepsilon}=\frac{1}{r^2}\frac{\partial(r^2u)}{\partial r}$, Eq. (11.12) can be integrated with respect r to obtain

$$\mathrm{tr}\,\boldsymbol{\varepsilon}-\ell_\varepsilon^2\nabla^2\mathrm{tr}\,\boldsymbol{\varepsilon}=\frac{2G+3\lambda}{2G+\lambda}M_o(\rho-\ell_\varepsilon^2\nabla^2\rho)+C(t), \quad (11.13)$$

where $C(t)$ is an integration function that depends on the mechanical boundary conditions. Using Eq. (11.13), the chemical potential in Eq. (11.5) can be expressed only in terms of the normalized concentration, i.e.,

$$\overline{\mu}=\ln\left(\frac{\rho}{1-\rho}\right)+\alpha(1-2\rho)+\beta\rho-(\ell_c^2+\beta\ell_\varepsilon^2)\nabla^2\rho, \quad (11.14)$$

where $\overline{\mu}:=(\mu-\mu^0-\Omega_{Li}C(t))/RT$ defines a dimensionless potential, $\ell_c:=\sqrt{\kappa c_{\max}/RT}$ denotes an internal length scale associated with the concentration gradient term of the Helmholtz free energy density, and $\beta:=4G(2G+3\lambda)M_o^2/(2G+\lambda)RTc_{\max}$ is a dimensionless material parameter. Equation (11.14) has the general form $\overline{\mu}=g(\rho)-\ell^2\nabla^2\rho$, where $\ell^2=\ell_c^2+\beta\ell_\varepsilon^2$. Therefore, the effects of concentration and strain gradients can be combined into a single internal length ℓ and hence, they are mathematically (but not physically) indistinguishable. Moreover, as long as there are non-vanishing misfit strains, the standard interfacial term $(\kappa/2)\nabla c\cdot\nabla c$ in Eq. (11.3) could be omitted, and yet the model could predict the width of the interphase because of the strain gradient length scale.

For a silicon particle of diameter d, Eqs. (11.10) and (11.14) can be recast into their dimensionless counterparts

$$\left.\begin{aligned}\frac{\partial\rho}{\partial\overline{t}}&=(1-2\rho)\overline{\nabla}\rho\cdot\overline{\nabla}\overline{\mu}+\rho(1-\rho)\overline{\nabla}^2\overline{\mu}\\ \overline{\mu}&=\ln\left(\frac{\rho}{1-\rho}\right)+\alpha(1-2\rho)+\beta\rho-\left(\overline{\ell}_c^2+\beta\overline{\ell}_\varepsilon^2\right)\overline{\nabla}^2\rho\end{aligned}\right\}, \quad (11.15)$$

where $\overline{\nabla}$ is the gradient operator with respect the normalized radial coordinate $\overline{r}=2r/d$, $\overline{t}=4D_ot/d^2$ is a dimensionless time parameter, while $\overline{\ell}_c=2\ell_c/d$ and $\overline{\ell}_\varepsilon=2\ell_\varepsilon/d$.

11.3.2 Material and Model Parameters

Suitable values of the material constants for the Si/Li_xSi system are obtained from the literature or by some simple calculations. In particular, at a stress-free state of full lithiation (i.e., $Li_{4.4}Si$ and $\rho = 1$), we have $\varepsilon_{rr} = \varepsilon_{\theta\theta} = \varepsilon_{\phi\phi} = M_o$ which gives $u(r) = M_o r$. Accordingly, for a corresponding 310% volume expansion [20], we obtain

$$\frac{\left[4\pi(r+M_o r)^3/3\right] - [4\pi r^3/3]}{4\pi r^3/3} = 3.1 \Rightarrow (1+M_o)^3 - 1 = 3.1 \Rightarrow M_o = 4.1^{1/3} - 1 \cong 0.6. \tag{11.16}$$

Experiments have shown that the Li-rich phase at room temperature likely consists of amorphous $Li_{3.75}Si$ [16, 17] rather than the fully lithiated alloy $Li_{4.4}Si$, and hence the normalized Li concentration in the actual Li-rich phase is $\rho_2 = 3.75/4.4 \cong 0.852$. The half of this value, i.e., $\rho = 0.426$ is used to calculate the elastic parameters via the linear rule of mixtures. In fact, nanoindentation experiments have shown that Young's modulus of lithiated silicon decline with increasing lithium content (see, for example, in [21] and references quoted therein). However, as noted in the previous section, a constant value is adopted in the present contribution for the sake of simplicity. In particular, the value $E = 77.5$ GPa is used which corresponds to the Young's modulus for $\rho = 0.426$ and it is calculated using a linear rule of mixtures between that of pure amorphous silicon (104.6 GPa) and fully lithiated silicon (41 GPa). A similar rule between Poisson's ratio of amorphous silicon (0.22) and that of pure lithium (0.36) gives $\nu = 0.28$.

The maximum nominal Li concentration (which corresponds to the fully lithiated alloy $Li_{4.4}Si$) is $c_{\max} = 3.667 \times 10^5$ mole/m^3 [18] and thus, at $T = 300$ K, we have $RTc_{\max} = 914.6$ MPa. The above values yield $\beta \cong 84.84$ for the dimensionless material parameter in Eq. $(11.15)_2$.

Equation $(11.15)_2$ can predict the occurrence of a phase transition as long as its homogeneous part

$$g(\rho) = \ln\left(\frac{\rho}{1-\rho}\right) + \alpha(1-2\rho) + \beta\rho, \tag{11.17}$$

is non-convex with a maximum followed by a minimum. Then, under quasistatic conditions in one-dimensional infinite medium, a transition solution between two phases of concentrations ρ_1 and ρ_2, respectively satisfies the following equations [22, 23]

$$\int_{\rho_1}^{\rho_2} [g(\rho) - \overline{\mu}] = 0, \quad \overline{\mu} = g(\rho_1) = g(\rho_2), \tag{11.18}$$

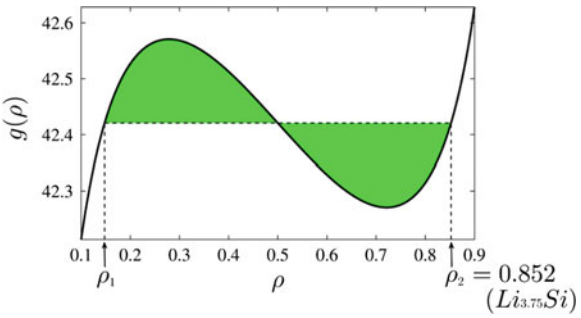

Fig. 11.1 Equal area rule satisfied by a transition solution between Li-poor and Li-rich phases

where the first relation is the Maxwell's equal area rule (Fig. 11.1). Given that $\rho_2 = 0.852$ (i.e. the concentration of the actual Li-rich phase), the system of Eq. (11.18) can be numerically solved with respect ρ_1, $\overline{\mu}$ and α. The calculated value for the last coefficient is $\alpha \cong 44.9$ and it is then employed for the dynamic problem of Eq. (11.15) in order to enforce the Li-rich phase to take its actual concentration $\rho_2 = 0.852$.

Concerning the concentration gradient coefficient, the value $\kappa = 1.49 \times 10^{-20}$ N m^6/mole^2 is computed from the corresponding constant $\overline{\kappa} = 2 \times 10^{-9}$ J/m found in [18], where $\overline{\kappa} = \kappa c_{\max}^2$. This gives $\ell_c = 1.48$ nm, which in turn for a silicon particle of diameter $d = 140$ nm corresponds to $\overline{\ell}_c = 0.0211$.

11.3.3 Initial and Boundary Conditions

For the solution of the Eq. (11.15), a state of uniform concentration $\rho_o = 10^{-4}$ is used as an initial condition to avoid the logarithmic singularity of chemical potential at $\rho = 0$. The corresponding uniform initial value of $\overline{\mu}$ is $\overline{\mu}_o = g(\rho_o)$. Throughout the lithiation process the so-called variational boundary condition $\nabla\rho \cdot \boldsymbol{n}|_{\overline{r}=1} = 0$ is employed. This is natural for systems without surface energies or surface diffusion, but it can also be used in time-dependent problems to enforce chemical potential continuity at the boundary of the system [24]. Concerning the second boundary condition the lithiation process is assumed divided in two stages. In the first one, the particle is charged galvanostatically, with a uniform lithium flux through its free surface, which is determined by the current equality condition [25] as $\boldsymbol{j}|_{\overline{r}=1} = i/zF$, where i is the surface current density (per area), $z = 1$ is the valence number of a Li-ion, and F is the Faraday constant. In terms of normalized quantities, this boundary condition reads

$$\rho(1-\rho)\frac{\partial \overline{\mu}}{\partial \overline{r}}\bigg|_{\overline{r}=1} = \overline{i}; \quad \overline{i} := \frac{d/2}{zFD_o c_{\max}} i. \tag{11.19}$$

Since the study of current density effects is beyond the scope of the present contribution, the fixed value $\bar{i} = 1$ is employed for the dimensionless current density.

The galvanostatic charging continues until the normalized concentration at the surface of the particle reaches the lithiated phase value $\rho_2 = 0.852$. Thereafter, the concentration on the boundary is held fixed at this value while the insertion process continues. As discussed in [26], this type of two-stage charging is quite close to the boundary conditions as applied using a battery simulator (Butler-Volmer kinetics), with the second stage being characterized as potentiostatic.

11.3.4 Numerical Solution

The system of Eq. (11.15) in association with the aforementioned initial and boundary conditions is solved numerically with aid of the method of lines. In particular, weighted residuals (Galerkin) method is employed and the variables ρ and $\bar{\mu}$ are interpolated in space using the spectral element method. The interior nodes of each element are distributed at the zeros of Lobatto polynomials over the canonical (local) interval $[-1,\ 1]$, and cubic splines with Lagrange end conditions are used for the interpolation within each element. The same set of nodes is also used to evaluate elemental integrals according to the Gauss-Lobatto quadrature. Since the system of ordinary differential equations resulting from this spatial discretization is usually stiff, it is integrated with respect to normalized time by the backward differentiation formulas (Gear's method). Numerical experimentation with different interpolation schemes shows that 40 spectral elements with 7 nodes each are enough to avoid spurious discretization effects.

The obtained normalized concentration profiles at different lithiation times and for negligible strain gradient effects (i.e., $\ell_\varepsilon = 0$) are depicted in Fig. 11.2, where the value $\bar{t} \approx 0.06$ corresponds to the ending of the galvanostatic stage and the initiation of the potentiostatic one. The rest of the concentration distributions show the migration of the interface between the Li-rich and the Li-poor phases, and they

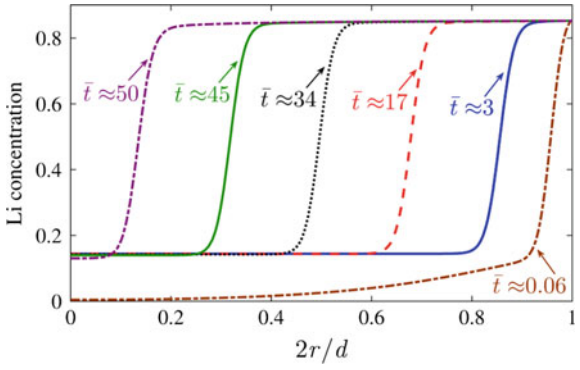

Fig. 11.2 Normalized concentration profiles during potentiostatic charging at different lithiation times and for negligible strain gradient effects (i.e., $\ell_\varepsilon = 0$)

are comparable with those presented in [18] using a model of finite elastoplasticity without strain gradients. It is also noted that identical profiles with these of Fig. 11.2 are obtained by setting $\ell_c = 0$ and $\ell_\varepsilon = 1.48/\sqrt{\beta} = 0.16$ nm, as follows from the coupling of the two internal lengths in Eq. (11.14).

From the profiles for $\bar{t} \approx 3$ to $\bar{t} \approx 45$ the average normalized velocity of the interface is estimated as $\bar{v} \approx 0.0132$. For a silicon particle of diameter $d = 140$ nm and an inter-diffusion coefficient $D_o = 10^{-16}$ m^2/s [27], this value yields a migration velocity $v \approx 0.018$ nm/s which is about 3.3 times smaller than the experimental value of 0.06 nm/s [17].

The effect of the strain gradient coefficient on the interface is depicted in Fig. 11.3, where the normalized concentration distributions are plotted when the interface is at the same position (determined by the position of $\rho = 0.5$), for different values of ℓ_ε. As expected from the concentration gradient coefficient in Eq. (11.15)$_2$, higher values of ℓ_ε render thicker (i.e. more diffused) interfaces. This, in turn, leads to higher lithiation rates as shown in Fig. 11.4, where the average normalized concentration of lithium vs. dimensionless time is illustrated. Consequently larger migration velocities of the interface are predicted. The aforementioned experimental value of 0.06 nm/s can be roughly approximated for some value of ℓ_ε between $0.3\ell_c$ and $0.4\ell_c$.

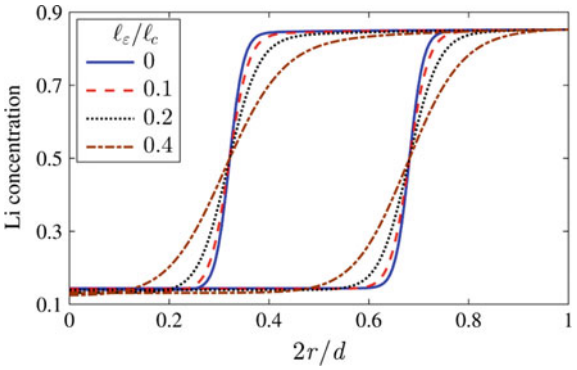

Fig. 11.3 Effect of the strain gradient length scale ℓ_ε on normalized concentration profiles at two different positions of the interface

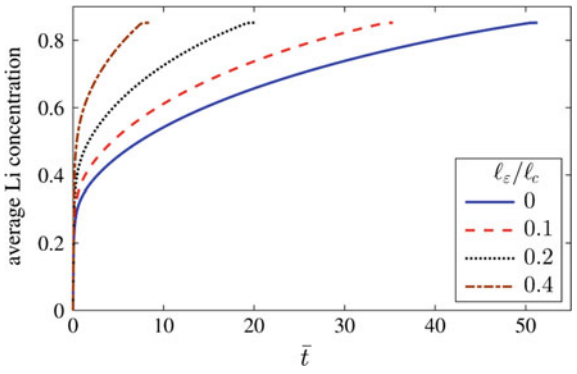

Fig. 11.4 Effect of the strain gradient length scale ℓ_ε on the evolution of the average Li concentration

11.3.5 Stress and Strain Radial Profiles

Regarding the mechanics boundary conditions, we assume that at the outer surface the silicon particle is traction free, i.e.,

$$\sigma_{rr}|_{\overline{r}=1}=0, \quad \ell_\varepsilon^2 \frac{\partial \sigma_{rr}^c}{\partial r}\bigg|_{\overline{r}=1}=0, \tag{11.20}$$

where the latter follows from Eq. $(11.8)_3$, while the former is the standard (physical) stress free condition rather than the full variationally consistent traction of Eq. $(11.8)_2$.

Then, Eq. (11.12) can be solved analytically to obtain the displacement profile in terms of the normalized concentration, i.e.,

$$u(r,t)=\frac{2G+3\lambda}{2G+\lambda}\frac{M_o}{r^2}\int_0^r \zeta\left[\rho(\zeta,t)-\ell_\varepsilon^2\nabla^2\rho(\zeta,t)\right]\left[\zeta+\ell_\varepsilon \sinh\left(\tfrac{r-\zeta}{\ell_\varepsilon}\right)-r\cosh\left(\tfrac{r-\zeta}{\ell_\varepsilon}\right)\right]\mathrm{d}\zeta+ \\ C_1(t)r+C_2(t)\sqrt{\tfrac{\pi\ell_\varepsilon}{2r}}I_{3/2}\left(\tfrac{r}{\ell_\varepsilon}\right)\Bigg\}, \tag{11.21}$$

where $C_1(t)$ and $C_2(t)$ are integration functions which are determined by Eq. (11.20), and $I_m(z)$ denotes the modified Bessel functions of the first kind and order m. The problem can then be solved by using the calculated concentration distributions $\rho(\zeta,t)$ and calculating numerically the integral in Eq. (11.21). Because $C_1(t)$ and $C_2(t)$ involve also lengthy integrals and have complicated expressions, an alternative numerical scheme is adopted. In particular, we start by considering the following weak form of the stress equilibrium equation

$$4\pi\int_0^1 \delta\overline{u}\left[\frac{\partial\sigma_{rr}}{\partial\overline{r}}+\frac{2}{\overline{r}}(\sigma_{rr}-\sigma_{\theta\theta})\right]\overline{r}^2 d\overline{r}=0, \tag{11.22}$$

where $\overline{u}=2u/d$ is a normalized displacement. Using the constitutive formula of stress tensor from Eq. (11.6), along with the boundary conditions of Eq. (11.20) and integrating by parts Eq. (11.22) yields

$$\int_0^1\left[\delta\varepsilon_{rr}\sigma_{rr}^H+2\delta\varepsilon_{\theta\theta}\sigma_{\theta\theta}^H+\ell_\varepsilon^2\left(\tfrac{\partial\delta\varepsilon_{rr}}{\partial\overline{r}}\tfrac{\partial\sigma_{rr}^H}{\partial\overline{r}}+2\tfrac{\partial\delta\varepsilon_{\theta\theta}}{\partial\overline{r}}\tfrac{\partial\sigma_{\theta\theta}^H}{\partial\overline{r}}\right)\right]\overline{r}^2 d\overline{r} \\ +\ell_\varepsilon^2\int_0^1 4(\delta\varepsilon_{rr}-\delta\varepsilon_{\theta\theta})\left(\sigma_{rr}^H-\sigma_{\theta\theta}^H\right)d\overline{r}-2\ell_\varepsilon^2\delta\overline{u}\tfrac{\partial\sigma_{\theta\theta}^H}{\partial\overline{r}}\Big|_{\overline{r}=1}= \\ =(2G+3\lambda)M_o\int_0^1\left[(\delta\varepsilon_{rr}+2\delta\varepsilon_{\theta\theta})\rho+\ell_\varepsilon^2\left(\tfrac{\partial\delta\varepsilon_{rr}}{\partial\overline{r}}+2\tfrac{\partial\delta\varepsilon_{\theta\theta}}{\partial\overline{r}}\right)\tfrac{\partial\rho}{\partial\overline{r}}\right]\overline{r}^2 d\overline{r}\Bigg\}, \tag{11.23}$$

where $\boldsymbol{\sigma}^H := 2G\boldsymbol{\varepsilon} + \lambda(\mathrm{tr}\,\boldsymbol{\varepsilon})\mathbf{1}$ denotes the Hookean stress. Equation (11.23) is numerically solved by interpolating the displacement as well as the already computed concentration profiles. In particular, because of the higher-order derivatives appeared in Eq. (11.23), C^1-continuous Hermite finite elements are employed, while the integrals are calculated by using 5-point Gauss quadrature. The same nodes used for the concentration problem are employed also for the mechanical one. The final linear system reads $\mathbf{KU} = \mathbf{f}$, where the vector $\mathbf{U}$ contains nodal displacements and their derivatives, the force-like vector depends on the concentration distribution and the stiffness matrix is constant. Then, total strains are calculated via the numerical counterpart of the relations $\varepsilon_{rr} = \partial u/\partial r$ and $\varepsilon_{\theta\theta} = u/r$, while the stresses are evaluated from Eq. (11.6). The obtained results are depicted in Figs. 11.5 and 11.6.

As shown, the thicker interface predicted by higher values of ℓ_ε results in more diffused stress and strain profiles around it. Moreover, the effect of ℓ_ε is more pronounced at the interface while it practically dies out within the two phases where gradients are vanished. It is noted that the stress values predicted are rather large ($\sigma/E_{Si} = 0.2$ corresponds to $\sigma \approx 21$ GPa), and hence plasticity and/or crack initiation are likely to occur at the early stages of lithiation. In this connection, it is noted that

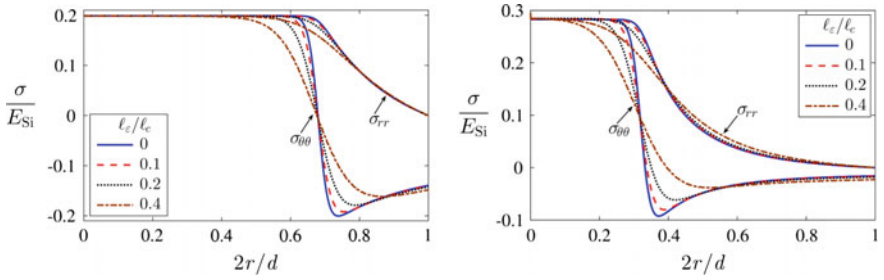

Fig. 11.5 Effect of the strain gradient length scale ℓ_ε on the stress distributions, for two different positions of the interface. The value $E_{Si} = 104.6$ GPa has been used for the Young's modulus of amorphous silicon [21]

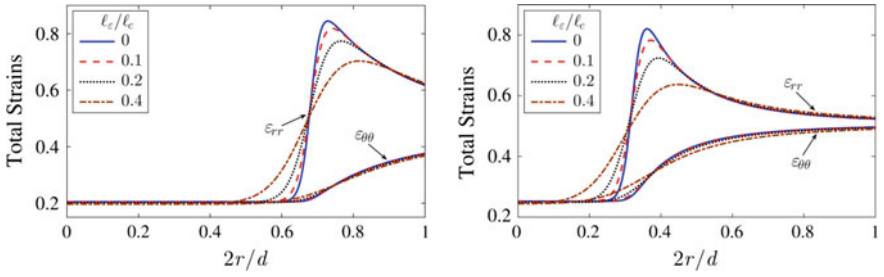

Fig. 11.6 Effect of the strain gradient length scale ℓ_ε on the total strain distributions, for two different positions of the interface

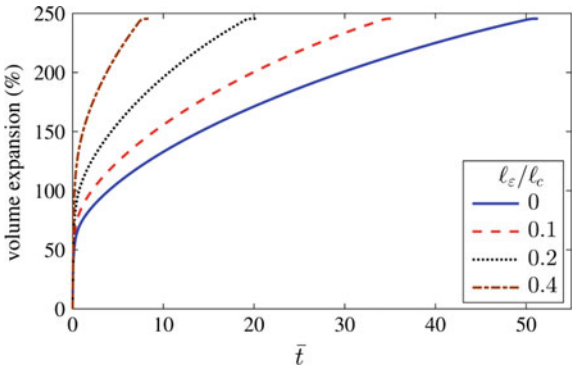

Fig. 11.7 Effect of the strain gradient length scale ℓ_ε on the evolution of the volume expansion

if a strain failure criterion is assumed then, higher values of ℓ_ε predict a stronger specimen, as implied by the maximum value of ε_{rr} in Fig. 11.5.

The evolution of the volume increase can be evaluated by the relation $\Delta V/V = [1 + \overline{u}(1, \overline{t})]^3 - 1$, and it is depicted in Fig. 11.7. Since volume expansion is an increasing function of the average concentration, their evolution graphs are similar as follows by comparing Figs. 11.4 and 11.7. Accordingly, faster lithiations predicted by higher values of ℓ_ε induce faster volume expansions.

11.4 Conclusions

A simple gradient chemoelasticity model was developed and applied to simulate the two-phase lithiation of a spherical Si nanoparticle that is free to expand. A two-stage charging process is considered, i.e., a galvanostatic stage followed by a pontetiostatice one, with the phase transition being developed in the latter. The model predicts velocities of the lithiation front in agreement with experimental observations as well as large internal stress and strain distributions which can be mediated by the action of an external pressure exerted by the surrounding matrix for a nanocomposite anode. This is a task to be undertaken in the future in a similar way done in [2] for the case of linear elasticity without explicit consideration of nonlocal diffusion and two-phase separation.

Acknowledgements The input and discussions with Professor Katerina Aifantis of the University of Florida on the topic of LIBs were very useful and deeply appreciated. The support of the Ministry of Education and Science of Russian Federation under Mega-Grant No.14.Z50.31.0039 is also gratefully acknowledged.

References

1. Aifantis, K.E., Hackney, S.A.: An ideal elasticity problem for Li-batteries. J. Mech. Behav. Mater. **14**(6), 413–427 (2003). https://doi.org/10.1515/JMBM.2003.14.6.413

2. Aifantis, K.E., Dempsey, J.P.: Stable crack growth in nanostructured Li-batteries. J. Power Sources **143**(1–2), 203–211 (2005). https://doi.org/10.1016/j.jpowsour.2004.11.037
3. Dimitrijevic, B.J., Aifantis, K.E., Hackl, K.: The influence of particle size and spacing on the fragmentation of nanocomposite anodes for Li batteries. J. Power Sources **206**, 343–348 (2012). https://doi.org/10.1016/j.jpowsour.2012.01.065
4. Aifantis, K.E., Hackney, S.A., Kumar, V.R. (Eds.): High Energy Density Lithium Batteries: Materials, Engineering, Applications. Wiley-VCH, Weinheim (2010). https://doi.org/10.1002/9783527630011
5. Cahn, J.W., Hilliard, J.E.: Free energy of a nonuniform system. I. Interfacial free energy. J. Chem. Phys. **28**(2), 258–267 (1958). https://doi.org/10.1063/1.1744102
6. Cahn, J.W.: On spinodal decomposition. Acta Metall. **9**(9), 795–801 (1961). https://doi.org/10.1016/0001-6160(61)90182-1
7. Ryu, I., Choi, J.W., Cui, Y., Nix, W.D.: Size-dependent fracture of Si nanowire battery anodes. J. Mech. Phys. Solids **59**(9), 1717–1730 (2011). https://doi.org/10.1016/j.jmps.2011.06.003
8. Bohn, E., Eckl, T., Kamlah, M., McMeeking, R.: A model for lithium diffusion and stress generation in an intercalation storage particle with phase change. J. Electrochem. Soc. **160** (10), A1638–A1652 (2013). https://doi.org/10.1149/2.011310jes
9. Haftbaradaran, H., Song, J., Curtin, W.A., Gao, H.: Continuum and atomistic models of strongly coupled diffusion, stress, and solute concentration. J. Power Sources **196**, 361–370 (2011). https://doi.org/10.1016/j.jpowsour.2010.06.080
10. Zhao, K., Pharr, M., Cai, S., Vlassak, J.J., Suo, Z.: Large plastic deformation in high-capacity lithium-ion batteries caused by charge and discharge. J. Am. Ceram. Soc. **94**(S1), S226–S235 (2011). https://doi.org/10.1111/j.1551-2916.2011.04432.x
11. Anand, L.: A Cahn–Hilliard-type theory for species diffusion coupled with large elastic-plastic deformations. J. Mech. Phys. Solids **60**, 1983–2002 (2012). https://doi.org/10.1016/j.jmps.2012.08.001
12. Cogswell, D.A., Bazant, M.Z.: Coherency strain and the kinetics of phase separation in $LiFePO_4$ nanoparticles. ACS Nano **6**(3), 2215–2225 (2012). https://doi.org/10.1021/nn204177u
13. Bagni, C., Askes, H., Aifantis, E.C.: Gradient-enriched finite element methodology for axisymmetric problems. Acta Mech. **228**(4), 1423–1444 (2017). https://doi.org/10.1007/s00707-016-1762-7
14. Tsagrakis, I., Aifantis, E.C.: Thermodynamic coupling between gradient elasticity and a Cahn–Hilliard type of diffusion: size-dependent spinodal gaps. Contin. Mech. Thermodyn. (2017). https://doi.org/10.1007/s00161-017-0565-y
15. Tsagrakis, I., Aifantis, E.C.: Gradient and size effects on spinodal and miscibility gaps. Contin. Mech. Thermodyn. (submitted) (2017)
16. Liu, X.H., Wang, J.W., Huang, S., Fan, F., Huang, X., Liu, Y., Krylyuk, S., Yoo, J., Dayeh, S. A., Davydov, A.V., Mao, S.X., Picraux, S.T., Zhang, S., Li, J., Zhu, T., Huang, J.Y.: In situ atomic-scale imaging of electrochemical lithiation in silicon. Natl. Nanotechnol. **7**, 749–756 (2012). https://doi.org/10.1038/nnano.2012.170
17. Wang, J.W., He, Y., Fan, F., Liu, X.H., Xia, S., Liu, Y., Harris, C.T., Li, H., Huang, J.Y., Mao, S.X., Zhu, T.: Two-phase electrochemical lithiation in amorphous silicon. Nano Lett. **13** (2), 709–715 (2013). https://doi.org/10.1021/nl304379k
18. Chen, L., Fan, F., Hong, L., Chen, J., Ji, Y.Z., Zhang, S.L., Zhu, T., Chen, L.Q.: A phase-field model coupled with large elasto-plastic deformation: application to lithiated silicon electrodes. J. Electrochem. Soc. **161**(11), F3164–F3172 (2014). https://doi.org/10.1149/2.0171411jes
19. Xie, Z., Ma, Z., Wang, Y., Zhou, Y., Lu, C.: A kinetic model for diffusion and chemical reaction of silicon anode lithiation in lithium ion batteries. RSC Adv. **6**, 22383–22388 (2016). https://doi.org/10.1039/C5RA27817A
20. Beaulieu, L.Y., Eberman, K.W., Turner, R.L., Krause, L.J., Dahna, J.R.: Colossal reversible volume changes in lithium alloys. Electrochem. Solid-State Lett. **4**(9), A137–A140 (2001). https://doi.org/10.1149/1.1388178

21. Berla, L.A., Lee, S.W., Cui, Y., Nix, W.D.: Mechanical behavior of electrochemically lithiated silicon. J. Power Sources **273**, 41–51 (2015). https://doi.org/10.1016/j.jpowsour.2014.09.073
22. Aifantis, E.C., Serrin, J.B.: The mechanical theory of fluid interfaces and Maxwell's rule. J. Colloid Interface Sci. **96**(2), 517–529 (1983). https://doi.org/10.1016/0021-9797(83)90053-X
23. Aifantis, E.C., Serrin, J.B.: Equilibrium solutions in the mechanical theory of fluid microstructures. J. Colloid Interface Sci. **96**(2), 530–547 (1983). https://doi.org/10.1016/0021-9797(83)90054-1
24. Burch, D., Bazant, M.Z.: Size-dependent spinodal and miscibility gaps for intercalation in nanoparticles. Nano Lett. **9**(11), 3795–3800 (2009). https://doi.org/10.1021/nl9019787
25. Bockris, J.O'M., Reddy, A.K.N., Gamboa-Aldeco, M.E.: Modern Electrochemistry 2A: Fundamentals of Electrodics, 2nd edn, p. 1213. Kluwer Academic Publishers (2002). https://doi.org/10.1007/0-306-47605-3_2
26. Purkayastha, R., McMeeking, R.: A parameter study of intercalation of lithium into storage particles in a lithium-ion battery. Comput. Mater. Sci. **80**, 2–14 (2013). https://doi.org/10.1016/j.commatsci.2012.11.050
27. Ding, N., Xu, J., Yao, Y.X., Wegner, G., Fang, X., Chen, C.H., Lieberwirth, I.: Determination of the diffusion coefficient of lithium ions in nano-Si. Solid State Ionics **180**, 222–225 (2009). https://doi.org/10.1016/j.ssi.2008.12.015

Chapter 12
Generalized Continua Concepts in Coarse-Graining Atomistic Simulations

Shuozhi Xu, Ji Rigelesaiyin, Liming Xiong, Youping Chen and David L. McDowell

Abstract Generalized continuum mechanics (GCM) has attracted increased attention in the context of multiscale materials modeling, an example of which is a bottom-up GCM model, called the atomistic field theory (AFT). Unlike most other GCM models, AFT views a crystalline material as a continuous collection of lattice points; embedded within each point is a unit cell with a group of discrete atoms. As such, AFT concurrently bridges the discrete and continuous descriptions of materials, two fundamentally different viewpoints. In this chapter, we first review the basics of AFT and illustrate how it is realized through coarse-graining atomistic simulations via a concurrent atomistic-continuum (CAC) method. Important aspects of CAC, including its advantages relative to other multiscale methods, code development, and numerical implementations, are discussed. Then, we present recent applications of CAC to a number of metal plasticity problems, including static dislocation properties, fast moving dislocations and phonons, as well as dislocation/grain boundary interactions. We show that, adequately replicating essential aspects of dislocation fields at a fraction of the computational cost of full

S. Xu
California NanoSystems Institute, University of California, Santa Barbara, Santa Barbara, CA 93106-6105, USA

J. Rigelesaiyin · L. Xiong
Department of Aerospace Engineering, Iowa State University, Ames, IA 50011, USA

Y. Chen
Department of Mechanical and Aerospace Engineering, University of Florida, Gainesville, FL 32611-6250, USA

D. L. McDowell
Woodruff School of Mechanical Engineering, Georgia Institute of Technology, Atlanta, GA 30332-0405, USA

D. L. McDowell (✉)
School of Materials Science and Engineering, Georgia Institute of Technology, Atlanta, GA 30332-0245, USA
e-mail: david.mcdowell@me.gatech.edu

H. Altenbach et al. (eds.), *Generalized Models and Non-classical Approaches in Complex Materials 2*, Advanced Structured Materials 90,
https://doi.org/10.1007/978-3-319-77504-3_12

atomistics, CAC is established as an effective tool for coarse-grained modeling of various nano/micro-scale thermal and mechanical problems in a wide range of monatomic and polyatomic crystalline materials.

12.1 Generalized Continuum Mechanics (GCM)

In classical continuum mechanics (CCM), a material consists of continuously distributed material points with infinitesimal size that fill the entire region of an infinite space they occupy [1]. The micro-scale kinetics or dynamics are implicitly averaged. The physical properties of each point are determined only by the deformation and history of that point, i.e., each point behaves independently following the same constitutive law. Interactions between these points take place only through the balance equations. Mechanics of real materials, however, deals with finite-sized materials with finite-sized material points, e.g., a large number of molecules, or the primitive unit cell of a crystal. From the atomic viewpoint, there is a lower limit to divisibility for any material, as continuum quantities such as mass density only have physical meaning in regions actually containing matter. Thus, CCM fails to describe the materials deformation at the atomic/nano-scale.

Limitations of CCM have motivated the development of various enhanced methods, a vast number of which aim at tackling the locality issue. Among these methods, a weakly nonlocal theory, named generalized continuum mechanics (GCM, also known as microcontinuum field theory), extends the classical field theory to microscopic space and time scales [2]. In GCM, materials are envisioned as a continuum collection of deformable point particles. Each point particle, with a finite size, has a continuous internal deformation which is represented by some vectors attached to it. Accordingly, a particle is identified by its position vector $\mathbf{R}$ and some director vectors attached to this point $\boldsymbol{\Xi}_\alpha$ in the undeformed state. In a solid crystal, $\mathbf{R}$ is employed to describe the continuous lattice deformation, in which the material is viewed as a collection of infinitesimal point particles, while $\boldsymbol{\Xi}_\alpha$ considers each point particle with finite size and describes its continuous internal deformation. Both $\mathbf{R}$ and $\boldsymbol{\Xi}_\alpha$ have their own motions or mappings to the deformed states $\mathbf{r}$ and ξ_α at time t, respectively, i.e.,

$$\mathbf{R} \rightarrow {}^{t}\mathbf{r},\ \boldsymbol{\Xi}_\alpha \rightarrow {}^{\mathbf{R},t}\xi_\alpha,\ \alpha = 1, 2, 3,\ \ldots,\ N \tag{12.1}$$

Such a medium is called microcontinuum of grade N. By introducing $\boldsymbol{\Xi}_\alpha$, the microcontinuum naturally brings length and time scales into the field theories; by considering the ratio of the external characteristic length to the internal characteristic length, the GCM theories are nonlocal in character. For the first grade microcontinuum ($N = 1$), $\boldsymbol{\Xi}_1$ are three deformable directors, conferring each point particle nine extra degrees of freedom (DOFs) compared to the local theory. This is the micromorphic continuum. The other two are the microstretch continuum and the

micropolar continuum, which can be achieved by constraining the director vectors in certain ways.

In the last seven years, Maugin [1–7] dedicated an extensive effort to the understanding and dissemination of GCM by offering a historical perspective, deep mathematical and physical insights, as well as a clear explanation of its essences. Maugin [3] summarized and discussed three possible paths towards the generalization of continuum mechanics: "*involving an additional microstructure at each material point*", "*introducing higher order gradients of the displacement in the energy density (weak nonlocal theory)*", and "*considering spatial functionals for the constitutive equations (strongly or truly nonlocal theory)*". Maugin [3] further posited and addressed three questions: "(1) *Do we need GCM at all? (2) Do we find the necessary tools in what exists nowadays? (3) What is the relationship between discrete and continuous descriptions if there must exist a consistent relationship between the two?*"

For the third question, Maugin [3] wrote "*the author personally believes that any relationship that can be established with a sub-level degree of physical description is an asset that no true physicist can discard*". This perspective is based on the distinction between atomic and continuous descriptions of matter; for the former, matter is manifested as discrete particles, whereas for the latter, matter is infinitely divisible. These two different views lead to fundamentally different theories. The "*material point*", Maugin [2] wrote, "*is quite suspiciously defined in a classical continuum*"; "*A point is the intersection of two immaterial (zero-thickness) curves on a two-dimensional surface. This, Newton already knew in his 'Principia Mathematica' where mass at a so-called 'material point' can only be defined by density multiplied by volume*". To avoid introducing the physical concept of a material point, CCM textbooks use global conservation laws to derive the local balance laws by purely mathematical means, leaving the question on the conditions under which the differential form of balance laws are valid unanswered. While continuum physics is always an approximation to the underlying discrete molecular physics, GCM is undoubtedly a better approximation than CCM to the description of real materials. It helps to bridge the gap between continuum and atomic views of materials.

12.2 Atomistic Field Theory (AFT)

In micromorphic field theory, the motion of point particles is governed by conservation equations of mass, microinertia, generalized spin, linear momentum, and energy. Based on micromorphic field theory, Chen and Lee [8] proposed a new GCM model, called the atomistic field theory (AFT), which treats a crystalline material as a continuous collection of material points (unit cells), but with each material point possessing internal DOFs that describe the movement of atoms inside each unit cell, as shown in Fig. 12.1. In this way, the micromorphic theory is

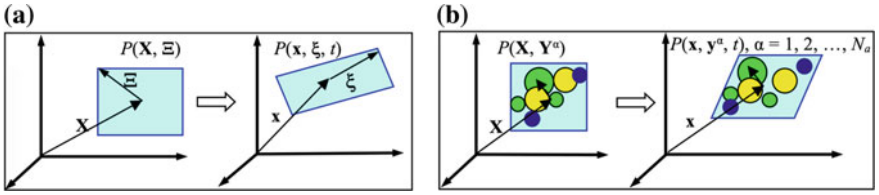

Fig. 12.1 Macro- and micro-motions of a material particle P in **a** micromorphic theory and **b** AFT. Left in **a** and **b** is the reference state at time 0 while right is the deformation state at time t. $\mathbf{X}$ and $\mathbf{x}$ are the positions of the mass center of the unit cell, $\boldsymbol{\Xi}$ and $\boldsymbol{\xi}$ are internal positions, $\mathbf{Y}^{\alpha}$ and $\mathbf{y}^{\alpha}$ are positions of atom α with respect to $\mathbf{X}$ and $\mathbf{x}$, respectively, N_a is the number of atoms in a unit cell. Reproduced with permission from Ref. [11]

connected with molecular dynamics (MD) and encompasses the atomic scale [9]. Here, the local density function is continuous at the level of the unit cell, but discrete in terms of the discrete atoms inside the unit cell [10, 11].

AFT differs from CCM in that it has two-level structure description of materials. It is also distinct from popular generalized continuum theories, such as the Cosserat theory [12], micropolar theory, [13, 14], micromorphic theory [15–20], or other generalized continuum theories [21, 22], in that the sub-level structure and physical description are not continuous but discrete. As a result of the discrete sub-level description in AFT, only balance of linear momentum is relevant to the dynamics. A comparison of the material description in AFT with those in GCM and CCM is presented in Table 12.1.

The main theoretical tool to link the atomic to the continuum description is statistical mechanics [23–26]. Statistical mechanics views thermodynamics and

Table 12.1 Comparison of CCM, top-down formulated theories of GCM, and AFT

Theory	Material description	Constituents of materials	Internal DOF	Governing laws	Constitutive relations
CCM	A single phase single component continuum	0D Material point without structure	None	Conservation of mass, linear and angular momentum, and energy	11 constitutive relations
GCM	A continuum with embedded microstructure	Finite-sized material particles	3 in micropolar, 9 in micromorphic	Conservation of mass, micro-inertia, linear and angular momentum, generalized spin, and energy	20 constitutive relations
AFT	A crystal structure as lattice + basis	Atoms	3 N_a (N_a is the number of atoms in one basis)	Conservation of mass, linear momentum, and energy	Interatomic potential

continuum mechanics as coarse-grained (CG) descriptions of classical *N*-body dynamics, and defines "coarse-graining" as "*the process of representing a system with fewer degrees of freedom than those actually present in the system*" [27]. From this definition, existing CG models are either atomistic CG models that are derived bottom-up from the underlying atomistic model or phenomenological models that have no direct connection to the underlying atomistic model. Existing coarse-graining methods for derivation of atomistic CG models can be further divided into three categories [11]: (1) reducing the order of particle representation of the molecular structure, e.g., the super-atom method, united-atom method, and multiscale-CG [28–31], (2) assuming continuous deformation of the lattice (affine or using some other imposed shape functions), e.g., quasicontinuum (QC) [32], hot-QC [33–35] and coarse-grained molecular dynamics (CGMD) [36], and (3) deriving an equivalent continuum field representation for the atomistic system, e.g., the Irving-Kirkwood (IK) statistical mechanics formulation of hydrodynamics [37], MD formulation of micromorphic theory [17–20], and the AFT formulation [8, 9]. These are shown in Table 12.2.

Different from other GCM theories that are derived via a top-down approach, AFT is bottom-up derived from the underlying atomistic model, and hence it is also a CG atomistic model. The AFT formulation is an extension of the IK formulation of "*the hydrodynamics equations for a single component, single phase system*" [37] to a two-level structural description of general crystalline materials. It employs the two-level crystalline materials description in solid state physics, i.e., crystal structure = lattice + basis [38]. As a result of its bottom-up atomistic formulation, all the

Table 12.2 Comparison of atomistic CG methods. ODE and PDE stand for ordinary differential equations and partial differential equations, respectively

Atomistic CG methods	Route to CG	Entities in simulations	Representative CG models	Governing laws	Governing equations
Structural reduction	From atoms to super-atoms through grouping many atoms into one super-atom	Super-atoms	Super-atom method, united atom method, multiscale-CG [28–31]	Newtonian Mechanics	2nd order ODE
Assuming homogeneous displacements of atoms	From atoms to rep-atoms using the Cauchy-Born rule or other prescribed shape functions	Representative atoms	QC [32], hot-QC [33–35]	Energy minimization	1st order ODE
Using continuum representation	From atomistic to continuum using statistical mechanics	Material points	IK hydrodynamics [37], AFT [8, 9]	Conservation laws	2nd order PDE

essential atomistic information of the material, including the atomic-level crystal structure and the interactions between atoms, is attained. The formulation naturally leads to a concurrent atomistic-continuum representation of the materials governed by a single set of balance equations for both atomic and continuum regions, as an exact consequence of Newton's second law [8, 9], in the following forms,

$$\frac{\mathrm{d}\rho^{\alpha}}{\mathrm{d}t}+\rho^{\alpha}\left(\nabla_{\mathbf{x}}\cdot\mathbf{v}+\nabla_{\mathbf{y}^{\alpha}}\cdot\Delta\mathbf{v}^{\alpha}\right)=0 \tag{12.2}$$

$$\rho^{\alpha}\frac{\mathrm{d}}{\mathrm{d}t}\left(\mathbf{v}+\Delta\mathbf{v}^{\alpha}\right)=\nabla_{\mathbf{x}}\cdot\mathbf{t}^{\alpha}+\nabla_{\mathbf{y}^{\alpha}}\cdot\boldsymbol{\tau}^{\alpha}+\mathbf{f}_{\mathrm{ext}}^{\alpha} \tag{12.3}$$

$$\rho^{\alpha}\frac{\mathrm{d}e^{\alpha}}{\mathrm{d}t}=\nabla_{\mathbf{x}}\cdot\mathbf{q}^{\alpha}+\nabla_{\mathbf{y}^{\alpha}}\cdot\mathbf{j}^{\alpha}+\mathbf{t}^{\alpha}\colon\nabla_{\mathbf{x}}\left(\mathbf{v}+\Delta\mathbf{v}^{\alpha}\right)+\boldsymbol{\tau}^{\alpha}\colon\nabla_{\mathbf{y}^{\alpha}}\left(\mathbf{v}+\Delta\mathbf{v}^{\alpha}\right) \tag{12.4}$$

where $\mathbf{x}$ is the physical space coordinate of the continuously distributed lattice; $\mathbf{y}^{\alpha}(\alpha=1,2,\ \ldots,N_a)$, with N_a being the total number of atoms in a unit cell, is the subscale internal variable describing the position of atom α relative to the mass center of the lattice located at $\mathbf{x}$; ρ^{α}, $\rho^{\alpha}\left(\mathbf{v}+\Delta\mathbf{v}^{\alpha}\right)$, and $\rho^{\alpha}e^{\alpha}$ are the local densities of mass, linear momentum, and internal energy, respectively; $\mathbf{v}+\Delta\mathbf{v}^{\alpha}$ is the atomic-level velocity and $\mathbf{v}$ is the velocity field; $\mathbf{f}_{\mathrm{ext}}^{\alpha}$ is the external force field; $\mathbf{t}^{\alpha}$ and $\mathbf{q}^{\alpha}$ are the momentum flux and heat flux due to the homogeneous deformation of lattice, respectively; $\boldsymbol{\tau}^{\alpha}$ and $\mathbf{j}^{\alpha}$ are the momentum flux and heat flux due to the reorganizations of atoms within the lattice cells, respectively.

For conservative systems, i.e., in the absence of an internal source that generates or dissipates energy, the energy equation (Eq. 12.4) is equivalent to the linear momentum equation (Eq. 12.3). We remark that, supplemented with the interatomic force field, the first two AFT balance equations (Eqs. 12.2 and 12.3) are sufficient for a wide range of thermal and mechanical problems, some of which will be discussed in Sect. 12.4. Employing the classical definition of kinetic temperature, which is proportional to the kinetic part of the atomic stress, the linear momentum equations can be expressed in a form that involves the internal force density and temperature T [39–41], i.e.,

$$\rho^{\alpha}\ddot{\mathbf{u}}^{\alpha}(\mathbf{x})+\frac{\gamma^{\alpha}k_{\mathrm{B}}}{\Delta V}\nabla_{\mathbf{x}}T=\mathbf{f}_{\mathrm{int}}^{\alpha}(\mathbf{x})+\mathbf{f}_{\mathrm{ext}}^{\alpha}(\mathbf{x}),\quad \alpha=1,2,\ \ldots,N_a \tag{12.5}$$

where $\mathbf{u}^{\alpha}(\mathbf{x})$ is the displacement of atom α at point $\mathbf{x}$; the superposed dots denote the material time derivative; ΔV is the volume of the finite-sized material particle (the primitive unit cell for crystalline materials) at $\mathbf{x}$; k_{B} is the Boltzmann constant; $\gamma^{\alpha}=\rho^{\alpha}/\sum_{\alpha=1}^{N_a}\rho^{\alpha}$, and $\mathbf{f}_{\mathrm{int}}^{\alpha}$ is the internal force density and is a nonlinear nonlocal function of relative atomic displacements. For systems with a constant temperature field or a constant temperature gradient, the temperature term in Eq. 12.5 can be considered as a surface traction on the boundary or a body force in the interior of the material, $\mathbf{f}_{\mathrm{T}}^{\alpha}(\mathbf{x})$ [40]. Denoting the finite element shape function as $\boldsymbol{\Phi}_{\xi}(\mathbf{x})$, the Galerkin weak form of Eq. 12.5 can be written as

$$\int_{\Omega(\mathbf{x})} \mathbf{\Phi}_{\xi}(\mathbf{x})\left(\rho^{\alpha}\ddot{\mathbf{u}}^{\alpha}(\mathbf{x}) + \mathbf{f}_{\mathrm{T}}^{\alpha}(\mathbf{x}) - \mathbf{f}_{\mathrm{int}}^{\alpha}(\mathbf{x}) - \mathbf{f}_{\mathrm{ext}}^{\alpha}(\mathbf{x})\right)\mathrm{d}\mathbf{x} = 0 \tag{12.6}$$

where $\Omega(\mathbf{x})$ is the simulation domain; the integral, using Gaussian quadrature, can be approximated by a weighted sum of the evaluations of the integrand at a set of integration points, leading to a set of discretized governing equations with the finite element nodal displacement as the unknowns to be solved.

In summary, AFT coarse-grains a discrete atomistic model by introducing an equivalent continuum description, i.e., by formulating a GCM representation of the underlying atomistic model. The field equations are then discretized and solved using finite element method (FEM). This process can be interpreted using Maugin's insightful and inspirational remarks: "*continualization*" is "*to construct sensible models*"; "*discretization*" is "*to be able to solve problems*" [2].

12.3 The Concurrent Atomistic-Continuum (CAC) Method

12.3.1 A Comparison Between CAC and Other Multiscale Methods

The AFT-based concurrent atomistic-continuum (CAC) method outlined in this chapter is an integral finite element approach for coarse-grained atomistics that admits description of dislocation nucleation, migration, and interaction with or without adaptive coarse-graining [9, 42–44], in contrast to QC. A CAC model, in general, has two domains: an atomistic domain containing atoms and a coarse-grained domain containing elements, as shown in Fig. 12.2. CAC employs a unified atomistic-continuum integral formulation (Eq. 12.6) with elements that have discontinuities between them and an underlying nonlocal interatomic force-displacement relation as the only constitutive relation. Ghost forces arising from a change of the underlying continuum formulation and energy summation rules in other approaches based on domain decomposition or coarse-graining are not an issue in CAC since the underlying integral formulation and constitutive framework do not change. Dislocations can be modeled throughout the entire domain, whether at full atomistic resolution or coarse-grained, because the elements are assumed to have faces on slip planes of the lattice, e.g., {111} and {110} planes in face-centered cubic (FCC) and body-centered cubic (BCC) lattices, respectively. This sets it apart from methods that require full atomistic resolution at the dislocation core. In contrast to QC, which has the objective of seeking convergence of the adaptively coarse-grained solution to that of the full atomistic solution for various field problems, CAC can have multiple purposes. On the one hand, it can coarse-grain in regions away from atomistic domains of interest and capture

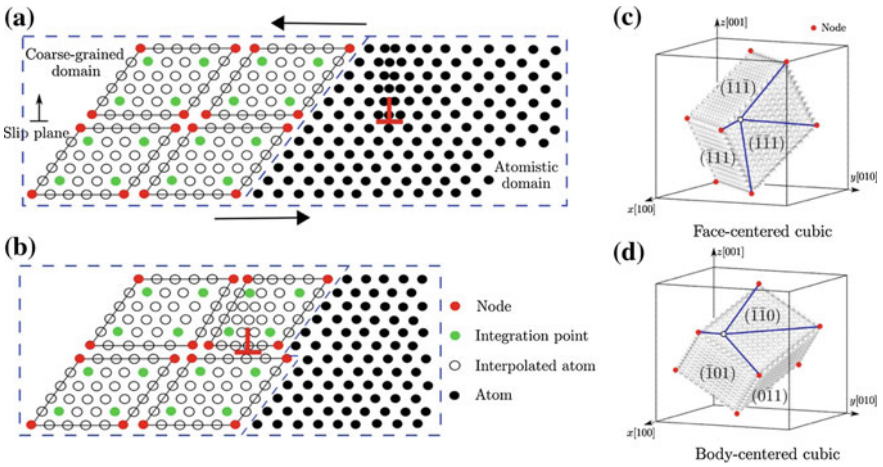

Fig. 12.2 **a–b** A 2-D CAC simulation domain consisting of an atomistic domain (right) and a coarse-grained domain (left). The atomistic domain is composed of atoms (black circles), which follow the same governing equations in the atomistic simulation. The coarse-grained domain consists of elements of varying size that have discontinuities between them, each of which contains a large number of underlying atoms with the nodes (red circles) as the only DOFs. Only the force/energy on integration points (green circles) and nodes are calculated. In **a**, an edge dislocation (red ⊥) is located in the atomistic domain. Upon applying a shear stress on the simulation cell, the dislocation migrates into the coarse-grained domain in **b**, where the Burgers vector spreads out between elements. **c–d** In 3-D, elements have faces on {111} planes and on {110} planes in an FCC and a BCC lattice, respectively. The positions of atoms within each element (open circles) are interpolated from the nodal positions. Reproduced with permission from Ref. [43]

long-range fields of dislocations, as in coupled atomistic and discrete dislocation (CADD) [45, 46]. On the other hand, it can model dislocations across a range of length scales to access trends and provide support for mechanistic understanding of coarse scale behavior of fields of dislocations, smearing individual cores but preserving the net Burgers vector, representing long-range and approximating short-range interactions. While QC typically seeks the most accurate and efficient solution to dislocation plasticity via adaptive remeshing of the domain near dislocations to full atomistic resolution, CAC can resolve full atomistics if necessary near interfaces or crack tips, but allows dislocations to nucleate, multiply, migrate, and interact even in the coarse-grained domain along interfaces between elements, introducing the option to coarse-grain dislocation fields over larger scales.

Like QC, CAC employs the same interatomic potential in both coarse-grained and atomistic domains where dislocations evolve and interact. This introduces systematic coarse-graining error, which originates from displacement approximation (i.e., the shape function) and the numerical integration. As the element size is reduced, the CAC predictions properly converge to the fully atomistic results. The coarse-graining error can be quantified and balanced with the high computational demands of remeshing, according to the purposes of the mesoscale modeling, for example in representation of dislocation core structures and short-range

interactions. It can also be minimized by use of adaptive remeshing, based on the level of the nodal displacement between elements [47]; this is necessary for general field problems to allow dislocation migration along arbitrary extended slip planes. However, remeshing need not be carried out to fully atomistic level, but can involve simply splitting larger continuum elements containing many atoms. Unlike QC, CAC does not employ the assumption of continuous lattice deformation throughout the coarse-grained domain and admits dislocation activity/displacement discontinuity between elements. As such, it pursues gradual coarse-graining from full atomistic resolution upward. For example, if trends of behavior or collective mechanisms are to be considered as a function of microstructure or stress state, as is often the case in applications of dislocation dynamics (DD) models [48–57], CAC may offer a means to support such parametric studies.

12.3.2 Code Development

The first version of the CAC numerical tool was developed by Xiong and Chen [57, 58] and Deng et al. [39, 59]. The reformulated balance equations [9] were numerically implemented using FEM with trilinear finite element shape functions and nodal integration. Later, the form and capabilities of the CAC method were extended substantially in modeling quasistatic and dynamics behavior of dislocations: elements that have discontinuities between them were employed, and the Gaussian quadrature was used for integration in the coarse-grained domain [42, 60–66]. Yang et al. [67–70] rewrote the CAC code for multiscale simulation of polycrystalline ionic materials. Based on this code, Chen et al. [71–74] extended the CAC method for space- and time-resolved simulation of the transient processes of the propagation of heat pulses in single crystals and across GBs [72] as well as the interactions between heat pulses and moving dislocations [71]; a new shape function was designed to facilitate the seamless passing of waves between the atomistic and coarse-grained domains [73]. More recently, Xu et al. [44] developed PyCAC, a novel numerical implementation of the CAC approach. In PyCAC, the CAC method is implemented in Fortran 2008 with a distributed-memory spatial decomposition parallel algorithm, while a Python scripting interface is built to provide a robust user interface to facilitate parametric studies via CAC simulations without interacting with the underlying Fortran code and to improve handling of input, output, and visualization options. For example, the finite element nodal positions obtained in CAC simulations can be mapped back to atomic positions through the Python interface; in this way, the atomic trajectories can be visualized using common atomistic configuration viewers such as AtomEye [75] and OVITO [76]. It has been demonstrated that the PyCAC code has a good parallel scaling performance and is an efficient, user-friendly, and extensible CAC simulation environment [44].

12.3.3 Numerical Implementations in PyCAC

The PyCAC code [44] can simulate monatomic pure FCC and pure BCC metals using the Lennard-Jones [77] and the many-body embedded-atom method (EAM) [78] interatomic potentials in a constant temperature field. The energy equation (Eq. 12.5) and the term $\mathbf{f}_{\mathrm{T}}^{\alpha}$ (Eq. 12.6) have not yet been implemented because they have small effects on mechanical response in the case of constant temperature. We remark that (i) there is ongoing work in interpreting $\mathbf{f}_{\mathrm{T}}^{\alpha}$ and in comparing different descriptions of temperature in the coarse-grained domain [25, 26], and (ii) for monatomic crystals $(N_a = 1)$, $\mathbf{y}^{\alpha}$ vanishes, and atom α sits at the nodal site; Eqs. 12.2–12.4 reduce to the balance equations in CCM.

In the coarse-grained domain, the integral in Eq. 12.6 is approximated using Gaussian quadrature, in which the positions and weights of the integration points are usually determined by the order of the integrand. It is, however, difficult to employ a unified set of integration points within an element because that the interatomic potential-based $\mathbf{f}_{\mathrm{int}}^{\alpha}(\mathbf{x})$ can be a complicated and highly non-linear function and that the variation of the integrand is not uniform within an element [43, 79]. To circumvent this problem, each element is divided into a number of non-overlapping subregions. In this way, one only needs to determine the order of the integrand within each subregion, which is usually lower than that within the entire element and is more easily approximated. In practice, either the first order [42] or the second order [43] Gaussian quadrature can be adopted, with a trilinear shape function $\mathbf{\Phi}_{\xi}(\mathbf{x})$, and the force on node ξ is

$$\mathcal{F}^{\xi} = \frac{\sum_{\mu} \omega_{\mu} \mathbf{\Phi}_{\mu\xi} \mathrm{F}^{\mu}}{\sum_{\mu} \omega_{\mu} \mathbf{\Phi}_{\mu\xi}} + \mathrm{F}_{\mathrm{ext}}^{\xi} \tag{12.7}$$

where ω_{μ} is the weight of integration point μ, $\mathbf{\Phi}_{\mu\xi}$ is the shape function of node ξ at integration point μ, F^{μ} is the interatomic potential-based atomic force on integration point μ, and $\mathrm{F}_{\mathrm{ext}}^{\xi}$ is the external force applied on node ξ. We refer the readers to Refs. [43, 79] where details of the Gaussian quadrature, subregion, and integration points are presented.

In the atomistic domain, an atom can be viewed as a special finite element for which the shape function $\mathbf{\Phi}_{\xi}$ in Eq. 12.6 reduces to 1 at the atomic site, and the force on atom α is simply

$$\mathrm{F}^{\alpha} = -\nabla_{\alpha} E + \mathrm{F}_{\mathrm{ext}}^{\alpha} \tag{12.8}$$

where E is the interatomic potential-based internal energy and $\mathrm{F}_{\mathrm{ext}}^{\alpha}$ is the external force applied on atom α. As such, common atomistic simulation techniques are employed: Newton's third law is employed to promote efficiency in calculating the force, pair potential, local electron density, and stress; the short-range neighbor search employs a combined cell list [80] and Verlet list [81] method.

Distinguished by how $\mathcal{F}$ and F are subsequently used, two main types of CAC simulations—dynamic CAC and quasistatic CAC, by analogy with MD and molecular statics (MS), respectively—have been developed. In dynamic CAC, the equation of motion (Eq. 12.6) or its modified form of each node/atom is solved directly using the velocity Verlet algorithm [82]. In quasistatic CAC, $\mathcal{F}$ and F are used to adjust the nodal and atomic positions, respectively, at each increment of system loading during energy minimization. For example, in both conjugate gradient and steepest descent algorithms, $\mathcal{F}$ and F are taken as the initial directions along which the nodes and atoms should move, respectively [43]. In practice, a third type of CAC simulation—hybrid CAC—can be employed to perform periodic energy minimization during a dynamic CAC simulation, so as to enable the constrained multiscale optimization for a sequence of non-equilibrium defect configurations in materials [83, 84]. In all types of CAC simulations, the nodes in the coarse-grained domain and the atoms in the atomistic domain interact with each other at each simulation step and are updated concurrently. More specific details of PyCAC, including the input script format and a few example problems, can be found in the PyCAC user's manual that is hosted on www.pycac.org.

12.4 Applications of the CAC Method to Metal Plasticity

Metal plasticity is a multiscale phenomenon that is manifested by irreversible microstructure rearrangement associated with nucleation, multiplication, interaction, and migration of dislocations [85]. Long-range field interactions between dislocations, along with the short-range dislocation reactions, are extremely important to describe in predicting the overall plastic behavior of materials at the macroscopic level. The former necessitates large solution scales, while the latter demands treatment of core effects using accurate underlying interatomic potentials. Metal plasticity therefore requires concurrent coupling across various scales.

In the context of dislocation/crack mediated metal plasticity, CAC has been used in a number of applications. These include impact of a rigid ball against a plate in an ideal FCC single crystal [59] and a $SrTiO_3$ polycrystal [69], brittle fracture in an ideal FCC crystal [39] and $SrTiO_3$ [67], ductile fracture in Cu [47], dislocation nucleation from notched specimens in Cu, Ni, and Al [42, 60, 61], nanoindentation in Cu [43, 60] and $SrTiO_3$ [67], nucleation and growth of dislocation loops in Cu, Al, and Si [62, 63], dislocation nucleation from GBs in $SrTiO_3$ [69], crack/GB interactions in $SrTiO_3$ [68], stationary dislocations in Cu, Ni, and Al [43, 86], quasistatic [43], subsonic [47], and transonic [66] dislocation migration in Cu, Ni, and Al, quasistatic dislocation migration across the atomistic/coarse-grained domain interface in Cu and Al [43], screw dislocation cross-slip in Ni [87], edge dislocations bowing out from obstacles in Al [88], dislocation multiplication from Frank-Read (FR) sources in Cu, Ni, and Al [86], dislocation/void interactions in Ni [65], dislocation/stacking fault interactions in Ni, Al, and Ag [89], sequential transfer of curved dislocations across GBs in Cu, Al, and Ni [83, 84], dislocation/phonon interactions in Cu [66, 71] and

Ni [64], phonon waves passing the atomistic/coarse-grained domain interface in 1D monatomic, diatomic, and triatomic crystals [90] and Cu single crystals [73], as well as phonon heat transport across a Σ19 symmetric tilt grain boundary (STGB) in Cu polycrystals [72]. The success of these calculations suggests the viability of using CAC simulations to study metal plasticity phenomena in a sufficiently large 3D model, which would normally be inaccessible to atomistics.

We remark that applications to date of the quasistatic CAC implementation [43] have been limited to monatomic crystals [43, 44, 79, 83, 84, 86, 87, 88, 89], while polyatomic crystals have been considered in dynamic CAC applications [57, 58, 62, 67, 68, 69, 70, 90]. Nevertheless, there is no theoretical challenge in applying quasistatic CAC to polyatomic crystals. The quasistatic implementation is considered useful for modeling reaction pathways for thermally activated dislocation processes in a manner that avoids the overdriven character of dynamic simulations. Hybrid CAC, with periodic energy minimization (e.g., every 50 time steps) while using quenched dynamics at each time step, may be regarded to accord with the concept of a sequence of constrained equilibrium states as espoused in internal state variable theory [91, 92], traversing the energy landscape such that each stage of the process (even with no dislocation flux) corresponds to a non-zero thermodynamic force (the Peach-Koehler force on a dislocation), due to elastic interactions. In the following, we discuss applications of the CAC method to static dislocation properties, fast moving dislocations and phonons, as well as dislocation/GB interactions.

12.4.1 Static Dislocation Properties

A question arises as to how well the non-singular dislocation core and associated Burgers vector [93–95] are described in the coarse-grained domain in CAC. For this purpose, quasistatic CAC simulations have been carried out to study certain benchmark problems, including generalized stacking fault energy (GSFE) [43], dislocation core structure/energy/stress fields [43, 86], and Peierls stress [86]. It is found that the coarse-grained domain predicts a less relaxed dislocation core. As a result, compared with atomistics, the coarse-grained domain exhibits a wider stacking fault width [43], a lower SFE [43], a larger core radius [86], a higher core energy [86], a lower Peierls stress [86], and a lower critical shear stress for dislocation bowing-out between obstacles [86, 88]; a dislocation also changes its local structure when passing across the numerical atomistic/coarse-grained domain interface [43].

To further understand the representation of dislocations in the coarse-grained domain in CAC, we calculate the disregistry and distribution of the Nye tensor [95, 96] around an edge and a screw dislocation in Cu. The fully coarse-grained simulation cell, with a size of 180 nm × 32 nm × 6.5 nm along the x, y, and z direction, respectively, contains about 3 million atoms; periodic boundary conditions (PBCs) are applied along the dislocation line direction, i.e., the z direction, while the x and y boundaries are assumed traction free. The interatomic interactions are

described using an EAM potential [97], which gives an equilibrium lattice constant $a_0 = 3.615$ Å. After displacing some nodes/atoms by $b = (\sqrt{2}/2)a_0$ along a $\langle 110 \rangle$ direction on a $\{111\}$ plane, a damped dynamic CAC simulation [42] is conducted for 1 million steps with a time step of 1 fs at a near zero temperature to achieve an equilibrium full dislocation, which is dissociated into two Shockley partial dislocations with an intrinsic stacking fault in between [93, 94]. For comparison, damped MD simulations are also performed using LAMMPS [98]. Based on the interpolated atomic positions in the CAC simulations or the atomic positions in the MD simulations, the disregistry along the Burgers vector direction and the Nye tensor $\boldsymbol{\alpha}$ are calculated, the latter of which uses Atomsk [99] following Hartley and Mishin [100]. The calculations of $\boldsymbol{\alpha}$ are conducted on atoms within an area around the dislocation: 10 nm by 4.5 nm along the x and y axes, respectively; larger calculation areas do not change the results.

Figure 12.3 shows that there exists a linear correlation between disregistry and atomic position within an element, because of the trilinear shape/interpolation functions employed in the coarse-grained domain. For the Nye tensor $\boldsymbol{\alpha}$, only α_{13} and α_{33} among the nine components are presented in Fig. 12.4 because they correspond to the edge and screw components of the partial dislocations, respectively. In both figures, with the smallest finite elements (64 atoms/element), results of the CAC simulations agree well with those of the MD simulations; with an increasing element size, the disregistry deviates and the separation between the two partial dislocations changes. Nevertheless, for the same dislocation, an integration of α within the calculation area, i.e., the Burgers vector, yields identical result between CAC and MD, suggesting that the net Burgers vector (and so the long-range stress field) of a dislocation is indeed preserved in the coarse-grained domain in CAC.

We emphasize it is not our intent here to shed light on improved understanding of static dislocation core level phenomena, but rather to establish that CAC

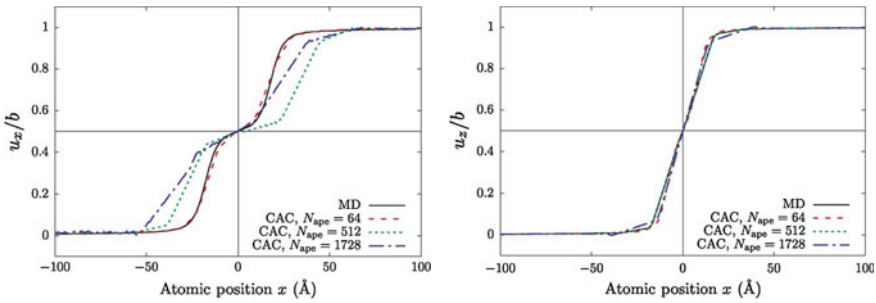

Fig. 12.3 Disregistry—the difference in the dislocation-induced displacement fields between two layers of atoms across the slip plane—of the **a** edge and **b** screw dislocations in Cu; The results in CAC with varying element size are compared with those of MD. u_x and u_z are the disregistry components along the Burgers vector direction, i.e., the x and z directions in cases of the edge and screw dislocation, respectively. $b = (\sqrt{2}/2)a_0$ is the magnitude of the Burgers vector of a dislocation, where a_0 is the lattice constant

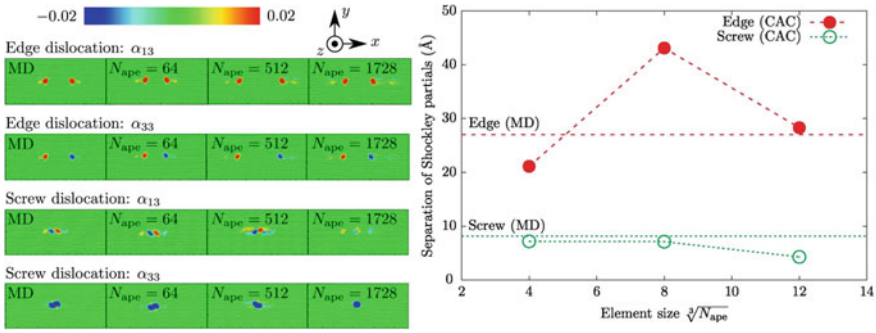

Fig. 12.4 Left: Nye tensor distribution around an edge or a screw dislocation in Cu, colored by the magnitude of two components α_{13} and α_{33}. CAC simulations with different element size (N_{ape} is the number of atoms per element) are employed, with the MD results also shown for comparison. Right: Separation of Shockley partial dislocations (based on α_{13}) with respect to the element size, in the cases of an edge and a screw dislocation. Both quantities converge to MD (horizontal lines) as each element has a smaller N_{ape}. The partial dislocation is assumed to sit at the mass center of the all surrounding atoms with the corresponding Nye tensor component that is larger than half the maximum value among all atoms. The partial dislocation position is unambiguously decided because most atoms have a value that is very close to either the maximum value or 0

adequately replicates essential aspects of dislocation fields, laying solid foundations for more complicated dislocation-mediated metal plasticity problems. The coarse-graining errors in the static dislocation properties are not essential in certain cases, e.g., dislocation/GB interactions (Sect. 12.4.3), because the dislocation has a correct core structure once it migrates into the atomistic domain in which the dislocation/defect interactions to be investigated take place.

12.4.2 Fast Moving Dislocations and Phonons

While much is known about static dislocations, the physics of dislocations moving near and above the sonic velocity in crystals remains relatively lightly explored [93, 94]. A dislocation moving in a lattice excites atomic vibrations and emits acoustic phonons [101]. The friction created by these interactions slows down the dislocation motion and reduces the mean distance between adjacent dislocations, leading to a stronger coupling between the long-range stress fields than that for static dislocations [66]. CAC is well-suited to explore fast moving dislocations and phonons because it concurrently captures the highly nonlinear time-dependent atomic-scale dislocation cores and the long-range elastic fields away from the cores.

For a fast moving dislocation in an otherwise perfect lattice, Xiong et al. [66] reported that (i) subject to the same resolved shear stress, the coarse-grained domain predicts a higher dislocation velocity, a larger phonon wavelength, and a larger

magnitude of the dislocation core stress field oscillation than the atomistic domain due to the linear shape/interpolation functions employed in the elements, and (ii) a fast moving dislocation has a velocity-dependent asymmetric stress field in which the leading partial dislocation possesses a higher stress level than the trailing partial dislocation as a result of the emitted phonon waves. In 1D monatomic, diatomic, and triatomic crystals, Xiong et al. [90] confirmed that the coarse-grained domain is able to reproduce complete phonon branches. In dynamic CAC simulations of dislocation/void interactions, Xiong et al. [65] discovered an inertia-induced transition from the Hirsch looping mechanism to the shearing mechanism, with the result that a relatively large void (~5 nm in diameter), which is a strong barrier for quasistatic dislocations, can behave as a weak barrier to dislocation motions under high strain-rate dynamic conditions. By performing fully coarse-grained atomistic simulations of dislocation/phonon interactions, Xiong et al. [64, 66] and Chen et al. [71] found that (i) the sub-THz phonon drag coefficient on dislocation migration increases with the increase of phonon wave packet magnitudes or sizes but is insensitive to the incident angles [64], and (ii) phonons reduce the dislocation energy, with some energy lagging behind the decelerated dislocation or dispersed around the arrested dislocation through emission of secondary phonon waves [66, 71]. In Cu polycrystals, Chen et al. [72] showed that the phonon/GB interactions alter the phonon focusing direction and locally reconstruct the GB, as shown in Fig. 12.5.

However, the fact that a dislocation may have different mobility, phonon wavelength, and dislocation core stress field in atomistic and coarse-grained domains raises the question of how the interface between the atomistic and coarse-grained domain affects the phonon transport in CAC [74]. The outstanding issue of a spurious wave reflection problem at the atomistic/continuum domain interface, encountered by many domain decomposition multiscale modeling methods [48], is mainly caused by the differences in material descriptions and

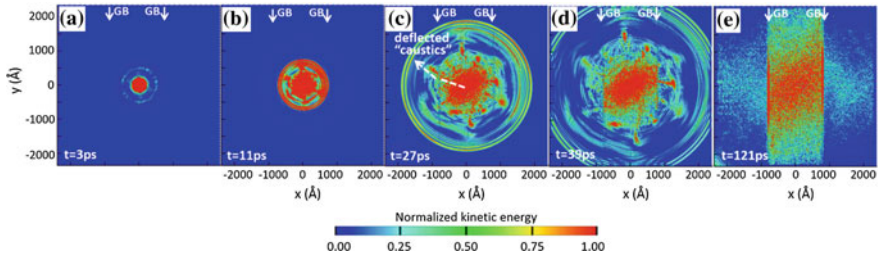

Fig. 12.5 Time sequences of the normalized kinetic energy of transient heat flow in CAC simulations of a 2D Cu polycrystal. The GBs, rendered in full atomistic resolution, are indicated by white solid arrows. The phonons, with a wavelength of 5–250 nm, are generated in the simulation cell center using a coherent phonon pulse model [102]. With simultaneous ballistic and diffusive thermal transport, the phonon-focusing caustics are deflected by the GBs, which are indicated by the dashed white arrows in **c**. In **e**, only 60% of the total kinetic energy initially excited by the heat pulse is transmitted across the GBs; the phonon/GB interactions also give rise to the local GB structure change. Adapted with permission from Ref. [72]

governing equations between the atomistic and continuum models, which results in a mismatch in phonon dispersion relations. In CAC, due to the fact that coarse-graining cuts off short wavelength phonons [72, 73, 90], the phonon dispersion relations in the atomistic and coarse-grained domains overlap with each other only for wavevector that is smaller than a certain value. For this reason, CAC simulations of phonon/GB interactions [72] only involved medium- or long-wavelength phonons because the GB region is rendered in atomistic resolution. Recently, new shape/interpolation functions, different from the original trilinear ones, have been developed and applied to 1D elements to preserve the complete phonon information when a short-wavelength phonon seamlessly propagates across multiple atomistic/coarse-grained domain interfaces [73]. Work is underway to extend the new shape/interpolation functions to 2D and 3D for more complicated crystalline materials.

12.4.3 Dislocation/GB Interactions

The mechanism for slip transfer of lattice dislocations that migrate to and interact with GBs is one of the most pressing yet unresolved issues facing GB engineering and polycrystal plasticity [103]. Although in situ transmission electron microscope experiments capture the real-time dynamic process of slip transfer, they are unable to discern 3D atomic-scale events at the dislocation/GB interaction sites to yield quantitative information [104]. The multiscale nature of the sequential transfer of slip across GBs, in which both the atomic scale structure of the interface and the long-range fields of dislocation pile-ups are important, also poses challenges from the perspective of computational simulation [85]. For example, dislocation-based continuum approaches such as the crystal plasticity FEM (CPFEM) and rule-based DD are not readily applicable to simulate the interactions between dislocations and GBs because they usually do not naturally incorporate the necessary microscopic DOFs associated with the GBs and other evolving internal state variables that relate to detailed slip transfer criteria [48, 105]. On the other hand, atomistic simulations, which are preferred for understanding local GB structure-specific slip transfer responses, are limited by the size of the computational cell in considering the long-range stress field [106].

We performed hybrid CAC simulations [44] to study the sequential slip transfer of mixed character dislocations across a $\Sigma 3\{111\}$ coherent twin boundary (CTB) in Cu, Ni, and Al [83, 84], as well as a $\Sigma 11\{113\}$ STGB in Ni [84]. In all simulations, the GBs are rendered in full atomistic resolution while the coarse-grained domain is used to accommodate long distance migration of dislocation pile-ups, which are introduced either by multiplication from an FR source [83, 86] or Volterra knives [84], the latter case is shown in Fig. 12.6a. The dislocations then move towards the GB subjected to a constant applied shear stress.

For a $\Sigma 3$ CTB in Cu and Al [83], it is found that, under a relatively small shear stress, (i) in Cu, the leading screw segment cuts into the twinned grain, i.e., the CTB

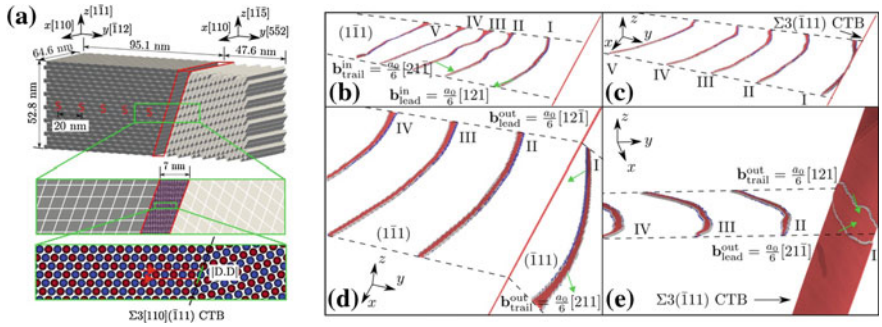

Fig. 12.6 **a** Bicrystal simulation cells used to study sequential slip transfer of five $(a_0/2)[110](1\bar{1}1)$ dislocations (red S) across a $\Sigma3(\bar{1}11)$ CTB in Ni. An atomistic domain is meshed in the vicinity the CTB; the jagged interstices at the cell boundaries are also filled in with atoms, which are not shown here. Away from the GBs and cell boundaries are coarse-grained finite elements, each containing 2197 atoms. All cell boundaries are assumed traction free to allow a full 3D description. Exploded views of the GB region appear in the lower region, where atoms in different (110) atomic layers have different colors; the Σ3 CTB is composed of all D structural units, and so all sites along the CTB are equivalent for dislocation impingement. **b–e** Snapshots of dislocation pile-up with dominant leading screw character impinging against the CTB. Atoms are colored by adaptive common neighbor analysis [107]: red are of hexagonal-close packed local structure, blue are BCC atoms, and all FCC atoms are deleted. In **a** five incoming dislocations approach the CTB subject to an applied shear stress. In **b** the leading dislocation is constricted at the CTB, where two Shockley partial dislocations are recombined into a full dislocation. In **c** with Mishin-EAM [108] and Voter-EAM [109] potentials, the dislocation effectively cross-slips into the outgoing twinned grain via redissociation into two partials. In **d** with Angelo-EAM [110], Foiles-EAM [111], and Zhou-EAM [112] potentials, the redissociated dislocation is absorbed by the CTB, with two partials gliding on the twin plane in opposite directions. Adapted with permission from Ref. [84]

acts as a barrier to dislocation motion; (ii) in Al, the leading segment is absorbed and glides on the CTB, which acts as sinks for lattice dislocations. In particular for Al, four dislocation/CTB interaction modes are identified, which are affected by applied shear stress, dislocation line length, and dislocation line curvature. This study highlights the complexity of dislocation/GB interactions, as well as the significance to let dislocations evolve freely in 3D and to probe the mechanisms of slip transfer in polycrystalline and twinned metals using sufficiently large models. In comparison, prior atomistic simulations in the literature [106] are limited to a small set of simulation parameters: low applied shear stresses and short/straight dislocation lines enforced by PBCs.

In Ni, five EAM potentials [108–112] were employed in CAC simulations of dislocation/GB interactions [84]. For the Σ3 CTB, the leading screw segment is transmitted into the twinned grain using two interatomic potentials (Fig. 12.6d), but is absorbed and glides on the CTB when the other three potentials are employed (Fig. 12.6e). In both reactions, each dislocation always follows the recombination-redissociation process, without forming any CTB dislocations in the process of recombination, as shown in Fig. 12.6c. For the Σ11 STGB, however,

all five EAM potential fits predict dislocation absorption, during which the leading partial dislocation in the incoming grain splits into a STGB partial dislocation and a stair-rod type dislocation, which subsequently reacts with the trailing partial dislocation in the incoming grain to form another STGB partial dislocation. This work highlights the uncertainty in computed dislocation-interface reactions associated with the deployment of a variety of interatomic potentials and suggests that the applicability of dislocation/GB interaction criteria in the literature derived from limited studies may be limited [106].

12.5 Conclusions

In this chapter, we first review the basics of GCM in Sect. 12.1 and establish, in accordance with the insights of Maugin, that GCM is a better approximation than CCM to the description of real materials. In Sect. 12.2, the theoretical foundations and governing equations of AFT are introduced, in comparison with several representative CG models in the literature. Fundamentally different from CG particle models and most field theories such as the micromorphic theory, AFT views a material as a continuous collection of material points, while embedded within each point there is a group of discrete atoms, providing an analytical link between the continuum quantities and the atomic variable. In Sect. 12.3, we discuss important aspects of the AFT-based CAC approach, including its advantages relative to other multiscale modeling methods, code development, and numerical implementations. Applications of CAC to metal plasticity are reviewed in Sect. 12.4, with an emphasis on static dislocation properties, fast moving dislocations and phonons, as well as dislocation/GB interactions. It is shown that CAC provides largely satisfactory predictive results at a fraction of the computational cost of the fully atomistic version of the same models.

The CAC applications discussed in this chapter, as well as all others in the last decade, establish that the CAC method is useful at intermediate length scales between fully-resolved atomistics and mesoscale modeling approaches such as DD, phase field method, and CPFEM. In this regard, CAC can serve as a complement to methods at the lower and higher length scales. The CAC method is especially useful to explore problems in which full atomistic resolution is required in some regions (e.g., complex atomistic phenomena involving dislocations reactions with other defects), with coarse-graining employed elsewhere to support representation of dislocation interactions and transport. In such cases, dislocation lines span between fully resolved atomistic and coarse-grained domains with the same constitutive equation used everywhere. Compared with MD/MS, CAC is advantageous in that with greatly reduced DOFs, the key characteristics of complex dislocation behavior can be reasonably well described, despite the coarse-graining errors. Compared with DD, in which only the dislocation lines are resolved, CAC simulations contain more DOFs and are less computationally efficient; however, CAC resolves dislocation core effects explicitly, in addition to long-range elastic interactions.

It is anticipated that CAC may assist in computational techniques at higher length scales by providing useful guidance regarding the form of higher scale constitutive models.

Future applications of the CAC method to metal plasticity include slip transfer of more general dislocation types with different curvatures across more general GBs, the "valve effect" in fracture [113], and dislocation substructure evolution [114]. In terms of the methodological development, we will implement higher order shape/interpolation functions and/or enrichment functions within elements to admit dislocations in element interior regions, as well as design adaptive mesh refinement schemes for dislocation migration. For finite temperature dynamic problems, the next step is to develop a novel description of the temperature in the coarse-grained domain such that it is consistent with that in MD [25]. Another future extension, which is more challenging, is to advance non-equilibrium finite temperature dynamic CAC for non-conservative systems, requiring the implementation of the balance equation of energy (Eq. 12.4).

Acknowledgements These results are in part based upon work supported by the National Science Foundation as a collaborative effort between Georgia Tech (CMMI-1232878) and University of Florida (CMMI-1233113). Any opinions, findings, and conclusions or recommendations expressed in this material are those of the authors and do not necessarily reflect the views of the National Science Foundation. The authors thank Dr. Jinghong Fan, Dr. Qian Deng, Dr. Shengfeng Yang, Dr. Xiang Chen, Mr. Rui Che, and Mr. Weixuan Li for helpful discussions, Mr. Kevin Chu for building the Python scripting interface in PyCAC, and Dr. Aleksandr Blekh for arranging execution of PyCAC via MATIN. The work of SX was supported in part by Georgia Tech Institute for Materials and in part by the Elings Prize Fellowship in Science offered by the California NanoSystems Institute (CNSI) on the UC Santa Barbara campus. SX also acknowledges support from the Center for Scientific Computing from the CNSI, MRL: an NSF MRSEC (DMR-1121053). LX acknowledges the support from the Department of Energy, Office of Basic Energy Sciences under Award Number DE-SC0006539. The work of LX was also supported in part by the National Science Foundation under Award Number CMMI-1536925. DLM is grateful for the additional support of the Carter N. Paden, Jr. Distinguished Chair in Metals Processing. This work used the Extreme Science and Engineering Discovery Environment (XSEDE), which is supported by National Science Foundation grant number ACI-1053575.

References

1. Maugin, G.A.: Non-Classical Continuum Mechanics: A Dictionary. Springer, Singapore (2016)
2. Maugin, G.A.: Some remarks on generalized continuum mechanics. Math. Mech. Solids **20**(3), 280–291 (2015)
3. Maugin, G.A.: Generalized continuum mechanics: various paths. In: Continuum Mechanics Through the Twentieth Century, pp. 223–241. Springer (2013)
4. Maugin, G.A.: Continuum Mechanics Through the Twentieth Century, Solid Mechanics and Its Applications, vol. 196, pp. 978–994. Springer, Berlin (2013)
5. Maugin, G.A.: Generalized continuum mechanics: what do we mean by that? In: Maugin, G., Metrikine, A. (eds.) Mechanics of Generalized Continua. Advances in Mechanics and Mathematics, pp. 3–13. Springer, New York, NY (2010)

6. Maugin, G.A.: A historical perspective of generalized continuum mechanics. In: Altenbach, H., Maugin, G., Erofeev, V. (eds.) Mechanics of Generalized Continua. Advanced Structured Materials, vol. 7. pp. 3–19 (2011)
7. Maugin, G.A., Metrikine, A.V.: Mechanics of Generalized Continua: One Hundred Years After the Cosserats. Springer, New York (2010)
8. Chen, Y., Lee, J.: Atomistic formulation of a multiscale field theory for nano/micro solids. Philos. Mag. **85**(33–35), 4095–4126 (2005)
9. Chen, Y.: Reformulation of microscopic balance equations for multiscale materials modeling. J. Chem. Phys. **130**(13), 134706 (2009)
10. Chen, Y., Lee, J., Xiong, L.: A generalized continuum theory and its relation to micromorphic theory. J. Eng. Mech. **135**(3), 149–155 (2009)
11. Chen, Y., Zimmerman, J., Krivtsov, A., McDowell, D.L: Assessment of atomistic coarse-graining methods. Int. J. Eng. Sci. **49**(12), 1337–1349 (2011)
12. Cosserat, E., Cosserat, F.: Théorie des corps déformables, vol. 3, pp. 17–29, Paris (1909)
13. Chen, Y., Lee, J.D., Eskandarian, A.: Micropolar theory and its applications to mesoscopic and microscopic problems. Comput. Model. Eng. Sci. **5**(1), 35–43 (2004)
14. Eringen, A.C.: Theory of micropolar elasticity. In: Microcontinuum Field Theories, pp. 101–248. Springer (1999)
15. Eringen, A.C.: Microcontinuum Field Theories: I. Foundations and Solids. Springer, New York (1999)
16. Eringen, A.C.: Mechanics of Micromorphic Continua. Springer (1968)
17. Chen, Y., Lee, J.D.: Connecting molecular dynamics to micromorphic theory. (I). Instantaneous and averaged mechanical variables. Phys. A **322**, 359–376 (2003)
18. Chen, Y., Lee, J.D.: Connecting molecular dynamics to micromorphic theory. (II). Balance laws. Phys. A **322**, 377–392 (2003)
19. Chen, Y., Lee, J., Eskandarian, A.: Atomistic counterpart of micromorphic theory. Acta Mech. **161**(1–2), 81–102 (2003)
20. Chen, Y., Lee, J.D.: Determining material constants in micromorphic theory through phonon dispersion relations. Int. J. Eng. Sci. **41**(8), 871–886 (2003)
21. Chen, Y., Lee, J.D., Eskandarian, A.: Atomistic viewpoint of the applicability of microcontinuum theories. Int. J. Solids Struct. **41**(8), 2085–2097 (2004)
22. Chen, Y., Lee, J.D., Eskandarian, A.: Examining the physical foundation of continuum theories from the viewpoint of phonon dispersion relation. Int. J. Eng. Sci. **41**, 61–83 (2003)
23. Hoover, W.G.: Computational Statistical Mechanics. Elsevier (1991)
24. Chen, Y.: Local stress and heat flux in atomistic systems involving three-body forces. J. Chem. Phys. **124**(5), 054113 (2006)
25. Chen, Y., Diaz, A.: Local momentum and heat fluxes in transient transport processes and inhomogeneous systems. Phys. Rev. E **94**(5), 053309 (2016)
26. Chen, Y.: The origin of the distinction between microscopic formulas for stress and Cauchy stress. EPL **116**(3), 34003 (2016)
27. Espanol, P.: Statistical mechanics of coarse-graining. In: Novel Methods in Soft Matter Simulations, pp. 69–115. Springer (2004)
28. Izvekov, S., Voth, G.A.: Multiscale coarse-graining of liquid-state systems. J. Chem. Phys. **123**(13), 134105 (2005)
29. Izvekov, S., Voth, G.A.: A multiscale coarse-graining method for biomolecular systems. J. Phys. Chem. B **109**(7), 2469–2473 (2005)
30. Noid, W., Chu, J.W., Ayton, G.S., Krishna, V., Izvekov, S., Voth, G.A., Das, A., Andersen, H.C.: The multiscale coarse-graining method. I. A rigorous bridge between atomistic and coarse-grained models. J. Chem. Phys. **128**(24), 244114 (2008)
31. Noid, W., Liu, P., Wang, Y., Chu, J.W., Ayton, G.S., Izvekov, S., Andersen, H.C., Voth, G.A.: The multiscale coarse-graining method. II. Numerical implementation for coarse-grained molecular models. J. Chem. Phys. **128**(24), 244115 (2008)
32. Tadmor, E.B., Ortiz, M., Phillips, R.: Quasicontinuum analysis of defects in solids. Philos. Mag. A **73**, 1529–1563 (1996)

33. Dupuy, L.M., Tadmor, E.B., Miller, R.E., Phillips, R.: Finite-temperature quasicontinuum: molecular dynamics without all the atoms. Phys. Rev. Lett. **95**, 060202 (2005)
34. Kulkarni, Y., Knap, J., Ortiz, M.: A variational approach to coarse-graining of equilibrium and non-equilibrium atomistic description at finite temperature. J. Mech. Phys. Solids **56**, 1417–1449 (2008)
35. Shenoy, V.B., Miller, R., Tadmor, E.B., Phillips, R., Ortiz, M.: Quasicontinuum models of interfacial structure and deformation. Phys. Rev. Lett. **80**, 742–745 (1998)
36. Rudd, R.E., Broughton, J.Q.: Coarse-grained molecular dynamics and the atomic limit of finite elements. Phys. Rev. B **58**(10), R5893 (1998)
37. Irving, J., Kirkwood, J.G.: The statistical mechanical theory of transport processes. IV. The equations of hydrodynamics. J. Chem. Phys. **18**(6), 817–829 (1950)
38. Kittel, C.: Introduction to Solid State Physics. Wiley, Inc (1956)
39. Deng, Q, Xiong, L., Chen, Y.: Coarse-graining atomistic dynamics of fracture by finite element method. Int. J. Plast. **26**(9), 1402–1414
40. Xiong, L., Chen, Y.: Coarse-grained simulations of single-crystal silicon. Modell. Simul. Mater. Sci. Eng. **17**, 035002 (2009)
41. Xiong, L., Chen, Y., Lee, J.D.: Atomistic simulation of mechanical properties of diamond and silicon carbide by a field theory. Model. Simul. Mater. Sci. Eng. **15**(5), 535 (2007)
42. Xiong, L., Tucker, G., McDowell, D.L., Chen, Y.: Coarse-grained atomistic simulation of dislocations. J. Mech. Phys. Solids **59**(2), 160–177 (2011)
43. Xu, S., Che, R., Xiong, L., Chen, Y., McDowell, D.L.: A quasistatic implementation of the concurrent atomistic-continuum method for FCC crystals. Int. J. Plast. **72**, 91–126 (2015)
44. Xu, S., Payne, T.G., Chen, H., Liu, Y., Xiong, L., Chen, Y., McDowell, D.L.: PyCAC:The concurrent atomistic-continuum simulation environment. J. Mater. Res. (2018) in press, https://doi.org/10.1557/jmr.2018.8
45. Shilkrot, L.E., Curtin, W.A., Miller, R.E.: A coupled atomistic/continuum model of defects in solids. J. Mech. Phys. Solids **50**, 2085–2106 (2002)
46. Shilkrot, L.E., Miller, R.E., Curtin, W.A.: Coupled atomistic and discrete dislocation plasticity. Phys. Rev. Lett. **89**, 025501 (2002)
47. Xu, S., Xiong, L., Deng, Q., McDowell, D.L.: Mesh refinement schemes for the concurrent atomistic-continuum method. Int. J. Solids Struct. **90**, 144–152 (2016)
48. Zbib, H.M., de la Rubia, T.D., Bulatov, V.: A multiscale model of plasticity based on discrete dislocation dynamics. ASME J. Eng. Mater. Technol. **124**(1), 78–87 (2002)
49. Hochrainer, T., Zaiser, M., Gumbsch, P.: A three-dimensional continuum theory of dislocation systems: kinematics and mean-field formulation. Philos. Mag. **87**, 1261–1282 (2007)
50. Arsenlis, A., Cai, W., Tang, M., Rhee, M., Oppelstrup, T., Hommes, G., Pierce, T.G., Bulatov, V.V.: Enabling strain hardening simulations with dislocation dynamics. Model. Simul. Mater. Sci. Eng. **15**, 553–595 (2007)
51. El-Azab, A., Deng, J., Tang, M.: Statistical characterization of dislocation ensembles. Philos. Mag. **87**(8–9), 1201–1223 (2007)
52. Devincre, B., Hoc, T., Kubin, L.: Dislocation mean free paths and strain hardening of crystals. Science **320**(5884), 1745–1748 (2008)
53. Motz, C., Weygan, D., Senger, J., Gumbsch, P.: Initial dislocation structures in 3-D discrete dislocation dynamics and their influence on microscale plasticity. Acta Mater. **57**(6), 1744–1754 (2009)
54. Zaiser, M., Sandfeld, S.: Scaling properties of dislocation simulations in the similitude regime. Model. Simul. Mater. Sci. Eng. **22**:065012, (2014)
55. Groma, I., Zaiser, M., Ispanovity, P.D.: Dislocation patterning in a two-dimensional continuum theory of dislocations. Phys. Rev. B **93**, 214110 (2016)
56. Xia, S., El-Azab, A.: Computational modelling of mesoscale dislocation patterning and plastic deformation of single crystals. Model. Simul. Mater. Sci. Eng. **23**(5), 55009 (2015)
57. Xiong, L., Chen, Y.: Effects of dopants on the mechanical properties of nanocrystalline silicon carbide thin film. Comput. Model. Eng. Sci. **24**, 203–214 (2008)

58. Xiong, L., Chen, Y.: Coarse-grained simulations of single-crystal silicon. Model. Simul. Mater. Sci. Eng. **17**, 035002 (2009)
59. Deng, Q., Chen, Y.: A coarse-grained atomistic method for 3D dynamic fracture simulation. Int. J. Multiscale Comput. Eng. **11**, 227–237 (2013)
60. Xiong, L., Deng, Q., Tucker, G., McDowell, D.L., Chen, Y.: A concurrent scheme for passing dislocations from atomistic to continuum domains. Acta Mater. **60**, 899–913 (2012)
61. Xiong, L., Deng, Q., Tucker, G., McDowell, D.L., Chen, Y.: Coarse-grained atomistic simulations of dislocations in Al, Ni and Cu crystals. Int. J. Plast. **38**, 86–101 (2012)
62. Xiong, L., McDowell, D.L., Chen, Y.: Nucleation and growth of dislocation loops in Cu, Al and Si by a concurrent atomistic-continuum method. Scr. Mater. **67**, 633–636 (2012)
63. Xiong, L., Chen, Y.: Coarse-grained atomistic modeling and simulation of inelastic material behavior. Acta Mech. Solida Sin. **25**, 244–261 (2012)
64. Xiong, L., McDowell, D.L., Chen, Y.: Sub-THz Phonon drag on dislocations by coarse-grained atomistic simulations. Int. J. Plast. **55**, 268–278 (2014)
65. Xiong, L., Xu, S., McDowell, D.L., Chen, Y.: Concurrent atomistic-continuum simulations of dislocation-void interactions in fcc crystals. Int. J. Plast. **65**, 33–42 (2015)
66. Xiong, L., Rigelesaiyin, J., Chen, X., Xu, S., McDowell, D.L., Chen, Y.: Coarse-grained elastodynamics of fast moving dislocations. Acta Mater. **104**, 143–155 (2016)
67. Yang, S., Xiong, L., Deng, Q., Chen, Y.: Concurrent atomistic and continuum simulation of strontium titanate. Acta Mater. **61**, 89–102 (2013)
68. Yang, S., Chen, Y.: Concurrent atomistic and continuum simulation of bi-crystal strontium titanate with tilt grain boundary. Proc. Roy. Soc. A **471**, 20140758 (2015)
69. Yang, S., Zhang, N., Chen, Y.: Concurrent atomistic-continuum simulation of polycrystalline strontium titanate. Philos. Mag. **95**, 2697–2716 (2015)
70. Yang, S., Chen, Y.: Concurrent atomistic-continuum simulation of defects in polyatomic ionic materials. In: Weinberger, C., Tucker, G. (eds.) Multiscale Materials Modeling for Nanomechanics. Springer International Publishing, Switzerland (2016)
71. Chen, X., Xiong, L., McDowell, D.L., Chen, Y.: Effects of phonons on mobility of dislocations and dislocation arrays. Scr. Mater. **137**, 22–26 (2017)
72. Chen, X., Li, W., Xiong, L., Li, Y., Yang, S., Zheng, Z., McDowell, D.L., Chen, Y.: Ballistic-diffusive phonon heat transport across grain boundaries. Acta Mater. **136**, 355–365 (2017)
73. Chen, X., Diaz, A., Xiong, L., Chen, Y.: Passing waves from atomistic to continuum. J. Comput. Phys. **354**, 393–402 (2018)
74. Chen, X., Li, W., Diaz, A., Li, Y., McDowell, D.L., Chen, Y.: Recent progress in the concurrent atomistic-continuum method and its application in phonon transport. MRS Commun. **7**(4), 785–797 (2017)
75. Li, J: AtomEye: an efficient atomistic configuration viewer. Model. Simul. Mater. Sci. Eng. **11**(2), 173 (2003)
76. Stukowski, A: Visualization and analysis of atomistic simulation data with OVITO—the Open Visualization Tool. Model. Simul. Mater. Sci. Eng. **18**(1), 015012 (2010)
77. Jones, J.E.: On the determination of molecular fields. II. From the equation of state of a gas. Proc. R. Soc. Lond. A **106**(738), 463–477 (1924)
78. Daw, M.S., Baskes, M.I.: Embedded-atom method: derivation and application to impurities, surfaces, and other defects in metals. Phys. Rev. B **29**(12), 6443–6453 (1984)
79. Xu, S.: The concurrent atomistic-continuum method: Advancements and applications in plasticity of face-centered cubic metals. Ph.D. Dissertation, Georgia Institute of Technology (2016)
80. Allen, M.P., Tildesley, D.J.: Computer Simulation of Liquids. Oxford University Press, USA (1989)
81. Verlet, L.: Computer "experiments" on classical fluids. I. Thermodynamical properties of Lennard-Jones molecules. Phys. Rev. **159**, 98–103 (1967)

82. Swope, W.C., Andersen, H.C., Berens, P.H., Wilson, K.R.: A computer simulation method for the calculation of equilibrium constants for the formation of physical clusters of molecules: Application to small water clusters. J. Chem. Phys. **76**(1), 637–649 (1982)
83. Xu, S., Xiong, L., Chen, Y., McDowell, D.L.: Sequential slip transfer of mixed-character dislocations across Σ3 coherent twin boundary in FCC metals: A concurrent atomistic-continuum study. npj Comput. Mater. **2**, 15016 (2016)
84. Xu, S., Xiong, L., Chen, Y., McDowell, D.L.: A concurrent atomistic-continuum study of slip transfer of sequential mixed character dislocations across symmetric tilt grain boundaries in Ni. JOM **69**, 814–821 (2017)
85. McDowell, D.L.: A perspective on trends in multiscale plasticity. Int. J. Plast. **26**, 1280–1309 (2010)
86. Xu, S., Xiong, L., Chen, Y., McDowell, D.L.: An analysis of key characteristics of the Frank-Read source process in FCC metals. J. Mech. Phys. Solids **96**, 460–476 (2016)
87. Xu, S., Xiong, L., Chen, Y., McDowell, D.L.: Shear stress- and line length-dependent screw dislocation cross-slip in FCC Ni. Acta Mater. **122**, 412–419 (2017)
88. Xu, S., Xiong, L., Chen, Y., McDowell, D.L.: Edge dislocations bowing out from a row of collinear obstacles in Al. Scr. Mater. **123**, 135–139 (2016)
89. Xu, S., Xiong, L., Chen, Y., McDowell, D.L.: Validation of the concurrent atomistic-continuum method on screw dislocation/stacking fault interactions. Crystals **7**, 120 (2017)
90. Xiong, L., Chen, X., Zhang, N., McDowell, D.L., Chen, Y.: Prediction of phonon properties of 1D polyatomic systems using concurrent atomistic-continuum simulation. Arch. Appl. Mech. **84**, 1665–1675 (2014)
91. Rice, J.R.: Inelastic constitutive relations for solids: An internal variable theory and its application to metal plasticity. J. Mech. Phys. Solids **19**, 433–455 (1971)
92. Muschik, W.: Non-Equilibrium Thermodynamics with Application to Solids. Springer, New York (1993)
93. Hull, D., Bacon, D.J.: Introduction to Dislocations, 5th edn. Butterworth-Heinemann, Oxford, UK (2011)
94. Anderson, P.M., Hirth, J.P., Lothe, J.: Theory of Dislocations, 3rd edn. Cambridge University Press (2017)
95. Nye, J.F.: Some geometrical relations in dislocated crystals. Acta Mater. **1**(2), 153–162 (1953)
96. Hill, R., Sneddon, I.N. (eds.): Progress in Solid Mechanics, vol. 1, p. 330. North-Holland Publishing Company (1960)
97. Mishin, Y., Mehl, M.J., Papaconstantopoulos, D.A., Voter, A.F., Kress, J.D.: Structural stability and lattice defects in copper: Ab initio, tight-binding, and embedded-atom calculations. Phys. Rev. B **63**(22), 224106 (2001)
98. Plimpton, S.: Fast parallel algorithms for short-range molecular dynamics. J. Comput. Phys. **117**, 1–19 (1995)
99. Hirel, P.: Atomsk: A tool for manipulating and converting atomic data files. Comput. Phys. Commun. **197**, 212–219 (2015)
100. Hartley, C.S., Mishin, Y.: Representation of dislocation cores using Nye tensor distributions. Mater. Sci. Eng. A **400**, 18–21 (2005)
101. Gurrutxaga-Lerma, B., Balint, D.S., Dini, D., Eakins, D.E., Sutton, A.P.: A dynamic discrete dislocation plasticity method for the simulation of plastic relaxation under shock loading. Proc. R. Soc. A **469**, 20130141 (2013)
102. Chen, X., Chernatynskiy, A., Xiong, L., Chen, Y.: A coherent phonon pulse model for transient phonon thermal transport. Comput. Phys. Commun. **195**, 112–116 (2015)
103. Ramesh, K.T.: Nanomaterials: Mechanics and Mechanisms. Springer (2009)
104. Kacher, J., Eftink, B.P., Cui, B., Robertson, I.M.: Dislocation interactions with grain boundaries. Curr. Opin. Solid State Mater. Sci. **18**, 227–243 (2014)
105. Counts, W.A., Braginsky, M.V., Battaile, C.C., Holm, E.A.: Predicting the Hall-Petch effect in fcc metals using non-local crystal plasticity. Int. J. Plast. **24**, 1243–1263 (2008)

106. Spearot, D.E., Sangid, M.D.: Insights on slip transmission at grain boundaries from atomistic simulations. Curr. Opin. Solid State Mater. Sci. **18**, 188–195 (2014)
107. Stukowski, A.: Structure identification methods for atomistic simulations of crystalline materials. Model. Simul. Mater. Sci. Eng. **20**, 045021 (2012)
108. Mishin, Y., Farkas, D., Mehl, M.J., Papaconstantopoulos, D.A.: Interatomic potentials for monoatomic metals from experimental data and ab initio calculations. Phys. Rev. B **59**, 3393 (1999)
109. Voter, A.F., Chen, S.P.: Accurate interatomic potentials for Ni, Al, and Ni_3Al. Mater. Res. Soc. Symp. Proc. **82**, 175 (1987)
110. Angelo, J.E., Moody, N.R., Baskes, M.I.: Trapping of hydrogen to lattice-defects in nickel. Model. Simul. Mater. Sci. Eng. **3**, 289 (1995)
111. Foiles, S.M., Hoyt, J.J.: Computation of grain boundary stiffness and mobility from boundary fluctuations. Acta Mater. **54**, 3351 (2006)
112. Zhou, X.W., Johnson, R.A., Wadley, H.N.G.: Misfit-energy-increasing dislocations in vapor-deposited CoFe/NiFe multilayers. Phys. Rev. B **69**, 144113 (2004)
113. Lipkin, D.M., Clarke, D.R., Beltz, G.E.: A strain-gradient model of cleavage fracture in plastically deforming materials. Acta Mater. **44**, 4051–4058 (1996)
114. Hussein, A.M., El-Awady, J.A.: Quantifying dislocation microstructure evolution and cyclic hardening in fatigued face-centered cubic single crystals. J. Mech. Phys. Solids **91**, 126–144 (2016)

Chapter 13
Bending of a Cantilever Piezoelectric Semiconductor Fiber Under an End Force

Chunli Zhang, Xiaoyuan Wang, Weiqiu Chen and Jiashi Yang

Abstract This paper presents a theoretical analysis on the bending and shear of a cantilever ZnO piezoelectric semiconductor fiber under a transverse end force. The phenomenological theory of piezoelectric semiconductors consisting of Newton's second law of motion, the charge equation of electrostatics, and the conservation of charge of electrons and holes is used. The equations are linearized for a small end force and small electromechanical fields as well as small carrier concentration perturbations. A first-order, one-dimensional theory for the bending of ZnO fibers with shear deformation is derived from the linearized three-dimensional equations. An analytical solution is obtained. The electromechanical fields and carrier concentrations are calculated. It is found that the electric potential is nearly constant along the fiber except near the fixed end of the cantilever, and that the electron distribution over a cross section is due to the transverse shear force and the piezoelectric constant e_{24}.

C. Zhang (✉) · X. Wang · W. Chen
Department of Engineering Mechanics, Zhejiang University,
Hangzhou 310027, China
e-mail: zhangcl01@zju.edu.cn

X. Wang
e-mail: 547134067@qq.com

W. Chen
e-mail: Chenwq@zju.edu.cn

J. Yang
Department of Mechanical and Materials Engineering,
The University of Nebraska-Lincoln, Lincoln, NE 68588-0526, USA
e-mail: jyang1@unl.edu

H. Altenbach et al. (eds.), *Generalized Models and Non-classical Approaches in Complex Materials 2*, Advanced Structured Materials 90,
https://doi.org/10.1007/978-3-319-77504-3_13

13.1 Introduction

Relatively recently, various one-dimensional piezoelectric semiconductor nanostructures have been synthesized such as ZnO fibers, tubes, belts and spirals [1–3]. They can be made into single structures [4–7] or in arrays [8–11], and have been used to make energy harvesters for converting mechanical energy into electrical energy [12–16], field effect transistors [1, 2, 17], acoustic charge transport devices [18], and strain, gas, humidity and chemical sensors [1, 19].

This paper is concerned with ZnO piezoelectric semiconductor fibers which have been used in the flexural deformation mode [2, 4, 5, 13, 20, 21] for various devices. We perform a theoretical analysis on the flexure of a cantilever ZnO nanofiber under a transverse end force. A deep understanding of this problem is fundamentally important to the development and optimization of devices based on the flexure of ZnO fibers. The basic behaviors of piezoelectric semiconductors can be described by the conventional phenomenological theory [22] consisting of the equations of linear piezoelectricity [23] and the equations of the conservations of charge of electrons and holes [24]. Because of the anisotropy of piezoelectric materials, the electromechanical couplings in them, and the nonlinearity associated with the drift currents of electrons and holes which are the products of the unknown carrier concentrations and the unknown electric field [24], theoretical analyses of piezoelectric semiconductor devices normally present considerable mathematical challenges. In the present paper the theory is linearized under the assumption of a small end force and hence small carrier concentration perturbations. A one-dimensional theory for the bending of ZnO fibers with shear deformation is then derived from the three-dimensional linearized theory in the manner of Mindlin [25–28]. The linearization and the development of the one-dimensional theory are crucial in the mathematical simplification of the problem and make the theoretical results in this paper possible.

13.2 Three-Dimensional Equations

We use the Cartesian tensor notation [23]. The indices i, j, k, l assume 1, 2, and 3. A comma followed by an index indicates a partial derivative with respect to the coordinate associated with the index. A superimposed dot represents a time derivative. For a piezoelectric semiconductor, the three-dimensional phenomenological theory consists of the equation of motion, the charge equation of electrostatics, and the conservation of charge for electrons and holes (continuity equations) [22–24, 29]:

$$\begin{aligned} T_{ji,j} &= \rho \ddot{u}_i, \\ D_{i,i} &= q\left(p - n + N_D^+ - N_A^-\right), \\ J_{i,i}^n &= q\dot{n}, \\ J_{i,i}^p &= -q\dot{p}, \end{aligned} \tag{13.1}$$

where $\mathbf{T}$ is the stress tensor, ρ the mass density, $\mathbf{u}$ the mechanical displacement vector, $\mathbf{D}$ the electric displacement vector, $q = 1.6 \times 10^{-19}$ coil the electronic charge, p and n the concentrations of holes and electrons, N_D^+ and N_A^+ the concentrations of impurities of donors and accepters, and J_I^P and J_I^b the hole and electron current densities. In (13.1), we have neglected carrier recombination and generation. Constitutive relations accompanying (13.1) can be written in the following form:

$$\begin{aligned} S_{ij} &= s_{ijkl}^E T_{kl} + d_{kij} E_k, \\ D_i &= d_{ikl} T_{kl} + \varepsilon_{ik}^T E_k, \\ J_i^n &= qn\mu_{ij}^n E_j + qD_{ij}^n n_{,j}, \\ J_i^p &= qp\mu_{ij}^p E_j - qD_{ij}^p p_{,j}, \end{aligned} \tag{13.2}$$

where $\mathbf{S}$ is the strain tensor, $\mathbf{E}$ the electric field vector, S_{ijkl}^E the elastic compliance, d_{kij} the piezoelectric constants, ε_{ij}^T the dielectric constants, μ_{ij}^n and μ_{ij}^p the carrier mobilities, and D_{ij}^n and D_{ij}^p the carrier diffusion constants. The superscripts "E" and "T" in S_{ijkl}^E and ε_{ij}^T will be dropped in the rest of the paper. The strain $\mathbf{S}$ and the electric field $\mathbf{E}$ are related to the mechanical displacement $\mathbf{u}$ and the electric potential φ through

$$S_{ij} = (u_{i,j} + u_{j,i})/2, \tag{13.3}$$

$$E_i = -\varphi_{,i}. \tag{13.4}$$

With the compressed matrix notation for tensor indices [23], the material constants s_{ijkl} and d_{ijk} in (13.2) can be represented by the matrices s_{pq} and d_{ir} with p, q, $r = 1, \ldots, 6$. Similarly, S_{ij} and T_{ij} are represented by S_p and T_q. We write

$$n = n_0 + \Delta n, \quad p = p_0 + \Delta p, \tag{13.5}$$

where

$$n_0 = N_D^+, \quad P_0 = N_A^-, \tag{13.6}$$

and they are constants for uniform impurities which we assume in this paper. Then $(13.1)_{2\text{-}4}$ become

$$\begin{aligned} D_{i,i} &= q(\Delta p - \Delta n)\,, \\ J^n_{i,i} &= q\frac{\partial \Delta n}{\partial t}, \\ J^p_{i,i} &= -q\frac{\partial \Delta p}{\partial t}. \end{aligned} \tag{13.7}$$

Consider the case of small Δn and Δp. We linearize $(13.2)_{3,4}$ as

$$\begin{aligned} J^n_i &= qn_0\mu^n_{ij}E_j + qD^n_{ij}(\Delta n)_{,j}, \\ J^p_i &= qp_0\mu^p_{ij}E_j - qD^p_{ij}(\Delta p)_{,j}. \end{aligned} \tag{13.8}$$

This type of linearization has been used in the analysis of piezoelectric semiconductors before [22, 30–35]. It has also been used in the macroscopic theory of ionic conductors [36, 37], a mathematically equivalent problem where the equilibrium or motion of ions are also governed by drift under an electric field and diffusion due to concentration gradients. Fully nonlinear theories for elastic semiconductors involving large deformations and strong fields can be found in [38–43].

13.3 One-Dimensional Equations

Consider a ZnO fiber with a circular cross section as shown in Fig. 13.1. It is slender with $L >> a$. The left end is fixed. The right end is under the action of a transverse shear force f_y.

To develop a one-dimensional theory for the bending and extension of the fiber in the y-z plane with shear deformation, we make the following approximations of the relevant mechanical displacements, electric potential, and carrier concentrations [25–28]:

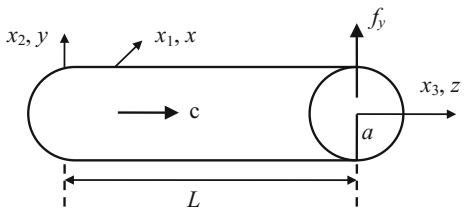

Fig. 13.1 A ZnO fiber with its c-axis along x_3

$$\begin{aligned}
u_2(\mathbf{x},t) &\cong v(x_3,t),\\
u_3(\mathbf{x},t) &\cong w(x_3,t)+x_2\psi(x_3,t),\\
\varphi(\mathbf{x},t) &\cong \phi^{(0)}(x_3,t)+x_2\phi^{(1)}(x_3,t),\\
\Delta n(\mathbf{x},t) &\cong n^{(0)}(x_3,t)+x_2 n^{(1)}(x_3,t),\\
\Delta p(\mathbf{x},t) &\cong p^{(0)}(x_3,t)+x_2 p^{(1)}(x_3,t),
\end{aligned} \tag{13.9}$$

where $v(x_3,t)$ is the flexural displacement, $w(x_3,t)$ the extensional displacement which is not present in the bending of the fiber in Fig. 13.1 but is included for other possible applications of the equations to be derived, and $\psi(x_3,t)$ the shear deformation associated with flexure. The relevant strains, electric fields and carrier concentration gradients are

$$\begin{aligned}
&S_3=S_{33}=u_{3,3}=w_{,3}+x_2\psi_{,3}, \quad S_4=2S_{23}=u_{2,3}+u_{3,2}=v_{,3}+\psi,\\
&E_2=-\varphi_{,2}=-\phi^{(1)}, \quad E_3=-\varphi_{,3}=-\phi^{(0)}_{,3}-x_2\phi^{(1)}_{,3},\\
&\Delta n_{,2}=n^{(1)}, \quad \Delta n_{,3}=n^{(0)}_{,3}+x_2 n^{(1)}_{,3},\\
&\Delta p_{,2}=p^{(1)}, \quad \Delta p_{,3}=p^{(0)}_{,3}+x_2 p^{(1)}_{,3}.
\end{aligned} \tag{13.10}$$

For bending in the y-z plane, the main stress components are T_3 and T_4. Therefore we introduce the following stress relaxation for thin fibers:

$$T_1=T_2=T_5=T_6\cong 0. \tag{13.11}$$

From the constitutive relations in $(13.2)_{1,2}$, for the relevant strain and electric displacement components, we have

$$\begin{aligned}
S_3&=s_{33}T_3+d_{33}E_3, \quad S_4=s_{44}T_4+d_{15}E_2,\\
D_2&=d_{15}T_4+\varepsilon_{11}E_2, \quad D_3=d_{33}T_3+\varepsilon_{33}E_3.
\end{aligned} \tag{13.12}$$

We invert $(13.12)_{1,2}$ for expressions of stresses in terms of strains and substitute the resulting expressions into $(13.12)_{3,4}$. Then (13.12) becomes

$$\begin{aligned}
T_3&=T_{33}=\bar{c}_{33}S_3-\bar{e}_{33}E_3=\bar{c}_{33}(w_{,3}+x_2\psi_{,3})+\bar{e}_{33}(\phi^{(0)}_{,3}+x_2\phi^{(1)}_{,3}),\\
T_4&=T_{32}=\bar{c}_{44}S_4-\bar{e}_{15}E_2=\bar{c}_{44}(v_{,3}+\psi)+\bar{e}_{15}\phi^{(1)},\\
D_2&=\bar{e}_{15}S_4+\bar{\varepsilon}_{11}E_2=\bar{e}_{15}(v_{,3}+\psi)-\bar{\varepsilon}_{11}\phi^{(1)},\\
D_3&=\bar{e}_{33}S_3+\bar{\varepsilon}_{33}E_3=\bar{e}_{33}(w_{,3}+x_2\psi_{,3})-\bar{\varepsilon}_{33}(\phi^{(0)}_{,3}+x_2\phi^{(1)}_{,3}),
\end{aligned} \tag{13.13}$$

where (13.10) has been used and the effective material constants for thin fibers are

$$\begin{aligned} &\bar{c}_{33} = 1/s_{33}, \quad \bar{c}_{44} = 1/s_{44}, \quad \bar{e}_{33} = d_{33}/s_{33}, \quad \bar{e}_{15} = d_{15}/s_{44}, \\ &\bar{\varepsilon}_{11} = \varepsilon_{11} - d_{15}^2/s_{44}, \quad \bar{\varepsilon}_{33} = \varepsilon_{33} - d_{33}^2/s_{33}. \end{aligned} \tag{13.14}$$

The relevant constitutive relations for the currents are the following ones from (13.8):

$$\begin{aligned} J_2^n &= qn_0\mu_{11}^n E_2 + qD_{11}^n \bar{n}_{,2} = -qn_0\mu_{11}^n \phi^{(1)} + qD_{11}^n n^{(1)}, \\ J_3^n &= qn_0\mu_{33}^n E_3 + qD_{33}^n \bar{n}_{,3} \\ &= -qn_0\mu_{33}^n (\phi_{,3}^{(0)} + x_2\phi_{,3}^{(1)}) + qD_{33}^n (n_{,3}^{(0)} + x_2 n_{,3}^{(1)}), \\ J_2^p &= qp_0\mu_{11}^p E_2 - qD_{11}^p \bar{p}_{,2} = -qp_0\mu_{11}^p \phi^{(1)} - qD_{11}^p p^{(1)}. \\ J_3^p &= qp_0\mu_{33}^p E_3 - qD_{33}^p \bar{p}_{,3} \\ &= -qp_0\mu_{33}^p (\phi_{,3}^{(0)} + x_2\phi_{,3}^{(1)}) - qD_{33}^p (p_{,3}^{(0)} + x_2 p_{,3}^{(1)}), \end{aligned} \tag{13.15}$$

where (13.10) has been used. Then the axial force N, the bending moment M, the transverse shear force Q, the zero-order and first-order moments of the relevant electric displacement and current components can be expressed as

$$\begin{aligned} N &= \int_A T_3 dA = \bar{c}_{33} A w_{,3} + \bar{e}_{33} A \phi_{,3}^{(0)}, \\ M &= \int_A x_2 T_3 dA = \bar{c}_{33} I \psi_{,3} + \bar{e}_{33} I \phi_{,3}^{(1)}, \\ Q &= \int_A T_4 dA = \bar{c}_{44} A (v_{,3} + \psi) + \bar{e}_{15} A \phi^{(1)}, \\ D_2^{(0)} &= \int_A D_2 dA = \bar{e}_{15} A (v_{,3} + \psi) - \bar{\varepsilon}_{11} A \phi^{(1)}, \\ D_3^{(0)} &= \int_A D_3 dA = \bar{e}_{33} A w_{,3} - \bar{\varepsilon}_{33} A \phi_{,3}^{(0)}, \\ D_3^{(1)} &= \int_A x_2 D_3 dA = \bar{e}_{33} I \psi_{,3} - \bar{\varepsilon}_{33} I \phi_{,3}^{(1)}, \end{aligned} \tag{13.16}$$

and

$$
\begin{aligned}
J_2^{n(0)} &= \int_A J_2^n dA = -qn_0\mu_{11}^n A\phi^{(1)} + qD_{11}^n An^{(1)},\\
J_3^{n(0)} &= \int_A J_3^n dA = -qn_0\mu_{33}^n A\phi_{,3}^{(0)} + qD_{33}^n An_{,3}^{(0)},\\
J_3^{n(1)} &= \int_A x_2 J_3^n dA = -qn_0\mu_{33}^n I\phi_{,3}^{(1)} + qD_{33}^n In_{,3}^{(1)},\\
J_2^{p(0)} &= \int_A J_2^p dA = -qp_0\mu_{11}^p A\phi^{(1)} - qD_{11}^p Ap^{(1)},\\
J_3^{p(0)} &= \int_A J_3^p dA = -qp_0\mu_{33}^p A\phi_{,3}^{(0)} - qD_{33}^p Ap_{,3}^{(0)},\\
J_3^{p(1)} &= \int_A x_2 J_3^p dA = -qp_0\mu_{33}^p I\phi_{,3}^{(1)} - qD_{33}^p Ip_{,3}^{(1)},
\end{aligned}
\tag{13.17}
$$

where I and A are the moment of inertia and the area of the fiber cross section, i.e.,

$$
I = \int_A x_2^2 dA = \frac{\pi a^4}{4}, \quad A = \pi a^2. \tag{13.18}
$$

The one-dimensional equations of motion, the charge equation of electrostatics and the conservation of charge for electrons and holes are obtained by integrating (13.1) and their products with x_2 over the fiber cross section. The results are

$$
\begin{aligned}
N_{,3} &= \rho A\ddot{w},\\
D_{3,3}^{(0)} &= qA(p^{(0)} - n^{(0)}),\\
J_{3,3}^{n(0)} &= qA\dot{n}^{(0)},\\
J_{3,3}^{p(0)} &= -qA\dot{p}^{(0)},
\end{aligned}
\tag{13.19}
$$

and

$$
\begin{aligned}
Q_{,3} &= \rho A\ddot{v},\\
M_{,3} - Q &= \rho I\ddot{\psi},\\
D_{3,3}^{(1)} - D_2^{(0)} &= qI(p^{(1)} - n^{(1)}),\\
J_{3,3}^{n(1)} - J_2^{n(0)} &= qI\dot{n}^{(1)},\\
J_{3,3}^{p(1)} - J_2^{p(0)} &= -qI\dot{p}^{(1)}.
\end{aligned}
\tag{13.20}
$$

The substitution of (13.16) and (13.17) into (13.19) and (13.20) gives two sets of second-order linear ordinary differential equations. One is for w, $\phi^{(0)}$, $n^{(0)}$, and $p^{(0)}$ which are related to extension. The other is for v, ψ, $\phi^{(1)}$, $n^{(1)}$ and $p^{(1)}$ which are related to flexure with shear deformation.

13.4 A Cantilever Under a Transverse End Force

For the cantilever in Fig. 13.1, since there is only a transverse shear force f_y at the right end which causes bending with shear but not extension, the extension-related fields of w, $\phi^{(0)}$, $n^{(0)}$, and $p^{(0)}$ all vanish and (13.19) is not needed. In addition, we limit ourselves to the case of an n-type semiconductor so that $p^{(1)}$ vanishes too and $(13.20)_5$ is trivially satisfied. The four remaining fields are v, ψ, $\phi^{(1)}$ and $n^{(1)}$. For static bending, the relevant equations from (13.20), (13.16) and (13.17) are

$$\begin{aligned} Q_{,3} &= 0, \\ M_{,3} - Q &= 0, \\ D_{3,3}^{(1)} - D_2^{(0)} &= qI(p^{(1)} - n^{(1)}), \\ J_{3,3}^{n(1)} - J_2^{n(0)} &= 0, \end{aligned} \tag{13.21}$$

$$\begin{aligned} Q &= \bar{c}_{44} A(v_{,3} + \psi) + \bar{e}_{15} A\phi^{(1)}, \\ M &= \bar{c}_{33} I\psi_{,3} + \bar{e}_{33} I\phi_{,3}^{(1)}, \\ D_2^{(0)} &= \bar{e}_{15} A(v_{,3} + \psi) - \bar{\varepsilon}_{11} A\phi^{(1)}, \\ D_3^{(1)} &= \bar{e}_{33} I\psi_{,3} - \bar{\varepsilon}_{33} I\phi_{,3}^{(1)}, \\ J_2^{n(0)} &= -qn_0\mu_{11}^n A\phi^{(1)} + qD_{11}^n An^{(1)}, \\ J_3^{n(1)} &= -qn_0\mu_{33}^n I\phi_{,3}^{(1)} + qD_{33}^n In_{,3}^{(1)}. \end{aligned} \tag{13.22}$$

The boundary conditions are

$$v(0) = 0, \quad \psi(0) = 0, \quad M(L) = 0, \quad Q(L) = f_y, \tag{13.23}$$

$$D_3^{(1)}(0) = 0, \quad J_3^{n(1)}(0) = 0, \quad D_3^{(1)}(L) = 0, \quad J_3^{n(1)}(L) = 0, \tag{13.24}$$

where we have assumed an electrically isolated fiber. There are no concentrated charges at the ends and there are no currents flowing in or out of the fiber at its ends. For bending without extension, the carrier concentration perturbation is simply $\Delta n = x_2 n^{(1)}$, an odd function of x_2 that satisfies the charge neutrality condition automatically.

The substitution of (13.22) into (13.21) gives four second-order ordinary differential equations with constant coefficients for v, ψ, $\phi^{(1)}$ and $n^{(1)}$. With some algebra, it can be found that the general solution of the four equations is

$$\begin{aligned}\phi^{(1)} = {} & C_1 \sinh \lambda_1 x_3 + C_2 \cosh \lambda_1 x_3 + C_3 \sinh \lambda_3 x_3 + C_4 \cosh \lambda_3 x_3 \\ & - \frac{D_{11}^n A}{D_{33}^n \varepsilon_{33} I} \left(\frac{\bar{e}_{33}\bar{c}_{44} - \bar{e}_{15}\bar{c}_{33}}{\bar{c}_{44}} \right) \frac{C_5}{a_2},\end{aligned} \tag{13.25}$$

$$\begin{aligned}\psi = {} & -\frac{\bar{e}_{33}}{\bar{c}_{33}} (C_1 \sinh \lambda_1 x_3 + C_2 \cosh \lambda_1 x_3 + C_3 \sinh \lambda_3 x_3 + C_4 \cosh \lambda_3 x_3) \\ & + \frac{C_5}{2} x_3^2 + C_6 x_3 + C_7 + \frac{D_{11}^n A \bar{e}_{33}}{D_{33}^n \varepsilon_{33} I \bar{c}_{33}} \left(\frac{\bar{e}_{33}\bar{c}_{44} - \bar{e}_{15}\bar{c}_{33}}{\bar{c}_{44}} \right) \frac{C_5}{a_2},\end{aligned} \tag{13.26}$$

$$\begin{aligned}n^{(1)} = {} & \frac{1}{qI} \Big[(\varepsilon_{33} I \lambda_1^2 - \varepsilon_{11} A)(C_1 \sinh \lambda_1 x_3 + C_2 \cosh \lambda_1 x_3) \\ & + (\varepsilon_{33} I \lambda_3^2 - \varepsilon_{11} A) \times (C_3 \sinh \lambda_3 x_3 + C_4 \cosh \lambda_3 x_3) \\ & - \frac{(D_{33}^n \varepsilon_{33} I^2 - D_{11}^n \varepsilon_{11} A^2)(\bar{e}_{33}\bar{c}_{44} - \bar{e}_{15}\bar{c}_{33})}{D_{33}^n \varepsilon_{33} I \bar{c}_{44}} C_5 \Big],\end{aligned} \tag{13.27}$$

$$\begin{aligned}v = {} & \left(\frac{\bar{e}_{33}}{\bar{c}_{33}} - \frac{\bar{e}_{15}}{\bar{c}_{44}}\right) \Big[\frac{1}{\lambda_1} (C_1 \cosh \lambda_1 x_3 + C_2 \sinh \lambda_1 x_3) \\ & + \frac{1}{\lambda_3} (C_3 \cosh \lambda_3 x_3 + C_4 \sinh \lambda_3 x_3) \Big] - \frac{C_5}{6} x_3^3 - \frac{C_6}{2} x_3^2 \\ & + \left[\left(\frac{\bar{c}_{33} I}{\bar{c}_{44} A} - \frac{D_{11}^n A (\bar{e}_{33}\bar{c}_{44} - \bar{e}_{15}\bar{c}_{33})^2}{D_{33}^n \varepsilon_{33} I \bar{c}_{33} \bar{c}_{44}^2 a_2} \right) C_5 - C_7 \right] x_3 + C_8,\end{aligned} \tag{13.28}$$

where C_1 through C_8 are eight arbitrary constants. λ_1 through λ_4 are the four roots of the following equation:

$$\lambda^4 - a_1 \lambda^2 + a_2 = 0 \tag{13.29}$$

where

$$a_1 = \frac{q \mu_{33}^n n_0}{D_{33}^n \varepsilon_{33}} + \frac{(D_{33}^n \varepsilon_{11} + D_{11}^n \varepsilon_{33}) A}{D_{33}^n \varepsilon_{33} I}, \quad a_2 = \frac{q \mu_{11}^n A n_0}{D_{33}^n \varepsilon_{33} I} + \frac{D_{11}^n \varepsilon_{11} A^2}{D_{33}^n \varepsilon_{33} I^2}. \tag{13.30}$$

Substituting (13.25)–(13.28) into the boundary conditions in (13.23) and (13.24), we obtain eight linear equations for C_1 through C_8. These equations are solved on a computer.

13.5 Numerical Results and Discussion

As an example, consider the ZnO fiber in [44]. The geometric parameters are that $L = 600$ nm and $a = 25$ nm. $f_y = 80$ nN. $n_0 = N_D^+ = 10^{23}$ m^{-3} [44]. The material constants of ZnO are from [23]. However, we were only able to find one of the diffusion constants for ZnO. Therefore $D_{11}^n = D_{33}^n$ is used in our calculation. For these parameters, λ_1 through λ_4 are all real and so are (13.25)–(13.28). In addition, $\lambda_1 = -\lambda_2$ and $\lambda_3 = -\lambda_4$. Numerical results show that in this case Δn is as large as n_0 and is no longer a small perturbation. Therefore, we reduce the end force to $f_y = 0.2$ nN while maintaining all other parameters the same as those in [44]. Then Δn is an order of magnitude smaller than n_0 and the linearization in (13.8) is valid.

The mechanical fields in the fiber are shown in Fig. 13.2 where $d = 2a$ is the diameter of the fiber. The shear force Q is a constant along the fiber. The bending moment M is a linear function along the fiber being equal to $-f_y L$ at the left end and vanishing at the right end. These are obvious from statics. The deflection u_2 in (a) is uniform over the cross section according to the displacement approximation in (13.9). It vanishes at the left fixed end and increases monotonically toward the right end. The axial displacement $u_3 = x_2\psi$ in (b) varies linearly in x_2 over a cross section and vanishes at the left end because of the prescribed boundary condition $\psi(0) = 0$ there. These are familiar mechanical behaviors of the bending of a cantilever. ψ in (c) contributes to the shear strain S_4 according to (13.10). It is related to the constant shear force Q by (13.16) and varies gradually along the fiber. It vanishes at the left end because of the boundary condition there. The shear strain S_4 in (d) is uniform over a cross section according to (13.10) within the approximation of the one-dimensional model. It varies very little along the fiber as dictated by the constant shear force Q except near the left end. The shear stress T_4 is a constant over a cross section according to (13.13). Since it produces a constant shear force along the fiber, T_4 is a constant everywhere in the fiber and hence is not plotted. The axial strain S_3 in (e) and the axial stress T_3 in (f) both vary linearly over a cross section according to (13.10) and (13.13). They are large at the left end where the bending moment is large and are small or vanish at the right end where the bending moment vanishes. From the three-dimensional theory of elasticity, it is well known that while the one-dimensional bending theory developed in this paper can predict the mechanical fields accurately along the most part of the fiber, it cannot predict the stresses (and strains) close to the fixed end. Therefore, the real stresses at the left end are more complicated than what is shown, but they are statically equivalent to the ones in Fig. 13.2.

Figure 13.3 shows the electrical fields in the fiber. (a) shows that the potential distribution varies very little along the fiber except near the left end. For the same fiber, the electric potential distribution obtained theoretically in [45] is constant along the entire fiber without the drastic change near the left end. Mathematically, what led to the z-independence of the potential in [45] is the reasoning after (21) of [45]. Because of the remnant charge on the right-hand side of (19) of [45] is z-independent, it is reasoned in [45] that the electric potential is also z-independent.

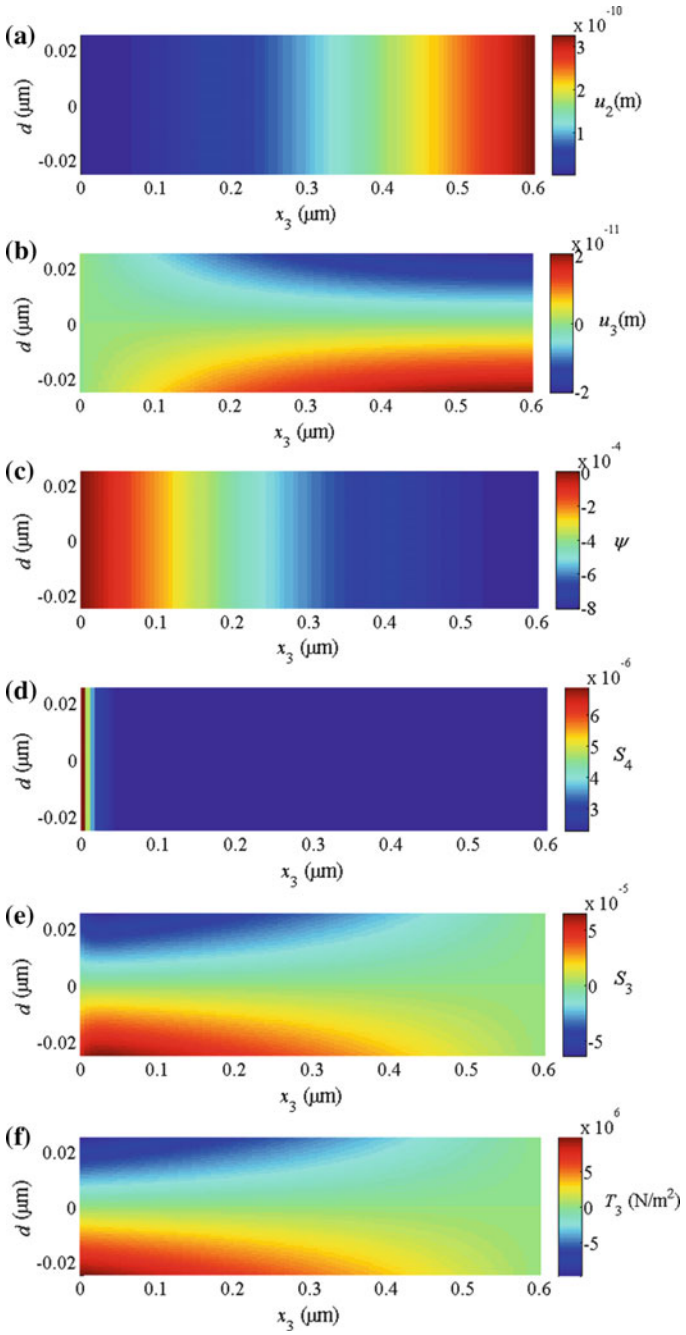

Fig. 13.2 Distributions of mechanical fields. $d = 2a$ is the diameter of the fiber. **a** Flexural displacement $u_2 = v$. **b** Axial displacement $u_3 = x_2\psi$. **c** ψ. **d** Shear strain S_4. **e** Axial strain S_3. **f** Axial stress T_3

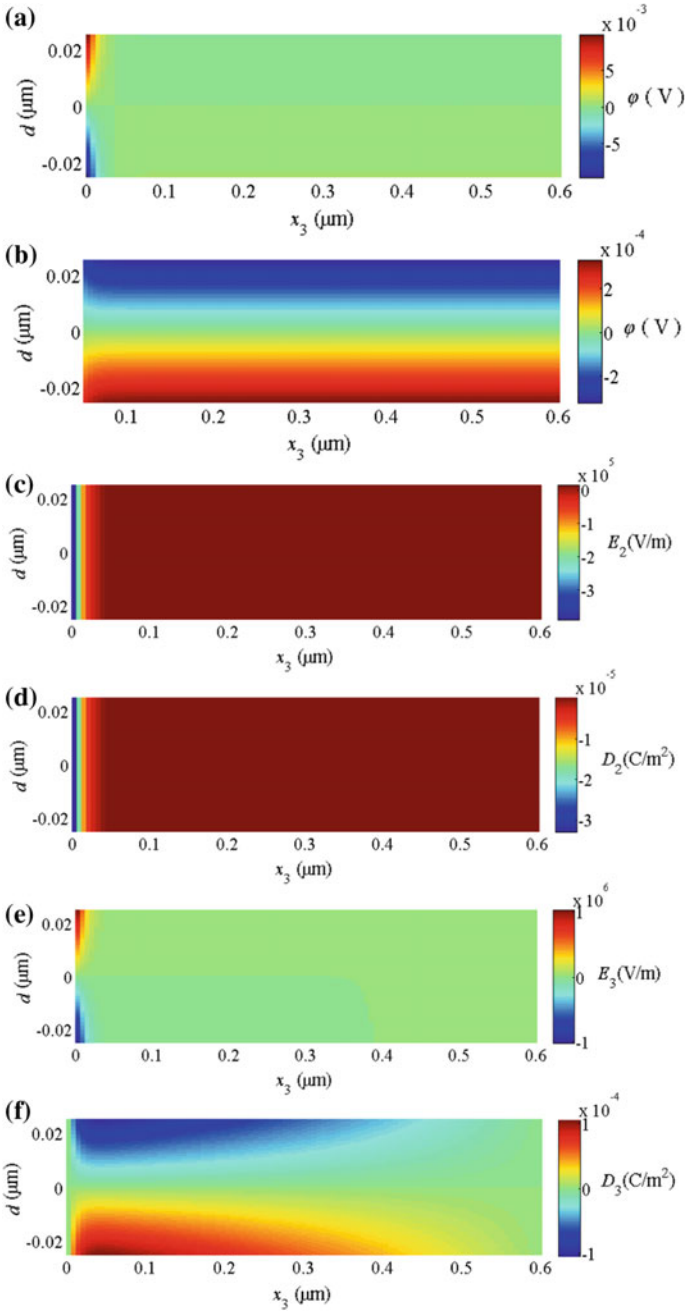

Fig. 13.3 Distributions of electrical fields. $d = 2a$ is the diameter of the fiber. **a** Electric potential $\varphi = x_2\phi^{(1)}$, $0 \le x_3 \le 600$ nm. **b** Electric potential, $50 \le x_3 \le 600$ nm. **c** Transverse electric field E_2. **d** Transverse electric displacement D_2. **e** Axial electric field E_3. **f** Axial electric displacement D_3

However, since the electric potential appears in (19) of [45] in its second-order spatial derivatives, it is only safe to say that some combination of the second-order derivatives of the potential is z-independent, but not necessarily the potential itself. Physically, the presence of T_3 in Fig. 13.2f can affect the axial electric field E_3 through the piezoelectric constant e_{33} and cause the z-dependence of the electric potential. (a) shows that the z-independence of the potential in [45] is a good approximation for the most part of the fiber except when it is very close to the left end. The potential varies linearly over the cross section according to (9) but the variation can hardly be seen in (a) because of the drastic variation of the potential near the left end. The potential distribution in (b) without a small region at the left end shows clearly the linear variation of the potential over the cross section, which is what matters in the application in [44, 45]. The behaviors of E_2 in (c) and D_2 in (d) are similar. They are both uniform over a cross section according to (13.10) and (13.13), and are nearly constant along the most part of the fiber except near the left end. The axial electric field E_3 in (e) and electric displacement D_3 in (f) both vary linearly over the cross section according to (13.10) and (13.13). E_3 is determined by $\phi^{(1)}_{,3}$ which is large at the left end. D_3 depends on $\psi_{,3}$ which varies along the entire fiber.

Figure 13.4a shows the carrier concentration perturbation $\Delta n = x_2 n^{(1)}$ in the fiber due to the end force. Since Δn varies drastically near the left end, we plot Δn again in (b) without a small region near the left end. (b) shows the linear variation of Δn over a cross section according to (13.9) clearly. Δn is produced by the E_2 in Fig. 13.3c which is negative. Therefore, the electrons move toward the upper surface of the fiber. We note that this electron distribution is caused by the shear force Q or the related shear stress T_4 through $e_{24} = e_{15}$, rather than the bending moment M or the axial stress T_3. The total electron concentration $n = n_0 + \Delta n$ is shown in (c) and (d) with or without a small region near the left end. There are more electrons at the upper surface of the fiber than at the lower surface.

$\varphi = x_2 \phi^{(1)}$ and $\Delta n = x_2 n^{(1)}$ show that the behaviors of the electric potential and the electron concentration perturbation are determined by $\phi^{(1)}$ and $n^{(1)}$. In Fig. 13.5, $\phi^{(1)}$ and $n^{(1)}$ are plotted for different values of the applied end force $f = f_y$ for a fixed $n_0 = 10^{23}/\text{m}^3$. (a) and (c) show that both $\phi^{(1)}$ and $n^{(1)}$ are nearly constant except near the fixed left end where they are large and vary rapidly. For the applications we are interested in, the behavior away from the fixed end is relevant and the one-dimensional model in this paper is effective there. To show the behavior of $\phi^{(1)}$ and $n^{(1)}$ away from the fixed end more clearly, they are plotted in (b) and (d) again, respectively, without a small region near the fixed end. It can be seen that a larger end force corresponds to a larger $\phi^{(1)}$ or $n^{(1)}$ as expected.

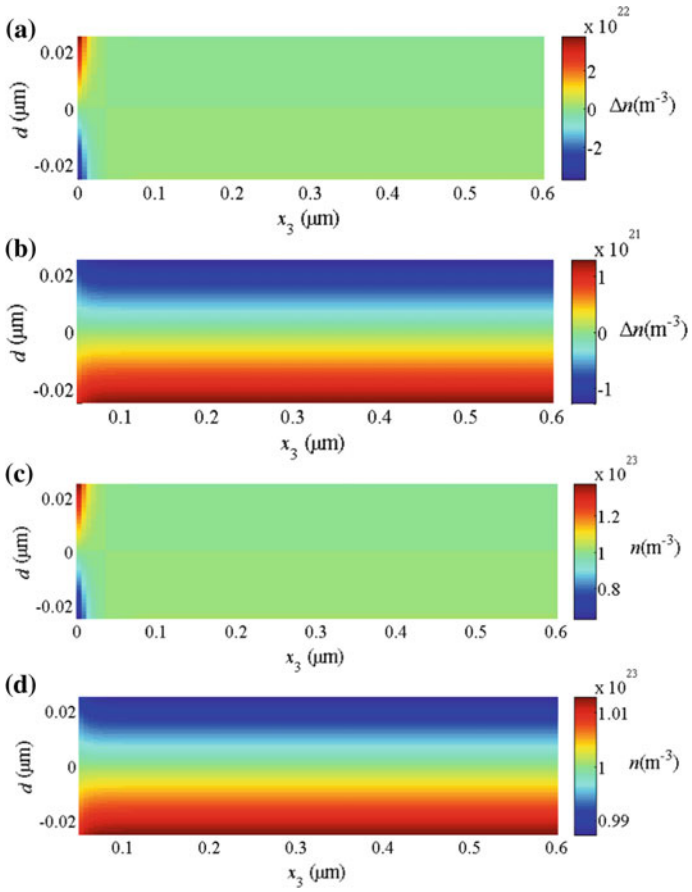

Fig. 13.4 Electron concentration. $d = 2a$ is the diameter of the fiber. **a** $\Delta n = x_2 n^{(1)}$, $0 \le x_3 \le 600$ nm. **b** $\Delta n = x_2 n^{(1)}$, $50 \le x_3 \le 600$ nm. **c** $n = n_0 + \Delta n$, $0 \le x_3 \le 600$. **d** $n = n_0 + \Delta n$, $50 \le x_3 \le 600$ nm

In Fig. 13.6, $\phi^{(1)}$ and $n^{(1)}$ are plotted for different values of the initial electron concentration n_0 for a fixed $f_y = 0.2$ nN. (b) and (d) show that a larger n_0 corresponds to a smaller $\phi^{(1)}$ and a larger $n^{(1)}$ away from the fixed end. This may be explained by that when n_0 is large there are more electrons participating in resisting the production of $\phi^{(1)}$.

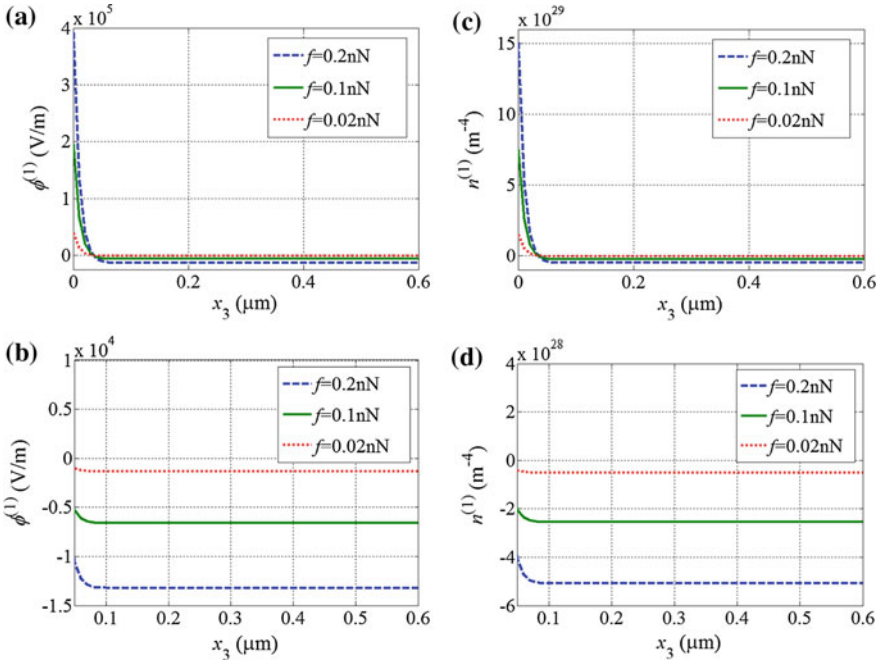

Fig. 13.5 Effects of the end force $f = f_y$. $n_0 = 10^{23}/\text{m}^3$. **a** Electric potential $\phi^{(1)}$. **b** Electric potential $\phi^{(1)}$ (magnified). **c** Electron concentration perturbation $n^{(1)}$. **d** Electron concentration perturbation $n^{(1)}$ (magnified)

13.6 Conclusions

The theoretical framework in this paper consisting of the macroscopic theory of piezoelectric semiconductors, its linearization for small fields, and the one-dimensional theory for thin fibers can produce basic theoretical results fundamental to the understanding of the behaviors of thin ZnO fibers. In the bending of a cantilever ZnO fiber by a transverse end force, the end force applied in [44] is relatively large and is beyond the linear theory in the present paper, but the results presented in the present paper for smaller end forces can still provide basic understanding of the problem. The electric potential is found to be nearly a constant for the most part along the fiber except near its fixed end. Therefore, treating the electric potential as z-independent [45] may be viewed as a good approximation. The variation of the electron concentration over a cross section is caused by the shear stress T_4 through the piezoelectric constant e_{24}. The perturbation of the electron concentration is similar to the electric potential, varying rapidly near the fixed end only.

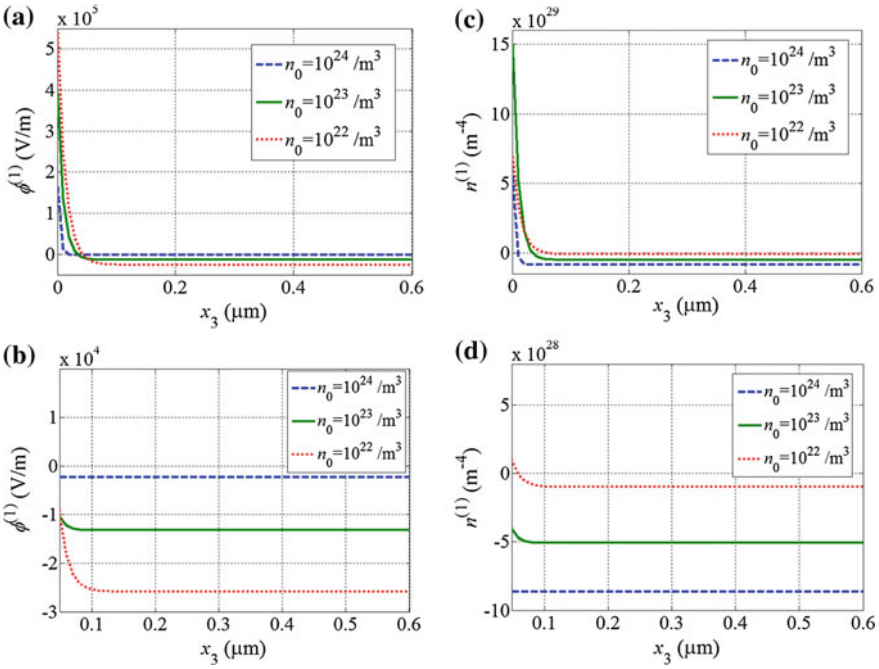

Fig. 13.6 Effects of the initial electron concentration n_0. $f_y = 0.2$ nN. **a** Electric potential $\phi^{(1)}$. **b** Electric potential $\phi^{(1)}$ (magnified). **c** Electron concentration perturbation $n^{(1)}$. **d** Electron concentration perturbation $n^{(1)}$ (magnified)

Acknowledgements This work was supported by the National Natural Science Foundation of China (Nos. 11202182, 11272281 and 11321202).

References

1. Wang, Z.L.: Nanobelts, nanowires, and nanodiskettes of semiconducting oxides-from materials to nanodevices. Adv. Mater. **15**, 432–436 (2003)
2. Wang, Z.L.: Piezopotential gated nanowire devices: piezotronics and piezo-phototronics. Nano Today **5**, 540–552 (2010)
3. Kumar, B., Kim, S.W.: Recent advances in power generation through piezoelectric nanogenerators. J. Mater. Chem. **21**, 18946–18958 (2011)
4. Gao, Y.F., Wang, Z.L.: Equilibrium potential of free charge carriers in a bent piezoelectric semiconductive nanowire. Nano Lett. **9**, 1103–1110 (2009)
5. Hu, Y.F., Chang, Y.L., Fei, P., Snyder, R.L., Wang, Z.L.: Designing the electric transport characteristics of ZnO micro/nanowire devices by coupling piezoelectric and photoexcitation effects. ACS Nano **4**, 1234–1240 (2010)
6. Araneo, R., Lovat, G., Burghignoli, P., Falconi, C.: Piezo-semiconductive quasi-1D nanodevices with or without anti-symmetry. Adv. Mater. **24**, 4719–4724 (2012)

7. Ji, J.L., Zhou, Z.Y., Yang, X., Zhang, W.D., Sang, S.B., Li, P.W.: One-dimensional nano-interconnection formation. Small **9**, 3014–3029 (2013)
8. Shen, Y., Hong, J., Xu, S., Lin, S.S., Fang, H., Zhang, S., Ding, Y., Snyder, R.L., Wang, Z.L.: A general approach for fabricating arc-shaped composite nanowire arrays by pulsed laser deposition. Adv. Func. Mater. **20**, 703–707 (2010)
9. Chen, T.T., Cheng, C.L., Fu, S.P., Chen, Y.F.: Photoelastic effect in ZnO nanorods. Nanotechnology **18**, 225705 (2007)
10. Yoo, J., Lee, C.H., Doh, Y.J., Jung, H.S., Yi, G.C.: Modulation doping in ZnO nanorods for electrical nanodevice application. Appl. Phys. Lett. **94**, 223117 (2009)
11. Xue, H.Z., Pan, N., Li, M., Wu, Y.K., Wang, X.P., Hou, J.G.: Probing the strain effect on near band edge emission of a curved ZnO nanowire via spatially resolved cathodoluminescence. Nanotechnology **21**, 215701 (2010)
12. Gao, P.X., Song, J.H., Liu, J., Wang, Z.L.: Nanowire piezoelectric nanogenerators on plastic substrates as flexible power sources for nanodevices. Adv. Mater. **19**, 67–72 (2007)
13. Choi, M.Y., Choi, D., Jin, M.J., Kim, I., Kim, S.H., Choi, J.Y., Lee, S.Y., Kim, J.M., Kim, S.W.: Mechanically powered transparent flexible charge-generating nanodevices with piezoelectric ZnO nanorods. Adv. Mater. **21**, 2185–2189 (2009)
14. Romano, G., Mantini, G., Garlo, A.D., D'Amico, A., Falconi, C., Wang, Z.L.: Piezoelectric potential in vertically aligned nanowires for high output nanogenerators. Nanotechnology **22**, 465401 (2011)
15. Asthana, A., Ardakani, H.A., Yap, Y.K., Yassar, R.S.: Real time observation of mechanically triggered piezoelectric current in individual ZnO nanobelts. J. Mater. Chem. C **2**, 3995–4004 (2014)
16. Liao, Q.L., Zhang, Z., Zhang, X.H., Mohr, M., Zhang, Y., Fecht, H.J.: Flexible piezoelectric nanogenerators based on a fiber/ZnO nanowires/paper hybrid structure for energy harvesting. Nano Res. **7**, 917–928 (2014)
17. Wang, X.D., Zhou, J., Song, J.H., Liu, J., Xu, N.S., Wang, Z.L.: Piezoelectric field effect transistor and nanoforce sensor based on a single ZnO nanowire. Nano Lett. **6**, 2768–2772 (2006)
18. Buyukkose, S., Hernandez-Minguez, A., Vratzov, B., Somaschini, C., Geelhaar, L., Riechert, H., van der Wiel, W.G., Santos, P.V.: High-frequency acoustic charge transport in GaAs nanowires. Nanotechnology **25**, 135204 (2014)
19. Yu, J., Ippolito, S.J., Wlodarski, W., Strano, M., Kalantar-Zadeh, K.: Nanorod based Shottky contact gas sensors in reversed bias condition. Nanotechnology **21**, 265502 (2010)
20. Chen, T.P., Young, S.J., Chang, S.J., Hsiao, C.H., Hsu, Y.J.: Bending effects of ZnO nanorod metal-semiconductor-metal photodetectors on flexible polyimide substrate. Nanoscale Res. Lett. **7**, 214 (2012)
21. Wang, C.H., Liao, W.S., Ku, N.J., Li, Y.C., Chen, Y.C., Tu, L.W., Liu, C.P.: Effects of free carriers on piezoelectric nanogenerators and piezotronic devices made of GaN nanowire arrays. Small **10**, 4718–4725 (2014)
22. Hutson, A.R., White, D.L.: Elastic wave propagation in piezoelectric semiconductors. J. Appl. Phys. **33**, 40–47 (1962)
23. Auld, B.A.: Acoustic Fields and Waves in Solids, vol. I. Wiley, New York (1973)
24. Pierret, R.F.: Semiconductor Fundamentals, 2nd edn. Addison-Wesley, Reading, Massachusetts (1988)
25. Mindlin, R.D.: Low frequency vibrations of elastic bars. Int. J. Solids Struct. **12**, 27–49 (1976)
26. Dokmeci, M.C.: A theory of high frequency vibrations of piezoelectric crystal bars. Int. J. Solids Struct. **10**, 401–409 (1974)
27. Chou, C.S., Yang, J.W., Huang, Y.C., Yang, H.J.: Analysis on vibrating piezoelectric beam gyroscope. Int. J. Appl. Electromagn. Mech. **2**, 227–241 (1991)
28. Yang, J.S.: Equations for the extension and flexure of a piezoelectric beam with rectangular cross section and applications. Int. J. Appl. Electromagn. Mech. **9**, 409–420 (1998)

29. Zhang, C.L., Wang, X.Y., Chen, W.Q., Yang, J.S.: Carrier distribution and electromechanical fields in a free piezoelectric semiconductor rod. J. Zhejiang Univ. SCIENCE A **17**, 37–44 (2016)
30. Wauer, J., Suherman, S.: Thickness vibrations of a piezo-semiconducting plate layer. Int. J. Eng. Sci. **35**, 1387–1404 (1997)
31. Yang, J.S., Song, Y.C., Soh, A.K.: Analysis of a circular piezoelectric semiconductor embedded in a piezoelectric semiconductor substrate. Arch. Appl. Mech. **76**, 381–390 (2006)
32. Hu, Y.T., Zeng, Y., Yang, J.S.: A Mode III crack in a piezoelectric semiconductor of crystals with 6 mm symmetry. Int. J. Solids Struct. **44**, 3928–3938 (2007)
33. Sladek, J., Sladek, V., Pan, E., Young, D.L.: Dynamic anti-plane crack analysis in functional graded piezoelectric semiconductor crystals. Comput. Model. Eng. Sci. **99**, 273–296 (2014)
34. Sladek, J., Sladek, V., Pan, E., Münsche, M.: Fracture analysis in piezoelectric semiconductors under a thermal load. Eng. Fract. Mech. **126**, 27–39 (2014)
35. Li, P., Jin, F., Yang, J.S.: Effects of semiconduction on electromechanical energy conversion in piezoelectrics. Smart Mater. Struct. **24**, 025021 (2015)
36. Golovnev, A., Trimper, S.: Exact solution of the Poisson-Nernst-Planck equations in the linear regime. J. Chem. Phys. **131**, 114903 (2009)
37. Zhou, S.A., Uesaka, M.: Modeling of transport phenomena of ions and polarizable molecules: a generalized Poisson-Nernst-Planck theory. Int. J. Eng. Sci. **44**, 938–948 (2006)
38. de Lorenzi, H.G., Tiersten, H.F.: On the interaction of the electromagnetic field with heat conducting deformable semiconductors. J. Math. Phys. **16**, 938–957 (1975)
39. McCarthy, M.F., Tiersten, H.F.: on integral forms of the balance laws for deformable semiconductors. Arch. Ration. Mech. Anal. **68**, 27–36 (1978)
40. Maugin, G.A., Daher, N.: Phenomenological theory of elastic semiconductors. Int. J. Eng. Sci. **24**, 703–731 (1986)
41. Daher, N., Maugin, G.A.: Waves in elastic semiconductors in a bias electric field. Int. J. Eng. Sci. **24**, 733–754 (1986)
42. Daher, N., Maugin, G.A.: Nonlinear electroacoustic equations in semiconductors with interfaces (relation between the macroscopic and the quasi-microscopic descriptions). Int. J. Eng. Sci. **26**, 37–58 (1988)
43. Daher, N., Maugin, G.A.: Bulk waves in elastic semiconductors in the presence of an initial state. Int. J. Eng. Sci. **26**, 993–1012 (1988)
44. Gao, Y.F., Wang, Z.L.: Equilibrium potential of free charge carriers in a bent piezoelectric semiconductive nanowire. Nano Lett. **9**, 1103–1110 (2009)
45. Gao, Y.F., Wang, Z.L.: Electrostatic potential in a bent piezoelectric nanowire. The fundamental theory of nanogenerator and nanopiezotrionics. Nano Lett. **7**, 2499–2505 (2007)

Chapter 14
Contact Mechanics in the Framework of Couple Stress Elasticity

Thanasis Zisis, Panos A. Gourgiotis and Haralambos G. Georgiadis

Abstract The purpose of this work is to present general solutions for two-dimensional (2D) plane-strain contact problems within the framework of the generalized continuum theory of couple-stress elasticity. This theory is able to capture the scale effects, which are often observed in indentation problems with contact lengths comparable to the material microstructure. To this end, we formulate a number of basic contact problems in terms of singular integral equations using the pertinent Green's function that corresponds to the solution of the analogue of the Flamant-Boussinesq problem of a half-space in couple-stress elasticity. In addition, we also provide results concerning the more complex traction boundary-value problem involving a deformable layer (again within couple-stress elasticity) of finite thickness superposed on a rigid half-space. We show that the contact behavior of materials with couple-stress effects depends strongly upon their microstructural characteristics, especially when the characteristic dimension of the microstructure becomes comparable to macroscopic characteristic dimensions of the contact problem. The latter lengths could be either the contact length/area or even the thickness of the layer.

Th. Zisis · H. G. Georgiadis (✉)
Mechanics Division, National Technical University of Athens,
15773 Zographou, Greece
e-mail: georgiad@central.ntua.gr

Th. Zisis
e-mail: zisis@mail.ntua.gr

P. A. Gourgiotis
School of Engineering & Computing Sciences, Durham University,
South Road, Durham DH1 3LE, UK
e-mail: panagiotis.gourgiotis@durham.ac.uk

H. G. Georgiadis
Office of Theoretical and Applied Mechanics, Academy of Athens, Athens, Greece

H. Altenbach et al. (eds.), *Generalized Models and Non-classical Approaches in Complex Materials 2*, Advanced Structured Materials 90,
https://doi.org/10.1007/978-3-319-77504-3_14

14.1 Introduction

Contact situations between two bodies occur in a multitude of engineering applications ranging from mechanical and civil engineering to materials science. On the one hand, small scale contacts appear in indentation tests for the extraction of material properties, in the area of mechanical engineering and/or material science while, on the other hand, a multitude of structures is founded in reinforced concrete footings or pads buried at relatively shallow depths beneath the ground surface. There, large-scale contacts take place between the footings and the deformable ground. Furthermore, the microscopic as well as the macroscopic behavior of most materials with distinct microstructural characteristics (i.e. non-homogeneous microstructure) like, for example, ceramics, composites, cellular materials, foams, masonry, bone tissues, glassy and semi-crystalline polymers, are strongly influenced by the microstructural lengths of the material, especially in the presence of large stress (or strain) gradients [1]. This effect of the microstructure upon the macroscopic mechanical response of the materials is usually referred to as "*size effect*".

Size effects have been observed in indentation tests especially when the contact area is comparable to the material microstructure. In particular, it has been shown that a strong size effect emerges upon the hardness in polycrystalline, cellular and polymer materials especially in the sub-micrometer depth regime. In fact, the indentation hardness of metals and ceramics increases by a factor of two as the width of the indent size decreases from 10 to 1 μm [2–4]. Moreover, indentation of thin films showed an increase in the yield stress with decreasing film thickness [5]. Fleck et al. [6] showed that the size effect on hardness is related to the high stress/strain gradients present in shallow indentations. Although material hardening is attributed to the combined presence of geometrically necessary dislocations associated with plastic strain gradients and statistically stored dislocations associated with plastic strains, strain gradients are also important for materials that deform purely elastically. In fact, there is evidence that certain polymers exhibit significant size effects under purely elastic deformation [7, 8]. In addition, Maraganti and Sharma [1] showed that gradient effects are expected to play a significant role in the elastic deformation of complex cellular-type materials with coarse-grained structure. In light of the above, and taking into account that the indentation technique has evolved to a standard method for material characterization, the investigation of the microstructural effects upon the macroscopic behavior of the indented material in the elastic regime is of paramount importance [9].

The study of size effects of microstructured materials upon various loading conditions involves roughly two different approaches. The first approach takes into account the discrete morphology of the material through discrete modeling and directly incorporates into the model the details of the material microstructure. The second approach involves the use of generalized continuum theories according to which the microstructural characteristics are smeared out but the characteristic microstructural length is retained. The generalized continuum approach is a very

powerful one since it can be incorporated efficiently into large computations. However, it lacks the detailed description of a discrete representation due to the fact that it treats the microstructural characteristic lengths in an average sense. Discrete modeling of the material microstructure during indentation has been carried out using classical theories [10–14], whereas phenomenological approaches based on generalized continua have been also extensively followed [15–20].

Couple-stress elasticity, also known as Cosserat theory of elasticity with constrained rotations, is an effective generalized continuum theory, successfully modeling size effects in many engineering problems. This theory is the simplest gradient theory in which couple-stresses appear. In particular, the couple-stress theory assumes an augmented form of the Euler-Cauchy principle with a non-vanishing couple traction, and a strain-energy density that depends upon both the strain and the gradient of rotation. Such assumptions are appropriate for materials with granular structure, where the interaction between adjacent elements may introduce internal moments. In this way, characteristic material lengths may appear representing in an average sense the material microstructure. The presence of these material lengths implies that the couple-stress theory encompasses the analytical possibility of size effects, which are absent in the classical theory. The fundamental concepts of the couple-stress theory were first introduced by Cauchy [21], Voigt [22] and the Cosserat brothers [23], but the subject was generalized and reached maturity only in the 1960s through the works of Toupin [24], Mindlin and Tiersten [25], and Koiter [26].

The physical relevance of the material length scales as introduced through generalized continuum theories has been the subject of numerous theoretical and experimental studies. For instance, Chen et al. [27] developed a continuum model for cellular materials showing that its continuum description obeys a gradient elasticity theory of the couple-stress type. The intrinsic material length was naturally identified with the cell size. Tekoglu and Onck [14] compared the analytical results of various gradient type generalized continuum theories with the computational results of discrete models of Voronoi representations of cellular microstructures. The analysis within the elastic regime assessed the capabilities of generalized continuum theories in capturing size effects in cellular solids. A recent study by Bigoni and Drugan [28] determined the couple-stress moduli via homogenization of heterogeneous materials. Moreover, Shodja et al. [29] utilizing ab initio DFT calculations evaluated the characteristic material lengths of the gradient elasticity theory for several *fcc* and *bcc* metal crystals.

Furthermore, experiments with phonon dispersion curves indicate that for most metals, the characteristic internal length is of the order of the lattice parameter, about 0.25 nm while other small-molecule materials have larger internal characteristic lengths [30]. For example, for the semiconductor gallium arsenide (GaAs), Zhang and Sharma [30] estimated a characteristic length of about 0.82 nm, while Lakes [31] estimated a microstructural length for graphite H257 of the order of 2.8 nm. On the other hand, in foams and cellular materials the characteristic lengths are comparable to the average cell size, whereas in laminates is of the order of the

laminate thickness. For example, dense polyurethane foams exhibit a microstructural length about 0.33 mm [32], while for human bones it is around 0.5 mm [33].

14.2 Basic Equations in Plane-Strain

Here, we briefly recall certain elements of the linearized plane-strain theory of couple-stress elasticity for homogeneous and isotropic elastic solids. A more detailed exposition of the theory under plane-strain conditions was given in the work by Muki and Sternberg [15] for the quasi-static case, and more recently by Gourgiotis and Piccolroaz [34] for the dynamical case (including micro-inertia effects).

The rectangular components of the asymmetric stress (σ_{xx}, σ_{xy}, σ_{yx}, σ_{yy}) and couple stress (m_{xz}, m_{yz}) are shown in Fig. 14.1, which act upon the faces of an infinitesimal rectangular element of unit thickness. If the stresses and couple stresses vary across the element, the shear stresses (σ_{xy}, σ_{yx}) are not necessarily equal and if the shear stresses are equal or even zero the couple stresses need not vanish.

For a body that occupies a domain in the (x, y)—plane under conditions of plane strain, the displacement field takes the general form

$$u_x \equiv u_x(x,y) \neq 0, \quad u_y \equiv u_y(x,y) \neq 0, \quad u_z \equiv 0. \tag{14.1}$$

Further, for the kinematical description, the following quantities are defined in the framework of the geometrically linear theory

$$\varepsilon_{xx} = \frac{\partial u_x}{\partial x}, \varepsilon_{yy} = \frac{\partial u_y}{\partial y}, \varepsilon_{xy} = \varepsilon_{yx} = \frac{1}{2}\left(\frac{\partial u_y}{\partial x} + \frac{\partial u_x}{\partial y}\right) \tag{14.2}$$

$$\omega = \frac{1}{2}\left(\frac{\partial u_y}{\partial x} - \frac{\partial u_x}{\partial y}\right), \kappa_{xz} = \frac{\partial \omega}{\partial x}, \kappa_{yz} = \frac{\partial \omega}{\partial y}, \tag{14.3}$$

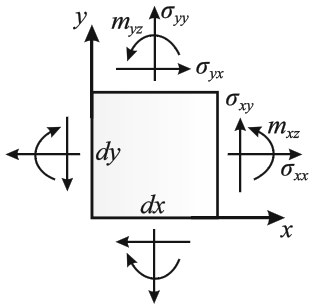

Fig. 14.1 Rectangular components of stress and couple stress

where $\boldsymbol{\varepsilon}$ is the usual strain tensor, ω is the rotation, and $(\kappa_{xz}, \kappa_{yz})$ are the non-vanishing components of the curvature tensor (i.e. the gradient of rotation) expressed in dimensions of [length]$^{-1}$.

Accordingly, assuming vanishing body forces and body couples, the equations of equilibrium in the present circumstances reduce to

$$\frac{\partial \sigma_{xx}}{\partial x} + \frac{\partial \sigma_{yx}}{\partial y} = 0, \quad \frac{\partial \sigma_{xy}}{\partial x} + \frac{\partial \sigma_{yy}}{\partial y} = 0, \quad \sigma_{xy} - \sigma_{yx} + \frac{\partial m_{xz}}{\partial x} + \frac{\partial m_{yz}}{\partial y} = 0, \tag{14.4}$$

Equations (14.4) are the Cosserat equations of equilibrium in two dimensions. Moreover, the constitutive equations read

$$\begin{aligned} &\varepsilon_{xx} = (2\mu)^{-1}\left[\sigma_{xx} - \nu\left(\sigma_{xx} + \sigma_{yy}\right)\right], \quad \varepsilon_{yy} = (2\mu)^{-1}\left[\sigma_{yy} - \nu\left(\sigma_{xx} + \sigma_{yy}\right)\right], \\ &\varepsilon_{xy} = (4\mu)^{-1}\left(\sigma_{xy} + \sigma_{yx}\right) \end{aligned} \tag{14.5}$$

and

$$\kappa_{xz} = \left(4\mu\ell^2\right)^{-1} m_{xz}, \quad \kappa_{yz} = \left(4\mu\ell^2\right)^{-1} m_{yz} \tag{14.6}$$

where μ, ν and ℓ stand, respectively, for the shear modulus, Poisson's ratio, and the characteristic material length of couple-stress theory.

The compatibility equations in terms of the stress and the couple stress components assume then the following form

$$\frac{\partial^2 \sigma_{xx}}{\partial y^2} - \frac{\partial^2}{\partial x \partial y}\left(\sigma_{xy} + \sigma_{yx}\right) + \frac{\partial^2 \sigma_{yy}}{\partial x^2} = \nu \nabla^2 \left(\sigma_{xx} + \sigma_{yy}\right), \tag{14.7}$$

$$\frac{\partial m_{xz}}{\partial y} = \frac{\partial m_{yz}}{\partial x}, \tag{14.8}$$

$$m_{xz} = -2\ell^2 \frac{\partial}{\partial y}\left[\sigma_{xx} - \nu\left(\sigma_{xx} + \sigma_{yy}\right)\right] + \ell^2 \frac{\partial}{\partial x}\left(\sigma_{xy} + \sigma_{yx}\right), \tag{14.9}$$

$$m_{yz} = 2\ell^2 \frac{\partial}{\partial x}\left[\sigma_{yy} - \nu\left(\sigma_{xx} + \sigma_{yy}\right)\right] - \ell^2 \frac{\partial}{\partial y}\left(\sigma_{xy} + \sigma_{yx}\right). \tag{14.10}$$

Notice that only three of the four equations of compatibility are independent. Indeed, Eqs. (14.8)–(14.10) imply (14.7), while Eqs. (14.7), (14.9) and (14.10) yield (14.8) [14, 15]. Furthermore, the complete solution of Eqs. (14.4) admits the following representation in terms of the Mindlin's stress functions [35]

$$\sigma_{xx}=\frac{\partial^2\Phi}{\partial y^2}-\frac{\partial^2\Psi}{\partial x\partial y},\sigma_{yy}=\frac{\partial^2\Phi}{\partial x^2}+\frac{\partial^2\Psi}{\partial x\partial y},\sigma_{xy}=-\frac{\partial^2\Phi}{\partial x\partial y}-\frac{\partial^2\Psi}{\partial y^2},\sigma_{yx}=-\frac{\partial^2\Phi}{\partial x\partial y}+\frac{\partial^2\Psi}{\partial x^2} \tag{14.11}$$

and

$$m_{xz}=\frac{\partial\Psi}{\partial x},m_{yz}=\frac{\partial\Psi}{\partial y}, \tag{14.12}$$

where $\Phi\equiv\Phi(x,\,y)$ and $\Psi\equiv\Psi(x,\,y)$ are two arbitrary but sufficiently smooth functions. Substitution of Eqs. (14.11) and (14.12) into (14.9) and (14.10) results in the following pair of differential equations, for the stress functions

$$\frac{\partial}{\partial x}\left(\Psi-\ell^2\nabla^2\Psi\right)=-2(1-\nu)\ell^2\nabla^2\left(\frac{\partial\Phi}{\partial y}\right), \tag{14.13}$$

$$\frac{\partial}{\partial y}\left(\Psi-\ell^2\nabla^2\Psi\right)=2(1-\nu)\ell^2\nabla^2\left(\frac{\partial\Phi}{\partial x}\right), \tag{14.14}$$

which, accordingly, lead to the uncoupled PDEs:

$$\nabla^4\Phi=0, \tag{14.15}$$

$$\nabla^2\Psi-\ell^2\nabla^4\Psi=0. \tag{14.16}$$

The above representation reduces to the classical Airy's representation as the quantities ℓ, $\partial_x\Psi$, and $\partial_y\Psi$ tend to zero. In addition, combining Eqs. (14.2)–(14.5), and (14.11)–(14.12), one can obtain the following relations connecting the displacement gradients with Mindlin's stress functions

$$\frac{\partial u_x}{\partial x}=\frac{1}{2\mu}\left(\frac{\partial^2\Phi}{\partial y^2}-\frac{\partial^2\Psi}{\partial x\partial y}-\nu\,\nabla^2\Phi\right), \tag{14.17}$$

$$\frac{\partial u_y}{\partial y}=\frac{1}{2\mu}\left(\frac{\partial^2\Phi}{\partial x^2}+\frac{\partial^2\Psi}{\partial x\partial y}-\nu\,\nabla^2\Phi\right), \tag{14.18}$$

$$\frac{\partial u_x}{\partial y}+\frac{\partial u_y}{\partial x}=-\frac{1}{2\mu}\left(2\frac{\partial^2\Phi}{\partial x\partial y}-\frac{\partial^2\Psi}{\partial x^2}+\frac{\partial^2\Psi}{\partial y^2}\right). \tag{14.19}$$

14.3 Green's Functions

The definition of a Green's function can be used mathematically to derive solutions to point load problems, either within the elastic body or on its surface. A multitude of Green's functions within the context of classical elasticity are available in the literature for different surface geometries (see e.g. [36]). In a 2D setting, the problem of determining the stress and displacement fields in an isotropic half-plane subjected to a concentrated line load on its surface is the celebrated Flamant-Boussinesq problem (see Fig. 14.2). The Flamant-Boussinesq solution of classical elasticity is discussed among others, e.g., by Love [37], Fung [38], Timoshenko and Goodier [39], and enjoys important applications mainly in Contact Mechanics and Tribology, since it can be used as a building block for the formulation of complicated contact problems [40–42].

In the context of generalized continuum theories, concentrated load problems have been extensively studied suggesting solutions that significantly depart from the predictions of classical elasticity (for a thorough review on the subject see the recent work of Anagnostou et al. [43]). Regarding the couple-stress theory, Muki and Sternberg [15] were the first to derive the asymptotic fields for the stress field in the Flamant-Boussinesq problem while Gourgiotis and Zisis [44] provided a full field solution for the same problem.

In what follows, we examine two basic 2D configurations: a half-plane $(-\infty < x < \infty,\ \ y \geq 0)$, and a layer of finite thickness h bonded on a rigid substrate $(-\infty < x < \infty,\ \ 0 \leq y \leq h)$ (see Fig. 14.2). In both cases plane strain conditions prevail. The point of application of the concentrated load is taken as the origin $(x = y = 0)$ of a Cartesian rectangular coordinate system. The intensities of the concentrated loads are expressed in dimensions of [force][length]$^{-1}$.

In both cases the boundary conditions along the surface $(y = 0)$ become

$$\sigma_{yy}(x,0) = -P\delta(x) \quad \text{for } -\infty < x < \infty, \tag{14.20}$$

$$\sigma_{yx}(x,0) = 0 \quad \text{for } -\infty < x < \infty, \tag{14.21}$$

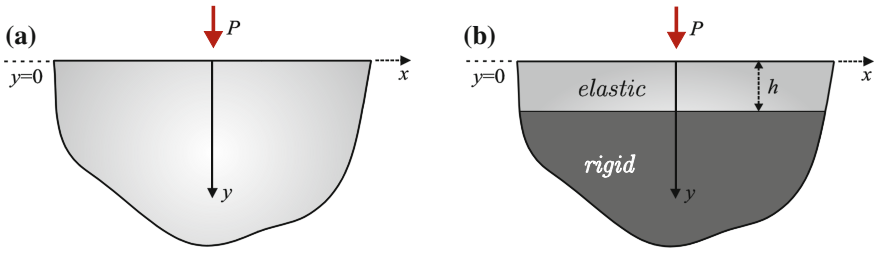

Fig. 14.2 Normal force acting on the surface of **a** an elastic half-plane and **b** an elastic layer of thickness bonded on a rigid substrate

$$m_{yz}(x,0)=0 \quad \text{for } -\infty<x<\infty, \tag{14.22}$$

where $\delta(x)$ is the Dirac delta distribution.

For the case of the layer of finite thickness, two sets of boundary conditions can be defined at the interface $(y=h)$ between the layer and the rigid substrate:

(i) The first set suggests vanishing displacements and rotations at the interface:

$$u_x(x,h)=0 \quad \text{for } -\infty<x<\infty, \tag{14.23}$$

$$u_y(x,h)=0 \quad \text{for } -\infty<x<\infty, \tag{14.24}$$

$$\omega_z(x,h)=0 \quad \text{for } -\infty<x<\infty, \tag{14.25}$$

(ii) The second set suggests vanishing displacements and couple stresses at the interface:

$$u_x(x,h)=0 \quad \text{for } -\infty<x<\infty, \tag{14.26}$$

$$u_y(x,h)=0 \quad \text{for } -\infty<x<\infty, \tag{14.27}$$

$$m_{yz}(x,h)=0 \quad \text{for } -\infty<x<\infty, \tag{14.28}$$

The boundary conditions (14.23)–(14.25) correspond to an over-constrained version of the classical elasticity solution, while boundary conditions (14.26)–(14.28) allow for a direct comparison of the current solution with the corresponding classical elasticity results. Finally, it is noted that the solution procedure for the case of a tangential load acting on the surface of a half-plane is directly analogous to what will be presented next and for this reason is omitted for sake of brevity.

The presented boundary value problems are attacked with the aid of the Fourier transform on the basis of the stress function formulation introduced earlier. The direct Fourier transform and its inverse are defined as follows

$$\hat{f}(\xi)=\int_{-\infty}^{\infty} f(x)\, e^{i\xi x}dx, \quad f(x)=\frac{1}{2\pi}\int_{-\infty}^{\infty} \hat{f}(\xi)\, e^{-i\xi x}d\xi, \tag{14.29}$$

where $i\equiv(-1)^{1/2}$.

The transformation of Eqs. (14.15) and (14.16) through $(14.29)_2$ yields the following ODEs for the transformed stress functions

$$\frac{d^4\hat{\Phi}}{dy^4} - 2\xi^2\frac{d^2\hat{\Phi}}{dy^2} + \xi^4\hat{\Phi} = 0, \tag{14.30}$$

$$\ell^2\frac{d^4\hat{\Psi}}{dy^4} - \left(1 + 2\ell^2\xi^2\right)\frac{d^2\hat{\Psi}}{dy^2} + \xi^2\left(1 + \ell^2\xi^2\right)\hat{\Psi} = 0. \tag{14.31}$$

Accordingly, the transformed displacements take the following form

$$\hat{u}_x = \frac{1}{2\mu\xi}\left(i(1-\nu)\frac{d^2\hat{\Phi}}{dy^2} - \xi\frac{d\hat{\Psi}}{dy} + i\nu\xi^2\hat{\Phi}\right), \tag{14.32}$$

$$\hat{u}_y = \frac{1}{2\mu\xi^2}\left((1-\nu)\frac{d^3\hat{\Phi}}{dy^3} - (2-\nu)\xi^2\frac{d\hat{\Phi}}{dy} - i\xi^3\hat{\Psi}\right). \tag{14.33}$$

The governing Eqs. (14.30) and (14.31) in conjunction with the compatibility Eqs. (14.13) and (14.14) assume the following general solutions

$$\hat{\Phi}(\xi, y) = [C_1(\xi) + yC_2(\xi)]e^{-|\xi|y} + [C_3(\xi) + yC_4(\xi)]e^{|\xi|y}, \tag{14.34}$$

$$\begin{aligned}\hat{\Psi}(\xi, y) = &-4i\ell^2(1-\nu)\xi C_2(\xi)e^{-|\xi|y} + C_5(\xi)e^{-\gamma y}\\ &-4i\ell^2(1-\nu)\xi C_4(\xi)e^{\xi y} + C_6(\xi)e^{\gamma y}.\end{aligned} \tag{14.35}$$

where $\gamma \equiv \gamma(\xi) = \left(\ell^{-2} + \xi^2\right)^{1/2}$. The functions $C_q(\xi)$ $(q = 1, \ldots, 6)$ will be determined through the enforcement of the pertinent boundary conditions. Note that in the case of a half-plane the solution should be bounded as $y \to \infty$ which implies that: $C_3 = C_4 = C_6 = 0$.

Utilizing the fact that $\hat{u}_x(x, \xi)$ and $\hat{u}_y(x, \xi)$ are odd and even functions of ξ, respectively, a general representation of the components of the displacement field reads

$$u_x(x, y) = \frac{-i}{\pi}\int_0^\infty \hat{u}_x(\xi, y)\sin(\xi x)\, d\xi, \tag{14.36}$$

$$u_y(x, y) = \frac{1}{\pi}\int_0^\infty \hat{u}_y(\xi, y)\cos(\xi x)\, d\xi. \tag{14.37}$$

It is worth noting that for the layer problem both $\hat{u}_x$ and $\hat{u}_y$ are bounded as $\xi \to 0$, which implies that the displacement field is also bounded as $x \to \infty$. On the other hand, for the half-plane problem, the integrand in (14.37) behaves as $\hat{u}_y = O\left(\xi^{-1}\right)$ for $\xi \to 0$, and, thus, u_y exhibits a logarithmic behavior as $x \to \infty$. These observations hold true also in the classical elasticity theory.

For the Flamant-Boussinesq problem in the context of couple stress theory the displacement field assumes the following form [44]

$$u_x(x,y) = \frac{P}{2\mu\pi}\int_0^\infty \frac{T_1(\xi)}{T_0(\xi)}\sin(\xi x)d\xi, \tag{14.38}$$

$$u_y(x,y) = \frac{P}{2\mu\pi}\int_0^\infty \frac{T_2(\xi)}{T_0(\xi)}\cos(\xi x)d\xi, \tag{14.39}$$

with

$$T_1(\xi) = 4\ell^2(1-\nu)\xi^2\gamma e^{-\gamma y} + \left(\gamma(y\xi - 1 + 2\nu) - 4\ell^2(1-\nu)\xi^3\right)e^{-\xi y},$$

$$T_2(\xi) = 4\ell^2(1-\nu)\xi^3 e^{-\gamma y} + \left(\gamma(y\xi + 2(1-\nu)) - 4\ell^2(1-\nu)\xi^3\right)e^{-\xi y},$$

$$T_0(\xi) = \xi\left(\gamma - 4(1-\nu)\ell^2\xi^2(\xi-\gamma)\right).$$

Note that analogous expressions for the displacement field have also been found for the layer problem, however these expressions are lengthy and are not reported here for the sake of brevity.

The asymptotic behavior of the tangential and normal displacements in the context of couple-stress elasticity for a half-space was examined near the point of the application of the concentrated load by Gourgiotis and Zisis [44] by employing theorems of the Abel-Tauber type and examining the behavior of the transformed solutions for the displacements as $\xi \to \infty$. In fact, it was shown that

$$u_x^{asympt}(x,y) = \frac{P}{2\mu\pi(3-2\nu)}\left[\tan^{-1}\left(\frac{x}{y}\right) - (1-2\nu)\frac{xy}{r^2}\right], \tag{14.40}$$

$$u_y^{asympt}(x,y) = -\frac{P}{2\pi\mu\,(3-2\nu)}\left[(1-2\nu)\frac{y^2}{r^2} + 2(1-\nu)\log(r)\right], \tag{14.41}$$

as $r \to 0$ with $r = (x^2+y^2)^{1/2}$. It is noted that the displacement components exhibit the same asymptotic behavior both in couple-stress and in classical elasticity, however, the detailed structure of these fields is different. The strain components can be readily calculated from Eqs. (14.36) and (14.37) through appropriate derivations. It can be shown that the strains remain singular and behave as $\varepsilon_{ij} = O(r^{-1})$ as $r \to 0$. However, in marked contrast with the classical theory, the rotation is bounded at the point of application of the load. It is recalled that in the classical theory the rotation is singular, exhibiting an $\sim r^{-1}$ variation as $r \to 0$.

In order to formulate the 2D contact problems, it is convenient to work in terms of the displacement gradients, thereby eliminating arbitrary constants [45]. To this respect, the quantity du_y/dx is evaluated at the surface of the half-plane ($y = 0$) as

$$\frac{du_y}{dx} = \frac{1}{\pi}\int_0^\infty g(\xi)\sin(\xi x)\,d\xi, \tag{14.42}$$

with $g(\xi) = -\xi\hat{u}_y(\xi, 0)$.The integral in (14.42) is divergent since $g(\xi) = O(1)$ as $\xi \to \infty$. In order to make $g(\xi)$ explicit and separate its singular and regular parts, it is expedient to examine the asymptotic behavior of $g(\xi)$ as $\xi \to \infty$. By using the Abel-Tauber theorem and noting that: $\lim_{\xi\to\infty} g(\xi) = g_\infty(\xi) = -\frac{P(1-\nu)}{\mu(3-2\nu)}$, we decompose $g(\xi)$ as

$$g(\xi) = g_\infty(\xi) + (g(\xi) - g_\infty(\xi)). \tag{14.43}$$

Equation (14.42) takes then the following form

$$\frac{du_y}{dx} = \underbrace{\frac{1}{\pi}\int_0^\infty g_\infty(\xi)\sin(\xi x)d\xi}_{\text{singular part}} + \underbrace{\frac{1}{\pi}\int_0^\infty [g(\xi) - g_\infty(\xi)]\sin(\xi x)d\xi}_{\text{regular part}}, \tag{14.44}$$

which, after utilizing results of the theory of the generalized functions and singular distributions [46], Eq. (14.44) can be finally written as

$$\frac{du_y}{dx} = -\frac{P}{\pi\mu}\frac{(1-\nu)}{(3-2\nu)}\frac{1}{x} + \frac{P}{\pi\mu}N(x), \tag{14.45}$$

where

$$N(x) = \frac{2(1-\nu)^2}{(3-2\nu)}\int_0^\infty \frac{2\ell^2\xi^2(\gamma-\xi)-\gamma}{\gamma+4(1-\nu)\ell^2\xi^2(\gamma-\xi)}\sin(\xi x)d\xi. \tag{14.46}$$

Equation (14.45) will be used next to construct the integral equations for the contact problems.

Before proceeding any further, we present some representative results regarding the displacements and the rotation for the Flamant-Boussinesq problem in the context of the couple-stress elasticity. In Fig. 14.3, the normal displacement and the rotation are illustrated at the surface of the half-plane ($y = 0$) for various Poisson's ratios. The classical elasticity results are also overlaid. Regarding the normal displacement u_y, it can be seen that the logarithmically singular response of the classical solution is retained in the couple-stress solution as well. Note that the

classical elasticity solution for the present normalization is independent of the Poisson's ratio, while the solution of the couple-stress elasticity for the same normalization retains dependence upon ν. Further, regarding the rotation ω, it is shown that the classical elasticity solution is unbounded at the point of the application of the load, however, this singular response is eliminated in the couple-stress elasticity, showing *zero* rotation at the same point. Of course, the effect of the Poisson's ratio in the case of the couple-stress elasticity is apparent in contrast to the classical elasticity case for the present normalization. It is emphasized that the effect of the couple stresses is significant near the point of the application of the load where the rotation/strain gradients are more pronounced. Indeed, the couple-stress solution approaches the classical one while the effect of the Poisson's ratio disappears moving further from the load source.

Results for the layer problem in couple-stress elasticity are presented in Fig. 14.4. In particular, Fig. 14.4 illustrates the variation of the normal displacement for selected values of the Poisson's ratio and the two different sets of boundary conditions that occur at the layer/rigid substrate interface, Eqs. (14.23)–(14.28). In the case of couple-stress elasticity the deformation and rotational characteristics at the surface depend upon both the Poisson's ratio and the normalized length h/ℓ. For fixed layer thickness h and increasing ℓ or increasing Poisson's ratio the layer becomes stiffer. In fact, it can be seen that both ℓ and ν play an important role in the qualitative characteristics of the behavior of the layer's surface. Note that in all the cases the classical elasticity layer solution is added. In general, all the significant variations are observed in a region that extends about $2h$ laterally to the point of the application of the load and the gradient effects become important for decreasing h/ℓ—a stiffer layer can be obtained by reducing the thickness h or increasing the microstructural length ℓ.

Moving further from the point of the application of the load the effect of the rotation gradients decreases and the results regarding all the measured quantities

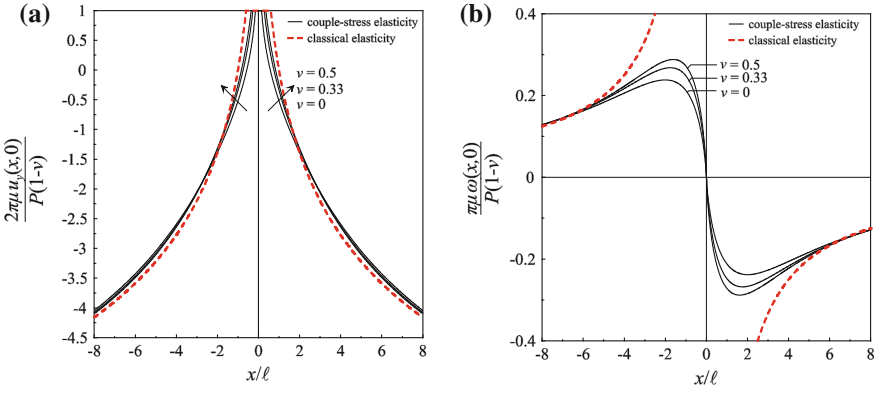

Fig. 14.3 Dimensionless **a** normal displacement and **b** rotation along the surface of the half-plane due to the application of normal point load P. Results are shown for different Poisson's ratios ν

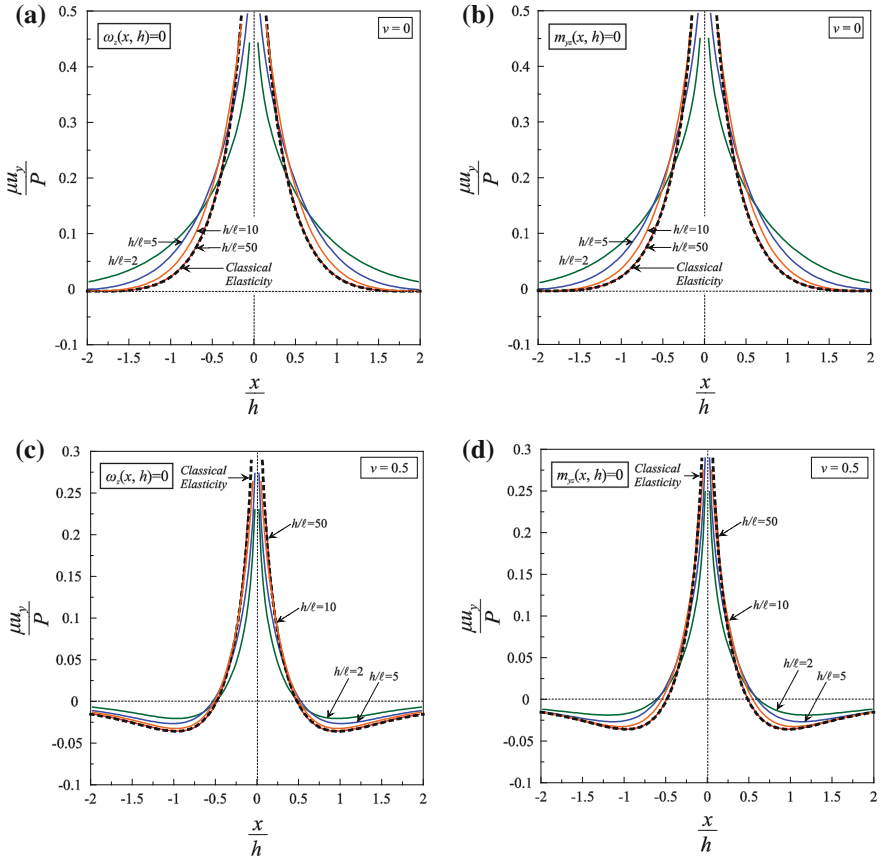

Fig. 14.4 The behavior of the surface of a layer of thickness h under the action of a normal point force in the context of couple stress elasticity. The normalized normal displacements $\mu u_y/P$ are presented as a function of the normalized distance x/h from the point of the application of the load P for two different Poisson's ratio and different boundary conditions at the interface. **a** $\nu=0,\ \omega_z(x,h)=0,$ **b** $\nu=0,\ m_{yz}(x,h)=0,$ **c** $\nu=0.5,\ \omega_z(x,h)=0,$ **d** $\nu=0.5,\ m_{yz}(x,h)=0$

converge to those of classical elasticity. In fact, for increasing h/ℓ ratio the region of significance of the effect of the rotation gradients decreases. It is concluded that for $h>50\ell$ the displacements and the rotation have essentially converged to those obtained by classical elasticity excluding of course the singular behavior of the rotation observed in classical elasticity.

Finally, it is instructive to examine the behavior of the equivalent stress in order identify the severest stress-states and accordingly the potential regions that plasticity may emerge. In the context of couple stress theory, the shape of the equivalent stress contours depends upon the microstructural characteristics of the material. For a plane-strain configuration, we introduce a general form of the equivalent stress as [47, 48]

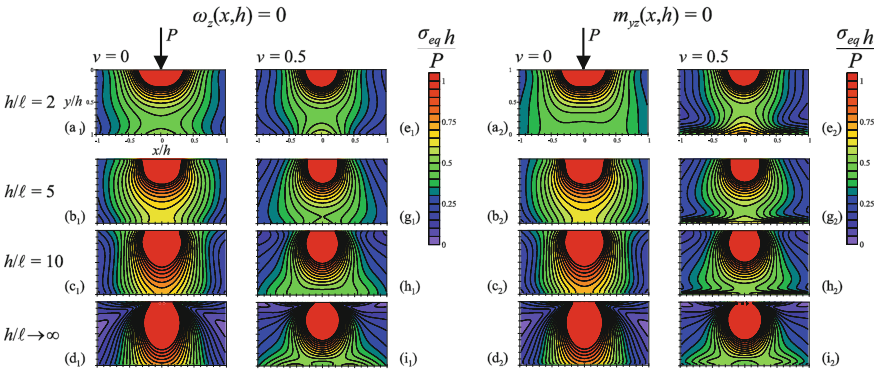

Fig. 14.5 Contours of normalized equivalent stress $\sigma_{eq}h/P$ for different ratios h/ℓ. Results are presented for the two different boundary conditions at the interface, namely $(a_1 - i_1)$ $\omega_z(x,h)=0$ and $(a_2 - i_2)$ $m_{yz}(x,h)=0$. Two different values of the Poisson's ratio are considered: $\nu=0$ and $\nu=0.5$

$$\sigma_{eq}=\sqrt{3\left[\frac{1}{2}\left(s_{xx}^2+s_{yy}^2+s_{zz}^2\right)+\frac{1}{4}\sigma_{xy}^2+\frac{1}{2}\sigma_{xy}\sigma_{yx}+\frac{1}{4}\sigma_{yx}^2+\frac{1}{2\ell^2}\left(m_{xz}^2+m_{yz}^2\right)\right]}, \tag{14.47}$$

with $s_{ij}=\sigma_{ij}-\frac{1}{3}\delta_{ij}\sigma_{\kappa\kappa}$ being the deviatoric stress. When the equivalent stress reaches the material yield stress yielding will commence. As it is shown in Fig. 14.5, the equivalent stress depends strongly upon the microstructural characteristic length ℓ and the Poisson's ratio ν, assuming fixed layer thickness h. In particular, it is observed that for decreasing ℓ the maximum equivalent stress increases and the region of maximum equivalent stress expands vertically while it rather shrinks horizontally. For $\ell\to 0$ ($h/\ell\to\infty$—classical elasticity solution), the maximum of the equivalent stress is shifted inside the layer and the potential yielding region increases substantially almost reaching the interface between the layer and the rigid substrate. We further note that the effect of the different boundary conditions at the interface is almost insignificant for the equivalent stress.

14.4 Formulation of Contact Problems

Consider now the stresses produced in an elastic half-plane by the action of a rigid indenter pressed into the surface as shown in Fig. 14.6. A Cartesian coordinate system $Oxyz$ is attached at the center line of the geometry. A load P is applied to the indenter which, in the plane strain case, has dimensions of [force][length]$^{-1}$.

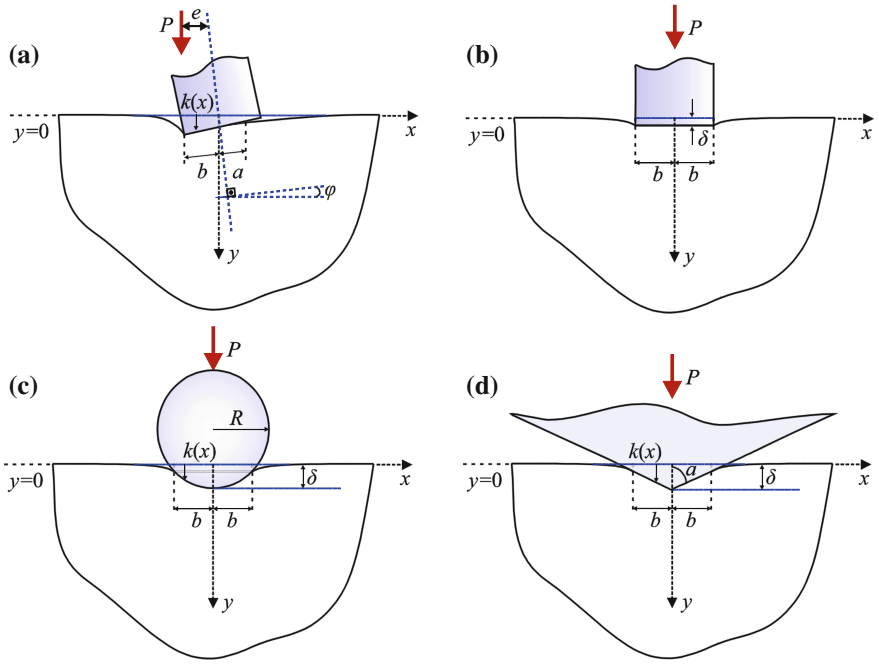

Fig. 14.6 **a** Tilted flat punch indentation problem, **b** 'Standard' flat punch indentation problem, **c** Indentation by a cylindrical indentor and **d** Indentation by a wedge indentor. The contact problem of the tilted flat punch leads to two different distinct cases depending upon the tilt angle φ. One case suggests that the contact is *complete* i.e. the contact width is $c = 2b$, while the second case suggests that the contact is *receding* i.e. the contact width is $c = a + b$

We begin by considering the case of the flat punch indenting a flat surface under the action of a vertical load P acting eccentrically by a distance e so that the punch tilts by an angle φ (Fig. 14.6a). In this case, the two bodies are making contact over a long strip of width c lying parallel to the z-axis. The type of contact depends upon the tilt angle φ and may be *complete* $(c = 2b)$ or *receding* $(c = a + b)$ as will be described later. If $e = 0$ then $\varphi = 0$ and consequently $c = 2b$—that is the classical flat punch contact problem (Fig. 14.6b).

Next, we examine the limit of the Hertzian elliptical contact where one axis of the ellipse becomes considerably larger than the other axis [40]. This limit corresponds to a cylindrical indenter of radius R with its axis lying parallel to the z-axis in the current coordinate system pressed in contact with a half-plane under the action of the force P. The two bodies are making contact over a long strip of width $c = 2b$ (Fig. 14.6c). Finally, results are given for the pressure below a wedge indenter pressed in contact with an elastic half-plane (Fig. 14.6d). In this case, in order for the deformations to be sufficiently small and lie within the frame of the

linear theory, the semi-angle α of the wedge must be close to 90° (in our analysis we have taken $\alpha = 88°$).

For the points lying within the contact area $D = \{-b < x < a,\ y = 0\}$ after loading, we have the following general geometrical boundary condition: $u_y = k(x)$, which, depending on the type of the profile, takes the following forms:

(a) $k(x) = \delta - \varphi x$, for the tilted flat punch,
(b) $k(x) = 0$, for the "standard" flat punch,
(c) $k(x) = \delta - \frac{1}{2R}x^2$, for the cylindrical indenter,
(d) $k(x) = \delta - |x|\cot(\alpha)$, for the wedge indenter.

where δ is a positive constant. Note that for cases (b), (c) and (d), the contact is complete so that $a = b$, whereas in case (a) the contact is receding i.e. $a < b$.

Regarding the traction boundary conditions, we note that since no restriction is imposed on u_x and du_x/dy under the indenter, the rotation ω is arbitrary at the contact area. Thus, by enforcing the principle of virtual power [26], we approximate zero shear and couple tractions under the indenter. In view of the above, the following traction boundary conditions hold for a frictionless and smooth contact [18]

$$\sigma_{yy}(x, 0) = 0 \quad \text{for } x \notin D, \tag{14.48}$$

$$\sigma_{yx}(x, 0) = 0 \quad \text{for } -\infty < x < \infty, \tag{14.49}$$

$$m_{yz}(x, 0) = 0 \quad \text{for } -\infty < x < \infty, \tag{14.50}$$

which are accompanied by the *auxiliary* conditions

$$\int_D \sigma_{yy}(x,\ 0)dx = -\int_D p(x)dx = -P, \tag{14.51}$$

and (for the case of the tilted flat punch)

$$\int_D \sigma_{yy}(x,\ 0)x\,dx = -\int_D p(x)x\,dx = -M, \tag{14.52}$$

where $p(x) \geq 0$ is the pressure below the indenter, P is the applied load, e is the load eccentricity and $M = Pe$ is the applied moment. Moreover, since the indented surface is an unbounded region, the above boundary conditions must be supplemented by the regularity conditions at infinity

$$\sigma_{ij} \to 0, m_{iz} \to 0 \quad as \quad r \to \infty. \tag{14.53}$$

14.5 Singular Integral Equation Approach

Our objective now is the determination of the contact-stress distribution below the rigid indenter and the determination of the associated contact length. Now suppose that the surface of the half-plane is subjected to a distributed normal load $p(\xi)$ per unit length. The stress and displacement fields can be found by superposition using the Flamant-Boussinesq solution as the pertinent Green's function—i.e. treating distributed load as the limit of a set of point loads of magnitude $p(\xi)d\xi$. It should be noted that the Flamant-Boussinesq solution automatically satisfies the traction-free boundary conditions (14.49) and (14.50).

In view of the above, the tangential gradient of the normal displacement at the surface of the half-plane (Eq. 14.45) assumes the following form

$$-\frac{(1-\nu)}{(3-2\nu)}\int_{-1}^{1}\frac{p(s)}{r-s}ds+\int_{-1}^{1}\tilde{N}(r-s)p(s)\,ds=\frac{2\pi\mu}{a+b}\frac{dk(r)}{dr},\quad |r|\le 1, \tag{14.54}$$

where the normalized regular kernel is defined now as

$$\tilde{N}(r-s)=\frac{2(1-\nu)^2}{(3-2\nu)}\int_{0}^{\infty}\left[\frac{\left(2q^2\zeta^2(\tilde{\gamma}-\zeta)-\tilde{\gamma}\right)}{\left(\tilde{\gamma}+4(1-\nu)q^2\zeta^2(\tilde{\gamma}-\zeta)\right)}\right]\sin(\zeta(r-s))d\zeta, \tag{14.55}$$

where $\tilde{\gamma}=\left(\zeta^2+q^{-2}\right)^{1/2}$ and

$$x=\frac{a+b}{2}(r+d),t=\frac{a+b}{2}(s+d),\xi=\frac{2}{a+b}\zeta,\ell=\frac{a+b}{2}q. \tag{14.56}$$

with $d=(a-b)/(a+b)$. Note that the first integral in the integral equation (14.54) is interpreted in the Cauchy principal value (CPV) sense. In fact, the CPV integral in Eq. (14.54) dominates the regular kernel and therefore determines the nature of the singularity of the pressure $p(s)$ at the endpoints of the contact region

The numerical solution of the singular integral Eq. (14.54) together with the complementary conditions (14.51) and (14.52) is accomplished by means of the collocation method for each indenter profile.

14.5.1 Indentation by a Flat Punch

Guided by the results concerning the modification of stress singularities in the presence of couple stresses [15, 45], the general solution for the pressure distribution admits the representation:

$$p(s) = w(s) \cdot \sum_{j=0}^{\infty} B_j P_j^{(\alpha,\beta)}(s), \quad |s| \le 1, \tag{14.57}$$

where $P_j^{(\alpha,\beta)}(s)$ are the Jacobi polynomials orthogonal to the weight function

$$w(s) = (1-s)^{\alpha}(1+s)^{\beta}, \quad (-1 < (\alpha,\beta) < 1), \tag{14.58}$$

with $\alpha = 1/2 + \mathrm{N}$, $\beta = -1/2 + \mathrm{M}$, and (N, M) arbitrary integers. The parameters (α, β) depend upon the type of contact (complete or receding) and the type of the indentor.

Employing now the well-known Gauss-Jacobi integration formulas for singular CPV integrals [49, 50], the integral Eq. (14.54) is reduced to a system of algebraic relations; viz.,

$$\sum_{j=0}^{\infty} B_j \left[-\frac{(1-\nu)}{(3-2\nu)} \frac{2^{-k}}{\sin \pi\alpha} P_{j-k}^{(-\alpha,-\beta)}(r) + Q_j(r) \right] = -\mu\varphi, \quad |r| < 1, \tag{14.59}$$

where $k = -\alpha - \beta$ is the index of the singular integral Eq. (14.54), and

$$Q_j(r) = \frac{1}{\pi} \int_{-1}^{1} w(s) P_j^{(\alpha,\beta)}(s) \tilde{N}(r-s)\, ds. \tag{14.60}$$

Furthermore, the auxiliary conditions (14.51) and (14.52) become now

$$\int_{-1}^{1} p(s) ds = \frac{2P}{(a+b)}, \qquad \int_{-1}^{1} p(s)\, s ds = \frac{4M + 2P(b-a)}{(a+b)^2}. \tag{14.61}$$

Two cases are now considered. In the first case, the applied moment is relatively small so that the contact is expected to be *complete* across the face of the punch ($c = 2b$, $a = b$). In the second case, the applied moment is sufficiently high, causing one corner of the punch to lift out of contact, and therefore for the contact extremity to be positioned at some point along the punch face ($c = a + b$, $|a| < b$)—see Fig. 14.6a, b.

14.5.1.1 Complete Contact

In this case, the pressure is singular at both ends of the contact width. Therefore, the weight function in Eq. (14.59) becomes: $w(s) = (1-s^2)^{-1/2}$ (i.e. $\alpha = \beta = -1/2$). In addition, the auxiliary conditions (14.62) are simplified to the following form:

$$\int_{-1}^{1} p(s)ds = \frac{P}{b}, \qquad \int_{-1}^{1} p(s)s\,ds = \frac{M}{b^2}, \tag{14.62}$$

which, taking into account (14.58), imply that

$$B_0 = \frac{P}{\pi b}, \quad B_1 = \frac{4M}{\pi b^2}. \tag{14.63}$$

Note that in complete contact the regular integral in (14.61) is evaluated using the standard Gauss-Chebyshev quadrature method.

The system of Eq. (14.60) is solved by truncating the series at $j = n$ and using a collocation technique with collocation points chosen as the roots of the second kind Chebyshev polynomial $U_n(r)$, viz. $r_j = \cos(j\pi/(n+1))$ with $j = 1, 2, \ldots, n$. In this way, a system of n linear algebraic equations is formed that enables us to evaluate the remaining n unknowns: the $n-1$ coefficients B_j $(j = 2, \ldots, n)$ and the unknown tilt angle φ. If $e = 0$ the moment M vanishes and consequently we have: $B_{2n+1} = 0$ (see Fig. 14.6b).

14.5.1.2 Receding Contact

Only the flat punch indenter exhibits receding contact characteristics. In this case, the pressure is zero at the right end of the contact area, so that $\alpha = 1/2$ and $\beta = -1/2$. Accordingly, the weight function becomes: $w(s) = (1-s)^{1/2}(1+s)^{-1/2}$ and the auxiliary conditions are given in Eq. (14.62), which, in view of (14.58), imply that

$$B_0 = \frac{2P}{\pi(a+b)}, \quad B_1 = \frac{4(4M + P(3b-a))}{\pi(a+b)^2}. \tag{14.64}$$

The system of equations in (14.60) is now solved by using a collocation method with collocation points chosen as the roots of the Jacobi polynomial $P_{n+1}^{(-1/2,\,1/2)}(r)$, viz. $r_j = \cos((2j-1)\pi/(2n+3))$ with $j = 1, 2, \ldots, n+1$. Here, in order to derive results for *constant* ratio ℓ/b, we consider the contact length a as a prescribed quantity and let the eccentricity e to float. The resulting $n+1$ linear algebraic equations are then utilized in conjunction with Eq. (14.65) to evaluate the coefficients B_j, the tilt angle φ, and the unknown eccentricity e.

14.5.2 Indentation by a Cylindrical Indenter

In classical elasticity the contact tractions for the cylindrical indenter problem are not singular at the end-points of the contact width $x=\pm b$ [46]. In this case, the weight function in Eq. (14.59) becomes: $w(s)=(1-s^2)^{1/2}$ that is $\alpha=\beta=1/2$. Accordingly, guided by the results concerning the modification of stress singularities in the presence of couple stresses [45], we assume that the pressure distribution assumes the following form:

$$p(s)=\sum_{n=0}^{\infty} a_n U_n(s)\sqrt{1-s^2}, \tag{14.65}$$

where $U_n(s)$ are the Chebyshev polynomials of the second kind. Employing now the well-known Gauss-Chebyshev integration formulas for singular CPV integrals [48–50], the integral Eq. (14.54) is reduced to a system of algebraic relations; viz.,

$$\sum_{n=0}^{\infty} a_n\left\{-\frac{(1-\nu)\pi}{3-2\nu}T_{n+1}(r)+W_n(r)\right\}=-\frac{\mu\pi b}{R}r, \quad |r|\le 1, \tag{14.66}$$

where $W_n(r)=\int_{-1}^{1} U_n(s)\sqrt{1-s^2}\tilde{N}(r-s)ds$ is regular integral which can be evaluated by the standard Gaussian quadrature method. It is remarked that the contact area b is not known a priori and will be determined from the solution of the boundary value problem. Now, Eq. (14.67) is solved using an appropriate collocation technique with collocation points chosen as the roots of $T_{n+1}(r)$, viz.$r_j=\cos((2j-1)\pi/(2(N+1)))$ with $j=1,2,\ldots,N+1$. The complementary condition (14.51) is then used for the evaluation of the unknown contact area b.

14.5.3 Indentation by a Wedge Indenter

Next, we consider the problem of the sharp wedge indenter. As in the classical theory [40], we assume that the pressure is non-singular at the end points of the contact area. In this case, the singular integral Eq. (14.53) takes the following form

$$-\frac{1-\nu}{3-2\nu}\int_{-1}^{1}\frac{p(s)}{r-s}ds+\int_{-1}^{1}\tilde{N}(r-s)p(s)\,ds=-\mu\pi\,\mathrm{sgn}(r)\cot\alpha, \tag{14.67}$$

where sgn() is the signum function, and α is the half-angle of the indenter (Fig. 14.6d). For the solution of the singular integral Eq. (14.68), the approach proposed by Ioakimidis [51] (see also [45]) is adopted where the loading function presents jump discontinuities. Again, as in the case of the cylindrical indenter, the

unknown contact length b will be determined from the solution of (14.67) together with the complementary condition (14.51). The functional equation is solved by employing the same collocation scheme as in the case of the cylindrical indenter noting however that the solution exhibits slower convergence.

14.6 Results and Discussion

We now proceed to the discussion of the results obtained for the indentation problems presented previously. In what follows, we investigate the effect of the ratio ℓ/b (normalized indent size) and the Poisson's ratio ν upon the contact pressure distribution, the contact width, and the average pressure. Finally contour plots of the equivalent stress are presented for the case of the cylindrical indenter.

Departing from Fig. 14.7, we present selected characteristic pressure distributions below the indenter resulting from the application of the load P at various normalized eccentricities e/b from the center of the punch. Results are shown for the cases of classical elasticity $(\ell/b=0)$ and couple-stress elasticity for a material with $\ell/b = 0.5$ and for two Poisson's ratios namely, $\nu = 0$ and $\nu = 0.5$.

We begin by reporting some general results that correspond to the case of $e/b=0$—the 'standard' flat punch indentation problem where no tilt is applied. As it has been shown by Muki and Sternberg [15] and Zisis et al. [45], when ℓ/b increases from zero the pressure distribution curves depart from and then again approach the classical elasticity result. As the load is translated from the center line of the punch $(e/b>0)$ the pressure distribution curves change qualitatively. At $e/b=0.5$ and independently of the Poisson's ratio, the pressure distribution attained for the classical elasticity case (red line) suggests that the punch is at the limit between the complete and the receding contact regime. In this case, the classical

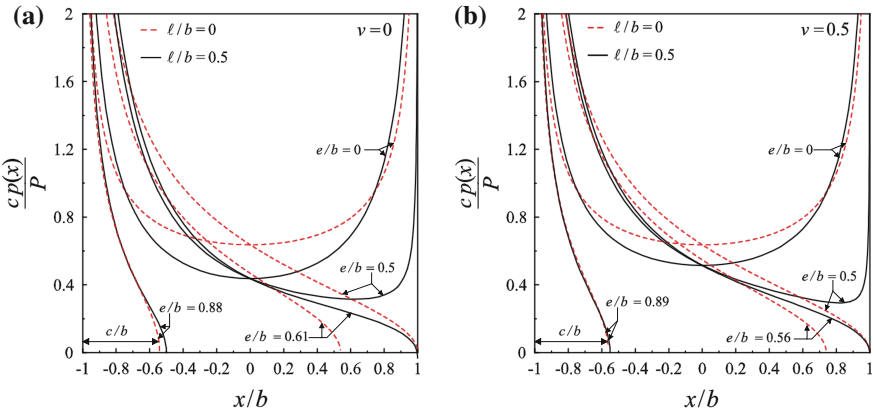

Fig. 14.7 The normalized pressure distribution $c\,p(x)/P$ as a function of the normalized distance x/b from the left corner of the indenter. Results are shown for two different Poisson's ratios **a** $\nu=0$ and **b** $\nu=0.5$

pressure at the right corner of the punch reduces to zero while at the left corner it remains *square-root* singular. However, the pressure distribution that corresponds to the couple-stress elasticity case shows that the flat punch is still in complete contact for a material with $\ell/b=0.5$. Further increase of the load eccentricity implies that the contact characteristics change from complete to receding also in couple-stress elasticity. Note that, unlike the classical elasticity, the limit eccentricity e^{lim} between complete to receding contact depends now, in addition to contact half-width b, upon the Poisson's ratio ν, and the characteristic material length ℓ. Nonetheless, the limit eccentricity in couple-stress elasticity is *independent* of the magnitude of the load P, as in the classical theory [52]. For example, when $\nu=0$ and $\ell/b=0.5$ the limit eccentricity is $e^{lim}=0.61b$. At this eccentricity, the contact region below the indenter for the classical elasticity case is equal to $c=1.59b$ (recall that $c=2b$ is the complete contact width). Larger values of eccentricity would produce receding contact conditions *both* in classical and in couple-stress theory and the contact widths would progressively reduce. This reduction is more pronounced for larger values of the Poisson's ratio. However, it should be mentioned that the difference in the extent of the receding contact region in couple-stress elasticity and in classical elasticity reduces as $e/b\to 1$. The response is qualitatively similar to the case of an incompressible material $(\nu=0.5)$ and for this reason no separate comment is required. The above results imply that for the same eccentricity, greater resistance against the reduction of the contact width is observed when couple-stress effects are taken into account.

Figure 14.8 presents details of the pressure distribution characteristics below the cylindrical indenter. It is observed that the cylindrical indenter suggests a pressure distribution that depends monotonically upon the ratio ℓ/b. Moreover, for increasing ratios ℓ/b, the pressure below the indenter increases significantly. In fact, as $\ell/b\to\infty$ the pressure tends to the limit $\sqrt{3-2\nu}p_{clas}(x)$. On the other hand, as $\ell/b\to 0$, we recover the classical elliptical pressure distribution. A qualitatively similar behavior is observed for the case of the wedge indenter in Fig. 14.9. The effect of the ratio ℓ/b upon the pressure ratio distribution becomes more significant as we approach the sharp tip of the indenter $(x\to 0)$ where both solutions exhibit logarithmic type singularities.

One of the most important information that one can obtain from indentation experiments is the indentation area (which essentially reduces to a contact width in the 2D case presented here) and the average pressure as a function of the ratio ℓ/b (indent size). To this purpose, the half-contact width b is normalized with the corresponding half contact width b_{clas} in classical elasticity. Note that $b_{clas}=(4(1-\nu^2)PR/(\pi E))^{1/2}$ (see for example [40]). In the same spirit, the average pressure $p_{av}\equiv P/(2b)$ is normalized with the corresponding $p_{av,clas}$. Results are shown for the two cases studied previously, i.e. the cylindrical and the wedge indenters.

In Fig. 14.10a, the dependence of the normalized contact width b/b_{clas} is shown as a function of the ratio ℓ/b, for different values of the Poisson's ratio ν. The contact width for both cylindrical and wedge indenters depends strongly upon the

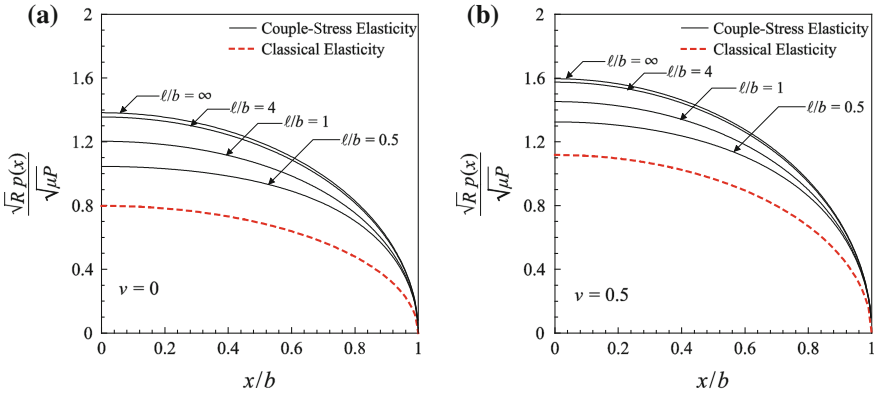

Fig. 14.8 Distribution of the pressure below the cylindrical indenter with respect to the normalized distance x/b for various ratios ℓ/b. Results are shown for Poisson's ratios: $\nu = 0$ and 0.5

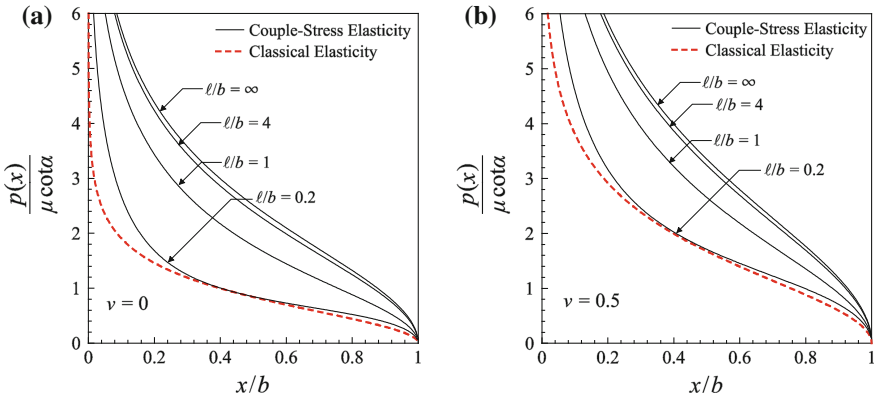

Fig. 14.9 Distribution of the pressure below the wedge indenter with respect to the normalized distance x/b for different ratios ℓ/b. Results are shown for Poisson's ratios: $\nu = 0$ and 0.5

ratio ℓ/b. Indeed, it is observed that for increasing ℓ/b the measured contact width b decreases significantly. The qualitative dependence of the contact width upon ℓ/b is the same for both the cylindrical and wedge indenters. For $\ell/b > 2$, a plateau is attained and no effect of the ratio ℓ/b upon the contact width is further observed. It should be emphasized that due to the characteristic dependence of the contact width upon the ratio ℓ/b, in practice, experimental results regarding the internal material length may be attained in the region $0.1 < \ell/b < 1$, where this dependence is more pronounced.

Next, Fig. 14.10b illustrates the effect of the ratio b/ℓ on the normalized average pressure (hardness) $p_{av}/p_{av,clas}$. It is observed that when couple-stress effects are taken into account ($\ell \neq 0$), the hardness increases significantly compared to the

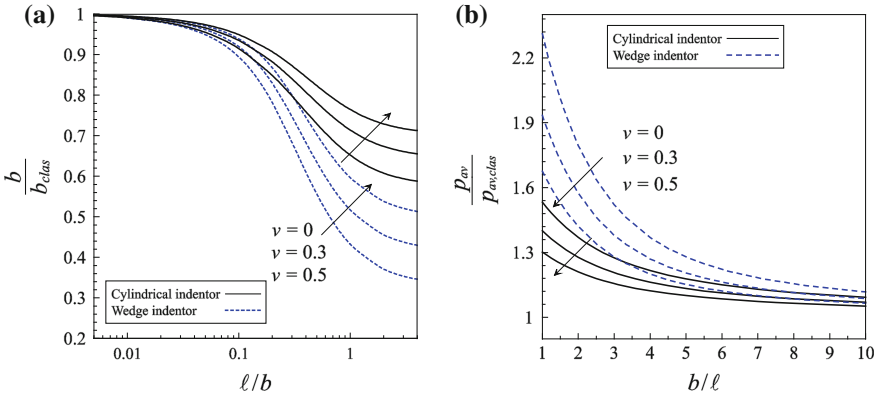

Fig. 14.10 **a** Dependence of the dimensionless contact radius b/b_{clas} upon the ratio ℓ/b and Poisson's ratio ν. **b** Dependence of the dimensionless average pressure $p_{av}/p_{av,\,clas}$ upon the ratio b/ℓ and Poisson's ratio ν. Results are shown for the cylindrical and wedge indenters

classical prediction. For example, in the case of a wedge indenter and for a material with $\nu = 0.3$ and $b/\ell = 2$, a 57% increase is noted in the average contact pressure. As b/ℓ increases the hardness decreases monotonically reaching the limit value of unity. Similar indentation size effects have been reported in the experiments performed by Han and Nikolov [8] during the elastic deformation of polymers and particularly of silicone. In fact, indentation experiments with a Berkovich indentor carried out on heterochain polymers such as polycarbonate (PC), epoxy, polyethylene terephthalate (PET) and polyamide 66 or nylon66 (PP66), showed an increased hardness with decreasing indentation depths, an experimental result which is qualitatively very similar to our p_{av} versus b relation presented in Fig. 14.8b. Furthermore, they reported that the depth at which the hardness starts to increase depends strongly, in the elastic deformation regime, upon the type of the polymer under consideration. In particular, they reported that the hardness at small indentation depths (or small contact areas) can increase from 0% to as much as 300%. In accord, our analysis showed that, depending on the Poisson ratio, a maximum increase of about 30–55% for the cylindrical and an increase of about 65–130% for the wedge indentor is attained for a contact area (length) twice the size of the characteristic material length ($b/\ell = 1$) (see Fig. 14.10).

For experimental purposes, both cylindrical and wedge indenters may be used in order to extract the characteristic material length ℓ of the indented material but from a practical perspective possible material failure in the highly stressed region immediately below the wedge tip, may limit the applicability of the present analysis. The cylindrical indenter, though less sensitive to the variations of ℓ/b, is not susceptible to these drawbacks and may in reality be the best geometry to investigate the effect of material length scale on the behavior of a microstructured elastic material.

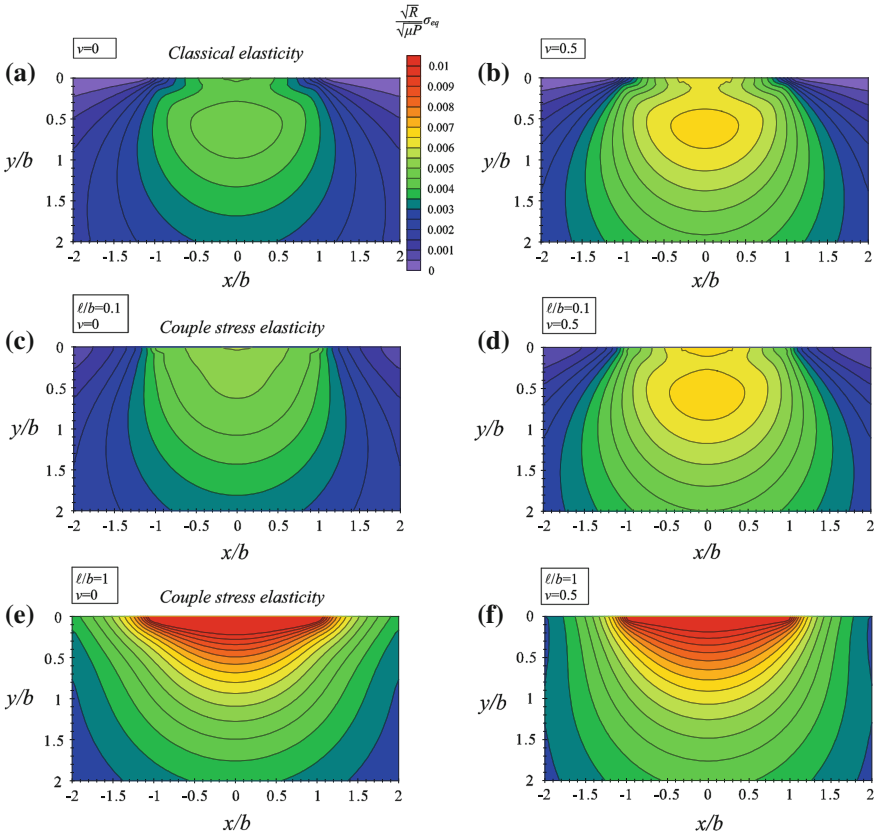

Fig. 14.11 Contour fields of normalized equivalent stress $\sqrt{R}/\sqrt{\mu P}\,\sigma_{eq}$ for the case of the cylindrical indentor for Classical elasticity and Couple stress elasticity ($\ell/b = 0.1,\ 0.1$ and 1) and selected values of Poisson's ratio ν

Finally, contours of the normalized equivalent stress $\sqrt{R}/\sqrt{\mu P}\,\sigma_{eq}$ are presented in Fig. 14.11 for the case of the cylindrical indenter in classical elasticity and couple stress elasticity ($\ell/b = 0.1,\ 0.1$ and 1) for selected values of Poisson's ratio ν. It is observed that for increasing ℓ/b the attained maximum equivalent stress increases while shifts to the surface of the half-plane. It should be noted that while in classical elasticity the equivalent stresses vanish outside the contact area, in the case of couple stress elasticity the equivalent stresses do not essentially vanish at the surface and extend laterally outside the contact area. This is due to the fact that the stress components ($\sigma_{xx},\ \sigma_{xy}$) as well as the couple-stress m_{xz} do not vanish at the surface in the case of the couple stress elasticity as opposed to the case of classical elasticity.

14.7 Conclusions

In the present study, the half-plane Green's functions have been derived within the framework of the generalized continuum theory of couple-stress elasticity. This theory introduces a characteristic material length in order to describe the pertinent scale effects that emerge from the underlying microstructure. Accordingly, the Green's function is used for the formulation of some classical two-dimensional plane strain contact problems in terms of singular integral equations. The present results exhibit significant departure from the predictions of classical elasticity. In particular, for the flat punch case the corresponding results showed that as ℓ/b increases from zero, the pressure departs from and then again approaches the classical solution. For the case of tilted punch, it was shown that the limit value of the load eccentricity e^{lim} between complete and receding contact strongly depends upon the Poisson's ratio and the micromechanical length ℓ. This is in marked contrast with the classical elasticity case where the limit eccentricity is always $e^{lim}_{clas} = 0.5b$, independently of the Poisson's ratio. On the other hand, for the cylindrical and wedge indentation problems, it was shown that for increasing ratio ℓ/b the pressure below the indenter increases significantly compared to the classical elasticity predictions. Moreover, it was in general shown that as the characteristic material length ℓ increases the contact width b decreases. With the presented results we shed light into salient details of the contact behavior of material with microstructure that may effectively act as general guidelines for the elastic indentation of microstructured solids. Indentation introduces a more complex loading situation, and can effectively act as a good alternative to common tests like simple shear and pure bending in order to identify the characteristic material length and provide more accurate information closer to real-life conditions.

References

1. Maranganti, R., Sharma, P.: A novel atomistic approach to determine strain-gradient elasticity constants: tabulation and comparison for various metals, semiconductors, silica, polymers and the (Ir) relevance for nanotechnologies. J. Mech. Phys. Solids **55**, 1823–1852 (2007)
2. Stelmashenko, N.A., Walls, M.G., Brown, L.M., Milman, Y.V.: Microindentations on W and Mo oriented single crystals: an STM study. Acta Metall. Mater. **41**, 2855–2865 (1993)
3. Ma, Q., Clarke, D.R.: Size dependent hardness of silver single crystals. J. Mater. Res. **10**, 853–863 (1995)
4. Poole, W.J., Ashby, M.F., Fleck, N.A.: Micro-hardness of annealed and work-hardened copper polycrystals. Scripta Mater. **34**, 559–564 (1996)
5. Huber, N., Nix, W.D., Gao, H.: Identification of elastic-plastic material parameters from pyramidal indentation of thin films. Proc. R. Soc. Lond. A **458**, 1593–1620 (2002)
6. Fleck, N.A., Muller, G.M., Ashby, M.F., Hutchinson, J.W.: Strain gradient plasticity: theory and experiment. Acta Metall. Mater. **42**, 475–487 (1994)
7. Larsson, P.L., Giannakopoulos, A.E., Söderlund, E., Rowcliffe, D.J., Vestergaard, R.: Analysis of Berkovich indentation. Int. J. Solids Struct. **33**, 221–248 (1996)

8. Han, C.-S., Nikolov, S.: Indentation size effects in polymers and related rotation gradients. J. Mater. Res. **22**, 1662–1672 (2007)
9. Fischer-Cripps, A.C.: Nanoindentation. Springer, New York (2004)
10. Chen, X., Hutchinson, J.W., Evans, A.G.: Simulation of the high temperature impression of thermal barrier coatings with columnar microstructure. Acta Mater. **52**, 565–571 (2004)
11. Stupkiewicz, S.: Micromechanics of contact and interphase layers. In: Lecture Notes in Applied and Computational Mechanics, vol. 30. Springer, Berlin (2007)
12. Fleck, N.A., Zisis, Th: The erosion of EB-PVD thermal barrier coatings: the competition between mechanisms. Wear **268**, 1214–1224 (2010)
13. Zisis, Th, Fleck, N.A.: The elastic–plastic indentation response of a columnar thermal barrier coating. Wear **268**, 443–454 (2010)
14. Tekoglu, C., Onck, P.R.: Size effects in two dimensional Voronoi foams. A comparison between generalized continua and discrete models. J. Mech. Phys. Solids **56**, 3541–3564 (2008)
15. Muki, R., Sternberg, E.: The influence of couple-stresses on singular stress concentrations in elastic solids. Z. Angew. Math. Phys. (ZAMP) **16**, 611–648 (1965)
16. Begley, M.R., Hutchinson, J.W.: The mechanics of size-dependent indentation. J. Mech. Phys. Solids **46**, 2049–2068 (1998)
17. Nix, W.D., Gao, H.: Indentation size effects in crystalline materials: a law for strain gradient plasticity. J. Mech. Phys. Solids **46**, 411–425 (1998)
18. Shu, J.Y., Fleck, N.A.: The prediction of a size effect in microindentation. Int. J. Solids Struct. **35**, 1363–1383 (1998)
19. Wei, Y., Hutchinson, J.W.: Hardness trends in micron scale indentation. J. Mech. Phys. Solids **51**, 2037–2056 (2003)
20. Nielsen, K.L., Niordson, C.F., Hutchinson, J.W.: Strain gradient effects in periodic flat punch indenting at small scales. Int. J. Solids Struct. **51**, 3549–3556 (2014)
21. Cauchy, A.L.: Note sur l' equilibre et les mouvements vibratoires des corps solides. Comptes-Rendus Acad. Paris **32**, 323–326 (1851)
22. Voigt, W.: Theoretische Studien uber die Elasticitatsverhaltnisse der Krystalle. Abh. Ges. Wiss. Gottingen **34**, 3–100 (1887)
23. Cosserat, E., Cosserat, F.: Theorie des Corps Deformables. Hermann et Fils, Paris (1909)
24. Toupin, R.A.: Theory of elasticity with couple-stress. Arch. Rat. Mech. Anal. **17**, 85–112 (1964)
25. Mindlin, R.D., Tiersten, H.F.: Effects of couple-stresses in linear elasticity. Arch. Ration. Mech. Anal. **11**, 415–448 (1962)
26. Koiter, W.T.: Couple-stresses in the theory of elasticity. Parts I and II. Proc. Ned Akad. Wet. **B67**, 17–44 (1964)
27. Chen, J.Y., Huang, Y., Ortiz, M.: Fracture analysis of cellular materials: a strain gradient model. J. Mech. Phys. Solids **46**, 789–828 (1998)
28. Bigoni, D., Drugan, W.J.: Analytical derivation of Cosserat moduli via homogenization of heterogeneous elastic materials. ASME J. Appl. Mech. **74**, 741–753 (2007)
29. Shodja, H.M., Zaheri, A., Tehranchi, A.: Ab initio calculations of characteristic lengths of crystalline materials in first strain gradient elasticity. Mech. Mater. **61**, 73–78 (2013)
30. Zhang, X., Sharma, P.: Inclusions and inhomogeneities in strain gradient elasticity with couple stresses and related problems. Int. J. Solids Struct. **42**, 3833–3851 (2005)
31. Lakes, R.S.: Experimental methods for study of Cosserat elastic solids and other generalized elastic continua. In: Continuum Models for Materials with Microstructure, pp. 1–25 (1995)
32. Lakes, R.S.: Strongly Cosserat elastic lattice and foam materials for enhanced toughness. Cell. Polym. **12**, 17–30 (1993)
33. Lakes, R.S.: Size effects and micromechanics of a porous solid. J. Mater. Sci. **18**, 2572–2580 (1983)
34. Gourgiotis, P.A., Piccolroaz, A.: Steady-state propagation of a Mode II crack in couple stress elasticity. Int. J. Fract. **188**, 119–145 (2014)

35. Mindlin, R.D.: Influence of couple-stresses on stress concentrations. Exp. Mech. **3**, 1–7 (1963)
36. Green, A.E., Zerna, W.: Theoretical Elasticity. Oxford University Press, Oxford (1968)
37. Love, A.E.H.: A Treatise on the Mathematical Theory of Elasticity. Cambridge University Press, New York (1952)
38. Fung, Y.C.: Foundations of Solid Mechanics. Prentice-Hall, Englewood Cliffs, NJ (1965)
39. Timoshenko, S.P., Goodier, J.N.: Theory of Elasticity. McGraw-Hill, New York (1970)
40. Johnson, K.: Contact Mechanics. Cambridge University Press, Cambridge, UK (1985)
41. Hills, D., Nowell, D.: Mechanics of Fretting Fatigue. Kluwer Academic Publishers, Dordrecht (1994)
42. Barber, J.R.: Elasticity. In: Solid Mechanics and its Applications, vol. 172. Springer, Netherlands (2010)
43. Anagnostou, D.S., Gourgiotis, P.A., Georgiadis, H.G.: The Cerruti problem in dipolar gradient elasticity. Math. Mech. Solids **20**, 1088–1106 (2013)
44. Gourgiotis, P.A., Zisis, Th: Two-dimensional indentation of microstructured solids characterized by couple-stress elasticity. J. Strain Anal. Eng. Design **51**, 318–331 (2016)
45. Zisis, Th, Gourgiotis, P.A., Baxevanakis, K.P., Georgiadis, H.G.: Some basic contact problems in couple-stress elasticity. Int. J. Solids Struct. **51**, 2084–2095 (2014)
46. Roos, B.W.: Analytic Functions and Distributions in Physics and Engineering. Wiley, New York (1969)
47. de Borst, R.: A generalisation of J2-flow theory for polar continua. Comput. Methods Appl. Mech. Eng. **103**, 347–362 (1993)
48. Vardoulakis, I., Sulem, J.: Bifurcation Analysis in Geomechanics. Blackie Academic & Professional (Chapman and Hall), London (1995)
49. Szegö, G.: Orthogonal Polynomials, vol. 23. Colloquium Publications, American Mathematical Society (1939)
50. Erdogan F., Gupta G.D., Cook T.S.: Numerical solution of singular integral equations. In: Sih, G.C. (ed.) Mechanics of Fracture: Methods of Analysis and Solutions of Crack Problems, vol. 1, pp. 368–425 (1973)
51. Ioakimidis, N.I.: The numerical solution of crack problems in plane elasticity in the case of loading discontinuities. Eng. Fract. Mech. **15**, 709–716 (1980)
52. Sackfield, A., Truman, C.E., Hills, D.A.: The tilted punch under normal and shear load (with application to fretting tests). Int. J. Mech. Sci. **43**, 1881–1892 (2001)

Chapter 15
Radiation from Equivalent Body Forces for Scattering of Surface Waves by a Near-Surface Cylindrical Cavity

Chao Yang and Jan D. Achenbach

Abstract The scattering of incident surface waves by a cylindrical cavity of arbitrary shape near the free surface of an elastic half-space is considered in this paper. The scattered field is represented by the radiation from equivalent body forces. The equivalent body forces due to the horizontal and vertical displacement components of the incident surface wave are determined separately. It is found that the equivalent body forces are double forces parallel and normal to the free surface of the half-space. By the use of the elastodynamic reciprocity theorem, the surface waves generated by the equivalent double forces are obtained in terms of properties of the incident wave, the cross-sectional area of the cavity and the elastic constants of the elastic half-space. The superposition of the surface waves generated by the equivalent body forces represents the scattered field of surface waves.

Keywords Scattering · Surface wave · Cavity · Equivalent body forces Reciprocity theorem

15.1 Introduction

Cavities are common defects in structures. They may form due to imperfection during the processing of materials or as a result of damage accumulation in service [1, 2]. Because the evolution of cavities has the potential to cause failures of

The original version of the book was inadvertently published without chapter 15. A correction to the book can be found at https://doi.org/10.1007/978-3-319-77504-3_16

C. Yang
School of Mechanical Engineering, Beijing Institute of Technology,
5 South Zhongguancun Street, Haidian District, Beijing 100081, China
e-mail: yangchaobit@gmail.com

J. D. Achenbach (✉)
McCormick School of Engineering and Applied Science, Northwestern University,
Evanston, IL 60208, USA
e-mail: achenbach@northwestern.edu

H. Altenbach et al. (eds.), *Generalized Models and Non-classical Approaches in Complex Materials 2*, Advanced Structured Materials 90,
https://doi.org/10.1007/978-3-319-77504-3_15

materials and structures [3, 4], it is of importance to nondestructively characterize cavities for structure health monitoring and other applications. One method that is used for cavity characterization is the evaluation of elastic wave scattering, since cavities are non-uniformities in structures and thus can act as scatterers for elastic waves.

Because surface waves are very sensitive to surface and near-surface defects, they can be usefully employed for the characterization of near-surface cavities. Although the propagation of surface waves in a homogenous elastic half-space is well understood [5, 6], since these waves were first investigated by Lord Rayleigh [7], analytical solutions for the scattering of surface waves are very complicated, especially for cavities of arbitrary shape. For wavelengths that are sufficiently larger than the largest characteristic dimension of the cavity, one potential method to simplify the analysis is to use the representation by equivalent body forces employed in acoustic emission [8–10]. In earlier work [11], it was shown that for long wavelengths the scattering of longitudinal waves by a cavity of general shape in a body of infinite extent can be represented by radiation from equivalent body forces in the undamaged body. By introducing the approximation that strains in the virtual cavity may be considered as constant for long wavelength incidence, the equivalent body forces were easily obtained and the scattered field was expressed in a simple form.

In this paper, we use the equivalent body force representation to consider the scattering of surface waves by a cylindrical cavity of general cross-section located near the free surface of a homogeneous, isotropic, linearly elastic half-space. For long wavelengths, the equivalent body forces for the scattering of an incident surface wave are decomposed into the equivalent body forces due to a locally plane longitudinal wave and the equivalent body forces due to a locally plane transverse wave. The equivalent body forces are double forces. Once the system of equivalent body forces has been formulated, the scattering of surface waves by a 2D cavity reduces to a radiation problem of determining the wave motion generated by time harmonic line loads.

The problem of the dynamic response to a time-harmonic line load applied to the surface as well as the interior of a half-space was first studied by Lamb [12]. Using integral transform techniques, the problem was discussed in some detail by Achenbach [5] and Graff [6]. Integral transform techniques are cumbersome because of the complicated integral evaluation involved. Based on the reciprocity theorem [13], an alternative approach without integral transforms was devised by Achenbach [14]. The reciprocity approach, which was discussed in some detail by Achenbach [15], is simple, straightforward, and makes it possible to separately calculate different wave modes by selecting suitable virtual wave solutions. The surface wave solutions obtained by the reciprocity approach were validated by Phan et al. [16, 17] for line loads applied to the surface of a half space.

In the present paper, the reciprocity approach is used to determine the surface wave radiation from equivalent body forces. The surface waves generated by the equivalent body forces are expressed in simple forms and are shown to be both symmetric and anti-symmetric with respect to the vertical plane where the forces are applied. For a few more recent applications of the reciprocity theorem, we refer to

Achenbach [18] for a review of related topics, Achenbach [19] for an elastic half-space with depth-dependent properties, Sergey [20] for a hierarchy of elastic waveguides, and Shi et al. [21] for randomly rough surfaces.

15.2 Formulation

Figure 15.1 shows the two-dimensional configuration of a plane surface wave, u_{in}, incident on a cylindrical cavity near the free surface of a homogeneous, isotropic, linearly elastic half-space, which is referred to a Cartesian coordinate system (x, z), such that the plane $z = 0$ coincides with the surface of the half-space. The interaction of the incident surface wave with the cavity generates scattered surface waves, u_{sc}, in both the forward and the backward directions. It should be noted that the scattered waves include both body waves and surface waves, but the surface waves predominate at some distance from the scatterer, since the body waves suffer geometrical attenuation.

For plane surface waves the following expressions for the displacement components in the frequency domain can be found in many textbooks, see, e.g.: [15, p. 133],

$$u_x^+ = iAU^R(z)e^{ikx}, \tag{15.1}$$

$$u_z^+ = AW^R(z)e^{ikx}, \tag{15.2}$$

for propagation in the positive x-direction, and

$$u_x^- = -iAU^R(z)e^{-ikx}, \tag{15.3}$$

$$u_z^- = AW^R(z)e^{-ikx}, \tag{15.4}$$

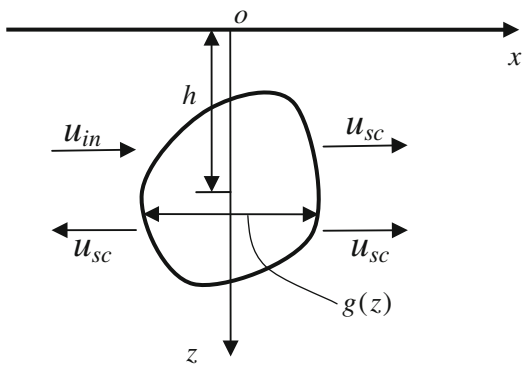

Fig. 15.1 The configuration of a plane surface wave incident on a near-surface cylindrical cavity

for propagation in the negative x-direction. In these expressions, A is the amplitude with length dimension, k is the wave number, $k=\omega/c_R$, where c_R is the phase velocity of surface waves, and the term $e^{-i\omega t}$ has been omitted. The functions $U^R(z)$ and $W^R(z)$ are defined by

$$U^R(z)=d_1e^{-pz}+d_2e^{-qz}, \tag{15.5}$$

$$W^R(z)=d_3e^{-pz}-e^{-qz}, \tag{15.6}$$

where

$$d_1=-\frac{1}{2}\frac{k^2+q^2}{kp},\quad d_2=\frac{q}{k},\quad d_3=\frac{1}{2}\frac{k^2+q^2}{k^2}. \tag{15.7a, b, c}$$

The quantities p and q are given by

$$p^2=k^2-\frac{\omega^2}{c_L^2}=k^2(1-\frac{c_R^2}{c_L^2}), \tag{15.8}$$

$$q^2=k^2-\frac{\omega^2}{c_T^2}=k^2(1-\frac{c_R^2}{c_T^2}), \tag{15.9}$$

where c_T and c_L are the phase velocities of transverse and longitudinal waves, respectively. Substitution of Eqs. (15.8) and (15.9) into Eq. (15.7) yields

$$\begin{aligned} d_1&=-\frac{1}{2}\frac{(2-c_R^2/c_T^2)}{(1-c_R^2/c_L^2)^{1/2}},\\ d_2&=(1-c_R^2/c_T^2)^{1/2},\\ d_3&=\frac{1}{2}(2-c_R^2/c_T^2). \end{aligned} \tag{15.10a, b, c}$$

The stress components corresponding to Eqs. (15.1)–(15.4) may be written as

$$\tau_{xx}^{+}=AT_{xx}(z)e^{ikx}, \tag{15.11}$$

$$\tau_{xz}^{+}=\tau_{zx}^{+}=iAT_{xz}(z)e^{ikx}, \tag{15.12}$$

for Eqs. (15.1) and (15.2), and

$$\tau_{xx}^{-}=AT_{xx}(z)e^{-ikx}, \tag{15.13}$$

$$\tau_{xz}^{-}=\tau_{zx}^{-}=-iAT_{xz}(z)e^{-ikx}, \tag{15.14}$$

for Eqs. (15.3) and (15.4). The plus and minus superscript signs correspond to surface waves propagating in the positive and the negative x-directions, respectively, and

$$T_{xx}(z) = \mu(d_4 e^{-pz} + d_5 e^{-qz}), \tag{15.15}$$

$$T_{xz}(z) = \mu(d_6 e^{-pz} + d_7 e^{-qz}), \tag{15.16}$$

$$d_4 = \frac{1}{2}(k^2+q^2)\frac{2p^2 - q^2 + k^2}{pk^2}, \quad d_5 = -2q, \tag{15.17a, b}$$

$$d_6 = \frac{k^2+q^2}{k}, \quad d_7 = -\frac{k^2+q^2}{k}. \tag{15.17c, d}$$

We also have

$$\tau_{zz}^{+} = AT_{zz}(z)e^{ikx}, \tag{15.18}$$

$$\tau_{zz}^{-} = AT_{zz}(z)e^{-ikx}, \tag{15.19}$$

where

$$T_{zz}(z) = \mu(d_8 e^{-pz} + d_9 e^{-qz}), \tag{15.20}$$

$$d_8 = -\frac{1}{2}\frac{(k^2+q^2)^2}{pk^2}, \quad d_9 = 2q. \tag{15.21a, b}$$

The boundary conditions at $z = 0$ are

$$\tau_{zz}|_{z=0} = 0, \quad \tau_{zx}|_{z=0} = 0. \tag{15.22a, b}$$

By virtue of Eqs. (15.12), (15.14), (15.18) and (15.19), Eq. (15.22) yields

$$d_6 + d_7 = \frac{k^2+q^2}{k} - \frac{k^2+q^2}{k} = 0, \tag{15.23}$$

$$d_8 + d_9 = -\frac{1}{2}\frac{(k^2+q^2)^2}{pk^2} + 2q = 0. \tag{15.24}$$

Equation (15.24) may be rewritten as

$$(k^2+q^2)^2 - 4pqk^2 = 0. \tag{15.25}$$

By substituting p and q from Eqs. (15.8) and (15.9) into Eq. (15.25), we then obtain the well-known equation for the phase velocity of Rayleigh surface waves:

$$\left(2-c_R^2/c_T^2\right)^2-4\left(1-c_R^2/c_L^2\right)^{1/2}\left(1-c_R^2/c_T^2\right)^{1/2}=0. \tag{15.26}$$

15.3 Equivalent Body Forces

The 2D superposition principle for the scattering by a cylindrical cavity in a half-space is shown in Fig. 15.2. Figure 15.2c shows that the scattered field is equivalent to the field generated by the application of tractions on the surface of the cavity. As shown in Fig. 15.2b, these tractions are the negative of the corresponding tractions generated by the incident wave on the boundary of a "virtual" cavity in the undamaged body. The virtual cavity is of the same shape as the actual cavity and is indicated by a dashed line in Fig. 15.2b.

It is difficult to rigorously solve for the field scattered by a cylindrical cavity in a half space. Thus in this section, following an earlier paper by Yang and

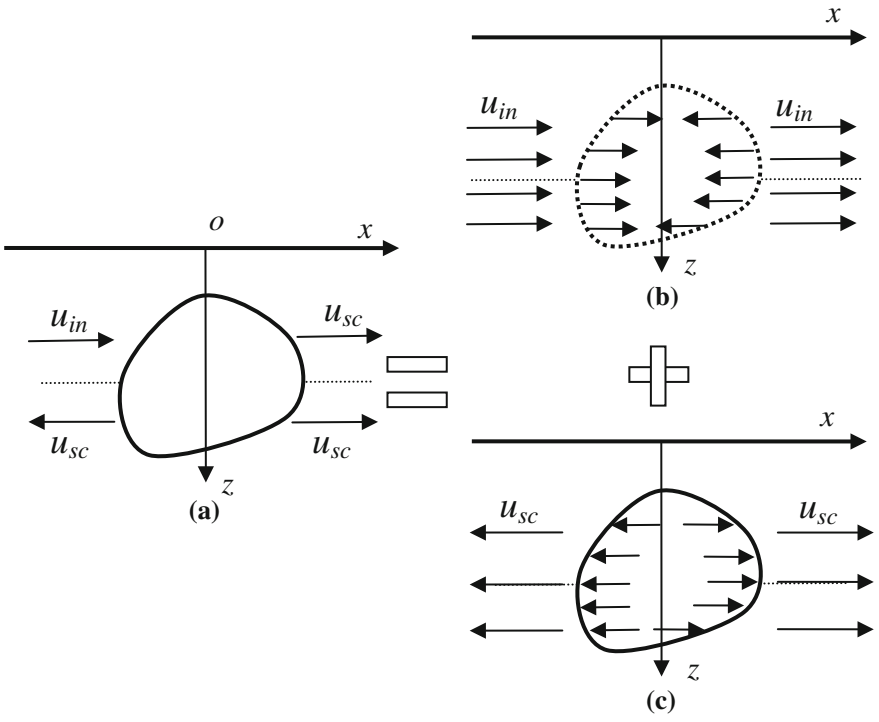

Fig. 15.2 The superposition principle for scattering by a cylindrical cavity

Achenbach [11], we seek solutions for equivalent body force loading in the undamaged half-space that produces elastodynamic radiation to represent the scattered field, for incident surface waves of wavelengths sufficiently larger than the largest characteristic length dimension of the cavity. The body force loading is determined on the basis of the loading on the surface of the virtual cavity, or equivalently on the deformation of the region inside the virtual cavity.

The displacements for the incident plane surface wave propagating in the positive x-direction are given by Eqs. (15.1) and (15.2), where A is the amplitude of the incident wave. For long wave incidence relative to the dimensions of the cavity, the displacements in the virtual cavity may be simplified to

$$u_x = iAU^R(h)e^{ikx}, \quad u_z = AW^R(h)e^{ikx}, \tag{15.27a, b}$$

where h is the depth of the cavity center from the free surface as shown in Fig. 15.1, and the time dependence term $e^{-i\omega t}$ has been omitted.

For the displacement given by Eq. (15.27a), the corresponding strain in the virtual cavity can be written as

$$\varepsilon_{xx} = -AkU^R(h)e^{ikx}. \tag{15.28}$$

For long wavelengths, Eq. (15.28) may be further simplified to

$$\varepsilon_{xx} = -AkU^R(h). \tag{15.29}$$

In the Cartesian coordinate system shown in Fig. 15.1, we may write the length increment across the virtual cavity in the x-direction at a fixed value of z as

$$\Delta u_x(x,z) = -g(z)AkU^R(h), \tag{15.30}$$

where $g(z)$ is the length at position z across the cavity in the x direction. The length increment given by Eq. (15.30) may then be represented by a concentrated strain along $x = 0$:

$$\overline{\Delta\varepsilon_{xx}(x,z)} = -g(z)AkU^R(h)\delta(x), \tag{15.31}$$

where $\delta(x)$ is the Dirac delta function. Note that Eq. (15.30) can be obtained by integrating Eq. (15.31) over x. Further integration over z yields the concentrated strain at $(0,h)$ as

$$\varepsilon^D_{xx}(x,z) = -AkU^R(h)\delta(x)\delta(z-h)\int_{z_{\min}}^{z_{\max}} g(z)dz. \tag{15.32}$$

Equation (15.32) may be rewritten as

$$\varepsilon_{xx}^{D}(x,z) = -A\tilde{A}kU^{R}(h)\delta(x)\delta(z-h), \tag{15.33}$$

where $\tilde{A}$ is the cross-sectional area of the cavity. Using Hooke's law, we may then write the stresses corresponding to the strain $\varepsilon_{xx}^{D}(x,z)$ as

$$\tau_{xx}^{D} = -(\lambda+2\mu)A\tilde{A}kU^{R}(h)\delta(x)\delta(z-h), \tag{15.34}$$

$$\tau_{zz}^{D} = -\lambda A\tilde{A}kU^{R}(h)\delta(x)\delta(z-h), \tag{15.35}$$

where λ and μ are the Lame elastic coefficients of the half space material.

Similarly, for the displacement given by Eq. (15.27b), the corresponding strains in the virtual cavity may be written as

$$\varepsilon_{xz} = \varepsilon_{zx} = \frac{1}{2}\frac{\partial u_z}{\partial x} = \frac{1}{2}ikAW^{R}(h)e^{ikx}. \tag{15.36}$$

For long wavelengths, Eq. (15.36) may be simplified to

$$\varepsilon_{xz} = \varepsilon_{zx} = \frac{1}{2}ikAW^{R}(h). \tag{15.37}$$

Completely analogous to the way shown before, the concentrated strains are obtained as integrations of ε_{xz} and ε_{zx} over the area $\tilde{A}$:

$$\varepsilon_{xz}^{D}(x,y,z) = \varepsilon_{zx}^{D}(x,y,z) = \frac{1}{2}ikA\tilde{A}W^{R}(h)\delta(x)\delta(z-h). \tag{15.38}$$

The stresses corresponding to the strains $\varepsilon_{xz}^{D}(x,y,z)$ and $\varepsilon_{zx}^{D}(x,y,z)$ can then be written as

$$\tau_{xz}^{D} = \tau_{zx}^{D} = \mu ikA\tilde{A}W^{R}(h)\delta(x)\delta(z-h). \tag{15.39}$$

The equations of motion in a region around the virtual cavity can now be written as

$$\frac{\partial \tau_{xx}^{D}}{\partial x} + \frac{\partial \tau_{xx}}{\partial x} + \frac{\partial \tau_{zx}^{D}}{\partial z} + \frac{\partial \tau_{zx}}{\partial z} = -\rho\omega^{2}u_x, \tag{15.40}$$

$$\frac{\partial \tau_{zz}^{D}}{\partial z} + \frac{\partial \tau_{zz}}{\partial z} + \frac{\partial \tau_{xz}^{D}}{\partial x} + \frac{\partial \tau_{xz}}{\partial x} = -\rho\omega^{2}u_z. \tag{15.41}$$

The body force terms follow from Eqs. (15.40) and (15.41). As an example, we consider

$$\overline{f_x} = \frac{\partial \tau_{xx}^D}{\partial x}. \tag{15.42}$$

Substitution of Eq. (15.34) in Eq. (15.42) yields

$$\overline{f_x} = (\lambda + 2\mu) A\tilde{A} k U^R(h) \delta'(x) \delta(z-h). \tag{15.43}$$

Note that the sign of $\overline{f_x}$ has been changed to make the fields generated by Eq. (15.43) applicable to the half-space with the actual cavity.

The body force in the z-direction follows from Eqs. (15.35) and (15.41) as

$$\overline{f_z} = \lambda A\tilde{A} k U^R(h) \delta(x) \delta'(z-h), \tag{15.44}$$

where the sign has been changed as in Eq. (15.43). The equivalent double forces corresponding to u_x are shown in Fig. 15.3.

By using Eqs. (15.39)–(15.41), we obtain the body forces corresponding to u_z as

$$\overline{f_{xz}} = \frac{\partial \tau_{xz}^D}{\partial x}, \tag{15.45}$$

and

$$\overline{f_{zx}} = \frac{\partial \tau_{zx}^D}{\partial z}. \tag{15.46}$$

In order that these body forces represent the loading on the actual cavity we change the signs as compared to Eq. (15.39), and we write

$$\overline{f_{xz}} = -i\mu k A\tilde{A} W^R(h) \delta'(x) \delta(z-h), \tag{15.47}$$

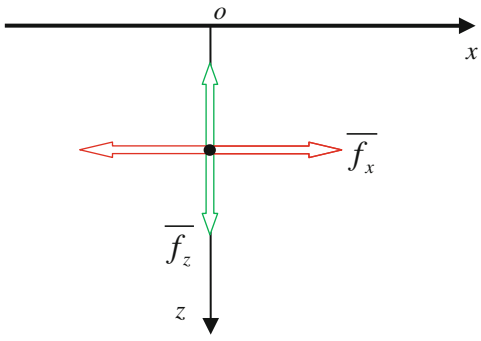

Fig. 15.3 Equivalent double forces corresponding to u_x

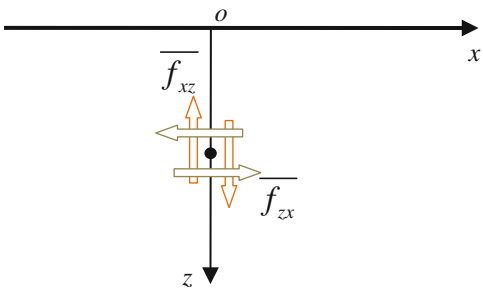

Fig. 15.4 Equivalent double forces corresponding to u_z

and

$$\overline{f_{zx}} = -i\mu kA\tilde{A}W^R(h)\delta(x)\delta'(z-h). \tag{15.48}$$

The corresponding equivalent double forces are shown in Fig. 15.4.

In the next section we determine the surface wave radiation generated by the equivalent body forces defined by Eqs. (15.43), (15.44), (15.47) and (15.48).

15.4 Surface Waves Generated by the Equivalent Body Forces

In Sect. 15.3, it has been shown that the equivalent body forces corresponding to an incident plane Rayleigh wave can be separated into those corresponding to u_x, the horizontal displacement component of the incident wave, and those corresponding to u_z, the vertical component of the incident wave. The equivalent body forces that will be taken into account are double forces.

15.4.1 Surface Waves Generated by the Equivalent Body Forces Due to u_x

Let us first consider the surface wave motion generated by the double force along the x-axis corresponding to u_x, which is given by Eq. (15.43) as,

$$f_x^{DF} = F_x^{DF}\delta'(x)\delta(z-h), \tag{15.49}$$

where

$$F_x^{DF} = (\lambda + 2\mu)A\tilde{A}kU^R(h). \tag{15.50}$$

In Eqs. (15.49) and (15.50) the superscript DF stands for a double force, and F_x^{DF} with dimension of force, is the magnitude of the double force. Since the double force given by Eq. (15.49) is symmetric with respect to $x=0$, the surface waves generated by the double force are also symmetric with respect to $x=0$. Following Eqs. (15.1)–(15.4) and (15.11)–(15.14), the corresponding surface wave displacement and stress components may then be written as

$$u_x^{+,DF_x} = iC_{DF_x}U^R(z)e^{ikx}, \quad u_z^{+,DF_x} = C_{DF_x}W^R(z)e^{ikx}, \tag{15.51}$$

$$\tau_{xx}^{+,DF_x} = C_{DF_x}T_{xx}(z)e^{ikx}, \quad \tau_{xz}^{+,DF_x} = \tau_{zx}^{+,DF_x} = iC_{DF_x}T_{xz}(z)e^{ikx}, \tag{15.52}$$

for $x>0$, and

$$u_x^{-,DF_x} = -iC_{DF_x}U^R(z)e^{-ikx}, \quad u_z^{-,DF_x} = C_{DF_x}W^R(z)e^{-ikx}, \tag{15.53}$$

$$\tau_{xx}^{-,DF_x} = C_{DF_x}T_{xx}(z)e^{-ikx}, \quad \tau_{xz}^{-,DF_x} = \tau_{zx}^{-,DF_x} = -iC_{DF_x}T_{xz}(z)e^{-ikx}, \tag{15.54}$$

for $x<0$, where $T_{xx}(z)$ and $T_{xz}(z)$ are defined by Eqs. (15.15)–(15.17a–d), and C_{DF_x} is the amplitude of the surface waves to be determined.

To determine C_{DF_x}, we employ the elastodynamic reciprocity theorem which was derived elsewhere [15, p. 41]. In a linearly elastic isotropic solid, for a region V with boundary S, the time-harmonic fields, u_i, τ_{ij} and body forces f_i of two distinct states, State A and State B, are related by

$$\int_V (f_i^A u_i^B - f_i^B u_i^A)dV = \int_S (u_i^A \tau_{ij}^B - u_i^B \tau_{ij}^A)n_j dS, \tag{15.55}$$

where n_j denotes the components of the unit vector along the outward normal to S. For V, we take the region defined by $a \le x \le b$, and $0 \le z < +\infty$. The geometry is shown in Fig. 15.5. For State A, the body force is defined by Eq. (15.49), and the

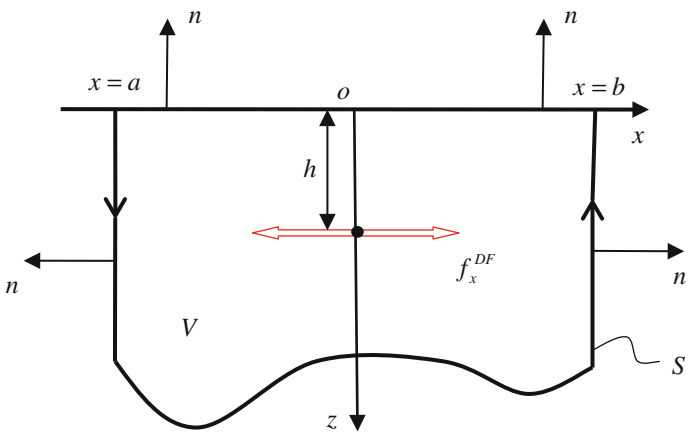

Fig. 15.5 Geometry of the region for the application of the reciprocity theorem

surface wave displacement and stress components are given by Eqs. (15.51)–(15.54). For state B, we take a virtual surface wave propagating in the positive x-direction with amplitude B:

$$u_x^B = iBU^R(z)e^{ikx}, \quad u_z^B = BW^R(z)e^{ikx}, \tag{15.56}$$

$$\tau_{xx}^B = BT_{xx}(z)e^{ikx}, \quad \tau_{xz}^B = \tau_{zx}^B = iBT_{xz}(z)e^{ikx}. \tag{15.57}$$

For the present application of the reciprocity theorem the contour is shown in Fig. 15.5. The reciprocity relation given by Eq. (15.55) then becomes

$$\int_V f_x^{DF} u_x^B dV = L_{DF_x}, \tag{15.58}$$

where

$$\begin{aligned} L_{DF_x} = &\int_0^{+\infty} (u_x^{+,DF_x}\tau_{xx}^B + u_z^{+,DF_x}\tau_{xz}^B - u_x^B\tau_{xx}^{+,DF_x} - u_z^B\tau_{xz}^{+,DF_x})\big|_{x=b} dz \\ &+ \int_0^{+\infty} (u_x^{-,DF_x}\tau_{xx}^B + u_z^{-,DF_x}\tau_{xz}^B - u_x^B\tau_{xx}^{-,DF_x} - u_z^B\tau_{xz}^{-,DF_x})\big|_{x=a}(-1)dz. \end{aligned} \tag{15.59}$$

Note that in Eq. (15.58), only the term $f_x^{DF}u_x^B$ appears, since only the body force f_x^{DF} is considered. In the right-hand side of Eq. (15.59), the first term is the contour integral along $x=b$ and the second term along $x=a$. The contour integral on the surface $z=0$ vanishes due to the traction-free boundary conditions, and the contour integral at $z\to+\infty$ does not contribute to Eq. (15.59) since the surface wave displacements are exponentially small far from the free surface.

For the integral in Eq. (15.58), by substituting Eq. (15.49) and u_x^B from Eq. (15.56), we obtain

$$\begin{aligned} \int_V f_x^{DF}u_x^B dV &= \int_V iBF_x^{DF}U^R(z)e^{ikx}\delta'(x)\delta(z-h)dV \\ &= iBF_x^{DF}\int_a^b e^{ikx}\delta'(x)dx\int_0^{+\infty} U^R(z)\delta(z-h)dz = kBF_x^{DF}U^R(h), \end{aligned} \tag{15.60}$$

where the following property of the Dirac delta function and its derivative has been used:

$$\phi(\xi)\delta'(\xi-\xi_0) = -\phi'(\xi_0)\delta(\xi_0). \tag{15.61}$$

By substituting expressions defined by Eqs. (15.51), (15.52), (15.56) and (15.57) in Eq. (15.59), the integral along $x=b$, i.e., the first term in the right-hand side of Eq. (15.59), becomes

$$\begin{aligned}&\int_0^{+\infty}\left(u_x^{+,DF_x}\tau_{xx}^B+u_z^{+,DF_x}\tau_{xz}^B-u_x^B\tau_{xx}^{+,DF_x}-u_z^B\tau_{xz}^{+,DF_x}\right)\Big|_{x=b}dz\\&=\int_0^{+\infty}\left\{\begin{array}{l}\left[iBC_{DF_x}U^R(z)T_{xx}(z)e^{2ikb}+iBC_{DF_x}W^R(z)T_{xz}(z)e^{2ikb}\right]-\\\left[iBC_{DF_x}U^R(z)T_{xx}(z)e^{2ikb}+iBC_{DF_x}W^R(z)T_{xz}(z)e^{2ikb}\right]\end{array}\right\}dz,\\&=0\end{aligned}\tag{15.62}$$

and the integral along $x=a$, i.e., the second term in the right-hand side of Eq. (15.59), becomes

$$\begin{aligned}&\int_0^{+\infty}\left(u_x^{-,DF_x}\tau_{xx}^B+u_z^{-,DF_x}\tau_{xz}^B-u_x^B\tau_{xx}^{-,DF_x}-u_z^B\tau_{xz}^{-,DF_x}\right)\Big|_{x=a}(-1)dz\\&=\int_0^{+\infty}\left(\begin{array}{l}\left[iBC_{DF_x}U^R(z)T_{xx}(z)-iBC_{DF_x}W^R(z)T_{xz}(z)\right]+\\\left[iBC_{DF_x}U^R(z)T_{xx}(z)-iBC_{DF_x}W^R(z)T_{xz}(z)\right]\end{array}\right)dz\\&=2iBC_{DF_x}\int_0^{+\infty}\left[U^R(z)T_{xx}(z)-W^R(z)T_{xz}(z)\right]dz\\&=2iBC_{DF_x}I\end{aligned},\tag{15.63}$$

where

$$I=\int_0^{+\infty}\left[U^R(z)T_{xx}(z)-W^R(z)T_{xz}(z)\right]dz,\tag{15.64}$$

Equations (15.62) and (15.63) show that at $x=b$, the two waves are co-propagating and yield no contribution to Eq. (15.59) as the relevant terms cancel out upon substitution. Thus the contribution to Eq. (15.59) is only from the counter-propagating waves at $x=a$.

Following Eqs. (15.62)–(15.64), the evaluation of Eq. (15.59) then results in

$$L_{DF_x}=2iIBC_{DF_x},\tag{15.65}$$

where I is defined by Eq. (15.64), and by using Eqs. (15.5), (15.6), (15.15) and (15.16) can be evaluated as

$$I=\mu J,\tag{15.66}$$

where

$$J=\frac{d_1d_4-d_3d_6}{2p}+\frac{d_1d_5+d_2d_4-d_3d_7+d_6}{p+q}+\frac{d_2d_5+d_7}{2q}.\tag{15.67}$$

Note that J is dimensionless.

The equality of Eqs. (15.58) and (15.63) yields

$$L_{DF_x} = 2i\mu JBC_{DF_x} = kBF_x^{DF}U^R(h). \tag{15.68}$$

We then obtain

$$C_{DF_x} = \frac{k}{2i}\frac{F_x^{DF}U^R(h)}{\mu J}. \tag{15.69}$$

By substituting F_x^{DF} given by Eq. (15.50), Eq. (15.69) becomes

$$C_{DF_x} = -\frac{\lambda+2\mu}{2\mu}\frac{iA\tilde{A}k^2[U^R(h)]^2}{J}. \tag{15.70}$$

For $x>0$, following Eqs. (15.51), (15.53) and (15.70), the displacements at position (x,z) of the surface waves generated by the equivalent double force in the x-direction corresponding to u_x may then be written as

$$u_x^{+,DF_x} = \frac{\lambda+2\mu}{2\mu}\frac{A\tilde{A}k^2[U^R(h)]^2}{J}U^R(z)e^{ikx}, \tag{15.71}$$

$$u_z^{+,DF_x} = -\frac{\lambda+2\mu}{2\mu}\frac{iA\tilde{A}k^2[U^R(h)]^2}{J}W^R(z)e^{ikx}, \tag{15.72}$$

while for $x<0$ we have

$$u_x^{-,DF_x} = -\frac{\lambda+2\mu}{2\mu}\frac{A\tilde{A}k^2[U^R(h)]^2}{J}U^R(z)e^{-ikx}, \tag{15.73}$$

$$u_z^{-,DF_x} = -\frac{\lambda+2\mu}{2\mu}\frac{iA\tilde{A}k^2[U^R(h)]^2}{J}W^R(z)e^{-ikx}. \tag{15.74}$$

The equivalent double force along the z-axis corresponding to u_x is

$$f_z^{DF} = F_z^{DF}\delta(x)\delta'(z-h), \tag{15.75}$$

where

$$F_z^{DF} = \lambda A\tilde{A}kU^R(h). \tag{15.76}$$

Due to the symmetric of the double force with respect to $x=0$, the corresponding displacements are also symmetric with respect to $x=0$ and may be written for $x>0$ as

$$u_x^{+,DF_z} = iC_{DF_z}U^R(z)e^{ikx}, \quad u_z^{+,DF_z} = C_{DF_z}W^R(z)e^{ikx}, \tag{15.77}$$

and for $x<0$:

$$u_x^{-,DF_z} = -iC_{DF_z}U^R(z)e^{-ikx}, \quad u_z^{-,DF_z} = C_{DF_z}W^R(z)e^{-ikx}. \tag{15.78}$$

In Eqs. (15.77) and (15.78) C_{DF_z} is the amplitude of the surface waves. For $x>0$, the corresponding stresses may then be written as

$$\tau_{xx}^{+,DF_z} = C_{DF_z}T_{xx}(z)e^{ikx}, \quad \tau_{xz}^{+,DF_z} = \tau_{zx}^{+,DF_z} = iC_{DF_z}T_{xz}(z)e^{ikx}, \tag{15.79}$$

while for $x<0$ we have

$$\tau_{xx}^{-,DF_z} = C_{DF_z}T_{xx}(z)e^{-ikx}, \quad \tau_{xz}^{-,DF_x} = \tau_{zx}^{-,DF_x} = -iC_{DF_x}T_{xz}(z)e^{-ikx}. \tag{15.80}$$

To determine C_{DF_z}, we again use the reciprocity relation given by Eq. (15.55), where the region V is taken as shown in Fig. 15.5. The virtual wave for State B is again selected as a surface wave propagating in the positive x-direction with amplitude B, and the displacement and stress components are given by Eqs. (15.56) and (15.57). For State A, the body force is given by Eq. (15.75) and the corresponding displacements and stresses are given by Eqs. (15.77)–(15.80). Equation (15.55) then becomes

$$\int_V f_z^{DF}u_z^B dV = L_{DF_z}, \tag{15.81}$$

where

$$\begin{aligned} L_{DF_z} = &\int_0^{+\infty} (u_x^{+,DF_z}\tau_{xx}^B + u_z^{+,DF_z}\tau_{xz}^B - u_x^B\tau_{xx}^{+,DF_z} - u_z^B\tau_{xz}^{+,DF_z})\big|_{x=b}dz \\ &+ \int_0^{+\infty} (u_x^{-,DF_z}\tau_{xx}^B + u_z^{-,DF_z}\tau_{xz}^B - u_x^B\tau_{xx}^{-,DF_z} - u_z^B\tau_{xz}^{-,DF_z})\big|_{x=a}(-1)dz. \end{aligned} \tag{15.82}$$

The integrals in Eq. (15.82) yield similar results as those given by Eqs. (15.62) and (15.63), where C_{DF_x} should be replaced by C_{DF_z}. Equation (15.82) then results in

$$L_{DF_z} = 2i\mu JBC_{DF_z}. \tag{15.83}$$

For the integral given Eq. (15.81) we obtain by substituting Eq. (15.75) and u_z^B from Eq. (15.56)

$$\int_V f_z^{DF} u_z^B dV = \int_V F_z^{DF} \delta(x)\delta'(z-h) B W^R(z) e^{ikx} dV$$
$$= BF_z^{DF} \int_0^{+\infty} W^R(z)\delta'(z-h)dz \int_a^b e^{ikx}\delta(x)dx = -BF_z^{DF} \left.\frac{dW^R(z)}{dz}\right|_{z=h}, \tag{15.84}$$

where $dW^R(z)/dz|_{z=h}$ is $dW^R(z)/dz$ at $z=h$.

The equality of Eqs. (15.83) and (15.84) then yields

$$C_{DF_z} = -\frac{F_z^{DF}}{2i\mu J} \left.\frac{dW^R(z)}{dz}\right|_{z=h}. \tag{15.85}$$

Using Eq. (15.76), Eq. (15.85) becomes

$$C_{DF_z} = \frac{\lambda}{2\mu} \frac{iA\tilde{A}kU^R(h)}{J} \left.\frac{dW^R(z)}{dz}\right|_{z=h}. \tag{15.86}$$

Using Eqs. (15.77), (15.78) and (15.86), the displacements at position (x,z) of the surface waves generated by the equivalent double force in the z-direction corresponding to u_x may then be written as

$$u_x^{+,DF_z} = -\frac{\lambda}{2\mu} \frac{A\tilde{A}kU^R(h)}{J} \left.\frac{dW^R(z)}{dz}\right|_{z=h} U^R(z)e^{ikx}, \tag{15.87}$$

$$u_z^{+,DF_z} = \frac{\lambda}{2\mu} \frac{iA\tilde{A}kU^R(h)}{J} \left.\frac{dW^R(z)}{dz}\right|_{z=h} W^R(z)e^{ikx}, \tag{15.88}$$

for $x>0$, and

$$u_x^{-,DF_z} = \frac{\lambda}{2\mu} \frac{A\tilde{A}kU^R(h)}{J} \left.\frac{dW^R(z)}{dz}\right|_{z=h} U^R(z)e^{-ikx}, \tag{15.89}$$

$$u_z^{-,DF_z} = \frac{\lambda}{2\mu} \frac{iA\tilde{A}kU^R(h)}{J} \left.\frac{dW^R(z)}{dz}\right|_{z=h} W^R(z)e^{-ikx}, \tag{15.90}$$

for $x<0$. Since $dW^R(z)/dz|_{z=h}$ is $O(k)$ the surface waves defined by Eqs. (15.87)–(15.90) are of the same order as Eqs. (15.71)–(15.74).

15.4.2 Surface Waves Generated by the Equivalent Body Forces Due to u_z

In Sect. 15.4.1, the elastodynamic reciprocity theorem has been used to determine the surface waves generated by the equivalent body forces corresponding to u_x, the horizontal displacement component of the incident surface wave. In this section we consider the surface waves generated by the equivalent body forces corresponding to u_z, the vertical displacement component of the incident wave, given by Eqs. (15.2) and (15.4). Corresponding to u_z, the equivalent body forces consist of a double force with forces in the z-direction and one with forces in the x-direction, which are shown in Fig. 15.4. We again use the elastodynamic reciprocity theorem to consider the surface waves generated by the two double forces.

The equivalent double force with forces in the z-direction corresponding to u_z is given by

$$f_{xz}^{DF} = F_{xz}^{DF}\delta'(x)\delta(z-h), \tag{15.91}$$

where

$$F_{xz}^{DF} = -i\mu k A\tilde{A}W^R(h). \tag{15.92}$$

As shown in Fig. 15.4, the equivalent double force in the z-direction is antisymmetric with respect to $x=0$. The corresponding surface waves are also antisymmetric. Following Eqs. (15.1)–(15.4) and (15.11)–(15.14), for the displacements and stresses corresponding to f_{xz}^{DF}, we may then write

$$u_x^{+,DF_{xz}} = iC_{DF_{xz}}U^R(z)e^{ikx}, \quad u_z^{+,DF_{xz}} = C_{DF_{xz}}W^R(z)e^{ikx}, \tag{15.93}$$

$$\tau_{xx}^{+,DF_{xz}} = C_{DF_{xz}}T_{xx}(z)e^{ikx}, \quad \tau_{xz}^{+,DF_{xz}} = \tau_{zx}^{+,DF_{xz}} = iC_{DF_{xz}}T_{xz}(z)e^{ikx}, \tag{15.94}$$

for $x>0$, and

$$u_x^{-,DF_{xz}} = iC_{DF_{xz}}U^R(z)e^{-ikx}, \quad u_z^{-,DF_{xz}} = -C_{DF_{xz}}W^R(z)e^{-ikx}, \tag{15.95}$$

$$\tau_{xx}^{-,DF_{xz}} = -C_{DF_{xz}}T_{xx}(z)e^{-ikx}, \quad \tau_{xz}^{-,DF_{xz}} = \tau_{zx}^{-,DF_{xz}} = iC_{DF_{xz}}T_{xz}(z)e^{-ikx}, \tag{15.96}$$

for $x<0$, where $C_{DF_{xz}}$ is the amplitude of the surface waves to be determined.

The region V is again taken as that shown in Fig. 15.5, and Eqs. (15.91)–(15.96) are the relevant expressions for the body force, and the displacements and the stresses corresponding to State A. For State B, we again select the virtual wave as a surface wave propagating in the positive x-direction with amplitude B, where the corresponding displacements and stress components are given by Eqs. (15.56) and (15.57). The reciprocity relation given by Eq. (15.55) then becomes

$$\int_V f_{xz}^{DF} u_z^B dV = L_{DF_{xz}}, \tag{15.97}$$

where

$$L_{DF_{xz}} = \int_0^{+\infty} (u_x^{-,DF_{xz}} \tau_{xx}^B + u_z^{-,DF_{xz}} \tau_{xz}^B - u_x^B \tau_{xx}^{-,DF_{xz}} - u_z^B \tau_{xz}^{-,DF_{xz}})\big|_{x=a}(-1)dz. \tag{15.98}$$

Note that in Eq. (15.98) the contour integral along $x = b$ again disappears because the surface waves are propagating in the same direction.

By substituting Eq. (15.91) and u_z^B from Eq. (15.56), the integral given by Eq. (15.97) yields

$$\begin{aligned}\int_V f_{xz}^{DF} u_z^B dV &= \int_V F_{xz}^{DF} \delta'(x)\delta(z-h) B W^R(z) e^{ikx} dV \\ &= B F_{xz}^{DF} \int_a^b e^{ikx}\delta'(x)dx \int_0^{+\infty} W^R(z)\delta(z-h)dz = -ikB F_{xz}^{DF} W^R(h).\end{aligned} \tag{15.99}$$

For the integral given by Eq. (15.98), by substituting Eqs. (15.56), (15.57), (15.95) and (15.96), we obtain

$$\begin{aligned}L_{DF_{xz}} &= \int_0^{+\infty} (u_x^{-,DF_{xz}} \tau_{xx}^B + u_z^{-,DF_{xz}} \tau_{xz}^B - u_x^B \tau_{xx}^{-,DF_{xz}} - u_z^B \tau_{xz}^{-,DF_{xz}})\big|_{x=a}(-1)dz \\ &= -\int_0^{+\infty} \left\{ \begin{array}{l} [iBC_{DF_{xz}} U^R(z) T_{xx}(z) - iBC_{DF_{xz}} W^R(z) T_{xz}(z)] + \\ \quad [iBC_{DF_{xz}} U^R(z) T_{xx}(z) - iBC_{DF_{xz}} W^R(z) T_{xz}(z)] \end{array} \right\} dz \\ &= -2iBC_{DF_{xz}} \int_0^{+\infty} [U^R(z) T_{xx}(z) - W^R(z) T_{xz}(z)] dz \\ &= -2iBC_{DF_{xz}} \mu J.\end{aligned} \tag{15.100}$$

The equality of Eqs. (15.99) and (15.100) then yields

$$C_{DF_{xz}} = -\frac{iA\tilde{A}k^2 [W^R(h)]^2}{2J}, \tag{15.101}$$

where Eq. (15.92) has been used, and J is defined by Eq. (15.67).

By using Eqs. (15.93), (15.95) and (15.101), the displacements at position (x, z) of the surface waves generated by the equivalent double force in the z-direction corresponding to u_z may then be written as

$$u_x^{+,DF_{xz}} = \frac{A\tilde{A}k^2[W^R(h)]^2}{2J} U^R(z)e^{ikx}, \tag{15.102}$$

$$u_z^{+,DF_x} = -\frac{iA\tilde{A}k^2[W^R(h)]^2}{2J} W^R(z)e^{ikx}, \tag{15.103}$$

for $x > 0$, and

$$u_x^{-,DF_{xz}} = \frac{A\tilde{A}k^2[W^R(h)]^2}{2J} U^R(z)e^{-ikx}, \tag{15.104}$$

$$u_z^{-,DF_{xz}} = \frac{iA\tilde{A}k^2[W^R(h)]^2}{2J} W^R(z)e^{-ikx}, \tag{15.105}$$

for $x < 0$.

The equivalent double force with forces in the x-direction corresponding to u_z is

$$f_{zx}^{DF} = F_{zx}^{DF}\delta(x)\delta'(z-h), \tag{15.106}$$

where

$$F_{zx}^{DF} = -i\mu kAA_0 W^R(h). \tag{15.107}$$

Similarly to Eqs. (15.93) and (15.95), the displacements of the corresponding surface waves are also antisymmetric and may be written as

$$u_x^{+,DF_{zx}} = iC_{DF_{zx}} U^R(z)e^{ikx}, \quad u_z^{+,DF_{zx}} = C_{DF_{zx}} W^R(z)e^{ikx}, \tag{15.108}$$

for $x > 0$, and

$$u_x^{-,DF_{zx}} = iC_{DF_{zx}} U^R(z)e^{-ikx}, \quad u_z^{-,DF_{zx}} = -C_{DF_{zx}} W^R(z)e^{-ikx}. \tag{15.109}$$

for $x < 0$, where $C_{DF_{zx}}$ is the amplitude of the surface waves to be determined. The corresponding stresses may then be written as

$$\tau_{xx}^{+,DF_{xz}} = C_{DF_{xz}} T_{xx}(z)e^{ikx}, \quad \tau_{xz}^{+,DF_{xz}} = \tau_{zx}^{+,DF_{xz}} = iC_{DF_{xz}} T_{xz}(z)e^{ikx}, \tag{15.110}$$

$$\tau_{xx}^{-,DF_{xz}} = -C_{DF_{xz}} T_{xx}(z)e^{-ikx}, \quad \tau_{xz}^{-,DF_{xz}} = \tau_{zx}^{-,DF_{xz}} = iC_{DF_{xz}} T_{xz}(z)e^{-ikx}. \tag{15.111}$$

For the application of the reciprocity relation given by Eq. (15.55), we take the region V as shown in Fig. 15.5, and State B as a virtual surface wave propagating in the positive x-direction with amplitude B, whose displacements and stresses are given by Eqs. (15.56) and (15.57). The body force, the displacements and the stresses for State A are defined by Eqs. (15.106)–(15.111).

The reciprocity relation given by Eq. (15.55) then reduces to

$$\int_V f_{zx}^{DF} u_x^B dV = L_{DF_{zx}}, \tag{15.112}$$

where

$$L_{DF_{zx}} = \int_0^{+\infty} \left(u_x^{-,DF_{zx}} \tau_{xx}^B + u_z^{-,DF_{zx}} \tau_{xz}^B - u_x^B \tau_{xx}^{-,DF_{zx}} - u_z^B \tau_{xz}^{-,DF_{zx}}\right)\Big|_{x=a} (-1) dz. \tag{15.113}$$

Again only the counter propagating waves contribute to the contour integral. Substitution of Eqs. (15.106)–(15.111) into Eqs. (15.112) and (15.113) yields

$$C_{DF_{zx}} = -\frac{ikA\tilde{A}W^R(h)}{2J} \frac{dU^R(z)}{dz}\bigg|_{z=h}, \tag{15.114}$$

where $dU^R(z)/dz|_{z=h}$ is $dU^R(z)/dz$ at $z = h$.

By using Eqs. (15.108), (15.109) and (15.114), the displacements at position (x, z) of the surface waves generated by the equivalent double force in the x-direction corresponding to u_z may then be written as

$$u_x^{+,DF_{zx}} = \frac{kA\tilde{A}W^R(h)}{2J} \frac{dU^R(z)}{dz}\bigg|_{z=h} U^R(z) e^{ikx}, \tag{15.115}$$

$$u_z^{+,DF_{zx}} = -\frac{ikA\tilde{A}W^R(h)}{2J} \frac{dU^R(z)}{dz}\bigg|_{z=h} W^R(z) e^{ikx}, \tag{15.116}$$

for $x > 0$, and

$$u_x^{-,DF_{zx}} = \frac{kA\tilde{A}W^R(h)}{2J} \frac{dU^R(z)}{dz}\bigg|_{z=h} U^R(z) e^{-ikx}, \tag{15.117}$$

$$u_z^{-,DF_{zx}} = \frac{ikA\tilde{A}W^R(h)}{2J} \frac{dU^R(z)}{dz}\bigg|_{z=h} W^R(z) e^{-ikx}, \tag{15.118}$$

for $x < 0$.

15.5 Conclusions

This paper proposes that the scattering of surface waves by a cylindrical cavity of general cross-section located near the free surface of an elastic half-space can be represented by the radiation from equivalent body forces. The equivalent body forces consist of those due to u_x, the horizontal displacement component of the

incident surface wave, and those due to u_z, the vertical component of the incident surface wave. The magnitudes of the equivalent body forces have been determined and the determination shows that the equivalent body forces are a combination of double forces. Using the elastodynamic reciprocity theorem, the surface waves generated by the equivalent double forces have been obtained. The surface waves generated by the equivalent double forces due to u_x and u_z are shown to be symmetric and antisymmetric, respectively, with respect to the plane $x = 0$.

The expressions given by Eqs. (15.1)–(15.2) and (15.3)–(15.4) represent surface waves propagating in the positive and the negative x-directions, respectively. Inspection of the pairs of surface wave displacements generated by equivalent body forces and given by Eqs. (15.71)–(15.72) and (15.73)–(15.74), Eqs. (15.87)–(15.88) and (15.89)–(15.90), as well as (15.93), and (15.95), (15.102)–(15.103) and (15.104)–(15.105), and (15.115)–(15.116) and (15.117)–(15.118), all have the same forms as Eqs. (15.1)–(15.2) and (15.3)–(15.4) albeit with different constants. Thus all these displacement pairs represent a surface wave. The superposition of the surface waves generated by the equivalent body forces represents the scattered field of surface waves.

The combined use of the equivalent body force representation and the elastodynamic reciprocity theorem shows potential for dealing with more complex scattering problems.

Acknowledgements This work was supported by the National Natural Science Foundation of China (No. 51335001). We thank the China Scholarship Council for the funding to support Chao Yang's study at Northwestern University.

References

1. Lange, F.F., Davis, B.I., Wright, E.: Processing-related fracture origins: IV, elimination of voids produced by organic inclusions. J. Am. Ceram. Soc. **69**(1), 66–69 (1986)
2. Heslehurst, R.B.: Defects and Damage in Composite Materials and Structures. CRC Press, Boca Raton, Florida (2014)
3. Rice, J.R., Tracey, D.M.: On the ductile enlargement of voids in triaxial stress fields. J. Mech. Phys. Solids **17**(3), 201–217 (1969)
4. Tvergaard, V., Hutchinson, J.W.: Two mechanisms of ductile fracture: void by void growth versus multiple void interaction. Int. J. Solids Struct. **39**(13), 3581–3597 (2002)
5. Achenbach, J.D.: Wave Propagation in Elastic Solids. North-Holland Publishing Company (1973). Paperback edition published by Elsevier (2012)
6. Graff, K.F.: Wave Motion in Elastic Solids. Courier Corporation, North Chelmsford, Massachusetts (2012)
7. Rayleigh, L.: On waves propagated along the plane surface of an elastic solid. Proc. Lond. Math. Soc. **1**(1), 4–11 (1885)
8. Aki, K., Richards, P.G.: Quantitative Seismology: Theory and Methods. W. H. Freeman and Company, San Francisco, California (1980)
9. Rice, J.R.: Elastic wave emission from damage processes. J. Nondestr. Eval. **1**(4), 215–224 (1980)

10. Zhang, H., Achenbach, J.D.: Use of equivalent body forces for acoustic emission from a crack in a plate. Mech. Res. Commun. **68**, 105–108 (2015)
11. Yang, C., Achenbach, J.D.: Time domain scattering of elastic waves by a cavity, represented by radiation from equivalent body forces. Int. J. Eng. Sci. **115**, 43–50 (2017)
12. Lamb, H.: On the propagation of tremors over the surface of an elastic solid. Philos. Trans. R. Soc. Lond. Ser. A **203**, 1–42 (1904)
13. Betti, E.: Teoria della elasticita'. Il Nuovo Cimento (1869–1876), 7(1), 69–97 (1872)
14. Achenbach, J.D., Xu, Y.: Wave motion in an isotropic elastic layer generated by a time-harmonic point load of arbitrary direction. J. Acoust. Soc. Am. **106**(1), 83–90 (1999)
15. Achenbach, J.D.: Reciprocity in Elastodynamics. Cambridge University Press, Cambridge (2003)
16. Phan, H., Cho, Y., Achenbach, J.D.: Application of the reciprocity theorem to scattering of surface waves by a cavity. Int. J. Solids Struct. **50**(24), 4080–4088 (2013)
17. Phan, H., Cho, Y., Achenbach, J.D.: Validity of the reciprocity approach for determination of surface wave motion. Ultrasonics **53**(3), 665–671 (2013)
18. Achenbach, J.D.: Reciprocity and related topics in elastodynamics. Appl. Mech. Rev. **59**(1), 13–32 (2006)
19. Achenbach, J.D.: A new use of the elastodynamic reciprocity theorem. Math. Mech. Solids **19**(1), 5–18 (2014)
20. Sorokin, S.V.: On the bi-orthogonality conditions for multi-modal elastic waveguides. J. Sound Vib. **332**(21), 5606–5617 (2013)
21. Shi, F., Lowe, M.J.S., Xi, X., Craster, R.V.: Diffuse scattered field of elastic waves from randomly rough surfaces using an analytical Kirchhoff theory. J. Mech. Phys. Solids **92**, 260–277 (2016)

Correction to: Generalized Models and Non-classical Approaches in Complex Materials 2

Holm Altenbach, Joël Pouget, Martine Rousseau, Bernard Collet and Thomas Michelitsch

Correction to:
H. Altenbach et al. (eds.), *Generalized Models and Non-classical Approaches in Complex Materials* 2, Advanced Structured Materials 90, https://doi.org/10.1007/978-3-319-77504-3

The original version of the book was inadvertently published without chapter 15.

The updated online version of the book can be found at https://doi.org/10.1007/978-3-319-77504-3

The online version of chapter 15 can be found at https://doi.org/10.1007/978-3-319-77504-3_15

H. Altenbach et al. (eds.), *Generalized Models and Non-classical Approaches in Complex Materials 2*, Advanced Structured Materials 90,
https://doi.org/10.1007/978-3-319-77504-3_16